

THE UNIVERSITY
of EDINBURGH

This thesis has been submitted in fulfilment of the requirements for a postgraduate degree (e.g. PhD, MPhil, DClinPsychol) at the University of Edinburgh. Please note the following terms and conditions of use:

This work is protected by copyright and other intellectual property rights, which are retained by the thesis author, unless otherwise stated.
A copy can be downloaded for personal non-commercial research or study, without prior permission or charge.
This thesis cannot be reproduced or quoted extensively from without first obtaining permission in writing from the author.
The content must not be changed in any way or sold commercially in any format or medium without the formal permission of the author.
When referring to this work, full bibliographic details including the author, title, awarding institution and date of the thesis must be given.



THE UNIVERSITY *of* EDINBURGH

The Limpet: A Multi-Sensing Robotic Platform For Monitoring Offshore Energy Platforms

Mohammed E. Sayed, *BSc (Hons)*, *MSc*

The University of Edinburgh
Institute for Integrated Micro and Nano Systems
Department of Electronics and Electrical Engineering
School of Engineering

Supervised by:
Dr. Adam A. Stokes

A Thesis Submitted for the Degree of
Doctor of Philosophy

2019

Lay Summary of Thesis

THE UNIVERSITY of EDINBURGH

The lay summary is a brief summary intended to facilitate knowledge transfer and enhance accessibility, therefore the language used should be non-technical and suitable for a general audience. (See the Degree Regulations and Programmes of Study, General Postgraduate Degree Programme Regulations. These regulations are available via: http://www.drps.ed.ac.uk/.)

Name of student:	Mohammed El-Sayed Mohammed	UUN	S1548415
University email:	m.mohammed@ed.ac.uk		
Degree sought:	Doctor of Philosophy	No. of words in the main text of thesis:	48000
Title of thesis:	The Limpet: A Multi-Sensing Robotic Platform For Monitoring Offshore Energy Platforms		

Insert the lay summary text here - the space will expand as you type.

This thesis describes a new multi-sensing robotic platform, the Limpet, which is designed to be low-cost and highly manufacturable, and thus can be deployed in large collectives for monitoring offshore energy platforms. The Limpet is developed as part of the flagship ORCA Hub in the United Kingdom. The Limpet is capable of sensing its environment, monitoring offshore structures, adhering to surfaces of different materials, and climbing surfaces at different angles. The work on offshore robotic technologies presented in this thesis pushes offshore robotic development and use towards more manufacturable, low-cost and more capable offshore robots, a research niche that has been barely studied. Large robot collectives with monitoring abilities, efficient navigation skills, and sensor fusion capabilities could become an important tool for industrial use in different applications, as well as key research tool to help develop and test different algorithms and processing techniques, and understand the science of complex systems. These uses and studies can become very important for offshore robotic applications such as inspection and monitoring of offshore energy platforms to make them a safer place to work and reduce risks to human lives.

Document control

Related policies/regulations: www.docs.sasg.ed.ac.uk/AcademicServices/Regulations/PGR_AssessmentRegulations.pdf	
If you require this document in an alternative format please email Academic.Services@ed.ac.uk or telephone 0131 650 2138.	Date last reviewed: 15.05.15

K:\AAPS\D-AcademicAdministration\02-CodesOfPractice,Guidelines&Regulations\24-MainReferencesCopiesPolicies\01-Current\Assessment BOE SCC & Feedback\Forms\ThesisLaySummary

If you can't
explain it simply,
you don't understand
it well enough.

Albert Einstein

Declaration of Authorship

I declare that this thesis was composed by myself, that the work contained herein is my own except where explicitly stated otherwise in the text, and that this work has not been submitted for any other degree or professional qualification except as specified.

Edinburgh, United Kingdom, 2019



I dedicate this thesis to my wife Lama Almajayda.

Acknowledgements

I would like to express my sincere gratitude to my supervisor Dr. Adam A. Stokes for his continuous guidance and support during my studies. I am grateful for the positive environment you have provided me with and for the extensive knowledge you have shared with me. I would also like to thank my parents, Naglaa and ElSayed for their constant inspiration, guidance and support. This would not have been possible without them and words cannot express my gratitude to them. My profound thanks goes to my beloved sister, Mayyada, and her husband, Amr, for their unconditional love and continuous advise in every aspect of my life and my studies. Last but not least, I would like to thank my Wife, Lama, for her unconditional support and constant sacrificies during my studies.

Abstract: The oil and gas industry faces increasing pressure to remove people from dangerous offshore environments for health and safety reasons, and to look for more cost-effective and safer methods for inspection, repair and maintenance of their offshore energy platforms. Robots are seen as key enablers in this regard, as they present a safer, cheaper, and more efficient way to inspect and monitor offshore infrastructure. In this thesis, I develop a new multi-sensing robotic platform, the Limpet, which is designed to be low-cost and highly manufacturable, and thus can be deployed in large collectives for monitoring offshore energy platforms. The Limpet is developed as part of the flagship ORCA (Offshore Robotics for Certification of Assets) Hub in the United Kingdom. The Limpet is designed to be one part of a heterogeneous collection of field robots (drones, UAVs, mobile legged robots etc.) that together with the offshore assets comprise the ORCA Hub System for asset certification and management. The Limpet comprises the sensing aspect of the ORCA Hub System, where sensing is a key element in asset monitoring, fault detection, mapping, environmental monitoring and helping other robots navigate around the platform. The Limpet has nine different sensing modalities, which are: temperature; pressure; humidity; optical; distance; sound; magnetic field; accelerometer; gyroscope. I have integrated the Limpet with Robot Operating System (ROS) to allow it to communicate with other robots within the ORCA Hub System, where the interaction between the different robots results in more complex and useful behavior. The Limpet was designed to have robust communication, where it can use one of multiple communication systems for data transmission or communication with other agents. In this thesis, I demonstrate how the Limpet could be used for real-time condition monitoring of offshore structures, by combining remote sensing with signal processing techniques. I show an example of the condition monitoring approach by using the system to monitor the condition of a wind turbine. I also show how the processing and analysis of the data from the sensors in the condition monitoring approach can be done on-board using the microcontroller, which can improve the communication requirements of the system. In this thesis, I also show a few examples of how the Limpet can be deployed in offshore environments using other robotic systems. To allow the Limpet to navigate the unstructured offshore environment efficiently after deployment and increase its accessible areas to be useful for monitoring and inspection tasks, I have developed an adhesion and locomotion mechanism for the Limpet based on electromagnetic modules (EMMs). These capabilities allows it to adhere to

and climb surfaces at different angles, which makes it a more useful tool for monitoring offshore environments. The adhesion and locomotion systems are designed in a modular fashion, as modular systems can be easily reconfigured, giving the robot more robustness and capability for achieving new tasks. Finally, due to the lack of accuracy that usually results from using single sensors for monitoring the condition of different structures, I have developed a multi-sensor fusion technique in this thesis that combines sensing modalities on different Limpets to achieve structural integrity monitoring.

Contents

Declaration of Authorship vi

Acknowledgements viii

List of Figures xix

List of Tables xxiii

List of QR Codes xxv

List of Abbreviations xxv

I Introduction and Background 1

1 Introduction, Overview and Aims 3
- 1.1 Introduction . . . 4
- 1.2 Motivation . . . 4
- 1.3 Problem Definition . . . 5
  - 1.3.1 Manufacturing Robots to Monitor Offshore Environments is Expensive . . . 5
  - 1.3.2 Deployment of Robotic Agents and Navigating Unstructured Offshore Environments is a Challenge . . . 5
  - 1.3.3 Uncertainty in Using a Single Sensor to Monitor Offshore Environments . . . 6
- 1.4 Aims and Objectives . . . 6
- 1.5 Preview of Contributions . . . 7
- 1.6 Publications . . . 8
- 1.7 2D Barcodes . . . 13
- 1.8 Thesis Tree . . . 14
- 1.9 Summary of Thesis Contents and Layout . . . 15

2 Background 17
- 2.1 Challenges Facing Offshore Industries . . . 18

2.2 Applications of Robotics in Offshore Industries 18
2.3 Offshore Robotics for Certification of Assets (ORCA Hub) 19
2.4 Offshore Environment Requirements 20
2.5 Current State-of-the-Art in Offshore Robotics 21
2.6 Condition Monitoring Systems in Offshore Environments 23
2.7 Adhesion Mechanisms for Climbing Robots 25
2.8 Modularity and Stacking of Modules 27
2.9 Multi-Sensor Data Fusion for Offshore Robotics 28

II A ROS-Enabled Multi-Sensing Robotic Platform for Monitoring Offshore Platforms "Limpet" 33

3 The Limpet: A ROS-Enabled Multi-Sensing Robotic Platform 35
3.1 Introduction and Background 36
3.2 Design and Fabrication of the Limpet Agent Version 1 39
3.2.1 Instrument Model of the Limpet 39
3.2.2 System Design 41
3.2.2.1 Choice of Sensing Modalities 42
3.2.2.2 Programming the Limpet 43
3.2.2.3 Cost and Dimensions of the Limpet 44
3.2.2.4 Bio-Inspiration 45
3.2.3 Electrical Design 46
3.2.3.1 Design of the Control Electronics 46
3.2.3.2 Power System 52
3.2.4 Mechanical Design 54
3.2.4.1 Fabrication of the Printed Circuit Board 54
3.2.4.2 Design of the Protective Housing 58
3.2.4.3 Ease of Robot Fabrication 60
3.2.5 ROS Interface 60
3.3 Design of the Communication Mechanisms and Communication Failover 63
3.3.1 WiFi Communication 65
3.3.2 Serial Communication 66
3.3.3 Long Range Wide Area Network (LoRaWAN) 66
3.3.4 Acoustic Communication 69
3.3.5 Optical Communication 71
3.4 Remote Sensing and Real-Time Condition Monitoring 74
3.4.1 Condition Monitoring Experimental Design 76
3.4.1.1 Design of the Distance-Based Condition Monitoring Experimental Setup 76
3.4.1.2 Design of the Offline Classification Experiments 79
3.4.1.3 Design of the Online Classification Experiments 81

3.4.1.4 Overview of the Communication Strategies in the Experiments . . . 84
3.4.1.5 Overview of the Classification Techniques in the Experiments . . . 85
3.4.2 Condition Monitoring Experimental Results . . . 88
3.4.3 Discussion . . . 105
3.4.3.1 Applicability to Other Faults . . . 105
3.4.3.2 Applicability to Other Sensors and Systems . . . 106
3.4.3.3 On-board (Online) Data Processing vs Offline Processing . . . 106
3.4.3.4 Mitigation of Interferences . . . 107
3.5 Summary . . . 108

III Limpet Deployment, Navigation and Adhesion 109

4 Deployment of the Limpet 111
4.1 Introduction and Background . . . 112
4.2 Deployment System Design . . . 114
4.2.1 Design of the Hardware . . . 114
4.2.2 Design of the Control Software . . . 116
4.2.3 Full System Assembly . . . 116
4.3 Experimental Design . . . 117
4.4 Experimental Results and Discussion . . . 119
4.5 Summary . . . 121

5 Limpet Navigation and Adhesion 123
5.1 Introduction and Background . . . 124
5.2 Electromagnetic Module (EMM) . . . 127
5.3 Limpet v2 - System Design . . . 129
5.3.1 Sensing Modalities, Communications and Progamming . 130
5.3.2 Cost and Dimensions . . . 131
5.4 Limpet v2 - Electrical Design . . . 132
5.4.1 Design of the Control Electronics . . . 132
5.4.1.1 Sensing Module . . . 132
5.4.1.2 Power Driver Module . . . 133
5.4.2 Power System . . . 134
5.5 Limpet v2 - Mechanical Design . . . 135
5.5.1 Design of the Electromagnetic Module . . . 135
5.5.2 Design of the Adhesion Module . . . 136
5.5.3 Design of the Locomotion Module . . . 142
5.5.4 Design of the Outer Body (Shell) . . . 142
5.6 Limpet v2 - Fabrication . . . 143

5.6.1 Fabrication of the Printed Circuit Boards 143
5.6.2 Fabrication of the Electromagnetic Module 143
5.6.3 Fabrication of the Adhesion Module 146
5.6.4 Fabrication of the Locomotion Module 146
5.7 Experimental Design 147
5.7.1 Characterisation of the Electromagnetic Module 147
5.7.1.1 Analysing Power Dissipation for Different Coil Thickness 147
5.7.1.2 Frequency Response Analysis 148
5.7.1.3 Evaluating the Spring Constant of the EMM . . 151
5.7.1.4 Determining the Output Force for Different Actuation Currents 151
5.7.2 Characterisation of the Adhesion Module 153
5.7.2.1 Strength of Attachment to Different Surfaces . 153
5.7.2.2 Closed Loop Control of the Adhesion System . 153
5.7.3 Characterisation of the Locomotion Module 154
5.7.3.1 Effect of Stacking the Locomotion Modules . . 154
5.7.3.2 Evaluating the Locomotion 155
5.8 Experimental Results 157
5.8.1 Characterisation of the Electromagnetic Actuator Unit . 157
5.8.1.1 Analysing Power Dissipation for Different Coil Thickness 157
5.8.1.2 Frequency Response Analysis 158
5.8.1.3 Evaluating the Spring Constant of the EMM . . 160
5.8.1.4 Determining the Output Force for Different Actuation Currents 162
5.8.2 Characterisation of the Adhesion Module 163
5.8.2.1 Strength of Attachment to Different Surfaces . 163
5.8.2.2 Closed Loop Control of the Adhesion System . 164
5.8.3 Characterisation of the Locomotion Module 165
5.8.3.1 Effect of Stacking the Locomotion Modules . . 165
5.8.3.2 Evaluating the Locomotion 170
5.9 Demonstrations 172
5.9.1 Untethered Sensory Control of the Limpet 172
5.9.2 Sound-Based Inter-Communication of Limpets 173
5.9.3 Climbing 174
5.10 Discussion 176
5.11 Summary 177

IV Multi-Sensor Data Fusion 179

6 Multi-Sensor Data Fusion Using Limpets 181

6.1 Introduction and Background 182
6.2 Multi-Sensor Data Fusion Architecture 183
6.3 Experimental Design 188
6.4 Results and Discussion 189
6.5 Summary 196

V Conclusions, Experimental and References 197

7 Impact, Field Tests and Commercialisation 199
7.1 Introduction 200
7.2 Fort William Test Trials 200
7.3 Fire Service College Test Trials 202
7.4 Environmental Water Monitoring 204
7.5 Commercialisation 207

8 Conclusions and Future Work 209
8.1 Conclusions 210
8.1.1 Limpets Are Low-Cost and Highly Manufacturable 210
8.1.2 Limpets Can Navigate Unstructured Environments . . . 210
8.1.3 Limpets Can Use Multi-Sensor Fusion For Monitoring Structures 211
8.2 Future Work 211
8.3 Impact of Work 213

References 214

VI Appendix 241

A Copyright Agreements 243
A.1 MDPI Sensors Copyright Agreement 244
A.2 Soft Robotics Copyright Agreement 246
A.3 WUWNet '18 Copyright Agreement 249

B Bill of Materials 253
B.1 Sensing Module (Limpet Version 1) Bill of Materials 253
B.2 Power Driver Module Bill of Materials 255

C Experimental 257
C.1 Custom-Designed Suction Cup Mould CAD Drawing 257
C.2 Loading Capacity Experimental Setup CAD Drawing 259
C.3 Multiple Weights Holder CAD Drawing 261
C.4 EMM Force Test Experimental Setup CAD Drawing 263

D Limpet User Guide **265**
D.1 Limpet Version 1 User Guide 265

E ESP8266 Tutorial **279**

F Printed Circuit Boards Design **305**
F.1 Infrared Handheld Transceiver Schematic 305
F.2 Infrared Handheld Transceiver PCB Layout 307
F.3 Sensing Module Schematic 309
F.4 Sensing Module PCB Layout 312
F.5 Power Driver Module Schematic 314
F.6 Power Driver Module PCB Layout 316

G Journal: The Limpet: A ROS-Enabled Multi-Sensing Platform for the ORCA Hub **319**

H Journal: Linbots: Soft Modular Robots Utilising Voice Coils **343**

I Journal: Limpet: A Modular, Untethered Soft Robot **355**

J Journal: Long Necked Turtle: A Soft/Hard Hybrid Mobile Robotic Platform for IoT Node Distribution **423**

K Conference Proceeding: Robust TDA-MAC for Practical Underwater Sensor Network Deployment: Lessons from USMART Sea Trials **443**

L Poster: A Multi-Sensing Robotic Platform for Inspection of Offshore Infrastructures **453**

M Poster: The Limpet: An Adaptable Multi-Sensor Inspection Robot **455**

N Code **457**

List of Figures

1.1 Thesis Tree 14

3.1 Conceptual Overview of the ORCA Hub System 38
3.2 Instrument Model 39
3.3 Limpet Version 1 System Overview 41
3.4 Connection between JTAG Adapter and Limpet JTAG Port . . . 44
3.5 Microcontroller (SAMD21G18) Schematic 48
3.6 Schematic of the Sensors on the Limpet 50
3.7 RGB LED Schematic 51
3.8 Crystal Oscillator Schematic 51
3.9 Power System Schematic 53
3.10 Breadboarded Limpet Version 1 54
3.11 Limpet In-House Fabricated PCB 55
3.12 Limpet with Solder Stencil 56
3.13 Limpet Externally Fabricated PCB 57
3.14 Polyurethane Protective Housing for the Limpet 59
3.15 Polydimethylsiloxane Protective Housing for the Limpet 59
3.16 Architecture of the Limpet Interface with ROS 62
3.17 Overview of the Communication Systems 64
3.18 Architecture of the WiFi Communication. 65
3.19 Architecture of the Serial Communication. 66
3.20 Architecture of the LoRaWAN communication. 68
3.21 Acoustic Communication Architecture 70
3.22 Light Intensity Interpretation. 72
3.23 Optical Sensor Calibration 73
3.24 Instrument Model for the Limpet for Distance-Based Fault Detection 75
3.25 Distance-Based Fault Detection Experimental Setup 78
3.26 Overview of the Offline Classification Approach 80
3.27 Overview of the Online Classification Approach 83
3.28 Condition Monitoring Experimental Results 90
3.29 Raw Sensor Data for Serial and WiFi Communication 91
3.30 Experimental Data After Outliers Elimination 92

3.31 Experimental Data After Low-Pass Filter Application 93
3.32 Downsampled Data 94
3.33 Raw Optical Sensor Data 95
3.34 Spectral Analysis for WiFi Communication Experiments 98
3.35 Spectral Analysis for Serial Communication Experiments 99
3.36 Spectral Analysis for Optical and LoRa Communication Experiments 100
3.37 First Additional Fault with WiFi Communication 101
3.38 Second Additional Fault with WiFi Communication 102
3.39 First Additional Fault with Serial Communication 103
3.40 Second Additional Fault with Serial Communication 104

4.1 Overview of the Deployment System 115
4.2 Schematic of the Experimental Setup for the Deployment System 117
4.3 Results of the Mapping Task Carried Out by the Deployment System 119
4.4 Results of the Placement Task Carried Out by the Deployment System 120

5.1 Electromagnetic Module (EMM) 128
5.2 Limpet version 2 System Overview 129
5.3 Infrared Handheld Transceiver 131
5.4 Labelled Picture of the Power Driver Module 134
5.5 Sketch of the EMM and the Actuation Mechanism 136
5.6 Adhesion Module 137
5.7 Suction Cup Mould 138
5.8 Horizontal and Vertical Loading Capacity on Commercial Suction Cup 139
5.9 Horizontal Loading Capacity of the Suction Cups 140
5.10 Vertical Loading Capacity of the Suction Cups 141
5.11 Locomotion Module 142
5.12 2D Patterns of the EMM components 144
5.13 Custom-Built Coil-Winding Machine 145
5.14 Experimental Setup for Heat Dissipation Measurements for Different Coils Thickness 148
5.15 Frequency Response Analysis Experimental Setup 150
5.16 Output Force of the EMM 152
5.17 Stacking of Locomotion Modules to form Locomotion Systems . 156
5.18 Experimental Results of the Heat Dissipation Experiment 157
5.19 Frequency Response Analysis Results 158
5.20 Sound Spectrogram of the EMM at Audible Frequency Levels . . 159
5.21 PWM Experiment Results 160
5.22 Spring Constant Evaluation Results 161

5.23 EMM Output Force Results 162
5.24 Results of the Attachment Strength of the Adhesion Module . . 163
5.25 Results of the Closed Loop Controller of the Adhesion System . 164
5.26 Modularity and Stacking of the Locomotion Modules (Single Locomotion Module) 167
5.27 Modularity and Stacking of the Locomotion Modules (Two Locomotion Modules) 168
5.28 A Locomotion System Composed of a Stack of Four Locomotion Modules 169
5.29 Characterisation of the Locomotion System with the Four Locomotion Modules 171
5.30 Configuration of the Limpet System for Climbing 175

6.1 Data Fusion Architecture Schematic 187
6.2 Multi-Sensor Fusion Experimental Setup 189
6.3 Fusion Processing Results For Limpet 1 190
6.4 Fusion Processing Results For Limpet 2 191
6.5 Fusion Processing Results For Limpet 3 192
6.6 Multi-Sensor Fusion Classification Results 195

7.1 Fort William Test Trials 201
7.2 Limpet Deployment in Fire Service College Using A Mobile Robotic Platform 202
7.3 Deployed Limpets in Fire Service College 203
7.4 Environmental Water Monitoring Using Limpets 204
7.5 Calibration Plot of the Hach Turbidimeter 205
7.6 Calibration Plot of the Limpet for Turbidity Measurements . . . 206

List of Tables

3.1 Limpet Measurands 43
3.2 Communication Methods Properties 73

5.1 Limpet Version 2 Cost Breakdown 132

6.1 Extracted Featues for the Multi-Sensor Data Fusion Approach . 185

7.1 Limpet Turbidity Measurements 207

List of QR Codes

Page:13 - Test your camera and link to my webpage.

Page:112 - Deployment of the Limpet Using Drones.

Page:113 - Deployment of the Limpet Using Hybrid System.

Page:126 - Overview of Limpet v2 System.

Page:137 - Adhesion Mechanism.

Page:149 - Frequency Response of the EMM.

Page:149 - PWM of the EMM.

Page:151 - Determining Output Force of the EMM.

Page:165 - Single Locomotion Module.

Page:166 - Two Module Locomotion System.

Page:166 - Four Module Locomotion System.

Page:170 - Rectangular Movement of the Locomotion System.

Page:170 - Height Tracking of the Locomotion System.

Page:172 - Light-based Control of the Limpet System.

Page:172 - Sound-based Control of the Limpet System.

Page:173 - Distance-based Control of the Limpet System.

Page:173 - IMU-based Control of the Limpet System.

Page:173 - Sound-based Inter-Communication of Limpets.

Page:174 - Climbing.

Page:201 - Fort William Test Trials Video.

Page:203 - Fire Service College Trials Video.

Page:253 - Limpet Version 1 Bill of Materials.

Page:255 - Power Driver Module PCB Bill of Materials.

Page:265 - Limpet Version 1 User Guide.

Page:279 - ESP8266 Tutorial.

Page:305 - Infrared Transceiver Schematic.

Page:307 - Infrared Transceiver PCB Layout.

Page:309 - Sensing Module Schematic.



Page:312 - Sensing Module PCB Layout.

Page:314 - Power Driver Module Schematic. 



Page:316 - Power Driver Module PCB Layout.

Page:319 - Sensors Journal Paper. 



Page:343 - Soft Robotics Journal Paper.

Page:443 - WUWNet ’18 Paper. 



Page:453 - Engineering Graduate Conference Poster.

Page:455 - Industry Engagement Poster. 



Page:458 - Code.

List of Abbreviations

ATEX	ATmosphères EXplosives
DNS	Domain Name System
EMM	Electromagnetic Module
DFT	Discrete Fourier Transform
FFT	Fast Fourier Transform
FoV	Field of View
FPSO	Floating Production Storage and Offloading
IC	Integrated Circuit
I^2C	Inter-Integrated Circuit
IMU	Inertial Measurement Unit
IoT	Internet of Things
IR	Infrared Light
LED	Light-Emitting Diode
LIN	Local Interconnect Network
LoRa	Long Range
MAD	Median Absolute Deviation
MQTT	Message Queuing Telemetry Transport
NTU	Nephelometric Turbidity Unit
ORCA Hub	Offshore Robotics for Certification of Assets Hub
OTA	Over the Air
PCB	Printed Circuit Board
PDMS	Polydimethylsiloxane
PMBUS	Power Management Bus
PSD	Power Spectral Density
PWM	Pulse Width Modulation
rpm	Revolutions Per Minute
RTAB-Map	Real-Time Appearance-Based Mapping
ROM	Read-Only Memory
ROS	Robot Operating System
RS-232	Recommended Standard 232
SDK	Software Development Kit
SERCOM	Serial Communication Interface

SF	Spreading Factor
SLAM	Simultaneous Localization And Mapping
SMBUS	System Management Bus
SPI	Serial Peripheral Interface
SOC	System-on-a-chip
SRAM	Static Random-Access Memory
SVC	Support Vector Classification
TDA-MAC	Time Division Access - Medium Access Control
ToF	Time of Flight
TTL	Transistor-Transistor Logic
WAN	Wide Area Network
UART	Universal Asynchronous Receiver/Transmitter
UAV	Unmanned Aerial Vehicle
UDP	User Datagram Protocol
USB	Universal Serial Bus
USART	Universal Synchronous/Asynchronous Receiver/Transmitter

Part I

Introduction and Background

Chapter 1

Introduction, Overview and Aims

1.1 Introduction

The urge to remove people from offshore platforms and hazardous environments for health and safety reasons has driven the offshore industries to look for more cost-effective and safer methods for inspection, repair and maintenance of their topside and marine offshore infrastructure. Advances in robotic technologies led people to believe that robots are the key to increase safety in monitoring offshore platforms as well as increase efficiency and reduce costs. This thesis deals with the improvement of current state-of-the-art offshore robotics technologies for utilisation in real monitoring use cases of offshore platforms and use in the general advancement of experimental research for offshore robotics.

1.2 Motivation

The underlying motivation for this work is to develop a new multi-sensing robotic platform for inspection and monitoring of offshore energy platforms. The aim is to make this robotic platform highly manufacturable to allow scalability and to deliver increased functionality at a low cost. I identify and address three main challenges in this thesis, which are:

- The expensive and complex manufacturing of offshore robots by developing a novel multi-sensing robotic platform that is low-cost and highly manufacturable.
- Deployment of the robotic agent and the challenging navigation around the unstructured offshore environment by developing modular low-cost adhesion and locomotion capabilities that allow the robot to climb surfaces at different angles.
- The lack of accuracy resulting from taking measurements offshore using a single sensor by developing a multi-sensor fusion approach combining sensing modalities on different agents to achieve structural integrity monitoring.

1.3 Problem Definition

There are three problems that I tackle in this thesis: I address the high manufacturing cost of offshore robots problem in Chapter 3, the deployment of the robot and navigation around unstructured environments problems in Chapters 4 and 5, and the uncertainty in using a single sensor for monitoring problem in Chapter 6.

1.3.1 Manufacturing Robots to Monitor Offshore Environments is Expensive

Currently, manufacturing robots for monitoring offshore environments is a complex and expensive process. Every extra component on the robot will add cost to the overall system. It is usually the case that functionality is sacrificed to keep the costs low. Developing highly manufacturable and low-cost systems without sacrificing functionality will allow mass-production of the system and the ability to deploy agents in huge collectives to monitor the different aspects of offshore energy platforms. To be useful for inspection and monitoring of the offshore platforms, it is crucial that the robot is equipped with multiple sensing modalities.

1.3.2 Deployment of Robotic Agents and Navigating Unstructured Offshore Environments is a Challenge

Offshore platforms are complex, unstructured environments, which consist of surfaces at different angles. Deploying robotic agents on the platform and enabling these robotic agents to navigate such unstructured environments efficiently are challenging tasks. The ability to adhere to and climb these surface will increase the accessible areas of terrestrial robots in such environments, which improves the capability of the robot to do inspection and monitoring of the offshore platform.

1.3.3 Uncertainty in Using a Single Sensor to Monitor Offshore Environments

Monitoring offshore environments and structures using single sensors or separately acting upon data from single sensors results in a high level of uncertainty. To form more accurate situation awareness and determine how to respond to it, more diverse data needs to be collected from multiple sensors and multiple agents, and this data then needs to be combined together and analysed. Fusing the sensor data will help achieve improved accuracy, more specific inference and enhancements in data authenticity than using data from a single sensor.

1.4 Aims and Objectives

At the outset of this research project, a list of aims and objectives was determined to act as a reference for the development of each of the different aspects of the project. The main objective was to develop a new low-cost and highly manufacturable multi-sensing robotic platform - the Limpet - that is capable of inspecting and monitoring offshore energy platforms. The list below summarises the major aims and objectives for this research project.

- Research the challenges facing offshore industries and the requirements robots need to operate in such environments.
- Conduct a literature review on current offshore robotic systems, analyse their sensing, locomotion, and adhesion capabilities, and understand their limitations.
- Develop a new low-cost and highly manufacturable multi-sensing robotic platform for the purpose of monitoring offshore energy platforms.
- Demonstrate the efficiency of the new robotic platform in monitoring the condition of offshore structures.
- Deployment of the robotic platform in the environment.
- Development of adhesion and locomotion mechanisms that allow the new robotic platform to efficiently navigate unstructured offshore environments.

- Demonstrate the capability of the new robotic platform in climbing inclined surfaces and responding to changes in its environment through the use of the on-board sensors.
- Develop a multi-sensor data fusion approach that combines the data from the sensors of multiple robotic agents.
- Demonstrate the usefulness of the multi-sensor fusion approach in offshore structural integrity monitoring.

1.5 Preview of Contributions

- The development of the Limpet system, a new low-cost and highly manufacturable multi-sensing robotic platform for monitoring offshore energy platforms.
- The integration of the Limpet system with Robot Operating System (ROS) to allow it to interact with other robots.
- The development of a robust communication scheme for the Limpet system.
- The use of the distance sensor on the Limpet system to gain multi-functional sensing capabilities.
- The development of an online classifier on the low-cost microcontroller of the Limpet system for achieving real-time and autonomous condition-monitoring of offshore structures.
- The deployment of the Limpet system using a custom-built hybrid hard/-soft robotic platform and using other robotic platforms.
- The development of an electromagnetic actuator that provides actuation, sound and communication capabilities.
- The use of the electromagnetic actuator to provide the Limpet system with adhesion and locomotion capabilities.
- The design of the new version of the Limpet as a modular system, which reduces costs and allows different tasks to be easily achieved by reconfiguring the modules.

- The development of the Limpet as an untethered system to remove dependence on electrical or pneumatic tethers which limits the applications that can be performed in the environment.
- The control of the Limpet system through its sensors, which demonstrates the capability of the Limpet to respond to changes in its environment.
- The use of the adhesion and locomotion capabilities of the Limpet system to climb inclined surfaces.
- The application of multi-sensor data fusion using the Limpets.
- Vibration monitoring data fusion approach that can be utilised in monitoring the structural integrity of conductor pipes installed offshore.
- Utilisation of the Limpet for other research outputs.
- Commercialisation of the Limpet technology.

1.6 Publications

This thesis represents my own work, and includes a number of original contributions to scientific knowledge. The work presented in this thesis has led to the following journal publications.

[J1] M. E. Sayed, M. P. Nemitz, S. Aracri, A. C. McConnell, R. M. McKenzie, and A. A. Stokes. **The Limpet: A ROS-Enabled Multi-Sensing Platform for the ORCA Hub**. *Sensors*. (2018) [1]

Summary of Contribution: lead author of the work; development of the Limpet system and classifier; design of the experimental setup; conducting the experiments; writing and revising the manuscript.

[J2] R. M. McKenzie*, M. E. Sayed*, M. P. Nemitz, B. W. Flynn, and A. A. Stokes. **Linbots: Soft, Modular Robots Utilising Voice Coils**. *Soft Robotics*. (2018). **(*The authors contributed equally to this work)** [2]

Summary of Contribution: co-first author on the work; design and development of the Linbot; development of the experimental scheme; writing half of the manuscript.

[J3] M. E. Sayed, Jamie O. Roberts, R. M. McKenzie, S. Aracri, A. Buchoux and A. A. Stokes. **Limpet: A Modular, Untethered Soft Robot**. *Soft Robotics*. (2019). *submitted* [3]

Summary of Contribution: lead author of the work; designing and creating the system; designing and conducting the experiments; analyzing the data; writing and revising the manuscript.

[J4] A. C. McConnell*, M. E. Sayed*, J. O. Roberts*, S. Aracri, R. M. McKenzie and A. A. Stokes. **Long Necked Turtle: A Soft/Hard Hybrid Mobile Robotic Platform for IoT Node Distribution**. *Frontiers in Robotics and AI*. (2019). *In Review*. **(*The authors contributed equally to this work)** [4]

Summary of Contribution: co-first author on the work; design and development of the long-necked turtle robot; development of the soft arm for limpet deployment; design of the control software; development of scheme for mapping of the environment; writing part of the manuscript.

The system I have developed during my doctoral studies has also been utilised by collaborators in some of their publications. The role of my system in the following publications will be explored further in this dissertation. The use of the system for other processes shows the great impact of this system.

[C1] S. Aracri, M. E. Sayed, J. O. Roberts, A. C. McConnell and A. A. Stokes. **Limpet: An Autonomous Bioinspired Robot For Environmental Monitoring**. *19th Biennial Seminar on Water Resources and Environmental Management*. (2018) [5]

Summary of Contribution: second author on the work; design and development of the Limpet system; advising on the experimental setup; conducting part of the experiments; helping in data analysis.

[C2] N. Morozs, P. D. Mitchell, Y. Zakharov, R. Mourya, Y. R. Petillot, T. Gibney, M. Dragone, B. Sherlock, J. A. Neasham, C. C. Tsimenidis, M. E. Sayed, A. C. McConnell, S. Aracri and A. A. Stokes **Robust TDA-MAC for Practical Underwater Sensor Network Deployment: Lessons from USMART Sea Trials**. *Proceedings of International Conference on UnderWater Networks and Systems (WUWNet'18)*. (2018) [6]

Summary of Contribution: first author from the University of Edinburgh group on the work; design and development of the Limpet system; help in conducting the experiments; writing part of the manuscript.

In addition to my own work, I have also contributed to other research outputs during my doctoral studies. The following publications have not been featured in this dissertation.

[J5] M. P. Nemitz, M. E. Sayed, J. Mamish, G. Ferrer, L. Teng, R. M. McKenzie, A. O. Hero, Edwin Olson, and A. A. Stokes, **HoverBots: Precise Locomotion Using Robots That Are Designed For Manufacturability**, *Frontiers in Robotics and Artificial Intelligence*. (2017) [7]

Summary of Contribution: second author on the work; design and development of the hoverbot platform; development of the experimental scheme; revising the manuscript.

[J6] M. P. Nemitz, Ryan Marcotte, M. E. Sayed, G. Ferrer, A. O. Hero, Edwin Olson, and A. A. Stokes, **Multi-Functional Sensing for Swarm Robots Using Time Sequence Classification: HoverBot, an Example**, *Frontiers in Robotics and Artificial Intelligence*. (2018) [8]

Summary of Contribution: third author on the work; design and development of the hoverbot platform; development of the experimental scheme; literature review; revising the manuscript.

[J7] S. T. Mahon, J. O. Roberts, M. E. Sayed, D. H. Chun, S. Aracri, R. M. McKenzie, M. P. Nemitz, and A. A. Stokes. **Capability by Stacking: The Current Design Heuristic for Soft Robots**. *Biomimetics*. (2018) [9]

Summary of Contribution: third author on the work; writing and revising the manuscript.

[J8] R. M. McKenzie, J. O. Roberts, M. E. Sayed, and A. A. Stokes. **PeriSim: a simulator for optimising peristaltic table control**. *Advanced Intelligent Systems*. (2019). *submitted* [10]

Summary of Contribution: third author on the work; assisting with the experiments; revising the manuscript.

[C3] J. Dodoo, M. E. Sayed, G. McHale and A. A. Stokes. **A Holistic Review of Wetting of Droplets**. *Electrowetting*. (2018) [11]

Summary of Contribution: second author on the work; development of the experimental scheme; conducting the experiments; revising the manuscript.

[C4] H. D. Chun, J. O. Roberts*, M. E. Sayed*, S. Aracri* and A. A. Stokes. **Towards more Energy Efficient Pneumatic Soft Actuators using a Port-Hamiltonian Approach**. *IEEE International Conference on Soft Robotics (RoboSoft 2019)*. (2019) **(*The authors contributed equally to this work)** [12]

Summary of Contribution: co-second author on the work; development of the experimental scheme; conducting the experiments; revising the manuscript.

[C5] S. T. Mahon, A. Buchoux, M. E. Sayed, L. Teng and A. A. Stokes. **Soft Robots for Extreme Environments: Removing Electronic Control**. *IEEE International Conference on Soft Robotics (RoboSoft 2019)*. (2019) [13]

Summary of Contribution: third author on the work; development of the experimental scheme; design of the circuits; development of the state machine; conducting the experiments; revising the manuscript.

During the course of my doctoral studies, I was involved in multiple different academic positions and extra-curricular outreach.

Post-Doctoral Research Associate
Connect-R: Industrial-Scale Self-Building Modular Robotics
2019
The University of Edinburgh, School of Engineering, United Kingdom

Research Assistant on the ORCA Hub
Offshore Robotics for Certification of Assets
2017-2019
The University of Edinburgh, School of Engineering, United Kingdom

Teaching Assistant
Introduction to Bioelectronics
2018
The University of Edinburgh, School of Engineering, United Kingdom

Teaching Assistant
Biosensors
2018
The University of Edinburgh, School of Engineering, United Kingdom

Consultant
Soft Robotics Project
2018
Khalifa University, Abu Dhabi, United Arab Emirates

Demonstrator
Electrical Engineering 1
2018
The University of Edinburgh, School of Engineering, United Kingdom

Marker
Electrical Engineering 1
2018
The University of Edinburgh, School of Engineering, United Kingdom

Project Manager
RAEng Ingenious Award
2019
The University of Edinburgh, School of Engineering, United Kingdom

Technical Committee
Royal Society Summer of Science Exhibition Demonstrations
2019
The University of Edinburgh, School of Engineering, United Kingdom

Certificate for Best Student Paper Award
Soft Robots for Extreme Environments: Removing Electronic Control
2019
IEEE International Conference on Soft Robotics (RoboSoft 2019)

Certificate of Achievement for Acting as
Vice President of the Engineering Graduate Society
2016-2017
The University of Edinburgh, School of Engineering, United Kingdom

1.7 2D Barcodes

Throughout this thesis, I use 2D barcodes to direct the reader towards important videos that help understand the context. The videos are directly relevant to the work shown in this dissertation. I used Latex's *qrcode* package for the 2D barcodes. This package encodes data (e.g. html links) into two-dimensional barcodes. A list of all the barcodes included in this dissertation can be found on Page xxvi. If any of the linked content asks for a password, please enter ***MESThesis***. The iPhones are capable of reading barcodes simply through the camera application on the phone. By opening the camera application and aiming at the barcode, a link should appear which will direct you to the linked file. Alternatively, you can download the free applications, ***QR Reader for iPhone*** in the AppStore or ***QR Code Reader*** in the Google Play Store.

Test your camera and link to my webpage.



1.8 Thesis Tree

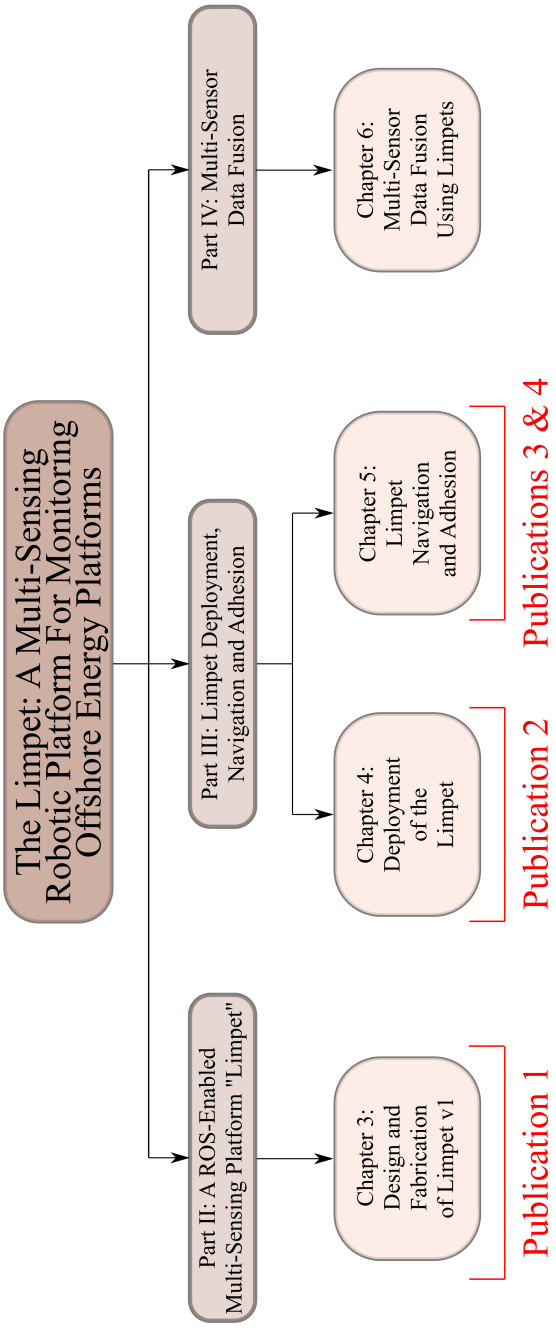

Figure 1.1: Thesis Tree.

1.9 Summary of Thesis Contents and Layout

A summary of the content of each chapter in this Thesis is given below:

- **Chapter 2 Background** An overview of challenges facing offshore industries, the need for robots on offshore platforms, requirements for these robots, current state-of-the-art in offshore robotics and the current limitations.
- **Chapter 3 The Limpet: A ROS-Enabled Multi-Sensing Robotic Platform** Development of version 1 of the Limpet, a new low-cost and highly manufacturable multi-sensing robotic platform, and the demonstration of condition monitoring of offshore structures using the Limpet.
- **Chapter 4 Deployment of the Limpet** Examples of how the Limpet can be deployed on structures in the offshore environment.
- **Chapter 5 Limpet Navigation and Adhesion** Development of version 2 of the Limpet, which has additional adhesion and locomotion capabilities, allowing it to adhere to offshore structures and navigate through the unstructured offshore environment.
- **Chapter 6 Multi-Sensor Data Fusion on the Limpet** Design and development of a multi-sensor data fusion approach for combining and analysing data from multiple Limpets, and the use of this approach for monitoring the structural integrity of conductor pipes.
- **Chapter 7 Impact, Field Tests and Commercialisation** An overview of the overall impact of the Limpet, its use in some field test trials and other scientific research outputs, and commercialisation of the Limpet technology.
- **Chapter 8 Conclusions and Future Work** Overview of the work, conclusions and possible future work.
- **Appendix** Copyright agreements, bill of materials, CAD design files, user guides, tutorials, schematics and board layouts, submitted and published journal papers, posters, source and main code files.

Chapter 2

Background

This chapter covers the background of, and literature related to, my thesis. In Section 2.1, I introduce some of the challenges facing offshore industries. In Section 2.2, I explain how robotics can help with the challenges facing the offshore industry. In Section 2.3, I give a brief overview on the flagship ORCA Hub in the United Kingdom, where the work presented in this thesis is undertaken as part of this flagship project. I give a brief introduction to the requirements that robots need to operate in such environments in Section 2.4. I give an overview of the current state-of-the-art in offshore robotics and limitations with current systems in Section 2.5. I explain how a robot is an important tool in condition monitoring systems for monitoring offshore platforms in Section 2.6. In Section 2.7, I explain the importance of climbing inclined surfaces for an offshore robot, and I give examples of the current adhesion and locomotion mechanisms used for climbing robots. In Section 2.8, I explain the importance of designing offshore robots in a modular fashion and how increased capability can be achieved by stacking modules together. I give a brief overview of multi-sensor data fusion and its importance in Section 2.9

2.1 Challenges Facing Offshore Industries

The international offshore energy industry currently faces the challenges of: a fluctuating oil price, significant and expensive decommissioning commitments for old infrastructure (especially North Sea), and small margins on the traded commodity price per kWh of offshore renewable energy [14]. Furthermore, the number of people available to work in offshore industries has reduced as graduates are shifting to less hazardous places onshore, and the current workforce is ageing.

The demand for oil and gas is increasing with the rapid growth of the world's population. Around 80% of the world's current energy demand comes from fossil fuels, and 60% of this energy from fossil fuels is generated by oil and gas alone [15, 16]. The need for higher amounts of oil and gas puts significant demands on the work force, financial abilities and technological capabilities. The depletion of shallow oil reservoirs (<400m) drove industries to explore deeper oil fields, often situated in high seas which are characterised by harsh and hostile environments. Hostile areas are by definition difficult to reach and to monitor leading to the urge to remove personnel from offshore platforms and hazardous environments [17]. As the oil and gas requirements increase, advanced technologies will become essential, and the cost of operating them will significantly rise due to the hostile and hard-to-reach nature of the environment [18].

There have been several reported accidents and explosions of offshore rigs, with the most widely reported and studied tragedy being the Deep Horizon oil spill in the Gulf of Mexico [19]. This accident was a huge setback for the offshore oil and gas industry, and it triggered the biggest debate from governments, academia, environmentalists and major companies of the oil and gas industry to look for safer ways to inspect, repair and maintain offshore platforms [17].

2.2 Applications of Robotics in Offshore Industries

The sensitivity of the product from offshore oil and gas platforms and the harshness of the environment leads to critical health and safety challenges.

Thus, continuous inspection and monitoring of the offshore facilities is a critical task and requires technologies to prevent accidents and ensure safety of human and marine lives. Operators are seeking more cost-effective and safer methods for inspection, repair and maintenance of their topside and marine offshore infrastructure. Robots are seen as key enablers in this regard to improve health, safety and environment, and increase the production and cost efficiency. Robots can be deployed in the air, on the rig or in the subsea.

In such a human–robot cooperation model, most of the cognitive ability to take decisions will come from human operators, while critical and dangerous tasks, and inspection and monitoring tasks will be achieved by robotic devices equipped with sensors [17]. On offshore energy platforms, robots could be used to remotely monitor pipelines, corrosion, natural gas leaks, equipment conditions, structural integrity and real-time reservoir status. The information gathered from these robots will significantly help the oil and gas industry in improving platform safety, optimising operations, preventing problems, fixing errors, reducing risk to human life, enabling control of operations remotely and reducing operating costs.

2.3 Offshore Robotics for Certification of Assets (ORCA Hub)

The UK Robotics and Artificial Intelligence Hub for Offshore Robotics for Certification of Assets (ORCA Hub) is a 3.5 year EPSRC funded, multi-site project with a vision to use teams of robots and autonomous intelligent systems (AIS) on remote energy platforms to enable cheaper, safer and more efficient working practices [14]. The ORCA Hub brings together top industrial companies (Total, Chevron, BP and many others) with academia (University of Edinburgh, Heriot-Watt University, University of Oxford, Imperial College London and University of Liverpool). The long-term vision for the ORCA Hub is an offshore platform that is completely autonomous and being operated and inspected from the shore, which will decrease the number of people working offshore.

The ORCA Hub System constitutes the offshore platform and the heterogeneous robotic systems. The ORCA Hub System provides remote solutions using robotics and Artificial Intelligence (AI) that are readily integratable with

existing and future assets and sensors, can operate and interact safely in autonomous or semi-autonomous modes in complex and cluttered environments, and can cooperate with remote operators [14]. The collaboration between topside (legged, wheeled and immobile), aerial, and marine robots, and their interaction with their environment (platform) are all considered part of the ORCA Hub System. The ORCA Hub System aims at achieving tasks that are not possible with a single robot due to the complex nature of offshore platforms. The ORCA Hub System includes many components such as robotic autonomy, mobility, manipulation, sensor processing, autonomous mapping, navigation, multimodal interfaces and human-machine collaboration. In this thesis, I focus on the sensing aspect of the ORCA Hub System. Sensing is a key element to the ORCA Hub System as it is important in asset monitoring, fault detection, mapping of the platform, helping other robots navigate around the platform, and monitoring the environmental conditions.

2.4 Offshore Environment Requirements

Robots on offshore platforms face many challenges and harsh working conditions. Some of these challenges include [18]:

- Dangerous atmospheric conditions resulting from gases, which can be explosive, toxic and corrosive
- Harsh weather conditions involving rain, hail and high speed winds
- Extreme ambient temperature and high humidity levels
- Absence of protection against saltwater spray and direct sunlight
- Constraint space and walkways

Robots on offshore platforms will have to operate with different degrees of autonomy: fully autonomous, semi-autonomous and manual. Fully autonomous operations do not require any human intervention, while semi-autonomous operations require varying degrees of human interaction [18]. For a robot to be suitable for operation on offshore platforms, there are some requirements regarding hardware, software and communication. Some of the hardware requirements for offshore robots include [18]:

- Making the electronics suitable for harsh environments
- Equipping the robot with highly reliable sensors to perceive its surroundings and monitor the offshore structure
- Ability to execute inspection and monitoring tasks autonomously, semi-autonomously or manually
- Certifying the robot to be used in explosive environments (ATEX Certification)

Offshore robots also have requirements for software development. Some of these requirements include [18]:

- Ability to control the robot manually, semi-automatically and autonomously
- Ability to control the robot from remote locations
- Quickly and easily program new inspection and manipulation tasks without the use of experts
- Display the sensor data on a remote screen
- Alert the remote operators when sensor values detected are abnormal
- Humans can safely interact with the robot

Communication requirements mainly includes the ability to communicate and transmit data to a remote control station or to neighbouring systems. The harsh offshore environment makes remote sensing extremely valuable, since it allows the gathering of data in remote and hostile areas. Recent advances in the Internet of Things (IoT) and the cloud computing model provide support for remote sensing [20].

2.5 Current State-of-the-Art in Offshore Robotics

Currently, the majority of offshore robotics are used for subsea tasks, such as mapping of the seabed and inspecting underwater equipment and pipelines using AUVs and ROVs [21, 22, 23, 24, 25, 26, 27]. However, offshore robots

for topside operations have started to gain the interest of researchers in recent years. Bengel et al. [28] were the first to demonstrate the application of robots for inspection and maintenance tasks in offshore platforms. Their work on the MIMROex inspection robot demonstrates the capability of a mobile robot to navigate safely through the platform, build maps of the platform and autonomously execute inspection tasks. The Sensabot [29] is a teleoperated offshore inspection robot developed by researchers at Carnegie Mellon University. It was designed to withstand extreme weather conditions, reach areas with difficult access, and operate in toxic, flammable and explosive environments.

Kyrkjebo et al. [30] developed an intelligent instrumentation system called the SINTEF Topside Robotic System, which can enable operators to control and monitor processes on the platform from onshore. Another robotic system developed for offshore inspection and monitoring of offshore platforms is DORIS [31]. DORIS moves through a rail and carries different sensors, where it can process the sensor data or store it for future analysis. The sensors can identify abnormalities such as intruders in restricted areas, smoke, fire, liquid and gas leakages [31]. The robot has an embedded manipulator that allows it to take samples and read instruments. Walloid [32] is a 4-arm quasistatic climbing robot designed for offshore platform topside automation. It is able to choose its adhesion force and thus capable of climbing walls of different materials. In 2009, Bengel et al. [33] developed another mobile offshore inspection robot equipped with a robotic arm and several application sensors such as a microphone, gas sensor and fire sensor. The robotic arm is equipped with a camera for visual inspection. The robotic prototype can autonomously execute pre-programmed inspection tasks in automatic mode. The prototype was tested and evaluated for inspection tasks in offshore environments.

Some of the main limitations of current offshore robotic systems are:

- Large size and high cost which limits the ability to deploy these systems in large quantities to monitor offshore structures
- Ability to easily navigate the unstructured offshore environment, which limits the accessible areas of the robot in such environments
- Limitations in using sensors from multiple different robots and fusing the sensor data to allow more accurate monitoring of the offshore platform

2.6 Condition Monitoring Systems in Offshore Environments

Robots can be important tools for fault detection and condition monitoring systems on offshore platforms. Condition monitoring techniques help describe complex faults, failure mode types and the observable signs generated by the presence of faults [34]. Offshore implementation of fault detection and condition monitoring is challenging due to the complexity of remote sensing, data collection, data processing and data analysis.

Condition monitoring systems play an important role in reducing maintenance and operational costs of offshore structures, e.g. wind turbines. Technological advances in the development of wind turbine blades have led to an increase in the blade span. This increase in the span enables wind turbines to harvest more wind energy. However, a larger blade span increases the aerodynamic load on the blades, which makes the blades more vulnerable to failure. The turbines also face harsh environmental conditions, which increases the chance of failure. Failure of wind turbines hinders the economic feasibility of offshore wind farms and, therefore, real-time condition-monitoring and fault detection for wind turbines is essential [35]. According to the Rules and Guidelines for Industrial Services, offshore wind turbines need to be equipped with blade condition monitoring systems to meet the safety requirements [36].

The turbines face harsh oceanic environmental conditions and this is the reason why a condition monitoring system is an important tool. Different techniques for condition-monitoring of wind turbines have been proposed in the literature [37, 38, 39, 40, 41]. Some of these techniques for fault diagnosis of wind turbines are based on piezoelectric sensors [42], acoustic emission sensors [43], fibre Bragg grating sensor system [44], piezo-ceramic and impedance sensing [45, 35]. Piezoelectric sensors utilise the piezoelectric effect, where mechanical stress generates an electric charge, to measure different parameters such as pressure, temperature, force, acceleration. Piezoelectric sensors have the advantage of small dimensions, good frequency response, and stable sensitivity [46]. Piezoelectric sensors have some limitations. They have a high temperature sensitivity, can only be used for dynamic measurements, and are greatly affected by humidity levels [46]. Acoustic emission sensors measure acoustic radiation from materials, which usually results from

the occurrence of micro-structural changes. Acoustic emission measurement has the advantage of being able to use information resulting from the damage process while it occurs. This advantage means that events can be detected as they occur and at any location on the structure [47]. Another advantage of the acoustic emission measurement technique is that it is non-directional. The structure under damage will emit radiation in all directions [47]. Acoustic emission sensors are sensitive to changes in the material rather than only being able to detect presence of defects [47]. Acoustic emission sensors have some limitations when used for condition monitoring systems. The acoustic emission technique provides a qualitative estimate on the amount of damage and how the long the structure will last, which means that other techniques will need to be used to provide quantitative results and do a more thorough examination on the structure [48]. Another limitation with acoustic emission sensors is the effect of the environment noise on the results. The environments where the sensors are used are usually very noisy and the acoustic emission signals are weak, which makes signal discrimination a challenging task [48]. Fibre bragg sensors are constructed from optical fibres, and they reflect light at specific wavelength while transmitting the light at all other wavelengths. Fibre bragg grating sensors have the advantage of small form factor, lightweight, elimination of electrical connections, and compatibility for non-invasive remote sensing [49]. They also have a high sensitivity, high resolution and wide dynamic range [49]. The limitations of fibre bragg sensors include thermal sensitivity, the high cost associated with the design and maintenance of the sensor, and difficulty in separately discriminating between a shift in the wavelength due to temperature or strain [49].

Real-time condition monitoring of wind turbines and fault detection has not been studied in great detail, due to the harsh environments surrounding wind turbines, which makes experimental research challenging. In this thesis, I introduce a novel method to achieve real-time condition monitoring and fault detection for offshore structures such as wind turbines. The approach involves combining signal processing methods with remote sensing to detect faults in the operation of equipment. The reliability of the monitoring system is enhanced by conducting all the data processing and analysis on the microcontroller, and transmitting data using high-range low-bandwidth communication systems only in the event of the presence of a fault.

2.7 Adhesion Mechanisms for Climbing Robots

Offshore platforms are massively complex and unstructured environments. The environment consists of structures at different angles, steep inclines, and inverted surfaces. To navigate such unstructured environments efficiently and to be useful for inspection and exploration tasks, a robot must be have a good adhesion mechanism and be capable of multiple locomotion modalities such as walking, running, and climbing [50]. The ability to adhere and to climb these inclined surfaces increases the accessible areas of terrestrial robots in such environments, which improves the capability of the robot to do inspection and monitoring of the offshore platform. Adhering to and climbing on these unstructured offshore environments alone is not enough for the robot to carry out inspection tasks; it must also be equipped with a sensor payload.

Climbing robots can be used for a wide range of applications in unstructured offshore environments. Some applications include: inspection of offshore structures and walls; object manipulation; long-term attachment to monitor structural health. The two key features for climbing robots are adhesion and locomotion mechanisms.

Reliable adhesion on surfaces is one of the key characteristics of climbing robots. Recent work on climbing robots have adapted different bio-inspired and engineered adhesion mechanisms. The adhesion mechanisms include gecko-inspired adhesion (molecular force) [51, 52, 53], magnetic adhesion [54, 55, 56, 57, 58, 59], electroadhesion [50, 60, 61, 62, 63, 64, 65, 66], adhesive materials [67] and negative pressure adhesion [68, 69]. Geckos adhere to surfaces via Van der Waals forces using a large number of very fine hair structures [70]. Gecko-inspired adhesion has been utilised by climbing robots of different scales to move on smooth inclined surfaces [69, 71, 72, 73, 74, 75, 76]. Magnetic adhesion relies on generating a magnetic force using permanent magnets, electromagnets or electro-permanent magnets. Magnetic adhesion has advantages of easy control, but it works only on ferromagnetic surfaces. Electroadhesion is achieved by using an applied electric field, and it can be tuned by changing the input voltage modulation [50]. Electroadhesion requires a large input voltage, and it also uses power tethers [50]. Adhesive materials for climbing robots are not very reliable and they require smooth and clean surfaces[67].

The most widely adopted adhesion mechanism for climbing robots is negative pressure adhesion using suction cups. This adhesion method has higher reliability, simpler design and easier application than other adhesion methods. When a suction cup is pushed down from the centre against a surface, air is squeezed out from the cavity between the suction cup and surface, which results in a decrease in pressure in the cavity. The internal pressure of the cavity is lower than atmospheric pressure, which keeps the suction cup adhered to the surface. When the suction cup is pulled up, air starts to leak into the cavity causing an increase in pressure, and eventually detaching the suction cup. Adhesion in nature based on suction can be seen in different animals including northern clingfish [77], limpet [78], octopus [79, 80] and squid [81]. The suction mechanism demonstrates effectiveness both in terrestrial [82, 83] and aquatic environments [84]. Negative pressure systems have used different methods to generate suction on a surface, which include high frequency vibrations, shape memory alloys, vacuum pumps, RC Servos and motors. Suction mechanisms have also been applied by robots in other applications, such as picking objects with variable shape and size [85]. It is important to have sensory feedback on the adhesion module, to inform the status of adhesion of the system and to implement closed-loop control systems that can enable robots to maintain their adhesion for longer periods of time. Robotic adhesion modules with the capability to adhere to surfaces for long durations are invaluable for industrial applications (e.g. inspection in offshore environment).

Locomotion types of climbing robots include crawlers [86, 87, 88, 89], wheels [90, 91], and legs [50, 92, 93, 94, 95, 96, 97]. Crawler-type climbing robots can move relatively fast, but are not adequate for rough environments as they cannot cross obstacles easily. The most common strategy for locomotion is using a two-wheel differential drive, where each wheel is powered by an electric motor. Wheeled robots are capable of achieving high velocities, do not need actuator calibration, and are platform independent. Wheeled locomotion, however, has a negative impact on the battery life and the cost of the robot. Another main disadvantage of using wheeled locomotion for robots that use suction force adhesion is the need to maintain an air gap between the robot base and the surface the robot is moving on. This feature will create some problems for the robot like loss of pressure or friction with the surface [98]. Legged robots allow the creation of a stable and strong adhesion force to the surface, and they can cope well with cracks or obstacles in their environment [98]. The disadvantage of legged robots is that they achieve low

speeds and may require complex control. There has been various other climbing robots based on different adhesion and locomotion mechanisms reported over the past years [67, 99, 100, 101, 102, 103, 104, 105, 106, 107].

2.8 Modularity and Stacking of Modules

Robots performing tasks in unstructured offshore environments need to adapt to variable constraints in their environment. Traditional robotics provide unique solutions to a specific real world application, but are usually hard to use in other applications [108]. Due to the lack of adaptive nature of traditional robots, they do not cope well with changes in their environment. Their repair and maintenance are also costly and generally require trained personnel [108]. Modular robots or assemblies of modular units make it easier to repair the system, to replace modules, and to control the robot. By building robots in a modular architecture, it is easy to adapt the robot to new tasks by simply adding or replacing modules. Modular units are easily reconfigured, giving the robot more robustness and capability for achieving new tasks.

Modular robotic systems have attracted major interest over the past years [109, 110, 111, 112, 113, 114, 115, 116, 117, 118, 119, 120]. A robotic module is defined as a unit that performs typical tasks of a robot, either fully or partially, and has the capability of interacting with other units or modules [121]. A modular robot is a robot consisting of units or modules that can interact with each other in different ways to create a system with new capabilities [121]. Modular robots are usually made of some primary structural actuated unit and some additional specialised units (e.g. grippers, sensor payload, feet, etc.) [122]. The interest in modular systems is due to the hypothesis that a single, advanced robot is more expensive and less robust than multiple low-cost modules [108, 122, 123]. Modular robots can be easily reconfigured for different tasks [108, 109, 112, 122, 124, 125, 126], making them different from monolithic robots. It is important to design the modules to be low cost and manufacturable to allow the modules to be easily developed and integrated into systems. Modular robots provide the advantage of: reconfigurability; reusability; versatility; robustness; ease of manufacturing over traditional robotic systems [108, 127]. Another important advantage of modular robots is the ability to develop low-cost systems. Building systems from the same module or a few types of modules allows mass production to

come into play. One set of modules can be used to develop a range of different complex systems, which saves costs through the reuse of units or modules.

The capability of single modules are limited, but modular robots consisting of multiple units have increased capability compared to the sum of their parts [9]. By stacking modules, one can increase the overall capability and the range of behaviours and motions of a system, and thus, utilise it to perform useful tasks. The term "stacking" refers to the ability to combine functional units to develop a system that has greater capability and complexity than the sum of its individual units [9]. There are multiple examples of systems where higher capability was achieved by stacking functional modules together [128, 129, 130, 131, 132, 83, 133, 134, 135, 136, 137, 138, 139, 140, 141, 142, 143, 144, 145, 146, 147, 148, 149].

The capability of a modular robotic system is usually dependent on the number of modules within it [122]. However, the number of modules are often limited by the cost of the unit, where systems with large number of modules sacrifice their functionality to keep the costs low. Creating low-cost modular robotic systems with higher capabilities is a key challenge in modular robotics. The use of hardware for multifunctional purposes is a great way to keep costs of the system low. Examples include the Kilobot system [150] and the Hoverbot system [7, 8].

2.9 Multi-Sensor Data Fusion for Offshore Robotics

Multi-sensor data fusion involves combining data and information from multiple sources to form a unified picture and a complete description of a process or environment [151, 152]. Data fusion is a multidisciplinary field of research and involves concepts from different research fields such as information theory, signal processing, artificial intelligence and statistical inference [151]. Data fusion is important in applications where a large amount of data needs to be combined together to form more accurate decisions [152]. It is used in a wide variety of applications, including robotics, sensor networks, image processing, artificial intelligence and video analysis [151]. A major advantage of data fusion is the enhancement in data authenticity and data availability, since it improves confidence and reliability of the data and increases the spatial and temporal coverage [151]. In networks consisting of large numbers

of agents, data fusion can solve problems with collision of data transmitted, which improves the scalability of the network [151].

Data fusion is mostly divided into a hierarchy of four processes [152]. The first and second processes are mostly about numerical information and fusion of this information from multiple sources [152]. Processes 3 and 4 of this hierarchy involve the extraction of useful information and knowledge from the fused data, and taking decisions and actions based on this information [152]. Multi-sensor data fusion faces various challenges, some of which are:

- Data imperfection. There is always some impreciseness and uncertainty in the data provided by sensors. Multisensor data fusion can exploit the data redundancy to reduce the effects of data imperfection [151].
- Data outliers and false data. Ambiguities and inconsistencies in the environment monitored also results in uncertainties in the sensor measurement [151]. The multisensor data fusion approaches should be able to make use of the redundant data to eliminate such effects.
- Data modaltities. Data collected by different sensors might be homogeneous or heterogenous data, such as sound, visual, proximity data [151]. Data fusion algorithms need to take into account the different data modalities and be able to handle them.
- Data correlation. In distributed fusion schemes, the data from the sensors are exposed to the same level of background noise. If these data dependencies are not accounted for by the sensor fusion algorithm, it will form over or under confidence in the results [151].
- Processing framework. Multisensor data fusion processing can be centralised or decentralised. In centralised frameworks, the data from all the sensors are sent to a central node for fusion processing. The centralised approach is more power demanding as it requires more communication to transmit a larger set of data. The decentralised approach involves processing the data locally on each node and communicating only the final result.
- Operational timing. The frequency or rate of measurements might be different depending on the part of the environment being monitored.

The multisensor fusion algorithm must account for this time variation between the measurements [151].

- Static vs dynamic events. The events being monitored by the sensors might be time-variant or time-invariant phenomena. For time-variant measurements, the multisensor data fusion algorithm needs to take into account the history of the measurements in the processing phase [153].
- Data dimensionality. The data measured by the sensors can be processed either on each node before transmission or on the fusion center after transmission, in order to compress it into a lower dimension [151]. If this processing is done on the node, it saves communication bandwidth and power required for transmission [154]. If the processing is done globally on the sensor fusion center, it will limit the computational load of the central fusion node [155].

No single sensor fusion approach can address all these challenges. Sensor fusion approaches presented in literature usually focus on a subset of these challenges. The imperfection of data is the most challenging problem in multisensor data fusion approaches [151]. Most of the work presented in literature has focused on addressing this challenge. There are different data fusion approaches related to data imperfection that have been proposed in literature, and these include:

- Probabilistic fusion [152, 156, 157]. Probabilistic data fusion use probability distributions fused together to represent sensor data and express the data uncertainty [151]. This data fusion approach is well understood and established for tackling data uncertainty problems, but is incapable of tackling any other data imperfection challenges [151].
- Evidential belief reasoning [158, 159, 160, 161, 162]. This data fusion approach deals with probability mass functions to characterise the data further using belief and plausibilities [151]. This approach cannot deal with any challenges of data imprecision, except for uncertain and ambiguous data. The approach is also inefficient when used for fusing highly conflicting data [151].
- Fusion and fuzzy reasoning [163, 164, 165]. The fuzzy reasoning approach uses fuzzy membership to represent vague data, and the fusion

approach is based on fuzzy rules. The approach, however, is limited mostly to vague data fusion [151].

- Possibilistic fusion [166, 167, 168]. Possibilistic fusion approach is based on fuzzy set theory, but represents incomplete data (common aspect in poorly informed environments) rather than vague data [151].
- Rough set based fusion [169, 170, 171, 172]. This fusion approach deals with ambiguous data using precise upper and lower bounds, which are manipulated using classical set theory operators [151]. The approach does not require any additional information and allows dealing with data granularity [151].
- Random set based fusion [173, 174, 175, 176]. This approach uses random subsets of measurement space to deal with multiple aspects of data imperfection [151].
- Hybrid fusion approaches [177, 178, 179, 165]. This approach aims at providing a more comprehensive framework for treatment of data imperfection by deploying fusion approaches in a complementary manner [151].

Many other data fusion approaches focus on data correlation challenges. Fusion algorithms require prior knowledge to covariance of data to be able to give consistent results [151]. If data correlation problem is not addressed in the fusion approach, it can lead to biased estimation [151]. Data fusion methods that address the data correlation challenge include correlation elimination framework or the correlation presence framework. The first framework tries to eliminate data correlation before fusion either by explicit removal [180, 181, 182] or implicit reconstruction of measurements [183, 184]. The latter framework accounts for correlated data rather than eliminating it [185, 186, 187, 188, 189].

Another data fusion framework that is studied in literature deals with data inconsistency, including spurious data or and conflicting data. If spurious data is fused with correct sensor data, it can result in inaccurate estimates [151]. The majority of work in addressing spurious data focused on predicting and

eliminating outliers before the fusion process, mainly through sensor validation techniques [190, 191, 192]. The problem with sensor validation techniques is that they require prior information or failure models. Another approach for dealing with spurious data is stochastic adaptive sensor modelling [193]. This approach does not require prior information and is a general framework for treating spurious data [151]. Fusing conflicting data is also a major challenge as it leads to non-intuitive results [151], and different combination rules and corrective strategies [175, 194, 195, 196, 197, 198] have been proposed to tackle this challenge.

Data fusion approaches have been studied widely for structural health monitoring [199, 200, 201, 202, 203, 204, 205, 206, 207], as all structures (e.g. offshore platforms) face challenges due to ageing problems, surrounding environment and natural hazards. Fusion based on acceleration and gyro data is quite common in these applications, and usually involves vibration monitoring aspects [208, 209, 210, 211]. Nowadays, inertial measurement units (accelerometers and gyroscopes) are manufactured in high numbers and are available at low cost. This is the reason why they are utilised extensively in sensor fusion approaches for monitoring structural health. The main advantage of vibration based monitoring is the ability to detect different types of distributed and localised faults, using a simple, accurate and low-cost setup [209]. In this thesis, I utilise IMU sensors on the Limpets to achieve vibration monitoring using a multi-sensor data fusion approach to infer the structural integrity and condition of a conductor pipe mock-up.

Part II

A ROS-Enabled Multi-Sensing Robotic Platform for Monitoring Offshore Platforms “Limpet”

Chapter 3

The Limpet: A ROS-Enabled Multi-Sensing Robotic Platform

3.1 Introduction and Background

At the outset of this work, important design requirements were determined to help determine necessary functions, designs and properties for the Limpet. The design objectives of the Limpet were:

- The Limpet needs to be low-cost and highly manufacturable.
- The Limpet needs to monitor the extreme environmental conditions surrounding the offshore platform (temperature, pressure, humidity).
- The Limpet needs to monitor different parameters that give an indication of the structural health of the offshore assets (vibration, corrosion, overheating).
- The Limpet needs to communicate or send data to a remote station.
- The Limpet needs to switch to secondary communication methods if the primary communication method fails.
- The Limpet needs to communicate and send its sensor data to other robots on the platform.
- The Limpet needs to have protection against salt-water spray and direct sunlight.
- The Limpet needs to be able to execute monitoring tasks autonomously or manually.
- The Limpet needs to be able to carry out real-time condition monitoring.

The Limpet is a miniature, multi-sensing robotic platform designed for monitoring offshore energy platforms. The Limpet is designed to be low-cost and highly manufacturable, and thus can be deployed in large collectives to monitor different parameters in the offshore environment. The Limpet is developed as part of the ORCA Hub System, which consists of the offshore assets and a heterogeneous collection of robots (UAVs, drones, mobile legged robots etc.) interacting with the assets as shown by Figure 3.1. The Limpet comprises the sensing aspect of the ORCA Hub System. Sensing is a key element to the

ORCA Hub System as it is important in asset monitoring, fault detection, mapping, environmental monitoring and helping other robots navigate around the platform. The Limpet is integrated with Robot Operating System (ROS), which allows it to interact with other robots in the ORCA Hub System. The Limpet was designed to have robust communication, where it can use one of multiple communication systems for data transmission or communication with other agents. In this Chapter, I discuss the design, fabrication, specifications and properties of version 1 of the Limpet system. I also discuss the iteration history of the Limpet version 1 system. In this Chapter, I also demonstrate how the Limpet can be used to achieve real-time condition monitoring for offshore structures, by combining remote sensing with signal-processing techniques. I show an example of this approach for monitoring offshore wind turbines, by designing an experimental setup to mimic a wind turbine using a stepper motor and custom-designed acrylic fan blades. I use the distance sensor on the Limpet, which is a Time-of-Flight sensor, to achieve the monitoring process. This Chapter is based on my published journal paper [1], which can be found in Appendix G on Page 319.

I show how the Limpet is modelled as an instrument of sensing and measurement in Subsection 3.2.1. In Subsection 3.2.2, I discuss the system design principles of the Limpet. Section 3.2.3 details the electrical design of the Limpet version 1 system. Section 3.2.4 depicts the mechanical design of the Limpet version 1. In Subsection 3.2.5, I explain how I integrate the Limpet with ROS to enable the interaction with other robots in the ORCA Hub System. In Section 3.3, I give an overview of the different communication strategies that can be used by the Limpet, the properties and specifications of each communication strategy, and how I achieved each strategy. The rest of the Chapter is organised as follows: Section 3.4.1.1 includes a detailed description of the experimental setup I designed to conduct all my experiments on wind turbine condition monitoring; Sections 3.4.1.2 and 3.4.1.3 describe the offline and online classification of faults using the Limpet and the signal-processing components involved in these classifications, respectively; Section 3.4.1.4 gives an overview of the different communication strategies I used in this Chapter and how I managed to achieve each strategy; Section 3.4.1.5 gives an overview of the signal processing and analysis tools used in the classification; Section 3.4.2 shows the results from the offline classification and online clasiffication experiments, respectively; Section 3.4.3 discusses how the monitoring approach

can be applied to different sensors and different faults, the advantages of online classification, and mitigation of interferences in this condition monitoring work.

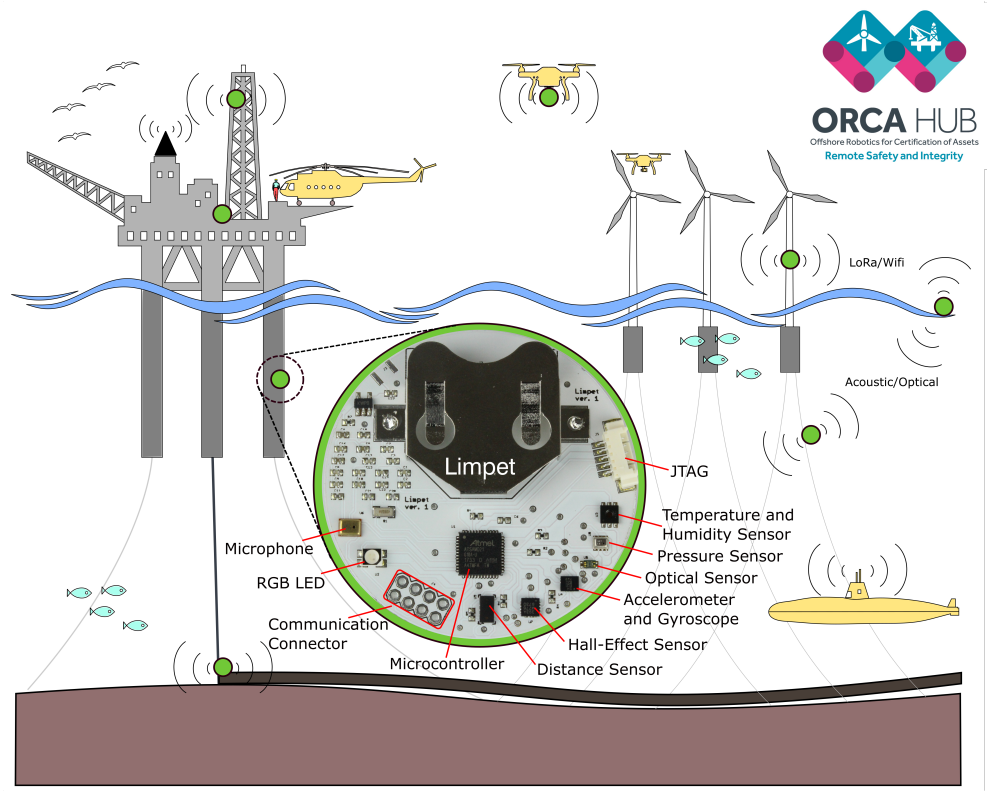

Figure 3.1: A conceptual overview of the ORCA Hub System. The Limpet version 1, a part of the heterogeneous collection of field robots that comprise the system, is shown in detail. The field robots and the Limpet communicate to each other, and the ORCA System controller, using ROS.

3.2 Design and Fabrication of the Limpet Agent Version 1

3.2.1 Instrument Model of the Limpet

The *instrument model* [212] is a simple generalised model accepted by the sensors community to describe an instrument or a measuring device. In abstract terms, an *instrument* is a device that transforms a physical variable of interest (*measurand*) into a form that is suitable for recording (*measurement*) as shown by Figure 3.2A. An example of a basic instrument is a ruler. In this case, the measurand is the length of some object, and the measurement is the number of units (meters, inches, etc.) that represents the length.

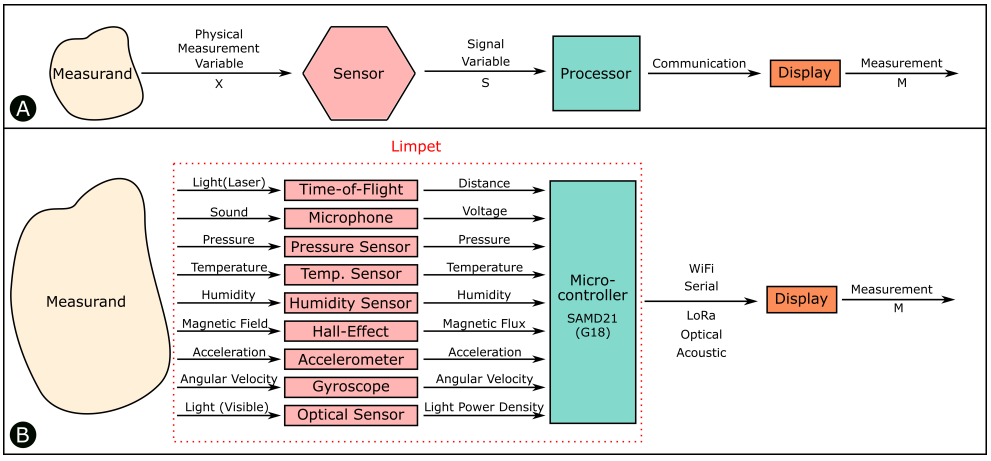

Figure 3.2: (A) Instrument Model [212]. A measurand is the physical variable of interest that is represented by a physical measurement variable. The sensor converts the physical measurement variable into a signal variable that is fed to the processor. Signal variables can be manipulated in a transmission system and transmitted to an output device that is remote from the sensor. The value displayed is the measurement. (B) Instrument model of the Limpet system showing the nine sensing modalities and their corresponding signal variables. The different physical measurement variables can be associated with several measurands. The signal variables are fed to the on-board microcontroller, which can then be transmitted by the Limpet using several communication strategies.

The measurand (physical process) is represented by an observable *physical measurement variable (X)*. There is a wide range of physical measurement variables. Common physical measurement variables include: force, temperature,

humidity, acceleration, velocity, pressure, frequency, time, length, capacitance, resistance, etc. It is important to know that the physical measurement variable (X) does not necessarily have to be the measurand, but can simply be related to the measurand. For example, the mass of an object is often measured by the process of weighing. In this case, the measurand is the mass but the physical measurement variable is the downward force the mass exerts in the Earth's gravitational field. Another example is vibration detection. A robot can detect the measurand *vibration* by measuring force or by relating the measurand to another physical measurement variable such as acceleration. Both implementations will allow the detection of vibration, however, the accelerometer is much cheaper than the force sensor. There are also other situations where a single measurement variable contains information about multiple measurands. I refer to this capability as multi-functional sensing. One example is Infrared (IR) light. IR light has been used by robots for proximity measurements and communication with other robots [213]. Receiving signals from an IR transmitter requires sensors, such as photodiodes that transduce IR light into electric signals. Therefore, communication using IR light can be considered a sensing task. Another example is the use of the magnetic flux density from a single hall-effect sensor to detect whether the robot had a successful movement, collision or rotation measurands [8].

The key element of the instrument model is the *sensor*. The function of the sensor is to convert the physical measurement variable X into a *signal variable S*. Signal variables can be manipulated in a transmission system, such as an electrical or mechanical circuit, which means that they can be transmitted to an output device that is remote from the sensor. The Limpet uses this property to be able to transmit the signal variable to a remote device using different communication or transmission systems. Typical signal variables include voltage displacement, current, force, frequency, light, pressure, etc. The output from the sensor is transmitted to a display or recording device, and the observed output is known as the measurement (M).

The Limpet can be modelled as an instrument, where each of its sensors converts a physical measurement variable into a corresponding signal variable as shown by Figure 3.2B. The signal variables are fed to the on-board microcontroller, which can then transmit the signal variable using one of several communication methods (WiFi, serial, LoRa, optical or acoustic communication).

3.2.2 System Design

The Limpet agent consists of a single PCB incorporating a microcontroller, several exteroceptive sensors, RGB LED, communication connector and on-board power source. The Limpet version 1 system overview is shown by Figure 3.3.

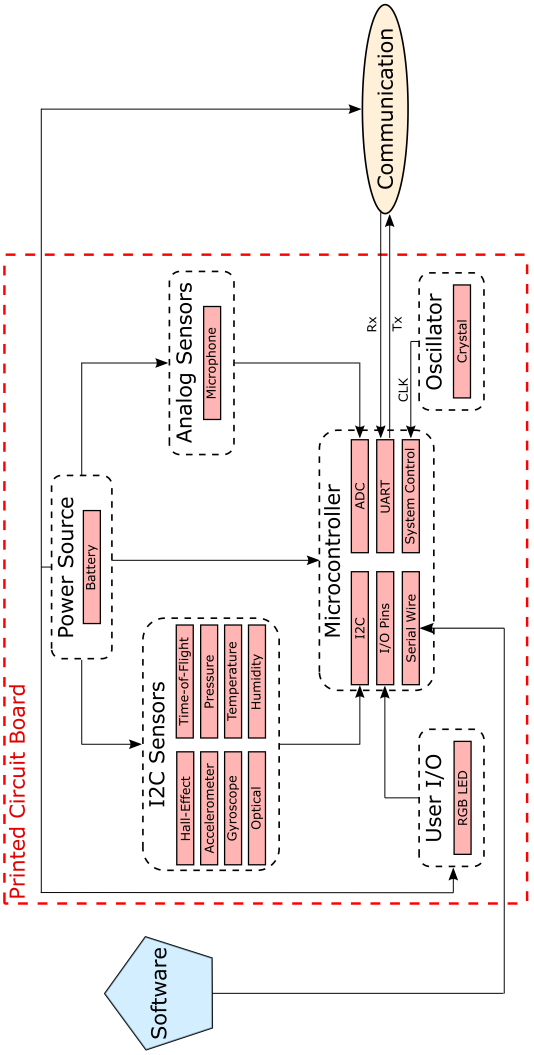

Figure 3.3: Limpet Version 1 System Overview. The Limpet possesses I^2C sensors, analog sensors, a microcontroller to process all inputs and outputs, an external crystal oscillator to adjust the clock speed, an RGB LED for local optical communication and outputing visual signals, an on-board power source (battery) and an interface to communication systems.

3.2.2.1 Choice of Sensing Modalities

The main purpose of the Limpet is to monitor the offshore assets and the environmental conditions surrounding them. Examples of the environmental conditions that need to be monitored are ambient temperature, ambient pressure, ambient light intensity, humidity level, toxic and explosive gases. Some of the characteristics of offshore assets that will need to be monitored by the Limpet include corrosion, vibration, thermal stress, fractures, fatigue loading, and over-heating. I equipped the Limpet with nine exteroceptive sensing modalities. The sensors incorporated in the Limpet are temperature, pressure, humidity, optical, distance, sound, magnetic field, accelerometer and gyroscope. The choice of sensing modalities were influenced by a literature survey that I conducted on parameters relevant to offshore environments and monitoring of offshore structures. Also, the discussions I had with the industrial partners involved in the ORCA Hub project on the parameters that are interesting to monitor in offshore platforms had a major influence on the choice of sensing modalities on the Limpet system. Table 3.1 describes how the physical measurement from each sensor on the Limpet can be related to different measurands on offshore platforms. The table is based on the instrument model described in Figure 3.2. It gives an example of a few potential measurands, and not all the measurands possible with each sensor, and it gives an overview of the multi-functionality that can be achieved with each sensor on the Limpet.

Sensor	**Physical Measurement Variable**	**Signal Variable**	**Measurands**
Accelerometer	Acceleration	Acceleration	Inclination, Collision, Vibration, Free-Fall Detection, Movement Acceleration
Gyroscope	Angular Velocity	Angular Velocity	Tilt Detection, Orientation
Temperature	Temperature	Temperature	Ambient Temperature, Over-heating, Fire Detection
Humidity	Humidity	Humidity	Relative Humidity
Microphone	Sound	Voltage	Speech Recognition, Noise Cancellation, Audible Fault Detection
Pressure	Pressure	Pressure	Ambient Pressure
Hall-Effect	Magnetic Field	Magnetic Flux Density	Locating Pipelines, Corrosion Detection
Optical	Light (Visible)	Light Intensity	Ambient Light Intensity, Local Communication, Colour Detection
Distance (Time-of-Flight)	Light (Laser)	Distance	Fault Detection, Proximity, Collision Detection, Object Identification

Table 3.1: The different physical measurements from each sensor on the Limpet and their relation to different possible measurands.

3.2.2.2 Programming the Limpet

The Limpet PCB has an on-board programming port (JTAG). I programmed the Limpet using a SEGGER J-Link programmer together with a JTAG Adapter (Olimex ARM-JTAG-20-10). The connection between the JTAG Adapter and the programming port on the Limpet is shown by Figure 3.4. I programmed the Limpet in C/C++ using Atmel Studio 7. The most recent version of the codes can be found in Appendix N on Page 457. The main.c file for Limpet

version 1 includes a variety of header files that give access to specialised functions, custom libraries and custom-written sensor libraries. The source and header files of the different sensors can also be found in Appendix N. I used the standard Universal Asynchronous Receiver-Transmitter (UART) protocol for communication. The UART protocol uses a high idle line, which is pulled low at the start of a message.

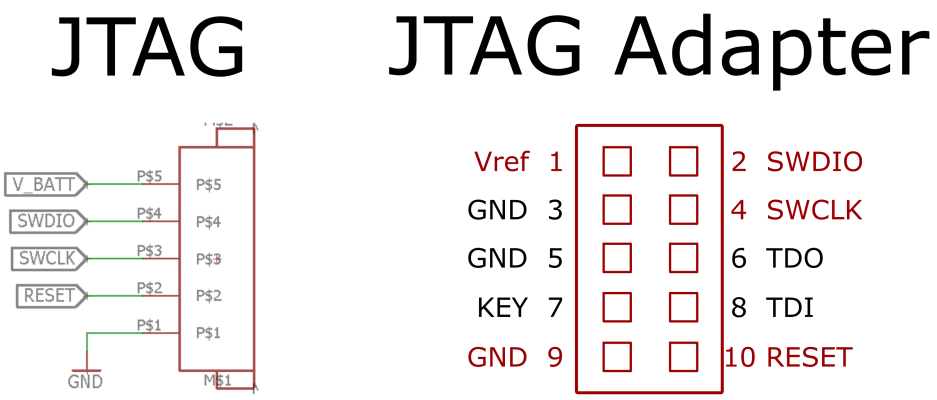

Figure 3.4: Connection between JTAG Adapter and programming port on the Limpet.

3.2.2.3 Cost and Dimensions of the Limpet

Cost and functionality are the most important factors considered when developing robots. These properties have a great effect on the scalability of a system to large number of agents. Any electronic component added to a robot will increase the cost as well as occupy space on the printed circuit board. Thus, it is beneficial to find specialised components for the required tasks.

Electronic components can be ordered in small or large quantities from suppliers. The batch quantities are usually supplied as 10, 50, 100, 500 or 1000 components, where the price decreases as the batch quantity increases. Thus, I always look for components that are lowest in cost but still satisfy the functional requirements. It is also good practice to compare the components across different suppliers to avoid shortages of components and to find the lowest cost for the component.

My rationale behind the Limpet system design was to keep the costs as low as possible without sacrificing functionality. The Limpet version 1 has a diameter of 50 mm, a height of 7 mm and weighs 17 g with, and 10 g without, the battery. I designed the Limpet to have a size and weight ideal for ease of fabrication, manufacturing and assembly. The total cost of electronic components used in the design of the Limpet version 1 is about £22. The bill of materials for Limpet version 1 can be found in Appendix B on Page 253.

Generally, any Integrated Circuit (IC) device will need additional components for its operation, and these components are usually found in the datasheet. The additional components are often smoothing capactiors, which ensure a stable voltage supply by smoothing or evening out the fluctuations in the voltage signal. Capacitors can also filter high frequency current that can damage the IC device. I usually look for components that do not require a large number of additional components as the circuit becomes more bulky, takes more space and increases in cost.

3.2.2.4 Bio-Inspiration

The Limpet system is inspired by patella vulgata [214], commonly known as Limpet, which is an aquatic snail with a conical shell that lives on rocks on land or in the sea. The patella vulgata has a strong shell that protects it from the external environment and predators. It can alternate between different adhesion mechanisms depending on the required period and strength of adhesion [78]. Suction is the primary adhesion mechanism used by the patella vulgata, where the suction force can reach up to 25N [215]. If the patella vulgata needs to attach for a longer time, it has been found that some of them use a stronger adhesion mechanism that is based on glue. It can alternate between suction and glueing depending on its activity and the tides [216].

The shell of the patella vulgata also plays an important role in the adhesion mechanism. The patella vulgata clamps its shell to increase friction with the surface and prevent any dislodgements caused by shear forces [215]. Shell clamping against the surface makes use of the vertical adherence strength of the suction mechanism to create a frictional force that resists the shear force of hydrodynamic drag [215]. The patella vulgata have rows of teeth that they use to scrape over rocks to feed. The teeth have been found to be the strongest

known biological material, with a tensile strength of 3 to 6.5 GPa [217]. The teeth consist of composite nanostructures with fractions of reinforcing geothite nanofibers within a softer chitin matrix [217]. The patella vulgata has an optic vesicle at the end of its tentacles that provides sensory function, and allows it to sense light and darkness levels [214].

I developed my bio-inspired system, the Limpet, for inspection and monitoring of offshore energy platforms. I integrated an adhesion mechanism on the Limpet system. I used permanent magnets for version 1 of the Limpet system, and a suction mechanism for version 2 of the Limpet. I also developed different protective cases for the Limpet versions, which act as a shell that can protect the circuitry from the harsh offshore weather conditions, as well as helping with other functions that the shell is involved in such as clamping to prevent shear forces.

3.2.3 Electrical Design

3.2.3.1 Design of the Control Electronics

The Limpet version 1 consists of a single two-layer PCB and a detachable lithium-ion coin cell battery. I designed a fully integrated PCB incorporating a low–power microcontroller (ATSAMD21G18A), RGB LED (LTST-N683EGBW), battery holder (BK-877) for a rechargeable Li-ion battery (LIR2477), charging IC (MCP73812), charger connector, programming port [JTAG] (Molex 532610571), and a communication connector as shown by Figure 3.1. The PCB includes several exteroceptive sensors, which are: temperature and humidity sensor (Si7006), inertial measurement unit (IMU) [accelerometer and gyroscope] sensor (LSM6DS3), optical sensor (VEML6040), sound sensor (SPU0414HR5H-SB), 3-Axis magnetic sensor (MLX90393), pressure sensor (BMP280), distance sensor (VL53L0). The communication connector is connected to the UART of the microcontroller. Therefore, I can use this connector to connect the Limpet to different communication systems. I designed the Limpet version 1 to use a single PCB for control, communication and sensing.

Microcontroller

I used an ATSAMD21G18A as a microprocessor for the Limpet. The SAMD21 microcontrollers are a series of low power, high performance microcontrollers that use the 32-bit ARM Cortex-M0+ processor. The SAMD21 microcontrollers operate at a maximum frequency of 48 MHz. The SAMD21G18 used on the Limpet features a 256KB in-system self-programmable Flash and 32KB SRAM memory. It also features six Serial Communication Interfaces (SERCOM), each configurable to operate as USART with full-duplex and single-wire half-duplex configuration, Inter-Integrated Circuit (I^2C) Bus up to 3.4MHz, System Management Bus (SMBUS)/Power Management Bus (PMBUS), Serial Peripheral Interface (SPI), or Local Interconnect Network (LIN) slave. The SAMD21G18A microcontroller costs £2.44 in small quantities (1s) and £2.01 in large quantities (100s) when purchased from *Digikey Electronics*. The SAMD21 also has the advantage of intelligent and flexible peripherals, where the peripheral functions can be multiplexed across the microcontroller pins. Figure 3.5 shows a schematic of the ATSAMD21G18A that I embedded in the Limpet system and the additional components (smoothing capacitors) required. The SAMD21 series have also been the choice of microprocessor for the new Arduino development boards including the Arduino Zero and Arduino M0 Pro. As such, it is easy for beginners to program the SAMD21 using the Arduino IDE by flashing any purchased SAMD21 microcontroller with the Arduino Bootloader and using a USB connection. This feature can make the Limpet an easy-to-use device if it becomes an open-source platform, where the only required addition to the Limpet PCB would be a USB port.

Sensors

Sensors are transducers that convert physical quantities or measurements from the environment to electrical signals. There are two different types of sensors: analog and digital sensors. Analog sensors produce a continuous analog output signal that is proportional to the measurand. Digital sensors on the other hand convert the measured signal into a digital output signal inside the sensor itself, and then transmits the digital signal. Digital sensors are usually preferred over analog sensors, as they are less susceptible to noise (undesirable variation in voltage). Small variations in the voltage of an analog signal can

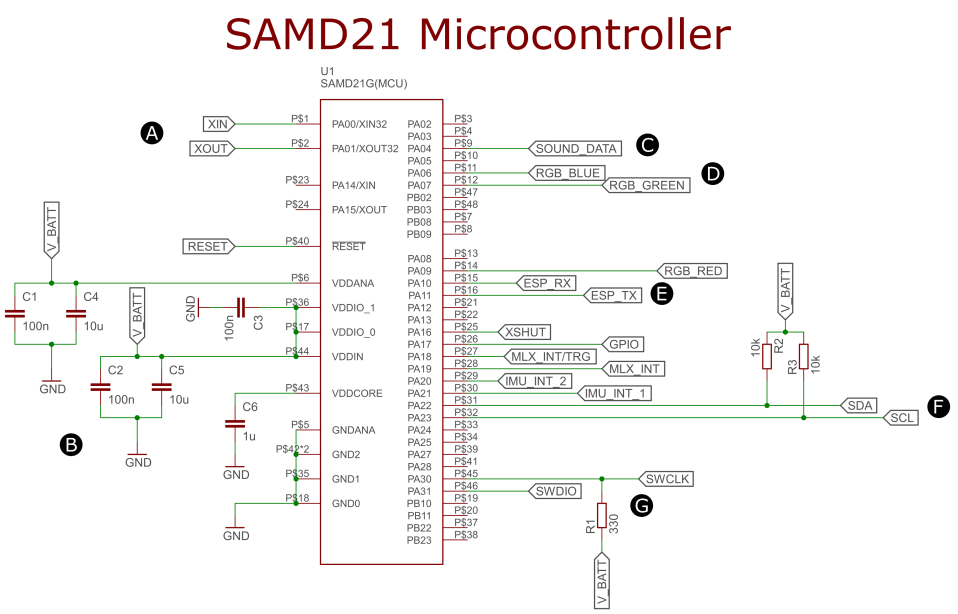

Figure 3.5: Schematic of the SAMD21G18 microcontroller used on the Limpet System. (A) Crystal Oscillator. (B) Decoupling Capacitors. (C) Sound Sensor. (D) RGB LED. (E) Communication Connector. (F) I^2C Bus. (G) JTAG Connector.

result in significant errors during the processing stage. Thus, digital sensors have a higher accuracy and throughput. Analog sensors are usually connected to analog-to-digital converters on the microcontroller. Digital sensors are usually connected to the I^2C bus or SPI on the microcontroller. There are different advantages for using the different bus systems on the microcontroller for digital sensors. The I^2C bus requires less wiring than the SPI bus, but it is slower in reading out sensor data. Most audio sensors are connected to a different bus, an Inter-IC Sound (I^2S). The I^2S is designed to handle audio data separately from clock signals. The sensors on the Limpet, except for the microphone, are controlled by the microcontroller through the I^2C bus. A schematic of the sensors is shown by Figure 3.6.

The microphone on the Limpet is an omnidirectional Micro-Electro-Mechanical System (MEMS) sensor, with an analogue output and a frequency range of 100 Hz to 10 KHz. The sensor has a signal-to-noise ratio and a sensitivity at 1KHz of 59 dB and -22 dBV, respectively. The microphone has a size of 3.76 x 2.95 x 1.1 mm with an acoustic port that is 0.5 mm in diameter. The distance sensor on the Limpet is a Time of Flight (ToF) sensor, which measures

the distance to an object based on the time difference between emission of a signal and reflection back to the sensor. This distance sensor is the smallest range sensor on the market today. It is a ToF laser-ranging module that can measure sub-mm distances for a range between 0 and 2.2 m. The distance sensor has a size of 4.4 x 2.4 x 1 mm. The optical sensor on the limpet can sense red, green and blue power density and ambient light intensity. It incorporates photodiodes, amplifiers and analog/digital circuits into a single chip. The optical sensor has a size of 2 x 1.25 x 1 mm and adopts a technology that allows it to achieve the closest ambient light spectral sensitivity to real human eye responses. The temperature and humidity sensor on the limpet are included in a single chip. The sensor integrates humidity and temperature sensor elements, an analog-to-digital converter, signal processing and calibration data. The sensor is factory-calibrated and the calibration data is stored in the on-chip non-volatile memory, which ensures that the sensors are fully interchangeable, with no recalibration or software changes required. The sensor has a size of 3 x 3 x 0.75 mm. The pressure sensor on the limpet is an absolute barometric pressure sensor based on piezo-resistive technology. It has a size of 2.0 $\times$ 2.5 x 0.95 mm and provides high accuracy and long term stability. The hall-effect sensor on the limpet is a 3-axis magnetometer and it has an on-board non-volatile memory to store calibration data on-chip. It has a size of 3 x 3 x 0.9 mm. The accelerometer and gyroscope on the limpet are included on a single chip (IMU sensor). The LSM6DS3 has a full-scale acceleration range of $\pm 2/\pm 4/\pm 8/\pm 16$ g and an angular rate range of $\pm 125/\pm 250/\pm 500/\pm 1000/\pm 2000$ dps. The sensor is highly robust to mechanical shock and has a size of 2.5 x 3 x 0.83 mm.

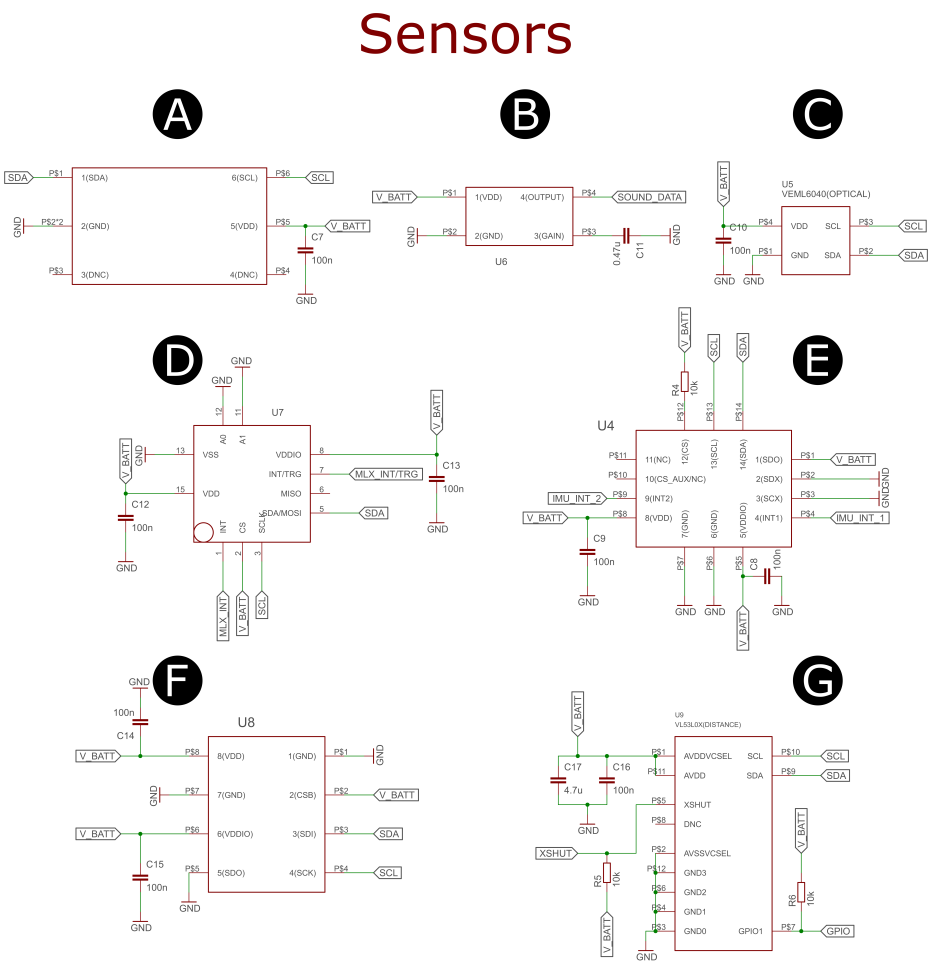

Figure 3.6: Schematic of the sensors used on the Limpet system. (A) Temperature and Humidity Sensor. (B) Sound Sensor. (C) Optical Sensor. (D) Hall-Effect Sensor. (E) IMU Sensor (Accelerometer and Gyroscope). (F) Pressure Sensor. (G) Distance Sensor.

RGB LED

The LED on the limpet is a compact tri-color RGB LED that has a size of 3.2 x 2.8 x 2.1 mm and costs £0.106 in large quantities (100s) when purchased from *RS Components*. The LED has a diffused lens and the RGB elements allow the creation of any colour within the visual spectrum, including white light. Each element (red, green, blue LED) can be addressed individually by the microcontroller as shown by the schematic in Figure 3.7. The RGB LED has a common anode configuration, where assigning a low value to any of the

LEDs from the microcontroller will turn it on. Each LED can be pulse-width modulated to different levels of intensity.

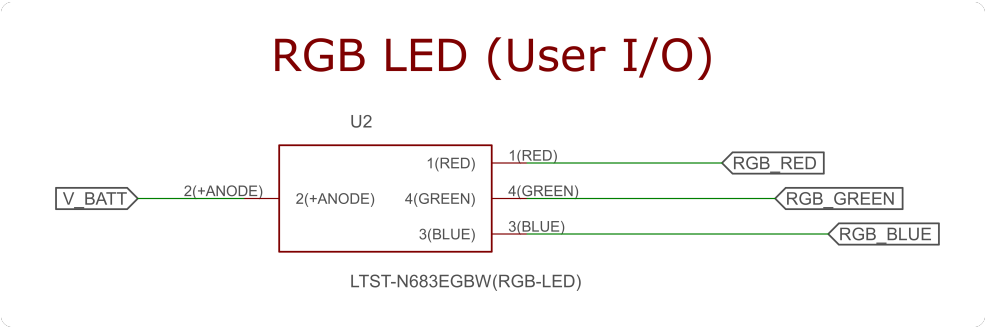

Figure 3.7: Schematic of the RGB LED used on the Limpet system, where the anode is connected to the voltage supply (battery) and the cathodes are connected to the microcontroller.

Crystal Oscillator

The Limpet PCB includes an external crystal oscillator that provides the clock signal to the microcontroller. The crystal has dimensions of 3.2 x 1.5 x 0.65 mm and costs £0.902 in small quantities (1s) and £0.676 in large quantities (100s). The crystal used has a frequency of 32.768 kHz and is highly stable. The application of the Limpet includes several sensors which use the clock signal in their operation and data transmission to the microcontroller. Thus, high stability of the oscillator is a very important parameter in the Limpet design.

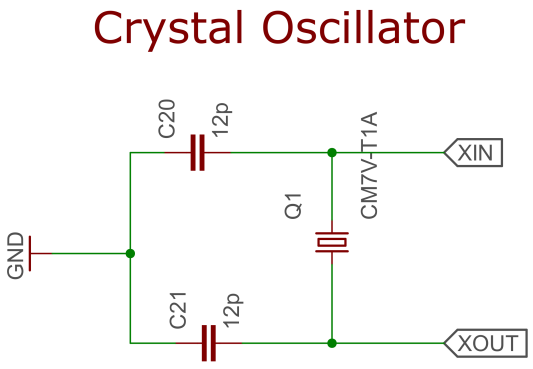

Figure 3.8: Schematic of the crystal oscillator used on the Limpet system.

3.2.3.2 Power System

The Limpet version 1 is powered by a 3.6V 160 mAh lithium-ion coin cell battery that fits into an SMD coin cell retainer. The lithium-ion battery (LIR2477) is a rechargeable battery and has a diameter of 24.5 mm. The battery can be recharged by using a 6Vdc plug-in power supply. I embedded a battery charging IC on the Limpet version 1 PCB, which means that the battery does not need to be removed from the robot to be charged. I included header pins on the PCB for connecting the power supply to recharge the battery. When the charging IC receives 6V dc, it will start charging the on-board battery until the battery is full. Figure 3.9 shows a schematic of the battery charging circuit on the Limpet version 1 PCB.

The Limpet has a battery life @160 mAh of 0.87 to 1600 hours. I calculated the minimum battery life by assuming the Limpet has all the sensors, RGB LED, microcontroller and communication continuously on. The Limpet will consume approximately 182.9 mA, with a power consumption of 658.44 mW (primary communication consumes 135 mA (486 mW), RGB LED consumes 20 mA (72 mW), sensors consume 20.9 mA (75.24 mW), microcontroller consumes 7 mA(25.2 mW)), which allows for a battery life of about 0.87 hours (52.2 minutes). I calculated the maximum battery life by assuming the Limpet is in sleep mode, where it consumes an average current of 0.1 mA, with a power consumption of 0.36 mW. In this mode, the battery life of the Limpet can reach about 1600 hours (67 days).

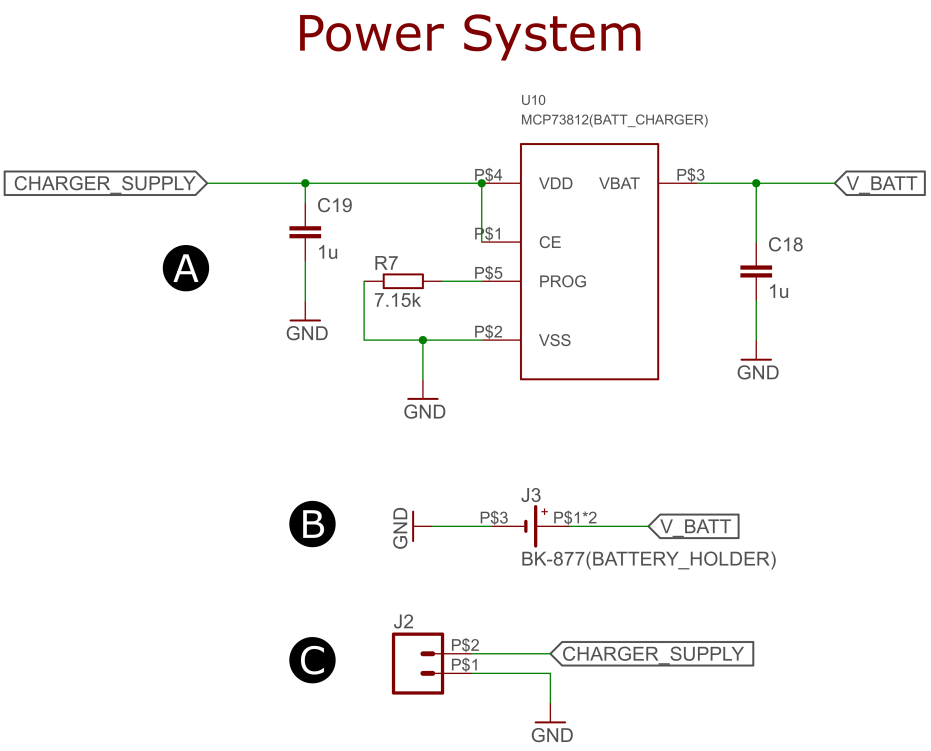

Figure 3.9: Schematic of the power circuit used on the Limpet system.

3.2.4 Mechanical Design

3.2.4.1 Fabrication of the Printed Circuit Board

The Limpet version 1 PCB went through five different stages in the fabrication process. In stage 1 of the fabrication process, I designed printed circuit boards for each individual component on the Limpet and fabricated them using the LPKF Protomat S63 milling machine. Each component was soldered onto its respective PCB and tested individually. Once each component is tested and the code for that component is developed, all the PCBs were connected together on a breadboard to create the Limpet circuit as shown by Figure 3.10.

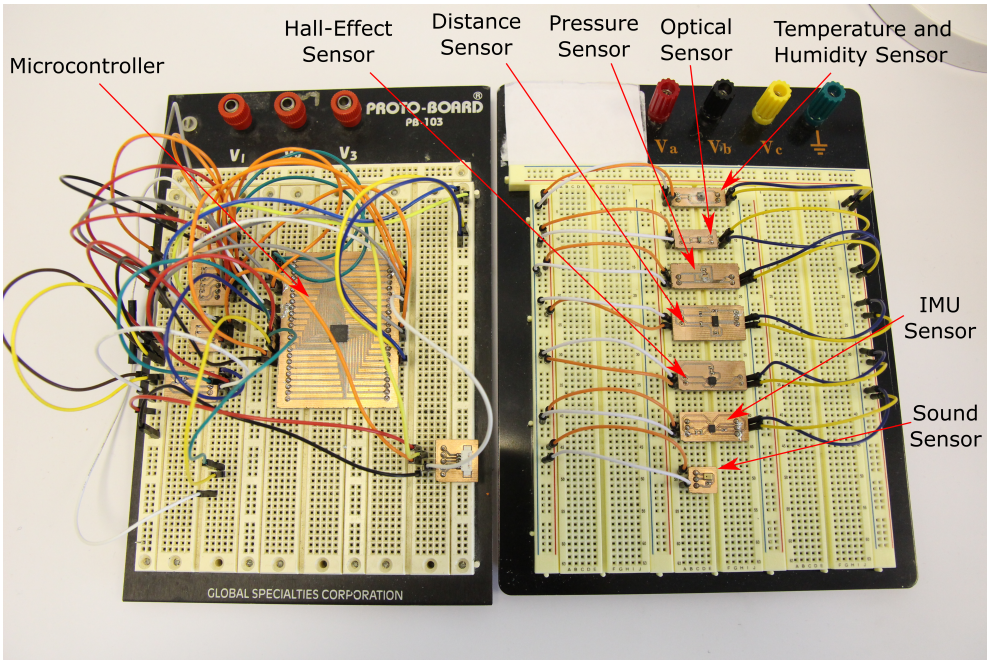

Figure 3.10: A picture showing the first stage of the Limpet version 1 PCB development, where each individual component was soldered onto its custom-designed PCB and the PCBs were connected together on a breadboard. The breadboard on the left contains all the power and computation modules, whereas the breadboard on the right contains all the sensors.

The second stage of the fabrication process was to design the Limpet PCB and fabricate it on the LPKF Protomat S63 to test it. The Limpet PCB that I fabricated in-house is shown by Figure 3.11.

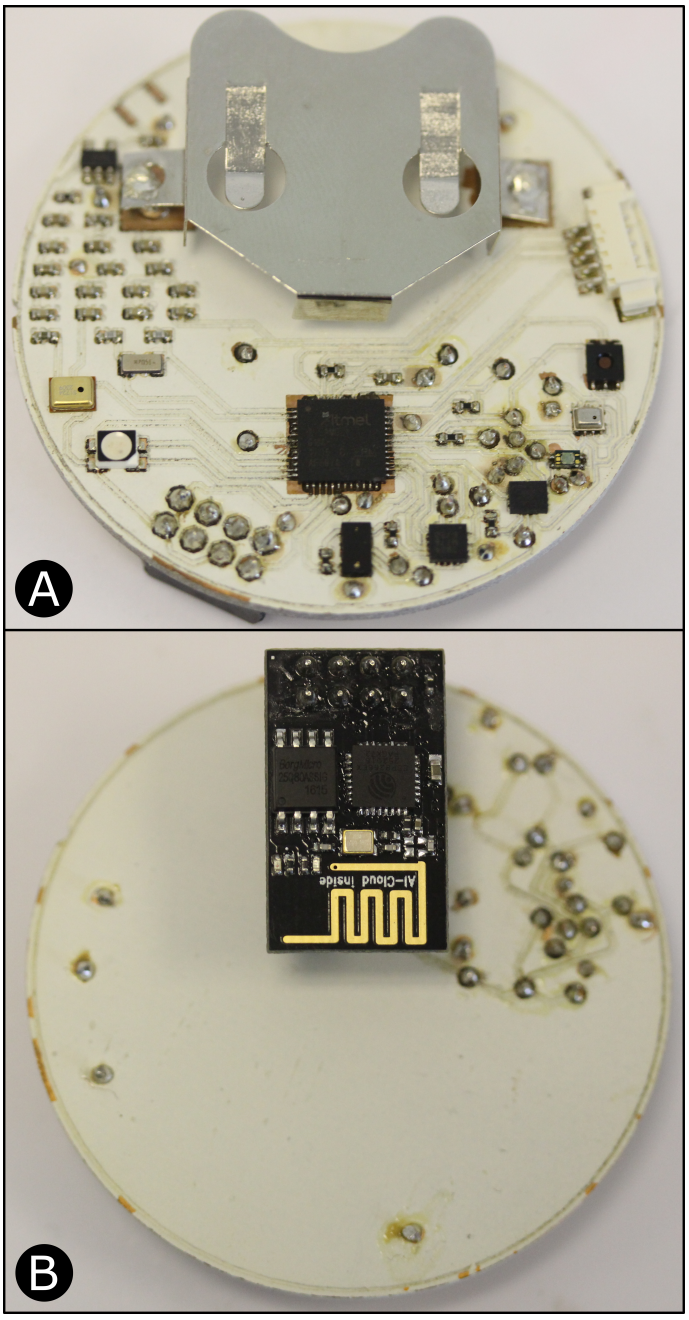

Figure 3.11: Picture of the (A) Top Side, (B) Bottom Side of the Limpet version 1 PCB fabricated in-house.

The third stage of the process is to solder all the components on the Limpet PCB. I soldered the components on the PCB using a reflow soldering process. In this process, I cut solder paste stencils from vinyl using a Laser Cutter (Epilog Laser Fusion 32). Then, I stick the stencil on the PCB and apply solder paste on the stencil and PCB. I remove the stencil and manually place the components on their respective pads. The PCB is then placed in an oven to reflow the solder. Figure 3.12 shows the Limpet PCB with the vinyl stencil.

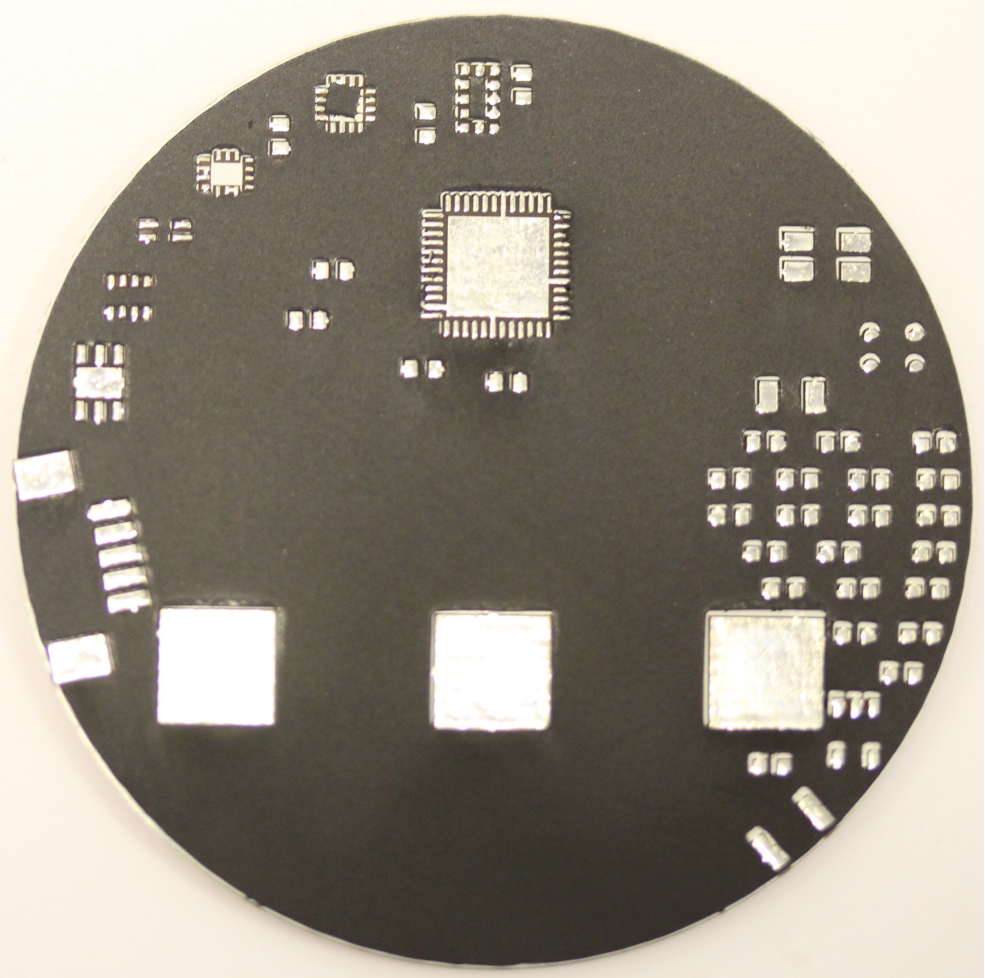

Figure 3.12: Picture of the Limpet PCB with the solder stencil.

After the Limpet PCB developed in-house was tested, I ordered several Limpet PCBs fabricated on double-sided Cu-FR4-Cu 0.1 mm boards from an external company called Minnitron Ltd. (Kent, UK). The final stage after receiving the PCBs from the company is soldering the components using the same solder reflow process. Figure 3.13 shows the unsoldered PCBs fabricated by the company. I designed all PCBs using Eagle PCB Design Software and purchased all electronic components from RS Components, Mouser Electronics and Digi-key Electronics.

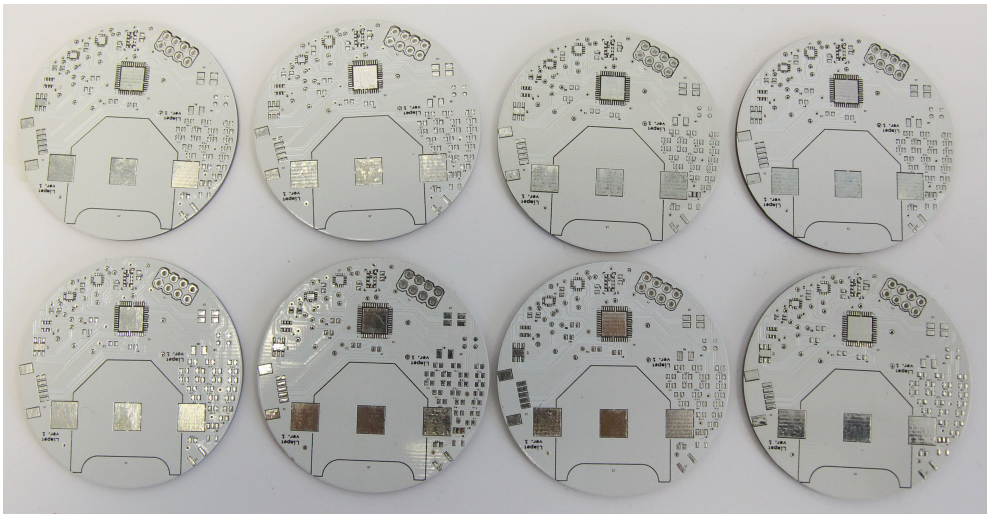

Figure 3.13: Picture of the unsoldered Limpet PCBs fabricated by the external company.

3.2.4.2 Design of the Protective Housing

The Limpet could be used in a wide variety of areas, which leads to a wide range of temperatures that the components have to be tolerant to. The datasheets of the sensors used on the Limpet show that they can be used in a wide range of temperatures. I designed the Limpet mainly for the North Atlantic region which has a water temperature range of between 6°C and 17°C. This temperature range was within the allowed range of all the components used on the Limpet. The sensors used on the Limpet also have a wide humidity range. Some of the sensors used are splash resistant such as the IMU, hall-effect, and optical sensors. If I were to deploy the Limpet for field tests, it would require encapsulation to ensure resistance to extreme temperatures, humidity conditions and saltwater spray. The casing would have to comply with the regulations used in the specific area it would be deployed in.

Figure 3.14 shows one example of a protective housing (shell) used with the Limpet version 1 when it is used for environmental monitoring or remote monitoring of equipment. I fabricated this protective housing from an optically clear, semi-rigid polyurethane resin. I developed the housing by casting the resin in a 3D printed mould. I did not cover the surfaces of the sensors by resin to keep them exposed to the external physical measurement variables. Figure 3.15 shows another protective housing used with Limpet version 1 when it is used to closely monitor status of equipment or pipelines. I fabricated the protective housing from polydimethylsiloxane (PDMS) by casting it in a 3D printed mould. I chose bright colours for the shell to be able to easily locate the Limpets in offshore platforms, where the surfaces are mostly metallic and rusty. The protective housing acts as a shell that can protect the circuitry from the harsh offshore weather conditions. I embedded permanent magnets in both shells to enable the Limpet to attach to metallic surfaces.

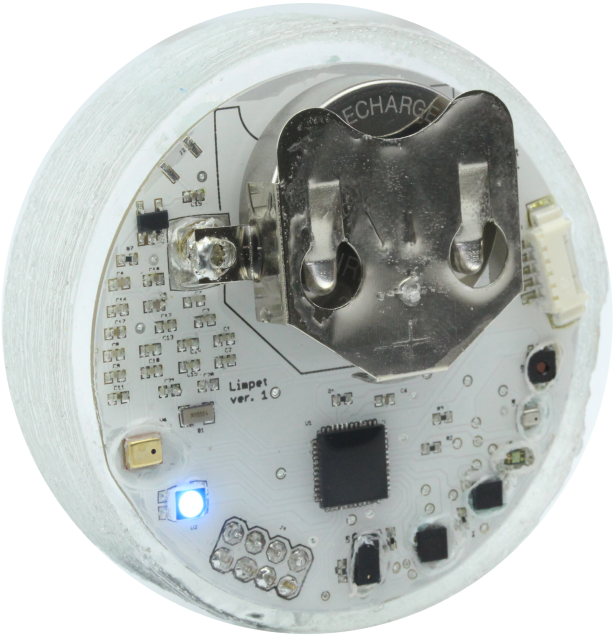

Figure 3.14: A picture of a Limpet in a protective housing made of clear polyurethane resin.

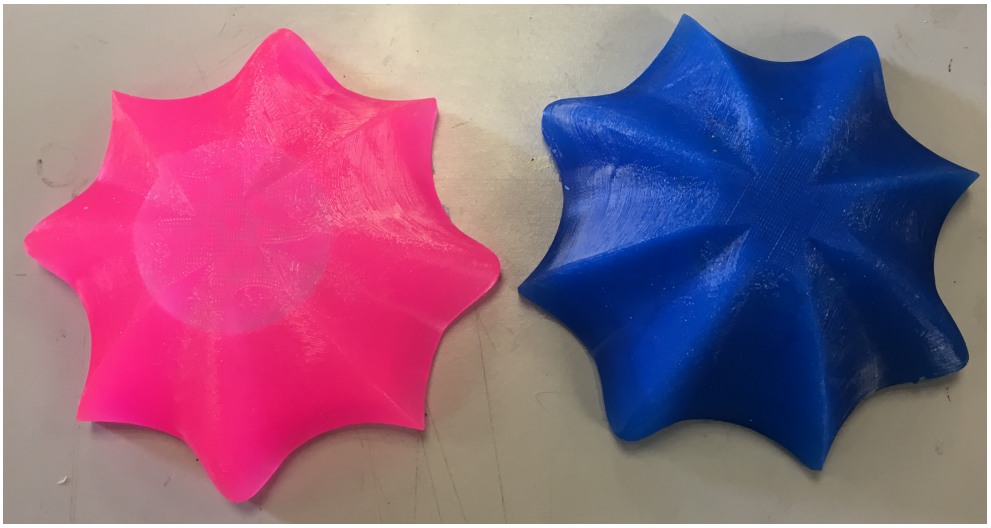

Figure 3.15: A picture of a protective housing for the Limpet made of polydimethylsiloxane mixed with silicone colour pigments.

3.2.4.3 Ease of Robot Fabrication

I designed the Limpet version 1 explicitly for manufacturability; it consists of a single PCB and therefore mass manufacture is a simple case of placing a batch order with a PCB foundry. I ordered 12 unassembled Limpet version 1 PCBs, shown by Figure 3.13, from a company called Minnitron. The Limpet PCB consists of surface mount components, except for the communication connector, and can be autonomously populated with pick-and-place machines at the point of manufacture. Systems that are made of a single PCB with mostly surface components allow for scaling up to huge collectives of agents easily without sacrificing functionality [7]. Assembly of one Limpet takes seconds as it is a matter of only connecting the coin cell battery. Once the battery is connected, there is no need to remove the battery from the Limpet again as it can be charged on-board. As a result of the Limpet being highly manufacturable and easy to assemble, it is easy to mass-produce Limpet agents and deploy them in huge collectives.

3.2.5 ROS Interface

ROS is a robotics middleware (collection of software frameworks) that provides libraries and tools to help software developers create robot applications [218]. It provides services such as hardware abstraction, device drivers, libraries, visualizers, low-level device control, implementation of commonly used functionality, message-passing, package management, and more [218]. ROS-based processes are represented in a graph architecture, where the processing occurs in nodes that can receive, send and multiplex data about sensors, control, state, planning, actuators, and other messages.

I can interface the Limpet with ROS, and the architecture of this interface is shown by Figure 3.16A. The sensor data are fed into the microcontroller, and the microcontroller then sends out the data to a converter. The converter is a custom-written python script on the remote PC, which receives the data from the Limpet through one of the communication strategies and converts this data into a ROS protocol. I can publish this data to a ROS topic, and any node running ROS can subscribe to that topic to read the sensor data. The integration of the Limpet with ROS is essential, as it allows the Limpet to communicate with other robots that constitute the ORCA Hub system. The

Limpet is designed to be one part (sensing) of the larger ORCA Hub System, where the system aims at realizing complex tasks that would not be possible with a single robot system. The different sensors on the Limpet have different physical measurement variables. When these measurement variables are fed into the microcontroller, it adds a label to the data to differentiate data from the different sensors (e.g. distance, temperature, pressure, etc). The data are published to the relative ROS topic based on this label as shown by the overview in Figure 3.16B. ROS nodes can subscribe to relevant topics to gain access to the sensor data. Figure 3.16C depicts an example of one of the results from integrating the Limpet with ROS. It shows a screenshot of the data published to the distance ROS Topic, and a graph of the distance measurement from the ROS Topic.

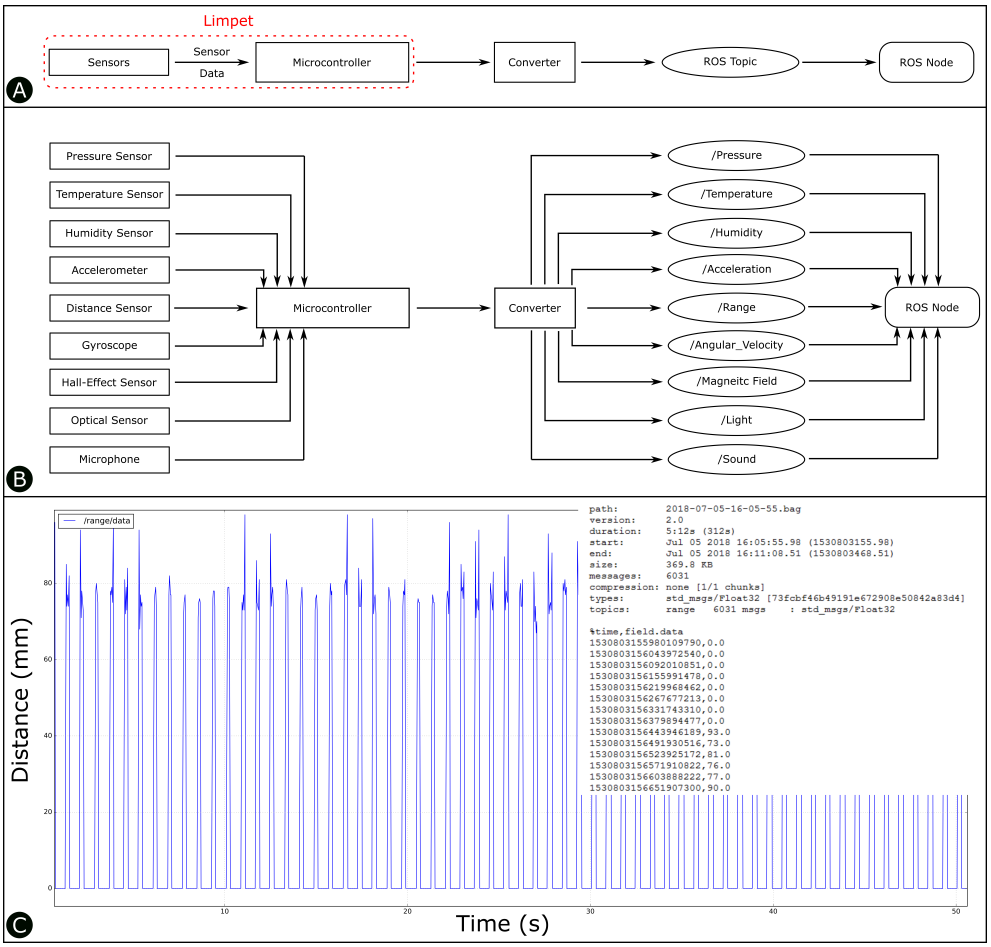

Figure 3.16: (A) Architecture of the Limpet interface with ROS. (B) An overview of the ROS Interface with the Limpet showing how the different physical measurement variables from the different sensors are published to different ROS Topics. (C) A figure showing a screenshot of the data published to the distance ROS Topic, and a graph of the distance measurement from the ROS Topic.

3.3 Design of the Communication Mechanisms and Communication Failover

I designed the Limpet to have robust communication. It can transmit data to a PC or other nodes using one of several different communication systems, including WiFi, serial, LoRa, optical and acoustic communication. WiFi and serial communication do not allow for communication with neighbouring Limpets, unlike LoRa, optical and acoustic communication.

The primary communication method of the Limpet is WiFi. I incorporated a communication fail-over mechanism on the Limpet. If the primary communication method (WiFi) fails for any reason, the functions of the WiFi are assumed by a secondary communication module, which makes the system more fault-tolerant and robust in communication and data transmission.

Figure 3.17 gives an overview of the communication strategies and how they are achieved. Serial and WiFi communication are high-bandwidth communication, and as such, I can send the sensor data from the Limpet continuously in real time to the PC. The data can then be analyzed on the PC using analysis tools such as MATLAB. In this regard, the Limpet is only making a measurement using the sensors and transmitting it instantly to the PC without doing any processing on the data, which means serial and Wi-Fi communication are not computationally demanding on the Limpet.

LoRa, optical and acoustic communication have a much lower communication bandwidth than serial and Wi-Fi communication. Thus, when these communication technologies are used with the Limpet, their limited bandwidth limits the ability to send the sensor data continuously in real time to the PC. Therefore, if the dataset is large, processing and analysis of the data need to be done on the microcontroller before transmission to allow for only small payloads of data to be transmitted. This on-board processing and analysis approach requires higher computational power than serial and Wi-Fi communication.

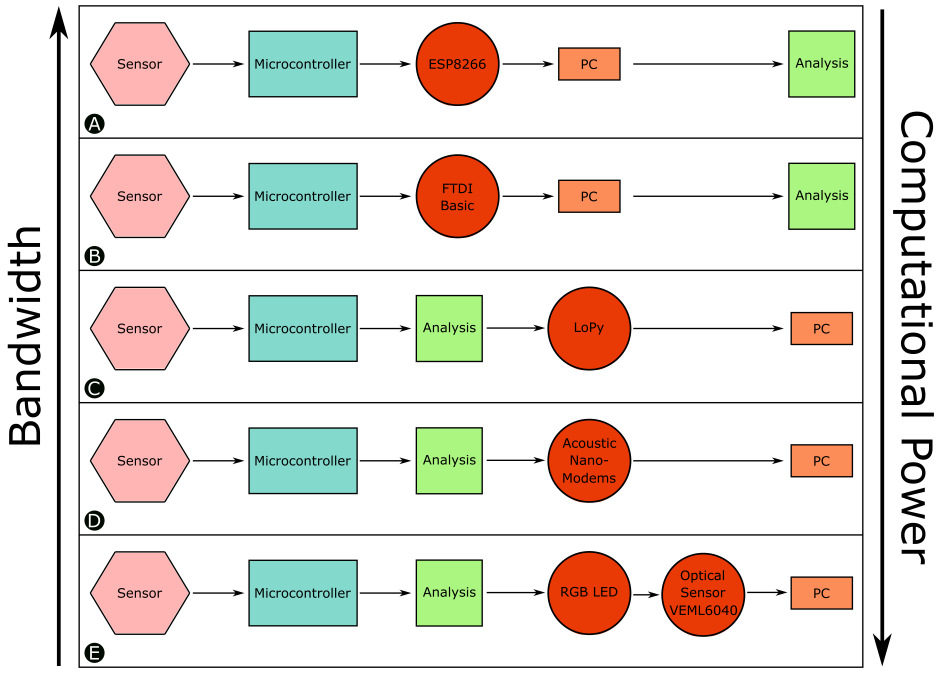

Figure 3.17: Overview of the communication strategies. The communication bandwidth decreases and the on-board computational power increases as we move from WiFi to acoustic communication. A) Overview of components involved in WiFi communication. In this communication strategy, the sensor data is fed into the microcontroller, which is then sent in real time to the PC. Transmission of data over WiFi is achieved using the ESP8266, a SOC WiFi module with integrated TCP/IP protocol stack that gives the Limpet access to the WiFi network. The data can then be analysed on the PC. B) Overview of components involved in serial communication. Similar to WiFi communication, the sensor data is fed into the microcontroller, which is then sent in real time to the PC. Transmission of data using serial communication is achieved using SparkFun's FTDI Basic Breakout - 3.3V. The FTDI Basic is a serial to USB converter. The Limpet transmits the data through the FTDI Basic, which can be recorded on the PC using a terminal program and analysed later. C) Overview of components involved in LoRa communication. LoRa has a much lower communication bandwidth than serial and WiFi communication, thus, processing and analysis need to be done before transmission to allow for only small packets of data to be transmitted. This on-board processing and analysis requires higher computational power than serial and WiFi communication. To transmit data via LoRa, I used the LoPy, which is a MicroPython enabled WiFi, Bluetooth and LoRa development board. D) Overview of components involved in optical communication. Optical communication has a lower bandwidth than LoRa. The processing and analysis also need to be done before the transmission of data. In this case, the transmission of data was achieved using the on-board RGB LED and the optical sensor. The data from the LED are transmitted by pulse-width modulating the LED to different levels. The optical sensor was used to read the light intensity and colour power density to interpret the data transmitted using the RGB LED. E) Overview of the components involved in acoustic communication. The acoustic communication is achieved using acoustic nano-modems developed by University of Newcastle under the EPSRC USMART Project. The transmission data rate is low and, thus, the processing and analysis needs to be done on the Limpet before transmitting the data.

3.3.1 WiFi Communication

In order to use WiFi for transmission of data from the Limpet to a node (e.g. PC), I incorporated an ESP8266, which is a low-cost System-on-a-Chip (SOC) WiFi module with integrated TCP/IP protocol stack capable of giving any microcontroller access to the WiFi network, on the Limpet. I use a software development kit (SDK), known as NodeMCU, to program the chip directly. NodeMCU is a lua-based firmware, where lua is lightweight multi-paradigm programming language that is used for embedded applications. The code for programming the ESP8266 can be found in Appendix N. I have also developed a tutorial on how to set up and program the ESP8266, which can be found in Appendix E. To send and receive the messages between the ESP8266 and the PC, I use Eclipse Mosquitto [219], which implements a messaging protocol known as Message Queuing Telemetry Transport (MQTT). MQTT is a lightweight publish/subscribe messaging protocol used for remote communication as shown by Figure 3.18. In this case, the Limpet is the publisher and the PC subscribes to the MQTT topic to receive the Limpet data. The received data can then be plotted in a real-time basis using Matlab, or saved on the PC and processed later.

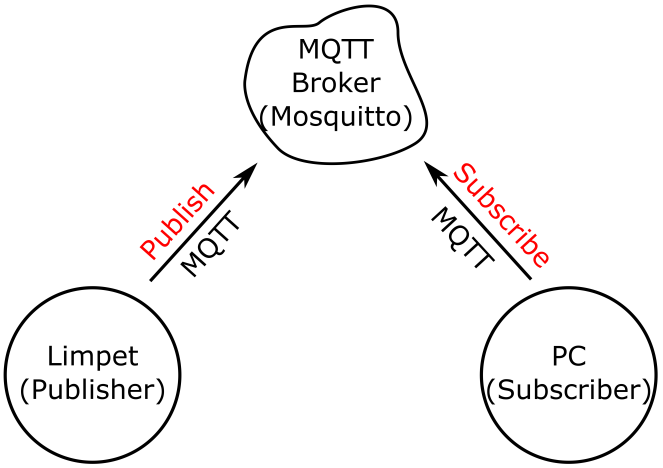

Figure 3.18: In the WiFi communication strategy using MQTT protocol, the Limpet is the publisher, where it publishes the different sensor data, and the subscriber is the PC, where it can subscribe to the MQTT topic to receive the sensor data. The nodes (Limpet and PC) communicate with a server, known as MQTT Broker. I use Mosquitto as the MQTT Broker.

3.3.2 Serial Communication

I transmit the data from the Limpet serially using SparkFun's FTDI Basic Breakout-3.3 V, which is a serial to USB convertor. The communication between the Limpet and the FTDI Basic Breakout occurs over UART. The transmitting UART (Limpet) converts parallel data from the microcontroller into serial form, transmits it in serial to the receiving UART (FTDI), which transmits the serial data back into parallel form for the PC. The UART transmits the data asynchronously, which means there is no clock synchronisation between sending data from the transmitting device to receiving data by the receiver. In UART, instead of the clock signal, the transmitting device adds a start bit and a stop bit to the data being sent, which defines the beginning and end of the data packet for the receiving UART. A schematic of the serial communication is shown by Figure 3.19.

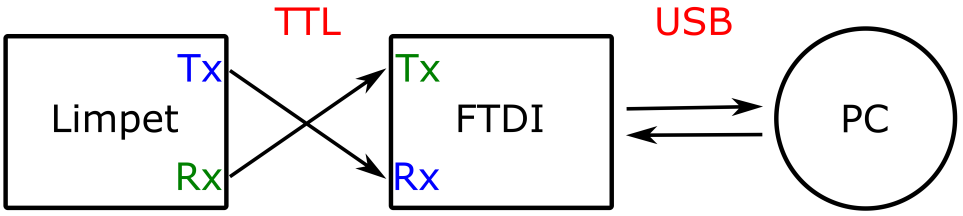

Figure 3.19: The Limpet sends the data serially to the computer using the FTDI Basic Breakout, which converts the TTL communication from the Limpet to USB signals for the PC.

3.3.3 Long Range Wide Area Network (LoRaWAN)

LoRaWAN is a new wide area network (WAN) technology that allows for long-range communication with low power consumption, but with a limited bandwidth [220]. LoRa technology is provided by the LoRa Alliance, which is a non-profit association of more than 500 member companies that are developing and promoting LoRaWAN open standard for Internet of Things (IoT). Low power WAN combines robust modulation and low data rate to achieve long-range communication, where LoRaWAN is one of the most successful tools in low power WAN technologies. It is a network stack rooted in the LoRa physical layer. LoRaWAN features a low data rate (a maximum of 27 kb/s with spreading factor 7 and 500 kHz channel) and long-range communication (2–5

km in urban areas and 15 km in suburban areas). There is a tradeoff between the spreading factor (SF) and communication range in LoRa. The higher the SF, which means a slower transmission, the longer the communication. Depending on the spreading factor used (7 to 12), LoRaWAN data rate ranges from 0.3 kb/s to 27 kb/s [221].

LoRa has a much lower communication bandwidth than serial and Wi-Fi communication. Thus, when I use LoRa technology with the Limpet for communication, the limited bandwidth limits the ability to send the sensor data continuously in real time to the PC. Therefore, if the dataset is large, processing and analysis of the data need to be done before transmission to allow for only small amounts of data to be transmitted. This on-board processing and analysis approach requires higher computational power than serial and Wi-Fi communication. I used the LoPy, which is a MicroPython enabled Wi-Fi, Bluetooth and LoRa development board, to gain access to the LoRa network.

In LoRa communication, devices or nodes send small data packets to a gateway, which can be several kilometers away from the node, using the LoRaWAN wireless protocol. The gateway then uses traditional communication mehtods (Ethernet, WiFi, mobile network) to forward the packets to a network server, which validates the packets and forwards it to an application server. Since the Limpet is designed to be used in offshore energy platforms, where data security is important and Internet connectivity is low, I have developed a local network for LoRaWAN communication for the Limpets, which can be used in any environment and allows for the data packets to be secure. The local network developed uses the LoRa Server project provided by CableLabs [222]. The architecture of the LoRa network is shown by Figure 3.20. The Limpet sends the sensor data through the UART to the LoPy nodes, which send these data packets to the LoRa gateway using the LoRaWAN wireless protocol. The gateway runs a packet-forwarder software, which is responsible for forwarding the incoming packets to a network server using a User Datagram Protocol (UDP). The network server and the LoRa gateway are given IP addresses through a local Domain Name System (DNS) server. The LoRa Gateway Bridge, which runs on the local machine or PC that runs the network server, is responsible for transforming the packet-forwarder UDP Protocol into an MQTT Protocol. I used Eclipse Mosquitto as the MQTT Broker. The MQTT messages are forwarded to the LoRa Server, which is the LoRaWAN network server component

running on the local machine. The LoRa Server manages the state of the network, where it handles the join requests by the devices and has knowledge of which devices are active on the network. The LoRa App Server component implements a LoRaWAN application-server compatible with the LoRa Server component. It provides a web-interface and APIs for management of users, organizations, applications, gateways and devices. The data payload sent by the devices can then be published from the LoRa App Server to an application using MQTT protocol.

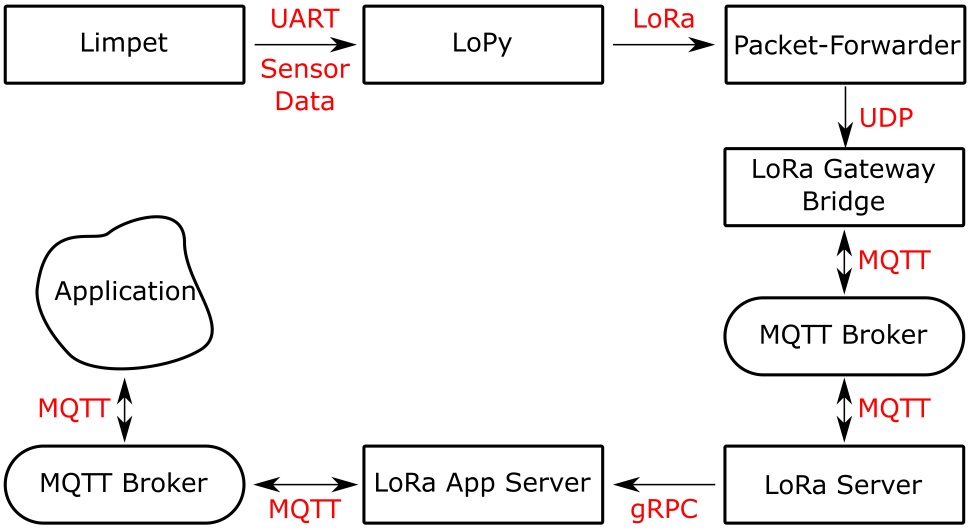

Figure 3.20: The Limpet sends the sensor data packets to the LoPy node through the UART. The LoPy sends these data packets to the LoRa gateway using the LoRaWAN wireless protocol. The gateway runs an implementation of the packet-forwarder software, which forwards the data packets to a network server (LoRa Server) using a UDP protocol. The LoRa Gateway Bridge transfers the packet-forwarder UDP protocol into messages over MQTT. The MQTT broker routes the MQTT messages between the nodes. The MQTT messages are forwarded to the LoRa server, which provides the LoRaWAN network server component. The LoRa App Server implements a LoRaWAN application server and provides a web interface and APIs. The data packets or payload can be published from the LoRa App Server to an application using the MQTT protocol. The application handles the application payloads sent by the Limpets.

3.3.4 Acoustic Communication

The Limpet can transmit data to a PC or another Limpet using acoustic communication. I achieved this by using the Limpet with acoustic nanomodems that were developed by University of Newcastle as part of the EPSRC USMART Project. The nanomodem is small in size (42 mm diameter and 60 mm long), low cost and low power. It operates in the acoustic frequency band of 24-28 kHz, and utilises simple but highly robust spread spectrum modulation scheme based on binary orthogonal keying using chirp waveforms (chirp-BOK). This modulation scheme allows the nanomodem to achieve a data transmission rate of 40 bps for a range of up to 2km.

The nanomodem uses RS-232 (Recommended Standard 232) serial communication, which is not compatible with the Limpet communication, which is TTL (Transistor-Transistor Logic) serial. TTL serial communication always remains between the limits of 0V and supply voltage (Vcc), which is 3.7V in this case. A logic low (0) is represented by 0V, while a logic high (1) is represented by Vcc. In RS-232 serial communication, logic low (0) is represented by a positive voltage between 3 and 25V, while logic high is represented by a negative voltage between -3 and -25V. Thus, to enable communication and transmission between the nanomodem and the Limpet, I used SparkFun's MAX3232, which is an RS-232 to TTL level converter. The schematic and architecture of the acoustic communication is given by Figure 3.21.

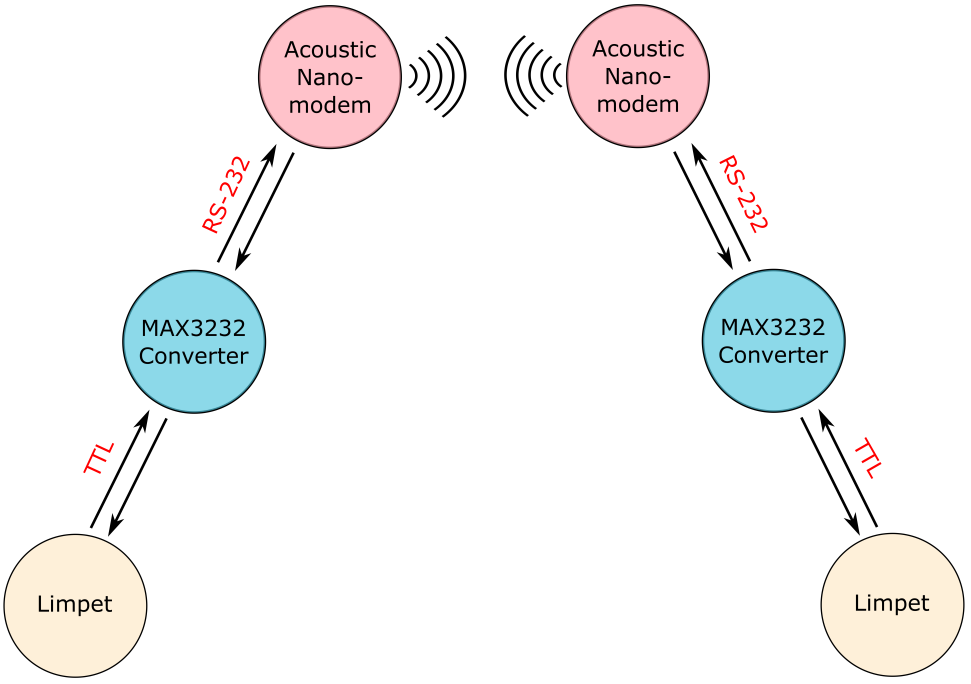

Figure 3.21: Each Limpet can send and receive data from the acoustic nano-modem using the MAX3232 converter, which is a TTL to RS232 communication converter. The nano-modems can communicate underwater with each other using acoustic waves.

3.3.5 Optical Communication

Optical communication has a lower bandwidth than LoRaWAN communication. The processing and analysis on the data also needs to be done before the transmission. I used the on-board RGB LED for transmission of data. I transmit the data by pulse-width modulating (PWM) the LED to different levels, where each level corresponds to a number from 0 to 9. I pulse-width modulate the RGB LED from 0 to 255 in steps of 25, which allows for ten different intensity levels corresponding to each of the numbers (0 to 9). I use the different LED colors to correspond to different measurements in a single experiment such as time, distance, index of measurement, etc. I can also use the other LED colors for other sensor measurements such as pressure, temperature, etc. The optical communication protocol transmits a single digit at a time. Therefore, I programmed the Limpet to divide any measurements into single digits and transmit the digits one after the other. The intensity of the transmission (PWM level) and the LED color (measurement type) allows reconstruction of the transmitted data from the RGB LED.

I used the optical sensor on the Limpet as a receiver, where it detects the light intensity (indication of the transmitted number) and color power density (indication of measurement type), to interpret the data transmitted using the RGB LED. Before conducting any experiments using optical communication, I ran a calibration experiment for the light sensor using two Limpets. I pulse-width modulated the RGB LED from 0 to 255 in steps of 25 on one Limpet. I pulse-width modulated the red LED first, followed by the green LED and the blue LED. I used the optical sensor on the other Limpet to read the light intensity and color power density of the LED for each PWM level. Figure 3.22 shows a plot of the power density from each LED for each of the numbers transmitted. Plots of the power density versus time for different numbers transmitted using the red, green, and blue LED is shown by Figure 3.23.

I used the results of this calibration experiment as a reference to interpret the data transmitted by the Limpet during any experiments with optical communication. The data transfer speed achieved in my optical communication protocol lies in the range of 6 bps to 53 bps. The extra step involved in the optical communication, which is the calibration and use of the optical sensor to infer the transmitted data, implies a higher computational power demand

for optical communication. Optical communication cannot be used for long-range communication, where the optical communication range in my work has a maximum range of about 20 cm. The optical communication range is a function of both the intensity of the RGB LED and the sensitivity of the optical sensor. Optical communication can be useful for communication with underwater vehicles, as it was discovered that blue light can propagate in seawater better than other frequencies of light [223]. In field conditions, the amount of ambient light intensity has an impact on the optical communication system.

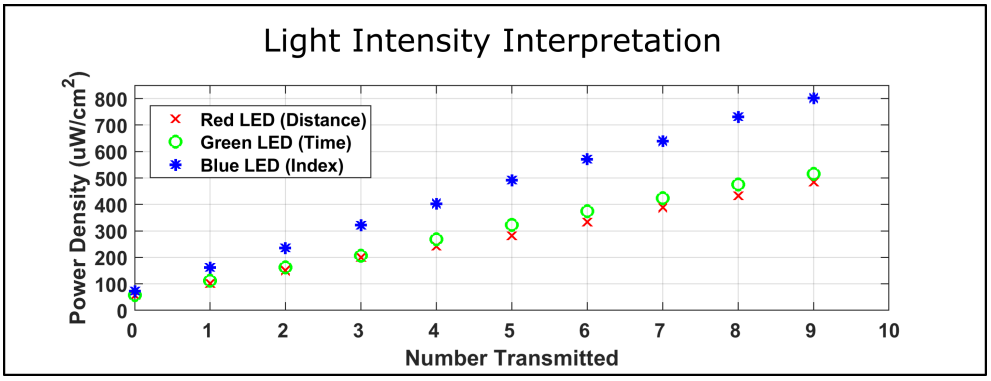

Figure 3.22: Light intensity interpretation for optical communication. This graph shows how the power density of the RGB LED represents a number transmitted by the Limpet. The red LED is used to send information about distance, green LED is used for timestamp information and blue LED is used for index information. The different power density for each LED corresponds to a number on a scale of 0 to 9. The different power densities are achieved by pulse-width modulating the RGB LED to different levels.

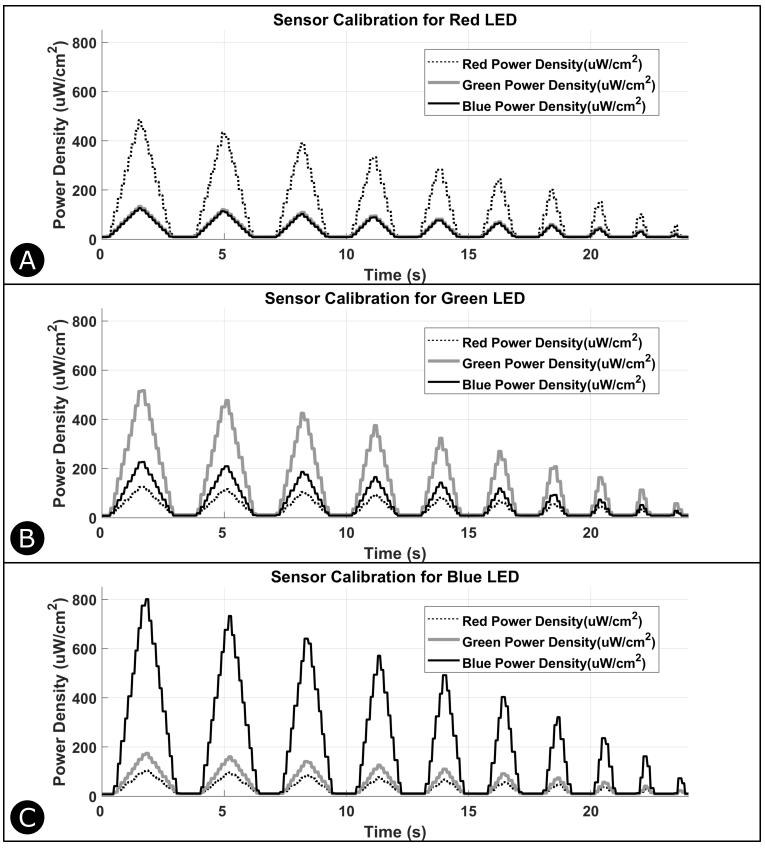

Figure 3.23: A plot of the power density data versus time from the optical sensor when transmitting numbers using the (A) red LED, (B) green LED, (C) blue LED. Each consecutive peak corresponds to a number from 9 to 0.

Communication Method	**Transmission Range**	**Communication Rate**	**Power Consumption**	**Environment**
WiFi	50-300 m	72.2 Mbps	135 mA	Terrestrial
Serial	N/A	115.200 Kbps	100 mA	Terrestrial
LoRa	2-15 km	0.3-27 Kbps	92.6 mA	Terrestrial
Acoustic	2 km	40 bps	300 mA	Underwater
Optical	20 cm	6-53 bps	20 mA	Terrestrial and Underwater

Table 3.2: Properties of the different communication methods.

3.4 Remote Sensing and Real-Time Condition Monitoring

I use two different approaches for the condition monitoring process in this Chapter: offline and online classification. I tested the offline classification approach using two different communication techniques: serial and Wi-Fi. I performed the online classification approach using two different communication techniques: LoRa and optical. I train the classifier offline and transfer its parameters to the Limpet for online classification. I simulated and classified four different faults in the operation of wind turbines. I tailored a data processing procedure for the gathered data and trained the Limpet to distinguish among each of the functioning states.

The results show successful classification using the online approach, where the processing and analysis of the data is done on-board by the microcontroller. By using online classification, I can reduce the information density of the transmissions, which allows me to substitute short-range high-bandwidth communication systems with low-bandwidth long-range communication systems. This Chapter shines light on how robots can perform on-board signal processing and analysis to gain multi-functional sensing capabilities, improve their communication requirements, and monitor the structural health of equipment. I show a use case of condition monitoring for offshore wind turbines. However, the approach presented here is applicable to other offshore structures in oil and gas platforms such as rotating machinery, gears, valves and cooling fans. The reliability of the monitoring system is enhanced by conducting all the data processing and analysis on the microcontroller, and transmitting data using high-range low-bandwidth communication systems only in the event of the presence of a fault.

I used the distance sensor on the Limpet for the condition monitoring process described in this Chapter, which not only achieves condition monitoring and fault detection remotely, but also gives an extra parameter, distance, that can be extremely useful in different applications (e.g. blade deflection monitoring), or when integrating it with other robots. The approach I used for the condition monitoring system requires a sensor that is capable of remotely

detecting the mechanical rotation of the wind turbine. For example, this approach can be performed using a magnetic sensor to measure magnetic reluctance. However, using a magnetic sensor would require the blades to be metallic. An accelerometer could also be used, by attaching it to the blade to monitor the speed and vibration, but the number of faults that can be detected are limited. A combination of a photodiode and phototransistor is another way to achieve fault detection in wind turbines, but it requires a complex setup and would only give indication of one parameter, which is absence of blade.

Figure 3.24 indicates the instrument model for the Limpet as considered for the condition monitoring process. The measurands normal operation and fault can be related to the physical measurement variable light. I use the distance sensor on the Limpet, which converts the physical measurement variable light to a signal variable distance, which is fed into the microcontroller's I2C bus. I use the microcontroller to process the sensor data on-board and check them against a classifier. I use the distance measurements to classify if the machine (wind turbine) is operating normally, or if there is a fault in the machine hindering its performance. The Limpet can send the data to a PC using one of several different communication systems. I can then use spectral analysis on the data to further reduce the information density and classify the type of fault detected.

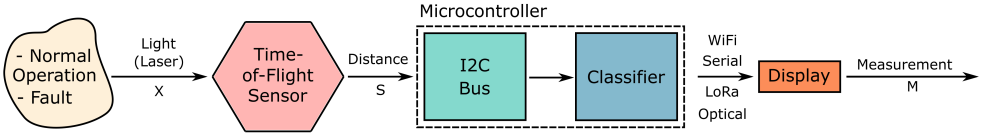

Figure 3.24: Instrument model for the Limpet for distance-based fault detection. I detect normal operation or fault measurands by using a time-of-flight sensor that converts the time of arrival of the reflected light into a distance measurement.

3.4.1 Condition Monitoring Experimental Design

The work presented on the condition monitoring process in this Chapter focuses on the sensing capabilities of the Limpet. I use the distance (ToF) sensor to demonstrate how distance measurements can be used to detect faults in the operating conditions of machines or equipment. I show how a measurement variable can be indirectly related to the measurand and demonstrate an example of how the Limpet could be used for condition monitoring. The approach presented here can used for monitoring different offshore structures. This section discusses the design of the experiments that I used to demonstrate the capabilities of a single Limpet in fault detection and condition monitoring.

3.4.1.1 Design of the Distance-Based Condition Monitoring Experimental Setup

The experimental setup consists of a platform containing the Limpet and a custom-designed fan with four blades rotating in front of the Limpet as shown by Figure 3.25A. I designed the fan blades by cutting a pattern out of an acrylic sheet using a laser cutter. I attached the fan blades to a stepper motor to achieve rotation. I used the fan to mimic a small wind turbine. I placed the fan 85 mm from the Limpet. I use the ToF sensor on the Limpet to measure distance to the fan blades as they rotate. I controlled the speed of rotation of the fan by controlling the speed of rotation of the stepper motor. When a blade passes in front of the Limpet, the blade is intercepted by the ToF sensor, and a distance measurement is recorded. I programmed the Limpet to interpret the absence of a blade as a zero measurement. Figure 3.25B shows a schematic of how the distance measurement was determined for the fan for normal operating conditions. It shows the distance profile, which depicts the distance measurement for each blade passage in front of the Limpet. The frequency of detection of the fan blades is 1.25 Hz under normal conditions. The fan has four blades, and each blade corresponds to a peak on the graph. In this case, the zero value represents the absence of a blade in front of the Limpet. I recorded the distance profile over a period of 3.2 s, which corresponds to the frequency of rotation of the fan. The difference in width between the peaks is due to the error in detection of the edges of the blade, which is discussed further in Section 3.4.3.4 on Page 107.

To evaluate the capability of distance-based fault detection using the Limpet, I divided the work into two parts: offline classification and online classification of faults. I tested the offline classification approach using two different communication techniques: serial and Wi-Fi. I performed the online classification approach using two different communication techniques: LoRa and optical. I conducted five experiments for each of the four communication systems. I conducted each of the five experiments separately for each communication system. I conducted all the experiments under normal laboratory conditions. I designed one of the five experiments to be normal operation of the fan. In the other four experiments, I introduce a fault to the system and check if the Limpet is capable of detecting this fault. Thus, I tested the detection of the fault using both approaches (offline and online classification). The faults introduced to the system are listed below and a schematic of these faults are shown by Figure 3.25C.

- Fault 1: I attach an object of 15 mm thickness to one of the four blades.
- Fault 2: I remove one of the four blades of the fan.
- Fault 3: I reduce the frequency of detection of a fan blade from 1.25 Hz to 0.25 Hz by reducing the speed of the stepper motor.
- Fault 4: I immobilize the rotation of the fan for a certain period during its normal operation.

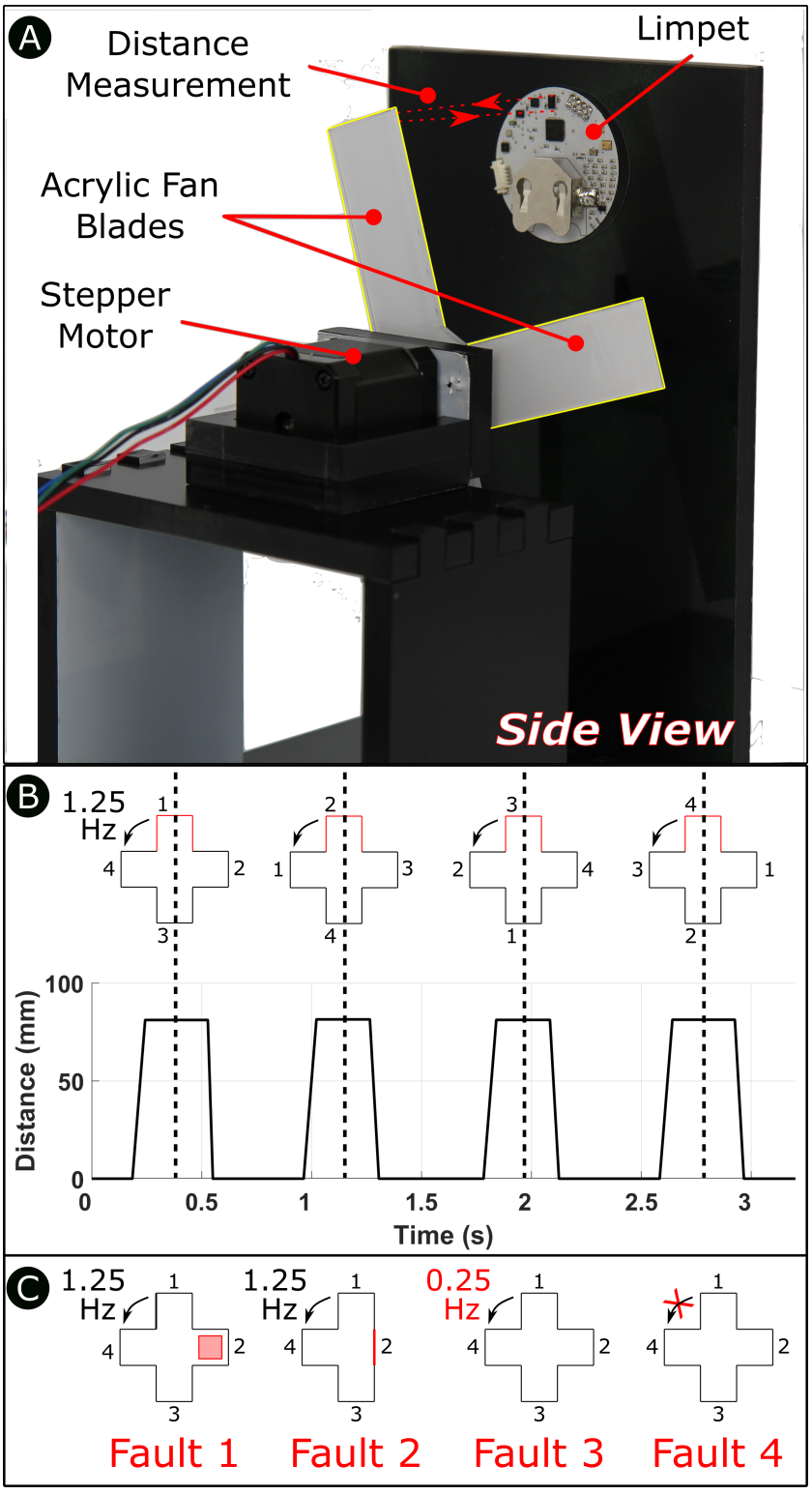

Figure 3.25: (A) Experimental setup for distance-based fault detection. I fixed the Limpet in place and used the fan to mimic a small wind turbine. (B) Schematic of the fan and distance profile for normal operation mode. Each peak corresponds to one of the four fan blades detected. (C) Schematic of the faults introduced to the system.

3.4.1.2 Design of the Offline Classification Experiments

Figure 3.26 gives an overview of the components included in the offline classification process of the system. First, I conduct the distance measurement experiment with the Limpet and record the data (distance measurement, timestamp). I transmit the data from the Limpet to the PC in a real-time manner using a high-bandwidth communication system such as serial or Wi-Fi communication. Since there is no memory limitation, as the data are not stored on the microcontroller in the offline classification approach, I recorded the sensor data over a period of 300 seconds. I then process the data on the PC using MATLAB. I apply a Median Absolute Deviation (MAD) algorithm to remove any outliers from the dataset. I then apply a low-pass filter (simple moving average) to the data to remove the fluctuations in the time-series signal. I also down-sample the data after application of the low-pass filter. In the presence of a fault, given this processed dataset, I apply spectral analysis to classify the type of fault. This offline classification process is used as a learning basis (training) for online classification on the Limpet. The parameters required for the online classification where calculated from the offline classification of normal operation of the fan. I calculated the average, standard deviation and frequency of rotation from the distance measurements and used these values as learning values for the microcontroller when performing the online classification process.

I conducted two additional experiments using Wi-Fi and serial communication (offline classification) to test for other types of scenarios. The first experiment involved sampling the distance to the fan using the sensor at a rate lower than the Nyquist frequency (sampling frequency < Nyquist frequency). This experiment was used to show that if we choose a wrong sampling frequency for the sensor, which is lower than the Nyquist frequency, the measurements cannot be used to infer any useful information. In the second experiment, I immobilize the fan twice during the 300 second measurement period.

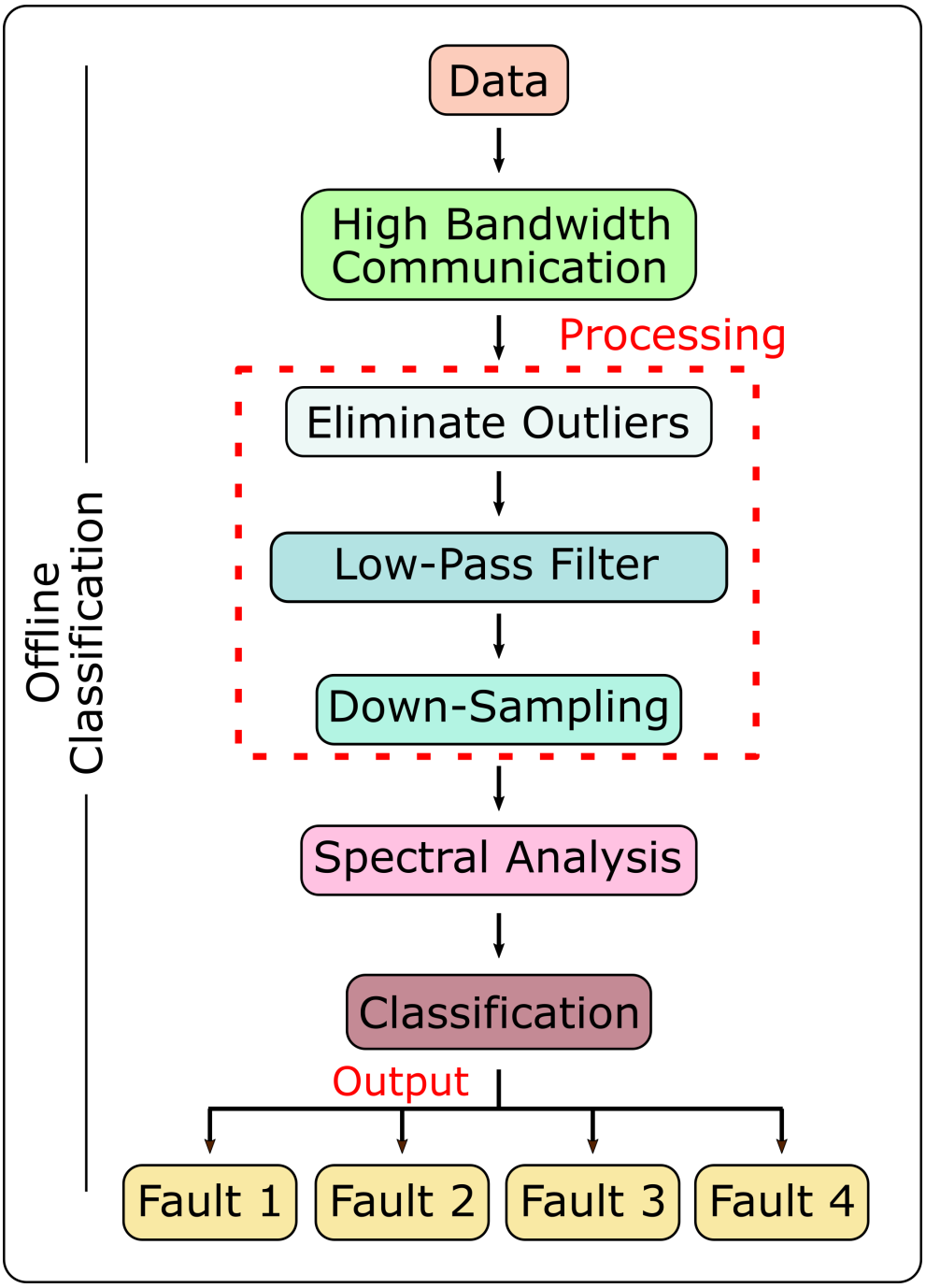

Figure 3.26: Overview of the signal-processing components for offline classification.

3.4.1.3 Design of the Online Classification Experiments

Figure 3.27 gives an overview of the online classification process. In the online classification approach, the Limpet does all the processing and analysis on-board, and then takes an autonomous decision based on the classification result. The Limpet starts sampling the distance to the fan using the ToF sensor. The Limpet stores several distance measurements into its memory (120 measurements). The Limpet processes the data, by first removing any outliers from the sensor data. The data are then down-sampled according to the down-sampling frequency to accord with the limitations of the microcontroller on the Limpet. The Limpet classifies the dataset using a sliding window algorithm. The sliding window algorithm is used to process data streams, where the input is presented as a sequence of items, and the function of interest is computed over a fixed-size window in the stream [224, 225]. The Limpet detects the first rising edge and the fourth falling edge and calculates the period between them. This period is checked against the frequency of normal operation stored in the microcontroller's memory during training of the classifier. The distance measurements are also compared to the average value and standard deviation of normal operation, which were stored in the microcontroller after training the classifier.

According to the offline training of the classifier, the distance measurement for each blade must fall within a range of average ± standard deviation. The parameters of the class representations (average, standard deviation, time period) were trained offline and do not change during operation. These parameters are stored on the Read-Only Memory (ROM) of the microcontroller. The amount of ROM used depends mainly on the number of points (120) in the dataset and their size (distance is 8-bit, time is 16-bit, distance index is 8-bit). After the Limpet checks the dataset for the presence of any faults, it makes an autonomous decision based on the result of the classification. Autonomy is the ability of a system to make its own decision and to act on its own without external intervention [226]. Within autonomy, there are many variations concerning where and how decisions are made, and actions are invoked. An automatic system carries out several fixed and prescribed activities, where there may be options, but they are fixed in advance and follow a rigid cycle [226]. An adaptive system uses feedback from the environment to improve its performance [226]. A completely autonomous system makes decisions based on the system's view of the situation at the time of decision and its current

view of the environment [226]. Decisions made by completely autonomous systems mimic human-level decisions.

Since the Limpet carries out several prescribed activities or checks during online classification, it can be considered an automatic system. If the dataset is within the specified range and frequency, the Limpet continues monitoring the system, but if the dataset fails any of the checks, the Limpet classifies the measurements as faulty operation. The Limpet then transmits the processed data using low-bandwidth communication systems such as LoRa and optical communication to the PC, where I perform spectral analysis on the data to classify the fault detected. For optical communication, I placed another Limpet in front of the Limpet that is part of the distance-based fault detection experimental setup. I aligned the second Limpet such that it does not block the distance sensor of the first Limpet, but at the same time with its optical sensor aligned with the RGB LED of the first Limpet.

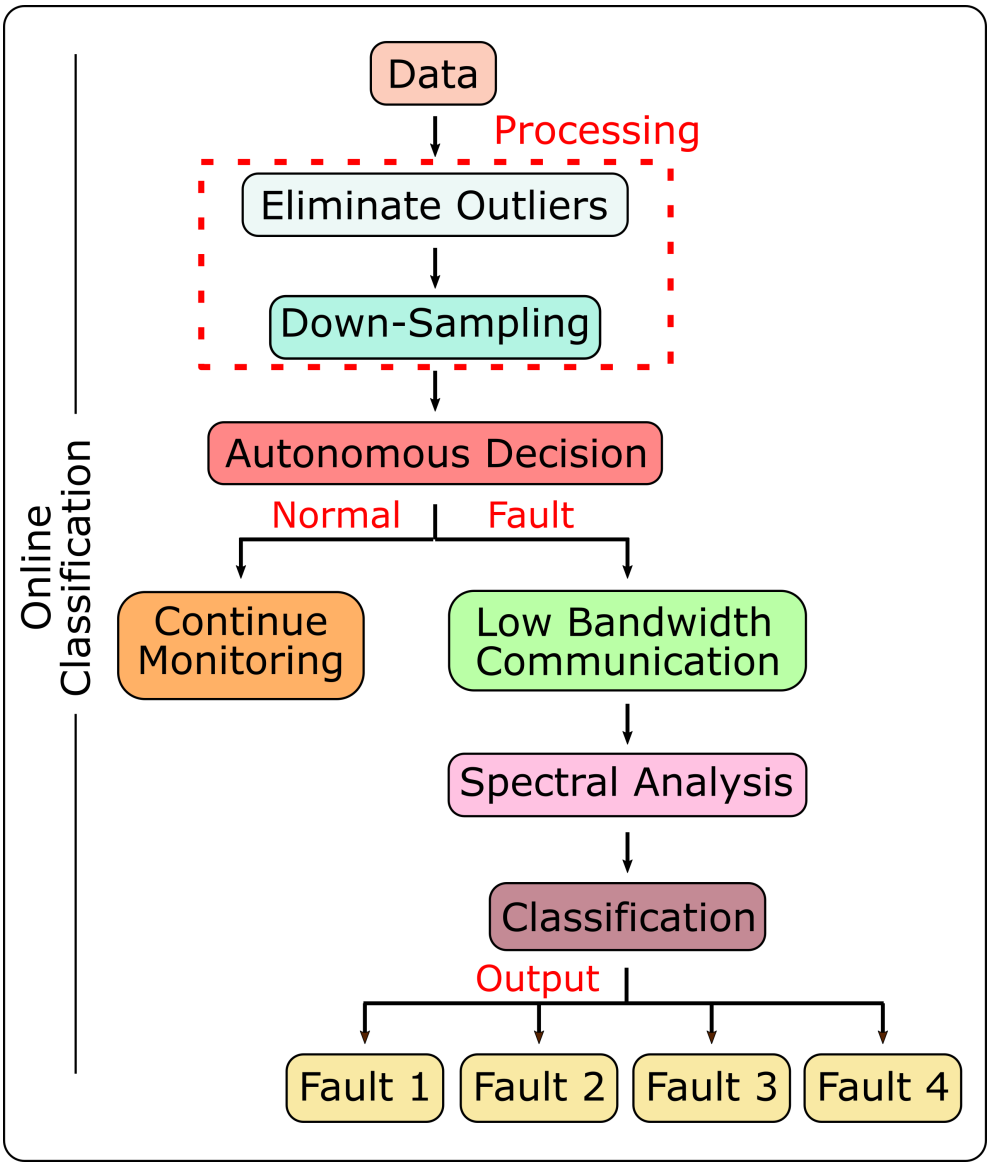

Figure 3.27: Overview of the signal-processing components for online classification.

3.4.1.4 Overview of the Communication Strategies in the Experiments

In the condition monitoring process discussed in this Chapter, I use four different communication methods (Wi-Fi, serial, LoRa, optical) to transmit the sensor data from the Limpet to the PC. For serial and Wi-Fi communication, the communication bandwidth is high, and I can send the sensor data from the Limpet continuously in real time to the PC. I can then analyze the data on the PC using analysis tools such as MATLAB. In this regard, the Limpet is only making a measurement and transmitting it instantly to the PC without doing any processing on the data, which means serial and Wi-Fi communication are not computationally demanding on the Limpet. I transmit the data from the Limpet over Wi-Fi using the ESP8266, and serially using SparkFun's FTDI Basic Breakout-3.3 V, which is a serial to USB convertor.

LoRa is a wide area network technology that allows for long-range communication, but with a limited bandwidth. LoRa has a much lower communication bandwidth than serial and Wi-Fi communication. Thus, when I use LoRa technology with the Limpet for communication, the limited bandwidth limits the ability to send the sensor data continuously in real time to the PC. Therefore, if the dataset is large, processing and analysis of the data need to be done before transmission to allow for only small amounts of data to be transmitted. This on-board processing and analysis approach requires higher computational power than serial and Wi-Fi communication. I used the LoPy, which is a MicroPython enabled Wi-Fi, Bluetooth and LoRa development board, to gain access to the LoRa network. The LoPy transmits the data from the Limpet to the local server running on the local machine, where the data can then be visualised.

Optical communication has the lowest bandwidth among the four communication strategies. The processing and analysis also need to be done before the transmission of data. In this case, I transmitted data by pulse-width modulating the on-board RGB LED to different levels, where each level corresponds to a number from 0 to 9. I used the different LED colors to correspond to different measurements such as time, distance, and index of measurement. The data is transmitted one digit at a time when using the optical communication protocol. Thus, I programmed the Limpet to divide all the measurements from the experiments into single digits and transmit the digits one after the other.

The intensity of the transmission (PWM level) and the LED color (measurement type) allows reconstruction of the transmitted data from the RGB LED using the optical sensor on another Limpet as a receiver. I used the optical sensor to read the light intensity (indication of the transmitted number) and color power density (indication of measurement type), to interpret the data transmitted using the RGB LED. In the experiments with optical communication, I used the red LED to send distance measurements, the green LED to send timestamps, and the blue LED to send the index of the data point.

3.4.1.5 Overview of the Classification Techniques in the Experiments

Signal Processing Tools

To eliminate outliers from the input signal, I applied a MAD Algorithm. MAD algorithm is used in statistics as a measure of the variability of a sample of quantitative data. MAD is more resilient to outliers in a dataset than the standard deviation. Since MAD is more robust to scale estimates than the standard deviation, it is better applied to data that is not normally distributed, which is the case for the work in this Chapter. For an input signal with length N, MAD is defined as the median of the absolute deviations from the dataset's median, and is given by

$$MAD = median(|x_i - median(x)|), i = 1, ..., N \tag{3.1}$$

In this work, I considered data points greater than 3 median absolute deviations from the dataset's median as outliers, and I replaced them with the mean of the dataset.

After the successful elimination of outliers, I applied a low-pass filter (simple moving average filter) to the data to smooth out the time-series signal and remove the fluctuations. In this stage, I calculate the mean from an equal number of data points on either side of a central value. By doing so, the variations in the mean are associated with the variations in the data instead of being shifted in time. For an input signal x and a positive integer k, the moving average y is computed by sliding a window of length k along x. Each element of y is the local mean of the corresponding values in the input signal

x within the window, and signal y is the same size as x. For a signal x made up of k scalar observations, the mean μ and the moving average y are given by

$$\mu = \frac{1}{k}\sum_{i=1}^{k} x_i \tag{3.2}$$

$$y = [\mu_i, ..., \mu_N] \tag{3.3}$$

I have chosen a moving average sliding window of size (k = 8) as the distance sensor records 8 data points for each blade passage in front of the sensor due to the sampling frequency I set for the sensor (25 Hz). The distance values of the peaks in the time series after application of the low-pass filter vary within a narrower range as compared to the signal after elimination of outliers.

After elimination of outliers and noise, I reduce the input signal with length N in size to accord with the computational limitations of the microcontroller. I reduce the length of the signal (N) by dividing the signal into L parts, each of which contains $M = \frac{N}{L}$ measurements. The value of each element $x^{'}_{M}$ of the down-sampled signal $x^{'}$ is given by

$$x^{'}_{M} = \frac{1}{M}\sum_{i=M(l-1)}^{Ml} x_i, l = 1, ..., L \tag{3.4}$$

In the work discussed in this Chapter, I down-sample the full distance measurement for one complete fan rotation to 8 measurements (M = 8) corresponding to the four peaks in the distance profile. I conduct the same process on the timestamp and index information sent with the original data. Down-sampling has an impact on the classifier's detection rate. The higher the down-sampling frequency on the input signal, the worse the detection rate becomes. Down-sampling potentially removes important features in the signal that can help the classifier discriminate between signals constituting normal operation or a fault. However, the higher the down-sampling frequency, the lower the memory required to store values of the cumulative distance matrix. Memory

reductions are useful since it lowers the requirements for our low-cost microcontroller. Therefore, there is a tradeoff between memory reduction and classifier performance. For the experiments conducted in this Chapter, I was able to achieve good classification performance with suitable memory usage as shown in Section 3.4.2 on Page 88. I determined the down-sampling frequency after conducting multiple experiments for normal operation of the fan and studying the signal for characterizing features in the distance profile. I conducted each experiment for a period of 300 seconds, during which I recorded 7322 data points. Among the recorded data, 802 data points corresponded to the detection of rising and falling edges, i.e., 401 peaks. Therefore, the down-sampling frequency is calculated to be 9 (7322/802).

Analysis Tools

After processing the input signal, I used spectral analysis to classify the fault detected. Spectral analysis has been used extensively in literature for fault detection [227, 228]. I first apply a Fast Fourier Transform (FFT) algorithm to the processed signal, which divides the time signal into its frequency components. These components are single sinusoidal oscillations at different frequencies, where each component has its own phase and amplitude. The FFT algorithm is the Discrete Fourier Transform (DFT) of a sequence. FFT computes the same results as DFT but can do it more quickly. In terms of time complexity, which is described as the amount of time needed to run an algorithm based on its computational complexity and expressed using big O notation, DFT takes $O(N^2)$ arithmetical operations, while FFT takes *O(N log N)* arithmetical operations for an input signal with N points. The N-point DFT equation for a finite-duration sequence x(n) is given by

$$X(f) = \sum_{n=1}^{N} x(n) e^{-j\frac{2\pi}{N}(f-1)(N-1)}, 1 \leq f \leq N \tag{3.5}$$

Following the application of the FFT algorithm, I compute the power spectral density function (PSD) of the signal. The PSD shows the variation of power as a function of frequency, which could be used to detect abnormal system behavior. Thus, observing the PSD of the recorded sensor data will enable

classifying the fault using a single parameter. The power spectral density for a signal x(n) with N points is given by

$$P(f) = \frac{1}{N} * |X(f)|^2 \tag{3.6}$$

For a periodic rectangular pulse function, the FFT divides the pulse signal into several harmonics (sine waves) to approximate the pulse signal. Adding more sine waves of increasingly higher frequencies improves the approximation of the rapid changes (discontinuity) in the pulse signal. In the frequency domain, a periodic rectangular pulse function results in a sinc() function centered around the dominant frequency. As the duty cycle or pulse-width of the signal is varied, the sinc() function changes. As the duty cycle is decreased, the width of the of the sinc() function broadens (i.e., it becomes less localized in frequency). Thus, if a function changes rapidly in time, the signal must contain high frequency component to allow for such a rapid change.

3.4.2 Condition Monitoring Experimental Results

Offline and Online Classification Results

Figure 3.28 depicts the results of the experiments for Wi-Fi (offline classification), LoRa and optical communication (online classification). The results from the experiments I conducted using serial communication (offline classification) were similar to the results from the Wi-Fi experiments. Figure 3.28 shows the distance profile resulting from each of the four faults introduced to the system. I constructed the distance profile for LoRa and optical communication (dotted lines) from the down-sampled results of the experiments (markers). Every two consecutive points (markers) on the graph represent a single peak or a fan blade. The distance profiles are shown within a period (T) of 3.2 s (corresponding to the frequency of rotation of the fan during normal operation). When a fault is introduced to the fan and stepper motor system, its distance profile looks distinctly different as compared to the distance profile of normal operation. Each fault also possesses a distinctive power spectral density plot as compared to other faults.

Figure 3.28A shows the distance profile acquired using Wi-Fi communication, and Figure 3.28E shows the distance profile for LoRa and optical communication, after I introduce Fault 1 to the system. As seen in both Figures, one of the peaks in the distance profile has an amplitude lower than the other peaks as a result of the object attached (extra thickness) to it. The results for Wi-Fi communication, and LoRa and optical communication after introducing fault 2 to the system are shown by Figures 3.28B and 3.28F, respectively. The results of the three communication systems show that one of the peaks in the distance profile is missing as compared to normal operation. For Fault 3, I reduced the frequency of detection of the fan blade to 0.25 Hz. The distance profile for Wi-Fi, LoRa and optical communication shows only a single peak within 3.2s as shown by Figures 3.28C and 3.28G, as the frequency of blade detection is lower than normal operation. For Fault 4, I immobilized the fan during its normal operation. The distance profile for Wi-Fi communication shows the absence of any peaks after the introduction of the fault to the system as shown by Figure 3.28D. Figure 3.28H shows the down-sampled results and the distance profile for LoRa and optical communication. The graph shows that two of the peaks are missing corresponding to where the fault is present. The fault period is slightly different for LoRa and optical communication experiments. The fault duration is also different for LoRa and optical communication as compared to Wi-Fi communication. For Wi-Fi communication, I recorded the distance measurements for a long period, and, thus the fault was introduced over a larger time window.

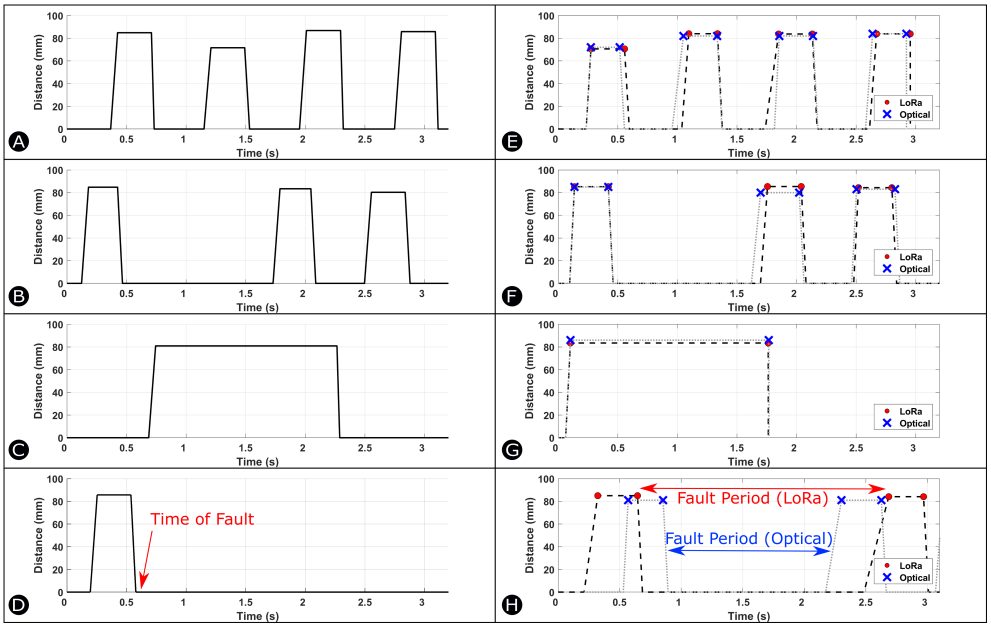

Figure 3.28: Distance Profile of Wi-Fi communication experiment for (A) Fault 1, (B) Fault 2, (C) Fault 3, (D) Fault 4. Distance Profile of LoRa and optical communication experiments for (E) Fault 1, (F) Fault 2, (G) Fault 3, (H) Fault 4.

Signal Processing and Analysis Results

The raw sensor data I recorded from the Limpet during each of the five experiments using Wi-Fi and serial communication are shown by Figure 3.29. The data after elimination of outliers, application of a low-pass filter, and downsampled results can be found in Figures 3.30, 3.31 and 3.32, respectively. Figure 3.33 shows the raw optical sensor data, which is obtained from the transmission of measurements using the RGB LED during the optical communication experiments.

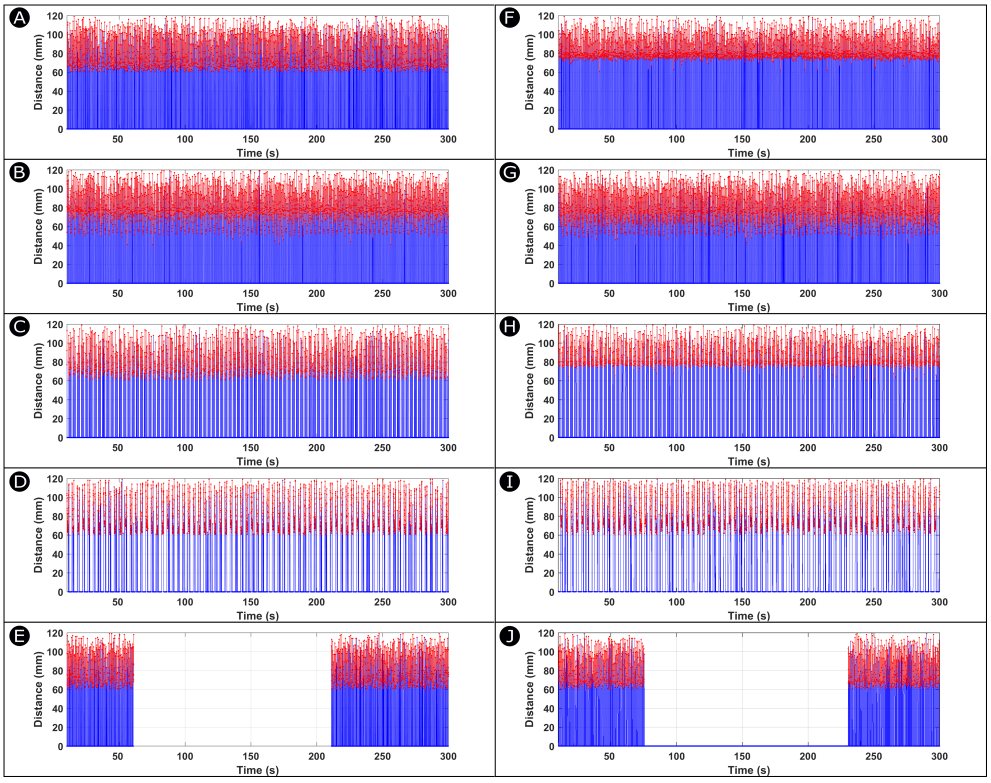

Figure 3.29: Raw sensor data transmitted by the Limpet via WiFi during (A) normal operation, (B) Fault 1, (C) Fault 2, (D) Fault 3, (E) Fault 4. Raw sensor data transmitted by the Limpet via serial communication during (F) normal operation, (G) Fault 1, (H) Fault 2, (I) Fault 3, (J) Fault 4. The sensor data has been recorded over a period of 300 seconds.

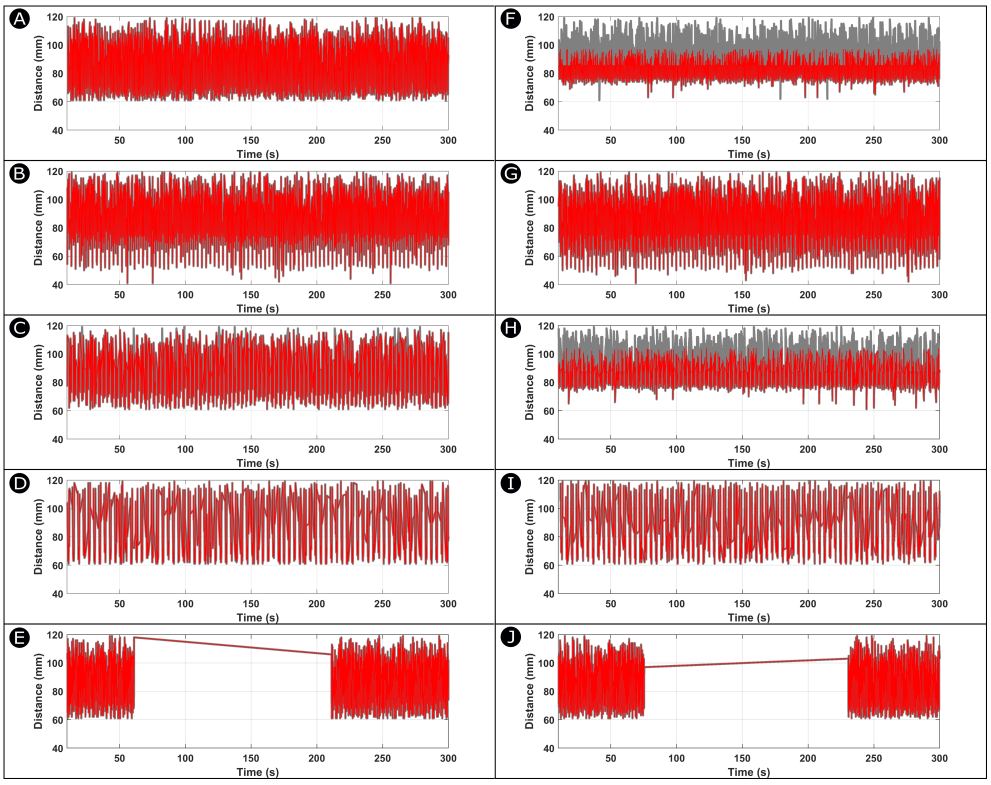

Figure 3.30: The sensor data, which was transmitted via WiFi, after elimination of outliers during (A) normal operation, (B) Fault 1, (C) Fault 2, (D) Fault 3, (E) Fault 4. The sensor data, which was transmitted via serial communication, after elimination of outliers during (F) normal operation, (G) Fault 1, (H) Fault 2, (I) Fault 3, (J) Fault 4. The sensor data has been recorded over a period of 300 seconds.

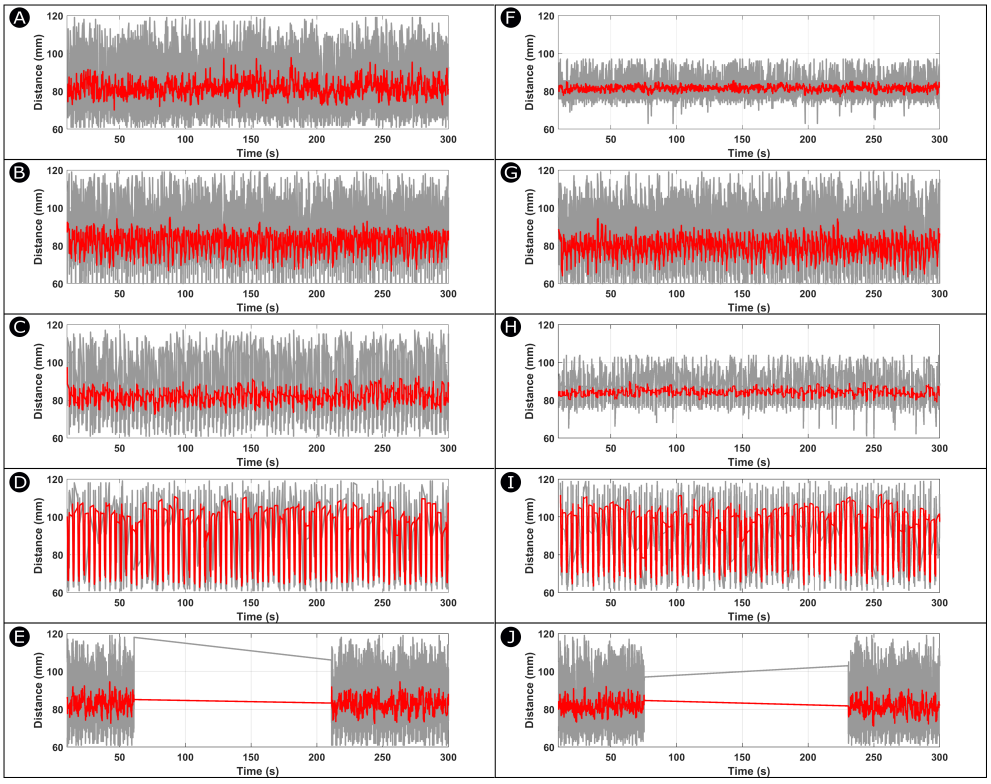

Figure 3.31: The sensor data, which was transmitted via WiFi, after application of a low-pass filter during (A) normal operation, (B) Fault 1, (C) Fault 2, (D) Fault 3, (E) Fault 4. The sensor data, which was transmitted via serial communication, after application of a low-pass filter during (F) normal operation, (G) Fault 1, (H) Fault 2, (I) Fault 3, (J) Fault 4. The sensor data has been recorded over a period of 300 seconds.

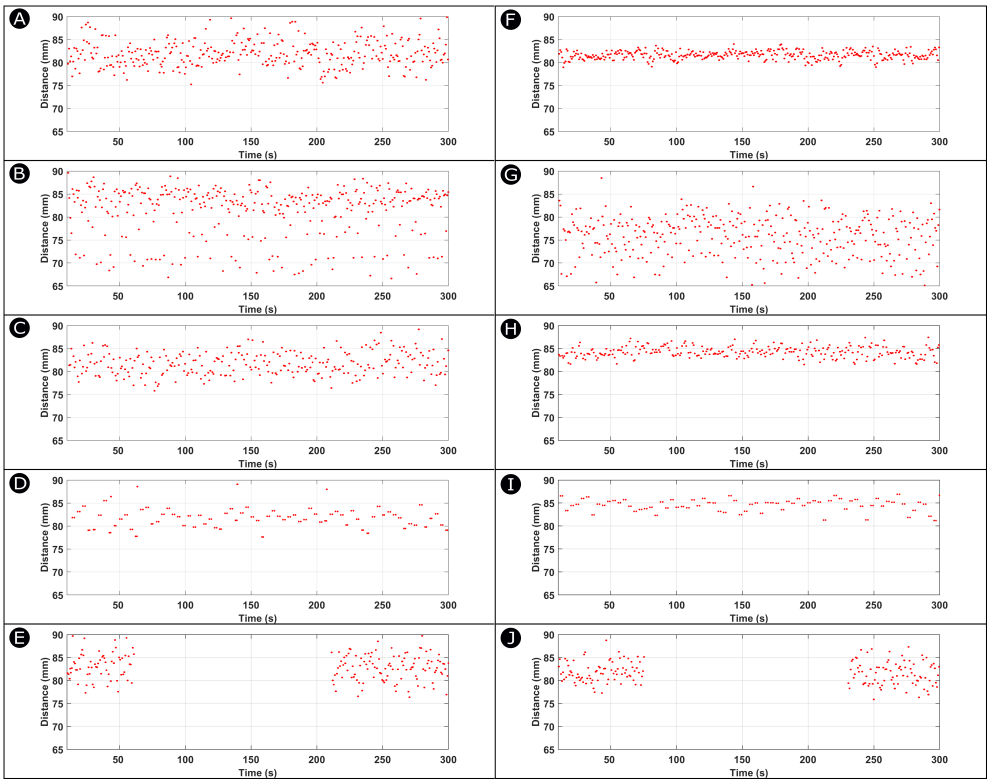

Figure 3.32: Down-sampling results from WiFi communication. This figure shows the effect of down-sampling on the sensor data, which was transmitted via WiFi, after removing the outliers and applying the low-pass filter. The sensor data was recorded over a period of 300 seconds. My down-sampling method decreases a signal's length to a number of averaged data points representing the fan blades. The effect of down-sampling on the sensor data for (A) normal operation mode, (B) Fault 1, (C) Fault 2, (D) Fault 3, (E) Fault 4. The down-sampled sensor data, which was transmitted via serial communication during (F) normal operation, (G) Fault 1, (H) Fault 2, (I) Fault 3, (J) Fault 4.

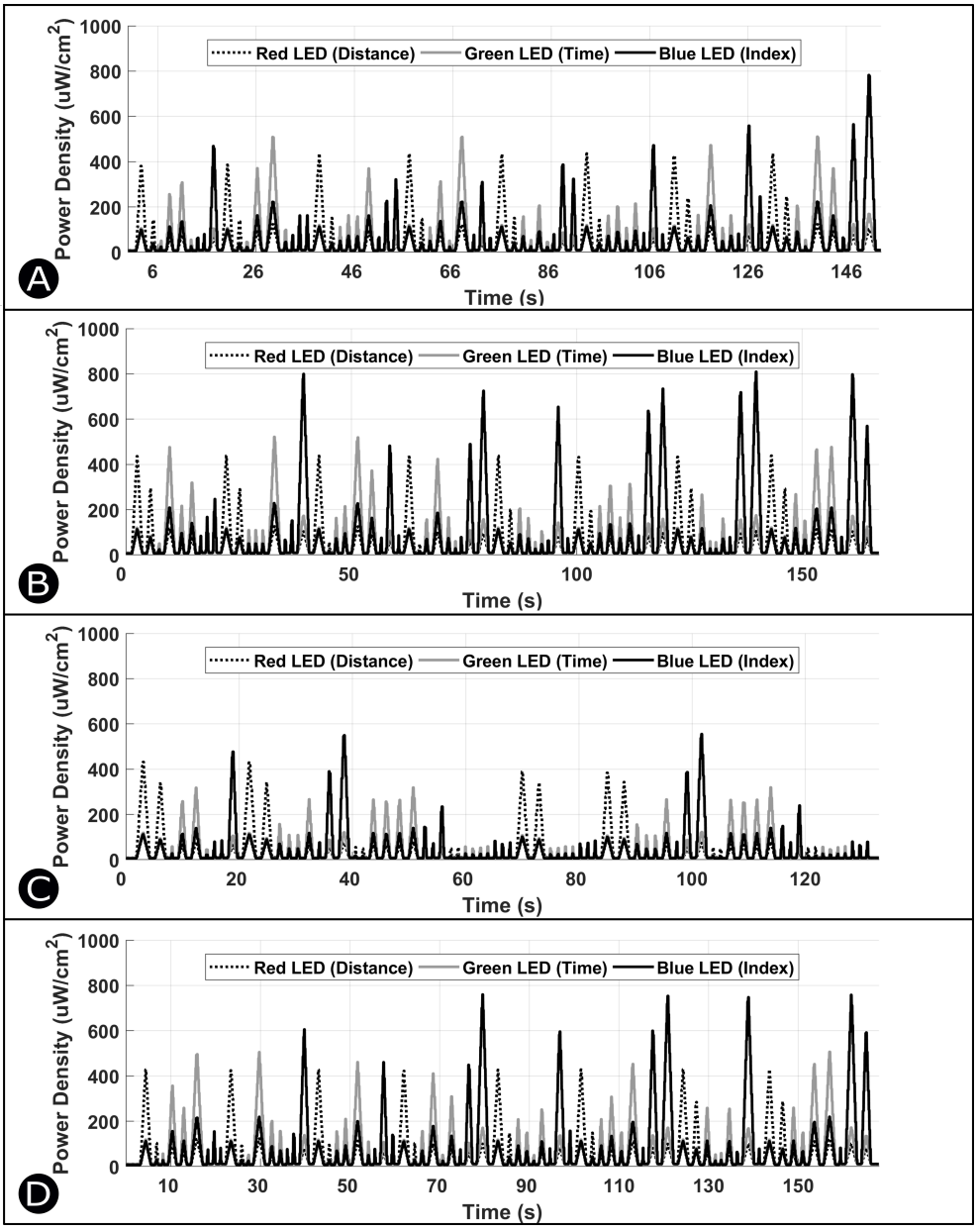

Figure 3.33: Colour power density from the optical sensor when (A) Fault 1, (B) Fault 2, (C) Fault 3, (D) Fault 4 are introduced to the system.

Spectral Analysis

Figure 3.34 shows the power spectral density plots for normal operation and each of the four faults. I obtained these results from the experiments using Wi-Fi communication. During normal operation, the spectral analysis gives a single output signal (peak) at a frequency of 1.3 Hz as shown by Figure 3.34A, which corresponds to the dominating harmonic frequency that best describes the signal in the time domain. In the time domain, the distance profile is a periodic rectangular pulse signal, therefore, in the frequency domain the harmonics exist around the same frequency. This collection of similar harmonics results in a peak in the frequency domain that is distributed around the dominating frequency. Figure 3.34B shows the power spectral density graph resulting from the introduction of Fault 1 to the system. There is a large peak at a frequency of 1.3 Hz, and three smaller peaks at frequencies of 0.35 Hz, 0.7 Hz and 1 Hz. The peak at 1.3 Hz represents the dominant harmonic in the time domain signal, while the other peaks are present because of the harmonics introduced to the system due to the presence of Fault 1. The PSD divides the signal into its single sinusoidal components at the different frequencies. In this case, the time domain signal is more complex, since the pulse signal is not periodic anymore. Therefore, the harmonics in this signal are more complex and introduce lower frequency components to describe the signal in the frequency domain. Figure 3.34C shows the power spectral density graph resulting from the introduction of Fault 2 to the system. There is a large peak at a frequency of 1.3 Hz, and three smaller peaks at frequencies of 0.35 Hz, 0.7 Hz and 1.1 Hz. The peak at 1.3 Hz represents the dominating harmonic in the time domain signal, while the other peaks are present because of the harmonics introduced to the system due to the presence of Fault 2. The absence of the peak in the time domain signal introduces new harmonics in the spectrum represented by the lower frequency components. This power spectrum is distinct from the power spectrum of Fault 1, as the power in the lower frequency harmonics is higher due to the larger difference in the amplitude between the peaks in the distance profile. The spectral analysis of Fault 3 shown by Figure 3.34D depicts a single large peak at a frequency of 0.25 Hz, which corresponds to the lower frequency of detection of the fan blades. The signal is a periodic rectangular pulse signal, and thus, results in a spectral plot with a peak around the dominant frequency. Since the duty cycle is increased as compared to normal operation, the peak is narrower and larger in the frequency domain. The

spectral analysis of Fault 4 shown by Figure 3.34E depicts a large peak at a frequency of 1.3 Hz representing the normal fan operation and another peak at a lower frequency representing the break of rotation of the fan. The amplitude of the peaks depends on the length of the jam introduced to the system.

Figure 3.35 shows the power spectral density plots from the serial communication experiments. The results of the spectral analysis on the serial communication experiments are similar to the spectral analysis of the Wi-Fi experiments. Figure 3.36 shows the spectral analysis performed on the data for both LoRa communication and optical communication after I introduce the four faults to the system. The frequency of the peaks in the power spectral density graph of LoRa and optical communication experiments are similar to those of serial and Wi-Fi experiments. The dominant frequency in Figure 3.36A is slightly different for the optical and LoRa communication. The reason behind this difference is that the transmitted data payload for both communications is small, and slight differences between those data causes an observable difference in the frequency in the spectral analysis plots. The frequency of both communications, however, is around the dominant frequency of 1.3 Hz, which is similar to the results of the serial and WiFi communication. The only difference is the amount of power or energy in each peak. The power in the sinusoidal oscillations is much higher in serial and Wi-Fi experiments as the results were recorded over a larger period. The results from the two additional experiments (jamming the fan twice and a lower rate of sampling) I conducted using Wi-Fi communication and serial communication are shown by Figures 3.37, 3.38, 3.39 and 3.40 .

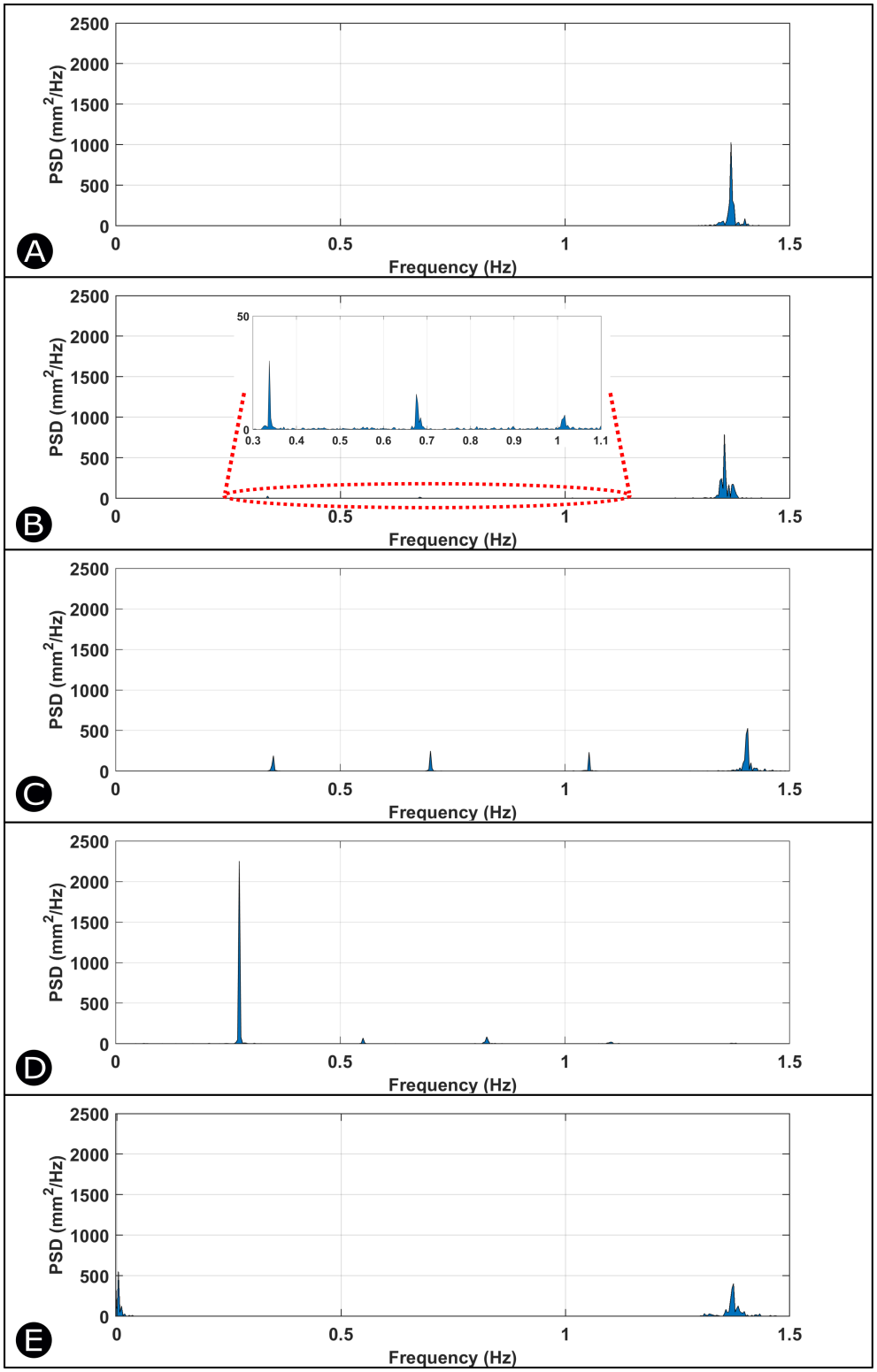

Figure 3.34: (A) Power spectral density plot of normal operation mode of the fan. There is a single peak at a frequency of 1.3 Hz, which corresponds to the frequency of detection of the fan blades. Spectral analysis of the data after introducing (B) Fault 1, (C) Fault 2, (D) Fault 3 and (E) Fault 4 to the system.

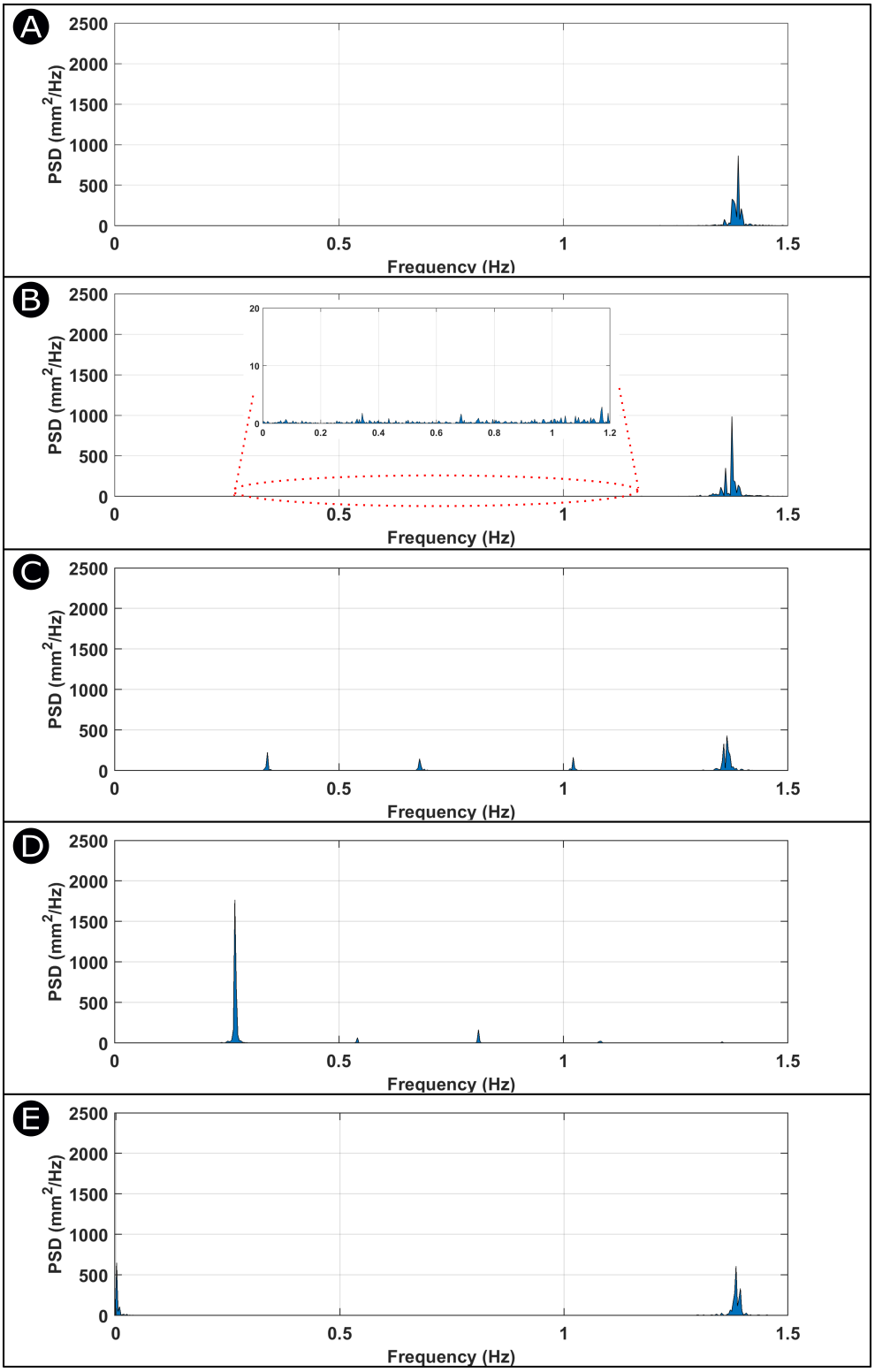

Figure 3.35: Power spectral density over frequency applied to the sensor data that was transmitted via serial communication during A) normal operation, B) Fault 1, C) Fault 2, D) Fault 3, E) Fault 4.

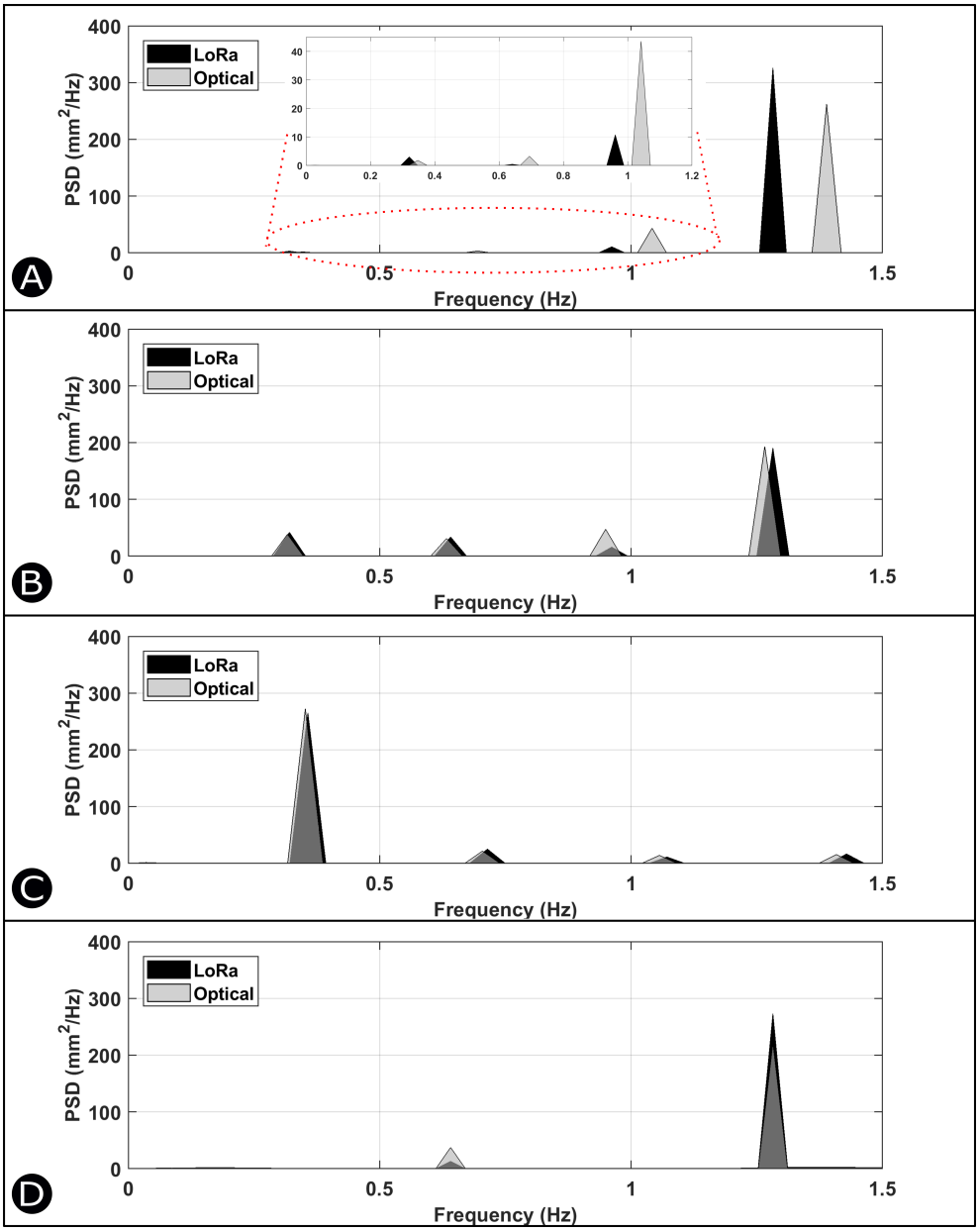

Figure 3.36: Spectral analysis of the data in the Optical and LoRa communication experiments after introducing (A) Fault 1, (B) Fault 2, (C) Fault 3 and (D) Fault 4 to the system.

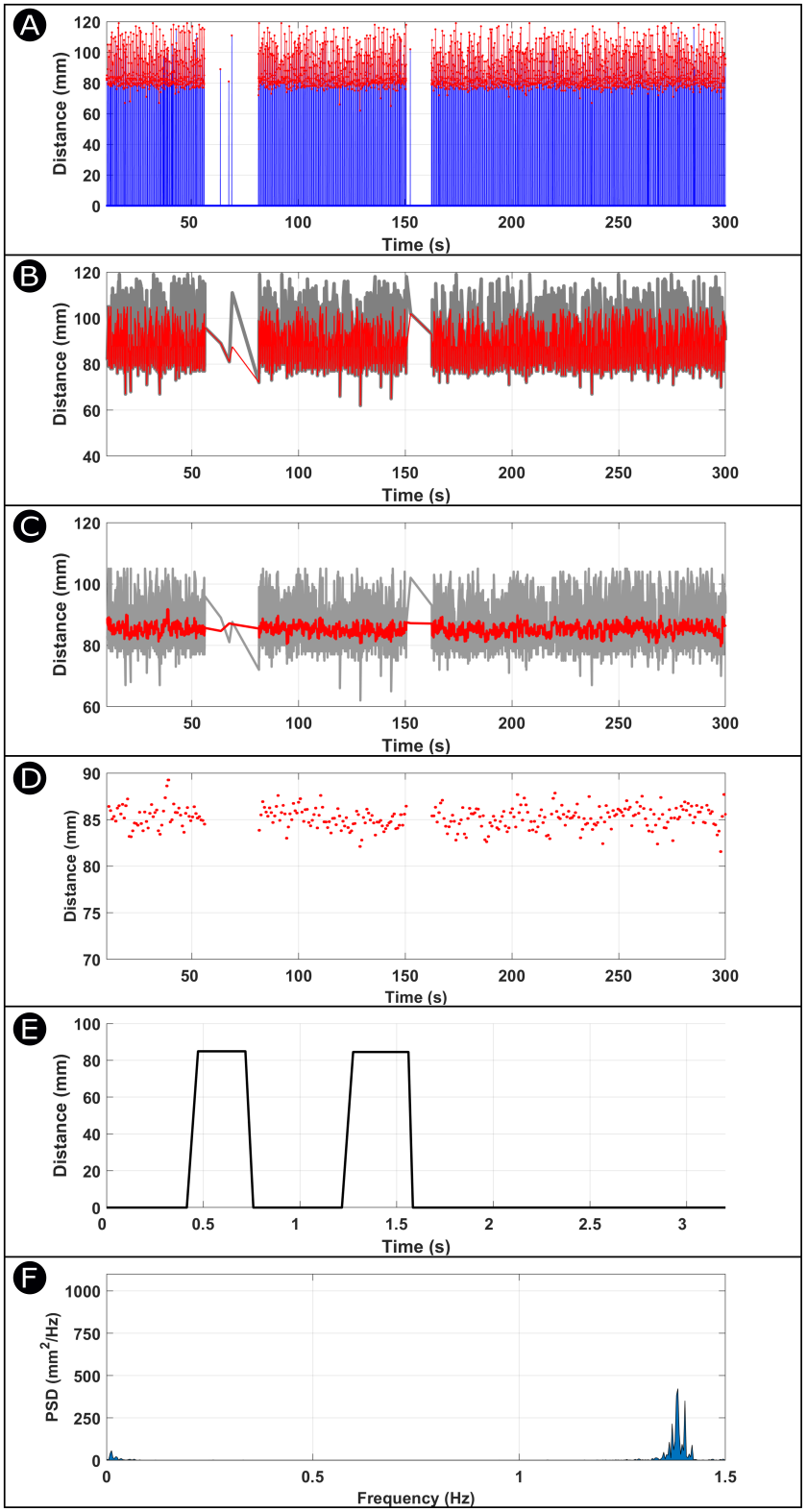

Figure 3.37: A figure showing a new type of fault introduced to the fan by stopping its rotation twice during operation. The sensor data was transmitted via WiFi. A) Raw sensor data. B) Sensor data after elimination of outliers. C) Sensor data after application of low-pass filter. D) Down-sampled sensor data. E) Distance profile. F) Power spectral density.

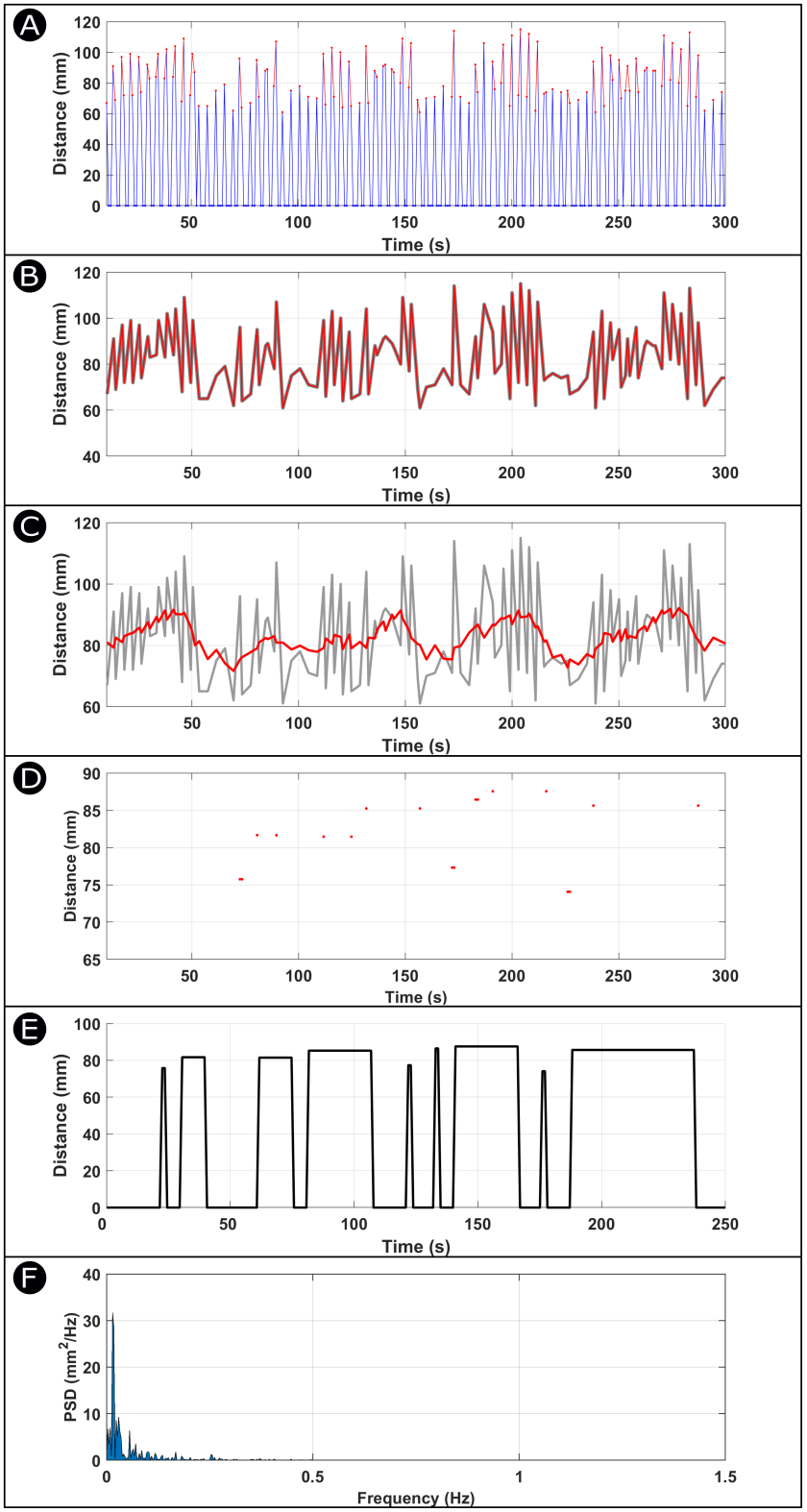

Figure 3.38: A figure showing an experiment conducted with a sampling rate lower than frequency of blade rotation. The sampling frequency used in this experiment is 1Hz. The frequency is lower than Nyquist frequency, showing that normal or fault measurands can not be identified. The sensor data was transmitted via WiFi. A) Raw sensor data. B) Sensor data after elimination of outliers. C) Sensor data after application of low-pass filter. D) Down-sampled sensor data. E) Distance profile. F) Power spectral density.

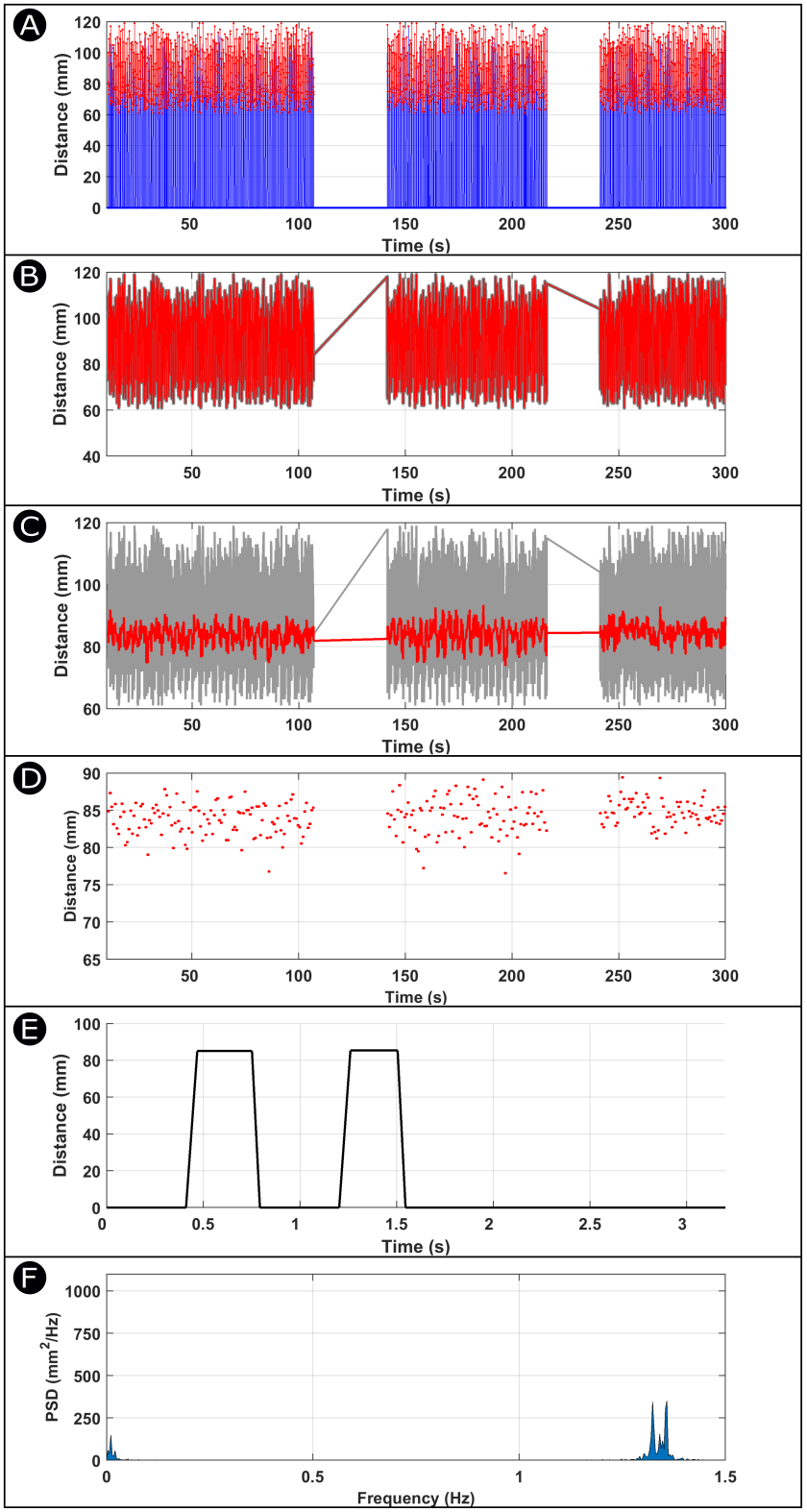

Figure 3.39: A figure showing a new type of fault introduced to the fan by stopping its rotation twice during operation. The sensor data was transmitted via serial communication. A) Raw sensor data. B) Sensor data after elimination of outliers. C) Sensor data after application of low-pass filter. D) Down-sampled sensor data. E) Distance profile. F) Power spectral density.

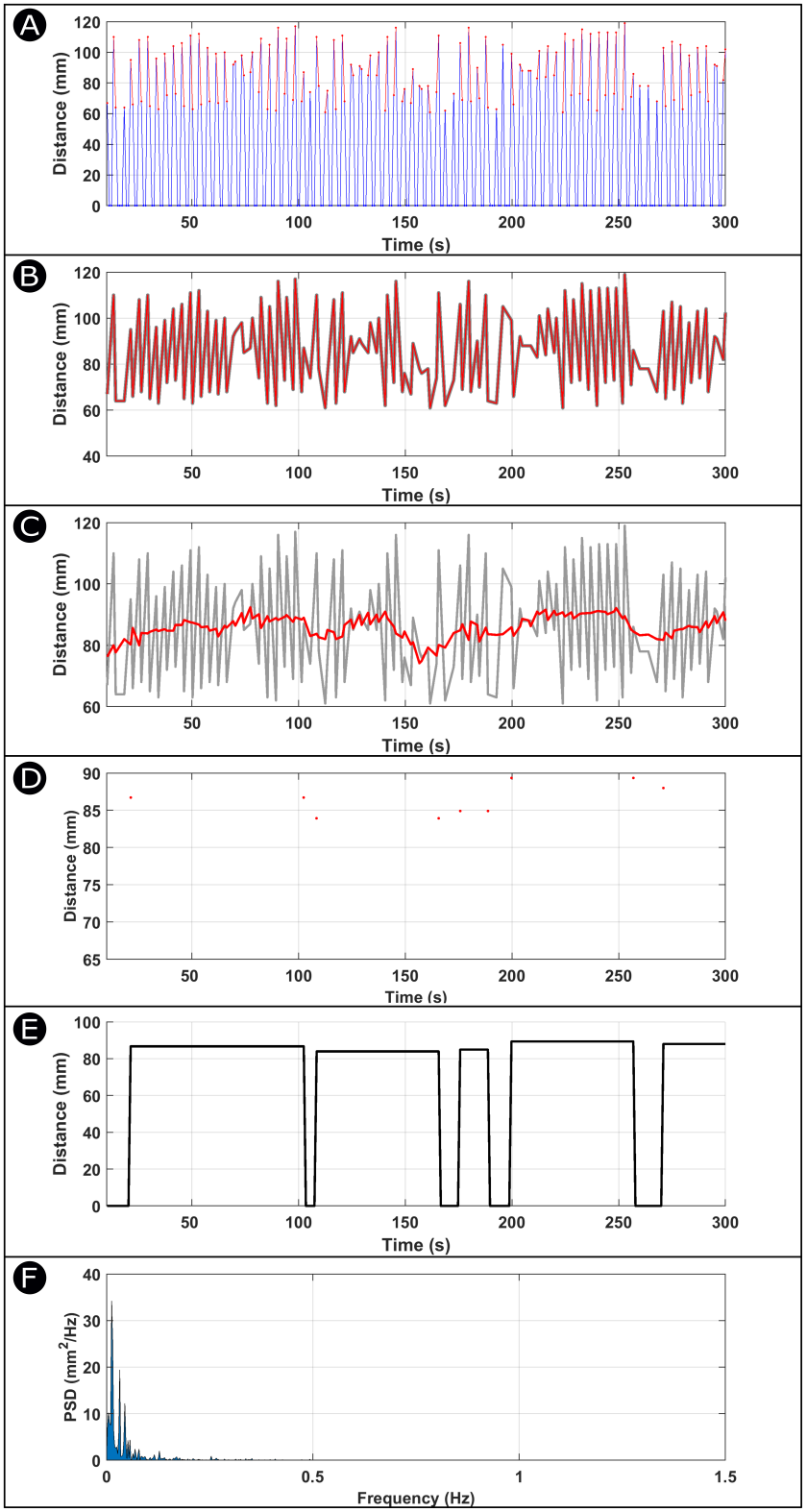

Figure 3.40: A figure showing an experiment conducted with a sampling rate lower than frequency of blade rotation. The sampling frequency used in this experiment is 1Hz. The frequency is lower than Nyquist frequency, showing that normal or fault measurands can not be identified. The sensor data was transmitted via serial communication. A) Raw sensor data. B) Sensor data after elimination of outliers. C) Sensor data after application of low-pass filter. D) Down-sampled sensor data. E) Distance profile. F) Power spectral density.

3.4.3 Discussion

In this Chapter, I combined ideas from the fields of offshore robotics, remote sensing and signal processing and designed a system to demonstrate that low-cost hardware can be a useful tool to monitor offshore energy platforms. The signal-processing techniques I used in this Chapter for condition monitoring were explicitly adapted to operate on my low-cost hardware. I used a down-sampling method to reduce the time taken to run the classifier and to decrease the size required in memory on the microcontroller. I performed a sliding window algorithm on-board as a rapid test of the system's functionality. The same approach can be applied to other faults and other sensors, which I discuss in Sections 3.4.3.1 and 3.4.3.2, respectively. I discuss, in Section 3.4.3.3, the advantages and disadvantages of on-board computation as compared to offline computation and the possible interferences to the measurements, and how I reduce them, in Section 3.4.3.4.

3.4.3.1 Applicability to Other Faults

The classification approach I adopted is a generic solution to condition monitoring and not specific to the faults I introduced to the system in this Chapter. My method depends on the change in normal operation conditions of equipment, where the change is associated with the presence of a fault in the system. I trained the classifier offline with conditions related to normal operation of the fan. The offline classification determines multiple parameters for normal operation including average distance to the fan blades, standard deviation of distance measurements, and frequency of rotation of the fan. These parameters are then transferred to the Limpet for online classification and do not change during operation. During the online classification, the Limpet checks the parameters of the class representations (average, standard deviation, period) to the parameters of normal operation stored on the microcontroller's memory. If any of the parameters fails the check, the Limpet classifies the measurement as a faulty operation. Thus, any fault that changes the normal operation conditions of the fan, which in turn results in a change in these parameters, will be detected and flagged as faulty operation by the Limpet. I believe that my method is applicable to several different fault types. I test my approach by introducing four specific faults to the system to determine if

the Limpet can detect these faults. Examples of other faults that could be detected for wind turbines or rotating machinery are bending of blades, change of distance between blades, or undesirable vibration or oscillation of blades.

3.4.3.2 Applicability to Other Sensors and Systems

In this Chapter, I have shown how a single sensor can be used to monitor the state of equipment by measuring several measurands, as well as how the data can be processed and analyzed on-board to improve communication requirements. My method is dependent on distinct measurement profiles associated with each measurand. The method also depends on time-varying measurements. I believe that this approach is applicable to other sensors and systems, if the measurement profile is (i) a time-varying measurement and (ii) distinctly different from other profiles. Thus, this method could be used by other sensors to identify different types of faults with equipment or to monitor different parameters on offshore platforms. It could also be easily adapted to other low-cost systems.

3.4.3.3 On-board (Online) Data Processing vs Offline Processing

By processing and analyzing data on-board using the microcontroller, I can improve the communication and power requirements of the system while still being able to perform same analysis. Data transmission does not need to occur continuously, but only in the case of a particular event. This design allows for the use of communication systems with high transmission distance, but low bandwidth (such as LoRaWAN), and increases the expected battery life of systems as the data transmission link is the most power-consuming part of a system. Offline processing involves continuously transmitting data and analyzing it to detect the presence of any faults. This approach is time-consuming, reduces battery life and requires high communication bandwidth, which lowers transmission distance. The major drawback of my approach is that low-cost hardware is limited in its computational power. As such, I am restricted to the types of algorithms that could be used on the system.

3.4.3.4 Mitigation of Interferences

Several parameters impact the sensor measurements and interferes with the classification process. Five of these parameters are: (1) Displacement of the Limpet during the experiment, which will affect the distance measurement to the equipment and will impact the classification process; (2) Change in the distance between the Limpet and the fan for the different set of experiments; (3) The target surface used for the fan blades. Different target surfaces will reflect light (laser) differently and might thus affect the distance measurements; (4) Presence of objects behind the experimental setup or fan. The distance sensor can detect distances up to 2 m, and the presence of any objects behind the fan would affect the distance measurement level (zero) for absence of fan blades; and (5) The Field of View (FoV) of the distance sensor, which is the angle at which the receiver on the sensor is sensitive to electromagnetic radiation. The distance sensor has a FoV of 25°, which causes it to detect the edge of the fan blade before the blade center is opposite the sensor. This error results in a larger number of distance measurements versus time as each blade passes in front of the limpet, and therefore, the blade appears wider than its actual width when observed by the receiver of the sensor.

In this Chapter, I reduce the effect of these parameters on our measurements in five ways: (1) I fixed the Limpet in place on a small wall in front of the fan to reduce any displacement by the Limpet; (2) I fixed the stepper motor in place in the experimental setup to minimize the errors in measurement by having the fan always at the same distance from the Limpet for all the experiments; (3) I used a white acrylic surface for the fan blades, as white targets cause maximum reflectance; (4) I place an acrylic sheet at a distance of 2.5 m behind the fan and setup, which is out of the range of measurement of the distance sensor, and thus ensures the same measurement level for absence of blades; and (5) I compute the moving average of our sensor measurements with a sliding window of size (8) to reduce the effect that the FoV introduces on our measurements. There are additional errors such as random noise or sensor drift that affect the robustness of the automatic decision-making process. The effect of these errors on the robustness of the online decision-making have not been considered in this work and will need to be investigated in future work.

3.5 Summary

A new multi-sensing platform, the Limpet, which is part of the ORCA Hub System is developed. I embedded the Limpet circuitry in a protective housing to protect it from the harsh offshore weather conditions. I have integrated the Limpet with ROS, which allows it to be used with other robots within the ORCA Hub System, where the interaction between different robots results in more complex and useful behavior. I designed the Limpet to be low-cost and highly manufacturable, which enables us to deploy it in huge collectives for inspecting offshore energy platforms. I show how the Limpet could be used for fault detection in wind turbines, by detecting multiple measurands from a single sensor. This demonstrates one of the possible multi-sensing capabilities of the Limpet in offshore monitoring. I demonstrate this approach using four different communication systems. I also show how the processing and analysis of the data from the sensor can be done on-board using the microcontroller, which can improve the communication requirements. The signal-processing techniques used are generally applicable to time-variant measurements; however, they must be applied to time-varying, distinct, and systematically reoccurring measurements to augment the sensing capabilities of a robot. I train the classifier offline and transfer its parameters to the Limpet for online classification. During online classification, the Limpet takes an autonomous decision of either transmitting the data or continuing the monitoring process based on whether a fault is detected or not. I apply spectral analysis to the data to classify the type of fault detected. The results in this Chapter shine light on how robots can perform on-board signal processing and analysis to gain multi-functional sensing capabilities, improve their communication requirements, and monitor the structural health of equipment or structures offshore.

Part III

Limpet Deployment, Navigation and Adhesion

Chapter 4

Deployment of the Limpet

4.1 Introduction and Background

Monitoring environmental and structural conditions in offshore platforms is an essential task, however, deployment of monitoring nodes such as the Limpet in such environments is an expensive task. Given the inherent nature of these environments, there has been a drive to remove humans from these environments and not involve them in such tasks. Robots are a key alternative, where they can be used to deploy monitoring nodes, such as the limpet, in such environments. A major challenge that robots face in offshore environments is the unstructured nature of the environment, where task planning will require increased complexity and intensive resources. In this Chapter, I present the design of a custom-built mobile soft/hard hybrid robotic platform that can robustly place the Limpet on an asset. This Chapter is based on my submitted journal paper [4], which can be found in Appendix J on Page 423. In this submitted journal paper, Alistair C. McConnell contributed to writing the manuscript and helping with conducting the experiments, Jamie O. Roberts contributed to the development of the robot and the control software, designing the vision software, and helping with conducting the experiments.

The focus of this chapter is not about the specific robot presented, but about demonstrating one way in which monitoring nodes like the Limpet can be deployed on offshore platforms without involving any humans, and showing how we can reduce the complexity of task planning in such deployment tasks. The deployment can be achieved using other robotic platforms as well, such as the mobile robotic platform shown in Chapter 7, or using drones. A video of the Limpet being deployed on a target using drones can be found here:

Deployment of the Limpet Using Drones. 

The design objectives of the robot in this Chapter were:

- The robot needs a mobile base to move in its environment.
- The robot needs to map its environment.
- The robot needs to locate a target surface in the environment.
- The robot needs an arm to pick up the Limpet.

- The robot needs a soft gripper to easily pick up the Limpet without previous knowledge of its shape, and robustly place the Limpet on the target surface regardless of the angle and roughness of the surface.
- The robot needs to be able to communicate with the Limpet.
- The robot needs to have a controller to control the movement, gripper, arm, and base.

In this Chapter, I demonstrate how my mobile hybrid robotic platform navigates an area and locates a target to place the Limpet. The robot uses the data provided from the Limpet to robustly place the Limpet on that target. I discuss the system design of the deployment system in Section 4.2, where the design of the hardware is discussed in Subsection 4.2.1, design of the control software is explained in Subsection 4.2.2, and the assembly of the system is depicted in Subsection 4.2.3. Section 4.3 includes a detailed description of the experimental setup I designed to conduct all my experiments, including the design of the mapping task, the design of the search and location task, and the design of the placement task. I explain the experimental results in Section 4.4. Section 4.5 gives a brief summary of this Chapter. A video of the system deploying the Limpet onto a target after mapping the environment and locating the target can be found here:

Deployment of the Limpet Using Hybrid System.



4.2 Deployment System Design

4.2.1 Design of the Hardware

The mobile hybrid deployment platform consists of six main parts as shown by Figure 4.1. The six main parts of the system include: Limpet, soft gripper, 2 degree of freedom robotic arm, mobile base, on-board controller and vision system. The Limpet node is discussed in details in Chapter 3. In this Chapter, I used the data collected by the Time-of-Flight sensor to measure the distance between the Limpet and the target area. The data from the Limpet is transmitted to rest of the system over Wi-Fi using the ESP8266 module. Figure 4.1 shows the Limpet mounted in its encapsulation while grasped by the hybrid deployment system. The encapsulation has been designed to protect it from damage and provide it with the ability to be mounted on magnetic surfaces.

The key aspect of the deployment system is the use of the soft gripper for deploying the Limpet. The design of the soft gripper needed to be able to hold the Limpet securely while the robot is traversing its environment, and then be able to robustly mount the Limpet on an uneven surface. I developed the soft gripper using four Pneunets [229] and a single pneumatic input line. The single line of control reduces the complexity of the robot, while providing suitable strength and compliance to carry and place the Limpet. Using a soft actuator allowed placement of the Limpet onto the wall regardless of its shape, as the soft actuator would conform to the shape of the surface.

The 2 degree of freedom arm was designed using acrylic layers and servo motors. The servo motors provide high torque, and thus increased the lifting capacity of the arm. The body of the deployment system is based on a wheeled hard robot (iRobot Create) [230], which I modified with an acrylic structure that the computer, arm and camera are mounted on. The wheeled robot, shown in Figure 4.1, is capable of travelling up to 500mm/s on a smooth, flat surface, and the robot is capable of carrying up to 3kg payload. The robot contains multiple sensors such as a front bump sensor, front mounted IR sensor, cliff sensors and drop sensor. The iRobot is operated via serial communication.

The on-board controller of the deployment system takes the form of an Intel NUC8i7HVK, running Linux. The Intel NUC is compact with dimensions of 220x140x44 mm. The Intel NUC, shown in Figure 4.1 is mounted on the

acrylic layer. The vision system of the deployment system consists of an Intel RealSense D415 camera [231]. This camera is a stereo depth camera that allows for 3D mapping and object recognition. In this Chapter, I used the camera for 3D mapping of the environment and detection of an AprilTag [232] to identify target location.

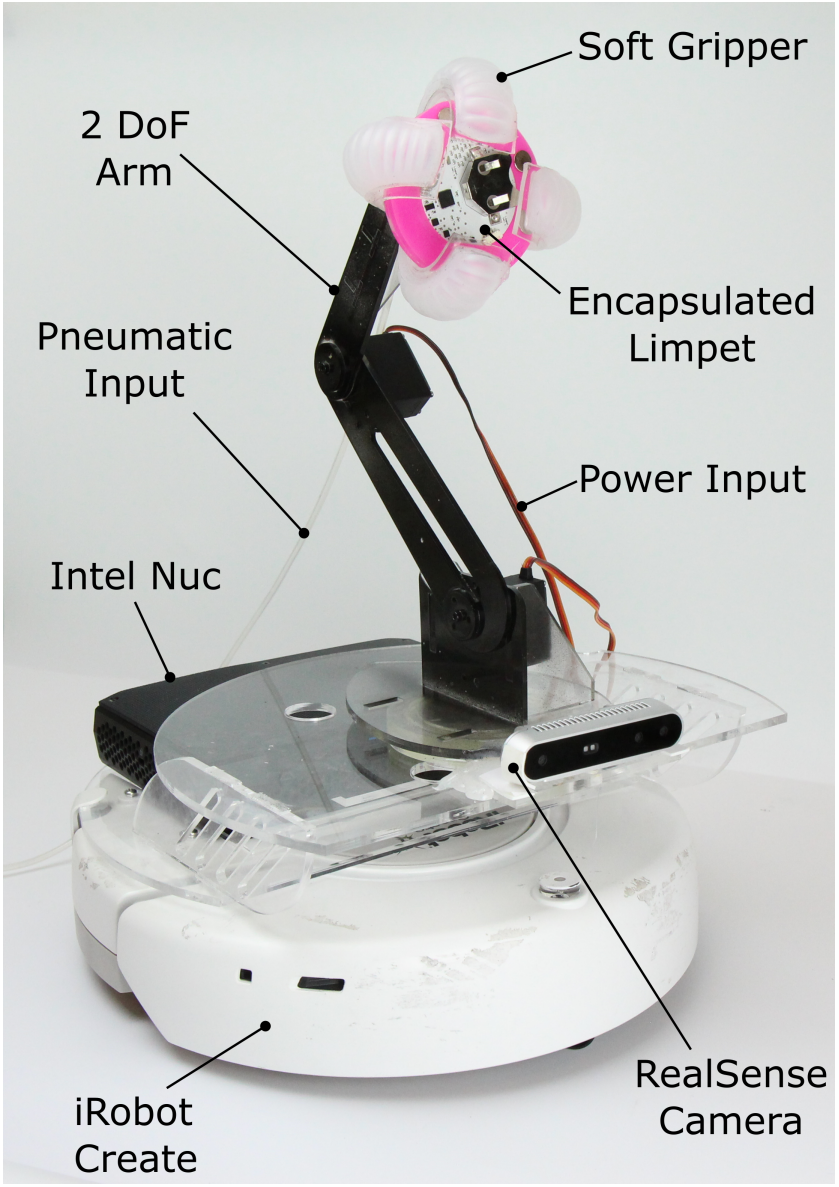

Figure 4.1: An image of the complete deployment system showing the iRobot Create Base, Power and Control Hardware, Intel NUC, RealSense D415 Camera, 2 Degree of Freedom Arm, Soft Robotic Actuator and Encapsulated Limpet.

4.2.2 Design of the Control Software

The deployment system control was provided by the Intel Nuc and the microprocessor (Arduino). The data flow in the system is linear, where the RealSense camera and the Limpet send data over USB and Wi-Fi, respectively, to the Intel NUC. The Intel Nuc processes the data and sends the appropriate commands to the microprocessor via USB, which in turn, sends the commands to either the arm, soft gripper or mobile base.

The control software on the deployment system consists of two parts: simultaneous localization and mapping (SLAM) navigation and limpet sensor feedback. The navigation of the deployment system was a combination of the SLAM navigation [233] in the form of Real-Time Appearance-Based Mapping (RTAB-Map) [234] and a visual fiducial system, AprilTags [232]. The RTAB-Map is an RGB-D Graph SLAM approach compatible with ROS. The SLAM approach was paired with the use of AprilTags. AprilTags are a form of open-source visual fiducial system that use a 2D bar code 'tag' which allows for six degree of freedom localisation and provides a marker point for the target where the Limpet needs to be mounted. AprilTags have been used in land robotics navigation and underwater navigation [235]. The Limpet communicates to the deployment system through the use of an ESP8266 Wi-Fi module. The Limpet sends its data wirelessly to the Intel Nuc through MQTT. The Intel Nuc can then act on the data it receives by sending control signals to the arm, soft gripper or the iRobot Create base.

4.2.3 Full System Assembly

Figure 4.1 shows the complete deployment system with the Limpet mounted in the soft gripper. It was autonomously controlled by an Arduino Mega 2560, and the data from the vision system was processed by a python script running on the Intel NUC which, in turn, passed the commands to the microprocessor (Arduino). The microprocessor sends control signal commands to the motor controls, electro-pneumatic controls and to the mobile base. The total additional payload I added to the wheeled base is 1.5kg. I use Slackbot [236] for sending commands, monitoring, controlling and shutting down the deployment system. Slackbot is a custom developed bot that functions with the Slack mobile application.

4.3 Experimental Design

In this section, I discuss the design of the experiments used to verify the functionality of the deployment system as a mobile platform capable of robustly and autonomously mounting Limpets on a target to monitor the structural or environmental parametrs. Figure 4.2 shows a schematic of the experimental setup used. The deployment system was placed in an enclosed arena, where an AprilTag and a steel plate are affixed to a section on one of the sides of the arena. The experiment is divided into three consecutive tasks: mapping, search and location, and placement.

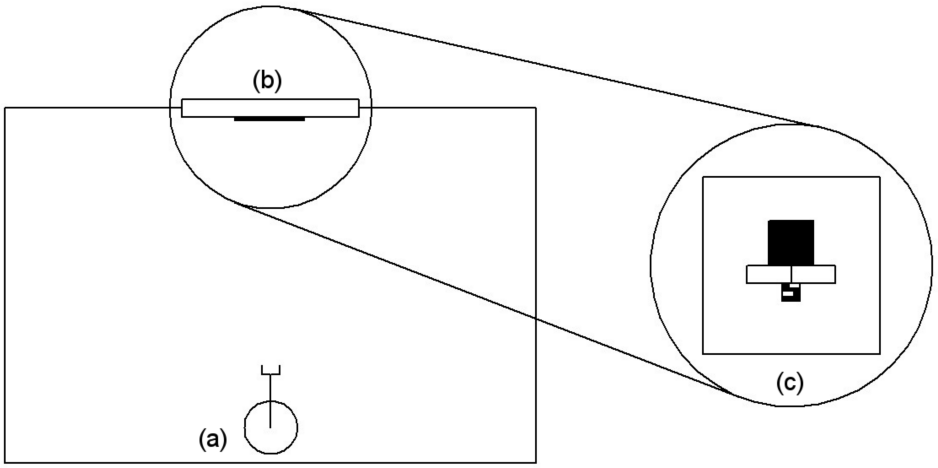

Figure 4.2: A schematic representation of the experimental setup. The schematic shows the layout of the test arena where (a) shows the intial start point of the deployment system , (b) the target area, (c) the breakdown of the target.

Design of the Mapping Task

The first task of the deployment system is to create a 3D map of its surrounding environment. The robot starts scanning the arena and building a map using RTAB-map. Once a full sweep of the environment is completed, the robot repeats the sweep once more. After the second sweep, the robot proceeds to carry out the search and location task.

Design of the Search and Location Task

The second task of the deployment system is a search and location task. An AprilTag was placed on a target surface in the experimental area. The robot starts navigating the environment and searching for the AprilTag to locate the target surface. Locating the AprilTag is carried out using the RealSense camera. Once the AprilTag is located, the robot will start approaching it to a minimum pre-defined distance. Once the robot is within the specified distance, it proceeds to the placement task.

Design of the Placement Task

The final task carried out by the robot is placement of the Limpet on the target surface. The deployment system first positions the soft gripper holding the Limpet within 200 mm of the surface. The robot will start receiving distance measurements from the Limpet to identify the distance to the target surface. The distance measurements is used by the robot to identify successful placement of the Limpet. The Limpet is then placed robustly on the target surface by extending the robot arm and opening the soft gripper.

4.4 Experimental Results and Discussion

In this section, I demonstrate the results of the deployment system in the different tasks conducted. Figure 4.3 shows the 3D map of the environment built by the robot. This first task serves the objective of building a map of the surrounding environment and checking the environment for obstacles.

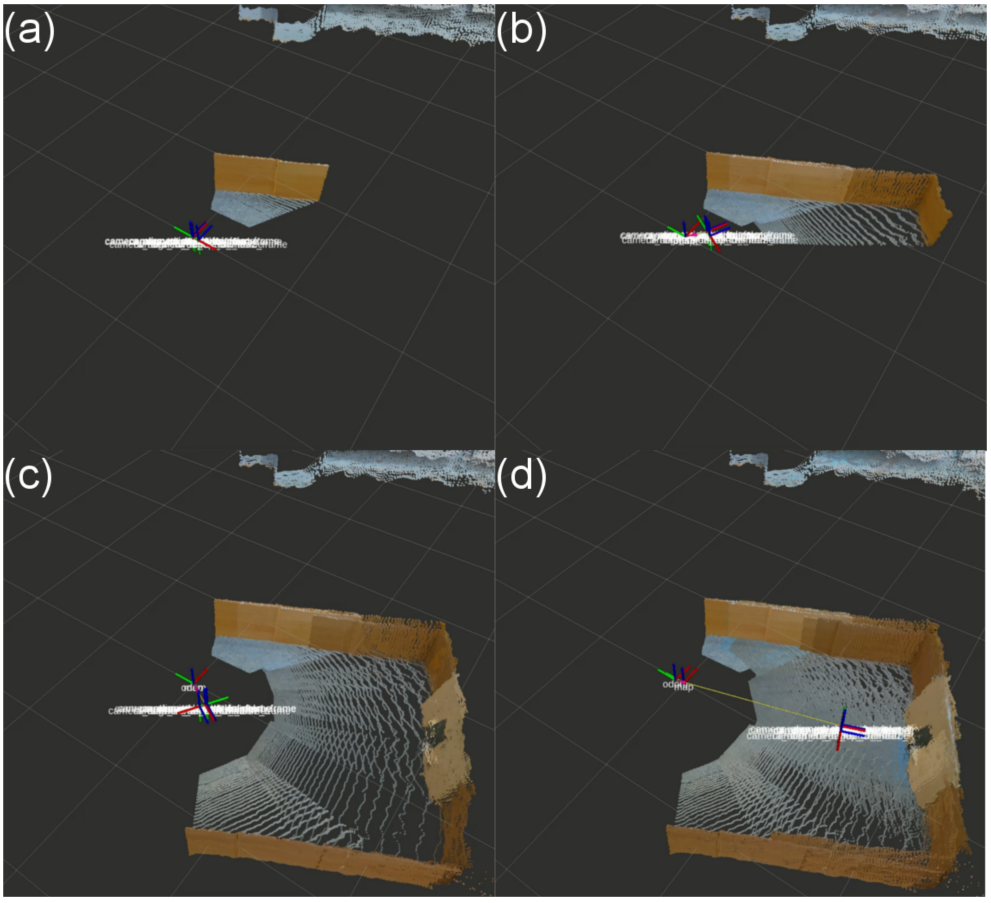

Figure 4.3: 3D mapping of the arena by the robot, where (a) the robot begins to map its surrounding area, (b) the robot continues to turn to map the surrounding environment, (c) a complete 180 degree arc in front of the robot has been mapped, and (d) the robot starts moving towards its target.

Figure 4.4 shows the progress of the deployment system as it progresses through its search and location task. The robot begins its navigation in Figure 4.4A, where it has located the AprilTag and is moving towards it. The robot then arrives within a pre-defined distance to the AprilTag as shown in Figure 4.4B. In both Figures 4.4A and 4.4B, the bottom right corner shows the view from the RealSense camera on the robot. The view from the RealSense camera shows the AprilTag being located and marked as the robot moves towards it. The robot then starts the placement task and raises the soft gripper to the target wall as shown by Figure 4.4C. Figure 4.4D shows the arm of the robot extending and placing the soft gripper against the wall to mount the Limpet on the target. The bottom right corner of Figures 4.4C and 4.4D shows the distance data from the Time-of-Flight sensor on the Limpet. The distance data does not change initially, as the Limpet stays at a constant distance from the wall. As the Limpet is placed on the target wall, the distance to the wall decreases significantly as shown in Figure 4.4D.

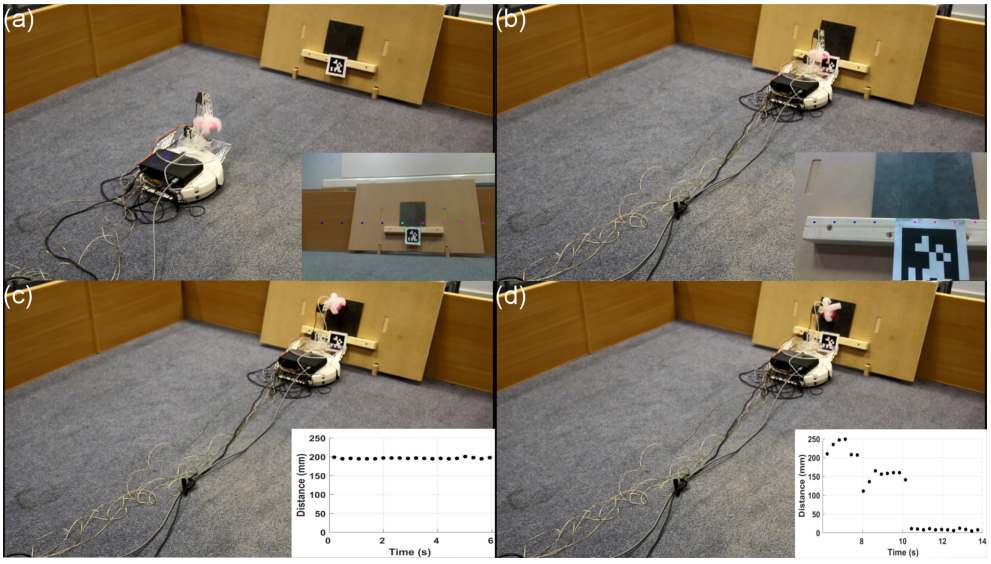

Figure 4.4: Still frames from the video of the robot performing a search, location and placement tasks with the Limpet. (a) the robot searches and locates the target which it moves towards, (b) the robot reaches the target and stops. Included in (a) and (b) in the bottom right of each frame is the view from the RealSense camera as it tracks the AprilTag. (c) the 2 DOF arm rises up to its mounting position and aims the Limpet at the target area, (d) the arm has extended and the soft actuator has placed the Limpet against the wall. Included in (c) and (d) is the data received from the Limpet regarding its distance from the target as the placement task proceeded.

4.5 Summary

In this Chapter, I present the design of a platform for deploying the Limpet in offshore environments. The system uses a conventional mobile robotic base and a soft gripper to deploy the Limpet in an unstructured environment. This work demonstrates an example of how to reduce the computational complexity of dynamic task planning by integrating soft materials with conventional robotic platforms, as the inherent compliance of the soft material reduces uncertainty in unstructured environment. The system is capable of creating a 3D map of its surrounding environment, moving rapidly over smooth surfaces, detecting a target (AprilTag), and placing the Limpet at the target for structural and environmental monitoring. Placement of nodes can be done in multiple different ways, but it would typically require an in-depth knowledge of the node and properties of the surface. The deployment system presented in this Chapter uses its soft robotic gripper to both handle the monitoring node "Limpet", of which it has no previous knowledge of, and robustly mount it on a target structure.

The communication system for the deployment system relies on Slackbot for its initial command before it runs autonomously. The deployment system is capable of carrying all of its necessary components, communications systems, motors, valves, a Limpet and a soft robotic gripper. In this Chapter, the presented system is currently tethered to a mains power supply for all its power requirements, but could run of a battery pack. This integration of hard robotics with soft robotic manipulation provides an advantage over other deployment techniques as it can lead to more complex tasks being achieved by simpler systems.

Chapter 5

Limpet Navigation and Adhesion

5.1 Introduction and Background

After deployment of the Limpet using another robotic system, it needs to navigate through the offshore environment and adhere to different surfaces in order to inspect and monitor the different offshore assets. Offshore platforms are massively complex and unstructured environments. The environment consists of surfaces at different angles, steep inclines, and inverted surfaces. To navigate such unstructured environments efficiently and be useful for inspection and exploration tasks, the Limpet must be have a good adhesion mechanism and be capable of multiple locomotion modalities such as walking, running, and climbing [237]. The ability to adhere to and climb these inclined surfaces would increase the accessible areas of the Limpet in such environments, which improves its capability to do inspection and monitoring of the offshore platform. Adhering and climbing on these unstructured offshore environments alone is not enough for the robot to carry out inspection tasks; it should also be equipped with a sensor payload. The Limpet is equipped with nine different sensing modalities, which makes it suitable for such tasks.

Robots performing tasks in unstructured environments, such as offshore platforms, need to adapt to variable constraints in their environment. Modular robots or assemblies of modular units are favoured on traditional robotics in these environments due to the lack of adaptive nature of traditional robots and the advantages that modular robots provide. Modular robots or assemblies of modular units make it easier to repair the system, replace modules, and control the robot. By building robots in a modular architecture, it is easy to adapt the robot to new tasks by simply adding or replacing modules. Modular units are easily reconfigured, giving the robot more robustness and capability for achieving new tasks. The capability of single modules are limited, but modular robots consisting of multiple units have increased capability compared to the sum of their parts [9]. By stacking or combining modules, we can increase the overall capability and the range of behaviours and motions of a system, and thus, utilise it to perform useful tasks.

In this Chapter, I discuss the design, fabrication, specifications and properties of version 2 of the Limpet system. Version 2 of the Limpet builds up on version 1 and is designed in a modular fashion. The Limpet version 2 uses a multi-functional electromagnetic module (EMM) and a sensing module to achieve increased capability and reconfigurability while keeping the costs low.

It is capable of climbing inclined surfaces, adhering to structures and sensing its environment. In this Chapter, I discuss the design of experiments used to characterise each of the modules on version 2 of the Limpet. I also show demonstrations where the Limpet system acts upon sensory change or input from its environment. Finally, I show the Limpet adhering to and climbing an inclined surface. This Chapter is based on my published journal paper [2] and my submitted journal paper [3], which can be found in Appendix H on Page 343 and Appendix I on Page 355, respectively.

The Limpet version 2 uses a low-cost and manufacturable EMM as its core module. The EMM can actuate linearly and produce sound output. I used the EMM to construct adhesion and locomotion modules, to give the Limpet the capability of locomotion, adhesion and sound communication. The Limpet has multi-sensing capabilities and was designed as a modular system. The modular architecture allows the Limpet to achieve multiple complex tasks in its environments including climbing, adhesion and monitoring the health of different structures. I designed most of the parts of the Limpet version 2 from soft materials as it gives the advantage of inherent compliance, low-cost manufacturing, and improved safety. The soft material compliance can immensely help robots in unstructured environments adapt to unexpected environmental changes such as slopes and obstacles. I have developed the Limpet version 2 as an untethered system. The dependence on electrical or pneumatic tethers limits the applications that can be performed by robots in their environment [238, 239]. For systems to be useful in field applications, all their vital components (e.g. actuation, power, communication and processing components) need to be fully integrated within their structure [239]. The experiments I conducted to characterise the different modules within the Limpet used power and pneumatic tethers. However, the final Limpet system was developed as an untethered system.

I based the Limpet version 2 presented in this Chapter on version 1 of the Limpet system [1] and the Linbot system [2]. Version 1 of the Limpet is a multi-sensing platform for monitoring offshore platforms. The Limpet version 1 was designed to be low-cost and highly manufacturable, and thus can be deployed in huge collectives for monitoring the offshore platforms. Version 1 of the Limpet is an integrated PCB with nine sensing modalities. It was integrated with ROS, to allow it to interact with other robots on the offshore platform. I demonstrate how the Limpet version 1 can be used to achieve

real-time condition monitoring for offshore structures, by combining remote sensing with signal processing techniques, in Chapter 3. The Linbots [2] were developed to show how a collective of low-cost robots can be reconfigured to achieve different useful tasks. The Linbot is a soft, modular robot that uses a multi-functional electromagnetic module for linear actuation, communication, sound output and tactile sensing. The Linbot and the Limpet version 1 are not capable of any locomotion or adhesion. In this Chapter, I define the Limpet version 1 as the sensing module. The EMM used for the Linbot is utilised in this Chapter to achieve locomotion and adhesion for version 2 of the Limpet. Figure 5.2 shows a picture of the overall Limpet version 2 system. A video showing the overall capabilities of the Limpet v2 system can be found here:

Overview of the Limpet v2 System. 

In Section 5.2, I explain how the electromagnetic module works, discuss its capabilities, and show how it was used for the Linbot system and the new Limpet system. I discuss the system design principles of Limpet version 2 in Section 5.3. Section 5.4 details the electrical design of the Limpet version 2. Section 5.5 depicts the mechanical design of the Limpet version 2, where I discuss the design of the different modules used to develop the system. The fabrication techniques for the different components in the system is demonstrated in Section 5.6. Section 5.7 discusses the design of the experiments I used to characterise the different modules in the Limpet version 2 system. In Subsection 5.7.1, I discuss the experiments designed to characterise the EMM. Subsections 5.7.2 and 5.7.3 demonstrate the experimental design used to characterise the adhesion and locomotion modules, respectively.

The rest of the Chapter is organised as follows: Subsection 5.8.1 discusses the results of the experiments used to characterise the EMM; Subsections 5.8.2 and 5.8.3 demonstrate the results of the experiments for characterising the adhesion and locomotion modules, respectively; Subsection 5.9.1 gives the results of the untethered sensory control demonstrations; Subsection 5.9.2 depicts the results of the sound-based communication demonstration between

different Limpets; Subsection 5.9.3 demonstrates the results of the demonstration involving the Limpet climbing an inclined surface; Section 5.10 summarizes the conclusions, elaborates on their implications and outlines the limitations of the results; Section 5.11 gives a brief summary of this Chapter.

5.2 Electromagnetic Module (EMM)

Figure 5.1 shows the EMM. The EMM is an electromagnetic system that is based on the same fundamental principles of loudspeakers. The EMM consists of an actuating electromagnetic coil and permanent magnets, which are attached together using a soft body that functions as a spring. The electromagnetic coil can repel or attract the permanent magnet depending on the direction of the current applied to the coil, and this force stretches or compresses the body of the robot, creating linear motion. The EMM is a hybrid hard/soft system. Hybrid systems can take advantage of rigid components while still being able to partially conform to their environment [240].

EMMs have been shown to be a useful system for soft robotics [145, 2]. They are multi-functional components that can generate different behaviours over a range of different control frequencies. At low frequencies, the EMM demonstrates linear actuation capabilities. At audible sound frequencies, the EMM acts as a loudspeaker and at even higher frequencies it can be used for communication [145, 2], where the communication is based on inductive data transmission. For Limpet version 2, I only use the actuation and sound capabilities of the EMM and do not utilise its communication capabilities.

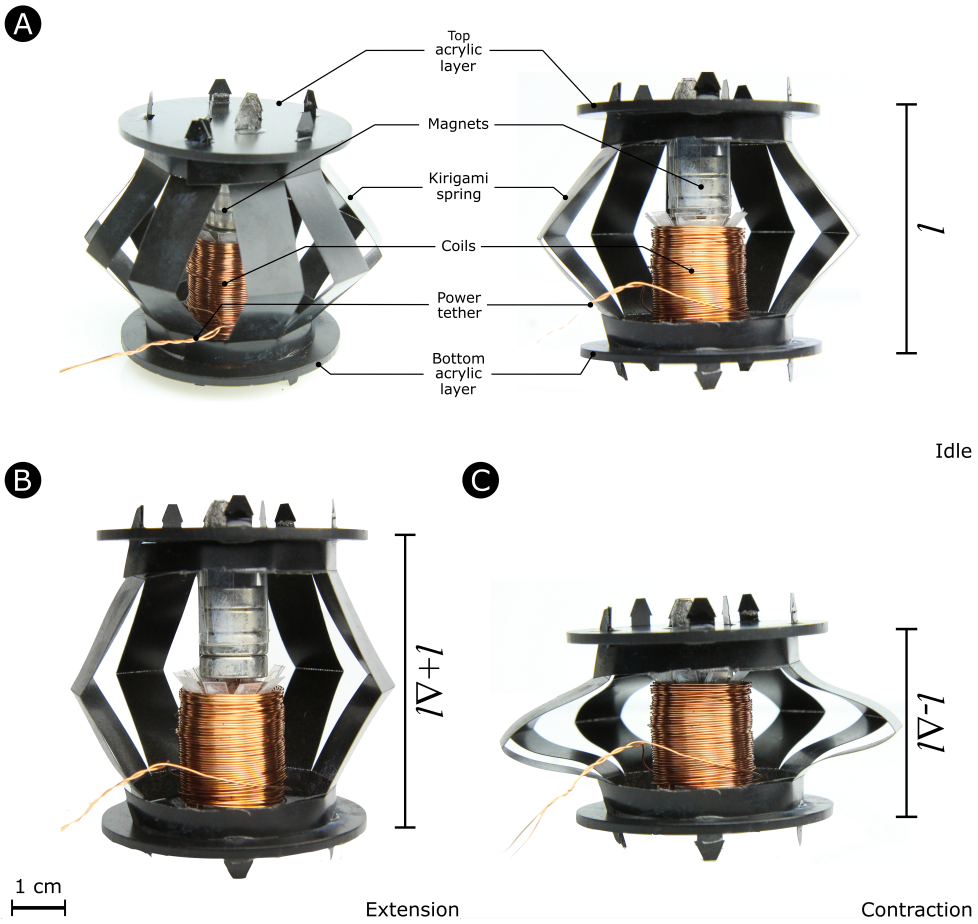

Figure 5.1: (A) A labelled picture of the EMM and a cross-sectional view of the EMM at rest position (l) showing the kirigami spring, coils, magnets, top and bottom acrylic layers. The coils interact with the magnets and either push or pull the kirigami spring. (B) An EMM extending which results in an increase in length of the module (l + δl). (C) An EMM contracting which results in a decrease in length of the module (l - δl).

5.3 Limpet v2 - System Design

The Limpet version 2 system consists of a sensing module (Limpet version 1), a power driver module, an adhesion module, a locomotion module and an outer protective shell as shown by Figure 5.2.

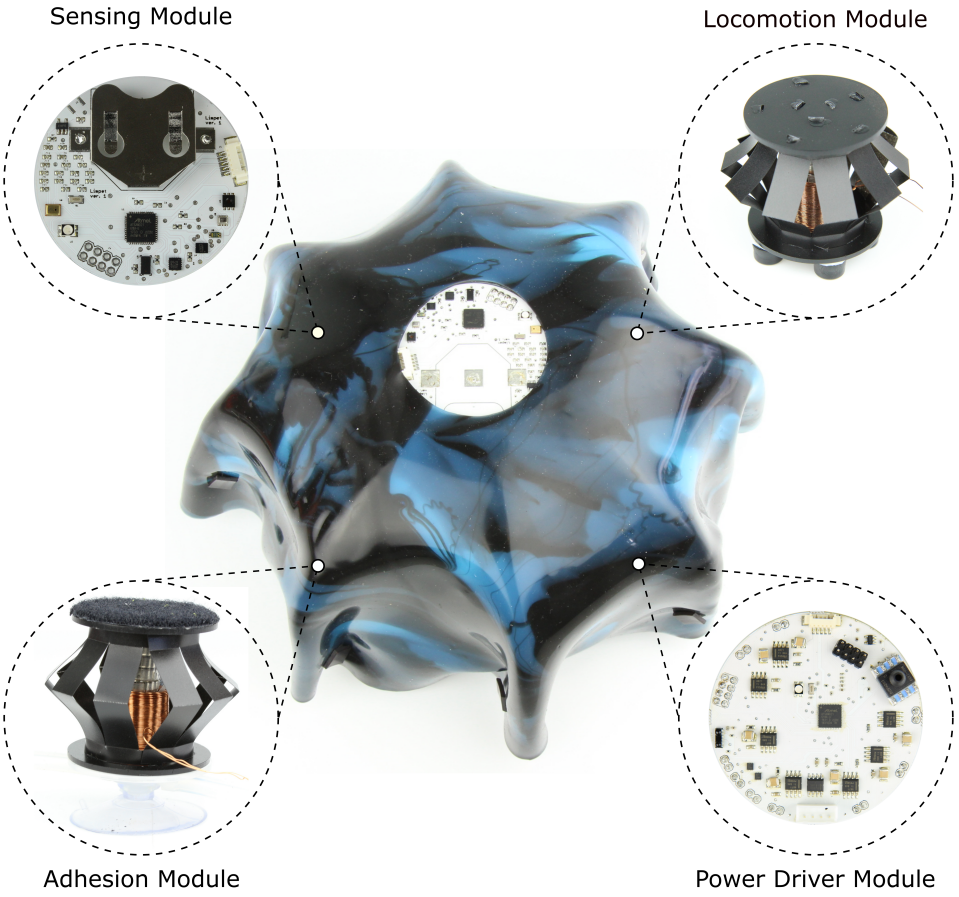

Figure 5.2: An overview of version 2 of the Limpet showing its main components: sensing module, power driver module, adhesion module, locomotion module, soft outer shell.

5.3.1 Sensing Modalities, Communications and Progamming

The sensing modalities on the Limpet version 2 system are all incorporated on the sensing module, which is based on version 1 of the Limpet. As such, the sensing modalities on version 2 are the same as version 1 of the Limpet, which include: temperature, pressure, humidity, optical, distance, sound, magnetic, accelerometer, and gyroscope.

The Limpet version 2 can use the same communication systems that are used with version 1, with the addition of infrared communication. I added an infrared data transceiver module on Limpet version 2. The module supports IrDA communication protocol with data rates up to 115200 bits per second and a transmission range of up to 8m. The module consists of an infrared emitter, a PIN photodiode and a low-power CMOS control IC. The infrared transceiver module allows the Limpet to communicate with local neighbours through IR or send its data to the computer at high rates for quick debugging. I use a custom-designed infrared handheld device to debug the Limpet using IR. A picture of the infrared handheld device can be found in Figure 5.3. A schematic of the PCB of the infrared handheld device can be found in Appendix F. The custom-designed infrared handheld device consists of an infrared transceiver module (TFBS4711), a microcontroller (ATSAMD21E16), and a USB-to-UART convertor (CP2102).

The sensing module and power driver module have an on-board programming port (JTAG). I program the Limpet version 2 via a SEGGER J-Link programmer together with a JTAG Adapter (Olimex ARM-JTAG-20-10) using a serial wire debug interface. I program the Limpet version 2 in C/C++ using Atmel Studio 7, and the main code includes online libraries and custom-written sensor libraries. I used the standard UART protocol for communication. The UART protocol uses a high idle line, which is pulled low at the start of a message.

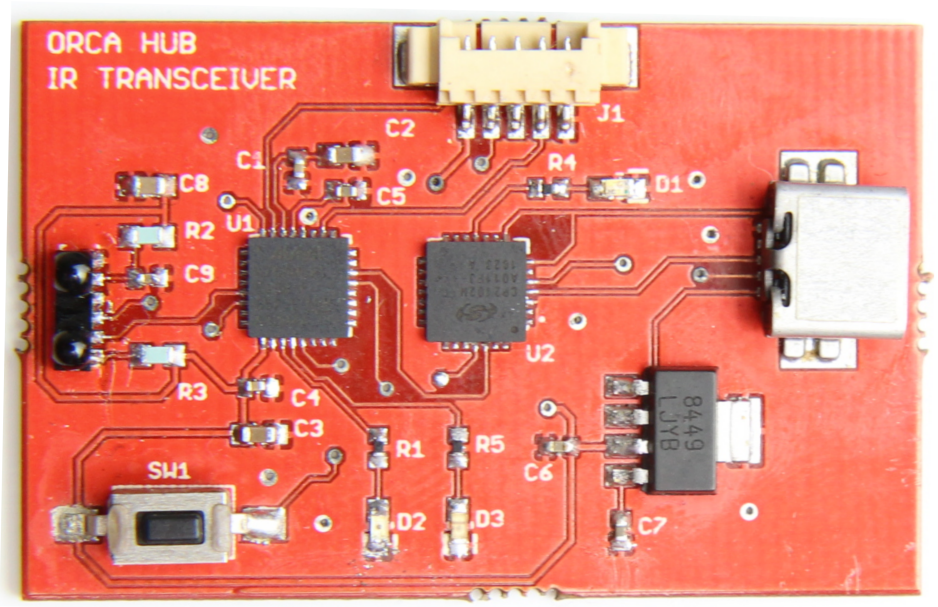

Figure 5.3: Picture of the Infrared Handheld Device.

5.3.2 Cost and Dimensions

The sensing module is an integrated PCB that has a diameter of 50 mm, a height of 3 mm and weighs 10 g. The power driver module is a PCB with a diameter of 65 mm, a height of 3 mm and weighs 15 g. The full Limpet system has a length of 250 mm, a width of 250 mm, a height of 140 mm, and weighs 450 g. I designed the Limpet to have a size and weight ideal for ease of fabrication, manufacturing and assembly. The total cost of the Limpet system is £112.3. The breakdown of the cost of the different components in the Limpet system is shown in Table 5.1.

Category	Components	Cost(£)
Sensing Module	Electronic Components	22
Power Driver Module	Electronic Components	47.96
Electromagnetic Module	Coils	1.22
	Magnets	3.08
	Acetate	0.054
	Acrylic	0.5
Adhesion Module	Electromagnetic Module	4.854
	Suction Cup	0.18
	Silicon Tubing	0.8
	Vacuum Pump	8.23
	Solenoid Valve	2
Locomotion Module	Electromagnetic Module	4.854
	Rubber Feet (x5)	0.773
Limpet Version 2	Adhesion Module (x1)	16.064
	Locomotion Module (x4)	22.508
	Sensing Module (x1)	22
	Power Driver Module (x1)	47.96
	Outer Body (Shell) (x1)	5
Total Cost		**112.3**

Table 5.1: Cost summary of the Limpet and its components.

5.4 Limpet v2 - Electrical Design

5.4.1 Design of the Control Electronics

5.4.1.1 Sensing Module

The sensing module is based on the Limpet version 1 PCB. The sensing module consists of a single two-layer PCB incorporating a low–power microcontroller (ATSAMD21G18A), a 32.768 KHz crystal oscillator (CM7V-T1A), RGB LED (LTST-N683EGBW), charging IC (MCP73812), programming port [JTAG] (Molex 532610571), nine sensing modalities and a communication connector.

The communication connector on the sensing module is connected to the UART of the microcontroller. Therefore, I can use this connector to connect the sensing module to multiple different communication systems. For the Limpet version 2, the communication connector on the sensing module is connected

to the power driver module. The microcontroller on the sensing module controls the sensing capabilities, and sends control messages to the power driver module based on the sensory input. The sensing module can also send the sensor data to the power driver module, which in turn, can forward the data to the PC or other node using one of the communication systems. The schematic of the sensing module is shown in Appendix F.

5.4.1.2 Power Driver Module

The power driver module consists of a single two-layer PCB incorporating a low–power microcontroller (ATSAMD21G18A), H-bridge drivers (DRV8871 and DRV8837), solenoid valve and air pump connectors, barbed absolute pressure sensor (HSCMANN015PA2A3), 3.5V voltage regulator (LP2985IM5), 5V voltage regulator (MC78L05ACDR2G), 32.768 KHz crystal oscillator (CM7V-T1A), infrared transceiver module (TFBS4711), connection to sensing module, battery connector, programming port and a communication connector. The frequency of actuation of the electromagnetic modules is controlled by the microcontroller, and the direction of actuation is also controlled by the microcontroller through the H-bridge drivers. The air pump and solenoid valve are controlled by the microcontroller through H-bridges drivers. The microcontroller on the power driver module is responsible for controlling the adhesion and locomotion capabilities. The pressure sensor is used as a feedback component for the closed loop controller of the adhesion system. The sensing module sends all the on-board sensor data to the power driver PCB, which then sends it to the computer through the IR transceiver or any other communication system (Serial, WiFi, LoRa, Optical) connected to the communication connector. A labelled picture of the power driver module is shown by Figure 5.4. The bill of materials for the power driver PCB can be found in Appendix B. The PCB schematic of the power driver module can be found in Appendix F.

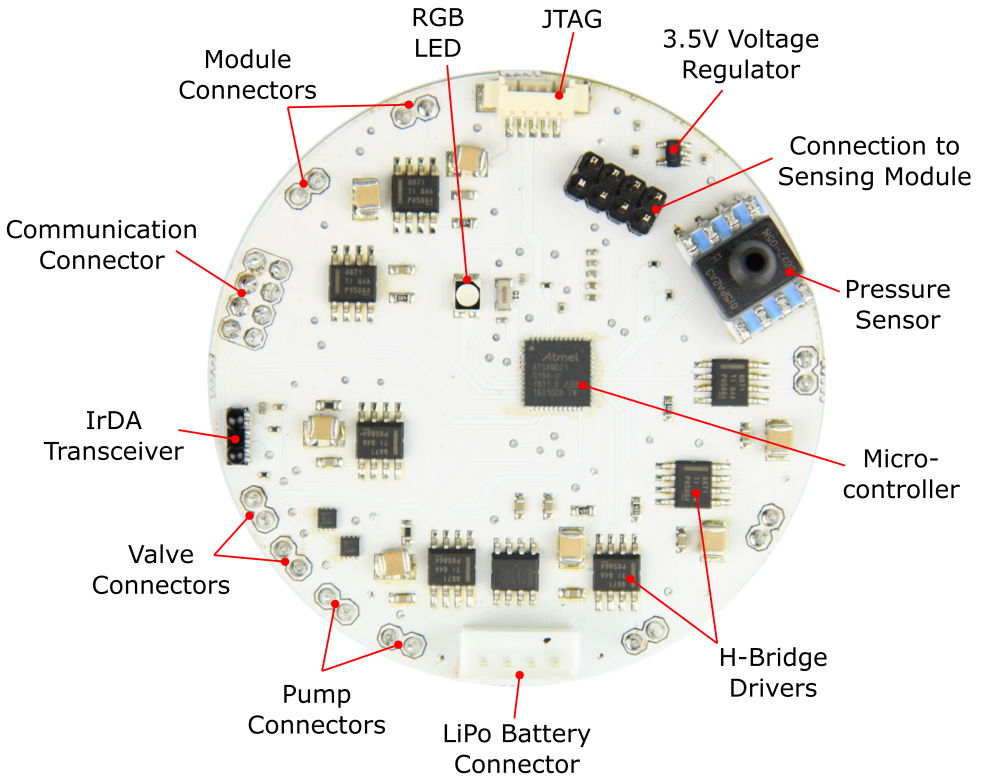

Figure 5.4: A labelled picture of the power driver PCB showing the pressure sensor, h-bridges, infrared transceiver, RGB LED, board-to-board connector, communication connector, JTAG, battery connector, microcontroller, valve connector, and pump connector.

5.4.2 Power System

The Limpet system is powered by a 450 mAh 11.1V lithium polymer (Li-Po) battery. The Li-Po battery is a rechargeable battery and has dimensions of 49 x 28.5 x 16 mm. In this Limpet version, I detach the Li-Po batteries for charging. The Limpet has a minimum battery life of 26 minutes and a maximum of 4500 hours. I calculated the minimum battery life by assuming the Limpet has all the sensors, RGB LED, microcontroller, infrared communication and electromagnetic module continuously on. The Limpet will consume approximately 1060 mA, with a power consumption of 11.766 W (communication consumes 10 mA (111 mW), RGB LED consumes 20 mA (222 mW), sensors consume 23 mA (255.3), microcontroller consumes 7 mA (77.7 mW), electromagnetic module consumes 1000 mA (11.1 W)), which allows for a battery life of about 26 minutes. I calculated the maximum battery life by assuming the Limpet is

in sleep mode, where it consumes an average current of 0.1 mA (1.11 mW). In this mode, the battery life of the Limpet can reach about 4500 hours (188 days). The other Limpet capabilities have different current consumption levels and thus can change the battery life. For example, when the limpet is static and adhered to a surface, the Limpet will have a battery lifetime of 50 hours. In this mode, the pressure sensor consumes 2.1 mA (23.31 mW) to achieve the closed loop control of the adhesion system, and the microcontroller consumes 7 mA (77.7 mW).

5.5 Limpet v2 - Mechanical Design

The Limpet is designed as a modular system consisting of an adhesion module, locomotion module, sensing module and power driver module. The main unit of the Limpet is the electromagnetic module, which is used as the core unit of the adhesion and locomotion modules.

5.5.1 Design of the Electromagnetic Module

The EMM consists of: electromagnetic coils wound around a reel; permanent magnets embedded in a holder; and a spring consisting of connected bent legs resembling a Chinese lantern as shown by Figure 5.1A. The magnet holder and the coil reel are attached to the spring using laser-cut circular acrylic layers. The EMM can be extended or contracted axially along its central axis from its rest position, depending on the polarity of current applied to the electromagnetic coil in the module as shown by Figure 5.1B and Figure 5.1C. The applied current induces a magnetic field in the coil, which either attracts or repels the permanent magnets resulting in this actuation mechanism. A sketch of the module and actuation mechanism is shown by Figure 5.5.

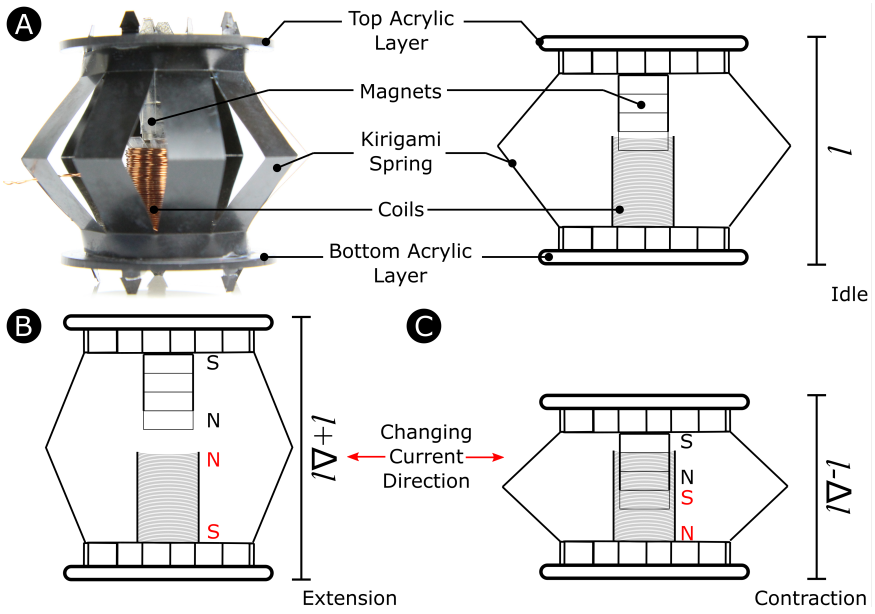

Figure 5.5: A labelled picture and sketch of the EMM showing all its components, and a sketch of the actuation mechanism.

5.5.2 Design of the Adhesion Module

To navigate the offshore environment efficiently and be useful for monitoring of offshore structures, the Limpet needs to have a good adhesion mechanism that allows robust adhesion to different surfaces. I developed a negative pressure adhesion module based on the EMM. The adhesion module also includes a suction cup, vacuum pump, a micro solenoid valve and a pressure sensor. The adhesion module is depicted in Figure 5.6A. Figure 5.6B shows a schematic representation of the adhesion system. I attached a T-connector to the suction cup. One side of the T-connector is connected to a pressure sensor. The other side of the T-connector is connected to a valve and pump. To attach to a surface, I program the EMM to push initially on the suction cup to flatten the suction cup and push out the air in the cavity between the cup and surface. I then open the valve and turn on the vacuum pump. The pump will remove any remaining air in the cavity and create a vacuum seal. After the seal is created, the solenoid valve is then closed and the pump is turned off. To detach the suction cup, I open the solenoid valve to atmosphere, which causes air to rush into the cavity and break the seal.

Adhesion Mechanism.

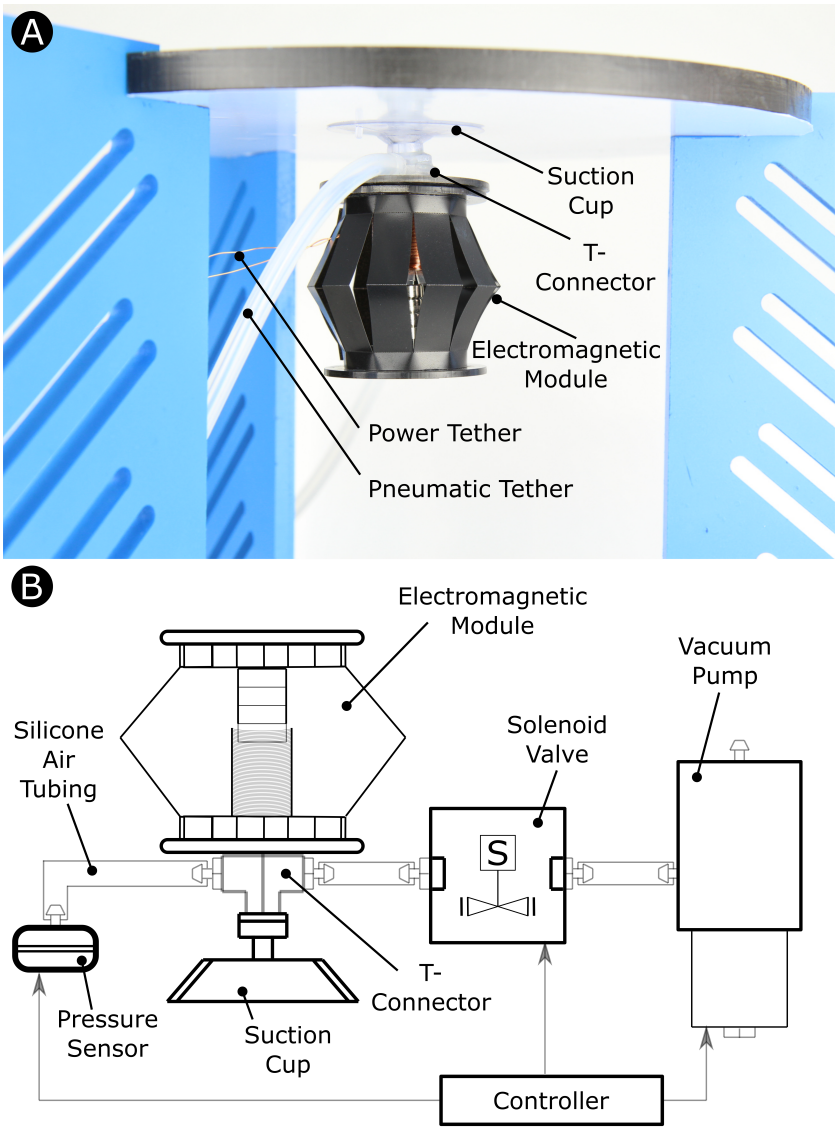

Figure 5.6: (A) A labelled picture of the adhesion module showing the EMM, suction cup, T-connector, and pneumatic and power tethers. (B) A schematic representation of the adhesion system.

I use a microcontroller (ATSAMD21G18) to control the pressure sensor, solenoid valve and air pump in the adhesion system. I chose a commercial suction cup for the adhesion module. I compared the commercial suction cup with two different groups of suction cups, which I fabricated out of different soft materials. The two groups of suction cups are: custom-designed suction cups and replicas of the commercial suction cup. I used six different soft materials for each group of suction cups which are Dragon Skin 10, Dragon Skin 20, Dragon Skin 30, Ecoflex 00-10, Ecoflex 00-30, Ecoflex 00-50. A picture of the mould used to fabricate the custom-designed suction cups is shown by Figure 5.7. The CAD design can be found in Appendix C.

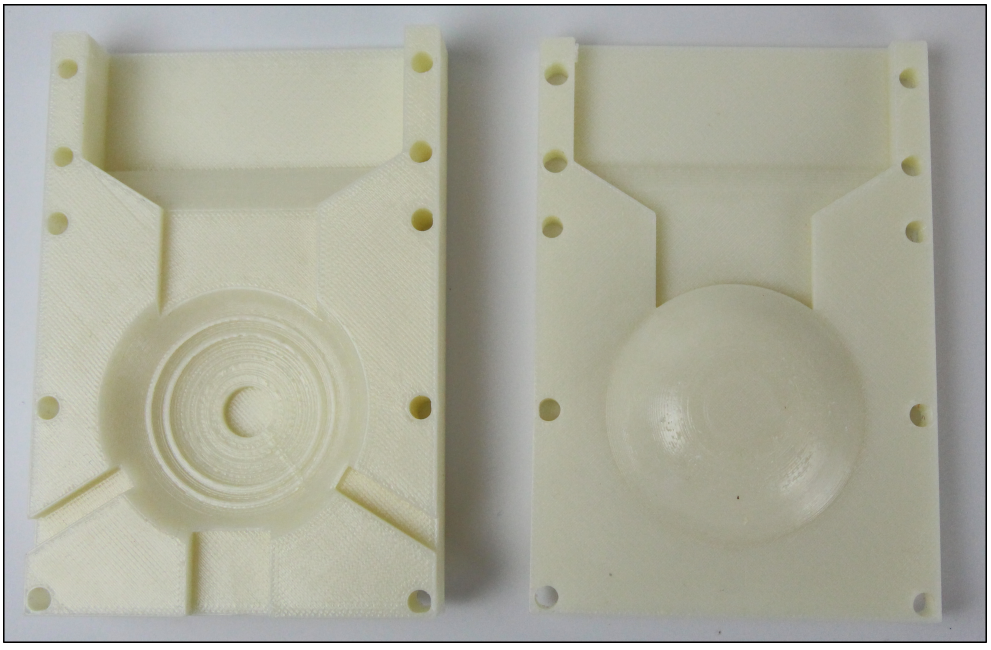

Figure 5.7: Picture of the mould used to fabricate the custom-designed suction cups.

I designed an experimental setup to test the maximum vertical loading capacity and maximum horizontal loading capacity of the suction cups I fabricated. I also conducted the same test for the commercial suction cup and the results are shown by Figure 5.8. A picture of the experimental setup and results of the maximum horizontal and vertical loading tests can be found in Figure 5.9 and Figure 5.10, respectively. The design of the experimental setup can be found in Appendix C. The commercial suction cup can handle a much higher loading capacity in both the vertical and horizontal direction, and, thus, I decided to use the commercial suction cup for the adhesion module in the Limpet version 2 system. From this experiment, I also found out that the custom-made suction cups deteriorate quickly (3-4 days) and lose adhesion strength over time.

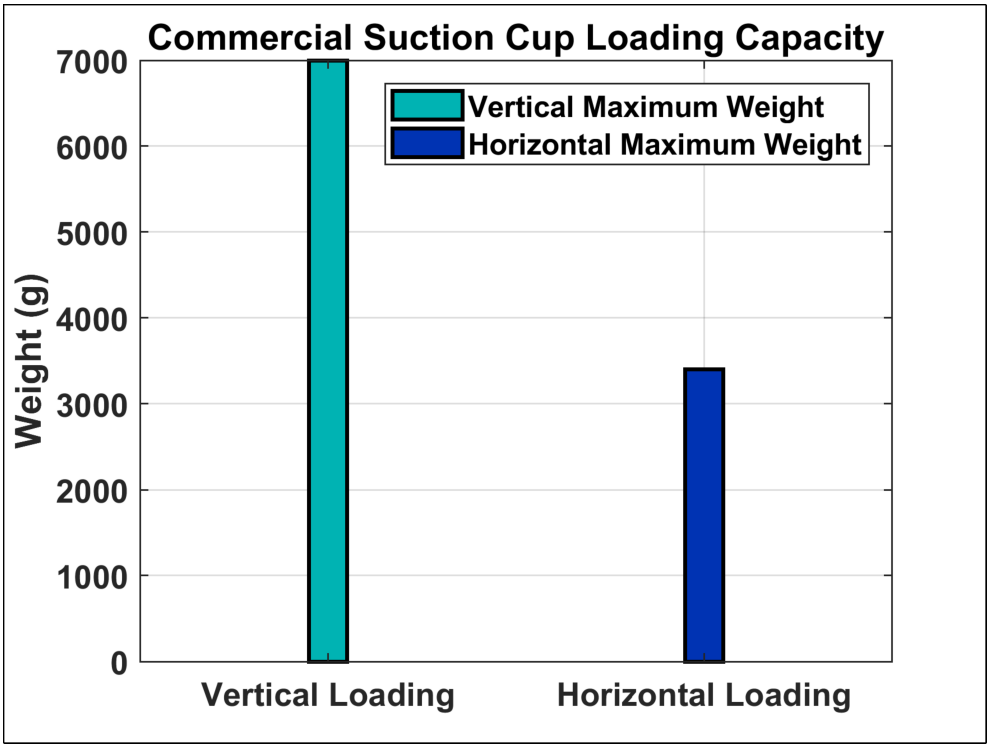

Figure 5.8: Maximum vertical and horizontal loading capacity on the commercial suction cup used for the Limpet. The graphs show the loading capacity of the suction cup before I make any changes to the suction cup.

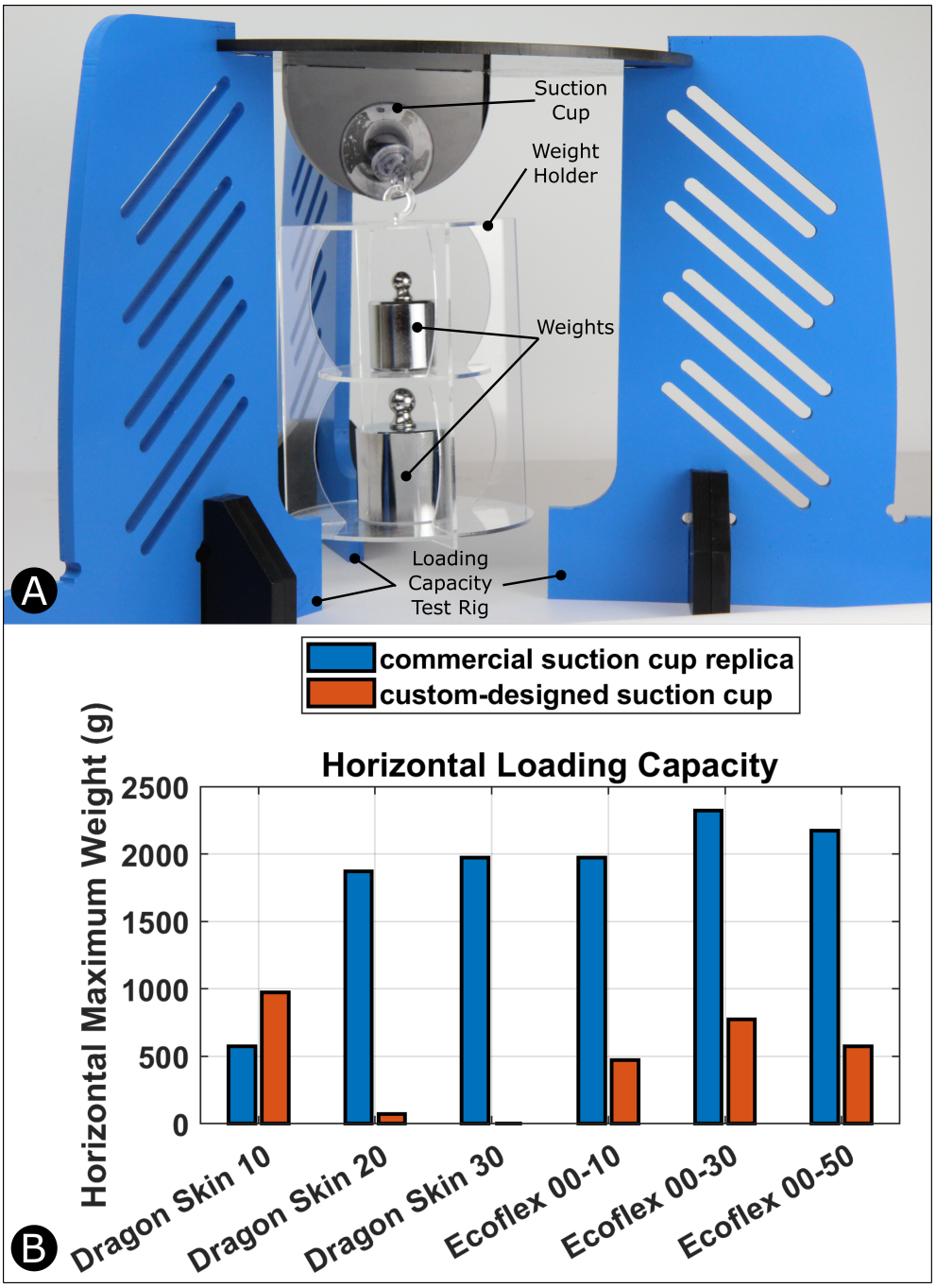

Figure 5.9: (A) A labelled picture of the experimental setup used to test the horizontal loading capacity of suction cups. In this experiment, we fabricated two different groups of suction cups, custom-designed suction cups and replicas of the commercial suction cup, out of different soft materials: Dragon Skin 10, Dragon Skin 20, Dragon Skin 30, Ecoflex 00-10, Ecoflex 00-30, Ecoflex 00-50. (B) Results of the horizontal loading capacity experiment showing the maximum loading capacity for the suction cups fabricated out of the different soft materials.

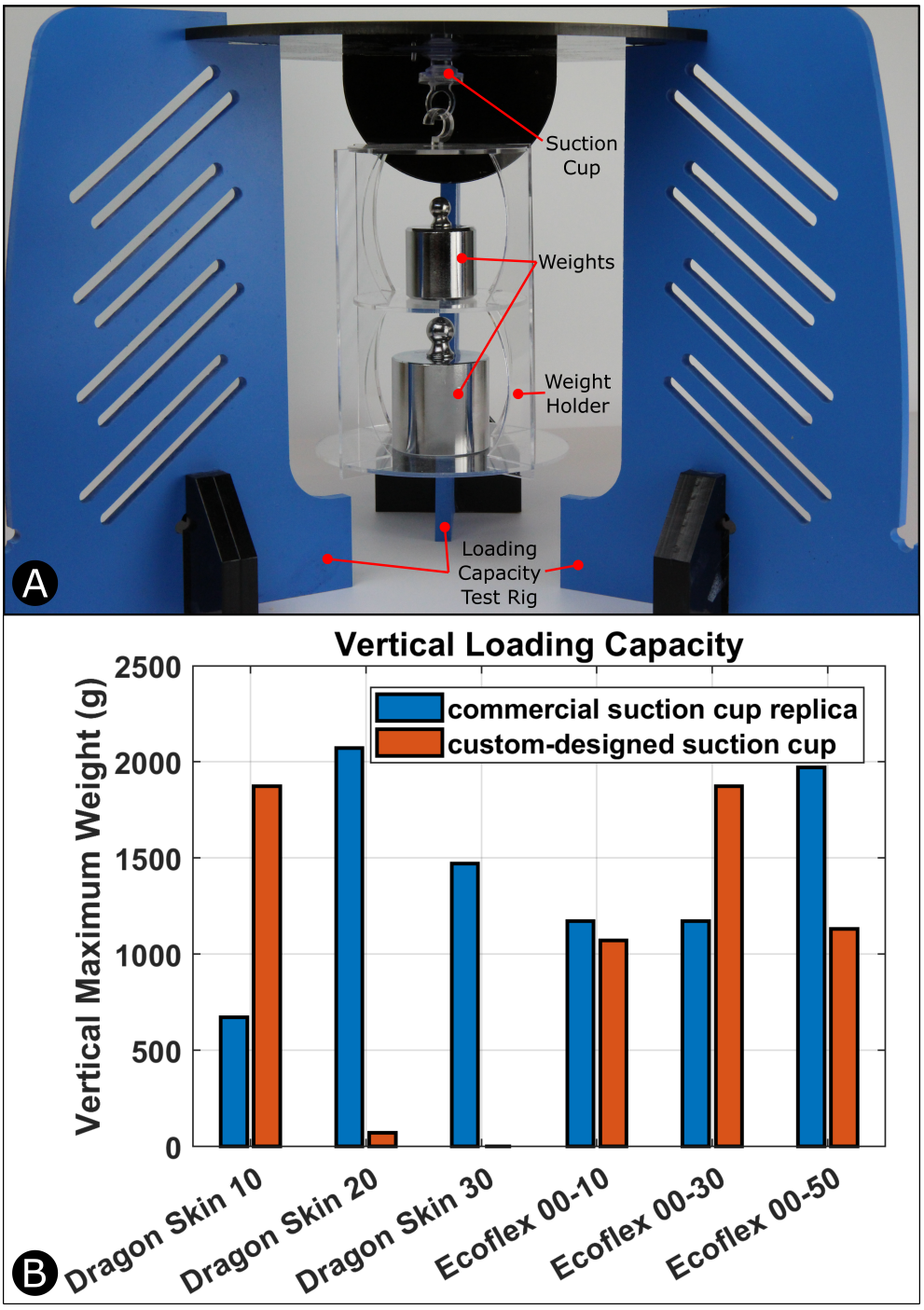

Figure 5.10: (A) A labelled picture of the experimental setup used to test the vertical loading capacity of suction cups. In this experiment, we fabricated two different groups of suction cups, custom-designed suction cups and replicas of the commercial suction cup, out of different soft materials: Dragon Skin 10, Dragon Skin 20, Dragon Skin 30, Ecoflex 00-10, Ecoflex 00-30, Ecoflex 00-50. (B) Results of the vertical loading capacity experiment showing the maximum loading capacity for the suction cups fabricated out of the different soft materials.

5.5.3 Design of the Locomotion Module

Locomotion is another important capability for inspection robots in offshore environments. I developed the locomotion module for Limpet version 2 using the EMM and rubber feet as shown by Figure 5.11. The locomotion is achieved by actuating the EMM at high frequencies, which results in vibrations. These vibrations are converted into a forward force that causes movement. The locomotion technique is thus based on slip-stick locomotion [241, 242]. By changing the amplitude and frequency of vibration, or number of locomotion modules, the Limpet is able to achieve movement in different directions.

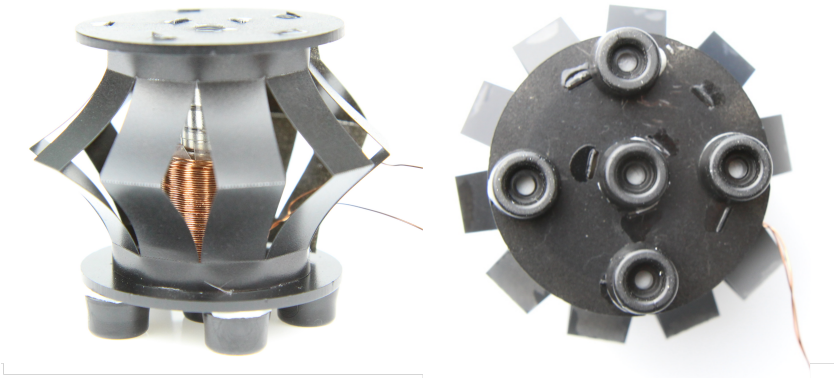

Figure 5.11: A side view picture and bottom view picture of the locomotion module based on the EMM.

5.5.4 Design of the Outer Body (Shell)

The shell acts as a protective housing for the Limpet components. The shell was fabricated using ecoflex 00-50. I first developed a flat mould, which I used to make a 1 mm layer of ecoflex 00-50. The soft layer was then bent into the right shape and used to cover the Limpet system components, with the sensing module exposed to the outer environment. The ecoflex 00-50 is a soft material and as such can be manufactured at low cost and allows the Limpet to be inherently complaint to its environment. In addition to that, the ecoflex is lightweight (reducing the overall weight of the Limpet), very strong (resistant to tearing) and very stretchy (capable of stretching multiple times of its original size without tearing and restores its original form without deforming).

5.6 Limpet v2 - Fabrication

5.6.1 Fabrication of the Printed Circuit Boards

I designed the sensing and power driver PCBs using Eagle PCB Design Software and fabricated them on double-sided Cu-FR4-Cu 0.1-mm boards. The sensing PCB and power driver PCB was fabricated using an external company called Minnitron Ltd. (Kent, UK). I purchased all electronic components from RS Components, Digi-key Electronics and Mouser Electronics. I soldered the components on the PCBs using a reflow soldering process. In this process, I cut solder paste stencils from vinyl using a Laser Cutter (Epilog Laser Fusion 32). I then stick the stencil on the PCB and apply solder paste on the stencil and PCB. I remove the stencil and manually place the components on their respective pads. Finally, I place the PCBs in an oven to reflow the solder.

5.6.2 Fabrication of the Electromagnetic Module

I fabricated the magnet holder, reel, and spring from acetate sheets using kirigami. Kirigami involves cutting a pattern out of sheets and folding it into the desired 3D configuration. The 2D patterns for the coil reel, magnet holder and spring are shown by Figure 5.12. I use kirigami as it allows our components to be low cost and highly manufacturable [243].

The output force from the EMM is a sum of the spring force from the kirigami spring and electromagnetic force from the interaction of the coils and permanent magnets. The total force generated by the EMM is given by

$$F_{output} = F_{spring} + F_{electromagnet} \tag{5.1}$$

The electromagnet force, when the coil and magnets are fully separated, is given by

$$F_{electromagnet} = \frac{\mu * q_{coil} * q_{pmag}}{4 * \pi * (d + r_o)^2} \tag{5.2}$$

Where μ is the permeability of free space, q_{coil} is the pole strength of the electromagnetic coil, q_{pmag} is the pole strength of the permanent magnets, d

is the distance from rest position, and r_o is the distance between center of coil and center of magnets at rest position. q_{coil} is given by

$$q_{coil} = \frac{NIA}{L} \tag{5.3}$$

Where N is the number of turns of the electromagnetic coil, I is the current supplied to the coil, A is the cross-sectional area of the coil, and L is the length of the coil.

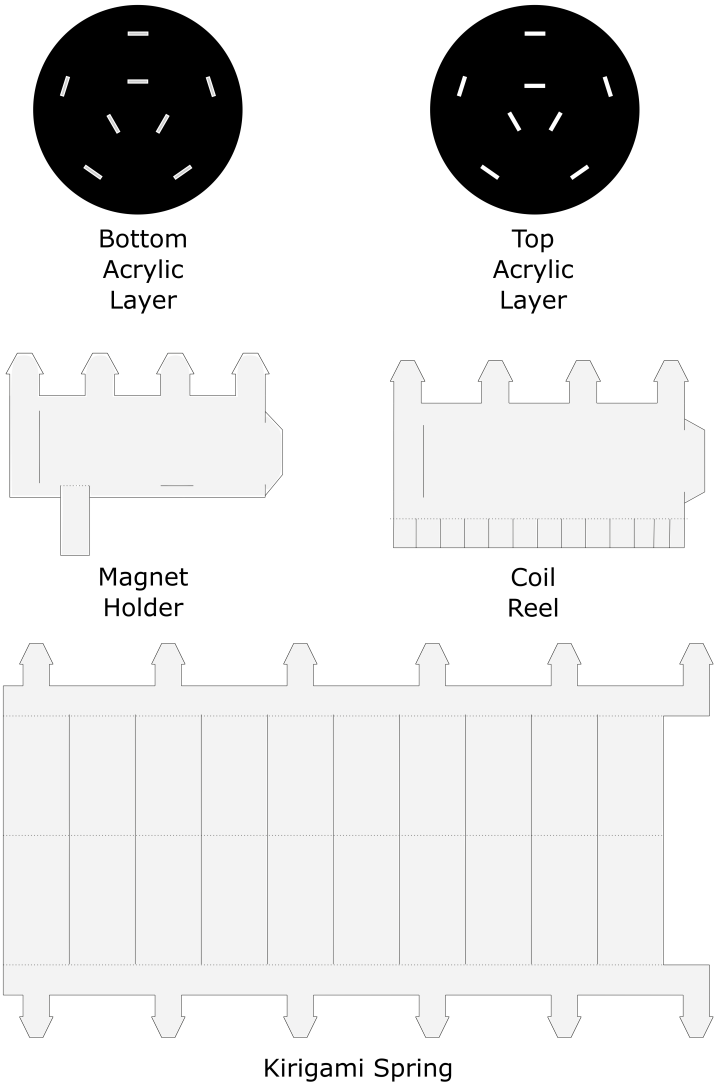

Figure 5.12: 2D design of the top acrylic layer, bottom acrylic layer, magnet holder, coil reel and kirigami spring of the EMM.

The fabricated electromagnetic coil consists of a 280-turn 0.35 mm insulated copper wire. I used 12 mm permanent neodymium magnets for our EMMs. I produced the actuation coils for the EMM using a custom-built coil-winding machine, which is shown by Figure 5.13. I purchased the 0.35 mm insulated copper wire from RS Components and the 12 mm permanent neodymium magnets from First4magnets. I use the custom-built coil-winding machine to wind the coils around the coil reel. The resulting reel with wound coils has an internal diameter of 14.5 mm, an outer diameter of 18.5 mm, and a height of 20 mm. The coil winding machine feeds the copper wire onto a rotating coil reel holder and I deposit superglue on the wire as it rotates so that the coil holds its shape. I fabricated the top and bottom layers of the EMM from a 2 mm acrylic sheet. I cut the patterns for the kirigami components (coil reel, magnet holder, spring) and the acrylic layers using a laser cutter (Epilog Laser Fusion 32).

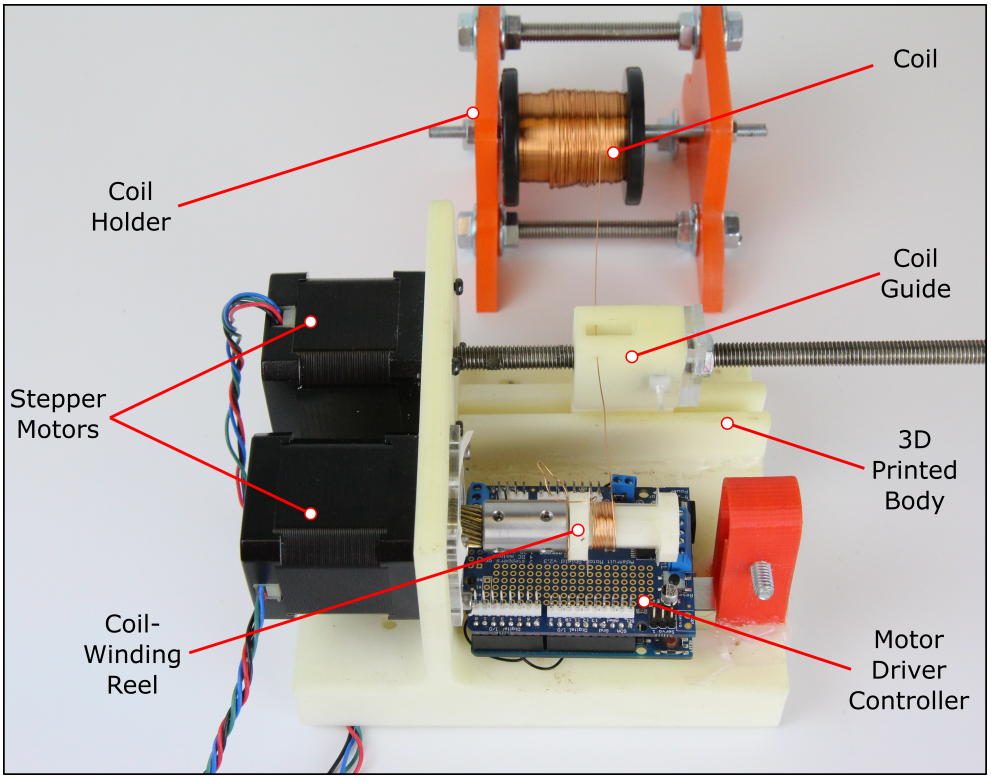

Figure 5.13: A labelled picture of the custom-built coil-winding machine used to produce the coils in the electromagnetic modules (EMMs).

5.6.3 Fabrication of the Adhesion Module

I fabricated the adhesion module from an EMM, suction cup, vacuum pump, solenoid valve and pressure sensor. I used 12 mm permanent magnets and a 280-turn 0.35 mm insulated copper wire coils for the EMM in the adhesion module. I drilled a hole in the suction cup and connected a plastic T-connector [3cm x 1.8cm x 0.6cm] to it. I used gorilla glue to seal the connection between the T-connector and the hole in the suction cup. I used a 1.6 mm diameter silicon tubing to connect the T-connector to the pressure sensor and the valve. I used the same silicon tubing to connect the valve and pump. I then glued the EMM on top of the T-connector and suction cup.

5.6.4 Fabrication of the Locomotion Module

I fabricated the locomotion module from an EMM. Similar to the EMM fabrication, I used 12 mm permanent magnets and a 280-turn 0.35 mm insulated copper wire coils for the locomotion module. I added round black soft-plastic feet to the bottom layer of the EMM. The plastic feet have a height of 7 mm and a diameter of 12 mm. I used 5 soft-plastic feet on the locomotion module, where one foot was placed in the center of the module and the four other feet where each placed on one of the edges of the module (right, left, top, bottom).

5.7 Experimental Design

5.7.1 Characterisation of the Electromagnetic Module

In this section, I discuss the design of the experiments I used to demonstrate the basic capabilities of the EMM. I conducted three different major experiments: frequency response analysis, evaluation of the spring constant and measurement of the output force for different input actuation currents. I also conducted an additional experiment to analyse the power dissipation from the coils for different coil thickness.

5.7.1.1 Analysing Power Dissipation for Different Coil Thickness

In this experiment, I analyse the effect of the coil wire thickness on the joule heating in the coils for different currents fed into the coil. I place the coils with different thicknesses in a custom-designed white acrylic box containing a temperature sensor. The temperature sensor is connected to a computational circuit consisting of a microcontroller and bypass capacitors. I feed different levels of current into the coils and measure the temperature rise as a result of the input current. A picture of the experimental setup is shown by Figure 5.14.

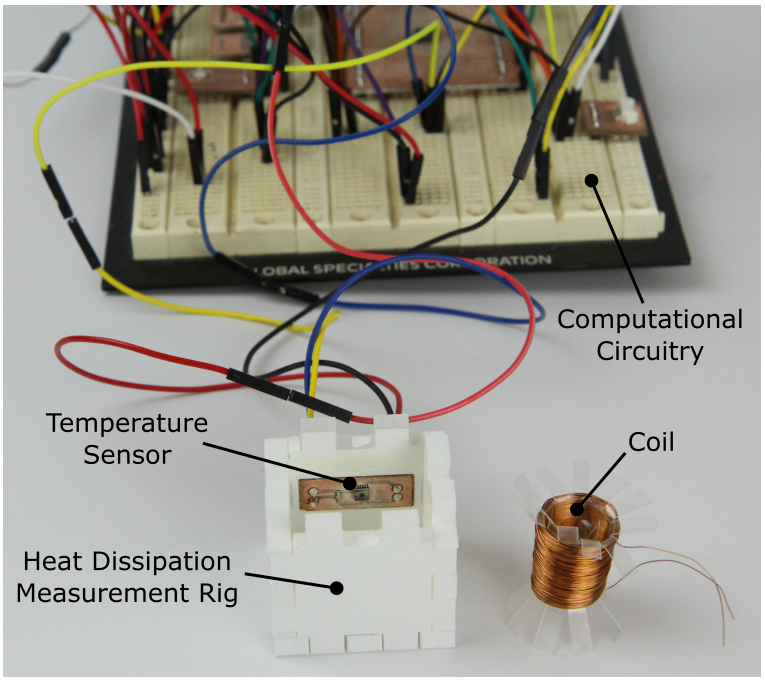

Figure 5.14: A picture of the experimental setup I used to analyse the effect of the coil wire thickness on the joule heating in the coils for different currents fed into the coil.

5.7.1.2 Frequency Response Analysis

The EMM provides different capabilities over a wide frequency range. The primary function of the EMM is actuation at low frequencies, but it can also produce an audio output at higher frequencies. I designed an experiment in which I programmed the microcontroller to vary the coil frequency from 1 Hz to 15 KHz. I measured the height of actuation of the top part of the EMM using a RealSense Camera mounted above the module. The RealSense Camera can detect the depth, and this function was used to track the movement of the top half of the EMM in the frequency response experiment. I also used an omni-directional sound sensor (-22 dB) to record the audio output produced by the EMM at high frequencies. The experimental setup is shown by Figure 5.15. I also recorded the frequency response analysis experiment with a Sony PlayStation 3 eyetoy camera, which provides a higher frame rate than the other camera. A video of the frequency response of the EMM from both cameras can be found here:

Frequency Response of the EMM. 

I designed an experiment to test the pulse-width scheme on the EMM and its effect on height of actuation by programming the microcontroller to provide a PWM signal to the coils of the EMM. I first sweep through duty cycles from 0% to 100% and then from 100% back to 0%. Following that, I increment the duty cycles applied to the EMM in steps of 20% from 0% to 100%, and measure the displacement at each step. I conducted the frequency response and PWM experiments only once to show the capabilities of the EMM over the range of different frequencies. I recorded the experiments using an 18-mp Canon EOS 100D camera and an EF-S 18–55mm f/3.5–5.6 IS STM lens. A video of the PWM experiment can be found here:

PWM of the EMM. 

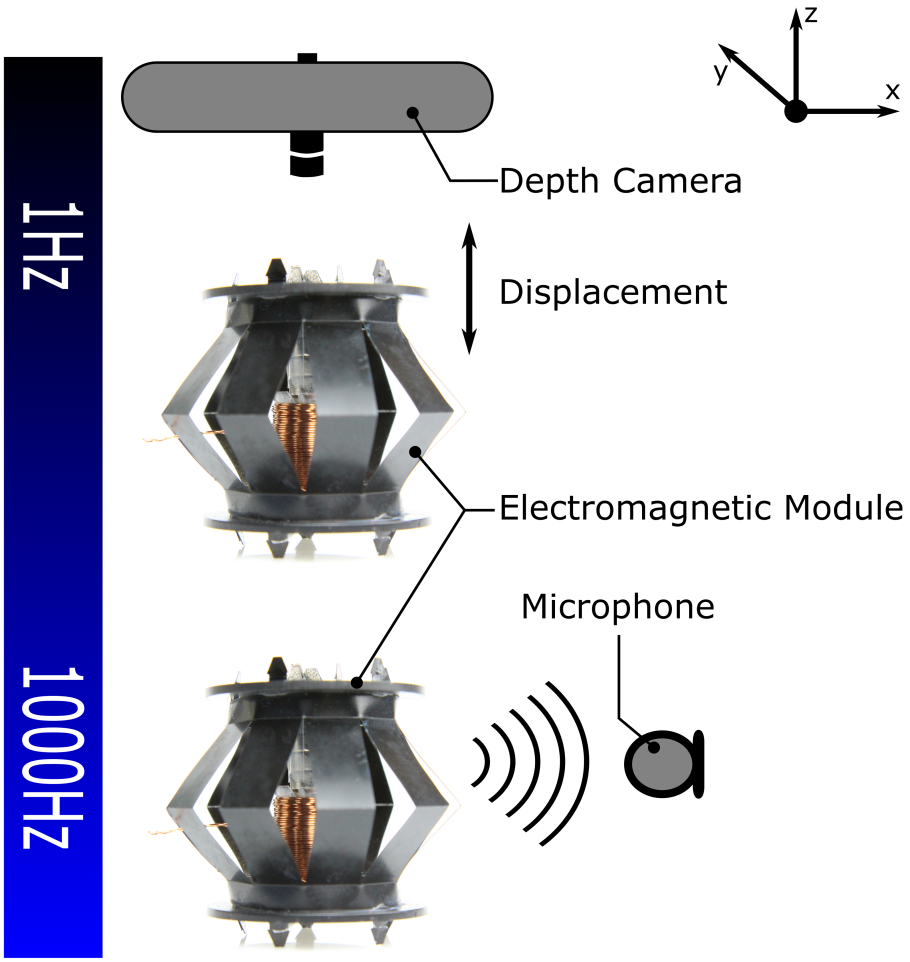

Figure 5.15: Schematic of the experimental setup used to characterize the frequency response of the EMM. At low frequencies, the EMM demonstrates linear actuation capabilities and acts as a loudspeaker at higher frequencies. I used a depth camera to track the height of actuation at low frequencies, and a microphone to detect the sound output at higher frequencies.

5.7.1.3 Evaluating the Spring Constant of the EMM

The output force of the EMM is a combination of a spring force and an electromagnetic force. To evaluate the spring force, I needed to quantify the spring constant (k), and thus, I designed an experiment to investigate the spring constant of the kirigami spring. The experimental setup consists of the kirigami spring (without the coils and magnets), ruler, and an ESM303 Tensile Compression Force Tester. The ESM303 Force Tester is a single column force tester for tension and compression measurement applications. In this experiment, I apply a force using the force tester on the kirigami spring in steps of 0.1N and measure the displacement of the spring. After reaching the maximum displacement of the spring, I start unloading the force on the spring in steps of 0.1N until it goes back to its resting position.

5.7.1.4 Determining the Output Force for Different Actuation Currents

To determine the output force for different current levels supplied to the EMM, I designed a controllable experimental setup consisting of a force testing rig, force gauge and a hook as shown by Figure 5.16. The force testing rig CAD design can be found in Appendix C.4. I designed the setup so that the force gauge and the EMM are fixed in place in the force testing rig, with the force gauge aligned perpendicularly above the EMM. I connected the EMM and the force gauge together with a hook and a laser-cut eye loop. I programmed the EMM to contract at maximum force and, thus, it pulls against the force gauge hook and gives a force measurement on the force gauge. I supplied the EMM with different current levels and measured the maximum force achieved at each current level. I increased the current from 0 to 1500 mA in steps of 50 mA. When the EMM pulls against the force gauge, it does not change its shape. Thus, the effect of the spring force does not affect the results of this experiment. For the electromagnetic force, the force measured is the force at zero displacement of the EMM. I repeated this experiment five times. One repeat of the experiment is shown in this video:

Determining Output Force of the EMM.

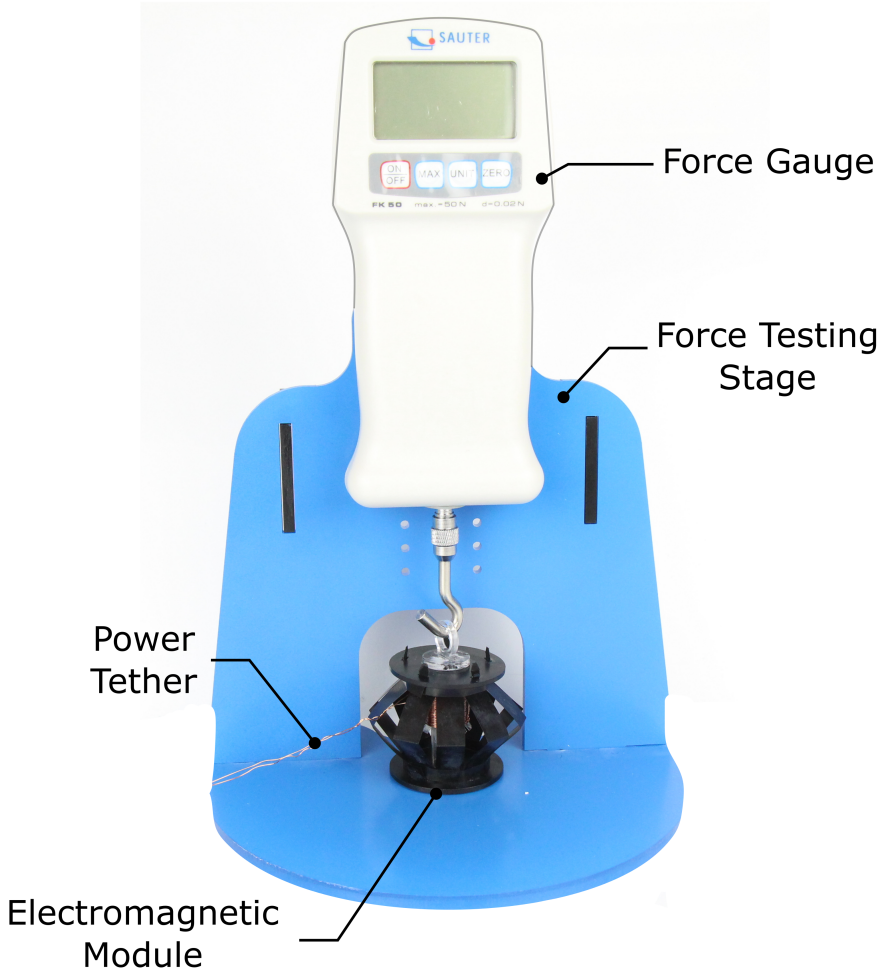

Figure 5.16: A labelled picture of the experimental setup used to measure the output electromagnetic force from the EMM for different current levels supplied to it. The force gauge is aligned vertically above the EMM, and the EMM pulls against the force gauge hook with maximum force.

5.7.2 Characterisation of the Adhesion Module

In this section, I discuss the design of the experiments used to characterise the adhesion module of the EMM. I conducted two different experiments: strength of attachment to different surfaces and closed loop control of the adhesion system. The first experiment evaluates the adhesion force of our adhesion module on surfaces with different roughness, and gives a safety factor indication for the design of the adhesion module for different surfaces. The second experiment demonstrates the capability of our closed loop controller implemented on the adhesion module.

5.7.2.1 Strength of Attachment to Different Surfaces

To characterise the ability of the adhesion module to stick to different surfaces, I designed an experimental setup consisting of the adhesion module, surfaces with different average surface roughness, laser-cut acrylic weight rig and weights. The CAD design of the weight rig can be found in Appendix C. I measured the average surface roughness of five different surfaces (acrylic, vinyl, copper, two different types of steel) using the Dektak XTL stylus profiler. The Dektak XTL provides a 2D roughness surface characterization by dragging a 2 um stylus across the surface. The average surface roughness gives an indication of surface texture and overall profile height characteristics of a surface. For each surface, I repeated the surface roughness measurement five times, and used the average of the five measurements. I conducted the experiment by attaching the adhesion module to each surface and testing the maximum vertical and horizontal loading capacity on the module. I attach the weight rig to the adhesion module and start adding weights to the rig in steps of 10g until the adhesion module fails and detaches from the surface.

5.7.2.2 Closed Loop Control of the Adhesion System

I designed a closed loop controller for the adhesion system. The closed loop controller monitors the pressure in the cavity between the suction cup and the surface. When the pressure reaches a certain threshold, which is lower than the pressure required to detach the suction cup (atmospheric pressure), the controller will open the valve and turn on the vacuum pump to restore the

pressure in the cavity. The controller ensures that if any leakage occurs in the suction cup, the adhesion module will not detach from the surface. To test the efficiency of the controller, I designed an experimental setup where I induce a leakage in the suction cup by opening the solenoid valve to atmosphere and then monitoring the effect of the closed loop controller on restoring the suction cup pressure.

5.7.3 Characterisation of the Locomotion Module

In this section, I discuss the design of the experiments used to characterise the locomotion module of the limpet. This section is divided into three parts. In the first part, I designed an experiment to show the modularity aspect of the system, and how I can achieve simpler controllers and more complex systems by stacking basic modules (EMMs) together. In the second part, I conducted an experiment to track the movement of my final locomotion system as it moves in a pre-defined geometry in its environment. Finally, I conducted an experiment to track the displacement of the top part of the final locomotion system as it moves in a straight line along one axis.

5.7.3.1 Effect of Stacking the Locomotion Modules

The locomotion using this module (EMM and rubber feet) can be achieved in multiple different ways depending on the number of modules used and the mechanical design of the system. The mechanical design of the system will affect the center of mass of the system. In this section, I designed an experiment to investigate the effect of stacking or combining basic functional modules (locomotion modules) to create a system that is more complex and has greater capability than the sum of its individual parts. I use three types of locomotion systems: using a single EMM, two EMMs, four EMMs. In this experiment, I have an environment with four targets in each of the four cardinal directions. The aim of this experiment is to show how I can stack or combine locomotion modules to produce a system that can achieve greater capability with simpler control. In the first part of the experiment, I used a single locomotion module and show the effect of weight biasing on the ability of module to reach the targets. I used a 20g weight to achieve the change in directions using the single locomotion module. I used an actuation frequency of 4 Hz, and supplied

the module with an actuation current of 300 mA and a voltage of 11.1 V. In the second part of this experiment, I demonstrate the capability of a system consisting of two combined locomotion modules and show the effect of both amplitude biasing and weight biasing on the performance of this system. For weight biasing, I change the direction of movement of the system using a 20g weight, while for amplitude biasing I actuate each of the locomotion modules in a different way to the other. The two locomotion modules are attached together using a 2mm acrylic piece. For this part of the experiment, one module was contracted fully while the other module was actuating at a frequency of 6.7 Hz. I supplied an actuation current of 750 mA to both modules and a voltage of 11.1 V. Finally, I designed a system with four different modules and used amplitude biasing on the system to try to reach the four targets, and I show the effect of this system on my controller and system design. Figure 5.17 shows pictures of the locomotion systems with two and four locomotion modules.

5.7.3.2 Evaluating the Locomotion

In this section, the locomotion system composed of four locomotion modules is investigated further. I conducted two different experiments to evaluate the locomotion of the system. In the first experiment, I programmed the system to travel in a rectangular path and track the position of the system using AprilTags [232]. Each side of the rectangular path is achieved by actuating a different combination of locomotion modules at different frequencies. I supplied a current of 2A and a voltage of 11.1 V to the system in this experiment. The system has no on-board odometry, but odometry can be achieved using the combination of the AprilTags surrounding the system and an off-board communication system (e.g. Infrared Transceiver). In the second experiment, I track the change in height of the top part of the locomotion system as it moves in a straight line along one axis. I track the displacement and change in height using a 3D printed black sphere that I attached to the top of the locomotion system. I recorded both experiments using an 18-mp Canon EOS 100D camera and an EF-S 18–55mm f/3.5–5.6 IS STM lens.

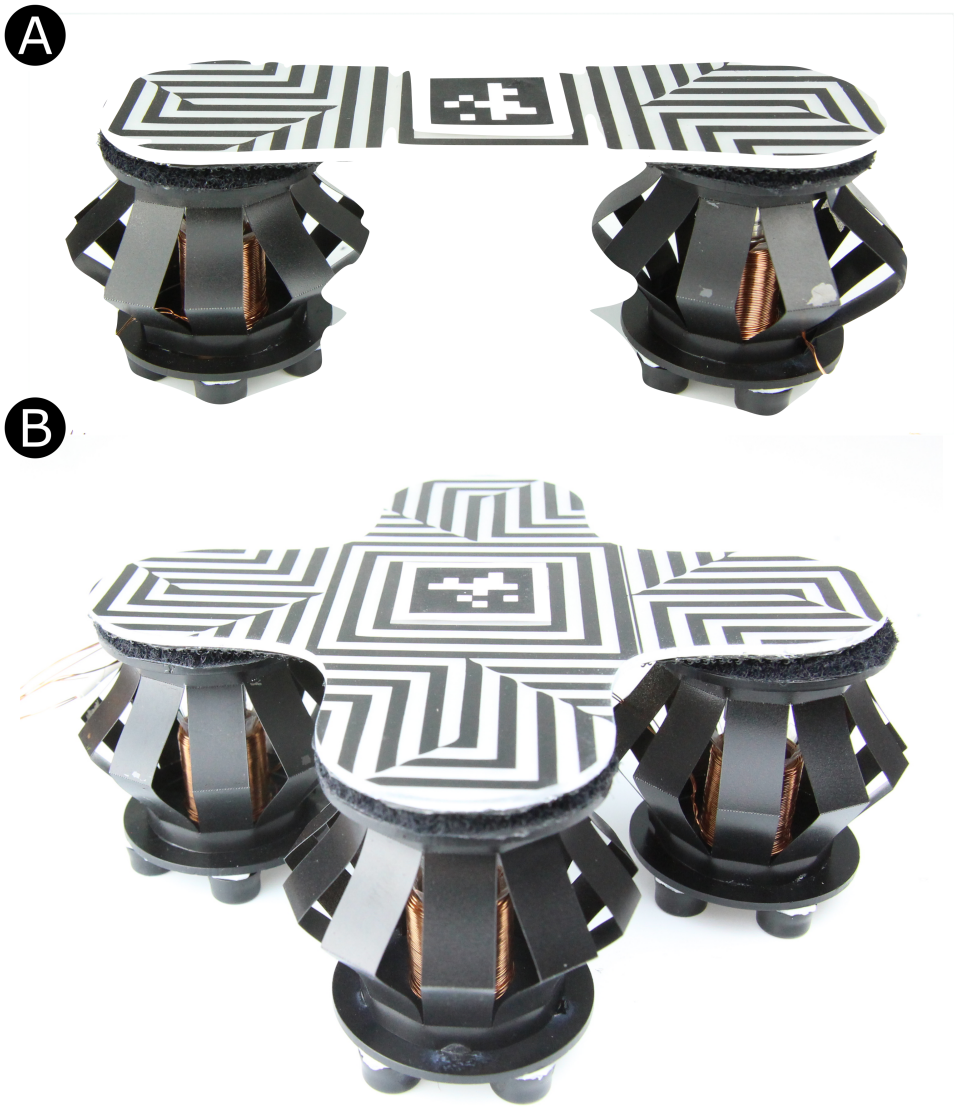

Figure 5.17: (A) A picture of the combination of two locomotion modules based on the EMMs. (B) A picture of 4 EMMs stacked together into a locomotion system.

5.8 Experimental Results

5.8.1 Characterisation of the Electromagnetic Actuator Unit

5.8.1.1 Analysing Power Dissipation for Different Coil Thickness

Figure 5.18 shows the experimental results of the heat dissipation from the coils at different current levels. The results show that the amount of current drawn by the coils is proportional to the rate of temperature rise. I analysed the temperature rise of the coils for a period of 150 seconds each. Each graph shows the rise in temperature over time for each of the coils at a different current level (1A, 2A, 3A, 4A). The voltage supplied to the coils in this experiment is 11.1 V. As such, the power consumption at each current level is 11.1 W, 22.2 W, 33.3 W and 44.4 W. The results also show that rate of temperature rise increases significantly as the wire thickness decreases.

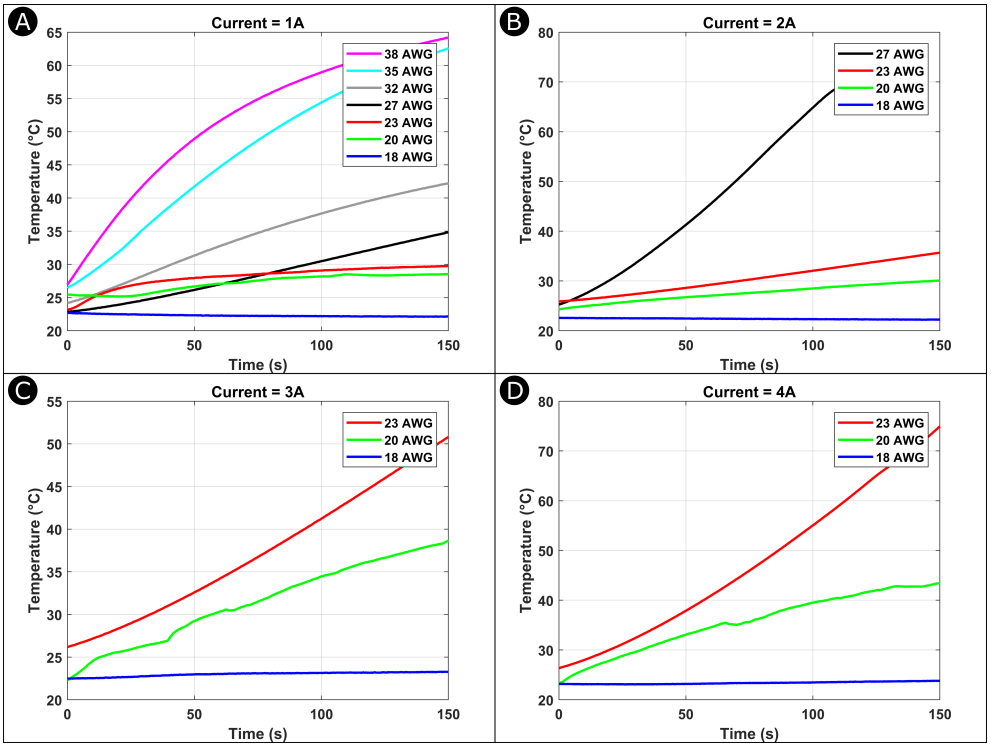

Figure 5.18: Results of the heat dissipation experiments showing the rise in temperature due to different currents for the different coil thicknesses.

5.8.1.2 Frequency Response Analysis

In this experiment, I demonstrate that the EMM can actuate at a low frequency and transition to sound output as the frequency increases to audible levels as shown by frequency response video in Section 5.7.1.2. The video shows the EMM actuating at increasing frequencies and then transitioning from actuation to sound output at higher frequencies. The change in height of the EMM against actuation frequency at low actuation frequencies is shown by Figure 5.19. As seen by the graph, as the actuation frequency increases the period for the EMM to extend and contract fully decreases. As the frequency increases further, the change in height decreases as the EMM is actuating at a very high speed. At even higher frequencies, the camera cannot pick up the change in height properly as the EMM is actuating at a frequency higher than the frame rate of the camera.

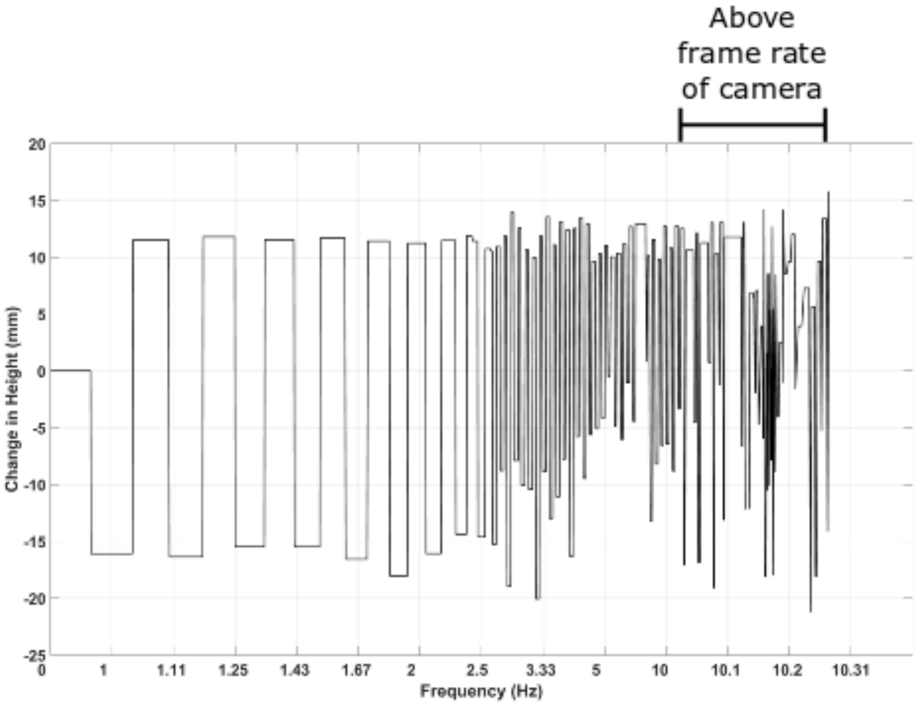

Figure 5.19: Results of the frequency response analysis experiment showing the change in height of the EMM against the actuation frequency.

The sound spectrogram for the EMM at audible frequency levels is shown by Figure 5.20. The spectrogram is based on the audio from seconds 24 to 42 in the frequency response video. The audio is sampled at a rate of 44,100 KHz and divided into windows of 8820 samples with an overlap of 2205 samples between neighbouring windows. Fast Fourier Transform (FFT) is conducted on each window. The amplitude of the powers in the FFT is then scaled [244] based on a Mel-Scale, which is a model of the sensitivity of the human ear to each frequency [245]. The resulting FFTs are used to create a heat map of frequency versus time called a Mel-Spectrogram.

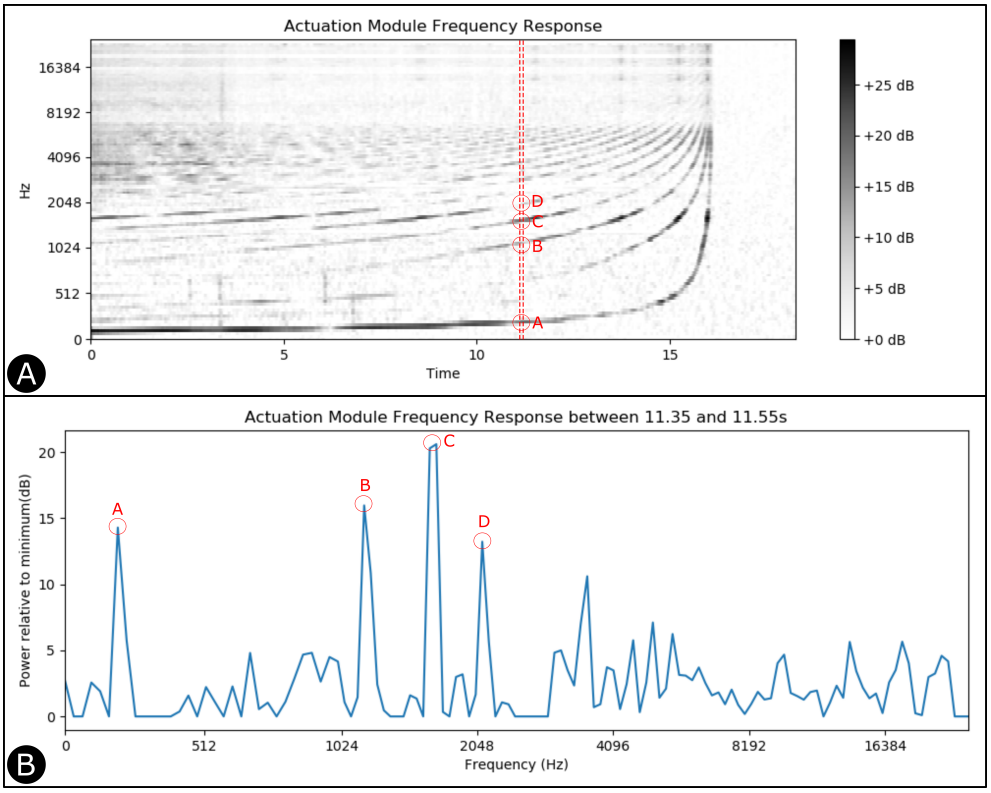

Figure 5.20: (A) A Mel-Spectrogram of the audio from seconds 24 to 42 of the frequency response video. The frequency axis is linear under 1000 Hz and is in log base 2 scale above 1000 Hz. (B) A vertical slice of the Mel spectrogram representing a Mel-Scaled FFT of the audio from 11.35s-11.55s of the video.

In this experiment, I also demonstrate how I can control the height of actuation by changing the PWM signal level. I expected that the use of PWM will change the actuation current to produce forces smaller than the maximum actuation force, and therefore, partial actuation. The use of a PWM actuation signal produced the expected partial actuation behavior. The partial actuation behavior resulting from the PWM signal is demonstrated by the video of the PWM experiment shown in Section 5.7.1.2. The change in height of the EMM with respect to the PWM duty cycle is shown by Figure 5.21. The change in height has a linear relationship with the PWM duty cycle.

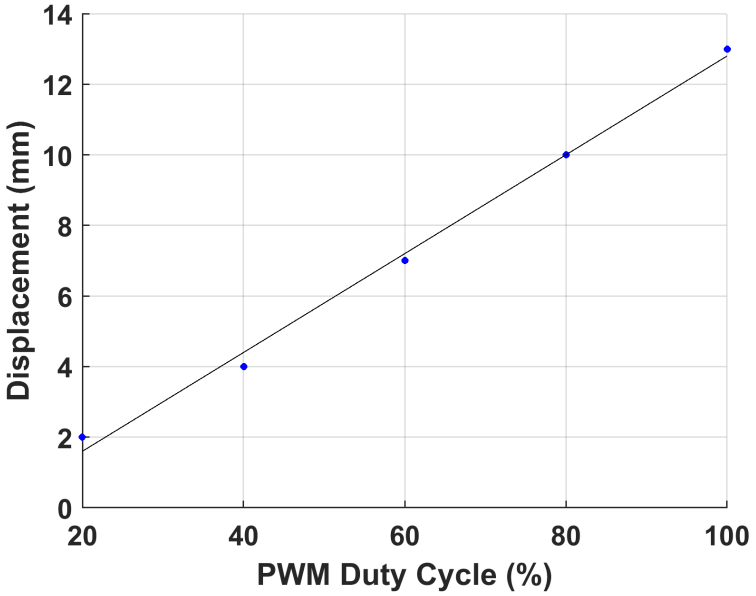

Figure 5.21: Results of the PWM test of the EMM showing the change in height of the EMM against the PWM duty cycle.

5.8.1.3 Evaluating the Spring Constant of the EMM

The force from the kirigami spring is part of the total output force produced by the EMM, and thus it is important to study the elasticity of the kirigami spring by measuring its spring constant. The spring constant represents the amount of force required to compress or extend a spring. Actuators that often move a large distance during actuation so that the restoring force varies nonlinearly with displacement, which is the case for the kirigami spring in this work, have the following relationship between the force applied to the spring and the displacement [246]:

$$F = K_1 x + K_3 x^3 + ... \tag{5.4}$$

Where F is the force applied, K is the spring constant, and x is the distance the spring is extended or compressed from its rest position. The graph of the force applied against the displacement for loading and unloading of the spring is shown by Figure 5.22. The spring constant is measured by fitting a third order polynomial function to the loading and unloading curves. For the loading curve, K_1 is 42.232 N/m and K_3 is 61501 N/m. For the unloading curve, K_1 is 14333 N/m and K_3 is 18.6 N/m. The hysteresis is measured by calculating the area between the loading and the unloading curves, which is 0.0014 N m. Since I took the measurements of displacement using a ruler the standard error is $\pm$0.5 mm.

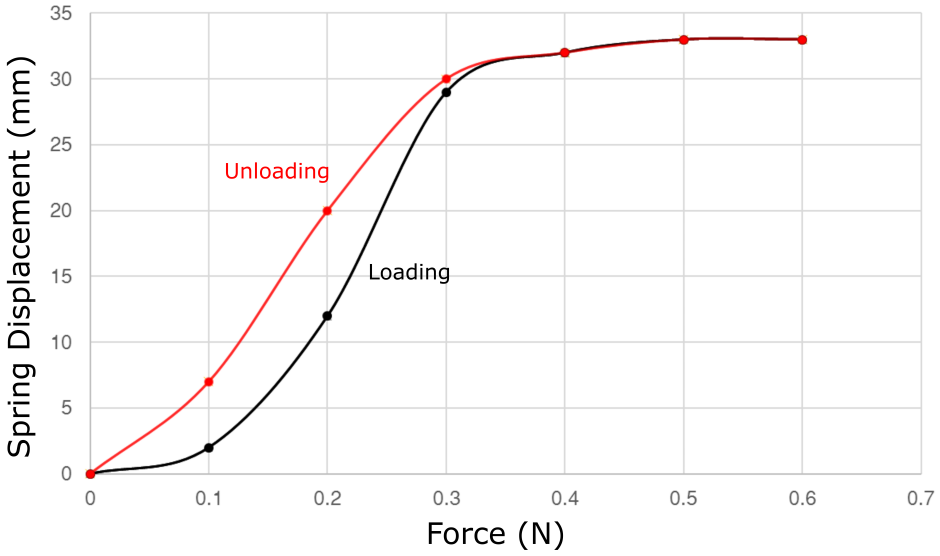

Figure 5.22: Results of the spring constant evaluation experiment showing the displacement of the spring against the force applied for loading and unloading of the spring.

5.8.1.4 Determining the Output Force for Different Actuation Currents

The mathematical model of the output force is shown in Section 5.6.2. In this experiment, the EMM was pulling against the force gauge with maximum force. The EMM did not change its height. Thus, the effect of the spring force does not affect the results of this experiment. For the electromagnetic force, the force measured is the force at zero displacement (d). The experimental results and mathematical model of the output force for different actuation currents is shown by Figure 5.23. There is a linear relationship between the current supplied and the actuation force. The standard deviation for all the five experiments is within the measurement error of the force gauge ($\pm$0.02N). The maximum force achieved by the EMM in this experiment was 1.8 N, which suggests that a single module could lift objects with masses below 184g when provided with an actuation current of 1500 mA.

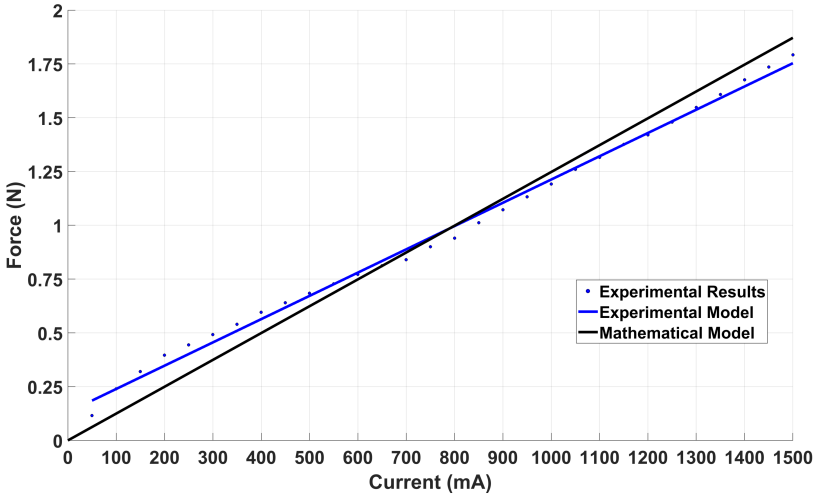

Figure 5.23: Results of the experiment used to evaluate the output force from the EMM against the current supplied to the EMM, and mathematical model of the output force versus current supplied. The experiment was repeated five times, and the standard deviation of all the five experiments are within the measurement error of the force gauge ($\pm$0.02N).

5.8.2 Characterisation of the Adhesion Module

5.8.2.1 Strength of Attachment to Different Surfaces

In this experiment, I observe that the adhesion force of the adhesion module decreases linearly with average surface roughness. Figure 5.24 shows the relationship between the vertical and horizontal adhesion force of the adhesion module and the average surface roughness. I measured the average surface roughness of five different target surfaces as shown by the points on the graph. I then plotted the best fit line through the points. I added a safety factor of 1.5 for the vertical and horizontal adhesion force. Taking into account the safety factor, the graph shows that on the surface with the highest measured surface roughness, the adhesion module can handle up to 26N in the vertical direction and up to 9N in the horizontal direction. These measurements indicate that the adhesion module can handle an average maximum weight of 920g in the horizontal direction if placed on a rough metallic surface. I used this measurement as a guide for the maximum allowed weight of the final Limpet system, if it is to be used for climbing rough surfaces in offshore environments.

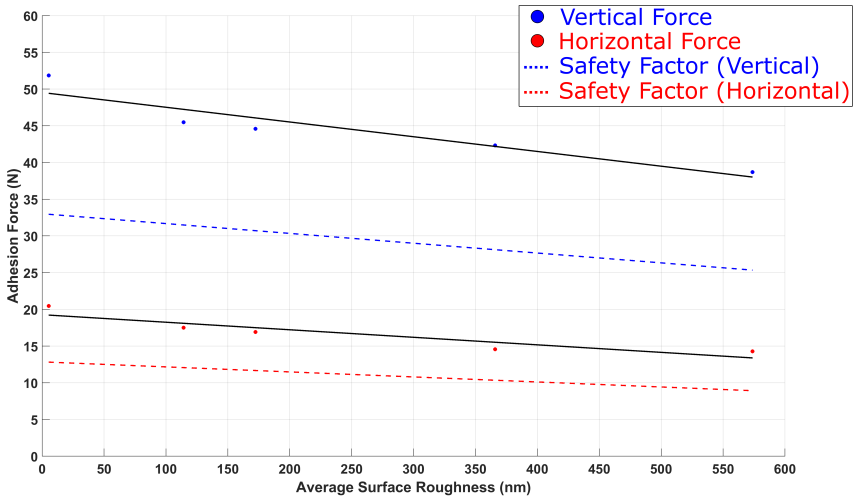

Figure 5.24: Results of the adhesion force of the adhesion module on different surfaces. The graph shows the maximum vertical and horizontal adhesion force of the module for surfaces with different surface roughness, and a safety factor of 1.5 for the vertical and horizontal adhesion forces.

5.8.2.2 Closed Loop Control of the Adhesion System

In this experiment, I first attach the adhesion module to the surface by pumping the air out of the cavity between the suction cup and the surface. At this point, the pressure of the suction cup is measured to be 435 mbar. The suction sup detaches from the surface when the pressure in the cavity reaches atmospheric pressure (1014 mbar). I developed a closed loop controller that monitors the pressure in the cavity, and if the pressure ever reaches 895 mbar, the controller will open the pump to restore the adhesion force to normal. In this experiment, I induced a leakage in the suction cup after attachment, by opening the valve to atmosphere, and monitor the pressure as it rises towards atmospheric pressure. When the pressure reaches 895 mbar, the pressure is restored back to 435 mbar as shown by Figure 5.25. I repeated this procedure multiple times, and the closed loop controller was always successful in restoring the adhesion of the module and preventing detachment of the suction cup.

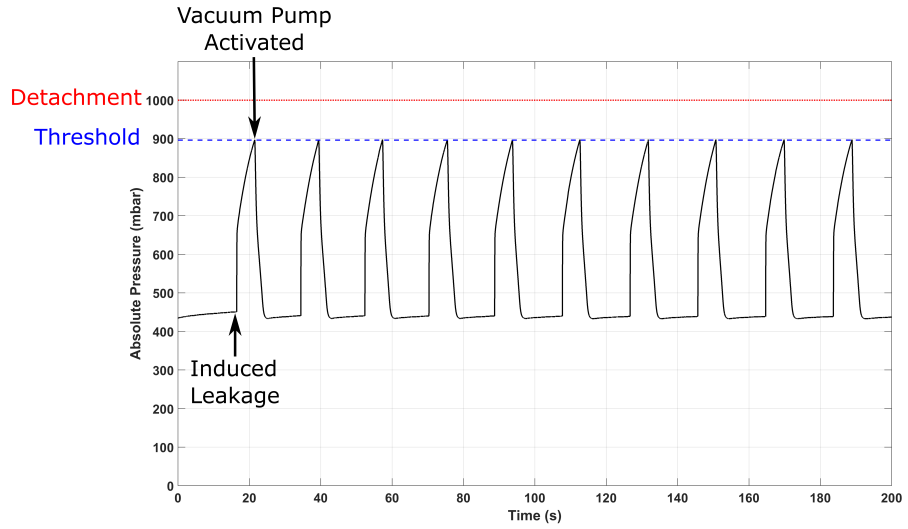

Figure 5.25: A graph demonstrating the closed loop control of the adhesion system. I induce a leakage in the suction cup, which causes the pressure in the cavity between the suction cup and surface to rise. When the pressure reaches a certain threshold, which is lower than the pressure required to detach the suction cup, the valve will open and the pump will switch back on to restore the pressure in the cavity.

5.8.3 Characterisation of the Locomotion Module

5.8.3.1 Effect of Stacking the Locomotion Modules

In this experiment, I observe that using one locomotion module to reach four targets in each cardinal direction requires a change in the mechanical structure of the module. I can bias the direction of movement by placing a weight at the edge of the EMM facing the desired direction of movement. I use a 20g weight for this experiment, and I repeat the experiment four times. In each repetition of the experiment, I have to manually change the location of the weight on the top acrylic layer of the module as shown by Figure 5.26. The weight tilts the EMM and shifts its center of mass allowing it to move to the desired direction. Thus, to use a single EMM as the final locomotion system, I would have to design a mechanical system that can shift the center of mass of the EMM towards the required direction, and I would have to develop a technique to allow the EMM to alter that mechanical system autonomously to achieve successful movement [247, 248, 249, 250]. This approach of using a single EMM would make the mechanical design and the controller of the Limpet very complex. The average speed of the single module in this experiment is 35.4 mm/s. The single locomotion module deviates from its path by 20 mm in the North direction, 17 mm in the South direction, 19 mm in the East direction, and 22 mm in the West direction. A video showing the single locomotion module reaching the four targets by biasing the direction using an external weight can be found here:

Single Locomotion Module. 

When I stack two EMM modules into one locomotion system, the system is capable of more complex motions with a simpler controller and design. The system can be biased in two ways. The center of mass of the system can be shifted using an external weight or using the combination of the two EMMs. The first method involves adding a 20g weight on either side of the space between the two EMMs. The weight tilts the system and results in a shift in the center of mass causing the locomotion system to move in the north or south directions as shown by Figure 5.27A and Figure 5.27B. The second method involves programming the EMMs to have different behaviours, which will also

result in a shift of the center of mass of the system. In my case, I program the EMM that is on the side closer to the target to actuate continuously in both directions, while the EMM further away from the target to be in continuous contraction at maximum force as shown by Figure 5.27C and Figure 5.27D. The average speed achieved by the system when biased by the weight is 70.7 mm/s. The average speed achieved by biasing the system using the combination of the EMMs is 31.4 mm/s. The two-module locomotion system deviates from its path by 11 mm in the North direction (weight bias), 22 mm in the South direction (weight bias), 15 mm in the East direction (amplitude bias), and 17 mm in the West direction (amplitude bias). The results of the locomotion system composed of two EMMs is shown by this video:

Two Module Locomotion System. 

Based on the results of these two experiments, I decided to develop a locomotion system using four EMMs. I can use this locomotion system to achieve motion in all cardinal directions using only the EMMs as shown in Figure 5.28. I use the EMMs to shift the center of mass of the locomotion system and achieve movement in the required direction. Thus, this system simplifies the mechanical design and the controller required for the system. The average speed achieved by this system is 37.1 mm/s. The four-module locomotion system deviates from its path by 4 mm in the North direction, 15 mm in the South direction, 14 mm in the East direction, and 17 mm in the West direction. All the targets are reached successfully and simply by the locomotion system without using any external weight bias, and the four-module locomotion systems achieves the least deviation in its path compared to the other locomotion systems. The results of the locomotion system composed of four EMMs is shown by this video:

Four Module Locomotion System. 

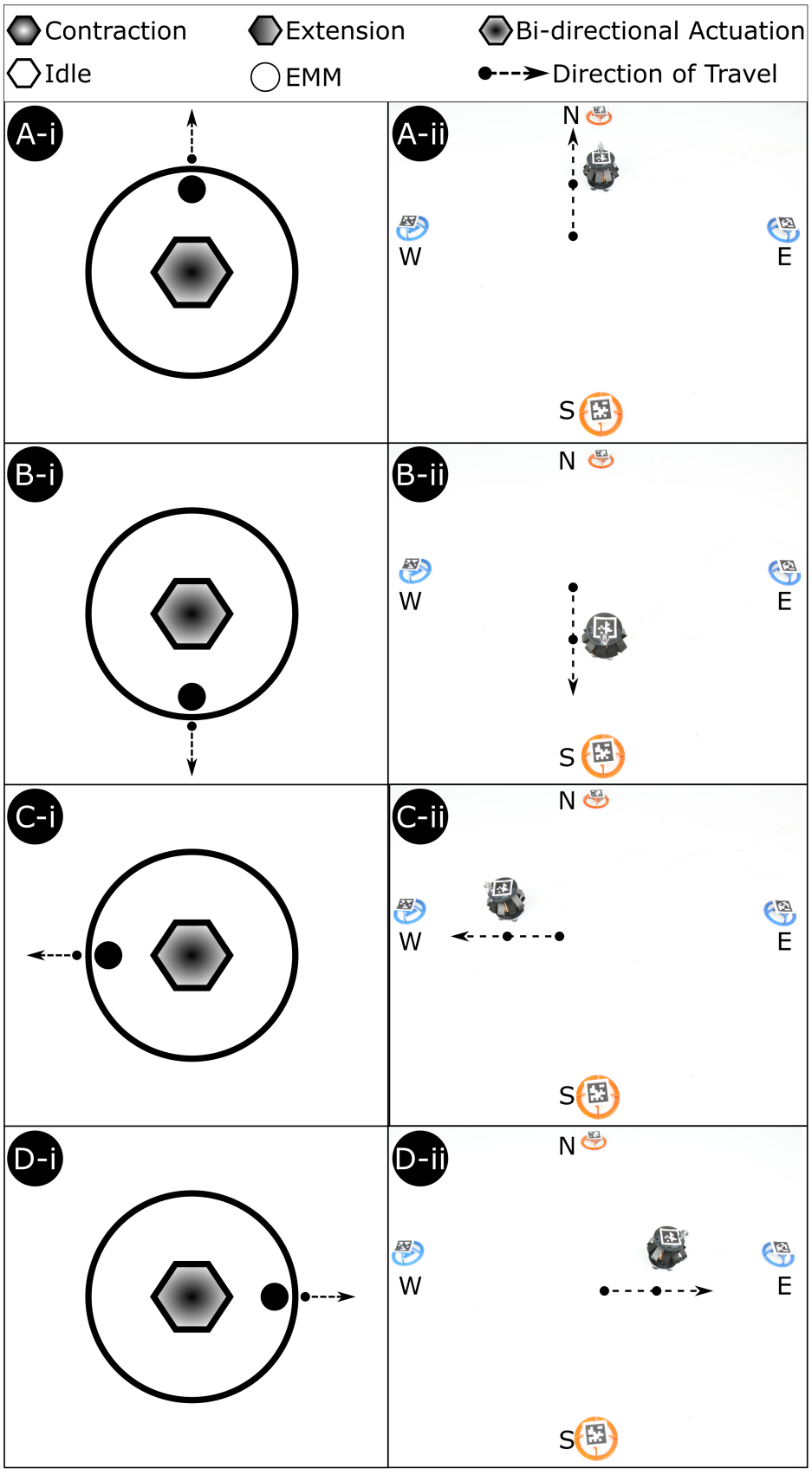

Figure 5.26: (Ai-Di) Schematic of the experimental setup used to analyse a single locomotion module and its ability to reach four different targets within its environment. I add a weight on one of the sides of the locomotion module to bias it to move in that direction. (Aii-Dii) Images of the single locomotion module with the weight on top of it trying to reach the targets at the different cardinal directions in the environment.

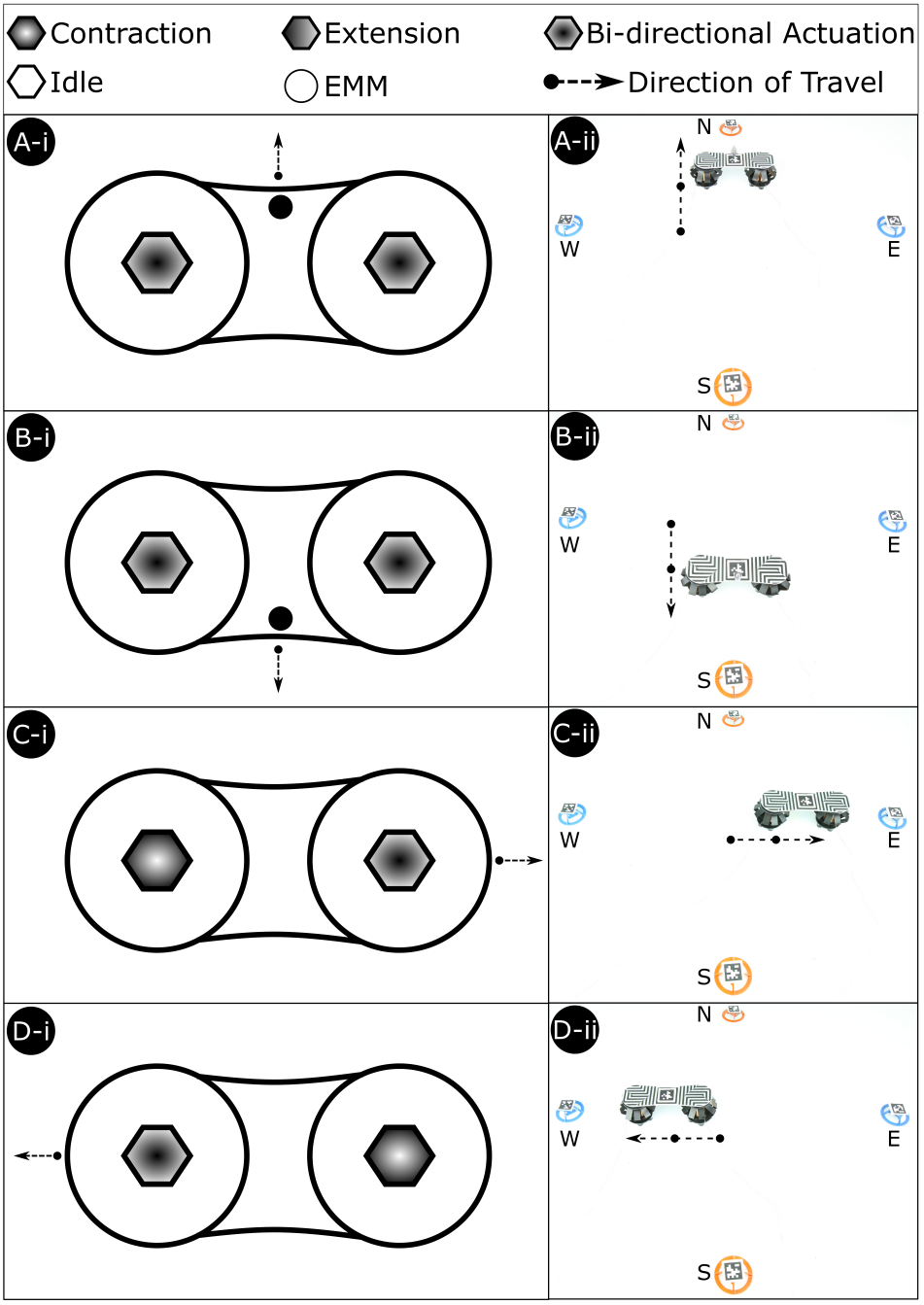

Figure 5.27: (Ai-Bi) Schematic of the experimental setup used to analyse a locomotion system made up of 2 EMMs, where the system is biased to move North and South by adding a weight on top of it. (Ci-Di) Schematic of the experimental setup used to analyse a locomotion system made up of 2 EMMs, where the system is biased to move East and West by actuating the 2 EMMs in different manners to each other. (Aii-Bii) Images of the double locomotion system trying to reach targets in the North and South directions by adding a weight to it and changing the positions of the weight manually. (Cii-Dii) Images of the double locomotion system trying to reach targets in the East and West directions by actuating one module in both directions, while only extending the other module.

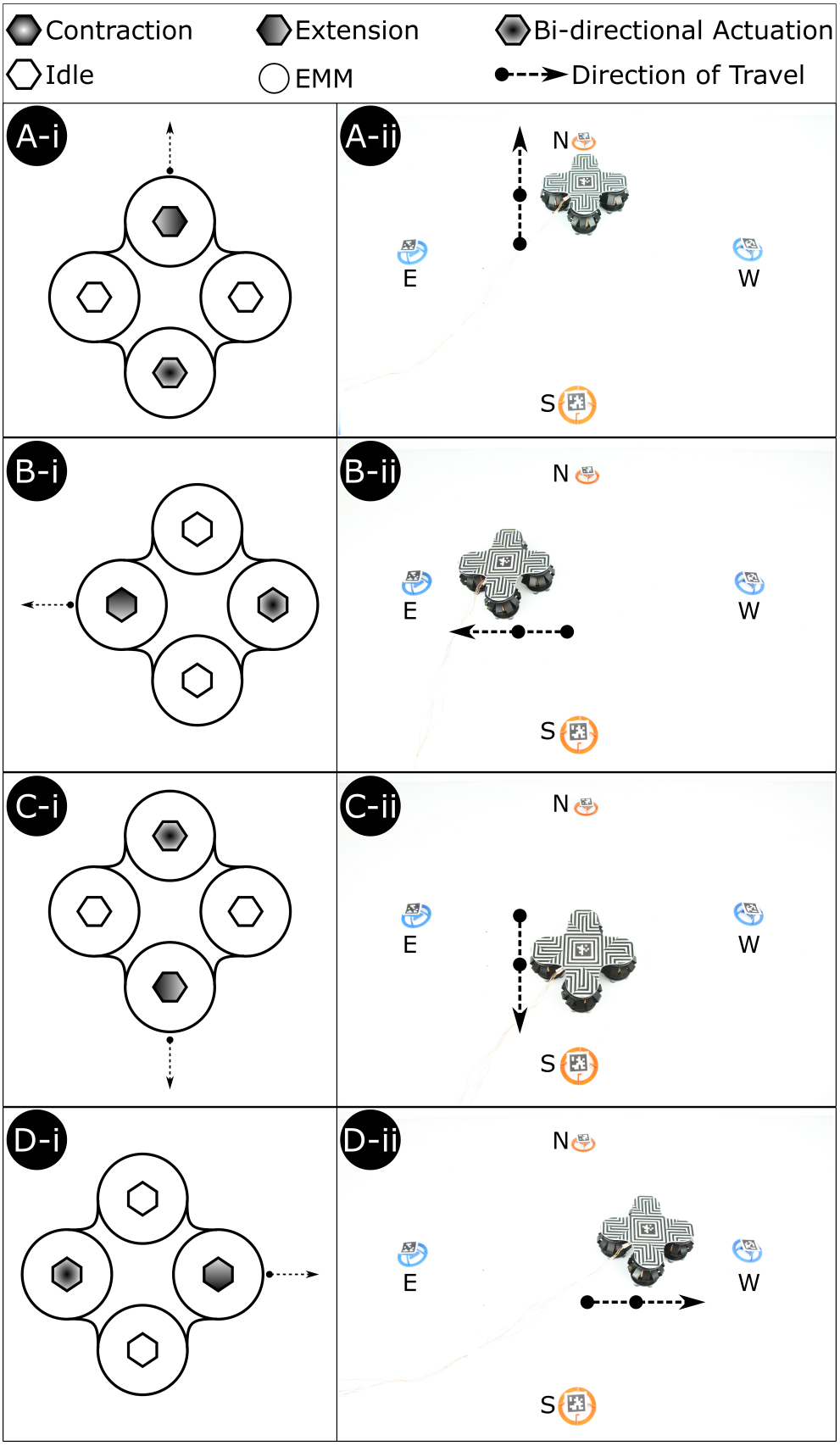

Figure 5.28: (A-D) Schematic of how each locomotion module within the locomotion system is actuated to achieve movement in the different directions, and pictures of the actual system reaching the targets using the different actuation mechanisms. In each case, two of the modules are idle, one module is actuating in both directions, while the final module is contracting to bias the direction of the movement.

5.8.3.2 Evaluating the Locomotion

I observe that stacking functional blocks results in systems that are increasingly capable of a diverse range of complex motions and behaviours. I decided to use the locomotion system composed of four EMMs and explore it further. This section discusses the results of the experiments carried out to further evaluate the locomotion of this system. The locomotion system is programmed to move in a rectangular fashion and can achieve so with a slight deviation in one of the rectangle sides as shown in Figure 5.29A. A video of the movement can be found here:

Rectangular Movement of the Locomotion System.



For tracking the displacement of the top part of the locomotion system during locomotion, I added a 3D printed black sphere on top of the system, and programmed the system to move in a straight line along one axis. I developed a custom-written script that can track the black sphere against the white background and record the change in position of the sphere vertically and horizontally. The change in height versus horizontal displacement is shown by Figure 5.29B. A video of the movement can be found here:

Height Tracking of the Locomotion System.



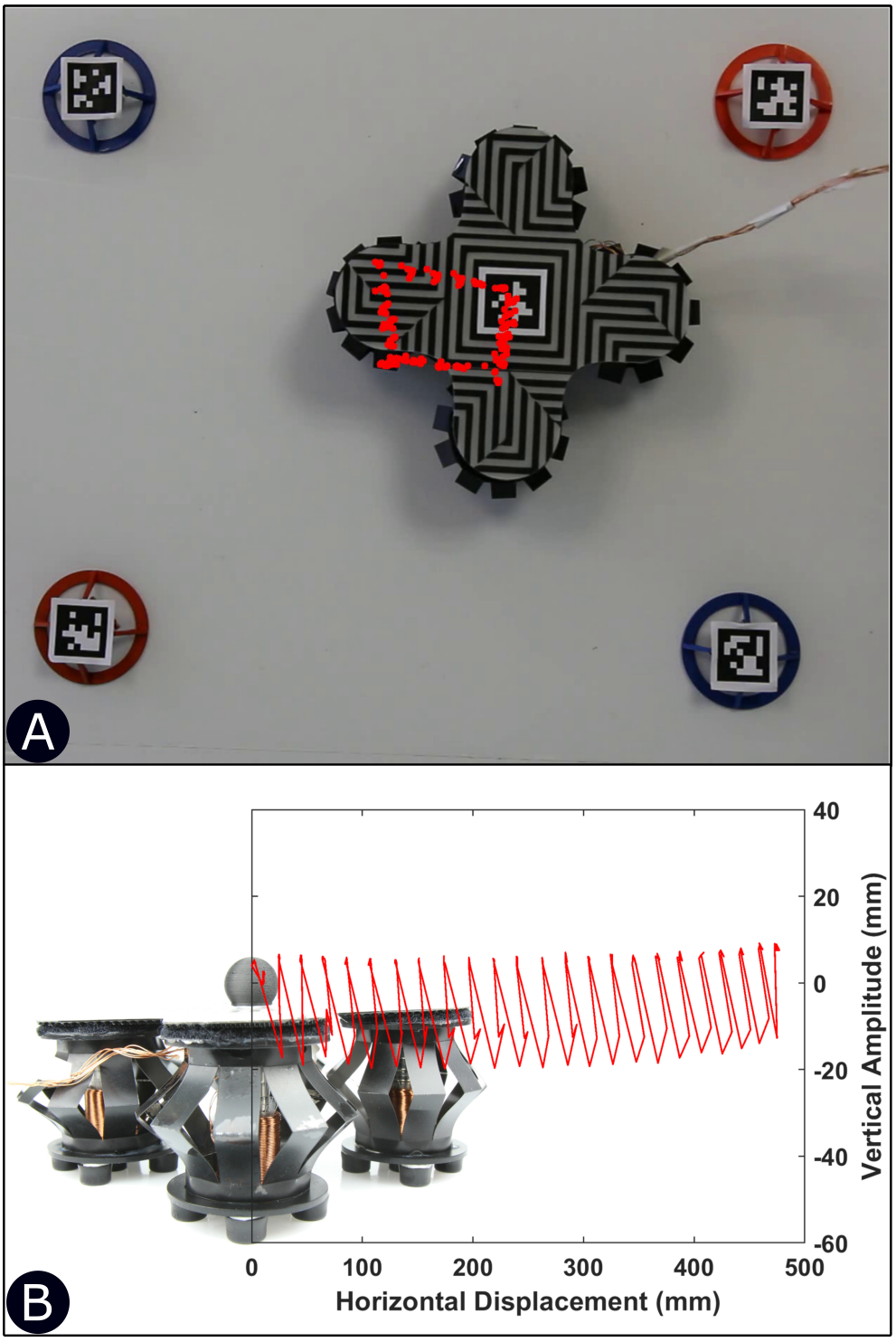

Figure 5.29: (A) The path of the locomotion system after being programmed to travel in a rectangular path and the position of the system is tracked using AprilTags. (B) Tracking the vertical displacement of the locomotion system as it moves horizontally in a straight line.

5.9 Demonstrations

In addition to the experiments that show the characterisation of the different modules included in the Limpet, I performed additional demonstrations to show how the Limpet can perform useful behaviours in its environment.

5.9.1 Untethered Sensory Control of the Limpet

In this experiment, I use the different sensors on the Limpet to control its locomotion and adhesion capabilities. I use the sound, distance, light, and IMU sensors to show an example of how the Limpet can respond to sensory input in its environment. These demonstrations shows how the Limpet can use this capability and the sensing measurements to map its environment and act upon changes in that environment. Such a capability is important for inspecting and monitoring offshore platforms. The video showing the Limpet responding to a light stimulus, where a change in the ambient light color will lead to movement in different directions can be found here:

Light-based Control of the Limpet System. 

In this demonstration, I use the light sensor on the Limpet, which is capable of measuring ambient light intensity, and power density of red, green and blue light. A video showing how the Limpet can change its movement direction or enable and disable its adhesion mechanism based on a change in frequency of a sound input signal that is measured by the sound sensor on the Limpet can be found here:

Sound-based Control of the Limpet System. 

The Limpet can also respond to the presence of objects at different proximity from it using the on-board distance sensor as shown by the following video:

Distance-based Control of the Limpet System.

In the video below, I poke the Limpet, which will cause it to start repositioning itself away and then adhering in place at the new position. I use the IMU sensor for this demonstration, where poking the Limpet will result in a small change in the acceleration and gyro data. This small change is picked up by the Limpet, which responds to this change by repositioning itself in its environment. The video can be found here:

IMU-based Control of the Limpet System.

5.9.2 Sound-Based Inter-Communication of Limpets

One of the capabilities of the EMM is generation of sound output. This capability can be used by the Limpets for communication with neighbouring Limpets. In this demonstration, I demonstrate how the sound capabilities of the EMM in the Limpet can be used for communication with other neighbouring Limpets. One Limpet generates a sound signal (distress signal), and the neighbouring Limpet around it will start moving away from that Limpet. This capability can be used in a situation where other communication systems (e.g. WiFi and LoRa) are down, and the Limpet needs to communicate to its neighbours. The idea behind this capability is that the Limpet can send out command signals to its neighbours, which can be for example, to start inspecting and mapping the structure for faults. The result of this demonstration is shown by the following video:

Sound-based Inter-Communication of Limpets.

5.9.3 Climbing

To highlight the capability of the Limpet in unstructured offshore environments, I designed an experiment to demonstrate the ability of the Limpet to climb an inclined surface. A video of the Limpet climbing the surface can be found here:

Climbing.

In this experiment, I reconfigured the electromagnetic and adhesion modules as shown by Figure 5.30. The Limpet configuration includes two vertical adhesion modules, and two horizontal electromagnetic modules connected between the adhesion modules. In this experiment, the surface is at an angle of 60°. The design of the climbing system can be changed to achieve vertical (90°) and inverted motion. I programmed the Limpet to follow a sequence of steps as follows:

- Top adhesion module adheres to the surface by activating its pump, closing its valve, and extending itself to push the suction cup on the surface.
- Bottom adhesion module contracts to lift its suction cup off the surface.
- Horizontal EMMs contract, which brings the bottom adhesion module closer to the top one.
- Bottom adhesion module adheres to the surface by activating its pump, closing its valve, and extending itself to push the suction cup on the surface.
- Top adhesion module detaches from the surface by opening its valve to atmosphere and contracting to lift its suction sup off the surface.
- Horizontal EMMs extend, which pushes the top adhesion module further away from the bottom one.
- Top adhesion module adheres to the surface by activating its pump, closing its valve and extending itself to push the suction cup on the surface.
- The motion is then repeated multiple times to achieve the vertical locomotion on the surface.

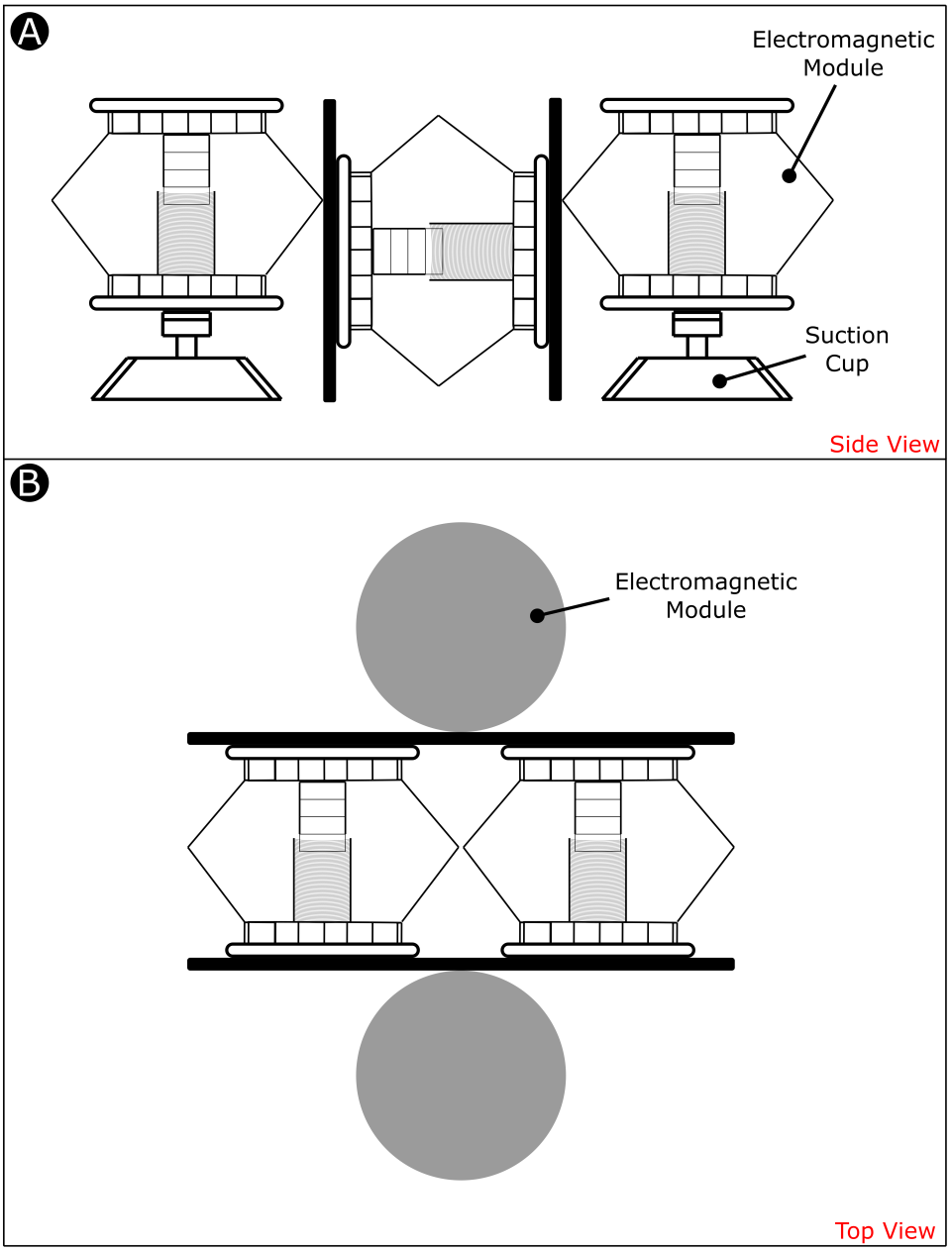

Figure 5.30: (A) Side view and (B) Top View of the configuration used for the Limpet system for climbing a surface.

5.10 Discussion

In this work, I present an untethered soft robot that integrates a sensing module, power driver module, adhesion and locomotion modules based on EMMs. The robot is designed in a modular fashion, equipped with nine exteroceptive sensing modalities, and features capabilities of simple and untethered control, adhering to different structures and materials (acrylic, vinyl, copper, steel), walking on horizontal and vertical surfaces, and sensing its environment.

The Limpet is a useful system for carrying out inspection tasks offshore as it capable of navigating on surfaces at different angles. Current climbing robots focus on the climbing capabilities and have limited or no sensing abilities onboard. Also, the existing systems mostly use rigid actuators, which does not allow the robot to easily conform to its environment and adds complexity in the task planning phase. Soft climbing robots that have been reported [66] are not fully untethered systems yet, which limits their capability to carry out useful tasks in such extreme environments. The Limpet uses hybrid actuators, which has the advantages of rigid components and can still partially conform to its environment. The Limpet is also developed as a fully, untethered system, which removes the limitations associated with power and communication tethers in performing tasks and allows for autonomous deployment of the system. The Limpet is equipped with nine sensing modalities, which allows it to sense its environment and monitor the conditions of the different offshore structures. The Limpet is developed in a modular fashion, which makes it easier to adapt the system to new tasks, to repair the system, to replace and reconfigure the modules.

One major drawback of the locomotion technique of the Limpet is that there is no real form of on-board odometry, which makes moving accurately and precisely for a long duration of time or for large distances a challenging task. However, I can achieve odometry using a combination of the AprilTags surrounding the system and an off-board communication system (e.g. Infrared Transceiver), to accurately estimate the change in position and achieve more precise movement over long distances. The speed achieved by the system in different tasks is not an important factor for comparison as I can easily alter the speed of the locomotion system. The speed is a function of the current supplied, frequency of actuation of the EMMs and the weight of the system. The speed achieved in climbing is smaller than that achieved in horizontal motion,

as the adhesion and locomotion forces are used to overcome the gravity force of the robot during climbing. The adhesion capability of the Limpet relies on materials and surface textures, and works best on flat surfaces. The adhesion can be used on rough and uneven surfaces, but will achieve shorter periods of adhesion. The Limpet system has a short battery life. The battery life can be increased by using larger batteries, but those batteries have larger weight and will affect the adhesion force and the climbing speed of the system.

5.11 Summary

Existing climbing robots mostly use rigid actuators, and robots that use soft actuators are not fully untethered yet. Current climbing robots are also not built in a modular fashion, which makes it harder to adapt the system to new tasks, to repair the system, to replace and reconfigure the modules. A modular, untethered soft robot - the Limpet v2 - capable of climbing surfaces, adhering to structures and sensing its environment, was designed in this Chapter. The Limpet v2 uses a hybrid electromagnetic module as its core unit to allow adhesion and locomotion capabilities. The adhesion capability is based on negative pressure adhesion utilising suction cups. The locomotion capability is based on slip-stick locomotion. The Limpet v2 also has a sensor payload (Limpet v1) with nine different sensing modalities, which can be used to inspect and monitor offshore structures and the conditions surrounding them. The Limpet was designed as a modular system, and as such the modules can be reconfigured to achieve different tasks. To demonstrate its potential for inspection of offshore platforms, I showed that the Limpet is capable of responding to different sensory inputs, repositioning itself within its environment, adhering to structures made of different materials, and climbing inclined surfaces.

Part IV

Multi-Sensor Data Fusion

Chapter 6

Multi-Sensor Data Fusion Using Limpets

6.1 Introduction and Background

Multi-sensor data fusion combines data from multiple sensors to form a complete picture of the task or environment. Multi-sensor data fusion is important in applications where one sensor does not give an accurate result to form a decision, and large amounts of data from different sources needs to be fused together to make more accurate and better informed decisions. One such application of multi-sensor data fusion in offshore environments is monitoring the condition of conductor pipes and managing them. The conductor pipe or drive pipe is usually set into the ground to provide the structural foundation for an oil well. In the offshore industry, the conductor pipe is set in the seabed and provides the foundation for subsea wellhead. The conductor pipes are usually set before the drilling operations are carried out. The conductor pipes are subject to constant waves from the sea causing continuous vibration, which can degrade the conductor pipe and affect its lifetime.

Thus, operators and offshore companies are interested in monitoring the condition of the conductors to predict their lifetime and perform maintenance when needed. Currently, the method used for conductor monitoring involves using human divers to inspect the condition of the conductors installed offshore by capturing images of the conductors at different points and then analysing these pictures later and making appropriate decisions accordingly. This method is an expensive one and poses risks to human safety.

The Limpet provides an option to do conductor monitoring without involvement of humans. Several Limpets can be stuck on the conductor for a long time, where they can use their IMU sensor to monitor the motion and vibration of the conductor, log the data and send it wirelessly to a central station. The data from all the Limpets need to be fused together and then classified to inform the operators of the status of the conductor (normal and damaged). In this Chapter, I discuss the design of a multi-sensor data fusion approach for multiple Limpets, and how this approach can be used to monitor the condition of conductor pipes offshore. I designed an experimental setup to mimic the conditions of conductor pipes monitoring. I use a stepper motor as a source of vibration with a constant frequency. I introduce faults to the conductor structure and use the Limpets data to classify the condition of the conductor as well as the type of fault. I use the IMU sensor on the Limpets to achieve the conductor monitoring process.

I discuss the architecture of the multi-sensor data fusion approach in Section 6.2. In Section 6.3, I show the design of the setup used to test the multi-sensor data fusion approach and a detailed description of the experiments conducted to test the fusion approach. I discuss the results of the experiments in Section 6.4. Section 6.5 gives a brief summary of this Chapter.

6.2 Multi-Sensor Data Fusion Architecture

Figure 6.1 shows the multi-sensor data fusion architecture used for this Chapter. The first stage is acquiring the raw sensor data from the Limpets. I used the IMU sensors on the Limpets for measuring the vibrations, where the source of vibrations was a stepper motor. The raw data of interest is the accelerometer data. The data from the sensors were sent to the computer through serial connection to each Limpet. The data from each Limpet was recorded for two minutes. I used two minutes as a proof of concept. As the volume of data changes, the classification accuracy and results will change. The second stage of the architecture is the signal processing phase. The signal processing phase is divided into three steps. The first step involves eliminating outliers and spikes using the median absolute deviation technique. The median absolute deviation is a measure of the median of the absolute deviations of the data points from the dataset's median. In this Chapter, data points are considered outliers if they have a value that is more than three scaled median absolute deviations from the median of the dataset. The median absolute deviation is calculated using the following formula:

$$MAD = median(|x_i - median(x)|), i = 1, ..., N \tag{6.1}$$

The second step in the signal processing phase is data smoothing using the moving average process. I applied a simple moving average filter to smooth out the short-term fluctuations in the data. I divide the dataset into windows of a specific size and calculate the mean from an equal number of data points on either side of a central value within each window. For an input signal x and a positive integer k, the moving average y is computed by sliding a window of length k along x. Each element of y is the local mean of the corresponding values in the input signal x within the window, and signal y is the same size as x. For a signal x made up of k scalar observations, the mean μ and the moving average y are given by

$$\mu = \frac{1}{k}\sum_{i=1}^{k} x_i \tag{6.2}$$

$$y = [\mu_i, ..., \mu_N] \tag{6.3}$$

The last step in the signal processing phase is dividing the dataset from each sensor into windows with a size of 1 second. After the signal processing phase, I carry out a feature extraction phase on each of the data windows. Diagnosis and monitoring are usually performed as classification using feature-based techniques. The feature extraction phase allows the original raw data to be mapped into fewer features (reducing dimensionality) without losing important information from the original measurements. At the feature extraction phase, important time-based and frequency-based features are calculated for the vibration data measured by the accelerometer. For the feature extraction phase, I used *tsfresh*, which is a python package that automatically calculates a large number of time-based and frequency-based features. Tsfresh package extracts a total of 30 features from each data window. The features extracted and their description are shown by Table 6.1.

Extracted Features	**Description**
Absolute Energy	Absolute energy of the time series signal computed by calculating the sum of the squared values of the signal
Absolute Sum of Changes	Sum of the absolute value of consecutive changes in the time series signal
Approximate Entropy	Uses a vectorized approximate entropy algorithm to estimate the entropy of the signal
Autoregressive Coefficient	Calculation of the autoregressive coefficient
Augmented Dickey-Fuller Test	Hypothesis test to check if the unit root is present in a time series signal.
Autocorrelation	Calculation of the autocorrelation of the time series signal with a specified lag.
Complexity-Invariant Distance	Estimation of the time series complexity based on the number of peaks and valleys
Continuous Wavelet Transform	Calculation of the continuous wavelet transform for the ricker wavelet

Energy Ratio Chunks	Division of the time series signal into chunks and calculation of the sum of squares for each chunk and expressed as a ratio with the sum of squares for the whole signal
Spectral Mean	Mean of the absolute fourier transform spectrum
Spectral Variance	Variance of the absolute fourier transform spectrum
Spectral Skewness	Skewness of the absolute fourier transform spectrum
Spectral Kurtosis	Kurtosis (measure of tailedness) of the absolute fourier transform spectrum
Spectral Coefficients	Coefficients of the one-dimensional discrete fourier transform of the time series signal by FFT algorithm
Friedrich Coefficients	Coefficients of the polynomial h(x) based on the Langevin model
Kurtosis	Kurtosis of the time series signal indicating the peakedness of the probability distribution function of the time series signal
Mean	Average of the time series signal
Mean Change	Average over the difference between subsequent time series values
Mean Absolute Change	Average over the absolute value of the difference between subsequent time series values
Median	Median of the time series signal
Peaks	Number of peaks in the time series signal
Re-occuring Datapoints	Percentage of the unique/re-occuring data-points in the time signal with respect to all data-points
RMS	Root-mean-square level of the time series signal
RSSQ	Root-sum-of-squares level of the time series signal
Sample entropy	Calculation of the sample entropy of the time series signal, which is used to asses the complexity of the signal
Skewness	Skewness of the time series signal, which is a measure of the assymetry of the probability density function
Welch Density	Cross power spectral density of the time series signal at different frequencies
Standard Deviation	Standard deviation of the time series signal
Sum of Re-occuring Datapoints	Sum of re-occuring data-points in the time series signal
Variance	Variance of the time series signal

Table 6.1: A list of the features extracted from the raw sensor data for the multi-sensor data fusion approach.

Generally, the sensor data fusion can be carried out at one of three different stages in fusion approaches. Data-level fusion involves combining the raw data from the sensors together before applying signal processing techniques to the dataset. The feature extraction is then performed on the fused data followed by the classification. In feature-level fusion, the features extracted from the data are fused together and used to inform the classification process. Decision-level fusion combines together the results of the classification from each sensor to provide a better result. In this Chapter, I use a feature-level fusion approach. After carrying out feature extraction on each window, the features extracted from the sensor data on all the different Limpets are fused together and fed into the classifier. The classification approach in this Chapter is based on offline classification.

The final stage of the multi-sensor data fusion approach presented in this Chapter is the classification. I used multiple different classifiers to identify the status of the conductor based on the fused features. The reason behind using multiple classifiers is to compare between the classification accuracy of the different classifiers and determine which classifier is best suited for such an application. The classifiers used are: Linear Support Vector Classifier (SVC), Ridge Regression Classifier, Decision Tree Classifier, Logistic Regression Classifier and Multi-layer Perceptron Neural Network. Linear SVC, logistic regression and ridge regression classifiers are linear classifiers, while decision tree and multi-layer perceptron neural network are non-linear classifiers. The multi-layer perceptron neural network used had the hidden layer size set to 100, the iterations size set to 200, the learning rate (regularisation term parameter) set to 0.0001, and the activation function for the hidden layers set to rectified linear unit function. The chosen classifiers are some of the most commonly used classifiers and represent different levels of complexity. The classification process in the multi-sensor fusion approach will identify if the structure is normal and healthy, or whether there is a fracture in the structure and locate the fracture position, or if there is fatigue loading on the structure and the location of that.

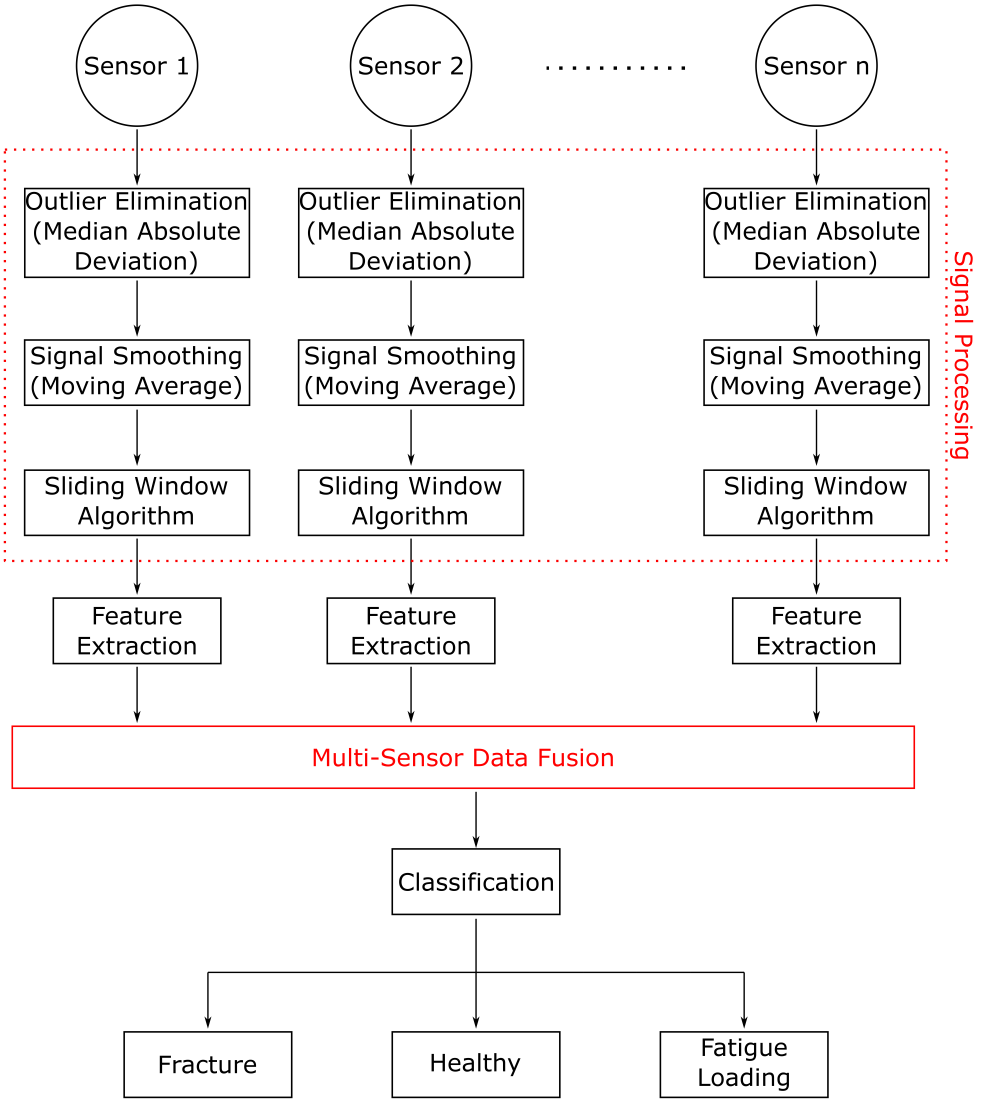

Figure 6.1: Schematic of the multi-sensor data fusion architecture.

6.3 Experimental Design

Figure 6.2 shows the experimental setup I designed to study the multi-sensor data fusion approach. The setup consists of an acrylic layer supported at the two ends by acrylic stands. I placed a stepper motor on one side of the acrylic layer. The stepper motor provides a continuous vibration signal, which travels down the acrylic layer. I run the stepper motor at a constant speed (80 rpm), which provides a constant frequency vibration signal. This setup mimics the conditions of a conductor pipe, since the pipe is laid in the ground, and so it is connected at the bottom to the ground and at the top to the offshore installation (two anchor points). The conductor pipe is exposed to vibrations at one point along the pipe resulting from the waves hitting the pipe. By placing multiple Limpets at different distances from the vibration source, we can pick up the vibration signal throughout the whole structure. By studying this vibration signal as it travels down the pipe, we can infer information about the structural integrity of the acrylic layer (conductor pipe). This scenario mimics the condition monitoring of conductor pipes, as it is important to monitor the vibrations along the pipe to identify any structural problems.

I used three Limpets, equally spaced from each other, to conduct the experiments for the multi-sensor data fusion. The Limpets send their data to the computer through serial communication. The sampling frequency used for the sensor is 200 Hz, and the data was transferred using a baud rate of 115200 bps. I conducted a set of five different experiments. The first experiment involved logging data from the Limpets at normal conditions and without changing anything in the setup. The second and third experiments involved adding an extra weight (100 g) on the acrylic layer between Limpet 1 and Limpet 2, and then between Limpet 2 and Limpet 3. In the fourth and fifth experiments, I introduce a fracture between Limpet 1 and Limpet 2, and then between Limpet 2 and Limpet 3. I repeated each experiment six times, and I used the first run of the experiments as training data for the classifier. After the experiments are conducted, the raw data from the sensors pass through the stages in the sensor fusion architecture shown by Figure 6.1.

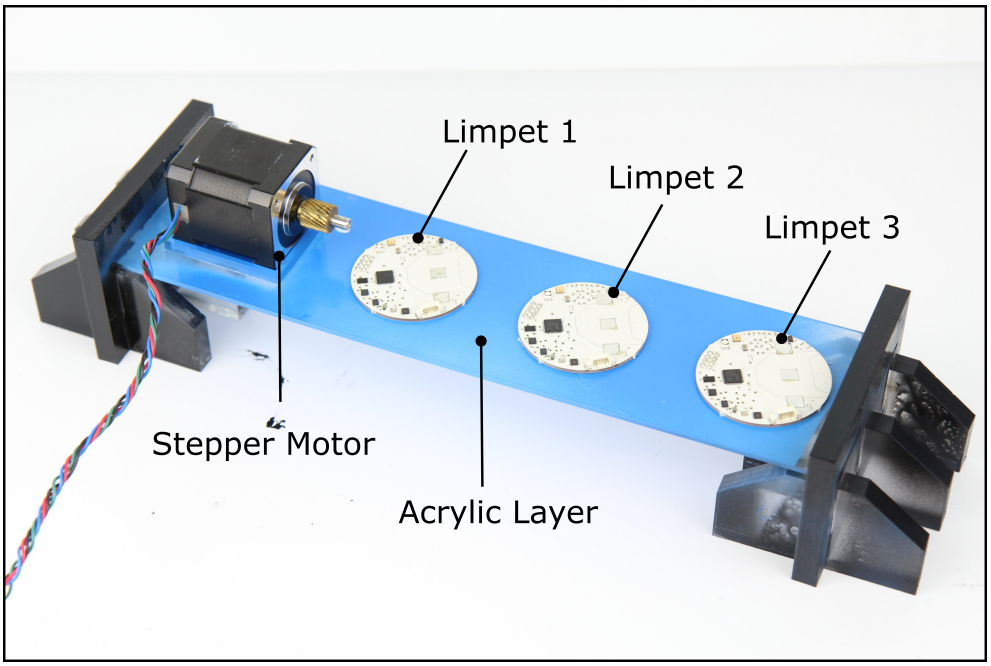

Figure 6.2: A picture of the multi-sensor fusion experimental setup showing the stepper motor, acrylic layer, and three Limpets used for measurement.

6.4 Results and Discussion

This section discusses the results of the fusion approach and the classification. The raw sensor data is the output of the first stage in data fusion architecture. The sensor data includes acceleration in the x, y, z for each of the three Limpets. The data is then processed and smoothed using MAD algorithm and a moving average filter. Figure 6.3 shows the processed data for Limpet 1 for normal conditions, a 100g weight placed between Limpets 1 and 2 (Fault 1), a 100g weight placed between Limpets 2 and 3 (Fault 2), a fracture introduced between Limpets 1 and 2 (Fault 3), and a fracture introduced between Limpets 2 and 3 (Fault 4). Figure 6.4 shows the processed data for Limpet 2 for normal conditions, Fault 1, Fault 2, Fault 3, and Fault 4. Figure 6.5 shows the processed data for Limpet 3 for normal conditions, Fault 1, Fault 2, Fault 3, and Fault 4.

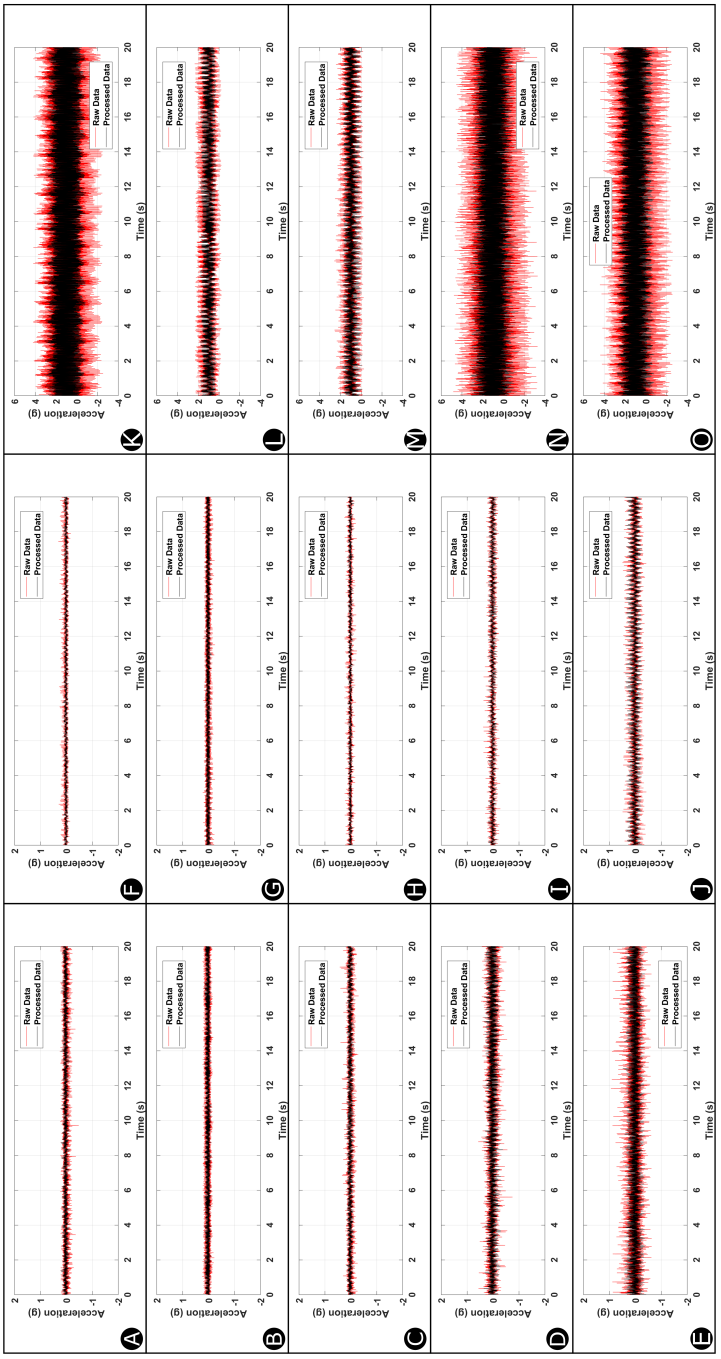

Figure 6.3: X-Acceleration data for Limpet 1 for (A) Normal Conditions, (B) Fault 1, (C) Fault 2, (D) Fault 3, (E) Fault 4. Y-Acceleration data for Limpet 1 for (F) Normal Conditions, (G) Fault 1, (H) Fault 2, (I) Fault 3, (J) Fault 4. Z-Acceleration data for Limpet 1 for (K) Normal Conditions, (L) Fault 1, (M) Fault 2, (N) Fault 3, (O) Fault 4.

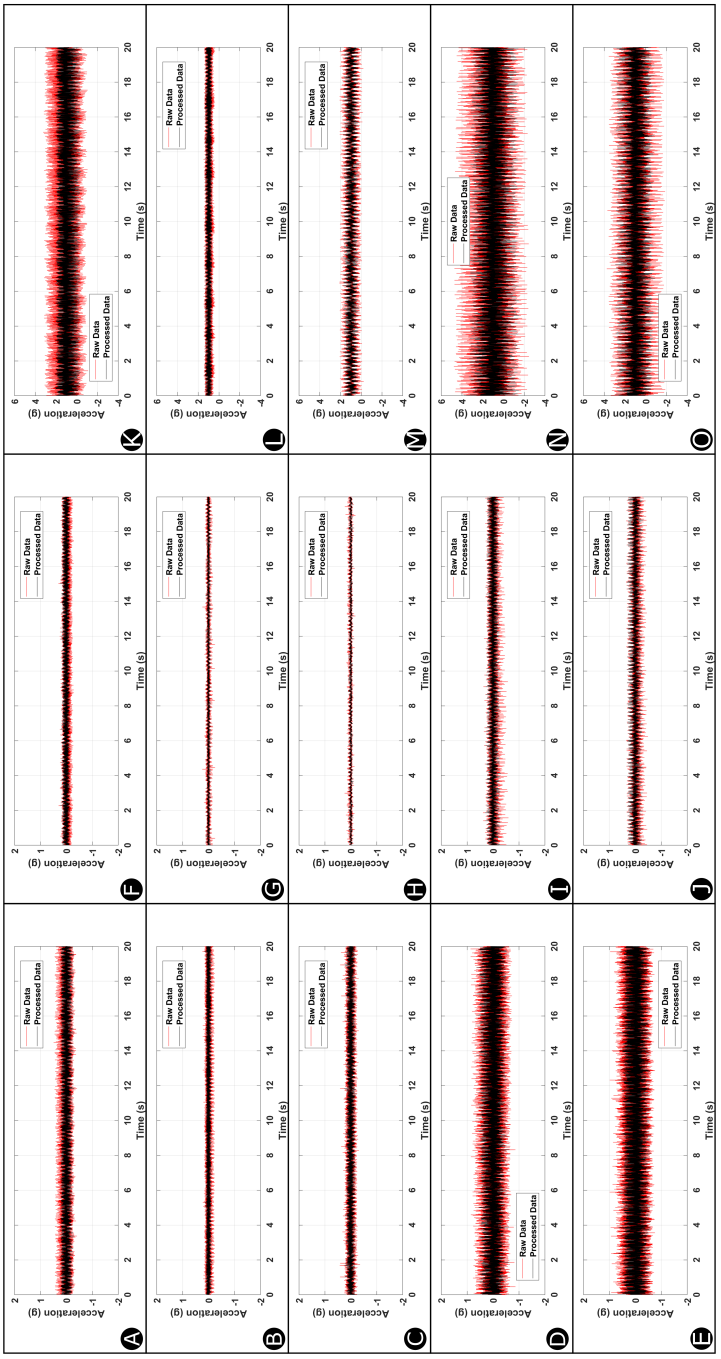

Figure 6.4: X-Acceleration data for Limpet 2 for (A) Normal Conditions, (B) Fault 1, (C) Fault 2, (D) Fault 3, (E) Fault 4. Y-Acceleration data for Limpet 2 for (F) Normal Conditions, (G) Fault 1, (H) Fault 2, (I) Fault 3, (J) Fault 4. Z-Acceleration data for Limpet 2 for (K) Normal Conditions, (L) Fault 1, (M) Fault 2, (N) Fault 3, (O) Fault 4.

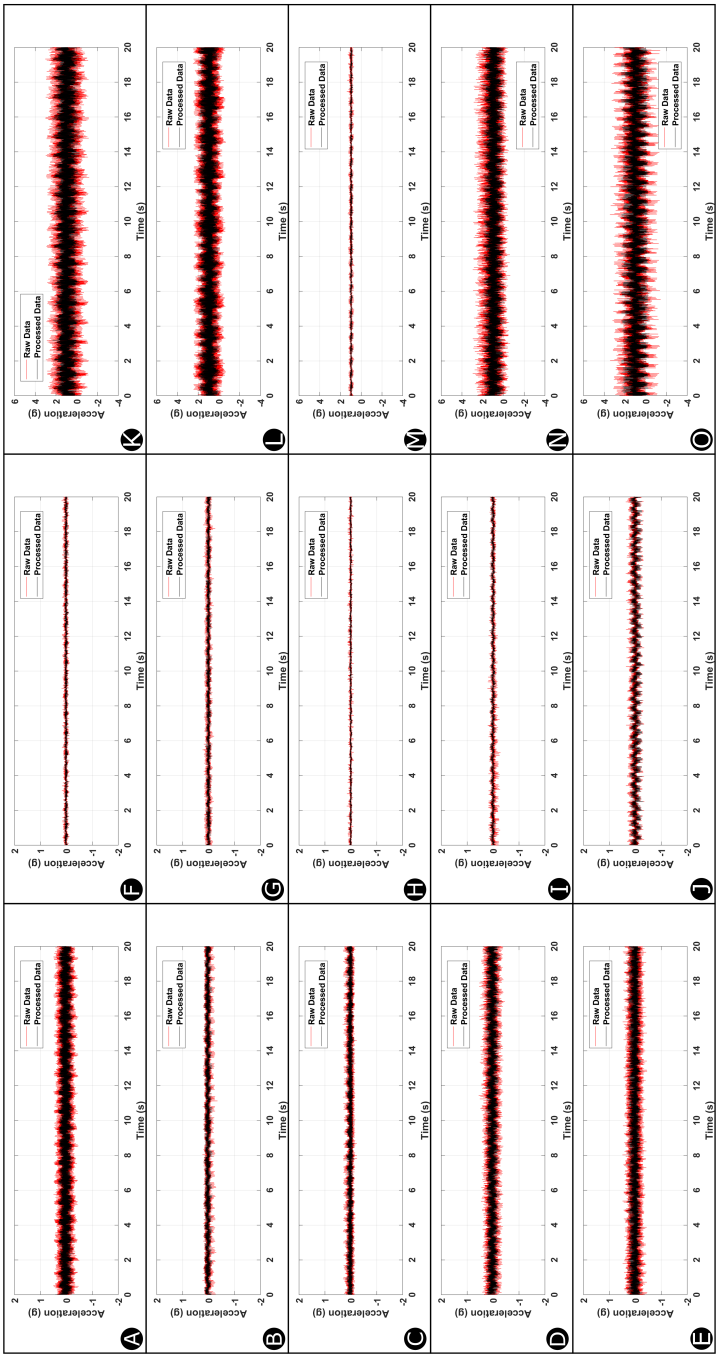

Figure 6.5: X-Acceleration data for Limpet 3 for (A) Normal Conditions, (B) Fault 1, (C) Fault 2, (D) Fault 3, (E) Fault 4. Y-Acceleration data for Limpet 3 for (F) Normal Conditions, (G) Fault 1, (H) Fault 2, (I) Fault 3, (J) Fault 4. Z-Acceleration data for Limpet 3 for (K) Normal Conditions, (L) Fault 1, (M) Fault 2, (N) Fault 3, (O) Fault 4.

Figure 6.6 shows the accuracy of the different classifiers for classification of the x-acceleration value (A), y-acceleration value (B), z-acceleration value (C) for the different faults introduced to the system. Non-linear classifiers (decision tree and neural networks) are usually better coped to deal with non-linear data, which is the case for the data in this scenario. Decision tree classifier gave good accuracy results in classification of the different faults across the x-acceleration (80%), y-acceleration (76%), and z-acceleration (77%). The multi-layer perceptron neural network, however, did not give good classification results as the accuracy of the classification was low for the x-acceleration (50%), y-acceleration (49%), and z-acceleration (67%). The main reason behind this poor accuracy is over-fitting of the data by the neural network. The error on the training data is usually driven to a very small value, but when the network is then presented with new values, the error becomes large. The neural network has memorised the training data, but it has not learned to adapt to new scenarios or data.

Linear classifiers are expected to give worse results than the non-linear classifiers in this experiment, since they are trying to classify non-linear data, and they do not cope well with that. Logistic regression and ridge classifiers gave poor accuracy results for the classification compared to other classifiers as shown in Figure 6.6. Although being a linear classifier, linear SVC classifier gave good classification accuracy for the classification of x-acceleration, y-acceleration and z-acceleration. The accuracy was similar to that of the decision tree classifier for the x and y accelerations, and even higher than the decision tree classifier for the z-acceleration. The linear SVC classifier was used on an input sample with a very large amount of data points. In scenarios where the input sample data (training data) is low, the accuracy of the linear SVC classifier decreases. I reduced the input sample data size by 90%, and re-classified the data using the decision tree and linear SVC classifiers to show how decreasing the input sample size would affect the accuracy of both classifiers. For the x-acceleration data, the decision tree accuracy did not change by a large amount (77%), but the linear SVC classification accuracy reduced significantly (57%). For the y-acceleration data, the decision tree classifier changed to 72%, while the linear SVC classifier accuracy reduced to about 56%. For the z-acceleration, the decision tree classifier accuracy increased to 86%, while the linear SVC classifier accuracy reduced significantly as compared to the accuracy of classification with a larger input sample (reduced from 92% to 60%).

The reason for using different classifiers is to test the accuracy of the classifiers in such applications and decide on which classifier is best-suited for this application. So, for the multi-sensor fusion approach for structural integrity monitoring of conductor pipes, I decided to use the decision tree as the main classifier since it classifies the different faults with high accuracy for all acceleration directions, and it works well for scenarios with lower input sample data as it is better coped to deal with non-linear data.

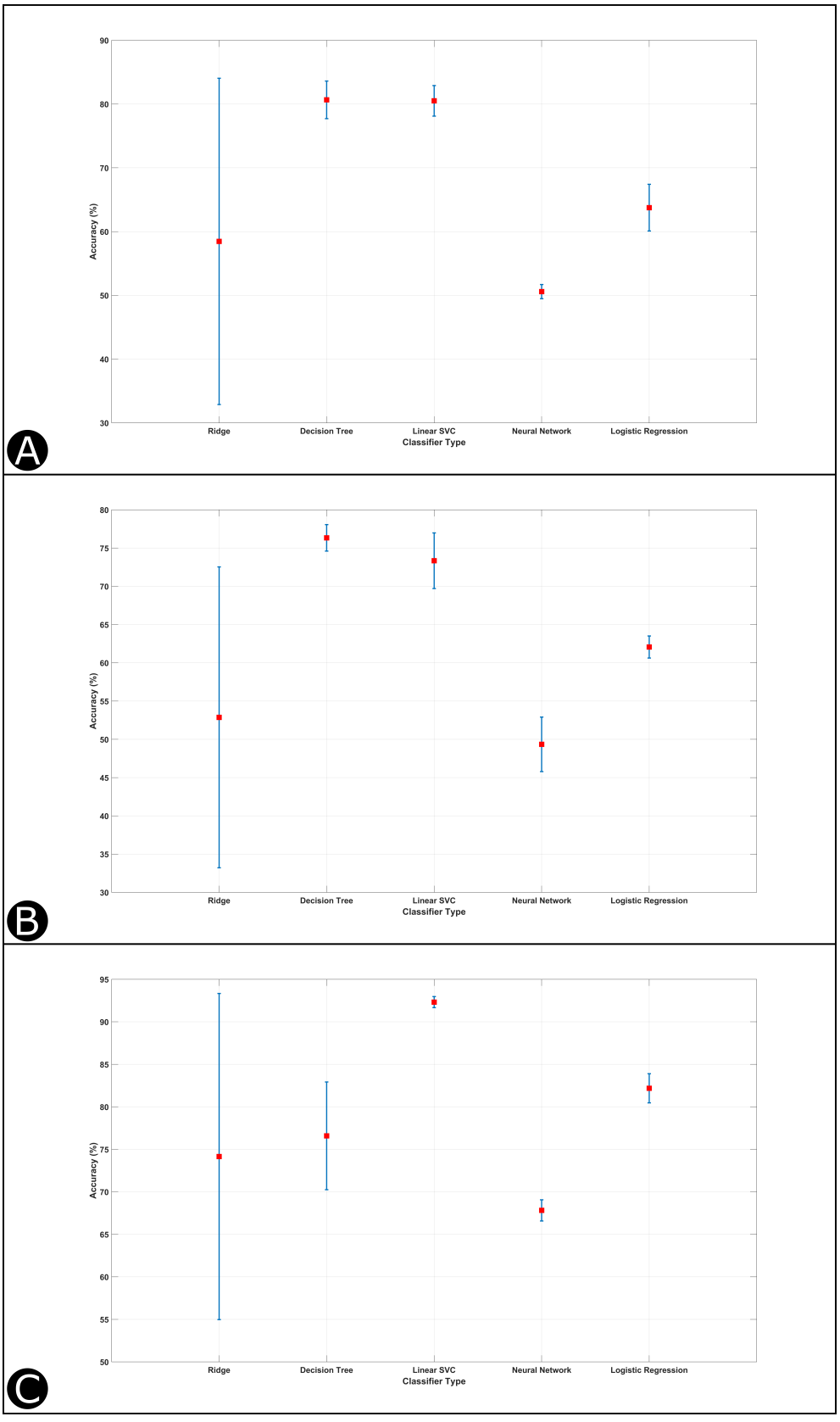

Figure 6.6: Accuracy of the different classifiers in classifying the different faults introduced to the system using (A) X-Acceleration, (B) Y-Acceleration, (C) Z-Acceleration.

6.5 Summary

Sensor fusion is important in applications where data from multiple sources need to be fused together to give a more accurate result and help in decision making. One such example is monitoring the structural integrity of conductor pipes offshore. Operators are interested in monitoring the vibration levels on the conductor pipes installed to inform the health of the pipe. In this Chapter, I used three Limpets for monitoring vibrations on a setup that mimics the pipe conditions. I used a multi-sensor data fusion approach to monitor the pipe and classify different faults introduced to the system (fatigue loading and fractures). The multi-sensor data fusion first involves processing the raw accelerometer data from the different Limpets and extracting important features from the data. The features from the different Limpets are then fused together and passed to the classifier. I used five different classifiers, both linear and non-linear classifiers, to classify the fused features. The classification results can be either normal structure, fatigue loading in position 1 (between Limpets 1 and 2), fatigue loading in position 2 (between Limpets 2 and 3), fracture in position 1 (between Limpets 1 and 2), or fracture in position 2 (between Limpets 2 and 3). The five classifiers successfully classified the fusion results but with different accuracies. Based on the accuracy of the classifiers, decision tree classifier (non-linear classifier) is better suited for this application than the other classifiers since it copes well with non-linear data, does not suffer from over-fitting of data, works well with smaller input samples, and has a high classification accuracy for the vibration data.

Part V

Conclusions, Experimental and References

Chapter 7

Impact, Field Tests and Commercialisation

7.1 Introduction

This Chapter demonstrates the use of the Limpet in some field test trials and use cases, as well as other scientific research that does not involve the offshore sector. The contribution of the Limpet to both industrial demonstrations and other research output shows its great impact and value. I discuss the use of the Limpet for underwater demonstrations in Fort William, Scotland, for the industrial partners of the ORCA Hub project in Section 7.2. Section 7.2 is based on our published conference proceeding [6]. Section 7.3 discusses the use of the Limpet for topside demonstrations for the industrial partners in ORCA Hub, where the demonstration took place on an oil rig mock-up in the Fire Service College, England. In Section 7.4, I show how the Limpet was used for environmental monitoring process as part of our conference publication [5]. Finally, I discuss the commercialisation of the Limpet technology in Section 7.5.

7.2 Fort William Test Trials

This section demonstrates how the Limpet was used as a part of a low-cost underwater sensor network in sea trials in Fort William, Scotland between 27/06/2018 and 03/07/2018. The section is based on our published conference proceeding [6], which can be found in Appendix K on Page 443. In this paper, we show the first ever hardware implementation of a robust Time Division Access – Medium Access Control (TDA-MAC) for data gathering in underwater acoustic sensor networks. The results show a successful application of TDA-MAC to remote environmental monitoring, integrating a range of different sensor nodes including the Limpet and other sensor nodes. Figure 7.1A shows a schematic of the overall system used in the test trials. The system consists of multiple sensor nodes monitoring the underwater environment and sending their data acoustically to a buoy floating on the surface of the water. The buoy acts as a gateway node and forwards the data using radio links to the terrestrial base station. In this work, the Limpet is connected to an acoustic underwater modem, and sends its data acoustically when requested by the buoy. The Limpet was contained in a watertight (up to 1000 m depth) glass encapsulation purchased from BlueRobotics as shown by Figure 7.1B.

The official video of the Fort William Test Trials from ORCA Hub can be found here:

Fort William Test Trials Video.

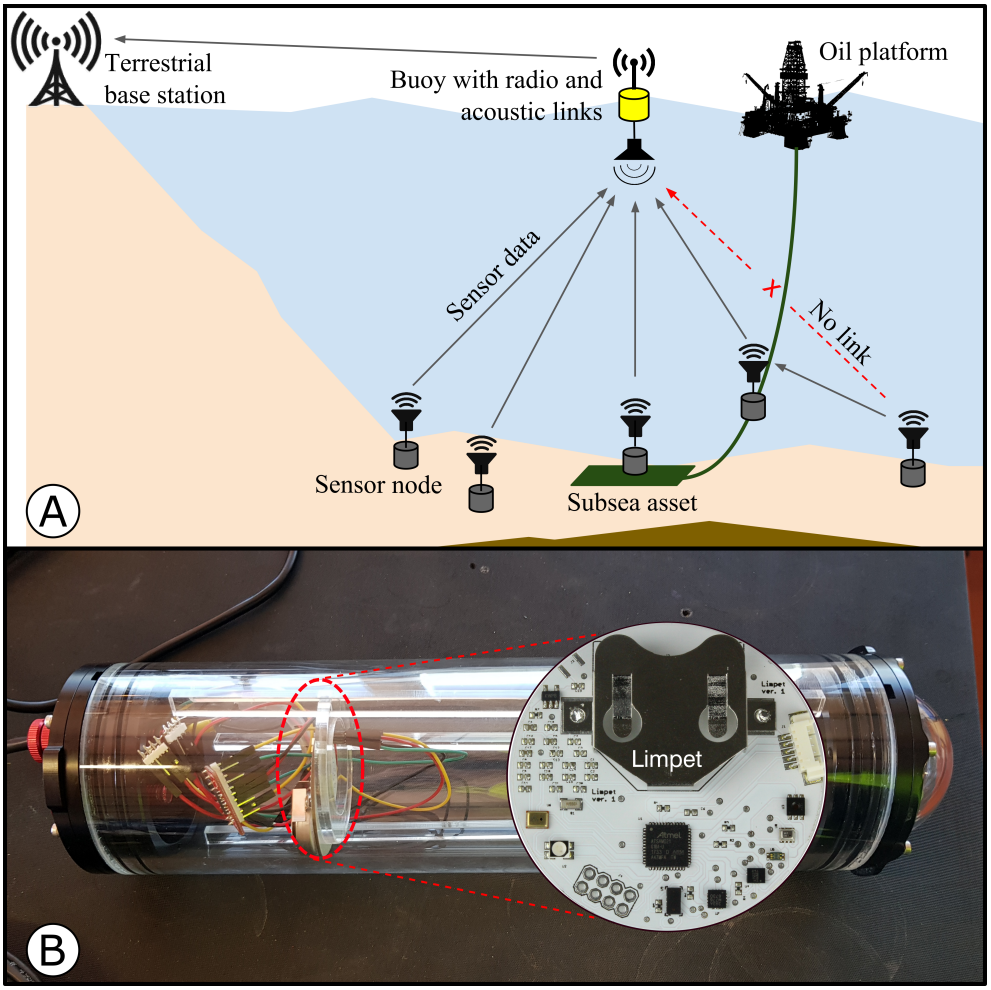

Figure 7.1: (A) A conceptual overview of the underwater wireless sensor network with a surface buoy used as a gateway node. (B) The Limpet in its encapsulation as used in the underwater wireless sensor network.

7.3 Fire Service College Test Trials

In this section, I demonstrate how the Limpet was used as part of the ORCA Hub demonstrations to the industrial partners, which took place in the Fire Service College, England. The Fire Service College has a mock-up of an oil rig on their site, where the demonstrations were held. The Limpet took part in two different demonstrations, which are: deployment of the Limpet using a mobile robotic platform; monitoring of the environmental conditions around the oil rig. The aim of the first demonstration was to show the capability of deploying a network of Limpets using a mobile robotic platform. Once the Limpet is deployed, it can adhere to the surface of the structure and monitor the condition of the structure and the environmental conditions surrounding it. Figure 7.2 shows the Limpet being deployed by the mobile robotic platform on a tank. The Limpet adheres to the surface of the tank using magnets embedded in its case.

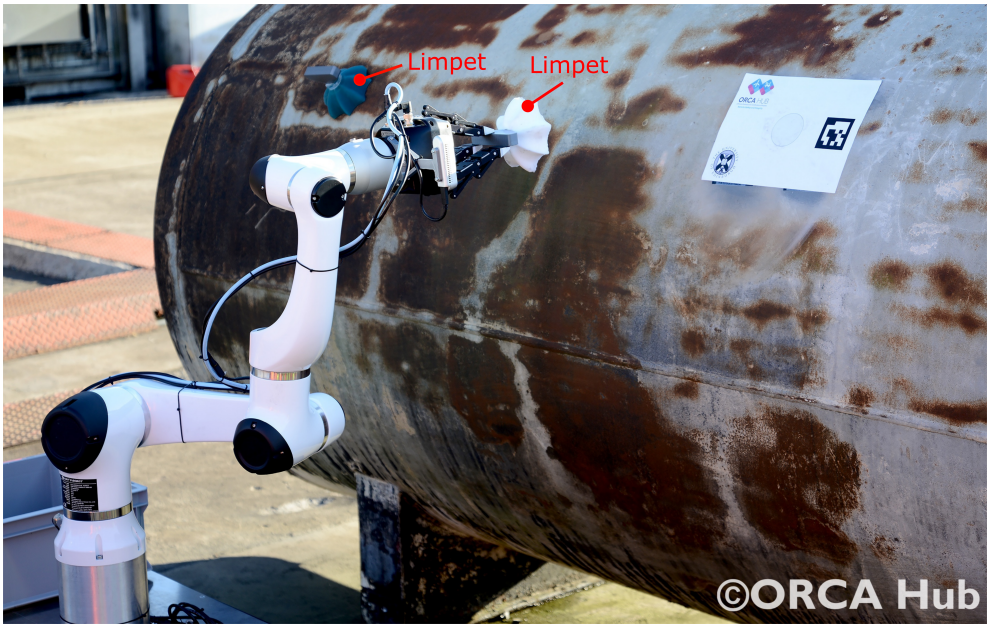

Figure 7.2: The Limper being deployed on a tank in a mock-up of an oil rig using a mobile robotic platform.

In the second demonstration, after multiple Limpets were deployed around the oil rig, they started monitoring the environmental conditions surrounding the platform. The Limpets then send the data back to a central monitoring station. Figure 7.3 shows some of the planted Limpets. The Limpet sends the data to the central station using LoRa communication. The main problem we faced in this demonstration is that our LoRa communication relied on having an internet connection. In the oil rig mock-up, we did not have any internet connection, which caused all our communication links to break down. There was also a firewall blocking any communication links over the internet. To fix this problem, we had to buy a Wi-Fi router with a Wi-Fi dongle and used it for our communications. After facing this problem, I had to develop our own local server for the LoRa communication that does not rely on any internet connection. Details of the server system developed is described in Chapter 3. An official video of the Fire Service College Test Trials from ORCA Hub can be found here:

Fire Service College Trials Video.

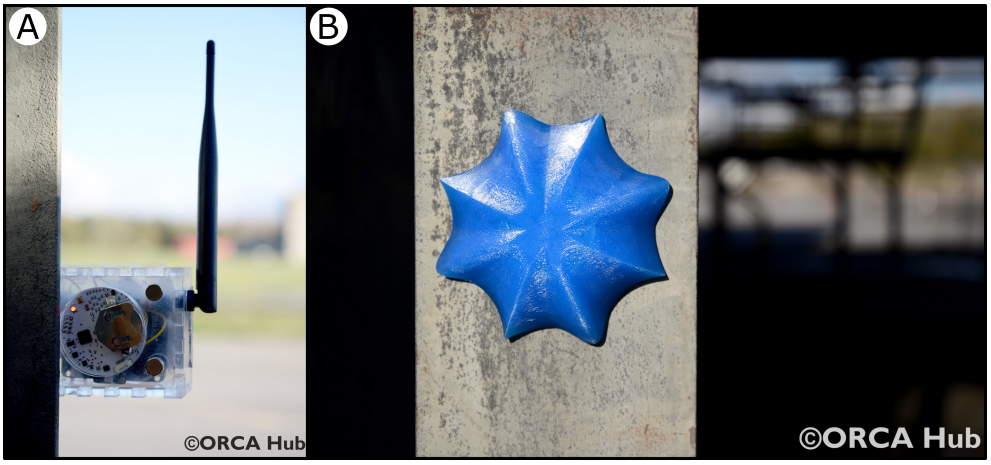

Figure 7.3: (A-B) Some of the Limpets deployed to monitor the environmental condition around the mock-up oil rig in the Fire Service College.

7.4 Environmental Water Monitoring

Currently, the environmental water monitoring field faces the challenge to create new integrated systems capable of measuring key indicators of the water quality in real-time. Important parameters to monitor include turbidity, pH, conductivity, chlorine and dissolved oxygen levels. The encouraged technology needs to be low-cost, low-maintenance, autonomous, long living, responsive, sensitive and accurate. The Limpet was shown to be useful for environmental water monitoring [5]. In this work, we used the Limpet to monitor the turbidity levels in water. By measuring the turbidity levels in water using the Limpet, we can identify drinkable and non-drinkable water. This process can also be used for other applications offshore like detecting and identifying offshore hazardous substances in water. We use a combination of the LED and optical sensor on the Limpet for measuring the water tubidity levels. The experimental setup is shown in Figure 7.4. The experimental setup consists of Limpet holders, light-guiding tunnels, and a sample holder. The light-guiding tunnels and sample holder are painted black to minimise light losses to the surrounding environment. The light emitted from the RGB LED of one Limpet is measured by the optical sensor of the Limpet facing it. The solutions with different turbidity levels are placed in the sample holder between the two Limpets.

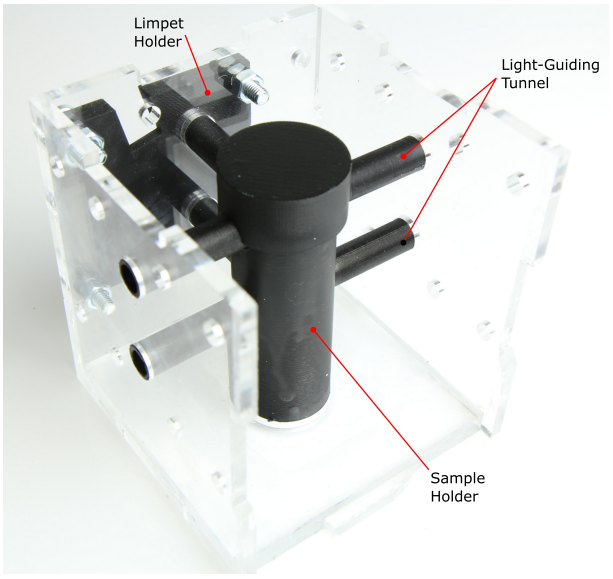

Figure 7.4: A picture of the experimental setup used for environmental water monitoring using the Limpets.

Before running any experiments with our setup, we ran measurements using solutions with a known turbidity level, which are Stabilized Formazin Turbidity Standards, using a Hach turbidimeter. The standards used have turbidity levels of 0,20,100,1000,4000 NTU. The Hach turbidimeter is a commercially available turbidity meter. This experiment is used to calibrate the Hach turbidimeter. The calibration plot of the Hach turbidimeter is shown by Figure 7.5.

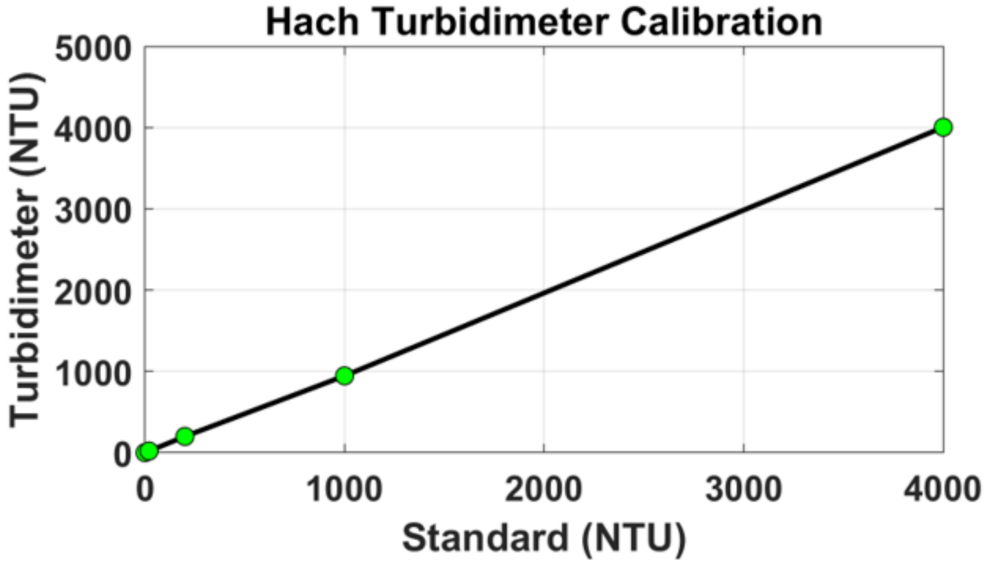

Figure 7.5: Calibration Plot of the Hach Turbidimeter using Stabilized Formazin Turbidity Standard. The graph shows the turbidity measurement from the Hach against the turbidity level of the standards.

The Limpet was first calibrated against the turbidity standards before using it to test turbidity levels of other samples. We used two different methods of measurement in this work. The first measurement involves using the white light on one Limpet and measuring the ambient light intensity using the optical sensor on the Limpet facing it. This measurement gives an indication of the amount of white light transmitted through the sample. The second measurement involves using the blue light on one Limpet and measuring the blue light power density using the optical sensor on the other Limpet. This measurement gives an indication of the amount of blue light transmitted through the sample. We repeated the measurements for all the different turbidity standards. The calibration plots for the white light transmission and blue light transmission for the Limpet is shown by Figure 7.6.

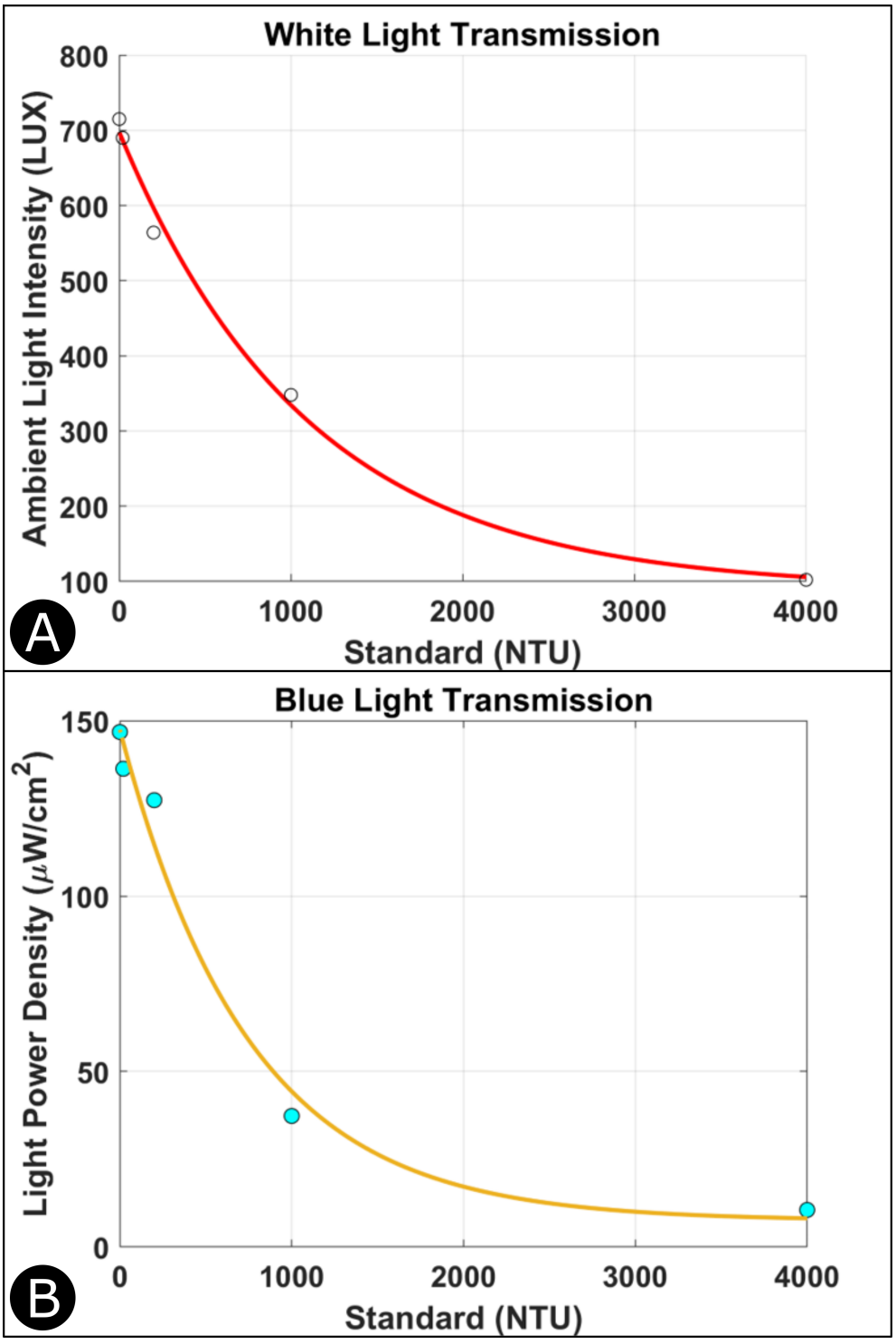

Figure 7.6: (A) Calibration plot of the Limpet for white light transmission. The graph shows the ambient light intensity (lux) measured by the optical sensor on the Limpet against the turbidity standards. (B) Calibration plot of the Limpet for blue light transmission. The graph shows the blue light power density (uW/cm2) against the turbidity standards.

After calibrating the Limpet, we used it to measure the turbidity level of lemon juice and compare it to the turbidity measurement from the Hach turbidimeter. The results of the measurement are shown in Table 7.1. The measurement using the blue light transmission is close to that of the hach turbidimeter. The white light transmission technique gave an inaccurate measurement. The reason behind the inaccuracy of the measurement is that we only calibrated the Limpet against five turbidity standards, and the range of turbidity between the standards is very large. We need more standards with closer turbidity values in order to calibrate the Limpet more accurately and come up with a better calibration plot for the Limpet.

Measurement Type	**Turbidity of Sample (NTU)**
Hach Turbidimeter	577.7
White Light Transmission (Limpet)	852
Blue Light Transmission (Limpet)	572

Table 7.1: Measurement of turbidity levels of lemon juice using the Hach turbidimeter, white light transmission technique with Limpets, and blue light transmission technique with Limpets.

7.5 Commercialisation

The Limpet technology and the work that I have developed in my research project have gained major interest from the industrial partners in the ORCA Hub project. We have been approached by multiple companies that want to buy the Limpet and use it for different monitoring use cases that fit with the work they do. Eventually, we decided to spin-off a company on this technology. The company is currently in the formation stage, and will be formed jointly with the Aerial Robotics Lab at Imperial College London. The aim of the company is to provide monitoring solutions for offshore platforms using some of the existing technologies and strategies developed.

Chapter 8

Conclusions and Future Work

8.1 Conclusions

8.1.1 Limpets Are Low-Cost and Highly Manufacturable

In this thesis, I develop a new low-cost and highly manufacturable multi-sensing robotic platform for inspection and monitoring of offshore energy platforms. In Chapter 3, I introduce the first version of the Limpet system and discuss its design, fabrication, specifications and properties. Due to its low cost and high manufacturability, the Limpet can be deployed in large collectives to monitor different parameters in the offshore environment. The Limpet has nine different on-board sensing modalities and comprises the sensing aspect of the ORCA Hub System, which consists of the offshore assets and the heterogeneous collection of robots interacting with the assets. In Chapter 3, I also show how the Limpet can be integrated with ROS to allow it to communicate and interact with other robots in the ORCA Hub System, where the interaction results in more complex and useful behaviours. I also show how the Limpet is robust in communication, where it can use one of multiple communication systems for data transmission or communication with other agents. I demonstrate how the Limpet can be used for real-time condition monitoring of offshore structures by designing an experiment to detect faults in the operation of a mock-up of a wind turbine. The results show how the Limpet can perform on-board signal processing and analysis to gain multi-functional sensing capabilities, improve its communication requirements, and monitor the structural health of equipment or structures offshore.

8.1.2 Limpets Can Navigate Unstructured Environments

In Chapter 5, I develop version 2 of the Limpet, where it can sense its surroundings and navigate around unstructured environments. The Limpet v2 is capable of adhering to and climbing different surfaces, which increases the accessible areas of the Limpet in offshore environments. The Limpet v2 is also equipped with a sensor payload (Limpet v1) which allows it to carry out inspection and monitoring tasks. In Chapter 5, I discuss the design, fabrication, specifications and properties of Limpet v2. Limpet v2 builds up on version 1 and is designed in a modular fashion. The Limpet v2 uses a hybrid electromagnetic module as its core unit to allow adhesion and locomotion capabilities.

The adhesion system is based on negative pressure adhesion utilising suction cups, and the locomotion system is based on slip-stick locomotion. The modularity aspect of Limpet v2 allows the different modules to be reconfigured for new tasks.

8.1.3 Limpets Can Use Multi-Sensor Fusion For Monitoring Structures

Due to the lack of accuracy that usually results from using single sensors for monitoring offshore structures, I have developed a multi-sensor fusion approach in Chapter 6 that combines sensing modalities on the different Limpets to achieve structural integrity monitoring of conductor pipes. In Chapter 6, I use three Limpets to monitor the vibration levels of an experimental setup that mimics the conductor pipe conditions. I developed a multi-sensor data fusion approach that combines the data of these three Limpets to infer the structural health of the conductor pipe. The result of the approach indicates if the conductor pipe is a healthy one, or if there is a structural problem (fatigue loading or fracture), and this will help operators make decisions on whether the pipe needs maintenance or replacement. For the multi-sensor data fusion approach described in Chapter 6, the accelerometers on the Limpet are used to measure the vibration levels. The raw acceleration data from the sensors is processed, and important time-based and frequency-based features are extracted from the processed data. The features are then fused together and fed into different classifiers (linear and non-linear classifiers) for classification of the faults. I used different classifiers to test the accuracy of the classifiers in such applications and take a decision on which classifier would be best suited for this application. Based on the resultant classifier accuracies, it was found that decision tree classifier (non-linear classifier) is best suited for this application since it copes well with non-linear data, does not suffer from over-fitting of data, works well with smaller input samples, and has a high classification accuracy for the vibration data.

8.2 Future Work

The work presented in this thesis presents a system with great research impact and high industrial value. This section provides the foundation for alot of

more interesting work that can be achieved with the system and maps out some additions that could be implemented to improve on the system. The list below summarises some of those key aspects.

- Floating production storage and offloading (FPSO) motion monitoring. The vessels are extensively used by the offshore industry and are one of the primary methods of oil and gas processing and storage. Therefore, monitoring the movement of the vessel at certain points and the effect of the waves on the vessel is a vital aspect. The Limpet can be stuck on the vessel and can use the IMU sensor to monitor the motion of the vessel, log the data and do the processing of the data on-board. It can then report back with major events to the central station.

- Subsea asset monitoring such as gas and water lift systems. It is important to monitor the flow within the production system, pressure, phase change, and motion. The Limpet can detect the vibration, sound and acceleration and use the combination of these sensing modalities to monitor the asset. The Limpet will need to operate underwater, do on-board processing and communicate back to a central station.

- Equipping the Limpet with an energy harvesting system, such that the battery and recharging requirements are not needed. Having on-board batteries adds to the cost, weight and complexity of the robot. The constant need to recharge batteries also presents a major limitation if Limpets are to be deployed for long times in such a hazardous environment, where access to the site is limited and the cost of access is high.

- Developing version 2 of the sensing module PCB, where the module can be designed in a modular architecture to enable easy replacement and addition of extra sensors and capabilities.

- Developing an underwater version of the Limpet. This version would require design of a new encapsulation that protects the Limpet circuitry from water and allows the sensors on the Limpet to be in contact with the structure or surface to be monitored.

- Equipping the Limpet with a natural language interface to allow easy interaction between operators and Limpets, and also eliminate the need to train any personnel on using the Limpets.

- Equipping the Limpet with an underwater adhesion mechanism to allow it to adhere to different surfaces underwater.
- Equipping the Limpet with satellite communication, which allows for communication over very large distances and will enable easy control of the Limpet remotely from various different areas.
- Providing the Limpet with extra storage in the form of a memory card or blockchain database (decentralised privacy oriented data storage).
- Conducting over-the-air (OTA) firmware updates on the Limpet. Over-the-air updates involves deploying new firware and configurations wirelessly to the Limpet, and it is a key element for robots in such industrial applications. Using OTA firware updates allows updating the Limpet software remotely and can be achieved for all Limpets at once.
- Equipping the Limpet with more advanced data analytics and allowing it to make its own decisions and control the status of other robots on the platform accordingly.

8.3 Impact of Work

As we push the boundaries of human endeavour, we are inevitably operating in more extreme environments (nuclear, offshore, space exploration, defence, subsea, deep mining) than ever before. Due to the hostile nature of extreme environments, they present a high risk to human life. The costs of operation associated with these extreme environments are also very high. Recently, extreme environments have been given considerable attention, and industries are looking for more cost-effective and safer methods to operate in such environments. The field of robotics and automation is seen as a key component in this regard. Robots can provide the capability required to exploit the harshest of environments, whilst reducing the risk to human life and operation costs. The work presented in this thesis demonstrates a more cost-effective and safer method for inspection and maintenance of offshore energy platforms, which helps protect people and keep them away from such dangerous environments.

References

[1] M. E. Sayed, M. P. Nemitz, S. Aracri, A. C. McConnell, R. M. McKenzie, and A. A. Stokes, "The limpet: A ros-enabled multi-sensing platform for the orca hub," *Sensors*, vol. 18, no. 10, p. 3487, 2018.

[2] R. M. McKenzie, M. E. Sayed, M. P. Nemitz, B. W. Flynn, and A. A. Stokes, "Linbots: Soft modular robots utilizing voice coils," *Soft Robotics*, vol. 6, no. 2, p. 11, 2019.

[3] M. E. Sayed, J. O. Roberts, R. M. McKenzie, S. Aracri, A. Buchoux, and A. A. Stokes, "Limpet: A modular, untethered soft robot," *Science Robotics*, 2019.

[4] A. C. McConnell, M. E. Sayed, J. O. Roberts, S. Aracri, R. M. McKenzie, and A. A. Stokes, "Long necked turtle: A soft/hard hybrid mobile robotic platform for iot node distribution," *Frontiers in Robotics and AI*, 2019.

[5] S. Aracri, M. E. Sayed, J. O. Roberts, A. C. McConnell, and A. A. Stokes, "Limpet: An autonomous bioinspired robot for environmental monitoring," in *19th Biennial Seminar on Water Resources and Environmental Management*, 2018.

[6] N. Morozs, P. D. Mitchell, Y. Zakharov, R. Mourya, Y. R. Petillot, T. Gibney, M. Dragone, B. Sherlock, J. A. Neasham, C. C. Tsimenidis, M. E. Sayed, A. C. McConnell, S. Aracri, and A. A. Stokes, "Robust tda-mac for practical underwater sensor network deployment: Lessons from usmart sea trials," in *Proceedings of International Conference on UnderWater Networks and Systems (WUWNet'18)*, ACM, 2018.

[7] M. P. Nemitz, M. E. Sayed, J. Mamish, G. Ferrer, L. Teng, R. McKenzie, A. O. Hero, E. Olson, and A. A. Stokes, "Hoverbots: Precise locomotion using robots that are designed for manufacturability," *Frontiers in Robotics and AI*, vol. 4, p. 55, 2017.

[8] M. P. Nemitz, R. Marcotte, M. E. Sayed, G. Ferrer, A. O. Hero, E. Olson, and A. A. Stokes, "Multi-functional sensing for swarm robots using time sequence classification: Hoverbot, an example," *Frontiers in Robotics and AI*, vol. 5, no. 55, 2018.

[9] S. T. Mahon, J. O. Roberts, M. E. Sayed, D. H.-T. Chun, S. Aracri, R. M. McKenzie, M. P. Nemitz, and A. A. Stokes, "Capability by stacking: The current design heuristic for soft robots," *Biomimetics*, vol. 3, no. 3, p. 16, 2018.

[10] R. M. McKenzie, J. O. Roberts, M. E. Sayed, and A. A. Stokes, "Perisim: a simulator for optimising peristaltic table control," *Advanced Intelligent Systems*, 2019.

[11] J. Dodoo, M. E. Sayed, L. Mackay, G. Mchale, and A. A. Stokes, "A holistic review of wetting of droplets," in *Electrowetting 2018*, 2018.

[12] H. D. Chun, J. O. Roberts, M. E. Sayed, S. Aracri, and A. A. Stokes, "Towards more energy efficient pneumatic soft actuators using a port-hamiltonian approach," in *2019 IEEE International Conference on Soft Robotics (RoboSoft 2019)*, IEEE, 2019.

[13] S. T. Mahon, A. Buchoux, M. E. Sayed, L. Teng, and A. A. Stokes, "Soft robots for extreme environments: Removing electronic control," in *2019 IEEE International Conference on Soft Robotics (RoboSoft 2019)*, IEEE, 2019.

[14] H. Hastie, K. S. Lohan, M. J. Chantler, D. Robb, S. Ramamoorthy, R. P. A. Petrick, S. Vijayakumar, and D. M. Lane, "The ORCA Hub: Explainable Offshore Robotics through Intelligent Interfaces," in *13th Annual ACM/IEEE International Conference on Human Robot Interaction*, mar 2018.

[15] Y. Bai and Q. Bai, *Subsea Engineering Handbook*. Gulf Professional Publishing, 1st ed., 2012.

[16] C. A. Miller, "Energy Resources and Policy," *Climate Vulnerability*, pp. 37–51, 2013.

[17] A. Shukla and H. Karki, "Application of robotics in offshore oil and gas industry— A review Part II," *Robotics and Autonomous Systems*, vol. 75, pp. 508–524, 1 2016.

[18] H. Chen, S. Stavinoha, M. Walker, B. Zhang, and T. Fuhlbrigge, "Opportunities and Challenges of Robotics and Automation in Offshore Oil & Gas Industry," *Intelligent Control and Automation*, vol. 05, pp. 136–145, 7 2014.

[19] J. W. Griggs, *Energy law journal.*, vol. 32. Federal Energy Bar Association, 2011.

[20] G. Mois, S. Folea, and T. Sanislav, "Analysis of Three IoT-Based Wireless Sensors for Environmental Monitoring," *IEEE Transactions on Instrumentation and Measurement*, vol. 66, pp. 2056–2064, aug 2017.

[21] J. Yuh and R. Lakshmi, "An intelligent control system for remotely operated vehicles," *IEEE Journal of Oceanic Engineering*, vol. 18, no. 1, pp. 55–62, 1993.

[22] J. Elvander and G. Hawkes, "ROVs and AUVs in support of marine renewable technologies," in *2012 Oceans*, pp. 1–6, IEEE, oct 2012.

[23] G. A. Raine and M. C. Lugg, *ROV Inspection of Welds - A Reality*. Underwater Intervention Conference, Underwater Intervention '95, 1995.

[24] L. Whitcomb, "Underwater robotics: out of the research laboratory and into the field," in *Proceedings of the 2000 IEEE International Conference on Robotics and Automation.*, vol. 1, pp. 709–716, IEEE, 2000.

[25] M. Bessa, "Controlling the dynamic positioning of a ROV," in *Oceans 2003*, p. Vol.2, IEEE, 2003.

[26] P. E. Hagen, T. G. Fossum, and R. E. Hansen, "Applications of AUVs with SAS," in *OCEANS 2008*, pp. 1–4, IEEE, 2008.

[27] M. J. Costa, P. Goncalves, A. Martins, and E. Silva, "Vision-based assisted teleoperation for inspection tasks with a small ROV," in *2012 Oceans*, pp. 1–8, IEEE, 10 2012.

[28] M. Bengel and K. Pfeiffer, "Mimroex mobile maintenance and inspection robot for process plants," tech. rep., Fraunhofer Institute for Manufacturing Engineering and Automation IPA, 2007.

[29] NREC/CMU, "Sensabot: A Safe and Cost-Effective Inspection Solution," *Journal of Petroleum Technology*, vol. 64, pp. 32–34, 10 2012.

[30] E. Kyrkjebo, P. Liljeback, and A. A. Transeth, "A Robotic Concept for Remote Inspection and Maintenance on Oil Platforms," in *ASME 2009 28th International Conference on Ocean, Offshore and Arctic Engineering*, pp. 667–674, ASME, 6 2009.

[31] M. Galassi, A. Royroy, G. Carvalho, G. Freitas, P. From, R. Costa, F. Lizarralde, L. Hsu, G. de Carvalho, J. de Oliveira, A. A. De Lima, T. D. M. Prego, S. L. Netto, and E. A. Da Silva, "DORIS - A Mobile Robot for Inspection and Monitoring of Offshore Facilities," in *Congresso Brasileiro de Automática*, 2014.

[32] A. F. Moghaddam, M. Lange, O. Mirmotahari, and M. Høvin, "Novel Mobile Climbing Robot Agent for Offshore Platforms," *International Journal of Mechanical, Aerospace, Industrial, Mechatronic and Manufacturing Engineering*, vol. 6, no. 8, 2012.

[33] M. Bengel, K. Pfeiffer, B. Graf, A. Bubeck, and A. Verl, "Mobile robots for offshore inspection and manipulation," in *2009 IEEE/RSJ International Conference on Intelligent Robots and Systems*, pp. 3317–3322, IEEE, 10 2009.

[34] M. J. Kabir, A. M. T. Oo, and M. Rabbani, "A brief review on offshore wind turbine fault detection and recent development in condition monitoring based maintenance system," in *2015 Australasian Universities Power Engineering Conference (AUPEC)*, pp. 1–7, IEEE, sep 2015.

[35] K.-Y. Oh, J.-Y. Park, J.-S. Lee, B. I. Epureanu, and J.-K. Lee, "A Novel Method and Its Field Tests for Monitoring and Diagnosing Blade Health for Wind Turbines," *IEEE Transactions on Instrumentation and Measurement*, vol. 64, no. 6, pp. 1726–1733, 2015.

[36] "GL Guideline for the Certification of Offshore Wind Turbines Edition 2012," tech. rep., GL Renewables Certification, 2012.

[37] W. Yang, P. Tavner, and M. Wilkinson, "Condition monitoring and fault diagnosis of a wind turbine synchronous generator drive train," *IET Renewable Power Generation*, vol. 3, no. 1, p. 1, 2009.

[38] R. Kryter and H. Haynes, "Condition monitoring of machinery using motor current signature analysis," *Power Plant Dynamics, Control and Testing Symposium*, vol. 20, no. 17, 1989.

[39] A. Cardoso and E. Saraiva, "Computer-aided detection of airgap eccentricity in operating three-phase induction motors by Park's vector approach," *IEEE Transactions on Industry Applications*, vol. 29, no. 5, pp. 897–901, 1993.

[40] Z. Hameed, Y. Hong, Y. Cho, S. Ahn, and C. Song, "Condition monitoring and fault detection of wind turbines and related algorithms: A review," *Renewable and Sustainable Energy Reviews*, vol. 13, pp. 1–39, jan 2009.

[41] B. Lu, Y. Li, X. Wu, and Z. Yang, "A review of recent advances in wind turbine condition monitoring and fault diagnosis," in *2009 IEEE Power Electronics and Machines in Wind Applications*, pp. 1–7, IEEE, 6 2009.

[42] T. Yuji, T. Bouno, and T. Hamada, "Suggestion of Temporarily for Forecast Diagnosis on Blade of Small Wind Turbine," *IEEJ Transactions on Power and Energy*, vol. 126, no. 7, pp. 710–711, 2006.

[43] T. Buono, T. Yuji, T. Hamada, and T. Hideaki, "Failure Forecast Diagnosis of Small Wind Turbine using Acoustic Emission Sensor," *KIEE International Transactions on Electrical Machinery and Energy Conversion Systems*, vol. 5-B, no. 1, pp. 78–83, 2005.

[44] K. Schroeder, W. Ecke, J. Apitz, E. Lembke, and G. Lenschow, "A fibre Bragg grating sensor system monitors operational load in a wind turbine rotor blade," *Measurement Science and Technology*, vol. 17, pp. 1167–1172, may 2006.

[45] J. Ruan, S. C. M. Ho, D. Patil, and G. Song, "Structural health monitoring of wind turbine blade using piezoceremic based active sensing and impedance sensing," in *Proceedings of the 11th IEEE International Conference on Networking, Sensing and Control*, pp. 661–666, IEEE, apr 2014.

[46] M. A. Trindade, "Applications of piezoelectric sensors and actuators for active and passive vibration control," in *7th Brazilian Conference on Dynamics, Control and Applications*, may 2008.

[47] M. Wevers and K. Lambrighs, *Applications of Acoustic Emission for SHM: A Review*, vol. 1. Wiley Online Library, september 2009.

[48] N. Godin, P. Reynaud, and G. Fantozzi, "Challenges and limitations in the identification of acoustic emission signature of damage mechanisms in composites materials," *Applied Sciences*, vol. 8, p. 1267, july 2018.

[49] C. E. Campanella, A. Cuccovillo, C. Campanella, A. Yurt, and V. M. N. Passaro, "Fibre bragg grating based strain sensors: Review of technology and applications," *Sensors*, vol. 18, p. 3115, september 2018.

[50] S. D. de Rivaz, B. Goldberg, N. Doshi, K. Jayaram, J. Zhou, and R. J. Wood, "Inverted and vertical climbing of a quadrupedal microrobot using electroadhesion," *Science Robotics*, vol. 3, p. eaau3038, 12 2018.

[51] K. Autumn, Y. A. Liang, S. T. Hsieh, W. Zesch, W. P. Chan, T. W. Kenny, R. Fearing, and R. J. Full, "Adhesive force of a single gecko foot-hair," *Nature*, vol. 405, pp. 681–685, 6 2000.

[52] K. Autumn, A. Dittmore, D. Santos, M. Spenko, and M. Cutkosky, "Frictional adhesion: A new angle on gecko attachment," *The Journal of Experimental Biology*, vol. 209, pp. 3569–79, 9 2006.

[53] M. Sitti and R. Fearing, "Synthetic gecko foot-hair micro/nano-structures for future wall-climbing robots," in *2003 IEEE International Conference on Robotics and Automation*, vol. 1, pp. 1164–1170, IEEE, 2003.

[54] F. Ochoa-Cardenas and T. J. Dodd, "Design of an active magnetic wheel with a varying Electro-Permanent Magnet adhesion mechanism," in *2015 IEEE/RSJ International Conference on Intelligent Robots and Systems (IROS)*, pp. 3340–3345, IEEE, 9 2015.

[55] J. Grieco, M. Prieto, M. Armada, and P. Gonzalez de Santos, "A six-legged climbing robot for high payloads," in *Proceedings of the 1998 IEEE International Conference on Control Applications*, vol. 1, pp. 446–450, IEEE, 1998.

[56] M. Eich and T. Vogele, "Design and control of a lightweight magnetic climbing robot for vessel inspection," in *2011 19th Mediterranean Conference on Control & Automation (MED)*, pp. 1200–1205, IEEE, 6 2011.

[57] Z. Xu and P. Ma, "A wall-climbing robot for labelling scale of oil tank's volume," *Robotica*, vol. 20, pp. 209–212, 3 2002.

[58] W. Shen, J. Gu, and Y. Shen, "Proposed wall climbing robot with permanent magnetic tracks for inspecting oil tanks," in *IEEE International Conference Mechatronics and Automation, 2005*, vol. 4, pp. 2072–2077, IEEE, 2005.

[59] W. Shen, J. Gu, and Y. Shen, "Permanent magnetic system design for the wall-climbing robot," in *IEEE International Conference Mechatronics and Automation, 2005*, vol. 4, pp. 2078–2083, IEEE, 2005.

[60] H. Wang, A. Yamamoto, and T. Higuchi, "Electrostatic-motor-driven electroadhesive robot," in *2012 IEEE/RSJ International Conference on Intelligent Robots and Systems*, pp. 914–919, IEEE, 10 2012.

[61] R. Liu, R. Chen, H. Shen, and R. Zhang, "Wall Climbing Robot Using Electrostatic Adhesion Force Generated by Flexible Interdigital Electrodes," *International Journal of Advanced Robotic Systems*, vol. 10, p. 36, 1 2013.

[62] H. Wang and A. Yamamoto, "Analyses and Solutions for the Buckling of Thin and Flexible Electrostatic Inchworm Climbing Robots," *IEEE Transactions on Robotics*, vol. 33, pp. 889–900, 8 2017.

[63] A. Yamamoto, T. Nakashima, and T. Higuchi, "Wall Climbing Mechanisms Using Electrostatic Attraction Generated by Flexible Electrodes," in *2007 International Symposium on Micro-NanoMechatronics and Human Science*, pp. 389–394, IEEE, 11 2007.

[64] H. Prahlad, R. Pelrine, S. Stanford, J. Marlow, and R. Kornbluh, "Electroadhesive robots—wall climbing robots enabled by a novel, robust, and electrically controllable adhesion technology," in *2008 IEEE International Conference on Robotics and Automation*, pp. 3028–3033, IEEE, may 2008.

[65] H. Wang, A. Yamamoto, and T. Higuchi, "A Crawler Climbing Robot Integrating Electroadhesion and Electrostatic Actuation," *International Journal of Advanced Robotic Systems*, vol. 11, p. 191, 12 2014.

[66] G. Gu, J. Zou, R. Zhao, X. Zhao, and X. Zhu, "Soft wall-climbing robots," *Science Robotics*, vol. 3, p. eaat2874, 12 2018.

[67] K. Daltorio, A. Horchler, S. Gorb, R. Ritzmann, and R. Quinn, "A small wall-walking robot with compliant, adhesive feet," in *2005 IEEE/RSJ International Conference on Intelligent Robots and Systems*, pp. 3648–3653, IEEE, 2005.

[68] J. Zhu, D. Sun, and S.-K. Tso, "Development of a Tracked Climbing Robot," *Journal of Intelligent and Robotic Systems*, vol. 35, no. 4, pp. 427–443, 2002.

[69] H. Kim, D. Kim, H. Yang, K. Lee, K. Seo, D. Chang, and J. Kim, "Development of a wall-climbing robot using a tracked wheel mechanism," *Journal of Mechanical Science and Technology*, vol. 22, pp. 1490–1498, aug 2008.

[70] K. Autumn and A. M. Peattie, "Mechanisms of Adhesion in Geckos," *Integrative and Comparative Biology*, vol. 42, pp. 1081–1090, 12 2002.

[71] M. P. Murphy, C. Kute, Y. Mengüç, and M. Sitti, "Waalbot II: Adhesion Recovery and Improved Performance of a Climbing Robot using Fibrillar Adhesives," *The International Journal of Robotics Research*, vol. 30, pp. 118–133, 1 2011.

[72] O. Unver, A. Uneri, A. Aydemir, and M. Sitti, "Geckobot: a gecko inspired climbing robot using elastomer adhesives," in *Proceedings 2006 IEEE International Conference on Robotics and Automation*, pp. 2329–2335, IEEE.

[73] Y. Li, A. Ahmed, D. Sameoto, and C. Menon, "Abigaille II: toward the development of a spider-inspired climbing robot," *Robotica*, vol. 30, pp. 79–89, 1 2012.

[74] M. Greuter, G. Shah, G. Caprari, F. Tâche, R. Siegwart, and M. Sitti, "Toward Micro Wall-Climbing Robots Using Biomimetic Fibrillar Adhesives," in *Proceedings of the 3rd International Symposium on Autonomous*

Minirobots for Research and Edutainment (AMiRE 2005), pp. 39–46, Springer-Verlag, 2006.

[75] E. W. Hawkes, D. L. Christensen, and M. R. Cutkosky, "Vertical dry adhesive climbing with a 100x bodyweight payload," in *2015 IEEE International Conference on Robotics and Automation (ICRA)*, pp. 3762–3769, IEEE, 5 2015.

[76] W. A. Breckwoldt, K. A. Daltorio, L. Heepe, A. D. Horchler, S. N. Gorb, and R. D. Quinn, "Walking inverted on ceilings with wheel-legs and micro-structured adhesives," in *2015 IEEE/RSJ International Conference on Intelligent Robots and Systems (IROS)*, pp. 3308–3313, IEEE, 9 2015.

[77] D. K. Wainwright, T. Kleinteich, A. Kleinteich, S. N. Gorb, and A. P. Summers, "Stick tight: suction adhesion on irregular surfaces in the northern clingfish," *Biology Letters*, vol. 9, pp. 20130234–20130234, 5 2013.

[78] A. M. Smith, "The role of suction in the adhesion of limpets," *The Journal of Experimental Biology*, vol. 161, p. 151, 1991.

[79] W. M. Kier and A. M. Smith, "The Structure and Adhesive Mechanism of Octopus Suckers," *Integrative and Comparative Biology*, vol. 42, pp. 1146–1153, 12 2002.

[80] J. Gray, H. W. Lissmann, and R. J. Pumphrey, "The Mechanism of Locomotion in the Leech (Hirudo Medicinalis Ray)," *Journal of Experimental Biology*, vol. 15, no. 3, 1938.

[81] J. Hou, E. Wright, R. H. Bonser, and G. Jeronimidis, "Development of Biomimetic Squid-Inspired Suckers," *Journal of Bionic Engineering*, vol. 9, pp. 484–493, dec 2012.

[82] H. Bing-Shan, W. Li-Wen, F. Zhuang, and Z. Yan-zheng, "Bio-inspired Miniature Suction Cups Actuated by Shape Memory Alloy," *International Journal of Advanced Robotic Systems*, vol. 6, p. 29, 9 2009.

[83] S. Sareh, K. Althoefer, M. Li, Y. Noh, F. Tramacere, P. Sareh, B. Mazzolai, and M. Kovac, "Anchoring like octopus: biologically inspired soft artificial sucker," *Journal of The Royal Society Interface*, vol. 14, p. 20170395, 10 2017.

[84] P. R. Bandyopadhyay, J. D. Hrubes, and H. A. Leinhos, "Biorobotic adhesion in water using suction cups," *Bioinspiration & Biomimetics*, vol. 3, p. 016003, 3 2008.

[85] Z. Zhakypov, F. Heremans, A. Billard, and J. Paik, "An Origami-Inspired Reconfigurable Suction Gripper for Picking Objects With Variable Shape and Size," *IEEE Robotics and Automation Letters*, vol. 3, pp. 2894–2901, 10 2018.

[86] H. Choi, S. Ryew, T. Kang, J. Lee, and H. Kim, "A wall climbing robot with closed link mechanism," in *Proceedings. 2000 IEEE/RSJ International Conference on Intelligent Robots and Systems (IROS 2000)*, vol. 3, pp. 2006–2011, IEEE, 2000.

[87] N. Elkmann, T. Felsch, M. Sack, J. Saenz, and J. Hortig, "Innovative service robot systems for facade cleaning of difficult-to-access areas," in *IEEE/RSJ International Conference on Intelligent Robots and System*, vol. 1, pp. 756–762, IEEE, 2002.

[88] J. Zhu, D. Sun, and S.-K. Tso, "Application of a Service Climbing Robot with Motion Planning and Visual Sensing," *Journal of Robotic Systems*, vol. 20, pp. 189–199, apr 2003.

[89] P. Backes, Y. Bar-Cohen, and B. Joffe, "The multifunction automated crawling system (MACS)," in *Proceedings of International Conference on Robotics and Automation*, vol. 1, pp. 335–340, IEEE, 1997.

[90] X. G. Gao and K. Kikuchi, "Study on a Kind of Wall Cleaning Robot," in *2004 IEEE International Conference on Robotics and Biomimetics*, pp. 391–394, IEEE, 2004.

[91] S. Park, H. D. Jeong, and Z. S. Lim, "Design of a mobile robot system for automatic integrity evaluation of large size reservoirs and pipelines in industrial fields," in *Proceedings 2003 IEEE/RSJ International Conference on Intelligent Robots and Systems (IROS 2003)*, vol. 3, pp. 2618–2623, IEEE, 2003.

[92] R. Pack, J. Christopher, and K. Kawamura, "A Rubbertuator-based structure-climbing inspection robot," in *Proceedings of International Conference on Robotics and Automation*, vol. 3, pp. 1869–1874, IEEE, 1997.

[93] R. Lal Tummala, R. Mukherjee, N. Xi, D. Aslam, H. Dulimarta, J. Xiao, M. Minor, and G. Dang, "Climbing the walls [robots]," *IEEE Robotics & Automation Magazine*, vol. 9, pp. 10–19, 12 2002.

[94] S. Krosuri and M. Minor, "A multifunctional hybrid hip joint for improved adaptability in miniature climbing robots," in *2003 IEEE International Conference on Robotics and Automation*, vol. 1, pp. 312–317, IEEE, 2003.

[95] J. Xiao, N. Xi, J. Xiao, and J. Tan, "Multi-sensor referenced gait control of a miniature climbing robot," in *Proceedings 2003 IEEE/RSJ International Conference on Intelligent Robots and Systems (IROS 2003)*, vol. 3, pp. 3656–3661, IEEE, 2003.

[96] B. Shores and M. Minor, "Design, Kinematic Analysis, and Quasi-Steady Control of a Morphic Rolling Disk Biped Climbing Robot," in *Proceedings of the 2005 IEEE International Conference on Robotics and Automation*, pp. 2721–2726, IEEE, 2005.

[97] W. Brockmann, "Concept for Energy-autarkic, Autonomous Climbing Robots," in *Climbing and Walking Robots*, pp. 107–114, Springer Berlin Heidelberg, 2006.

[98] M. F. Silva, J. A. T. Machado, and J. K. Tar, "A Survey of Technologies for Climbing Robots Adhesion to Surfaces," in *2008 IEEE International Conference on Computational Cybernetics*, pp. 127–132, IEEE, 11 2008.

[99] G. La Rosa, M. Messina, G. Muscato, and R. Sinatra, "A low-cost lightweight climbing robot for the inspection of vertical surfaces," *Mechatronics*, vol. 12, pp. 71–96, 2 2002.

[100] M. Murphy, W. Tso, M. Tanzini, and M. Sitti, "Waalbot: An Agile Small-Scale Wall Climbing Robot Utilizing Pressure Sensitive Adhesives," in *2006 IEEE/RSJ International Conference on Intelligent Robots and Systems*, pp. 3411–3416, IEEE, 10 2006.

[101] C. Menon, M. Murphy, and M. Sitti, "Gecko Inspired Surface Climbing Robots," in *2004 IEEE International Conference on Robotics and Biomimetics*, pp. 431–436, IEEE, 2004.

[102] K. Sangbae, A. Asbeck, M. Cutkosky, and W. Provancher, "SpinybotII: climbing hard walls with compliant microspines," in *ICAR '05. Proceedings., 12th International Conference on Advanced Robotics, 2005.*, pp. 601–606, IEEE, 2005.

[103] D. Longo and G. Muscato, "A modular approach for the design of the Alicia ³ climbing robot for industrial inspection," *Industrial Robot: An International Journal*, vol. 31, pp. 148–158, 4 2004.

[104] H. L. Rodriguez, B. Bridge, and T. P. Sattar, "Climbing Ring Robot For Inspection of Offshore Wind Turbines," in *Advances in Mobile Robotics*, pp. 555–562, WORLD SCIENTIFIC, aug 2008.

[105] K. Daltorio, T. Wei, S. Gorb, R. Ritzmann, and R. Quinn, "Passive Foot Design and Contact Area Analysis for Climbing Mini-Whegs," in *Proceedings 2007 IEEE International Conference on Robotics and Automation*, pp. 1274–1279, IEEE, 4 2007.

[106] K. A. Daltorio, S. Gorb, A. Peressadko, A. D. Horchler, R. E. Ritzmann, and R. D. Quinn, "A Robot that Climbs Walls using Micro-structured Polymer Feet," in *Climbing and Walking Robots*, pp. 131–138, Springer Berlin Heidelberg, 2006.

[107] T. Kang, H. Kim, T. Son, and H. Choi, "Design of quadruped walking and climbing robot," in *Proceedings 2003 IEEE/RSJ International Conference on Intelligent Robots and Systems (IROS 2003)*, vol. 1, pp. 619–624, IEEE, 2003.

[108] S. S. R. Chennareddy, A. Agrawal, and A. Karuppiah, "Modular Self-Reconfigurable Robotic Systems: A Survey on Hardware Architectures," *Journal of Robotics*, vol. 2017, pp. 1–19, mar 2017.

[109] S. Li, R. Batra, D. Brown, H.-D. Chang, N. Ranganathan, C. Hoberman, D. Rus, and H. Lipson, "Particle robotics based on statistical mechanics of loosely coupled components," *Nature*, vol. 567, pp. 361–365, 3 2019.

[110] D. Rus and M. Vona, "A physical implementation of the self-reconfiguring crystalline robot," in *IEEE international conference on robotics and automation (ICRA)*, vol. 2, pp. 1726–1733, IEEE, 2000.

[111] X. Jia, M. Frenger, Z. Chen, W. R. Hamel, and M. Zhang, "An alligator inspired modular robot," in *2015 IEEE International Conference on Robotics and Automation (ICRA)*, pp. 1949–1954, IEEE, 5 2015.

[112] S. Murata, E. Yoshida, A. Kamimura, H. Kurokawa, K. Tomita, and S. Kokaji, "M-TRAN: self-reconfigurable modular robotic system," *IEEE/ASME Transactions on Mechatronics*, vol. 7, pp. 431–441, 12 2002.

[113] M. Yim, D. G. Duff, and K. D. Roufas, "PolyBot: a modular reconfigurable robot," in *IEEE international conference on robotics and automation (ICRA)*, IEEE, 2000.

[114] J. Suh, S. Homans, and M. Yim, "Telecubes: mechanical design of a module for self-reconfigurable robotics," in *IEEE international conference on robotics and automation (ICRA)*, (Washington), pp. 4095–4101, IEEE, 2002.

[115] B. Salemi, M. Moll, and W.-m. Shen, "SUPERBOT: A Deployable, Multi-Functional, and Modular Self-Reconfigurable Robotic System," in *2006 IEEE/RSJ International Conference on Intelligent Robots and Systems*, IEEE, 10 2006.

[116] G. G. Ryland and H. H. Cheng, "Design of iMobot, an intelligent reconfigurable mobile robot with novel locomotion," in *2010 IEEE International Conference on Robotics and Automation*, (Anchorage), IEEE, 5 2010.

[117] K. Gilpin, A. Knaian, and D. Rus, "Robot pebbles: One centimeter modules for programmable matter through self-disassembly," in *2010 IEEE International Conference on Robotics and Automation*, IEEE, 5 2010.

[118] J. Zhao, X. Cui, Y. Zhu, and S. Tang, "A new self-reconfigurable modular robotic system UBot: Multi-mode locomotion and self-reconfiguration," in *2011 IEEE International Conference on Robotics and Automation*, IEEE, 5 2011.

[119] J. W. Romanishin, K. Gilpin, and D. Rus, "M-blocks: Momentum-driven, magnetic modular robots," in *2013 IEEE/RSJ International Conference on Intelligent Robots and Systems*, IEEE, 11 2013.

[120] J. Baca, S. Hossain, P. Dasgupta, C. A. Nelson, and A. Dutta, "ModRED: Hardware design and reconfiguration planning for a high dexterity modular self-reconfigurable robot for extra-terrestrial exploration," *Robotics and Autonomous Systems*, vol. 62, pp. 1002–1015, 7 2014.

[121] A. Brunete, J. E. Torres, and M. Hernando, "Arquitectura para robots modulares multiconfigurables heterogéneos de tipo cadena," *Arquit. Control Para Robot. Sección publicaciones la Esc. Técnica Super. Ing. Ind.*, pp. 151–167, 2007.

[122] M. Yim, W.-m. Shen, B. Salemi, D. Rus, M. Moll, H. Lipson, E. Klavins, and G. Chirikjian, "Modular Self-Reconfigurable Robot Systems [Grand Challenges of Robotics]," *IEEE Robotics & Automation Magazine*, vol. 14, pp. 43–52, 3 2007.

[123] J. Clune, J.-B. Mouret, and H. Lipson, "The evolutionary origins of modularity," *Proceedings of the Royal Society B: Biological Sciences*, vol. 280, pp. 20122863–20122863, 1 2013.

[124] C. H. Belke and J. Paik, "Mori: A Modular Origami Robot," *IEEE/ASME Transactions on Mechatronics*, vol. 22, pp. 2153–2164, 10 2017.

[125] J. Neubert, A. Rost, and H. Lipson, "Self-Soldering Connectors for Modular Robots," *IEEE Transactions on Robotics*, vol. 30, pp. 1344–1357, 12 2014.

[126] K. Stoy, "Reconfigurable Robots," in *Springer Handbook of Computational Intelligence* (J. Kacprzyk and W. Pedrycz, eds.), pp. 1407–1419, Springer, 2015.

[127] A. Brunete, A. Ranganath, S. Segovia, J. P. de Frutos, M. Hernando, and E. Gambao, "Current trends in reconfigurable modular robots design," *International Journal of Advanced Robotic Systems*, vol. 14, p. 172988141771045, 5 2017.

[128] S.-R. Kim, D.-Y. Lee, J.-S. Koh, and K.-J. Cho, "Fast, compact, and lightweight shape-shifting system composed of distributed self-folding origami modules," in *2016 IEEE International Conference on Robotics and Automation (ICRA)*, pp. 4969–4974, IEEE, 5 2016.

[129] A. A. Stanley and A. M. Okamura, "Controllable Surface Haptics via Particle Jamming and Pneumatics," *IEEE Transactions on Haptics*, vol. 8, pp. 20–30, j1 2015.

[130] C. Christianson, N. N. Goldberg, D. D. Deheyn, S. Cai, and M. T. Tolley, "Translucent soft robots driven by frameless fluid electrode dielectric elastomer actuators," *Science Robotics*, vol. 3, p. eaat1893, 4 2018.

[131] S. Li, D. M. Vogt, D. Rus, and R. J. Wood, "Fluid-driven origami-inspired artificial muscles.," *Proceedings of the National Academy of Sciences of the United States of America*, vol. 114, pp. 13132–13137, 12 2017.

[132] B. Mosadegh, A. D. Mazzeo, R. F. Shepherd, S. A. Morin, U. Gupta, I. Z. Sani, D. Lai, S. Takayama, and G. M. Whitesides, "Control of soft machines using actuators operated by a Braille display.," *Lab on a chip*, vol. 14, pp. 189–99, 1 2014.

[133] R. K. Katzschmann, A. D. Marchese, and D. Rus, "Hydraulic Autonomous Soft Robotic Fish for 3D Swimming," in *Experimental Robotics*, pp. 405–420, Springer, Cham, 2016.

[134] M. Wehner, R. L. Truby, D. J. Fitzgerald, B. Mosadegh, G. M. Whitesides, J. A. Lewis, and R. J. Wood, "An integrated design and fabrication strategy for entirely soft, autonomous robots," *Nature*, vol. 536, pp. 451–455, 8 2016.

[135] A. A. Stokes, R. F. Shepherd, S. A. Morin, F. Ilievski, and G. M. Whitesides, "A Hybrid Combining Hard and Soft Robots," *Soft Robotics*, vol. 1, no. 1, 2013.

[136] N. Kellaris, V. Gopaluni Venkata, G. M. Smith, S. K. Mitchell, and C. Keplinger, "Peano-HASEL actuators: Muscle-mimetic, electrohydraulic transducers that linearly contract on activation," *Science Robotics*, vol. 3, p. eaar3276, 1 2018.

[137] N. W. Bartlett, M. T. Tolley, J. T. B. Overvelde, J. C. Weaver, B. Mosadegh, K. Bertoldi, G. M. Whitesides, and R. J. Wood, "A 3D-printed, functionally graded soft robot powered by combustion.," *Science*, vol. 349, pp. 161–5, 7 2015.

[138] B. Mosadegh, P. Polygerinos, C. Keplinger, S. Wennstedt, R. F. Shepherd, U. Gupta, J. Shim, K. Bertoldi, C. J. Walsh, and G. M. Whitesides,

"Pneumatic Networks for Soft Robotics that Actuate Rapidly," *Advanced Functional Materials*, vol. 24, pp. 2163–2170, 4 2014.

[139] T. Wei, A. Stokes, and B. Webb, "A Soft Pneumatic Maggot Robot," in *Biomimetic and Biohybrid Systems*, pp. 375–386, Springer, Cham, 2016.

[140] A. Nemiroski, Y. Y. Shevchenko, A. A. Stokes, B. Unal, A. Ainla, S. Albert, G. Compton, E. MacDonald, Y. Schwab, C. Zellhofer, and G. M. Whitesides, "Arthrobots," *Soft Robotics*, vol. 4, pp. 183–190, 9 2017.

[141] G. Agarwal, M. A. Robertson, H. Sonar, and J. Paik, "Design and Computational Modeling of a Modular, Compliant Robotic Assembly for Human Lumbar Unit and Spinal Cord Assistance," *Scientific Reports*, vol. 7, p. 14391, 12 2017.

[142] M. A. Robertson and J. Paik, "New soft robots really suck: Vacuum-powered systems empower diverse capabilities," *Science Robotics*, vol. 2, p. eaan6357, 8 2017.

[143] M. T. Tolley, R. F. Shepherd, B. Mosadegh, K. C. Galloway, M. Wehner, M. Karpelson, R. J. Wood, and G. M. Whitesides, "A Resilient, Untethered Soft Robot," *Soft Robotics*, vol. 1, pp. 213–223, 9 2014.

[144] D. Keithly, J. Whitehead, A. Voinea, D. Horna, S. Hollenberg, M. Peck, J. Pikul, and R. F. Shepherd, "A cephalopod-inspired combustion powered hydro-jet engine using soft actuators," *Extreme Mechanics Letters*, vol. 20, pp. 1–8, 4 2018.

[145] M. P. Nemitz, P. Mihaylov, T. W. Barraclough, D. Ross, and A. A. Stokes, "Using voice coils to actuate modular soft robots: Wormbot, an example," *Soft Robotics*, vol. 3, no. 4, pp. 198–204, 2016.

[146] R. F. Shepherd, F. Ilievski, W. Choi, S. A. Morin, A. A. Stokes, A. D. Mazzeo, X. Chen, M. Wang, and G. M. Whitesides, "Multigait soft robot," *Proceedings of the National Academy of Sciences*, vol. 108, pp. 20400–20403, 12 2011.

[147] E. Acome, S. K. Mitchell, T. G. Morrissey, M. B. Emmett, C. Benjamin, M. King, M. Radakovitz, and C. Keplinger, "Hydraulically amplified self-healing electrostatic actuators with muscle-like performance.," *Science*, vol. 359, pp. 61–65, 1 2018.

[148] C. Laschi, M. Cianchetti, B. Mazzolai, L. Margheri, M. Follador, and P. Dario, "Soft Robot Arm Inspired by the Octopus," *Advanced Robotics*, vol. 26, pp. 709–727, jan 2012.

[149] S. Follmer, D. Leithinger, A. Olwal, A. Hogge, and H. Ishii, "inFORM: Dynamic Physical Affordances and Constraints through Shape and Object Actuation," in *ACM Symposium on User Interface Software and Technology (UIST)*, (St Andrews), ACM, 2013.

[150] M. Rubenstein, C. Ahler, and R. Nagpal, "Kilobot: A low cost scalable robot system for collective behaviors," in *2012 IEEE International Conference on Robotics and Automation*, pp. 3293–3298, IEEE, 5 2012.

[151] B. Khaleghi, A. Khamis, F. O. Karray, and S. N. Razavi, "Multisensor data fusion: A review of the state-of-the-art," *Information Fusion*, vol. 14, pp. 28–44, jan 2013.

[152] H. Durrant-Whyte and T. C. Henderson, "Multisensor Data Fusion," in *Handbook of Robotics* (B. Siciliano and O. Khatib, eds.), ch. 25, pp. 585–610, Springer, 1 ed., 2008.

[153] R. Joshi and A. Sanderson, "Minimal representation multisensor fusion using differential evolution," *IEEE Transactions on Systems, Man, and Cybernetics - Part A: Systems and Humans*, vol. 29, no. 1, pp. 63–76, 1999.

[154] Yunmin Zhu, Enbin Song, Jie Zhou, and Zhisheng You, "Optimal dimensionality reduction of sensor data in multisensor estimation fusion," *IEEE Transactions on Signal Processing*, vol. 53, pp. 1631–1639, may 2005.

[155] B. Milenova and M. Campos, "Mining high-dimensional data for information fusion: a database-centric approach," in *2005 7th International Conference on Information Fusion*, p. 7 pp., IEEE, 2005.

[156] G. Welch and G. Bishop, "An Introduction to the Kalman Filter," tech. rep., University of North Carolina, 1995.

[157] D. Crisan and A. Doucet, "A survey of convergence results on particle filtering methods for practitioners," *IEEE Transactions on Signal Processing*, vol. 50, pp. 736–746, mar 2002.

[158] G. Shafer, *A mathematical theory of evidence*. Princeton University Press, 1 ed., 1976.

[159] T. D. Garvey, J. D. Lowrance, and M. A. Fischler, "An inference technique for integrating knowledge from disparate sources," in *Proceedings of the International Joint Conference on Artificial Intelligence*, (Vancouver), pp. 319–325, Morgan Kaufmann Publishers, 1981.

[160] B. Bracio, W. Horn, and D. Moller, "Sensor fusion in biomedical systems," in *Proceedings of the 19th Annual International Conference of the IEEE Engineering in Medicine and Biology Society.*, vol. 3, pp. 1387–1390, IEEE.

[161] J. A. Barnett, "Computational Methods for A Mathematical Theory of Evidence," in *Classic Works of the Dempster-Shafer Theory of Belief Functions*, pp. 197–216, Berlin, Heidelberg: Springer Berlin Heidelberg, 2008.

[162] A. Benavoli, B. Ristic, A. Farina, M. Oxenham, and L. Chisci, "An approach to threat assessment based on evidential networks," in *2007 10th International Conference on Information Fusion*, pp. 1–8, IEEE, jul 2007.

[163] P. Escamilla-Ambrosio and N. Mort, "Hybrid Kalman filter-fuzzy logic adaptive multisensor data fusion architectures," in *42nd IEEE International Conference on Decision and Control (IEEE Cat. No.03CH37475)*, pp. 5215–5220, IEEE.

[164] J. Sasiadek and P. Hartana, "Sensor data fusion using Kalman filter," in *Proceedings of the Third International Conference on Information Fusion*, pp. WED5/19–WED5/25 vol.2, IEEE, 2000.

[165] H. Zhu and O. Basir, "A novel fuzzy evidential reasoning paradigm for data fusion with applications in image processing," *Soft Computing*, vol. 10, pp. 1169–1180, oct 2006.

[166] M. C. Florea, A.-L. Jousselme, and E. Bosse, "Fusion of Imperfect Information in the Unified Framework of Random Sets Theory: Application to Target Identification," tech. rep., Defence R&D Canada, 2007.

[167] D. Dubois and H. Prade, "Possibility theory and data fusion in poorly informed environments," *Control Engineering Practice*, vol. 2, pp. 811–823, oct 1994.

[168] H. Borotschnig, L. Paletta, and A. Pinz, "A Comparison of Probabilistic, Possibilistic and Evidence Theoretic Fusion Schemes for Active Object Recognition," *Computing*, vol. 62, pp. 293–319, jun 1999.

[169] Z. Pawlak, *Rough Sets : Theoretical Aspects of Reasoning about Data*. Springer Netherlands, 1991.

[170] W. Haijun and C. Yimin, "Sensor Data Fusion Using Rough Set for Mobile Robots System," in *2006 2nd IEEE/ASME International Conference on Mechatronics and Embedded Systems and Applications*, pp. 1–5, IEEE, aug 2006.

[171] Mingge Xia, You He, Xiaodong Huang, and Feng Su, "Image fusion algorithm using rough sets theory and wavelet analysis," in *Proceedings 7th International Conference on Signal Processing, 2004. Proceedings. ICSP '04. 2004.*, vol. 2, pp. 1041–1044, IEEE.

[172] Liu Yong, Xu Congfu, and Pan Yunhe, "A new approach for data fusion: implement rough set theory in dynamic objects distinguishing and tracing," in *2004 IEEE International Conference on Systems, Man and Cybernetics*, pp. 3318–3322, IEEE.

[173] I. R. Goodman, R. P. S. Mahler, and H. T. Nguyen, *Mathematics of Data Fusion*. Springer Netherlands, 1997.

[174] R. Mahler, "Statistics 101 for multisensor, multitarget data fusion," *IEEE Aerospace and Electronic Systems Magazine*, vol. 19, pp. 53–64, jan 2004.

[175] R. P. S. Mahler, *Statistical Multisource-Multitarget Information Fusion*. Boston: Artech House, Inc., 2007.

[176] R. Mahler, "Random sets: Unification and computation for information fusion - a retrospective assessment," in *Proceedings of the Seventh International Conference on Information Fusion*, pp. 1–20, 2004.

[177] J. Yen, "Generalizing the Dempster–Shafer Theory to Fuzzy Sets," in *Classic Works of the Dempster-Shafer Theory of Belief Functions*, pp. 529–554, Berlin, Heidelberg: Springer Berlin Heidelberg, 2008.

[178] R. R. Yager, "Generalized probabilities of fuzzy events from fuzzy belief structures," *Information Sciences*, vol. 28, pp. 45–62, oct 1982.

[179] O. Basir, F. Karray, and H. Zhu, "Connectionist-Based Dempster–Shafer Evidential Reasoning for Data Fusion," *IEEE Transactions on Neural Networks*, vol. 16, pp. 1513–1530, nov 2005.

[180] S. McLaughlin, R. Evans, and V. Krishnamurthy, "Data incest removal in a survivable estimation fusion architecture," in *Sixth International Conference of Information Fusion, 2003. Proceedings of the*, pp. 229–236, IEEE, 2003.

[181] S. McLaughlin, R. Evans, and Vikram Krishnamurthy, "A graph theoretic approach to data incest management in network centric warfare," in *2005 7th International Conference on Information Fusion*, p. 8 pp., IEEE, 2005.

[182] T. Brehard and V. Krishnamurthy, "Optimal Data Incest Removal in Bayesian Decentralized Estimation Over a Sensor Network," in *2007 IEEE International Conference on Acoustics, Speech and Signal Processing - ICASSP '07*, pp. III–173–III–176, IEEE, apr 2007.

[183] L. Pao and M. Kalandros, "Algorithms for a class of distributed architecture tracking," in *Proceedings of the 1997 American Control Conference (Cat. No.97CH36041)*, pp. 1434–1438 vol.3, IEEE, 1997.

[184] W. Khawsuk and L. Pao, "Decorrelated state estimation for distributed tracking of interacting targets in cluttered environments," in *Proceedings of the 2002 American Control Conference (IEEE Cat. No.CH37301)*, pp. 899–904 vol.2, IEEE, 2002.

[185] S. Julier and J. Uhlmann, "A non-divergent estimation algorithm in the presence of unknown correlations," in *Proceedings of the 1997 American Control Conference (Cat. No.97CH36041)*, pp. 2369–2373 vol.4, IEEE, 1997.

[186] M. Hurley, "An information theoretic justification for covariance intersection and its generalization," in *Proceedings of the Fifth International Conference on Information Fusion.*, vol. 1, pp. 505–511, Int. Soc. Inf. Fusion, 2002.

[187] W. Niehsen, "Information fusion based on fast covariance intersection filtering," in *Proceedings of the Fifth International Conference on Information Fusion.*, vol. 2, pp. 901–904, Int. Soc. Inf. Fusion.

[188] D. Franken and A. Hupper, "Improved fast covariance intersection for distributed data fusion," in *2005 7th International Conference on Information Fusion*, p. 7 pp., IEEE, 2005.

[189] A. Benaskeur, "Consistent fusion of correlated data sources," in *IEEE 2002 28th Annual Conference of the Industrial Electronics Society. IECON 02*, pp. 2652–2656, IEEE.

[190] S. Wellington, J. Atkinson, and R. Sion, "Sensor validation and fusion using the Nadaraya-Watson statistical estimator," in *Proceedings of the Fifth International Conference on Information Fusion.*, vol. 1, pp. 321–326, Int. Soc. Inf. Fusion.

[191] P. Ibarguengoytia, L. Sucar, and S. Vadera, "Real time intelligent sensor validation," *IEEE Transactions on Power Systems*, vol. 16, no. 4, pp. 770–775, 2001.

[192] J. Frolik, M. Abdelrahman, and P. Kandasamy, "A confidence-based approach to the self-validation, fusion and reconstruction of quasi-redundant sensor data," *IEEE Transactions on Instrumentation and Measurement*, vol. 50, no. 6, pp. 1761–1769, 2001.

[193] M. Kumar, D. P. Garg, and R. A. Zachery, "A Method for Judicious Fusion of Inconsistent Multiple Sensor Data," *IEEE Sensors Journal*, vol. 7, pp. 723–733, may 2007.

[194] R. R. Yager, "On the dempster-shafer framework and new combination rules," *Information Sciences*, vol. 41, pp. 93–137, mar 1987.

[195] P. Smets, "The combination of evidence in the transferable belief model," *IEEE Transactions on Pattern Analysis and Machine Intelligence*, vol. 12, pp. 447–458, may 1990.

[196] E. Lefevre, O. Colot, and P. Vannoorenberghe, "Belief function combination and conflict management," *Information Fusion*, vol. 3, pp. 149–162, jun 2002.

[197] F. Voorbraak, "On the justification of Dempster's rule of combination," *Artificial Intelligence*, vol. 48, pp. 171–197, mar 1991.

[198] R. Haenni, "Are alternatives to Dempster's rule of combination real alternatives?," *Information Fusion*, vol. 3, pp. 237–239, sep 2002.

[199] R.-T. Wu and M. R. Jahanshahi, "Data fusion approaches for structural health monitoring and system identification: Past, present, and future," *Structural Health Monitoring*, p. 147592171879876, sep 2018.

[200] N.-E. E. Faouzi, "Data fusion in intelligent transportation systems: Progress and challenges – A survey," *Information Fusion*, vol. 12, pp. 4–10, jan 2011.

[201] I. Lopez and N. Sarigul-Klijn, "A review of uncertainty in flight vehicle structural damage monitoring, diagnosis and control: Challenges and opportunities," *Progress in Aerospace Sciences*, vol. 46, pp. 247–273, oct 2010.

[202] M. G. Kogan, W.-Y. Kim, Y. Bock, and A. W. Smyth, "Load Response on a Large Suspension Bridge during the NYC Marathon Revealed by GPS and Accelerometers," *Seismological Research Letters*, vol. 79, pp. 12–19, jan 2008.

[203] F.-C. Chen and M. R. Jahanshahi, "NB-CNN: Deep Learning-Based Crack Detection Using Convolutional Neural Network and Naïve Bayes Data Fusion," *IEEE Transactions on Industrial Electronics*, vol. 65, pp. 4392–4400, may 2018.

[204] J. Ching, M. Muto, and J. L. Beck, "Structural Model Updating and Health Monitoring with Incomplete Modal Data Using Gibbs Sampler," *Computer-Aided Civil and Infrastructure Engineering*, vol. 21, pp. 242–257, may 2006.

[205] E. Ntotsios, C. Papadimitriou, P. Panetsos, G. Karaiskos, K. Perros, and P. C. Perdikaris, "Bridge health monitoring system based on vibration measurements," *Bulletin of Earthquake Engineering*, vol. 7, pp. 469–483, may 2009.

[206] V. H. Jaramillo, J. R. Ottewill, R. Dudek, D. Lepiarczyk, and P. Pawlik, "Condition monitoring of distributed systems using two-stage Bayesian inference data fusion," *Mechanical Systems and Signal Processing*, vol. 87, pp. 91–110, mar 2017.

[207] R. P. Palanisamy, W. Kim, S.-H. Sim, and J.-H. Yi, "Reconstruction of Unmeasured Strain Responses in Bottom-fixed Offshore Structures by Multimetric Sensor Data Fusion," *Procedia Engineering*, vol. 188, pp. 96–101, jan 2017.

[208] P. Patonis, P. Patias, I. N. Tziavos, D. Rossikopoulos, and K. G. Margaritis, "A Fusion Method for Combining Low-Cost IMU/Magnetometer Outputs for Use in Applications on Mobile Devices," *Sensors*, vol. 18, p. 2616, aug 2018.

[209] M. Safizadeh and S. Latifi, "Using multi-sensor data fusion for vibration fault diagnosis of rolling element bearings by accelerometer and load cell," *Information Fusion*, vol. 18, pp. 1–8, jul 2014.

[210] W. Kim, J.-H. Yi, J.-T. Kim, and J.-H. Park, "Vibration-based Structural Health Assessment of a Wind Turbine Tower Using a Wind Turbine Model," *Procedia Engineering*, vol. 188, pp. 333–339, jan 2017.

[211] W. Yan and K. F. Goebel, "Sensor validation and fusion for gas turbine vibration monitoring," pp. 106–117, aug 2003.

[212] J. G. Webster, *The Measurement, Instrumentation, and Sensors Handbook*. Boca Raton, Florida: CRC Press LLC, 1999.

[213] N. Farrow, J. Klingner, D. Reishus, and N. Correll, "Miniature six-channel range and bearing system: Algorithm, analysis and experimental validation," in *IEEE International Conference on Robotics and Automation (ICRA)*, pp. 6180–6185, IEEE, 2014.

[214] D. Marshall and A. Hodgson, "Structure of the cephalic tentacles of some species of prosobranch limpet (patellidae and fissurellidae)," *Journal of Molluscan Studies*, vol. 56, no. 3, p. 415, 1990.

[215] G. K. Ellem, J. E. Furst, and K. D. Zimmerman, "Shell clamping behaviour in the limpet cellana tramoserica," *The Journal of Experimental Biology*, vol. 205, no. 4, p. 539, 2002.

[216] A. M. Smith, "Alternation between attachment mechanisms by limpets in the field," *Journal of Experimental Marine Biology and Ecology*, vol. 160, no. 2, p. 205, 1992.

[217] A. H. Barber, D. Lu, and N. M. Pugno, "Extreme strength observed in limpet teeth," *Journal of the Royal Society, Interface*, vol. 12, no. 105, 2015.

[218] "Ros," 2009.

[219] R. A. Light, "Mosquitto: server and client implementation of the mqtt protocol," *Journal of Open Source Software*, vol. 2, no. 13, 2017.

[220] N. Sornin, M. Luis, T. Eirich, T. Kramp, and O. Hersent, *LoRaWAN Specification*. LoRa Alliance.

[221] F. Adelantado, X. Vilajosana, P. Tuset-Peiro, B. Martinez, J. Melia-Segui, and T. Watteyne, "Understanding the limits of lorawan," *IEEE Communication Magazine*, vol. 55, no. 9, p. 34, 2017.

[222] CableLabs, "Lora server, open-source lorawan network-server."

[223] M.-C. Jin, J. Pierce, J. Lambiotte, J. Fite, J. Marshall, and M. Huntley, "Underwater free-space optical power transfer: An enabling technology for remote underwater intervention," in *Proceedings of the Offshore Technology Conference*, 2018.

[224] J. Wang, R. Wang, and T. Li, "Analysis of the data streams trend in sensor network based on sliding window," in *Proceedings of the 2012 IEEE International Conference on Computer Science and Automation Engineering (CSAE)*, pp. 224–228, IEEE, 2012.

[225] M. Vafaeipour, O. Rahbari, M. A. Rosen, F. Fazelpour, and P. Ansarirad, "Application of sliding window technique for prediction of wind velocity time series," *International Journal of Energy and Environmental Engineering*, vol. 5, no. 2, p. 105, 2014.

[226] L. A. Dennis, M. Fisher, J. M. Aitken, S. M. Veres, Y. Gao, A. Shaukat, and G. Burroughes, "Reconfigurable autonomy," *KI - Künstliche Intelligenz*, vol. 28, no. 3, pp. 199–207, 2014.

[227] M. Pineda-Sanchez, R. Puche-Panadero, J. Martinez-Roman, A. Sapena-Bano, M. Riera-Guasp, and J. Perez-Cruz, "Partial inductance model of induction machines for fault diagnosis," *Sensors*, vol. 18, no. 7, p. 2340, 2018.

[228] M. E. H. Benbouzid, "A review of induction motors signature analysis as a medium for faults detection," *IEEE Transactions on Industrial Electronics*, vol. 47, no. 5, pp. 984–993, 2000.

[229] F. Ilievski, A. D. Mazzeo, R. F. Shepherd, X. Chen, and G. M. Whitesides, "Soft robotics for chemists," *Angewandte Chemie*, vol. 123, no. 8, pp. 1930–1935, 2011.

[230] J. L. Jones, "Robots at the tipping point: the road to irobot roomba," *IEEE Robotics and Automation Magazine*, vol. 13, no. 1, pp. 76–78, 2006.

[231] "Realsense camera d415," 2017.

[232] E. Olson, "Apriltag: A robust and flexible visual fiducial system," in *IEEE International Conference on Robotics and Automation (ICRA)*, IEEE, 2011.

[233] H. Temeltas and D. Kayak, "Slam for robot navigation," *IEEE Aerospace and Electronic Systems Magazine*, vol. 23, no. 12, pp. 16–19, 2008.

[234] M. Labbe and F. Michaud, "Online global loop closure detection for large-scale multi-session graph-based slam," in *IEEE/RSJ International Conference on Intelligent Robots and Systems*, IEEE, 2014.

[235] E. Westman and M. Kaess, "Underwater apriltag slam and calibration for high precision robot localization," Tech. Rep. CMU-RI-TR-18-43, Carnegie Mellon University, Pittsburgh, PA, October 2018.

[236] "Slackbot api," 2018.

[237] S. D. de Rivaz, B. Goldberg, N. Doshi, K. Jayaram, J. Zhou, and R. J. Wood, "Inverted and vertical climbing of a quadrupedal microrobot using electroadhesion," *Science Robotics*, vol. 3, no. 25, p. eaau3038, 2018.

[238] M. T. Tolley, R. F. Shepherd, B. Mosadegh, K. C. Galloway, M. Wehner, M. Karpelson, R. J. Wood, and G. M. Whitesides, "A resilient, untethered soft robot," *Soft Robotics*, vol. 1, no. 3, 2014.

[239] S. I. Rich, R. J. Wood, and C. Majidi, "Untethered soft robotics," *Nature Electronics*, vol. 1, pp. 102–112, 2018.

[240] A. A. Stokes, R. F. Shepherd, S. A. Morin, F. Ilievski, and G. M. Whitesides, "A hybrid combining hard and soft robots," *Soft Robotics*, vol. 1, no. 1, pp. 70–74, 2013.

[241] M. Rubenstein, C. Ahler, and R. Nagpal, "Kilobot: A low cost scalable robot system for collective behaviors," in *IEEE International Conference on Robotics and Automation*, p. 3293–3298, IEEE, 2012.

[242] P. Vartholomeos and E. Papadopoulos, "Analysis, design and control of a planar micro-robot driven by two centripetal-force actuators," in *IEEE International Conference on Robotics and Automation*, pp. 649–654, IEEE, 2006.

[243] C. Sung and D. Rus, *Automated Fabrication of Foldable Robots Using Thick Materials*, pp. 253–266. Springer International Publishing, 2018.

[244] M. Slaney, "Auditory toolbox version 2."

[245] S. S. Stevens, J. Volkmann, and E. B. Newman, "A scale for the measurement of the psychological magnitude pitch," *The Journal of the Acoustical Society of America*, vol. 8, no. 3, pp. 185–190, 1937.

[246] M. T. A. Saif and N. C. MacDonald, "Measurement of forces and spring constants of microinstruments," *Review of Scientific Instruments*, vol. 69, p. 1410, 1998.

[247] W. P. Weston-Dawkes, A. C. Ong, M. R. Abdul Majit, F. Joseph, and M. T. Tolley, "Towards rapid mechanical customization of cm-scale self-folding agents," in *2017 IEEE/RSJ International Conference on Intelligent Robots and Systems (IROS)*, IEEE, 2017.

[248] P. Vartholomeos and E. Papadopoulos, "Dynamics, design and simulation of a novel microrobotic platform employing vibration microactuators," *Journal of Dynamic Systems, Measurement, and Control*, vol. 128, no. 1, pp. 122–133, 2005.

[249] P. Vartholomeos and E. Papadopoulos, "Analysis, design and control of a planar micro-robot driven by two centripetal-force actuators," in *2006 IEEE International Conference on Robotics and Automation*, IEEE, 2006.

[250] K. Vlachos, D. Papadimitriou, and E. Papadopoulos, "Vibration-driven microrobot positioning methodologies for nonholonomic constraint compensation," *Engineering*, vol. 1, no. 1, pp. 066–072, 2015.

Part VI

Appendix

Appendix A

Copyright Agreements

A.1 MDPI Sensors Copyright Agreement

Journal: Sensors

Publisher: MDPI

Article: The Limpet: A ROS-Enabled Multi-Sensing Platform for the ORCA Hub

Re: Referencing and copying my own published work in Sensors

Sensors Editorial Office <sensors@mdpi.com>

Mon 12/08/2019 03:47

To: MOHAMMED Mohammed <s1548415@sms.ed.ac.uk>;

Cc: sensors@mdpi.com <sensors@mdpi.com>;

Dear Dr. El-Sayed,

It is fine to reference and copy your own published work "The Limpet: A ROS-Enabled Multi-Sensing Platform for the ORCA Hub" in your upcoming PhD Thesis.

Please do not hesitate to contact us if you have any other questions.

Kind regards,
Dr. Camilla Zhang
Managing Editor
http://www.mdpi.com/journal/sensors/
The latest Impact Factor for the year 2018 is 3.031

--
MDPI Branch Office, Beijing
Sensors Editorial Office

A.2 Soft Robotics Copyright Agreement

Journal: Soft Robotics

Publisher: Mary Ann Liebert, Inc.

Article: Linbots: Soft Modular Robots Utilizing Voice Coils

Copyright Clearance Center

Confirmation Number: 11840421
Order Date: 08/11/2019

Customer Information

Customer: Mohammed Mohammed
Account Number: 3001499658
Organization: Mohammed Mohammed
Email: m.mohammed@ed.ac.uk
Phone: +44 7490208431
Payment Method: Invoice

This is not an invoice

Order Details

Soft robotics

Billing Status: **N/A**

Order detail ID: 71977000
ISSN: 2169-5180
Publication Type: Journal
Volume:
Issue:
Start page:

Permission Status: **Granted**
Permission type: Republish or display content
Type of use: Thesis/Dissertation
Order License Id: 4645881242809

Requestor type	Academic institution
Format	Print, Electronic
Portion	chapter/article
The requesting person/organization	Mohammed E. Sayed
Title or numeric reference of the portion(s)	Full Article
Title of the article or chapter the portion is from	Linbots: Soft Modular Robots Utilizing Voice Coils
Editor of portion(s)	Barry A. Trimmer
Author of portion(s)	Ross M. McKenzie
Volume of serial or monograph	6
Issue, if republishing an article from a serial	2
Page range of portion	
Publication date of portion	16 Apr 2019
Rights for	Main product
Duration of use	Life of current edition
Creation of copies for the disabled	no
With minor editing privileges	no
For distribution to	Worldwide
In the following language(s)	Original language of publication
With incidental promotional use	no
Lifetime unit quantity of new product	Up to 499
Title	The Limpet: A Multi-Sensing Robotic Platform For Monitoring Offshore Energy Platforms

Institution name	University of Edinburgh
Expected presentation date	Aug 2019

Note: This item was invoiced separately through our **RightsLink service.** More info **$ 0.00**

Total order items: 1 **Order Total: $0.00**

About Us | Privacy Policy | Terms & Conditions | Pay an Invoice

Copyright 2019 Copyright Clearance Center

A.3 WUWNet '18 Copyright Agreement

Conference: Proceedings of the Thirteenth ACM International Conference on Underwater Networks and Systems (WUWNet '18)

Publisher: Association for Computing Machinery

Article: Robust TDA-MAC for practical underwater sensor network deployment: lessons from USMART sea trials

Copyright Clearance Center

Confirmation Number: 11840418
Order Date: 08/11/2019

Customer Information

Customer: Mohammed Mohammed
Account Number: 3001499658
Organization: Mohammed Mohammed
Email: m.mohammed@ed.ac.uk
Phone: +44 7490208431
Payment Method: Invoice

This is not an invoice

Order Details

Proceedings, Association for Computing Machinery

Billing Status: **N/A**

Order detail ID: 71976996
ID Number: PJC02
Publication Type: Journal
Volume:
Issue:
Start page:
Publisher: Association for Computing Machinery

Permission Status: **Granted**
Permission type: Republish or display content
Type of use: Republish in a thesis/dissertation
Order License Id: 4645880103120

Requestor type	Academic institution
Format	Print, Electronic
Portion	chapter/article
The requesting person/organization	Mohammed E. Sayed
Title or numeric reference of the portion(s)	Full Article
Title of the article or chapter the portion is from	Robust TDA-MAC for practical underwater sensor network deployment: lessons from USMART sea trials
Editor of portion(s)	Jingdong Chen
Author of portion(s)	Nils Morozs
Volume of serial or monograph	N/A
Page range of portion	
Publication date of portion	December 03 - 05, 2018
Rights for	Main product
Duration of use	Life of current edition
Creation of copies for the disabled	no
With minor editing privileges	no
For distribution to	Worldwide
In the following language(s)	Original language of publication
With incidental promotional use	no
Lifetime unit quantity of new product	Up to 499
Title	The Limpet: A Multi-Sensing Robotic Platform For Monitoring Offshore Energy Platforms

Institution name	University of Edinburgh
Expected presentation date	Aug 2019

Note: This item was invoiced separately through our **RightsLink service.** More info **$ 0.00**

Total order items: 1 **Order Total: $0.00**

About Us | Privacy Policy | Terms & Conditions | Pay an Invoice

Copyright 2019 Copyright Clearance Center

Appendix B

Bill of Materials

B.1 Sensing Module (Limpet Version 1) Bill of Materials

Title: Bill of Materials for Limpet Version 1.

Designer: Mohammed E. Sayed.

Limpet Version 1 Bill of Materials

Part Number	Reference	Description	Value	Manufacturer	Manufacturer Part Number	Supplier	Supplier Part Number	Package	Cost Per Unit(£)
				Computation					
U1	**Microcontroller**	ATSAMD21 IC MCU - 32 Bit, 256 KB Flash	ATSAMD21G	Microchip	ATSAMD21G18A-MU	Digi-Key Electronics	ATSAMD21G18A-MU-ND	48-QFN	2.38
C1	Capacitor	Bypass Capacitor - 0402	100 nF	AVX	0402YD104KAT2A	RS Components	698-3197	0402	0.008
C2	Capacitor	Bypass Capacitor - 0402	100 nF	AVX	0402YD104KAT2A	RS Components	698-3197	0402	0.008
C3	Capacitor	Bypass Capacitor - 0402	100 nF	AVX	0402YD104KAT2A	RS Components	698-3197	0402	0.008
C4	Capacitor	Bypass Capacitor - 0402	10 uF	Murata	GRM155R60G106ME44D	Digi-Key Electronics	490-10693-1-ND	0402	0.1
C5	Capacitor	Bypass Capacitor - 0402	10 uF	Murata	GRM155R60G106ME44D	Digi-Key Electronics	490-10693-1-ND	0402	0.1
C6	Capacitor	Bypass Capacitor - 0402	1 uF	Murata	GRM155R61A105ME15D	RS Components	814-5237	0402	0.009
R1	Resistor	SWCLK Pull-up Resistor - 0402	330 ohm	Panasonic	ERJ-2RKF3300X	Digi-Key Electronics	P330LCT-ND	0402	0.07
R2	Resistor	SDA Pull-up Resistor - 0402	10 kohm	Panasonic	ERJ-2RKF1002X	Digi-Key Electronics	P10.0KLCT-ND	0402	0.07
R3	Resistor	SCL Pull-up Resistor - 0402	10 kohm	Panasonic	ERJ-2RKF1002X	Digi-Key Electronics	P10.0KLCT-ND	0402	0.07
				User I/O					
U2	**RGB LED**	3 RGB LED, PLCC 4 SMD package	PWM	Lite-On	LTST-N683EGBW	RS Components	127-8444	PLCC 4 SMD	0.106
				Connectors					
J1	JTAG Connector/Programming Port	5 Way 1 Row Shrouded Right Angle PCB Header, Surface Mount	JTAG	Molex	532610571	RS Components	542-7270	1 row (5 positions)	0.838
J2	Charger Connector	2 Positions Header Connector , Surface Mount, Right Angle, Tin	2.54 mm	Samtec	TSM-102-01-T-SH	Digi-Key Electronics	SAM10785-ND	1 row (2 positions)	0.21
				Sensing					
U3	**Temperature and Humidity Sensor**	Temperature & Humidity Sensor	I2C	Silicon Labs	Si7006-A20-IM	RS Components	865-2274	6-DFN	1.22
C7	Capacitor	Bypass Capacitor - 0402	100 nF	AVX	0402YD104KAT2A	RS Components	698-3197	0402	0.008
U4	**IMU - Accelerometer/Gyroscope**	Accelerometer, Gyroscope, 3 Axis	I2C	STMicroelectronics	LSM6DS3USTR	Digi-Key Electronics	497-16910-1-ND	LGA-16L	2.26
R4	Resistor	Resistor - 0402	10 kohm	Panasonic	ERJ-2RKF1002X	Digi-Key Electronics	P10.0KLCT-ND	0402	0.07
C8	Capacitor	Bypass Capacitor - 0402	100 nF	AVX	0402YD104KAT2A	RS Components	698-3197	0402	0.008
C9	Capacitor	Bypass Capacitor - 0402	100 nF	AVX	0402YD104KAT2A	RS Components	698-3197	0402	0.008
U5	**Optical Sensor**	RGBW Color Sensor	I2C	Vishay Semiconductor	VEML6040A3OG	RS Components	122-6788	4-TFLGA	1.516
C10	Capacitor	Bypass Capacitor - 0402	100 nF	AVX	0402YD104KAT2A	RS Components	698-3197	0402	0.008
U6	**Sound Sensor**	Omnidirectional Microphone - MEMS (Silicon) [100Hz ~ 10kHz]	Analog	Knowles	SPU0414HR5H-SB	Mouser Electronics	721-SPU0414HR5H-SB	custom	1.25
C11	Capacitor	Bypass Capacitor - 0402	0.47 uF	Kemet	C0402C474K9PACTU	Digi-Key Electronics	399-4899-1-ND	0402	0.07
U7	**Magnetic Sensor**	3-Axis Linear Hall-Effect Sensor	I2C	Melexis Technologies	MLX90393SLW-ABA-011-SP	Mouser Electronics	482-90393SLWABA011SP	16-QFN	1.56
C12	Capacitor	Bypass Capacitor - 0402	100 nF	AVX	0402YD104KAT2A	RS Components	698-3197	0402	0.008
C13	Capacitor	Bypass Capacitor - 0402	100 nF	AVX	0402YD104KAT2A	RS Components	698-3197	0402	0.008
U8	**Pressure Sensor**	Absolue Pressure Sensor	I2C	Bosch Sensortec	BMP280	Digi-key Electronics	828-1064-1-ND	8-SMD	2.61
C14	Capacitor	Bypass Capacitor - 0402	100 nF	AVX	0402YD104KAT2A	RS Components	698-3197	0402	0.008
C15	Capacitor	Bypass Capacitor - 0402	100 nF	AVX	0402YD104KAT2A	RS Components	698-3197	0402	0.008
U9	**Distance/Proximity Sensor**	ToF Laser Distance Sensor	I2C	STMicroelectronics	VL53L0CXV0DH/1	Digi-Key Electronics	497-16538-1-ND	custom	4.09
C16	Capacitor	Bypass Capacitor - 0402	100 nF	AVX	0402YD104KAT2A	RS Components	698-3197	0402	0.008
C17	Capacitor	Bypass Capacitor - 0402	4.7 uF	Murata	GRM155B30J475ME47D	RS Components	884-7065	0402	0.018
R5	Resistor	Pull-up Resistor - 0402	10 kohm	Panasonic	ERJ-2RKF1002X	Digi-Key Electronics	P10.0KLCT-ND	0402	0.07
R6	Resistor	Pull-up Resistor - 0402	10 kohm	Panasonic	ERJ-2RKF1002X	Digi-Key Electronics	P10.0KLCT-ND	0402	0.07
				Power					
J3	**Battery Holder**	Coin Cell Battery SMD Retainer	24.5mm	MPD	BK-877	Digi-key Electronics	BK-877-ND	SMD	0.31
N/A	**Battery**	LIR2477 - Rechargeable Lithium Ion Coin Cell Battery	3.6 V, 150 mAh	Conrad Energy	LIR2477	Amazon UK	LIR2477	SMD	1.82
U10	**Battery Charger**	Battery Charging IC	150 mAh	Microchip	MCP73812T-420I/OT	Digi-key Electronics	MCP73812T-420I/OTCT-ND	SOT-23-5	0.43
R7	Resistor	Setup Resistor - 0402	7.15 kohm	Panasonic	ERJ-2RKF7151X	Digi-Key Electronics	P7.15KLCT-ND	0402	0.007
C18	Capacitor	Bypass Capacitor - 0402	1 uF	Murata	GRM155R61A105ME15D	RS Components	814-5237	0402	0.009
C19	Capacitor	Bypass Capacitor - 0402	1 uF	Murata	GRM155R61A105ME15D	RS Components	814-5237	0402	0.009
				Crystal Oscillator					
Q1	Crystal Unit	SMD Crystal (32.768 KHz), ±20ppm	32.768 KHz	Micro Crystal	CM7V-T1A	RS Components	729-3271	SMD	0.902
C20	Capacitor	Capacitor -0402	12 pF	Murata	GRM1555C1H120FA01D	RS Components	814-5498	0402	0.017
C21	Capacitor	Capacitor -0402	12 pF	Murata	GRM1555C1H120FA01D	RS Components	814-5498	0402	0.017
				Communication					
N/A	**ESP8266**	RF Transceievr Module	ESP8266	Sparkfun Electronics	WRL-13678	Digi-Key Electronics	1568-1235-ND	N/A	5.18
J4	ESP Connector	8 Way, 2 Row Unshrouded, Straight Pin Header, Through Hole	2.54 mm	Harwin	M20-9980446	RS Components	745-7040	2 row (8 positions)	0.173
				External Components					
N/A	**JTAG/Debugger**	JTAG Emulator for ARM Cores	JTAG	Segger	8.08.90 J-LINK EDU	Digi-Key Electronics	899-1008-ND	N/A	47.78
N/A	**JTAG Adapter**	JTAG Adapter for ARM-USB (20-10)	Adapter	Olimex LTD	ARM-JTAG-20-10	Digi-Key Electronics	1188-1016-ND	N/A	4.45
N/A	JTAG Connector Receptacle	5 Position Rectangular Housing Connector Receptacle (1.25 mm)	JTAG	Molex	0510210500	Digi-Key Electronics	WM1723-ND	1 row (5 positions)	0.31
N/A	JTAG Connector Crimp	Socket Contact Tin 26-28 AWG Crimp	Crimp	Molex	0500798000	Digi-Key Electronics	WM1142CT-ND	26-28 AWG	0.07
								Total without Communication	**22.547**
								Total with Communication	**27.727**

B.2 Power Driver Module Bill of Materials

Title: Bill of Materials for Power Driver Module PCB.

Designer: Mohammed E. Sayed.

Power Driver Module PCB Bill of Materials 

Part Number	Reference	Description	Value	Manufacturer	Manufacturer Part Number	Supplier	Supplier Part Number	Package	Cost Per Unit(£)
				Computation					
U1	**Microcontroller**	ATSAMD21 IC MCU - 32 Bit, 256 KB Flash	ATSAMD21G	Microchip	ATSAMD21G18A-MU	Digi-Key Electronics	ATSAMD21G18A-MU-ND	48-QFN	2.43
C1	Capacitor	0402 Bypass Capacitor	100 nF	AVX	0402ZD104KAT2A	RS Components	698-3207	0402	0.017
C2	Capacitor	0402 Bypass Capacitor	100 nF	AVX	0402ZD104KAT2A	RS Components	698-3207	0402	0.017
C3	Capacitor	0402 Bypass Capacitor	100 nF	AVX	0402ZD104KAT2A	RS Components	698-3207	0402	0.017
C4	Capacitor	Bypass Capacitor - 0402	10 uF	Murata	GRM155R60G106ME44D	Digi-Key Electronics	490-10693-1-ND	0402	0.16
C5	Capacitor	Bypass Capacitor - 0402	10 uF	Murata	GRM155R60G106ME44D	Digi-Key Electronics	490-10693-1-ND	0402	0.16
C6	Capacitor	Bypass Capacitor - 0402	1 uF	Samsung Electro-Mechanics	CL05A105MP5NNNC	Digi-Key Electronics	1276-1448-1-ND	0402	0.08
R1	Resistor	SWCLK Pull-up Resistor - 0402	330 Ω	Panasonic	ERJ-2RKF3300X	Digi-Key Electronics	P330LCT-ND	0402	0.07
R2	Resistor	SDA Pull-up Resistor - 0402	10 kΩ	Panasonic	ERJ-2RKF1002X	RS Components	665-0856	0402	0.013
R3	Resistor	SCL Pull-up Resistor - 0402	10 kΩ	Panasonic	ERJ-2RKF1002X	RS Components	665-0856	0402	0.013
				Valve Controller					
U18	**H-Bridge**	Brushed Motor Driver IC	11V, 1.8A	Texas Instruments	DRV8837DSGT	RS Components	813-6497	WSON	1.074
U3	**Valve**	Solenoid Valve	5V	-	-	-	-	-	-
				Sensing					
U4	**Pressure Sensor**	Absolute Pressure Sensor	0 - 15 psi	Honeywell	HSCMANN015PA2A3	Mouser Electronics	785-HSCMANN015PA2A3	SMD-8	26.62
				Pump Controller					
U5	**Pump**	Air Pump Motor	12V	Makeblock Co.	50000	Digi-Key Electronics	1890-1035-ND	-	8.23
U6	**H-Bridge**	Brushed DC Motor Driver with Integrated Current Sensing	3.6A, 6.5V to 45V	Texas Instruments	DRV8871DDAR	Mouser Electronics	595-DRV8871DDAR	SO-PowerPad-8	1.34
R5	Resistor	0603 SMD Resistor	82 kΩ	Panasonic	ERJ3RBD8202V	RS Components	810-2334	0603	0.019
C7	Capacitor	0603 SMD Capacitor	0.1 uF	Samsung Electro-Mechanics	CL10B104KB8NNNC	Digi-Key Electronics	1276-1000-1-ND	0603	0.07
C8	Capacitor	1210 SMD Capacitor	47 uF	Murata	GRM32EC81C476KE15L	RS Components	846-7369	1210	0.473
				Adhesion Module Controller					
U7	**H-Bridge**	Brushed DC Motor Driver with Integrated Current Sensing	3.6A, 6.5V to 45V	Texas Instruments	DRV8871DDAR	Mouser Electronics	595-DRV8871DDAR	SO-PowerPad-8	1.34
R6	Resistor	0603 SMD Resistor	43 kΩ	Panasonic	ERA3AEB433V	RS Components	828-0762	0603	0.452
C9	Capacitor	0603 SMD Capacitor	0.1 uF	Samsung Electro-Mechanics	CL10B104KB8NNNC	Digi-Key Electronics	1276-1000-1-ND	0603	0.07
C10	Capacitor	1210 SMD Capacitor	47 uF	Murata	GRM32EC81C476KE15L	RS Components	846-7369	1210	0.473
				Locomotion Module Controller					
U8	**H-Bridge**	Brushed DC Motor Driver with Integrated Current Sensing	3.6A, 6.5V to 45V	Texas Instruments	DRV8871DDAR	Mouser Electronics	595-DRV8871DDAR	SO-PowerPad-8	1.34
R7	Resistor	0603 SMD Resistor	43 kΩ	Panasonic	ERA3AEB433V	RS Components	828-0762	0603	0.452
C11	Capacitor	0603 SMD Capacitor	0.1 uF	Samsung Electro-Mechanics	CL10B104KB8NNNC	Digi-Key Electronics	1276-1000-1-ND	0603	0.07
C12	Capacitor	1210 SMD Capacitor	47 uF	Murata	GRM32EC81C476KE15L	RS Components	846-7369	1210	0.473
U9	**H-Bridge**	Brushed DC Motor Driver with Integrated Current Sensing	3.6A, 6.5V to 45V	Texas Instruments	DRV8871DDAR	Mouser Electronics	595-DRV8871DDAR	SO-PowerPad-8	1.34
R8	Resistor	0603 SMD Resistor	43 kΩ	Panasonic	ERA3AEB433V	RS Components	828-0762	0603	0.452
C13	Capacitor	0603 SMD Capacitor	0.1 uF	Samsung Electro-Mechanics	CL10B104KB8NNNC	Digi-Key Electronics	1276-1000-1-ND	0603	0.07
C14	Capacitor	1210 SMD Capacitor	47 uF	Murata	GRM32EC81C476KE15L	RS Components	846-7369	1210	0.473
U10	**H-Bridge**	Brushed DC Motor Driver with Integrated Current Sensing	3.6A, 6.5V to 45V	Texas Instruments	DRV8871DDAR	Mouser Electronics	595-DRV8871DDAR	SO-PowerPad-8	1.34
R9	Resistor	0603 SMD Resistor	43 kΩ	Panasonic	ERA3AEB433V	RS Components	828-0762	0603	0.452
C15	Capacitor	0603 SMD Capacitor	0.1 uF	Samsung Electro-Mechanics	CL10B104KB8NNNC	Digi-Key Electronics	1276-1000-1-ND	0603	0.07
C16	Capacitor	1210 SMD Capacitor	47 uF	Murata	GRM32EC81C476KE15L	RS Components	846-7369	1210	0.473
U11	**H-Bridge**	Brushed DC Motor Driver with Integrated Current Sensing	3.6A, 6.5V to 45V	Texas Instruments	DRV8871DDAR	Mouser Electronics	595-DRV8871DDAR	SO-PowerPad-8	1.34
R10	Resistor	0603 SMD Resistor	43 kΩ	Panasonic	ERA3AEB433V	RS Components	828-0762	0603	0.452
C17	Capacitor	0603 SMD Capacitor	0.1 uF	Samsung Electro-Mechanics	CL10B104KB8NNNC	Digi-Key Electronics	1276-1000-1-ND	0603	0.07
C18	Capacitor	1210 SMD Capacitor	47 uF	Murata	GRM32EC81C476KE15L	RS Components	846-7369	1210	0.473
				Crystal Oscillator					
Q1	**Crystal Unit**	SMD Crystal (32.768 KHz), ±20ppm	32.768 KHz	Micro Crystal	CM7V-T1A	RS Components	729-3271	SMD	0.902
C19	Capacitor	Capacitor -0402	12 pF	Samsung Electro-Mechanics	CL05C120JB5NNNC	Digi-Key Electronics	1276-1178-1-ND	0402	0.07
C20	Capacitor	Capacitor -0402	12 pF	Samsung Electro-Mechanics	CL05C120JB5NNNC	Digi-Key Electronics	1276-1178-1-ND	0402	0.07
				Communication					
U12	**IrDA Transceiver**	115.2kbs (SIR) IRDA Transceiver Module	SERCOM	Vishay	TFBS4711-TT1	Digi-Key Electronics	751-1068-1-ND	-	3.47
C21	Capacitor	0402 Bypass Capacitor	100 nF	AVX	0402ZD104KAT2A	RS Components	698-3207	0402	0.017
C22	Capacitor	Bypass Capacitor - 0402	4.7 uF	Murata	GRM155B30J475ME47D	RS Components	884-7065	0402	0.02
R11	Resistor	Resistor - 0402	47 ohm	Panasonic	ERJ-2RKF47R0X	Digi-Key Electronics	P47.0LCT-ND	0402	0.07
R12	Resistor	Resistor - 0402	47 ohm	Panasonic	ERJ-2RKF47R0X	Digi-Key Electronics	P47.0LCT-ND	0402	0.07
				User I/O					
U13	**RGB LED**	3 RGB LED, PLCC 4 SMD package	PWM	Broadcom	ASMB-MTB1-0A3A2	RS Components	830-5079	PLCC 4 SMD	0.274
				Power					
U14	**Voltage Regulator**	3.5V Voltage Regulator (Limpet and Pressure Sensor)	3.5V, 150 mA	Texas Instruments	LP2985IM5-3.5/NOPB	Digi-Key Electronics	LP2985IM5-3.5/NOPBCT-ND	SOT23-5	0.61
C23	Capacitor	0402 SMD Capacitor	1 uF	Samsung Electro-Mechanics	CL05A105MP5NNNC	Digi-Key Electronics	1276-1448-1-ND	0402	0.08
C24	Capacitor	0402 SMD Capacitor	2.2 uF	Murata	GRM155C81C225ME15D	Digi-Key Electronics	490-10444-1-ND	0402	0.16
C25	Capacitor	0402 SMD Capacitor	0.01 2uF	Kemet	C0402C123K4RACTU	Digi-Key Electronics	399-4875-1-ND	0402	0.07
U15	**Voltage Regulator**	5V Voltage Regulator (Valve)	5V, 100 mA	ON Semiconductior	MC78L05ACDR2G	Digi-Key Electronics	MC78L05ACDR2GOSCT-ND	8-SOIC	0.3
C26	Capacitor	0402 SMD Capacitor	0.1 uF	Samsung Electro-Mechanics	CL10B104KB8NNNC	Digi-Key Electronics	1276-1000-1-ND	0603	0.07
C27	Capacitor	0402 SMD Capacitor	0.33 uF	Samsung Electro-Mechanics	CL10B334KO8NNNC	Digi-Key Electronics	1276-2048-1-ND	0603	0.1
				Connectors					
J1	Header Pin Connector (2 Way)	Adhesion Coil Connector	2.54 mm	Harwin	M20-7823646	RS Components	173-1065	Through Hole	0.084
J2	Header Pin Connector (2 Way)	Locomotion 1 Coil Connector	2.54 mm	Harwin	M20-7823646	RS Components	173-1065	Through Hole	0.084
J3	Header Pin Connector (2 Way)	Locomotion 2 Coil Connector	2.54 mm	Harwin	M20-7823646	RS Components	173-1065	Through Hole	0.084
J4	Header Pin Connector (2 Way)	Locomotion 3 Coil Connector	2.54 mm	Harwin	M20-7823646	RS Components	173-1065	Through Hole	0.084
J5	Header Pin Connector (2 Way)	Locomotion 4 Coil Connector	2.54 mm	Harwin	M20-7823646	RS Components	173-1065	Through Hole	0.084
J6	Board to board Connection	Sensing and Power Driver Modules Connector	2.54 mm	Valcon	FTHS-08R-235-180-030	Toby Electronics	FTHS-08R-235-180-030	Through Hole	0.36
J7	Battery Connector	JST XH Battery Connector	2.54 mm	JST	B4B-XH-A(LF)(SN)	RS Components	820-1551	Through Hole	0.38
J8	Communication Connector	Communication Connector	2.54 mm	Harwin	M20-7823646	RS Components	173-1065	Through Hole	0.336
				JTAG					
J9	**JTAG Connector/Programming Port**	5 Way 1 Row Shrouded Right Angle PCB Header, Surface Mount	JTAG	Molex	532610571	RS Components	542-7270	1 row (5 positions)	0.838
				Additional					
-	**LiPo Battery**	450 mAh LiPo Battery (11.1 V)	Battery	Nano-Tech	-	HobbyKing	9210000130-0	LiPo	5.55
-	**JTAG Programmer**	JTAG Emulator for ARM Cores	JTAG	Segger	8.08.90 J-LINK EDU	Digi-Key Electronics	899-1008-ND	-	47.74
-	**JTAG Adapter**	JTAG Adapter for ARM-USB (20-10)	Adapter	Olimex LTD	ARM-JTAG-20-10	Digi-Key Electronics	1188-1016-ND	N/A	4.57
-	**JTAG Connector Receptacle**	5 Position Rectangular Housing Connector Receptacle (1.25 mm)	JTAG	Molex	0510210500	Digi-Key Electronics	WM1723-ND	1 row (5 positions)	0.32
-	**JTAG Connector Crimp**	Socket Contact Tin 26-28 AWG Crimp	Crimp	Molex	0500798000	Digi-Key Electronics	WM1142CT-ND	26-28 AWG	0.07

Appendix C

Experimental

C.1 Custom-Designed Suction Cup Mould CAD Drawing

Software: Autodesk Inventor

Authors: Mohammed E. Sayed and Jamie O. Roberts

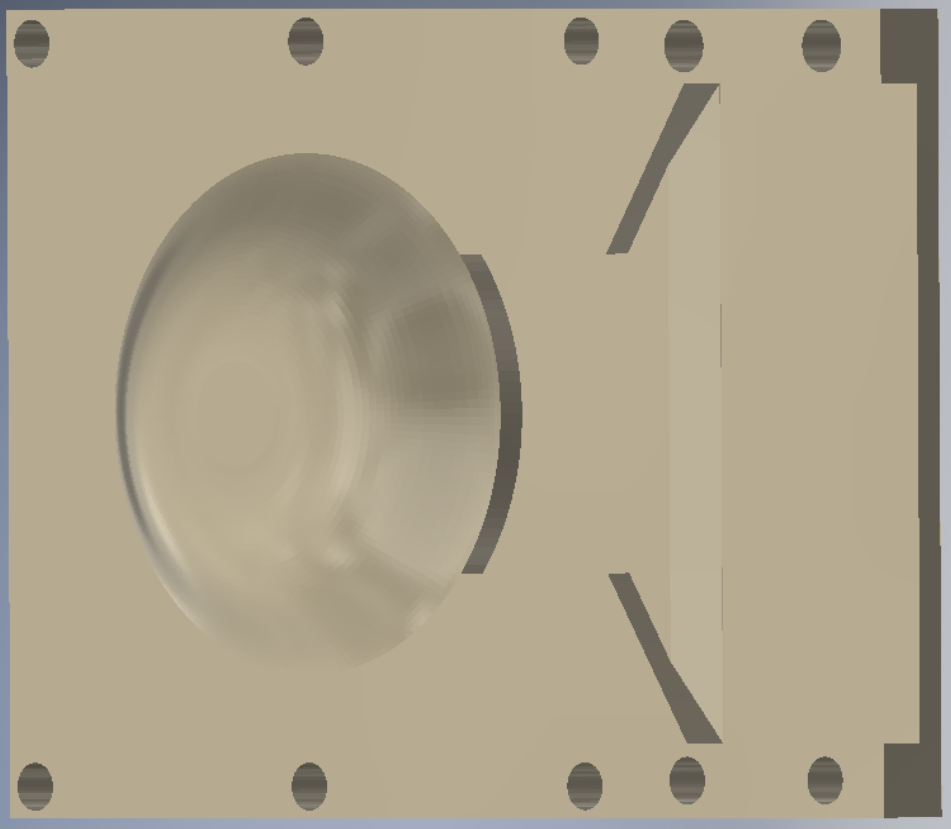

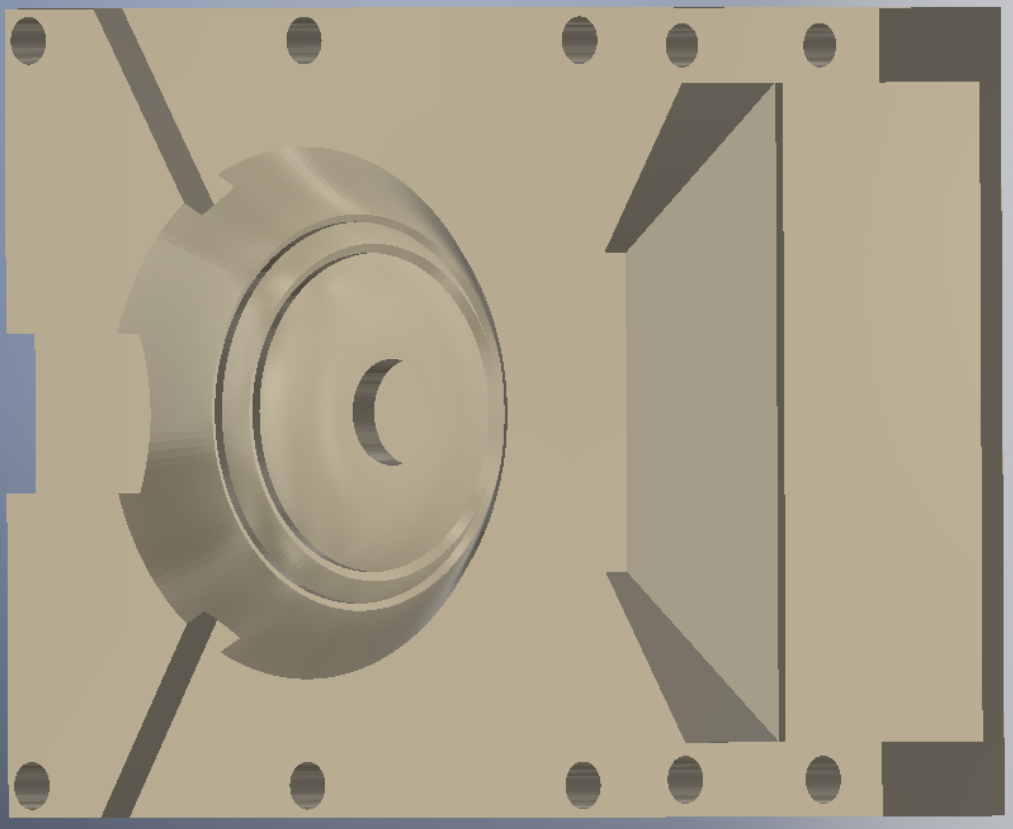

C.2 Loading Capacity Experimental Setup CAD Drawing

Software: Autodesk Inventor

Authors: Mohammed E. Sayed and Jamie O. Roberts

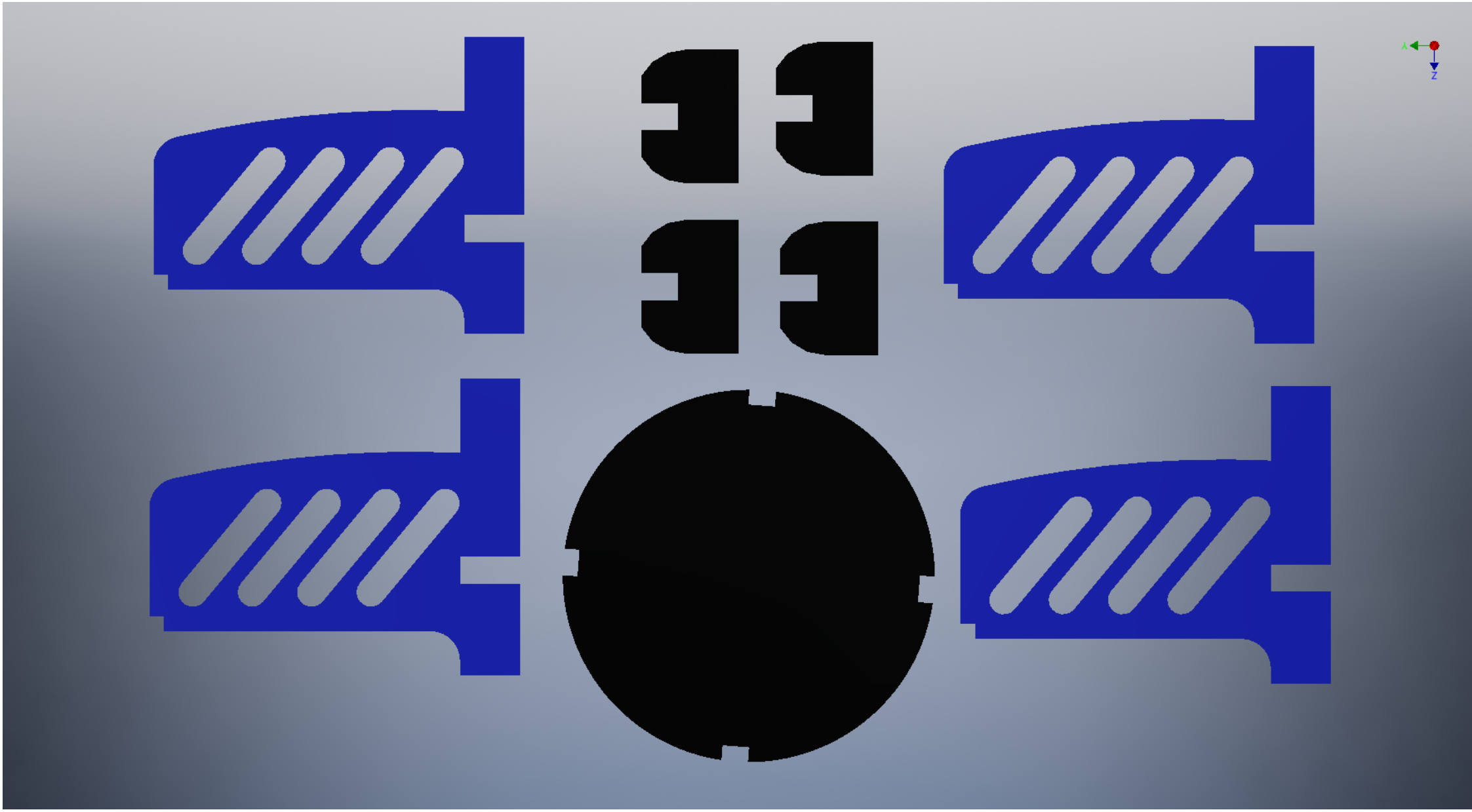

C.3 Multiple Weights Holder CAD Drawing

Software: Autodesk Inventor

Authors: Mohammed E. Sayed and Jamie O. Roberts

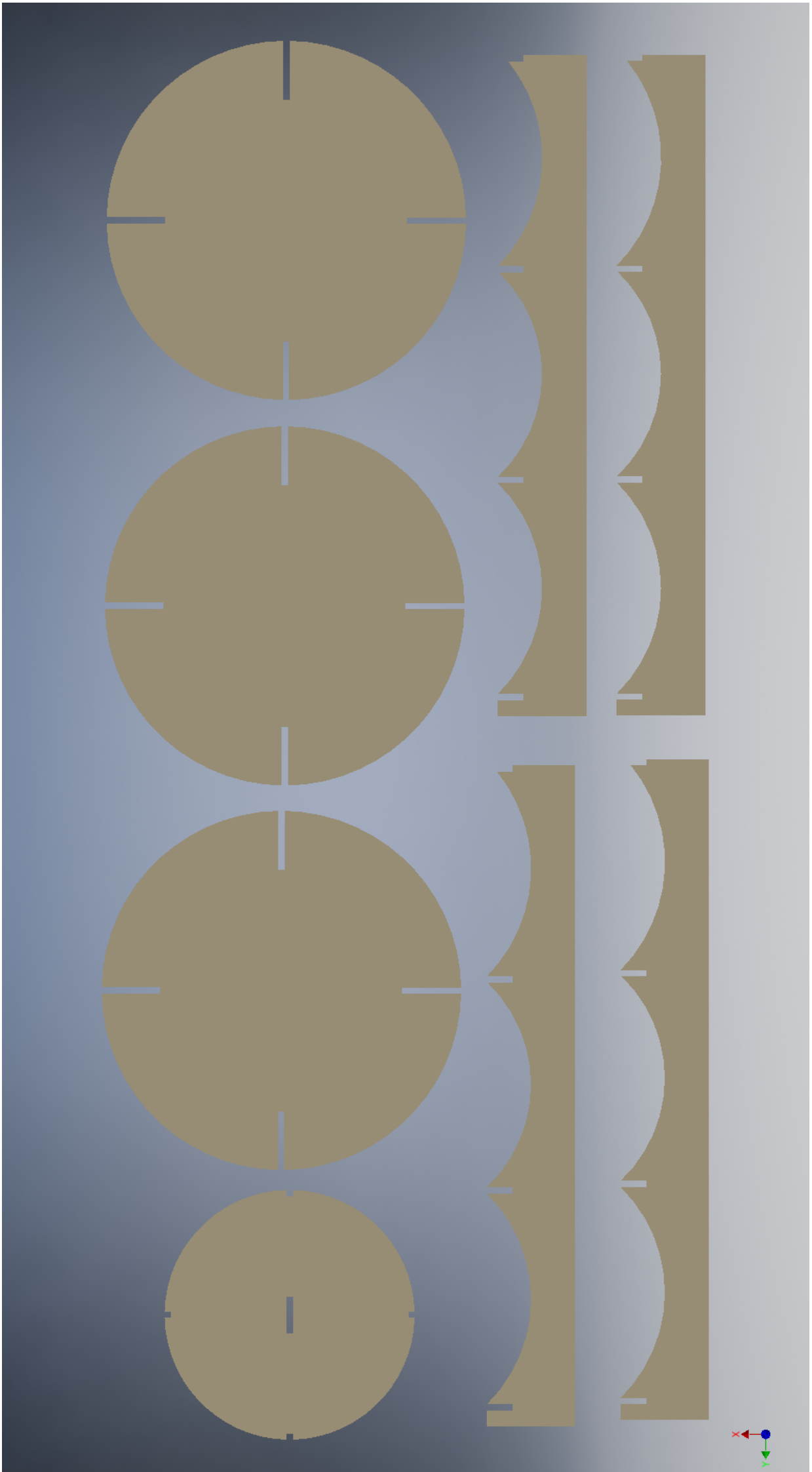

C.4 EMM Force Test Experimental Setup CAD Drawing

Software: Autodesk Inventor

Authors: Mohammed E. Sayed and Jamie O. Roberts

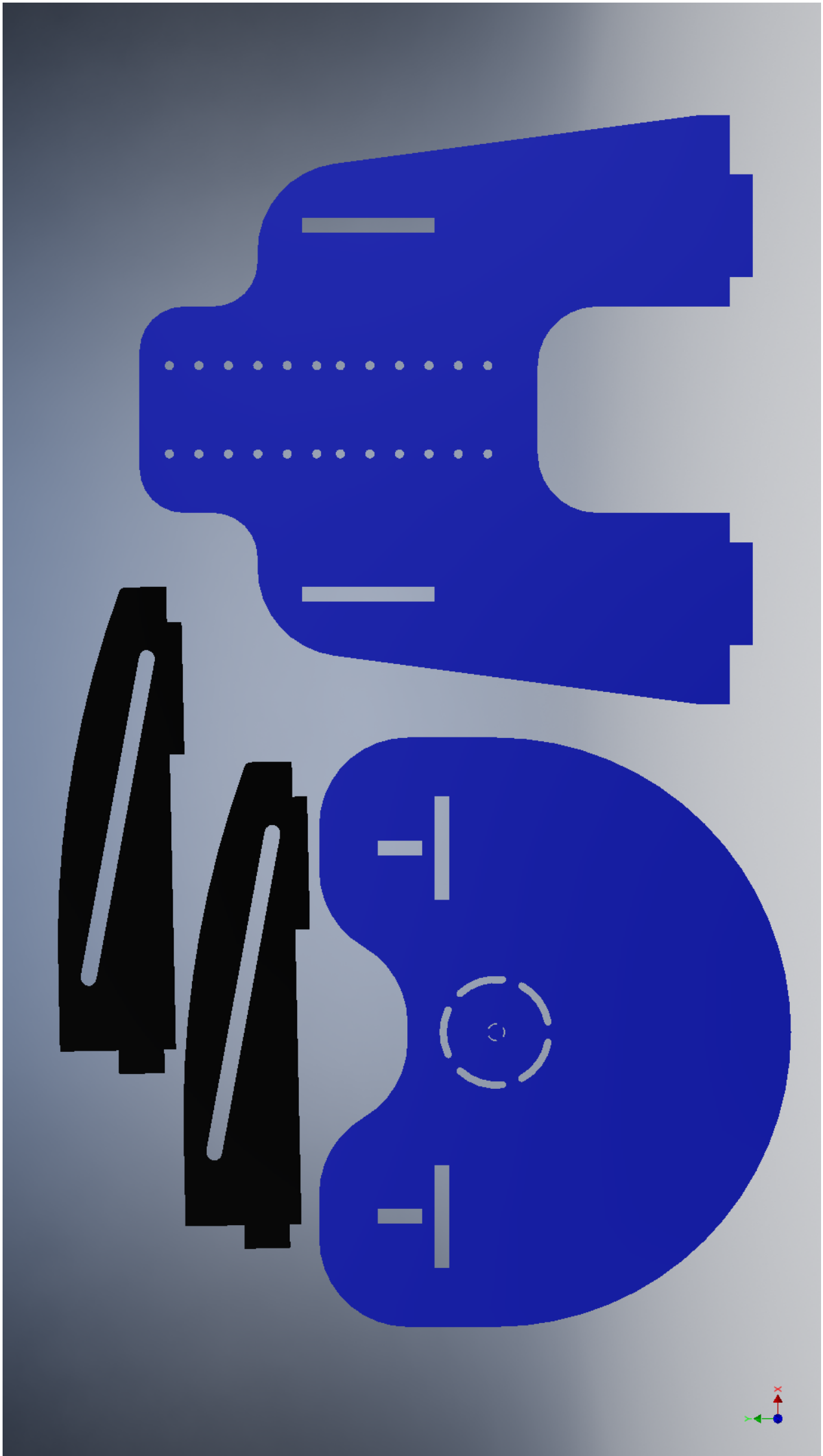

Appendix D

Limpet User Guide

D.1 Limpet Version 1 User Guide

Authors: Mohammed E. Sayed

Limpet Version 1 User Guide 

Stokes Research Group
Bioinspired Engineering

LIMPET V1.0
USER GUIDE

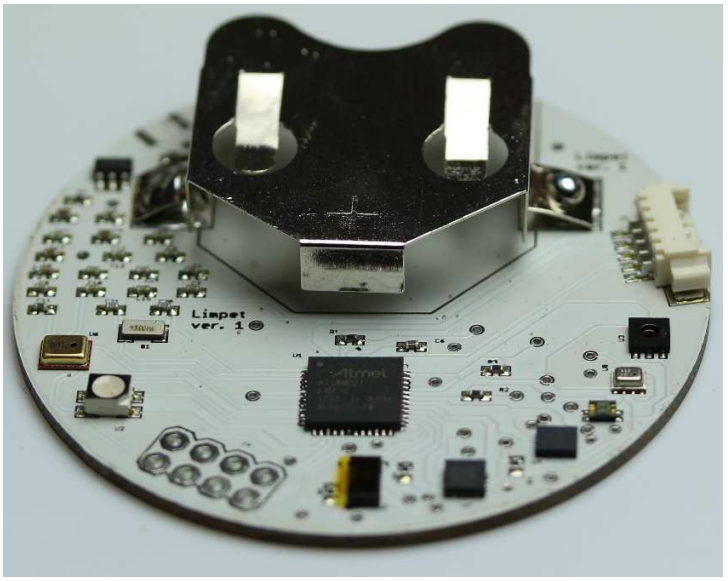

Mohammed El-Sayed

Stokes Research Group

The Institute for Integrated Micro and Nano Systems

School of Engineering

The University of Edinburgh

INTRODUCTION

The Limpet is a low cost, miniature and robust robotic platform designed for manufacturability. The Limpet is designed to be part of the ORCA (Offshore Robotics for Certification of Assets) Hub System, which consists of the offshore assets and all the robots (UAVs, drones, mobile legged robots etc.) interacting with them. The Limpet comprises the sensing aspect of the ORCA Hub System. We integrated the Limpet with Robot Operating System (ROS), which allows it to interact with other robots in the ORCA Hub System. The Limpet consists of a single two-layer Printed Circuit Board (PCB) and a detachable Li-Ion coin cell battery. The limpet possesses a low-power microcontroller, programming port, exteroceptive sensors and a communication connector. It is a multi-sensing platform, equipped with nine exteroceptive sensing modalities, that can be used to monitor a wide range of environmental and physical parameters in offshore platforms. We designed version 1.0 of the Limpet as an immobile robot that can attach to metallic surfaces using permanent magnets embedded in its protective housing. The protective housing (polyurethane) acts as a shell protecting the circuitry of the Limpet from the harsh offshore weather conditions. Robust agents will have a longer lifetime, need less maintenance and require lower repair costs. The Limpet is designed explicitly for manufacturability; it consists of a single PCB and therefore mass manufacture is a simple case of placing a batch order with a PCB foundry. The PCB consists of SMD-only components, except for the ESP8266, and can be autonomously populated with pick-and-place machines at the point of manufacture. Assembly of one robot takes seconds as it is a matter of only connecting the coin cell battery. Therefore, it is easy to mass-produce Limpet agents and deploy them in huge collectives for inspecting offshore infrastructures. This guide describes the system's operation, specifications, properties and usage.



Limpet Schematic

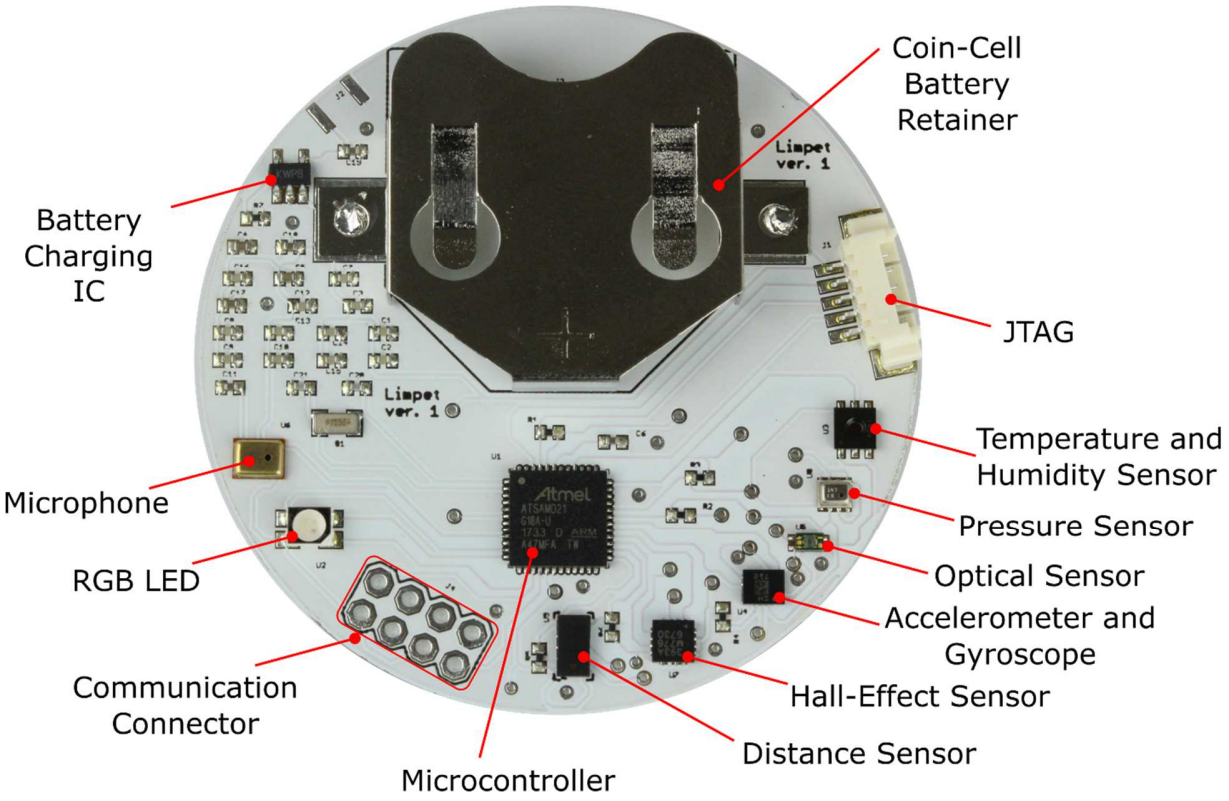

Limpet Board Layout

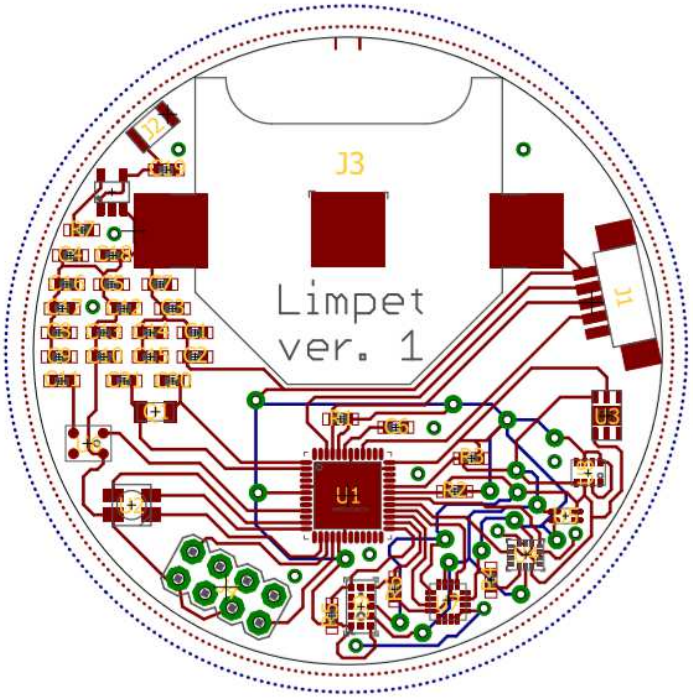

ELECTRICAL SPECIFICATIONS

	Min.	Typ.	Max.	Units
Supply Voltage	1.62	3.3	3.63	V
Supply Current	-	-	130	mA
Current Consumption	0.1	20	48 mA	mA
Storage Temperature	-40	25	85	°C

COMPONENTS

The Limpet PCB incorporates a microcontroller (ATSAMD21G18A), RGB LED (LTST-N683EGBW), battery holder (BK-877) for a rechargeable Li-ion battery (LIR2477), charging IC (MCP73812T), charger connector, JTAG connector (Molex 532610571), and an ESP connector to connect a SOC Wi-Fi module (ESP8266). The ESP connector (J4) is connected to the serial port (UART) of the MCU. Therefore, this connector can be used to connect other communication modules, where the picture below demonstrates the pins that can be used to do so. The Limpet PCB includes several exteroceptive sensors, which are:

- Temperature and Humidity Sensor (Si7006)
- IMU [Accelerometer and Gyroscope] Sensor (LSM6DS3)
- Optical Sensor (VEML6040)
- Sound Sensor (SPU0414HR5H-SB)
- 3-Axis Magnetic Sensor (MLX90393)
- Pressure Sensor (BMP280)
- Distance Sensor (VL53L0)

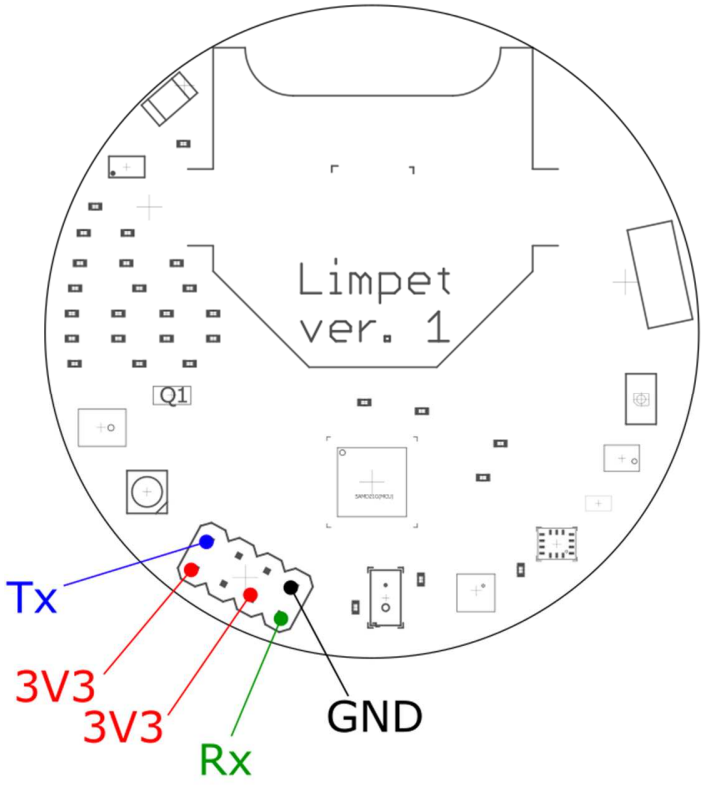

SENSORS

Sensor	Sensor Modality	Measurements
Accelerometer	Acceleration	• Acceleration (x) • Acceleration (y) • Acceleration (z) • Temperature
Gyroscope	Angular Velocity	• Angular Velocity (x) • Angular Velocity (y) • Angular Velocity (z) • Temperature
Temperature Sensor	Temperature	• Temperature
Humidity Sensor	Humidity	• Relative Humidity
Microphone	Sound	• Sound Frequency
Pressure Sensor	Pressure	• Temperature • Pressure • Altitude
Hall-Effect Sensor	Magnetic Field Strength	• Magnetic Field Strength (x) • Magnetic Field Strength (y) • Magnetic Field Strength (z) • Temperature
Optical Sensor	Light Frequency	• Correlated Color Temperature • Red Light Power Density • Green Light Power Density • Blue Light Power Density • Ambient Light Intensity
Distance (Time-of-Flight) Sensor	Laser	• Distance (Range)

BATTERY

The Limpet is powered by a 3.6V 160 mAh lithium-ion coin cell battery. The Li-ion battery (LIR2477) is a rechargeable battery and has a diameter of 24.5 mm. The battery can be recharged by using a 6Vdc plug-in power supply. The limpet includes header pins (J2) on the PCB for connecting the power supply to recharge the battery. When the charging IC receives 6V dc, it will start charging the onboard battery until the battery is full.

LIFETIME

The Limpet has a battery life @160 mAh of 0.87 to 1600 hours. The minimum battery life is calculated by assuming the Limpet has all the sensors, RGB LED, MCU and communication constantly on. The Limpet will consume approximately 182.9 mA (ESP8266 consumes 135 mA, RGB LED consumes 20 mA, sensors consume 20.9 mA, MCU consumes 7 mA) which allows for a battery life time of about 0.87 hours or 52.2 minutes. The maximum battery life is calculated by assuming the Limpet is in sleep mode, where it consumes an average current of 0.1 mA. In this mode, the battery life time of the Limpet can reach about 1600 hours or 67 days.

COST AND DIMENSIONS

The Limpet has a diameter of 50 mm, a height of 7 mm and weighs 17g with, and 10g without, the battery. The total cost of electronic components used in the limpet design is about £22. The cost of the ESP8266 module is £5.

ADHESION MECHANISM

Limpet v1 incorporates permanent magnets in the bottom layer for adhesion to metal surfaces. Limpet v2 will include an adhesion mechanism to attach to multiple different surfaces.

PRIMARY COMMUNICATION METHOD

The Limpet uses Wi-Fi to communicate and send data to the PC. It incorporates the ESP8266, which is a SOC Wifi module with integrated TCP/IP protocol stack capable of giving any microcontroller access to the WiFi network. The ESP8266 sends the data wirelessly to the PC using a messaging protocol known as MQTT. MQTT is a light-weight publish/subscribe messaging protocol used for remote communication. The received data can then be plotted in a real-time basis using Matlab, or saved and processed later.

OTHER COMMUNICATION METHODS

The Limpet was designed to have robust communication. It can use one of multiple communication methods, including *Serial*, *WiFi*, *LoRa, Optical* and *Acoustic Communication*. These communication methods have been successfully tested on the Limpet. This gives the

Limpet robustness in communication because if the primary communication method (WiFi) fails for any reason, secondary communication methods are available to achieve communication fail-over.

WiFi and serial communication do not allow for robot-to-robot communication. LoRaWAN, Acoustic and optical communication allow for robot-to-robot communication. Optical communication is achieved with a combination of the RGB LED and optical sensor. The messages are encoded in the LED signal by pulse-width modulating the LED to provide a range of different intensities. Each intensity corresponds to a different number from 0 to 9. The different LED colors can be used to correspond to different measurements such as time, distance, pressure, temperature, etc. The optical sensor can measure the red, blue and green light power density as well as the ambient light intensity. The optical sensor can thus use the light intensity and color power density measurements to infer transmitted messages. LoRaWAN is a digital wireless data communication technology that enables long-range transmission with low power consumption. LoRaWAN technology is provided by the LoRa Alliance, which is a non-profit association of more than 500 member companies that are developing and promoting LoRaWAN open standard for IoT.

SETTING UP THE ESP8266

Please refer to the ESP8266 tutorial for information on how to setup the ESP8266.

PROGRAMMING THE LIMPET

The limpet has an onboard programming port (JTAG). The limpet is programmed using a J-Link programmer together with a JTAG Adapter (Olimex ARM-JTAG-20-10). The limpet is programmed in C/C++ using Atmel Studio 7. The connection between the JTAG Adapter and the programming port
(JTAG) is shown below.

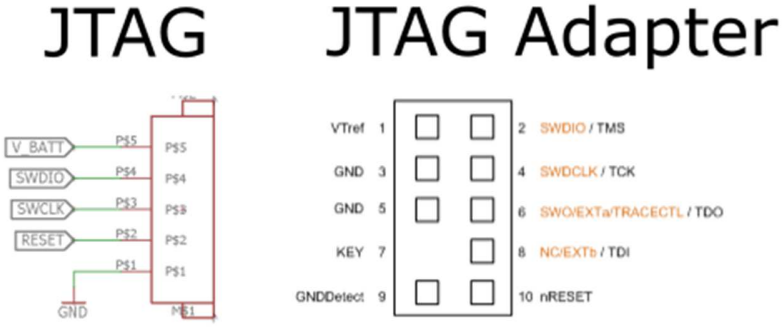

DATA TREATMENT ON THE LIMPET

In data treatment, there are two distinguished phases: data processing and data analysis. Data processing includes data visualization, eliminating outliers, averaging, smoothing, down sampling, quality check, etc. This phase aims to remove noise and outliers from the data to prepare it for further processing and analysis. The optimum data product is the collection of information that best represents the measured parameter and that requires the minimum manipulation to be embedded in a particular analysis.

The Limpet allows for on-board processing and analysis of data collected from the various sensors. The on-board processes can eliminate any noise and outliers, smooth the data, down-sample the data to accord with computational limitations of the microcontroller, and check the data against pre-stored values. These processing capabilities are just a few of the on-board processing techniques that can be carried out on the Limpet. The Limpet can use these processing capabilities to make autonomous decisions during inspection and monitoring of offshore energy platforms. The user can remove or add new data processing stages if required. The choice of data treatment ultimately depends on the nature of the monitored variable, the final usage of the data, the environmental conditions, the monitoring setup, power consumption and communication method. Each use case can have its own customized set of processing on the Limpet. The Limpet can also perform multiple on-board analysis processes such as: Spectral Analysis, Acoustic Fingerprinting, Sliding Window Analysis, and many others.

ROS INTERFACE

The Limpet can be integrated with ROS interface. The figure below shows an overview of the ROS interface with the Limpet. The sensor data is fed into the microcontroller. The microcontroller sends out the data to a converter, which converts this data into a ROS protocol. The data can be published to a ROS topic and any ROS node can subscribe to that topic to read the sensor data. The different sensors on the Limpet have different physical measurement variables. These measurement variables are fed into the microcontroller, where it adds a label to the data to differentiate data from the different sensors (e.g. distance, temperature, pressure, etc). The microcontroller sends out the data to a converter, which converts this data into a ROS protocol. The data can be published to a ROS topic and based on the label sent with the data, the

converter can decide which topic to publish the data to. ROS nodes can subscribe to the different topics to gain access to the sensor data. This enables the Limpet to be used as part of a multi-robotic system, where the interaction between different robots results in a more complex and useful behavior. For example, Limpets can be deployed from onshore to offshore platforms using drones, and they can then be repositioned using the drones to create a dynamic multi-sensing robotic system.

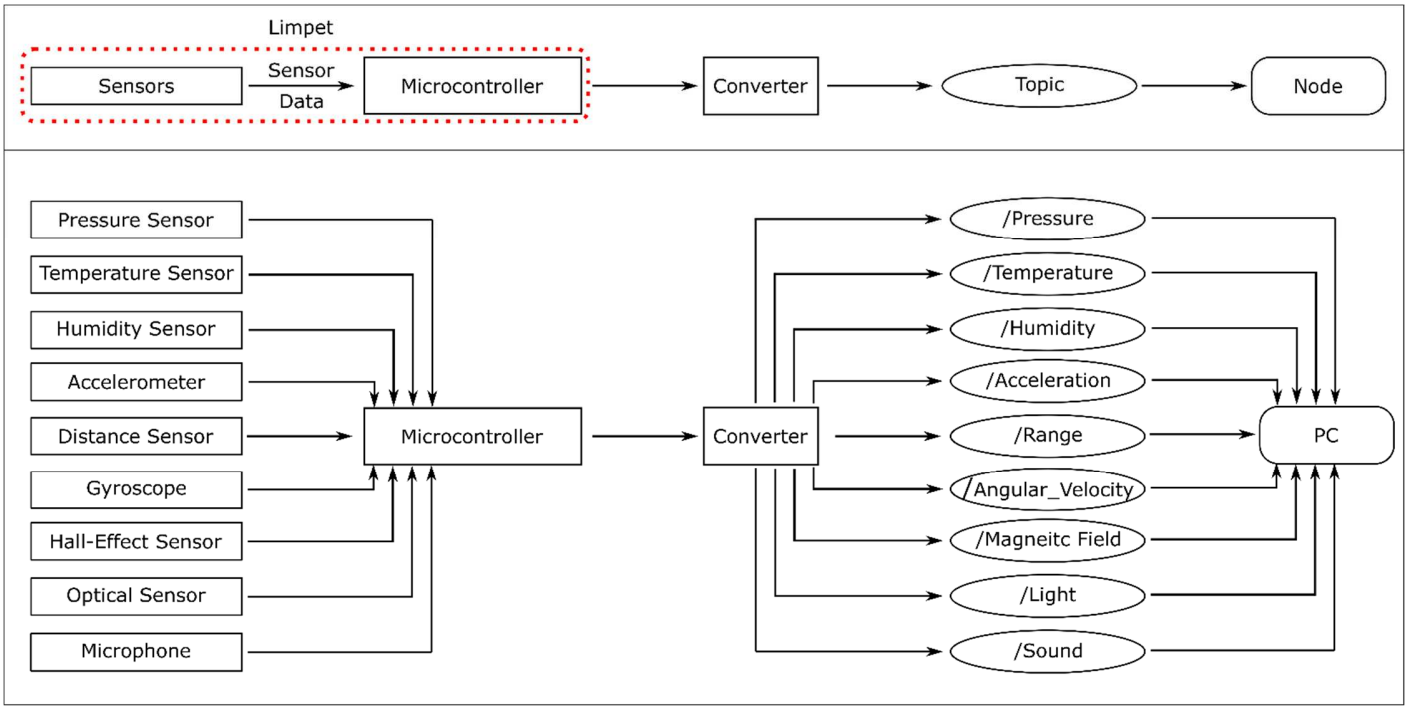

LIMPET ACOUSTIC COMMUNICATION PROTOCOL

The Limpet can be integrated with acoustic modems. The Limpet was tested with acoustic USMART Nanomodem, and the table below shows the communication protocol.

Command String	Description	Response String	Description
Broadcast			
$Bnddddddd	**Broadcast data message. Send n bytes (ddd…) to all units. Data bytes (d) can be any printable or non-printable char**	**#Bxxxnddddddd**	**The unit will output #Bxxxnddddddd (where xxx is the transmitting unit and ddddddd is data from the sensor)**
$B7000000U	Send 7 bytes to all units requesting	#Bxxx7U±d.ddd	Send 7 bytes of acceleration data in x direction to the requesting

	acceleration in x direction		unit. d(1) is the sensor identification char (U), d(2) is the sign and d(4) is the decimal sign '.'
$B7000000V	Send 7 bytes to all units requesting acceleration in y direction	#Bxxx7V±d.ddd	Send 7 bytes of acceleration data in y direction to the requesting unit. d(1) is the sensor identification char (V), d(2) is the sign and d(4) is the decimal sign '.'
$B7000000W	Send 7 bytes to all units requesting acceleration in z direction	#Bxxx7W±d.ddd	Send 7 bytes of acceleration data in z direction to the requesting unit. d(1) is the sensor identification char (W), d(2) is the sign and d(4) is the decimal sign '.'
$B7000000P	Send 7 bytes to all units requesting pressure measurement	#Bxxx7Pdddddd	Send 7 bytes of pressure data (P) to the requesting unit. d(1) is the sensor identification char (P)
$B7000000H	Send 7 bytes to all units requesting humidity measurement	#Bxxx7Hddd.dd	Send 7 bytes of humidity data to the requesting unit. d(1) is the sensor identification char (H), d(2) is the sign and d(5) is the decimal sign '.'
$B7000000D	Send 7 bytes to all units requesting distance measurement	#Bxxx7Ddddddd	Send 7 bytes of distance data to the requesting unit. d(1) is the sensor identification char (D)
$B7000000T	Send 7 bytes to all units requesting temperature measurement	#Bxxx7Tddd.dd	Send 7 bytes of temperature data to the requesting unit. d(1) is the sensor identification char (T) and d(5) is the decimal sign '.'
$B7000000L	Send 7 bytes to all units requesting ambient light intensity data	#Bxxx7Lddd.dd	Send 7 bytes of light intensity data to the requesting unit. d(1) is the sensor identification char (L), d(2) is the sign and d(4) is the decimal sign '.'
$B7000000R	Send 7 bytes to all units requesting red light power density	#Bxxx7Rddd.dd	Send 7 bytes of red light power density data to the requesting unit. d(1) is the

			sensor identification char (R), d(2) is the sign and d(4) is the decimal sign '.'
$B7000000G	Send 7 bytes to all units requesting green light power density	#Bxxx7Gddd.dd	Send 7 bytes of green light power density data to the requesting unit. d(1) is the sensor identification char (G), d(2) is the sign and d(4) is the decimal sign '.'
$B7000000B	Send 7 bytes to all units requesting blue light power density	#Bxxx7Bddd.dd	Send 7 bytes of blue light power density to the requesting unit. d(1) is the sensor identification char (B), d(2) is the sign and d(4) is the decimal sign '.'
$B7000000C	Send 7 bytes to all units requesting correlated colour temperature	#Bxxx7Cdddddd	Send 7 bytes of correlated colour temperature data to the requesting unit. d(1) is the sensor identification char (C)
$B7000000M	Send 7 bytes to all units requesting magnetic field strength in x direction	#Bxxx7M±dd.dd	Send 7 bytes of magnetic field strength data in x direction to the requesting unit. d(1) is the sensor identification char (M), d(2) is the sign and d(5) is the decimal sign '.'
$B7000000N	Send 7 bytes to all units requesting magnetic field strength in y direction	#Bxxx7N±dd.dd	Send 7 bytes of magnetic field strength data in y direction to the requesting unit. d(1) is the sensor identification char (N), d(2) is the sign and d(5) is the decimal sign '.'
$B7000000O	Send 7 bytes to all units requesting magnetic field strength in z direction	#Bxxx7O±dd.dd	Send 7 bytes of magnetic field strength data in z direction to the requesting unit. d(1) is the sensor identification char (O), d(2) is the sign and d(5) is the decimal sign '.'
$B7000000X	Send 7 bytes to all units requesting gyroscope measurement in x direction	#Bxxx7X±d.ddd	Send 7 bytes of gyroscope data in x direction to the requesting unit. d(1) is the sensor identification char (X), d(2) is the sign and d(4) is the decimal sign '.'

$B7000000Y	Send 7 bytes to all units requesting gyroscope measurement in y direction	#Bxxx7Y±d.ddd	Send 7 bytes of gyroscope data in y direction to the requesting unit. d(1) is the sensor identification char (Y), d(2) is the sign and d(4) is the decimal sign '.'
$B7000000Z	Send 7 bytes to all units requesting gyroscope measurement in z direction	#Bxxx7Z±d.ddd	Send 7 bytes of gyroscope data in z direction to the requesting unit. d(1) is the sensor identification char (Z), d(2) is the sign and d(4) is the decimal sign '.'
Unicast			
$Uxxxnddddddd	**Broadcast data message. Send n bytes (ddd…) to unit xxx. Data bytes (d) can be any printable or non-printable char**	**#Undddddddd**	**The unit will output #Bxxxnddddddd (where xxx is the transmitting unit and ddddddd is data from the sensor)**
$Uxxx7000000U	Send 7 bytes to unit xxx requesting acceleration in x direction	#U7U±d.ddd	Send 7 bytes of acceleration data in x direction to the requesting unit. d(1) is the sensor identification char (U), d(2) is the sign and d(4) is the decimal sign '.'
$Uxxx7000000V	Send 7 bytes to unit xxx requesting acceleration in y direction	#U7V±d.ddd	Send 7 bytes of acceleration data in y direction to the requesting unit. d(1) is the sensor identification char (V), d(2) is the sign and d(4) is the decimal sign '.'
$Uxxx7000000W	Send 7 bytes to unit xxx requesting acceleration in z direction	#U7W±d.ddd	Send 7 bytes of acceleration data in z direction to the requesting unit. d(1) is the sensor identification char (W), d(2) is the sign and d(4) is the decimal sign '.'
$Uxxx7000000P	Send 7 bytes to unit xxx requesting pressure measurement	#U7Pdddddd	Send 7 bytes of pressure data (P) to the requesting unit. d(1) is the sensor identification char (P)
$Uxxx7000000H	Send 7 bytes to unit xxx requesting	#U7Hddd.dd	Send 7 bytes of humidity data to the requesting unit. d(1) is the sensor

	humidity measurement		identification char (H), d(2) is the sign and d(5) is the decimal sign '.'
$Uxxx7000000D	Send 7 bytes to unit xxx requesting distance measurement	#U7Ddddddd	Send 7 bytes of distance data to the requesting unit. d(1) is the sensor identification char (D)
$Uxxx7000000T	Send 7 bytes to unit xxx requesting temperature measurement	#U7Tddd.dd	Send 7 bytes of temperature data to the requesting unit. d(1) is the sensor identification char (T) and d(5) is the decimal sign '.'
$Uxxx7000000L	Send 7 bytes to unit xxx requesting light intensity data	#U7Lddd.dd	Send 7 bytes of light intensity data to the requesting unit. d(1) is the sensor identification char (L), d(2) is the sign and d(4) is the decimal sign '.'
$Uxxx7000000R	Send 7 bytes to unit xxx requesting red light power density	#U7Rddd.dd	Send 7 bytes of red light power density data to the requesting unit. d(1) is the sensor identification char (R), d(2) is the sign and d(4) is the decimal sign '.'
$Uxxx7000000G	Send 7 bytes to unit xxx requesting green light power density	#U7Gddd.dd	Send 7 bytes of green light power density data to the requesting unit. d(1) is the sensor identification char (G), d(2) is the sign and d(4) is the decimal sign '.'
$Uxxx7000000B	Send 7 bytes to unit xxx requesting blue light power density	#U7Bddd.dd	Send 7 bytes of blue light power density to the requesting unit. d(1) is the sensor identification char (B), d(2) is the sign and d(4) is the decimal sign '.'
$Uxxx7000000C	Send 7 bytes to unit xxx requesting correlated colour temperature	#U7Cdddddd	Send 7 bytes of correlated colour temperature data to the requesting unit. d(1) is the sensor identification char (C)
$Uxxx7000000M	Send 7 bytes to unit xxx requesting magnetic field strength in x direction	#U7M±dd.dd	Send 7 bytes of magnetic field strength data in x direction to the requesting unit. d(1) is the sensor identification char (M),

Appendix E

ESP8266 Tutorial

Authors: Mohammed E. Sayed

Description: Beginners guide for setting up and using the ESP8266 chip. The ESP8266 can be used to get access to the WiFi network and achieve communication between devices using WiFi.

ESP8266 Tutorial 

ESP8266 GUIDE

Mohammed El-Sayed
Stokes Research Group
Institute of Integrated Micro and Nano Systems
School of Engineering
University of Edinburgh



DOWNLOADING ESP8266FLASHER (V1.0)

- The ESP8266Flasher flashes your ESP8266 module with NodeMCU.
- NodeMCU is a firmware that allows the user to program ESP8266 modules using LUA scripts. More information about NodeMCU can be found here.
- The ESP8266Flaser can be downloaded from:
  - Win32
  - Win64
- For more information about NodeMCU flasher, click here.

DOWNLOADING ESPLORER (V0.2.0-RC6)

- ESPLorer can be downloaded here.
- Download the zip folder (ESPlorer.zip (v 0.2.0-rc6)).



DOWNLOADING ESPLORER

- After the zip folder is downloaded, extract the files from the zip folder.
- The ESPLorer executable file can be found in the folder as shown in the picture below.

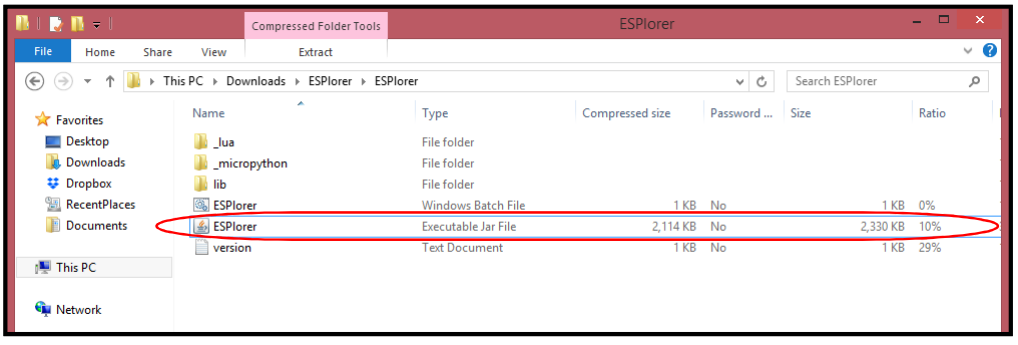

DOWNLOADING MOSQUITTO

- First, you need to download Mosquitto here.
- This will take you to the Eclipse repository with mirror options through which you can download the exe file.

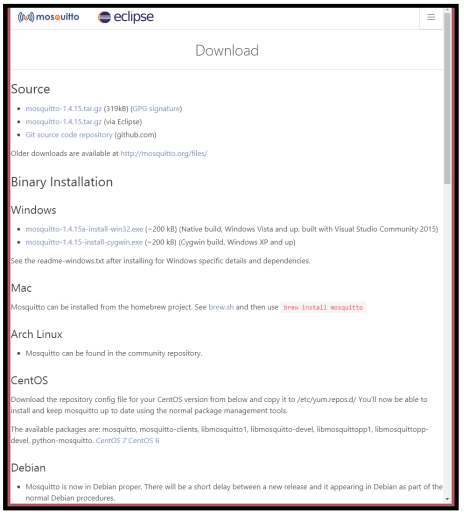

DOWNLOADING MOSQUITTO

- After downloading the exe file, run it. This will give you the following screen, requesting that you download Mosquitto dependencies.

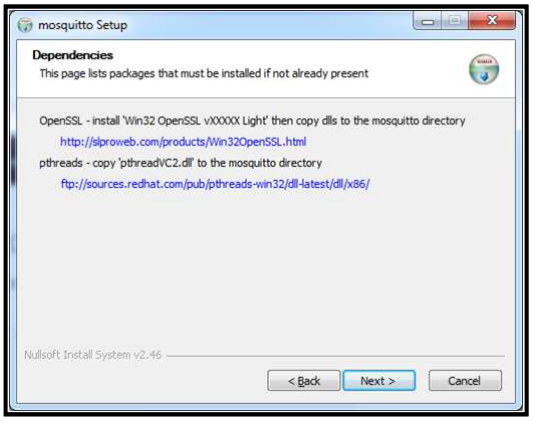

DOWNLOADING MOSQUITTO

- Download the Win32 OpenSSL v1.0.2c Light setup file here.
- Next, you need to download Pthreadvc2.dll given here.
- Continue running the Mosquitto installer. It will then ask you if you want to install the service too. Select the service and click next.

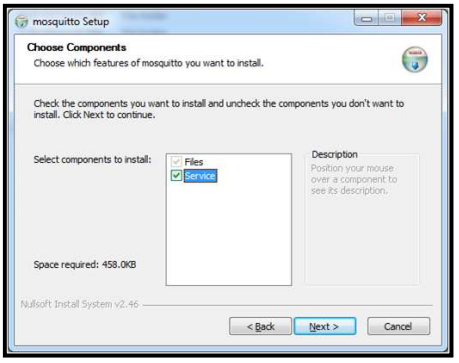

DOWNLOADING MOSQUITTO

- Select the installation location and press on Install. Once the installation is done, the dependencies should be copied to the folder where Mosquitto is installed.
- The required DLLS are:
  - pthreadVC2.dll
  - libeay32.dll (This can be found in the download OpenSSL-Win32)
  - ssleay32.dll (This can be found in the download OpenSSL-Win32)
- Make sure that the required DLLs are on the system path or in the same directory as mosquito executable.
- The next step is uninstalling mosquitto and reinstalling it in the same location (so that now it has all the dependencies in the folder).

DOWNLOADING MOSQUITTO

- To check that the Mosquitto broker works, open **Services** on your computer and start the Mosquitto Broker as shown in the picture.

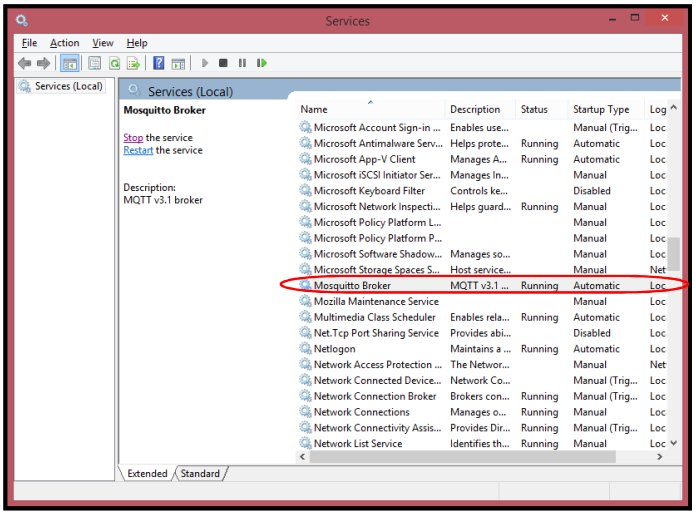

DOWNLOADING MOSQUITTO

- Run the command prompt and use the command **netstat –an** to check that the Mosquitto Broker is running. (Note: Do not forget to stop the Mosquitto Broker from **Services** after doing the check).

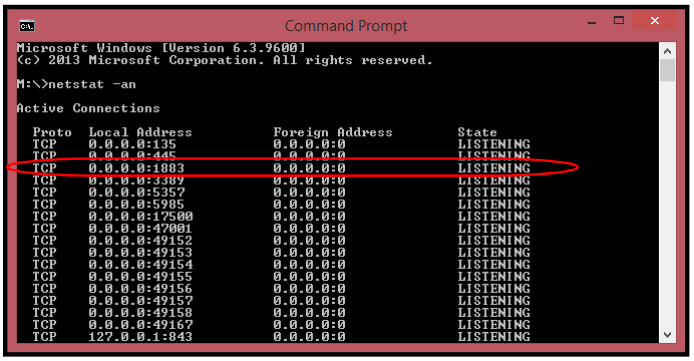

FLASHING ESP8266 WITH NODEMCU

- To flash your ESP8266 with NodeMCU, you will need a 3.3V FTDI Programmer.
- A good FTDI Programmer to use for this purpose is the SparkFun FTDI Basic Breakout – 3.3V, which can be found here.
- The connection between the ESP8266 module and the FTDI Programmer is as follows:
  - RXI (ESP8266) -> TXO (FTDI Programmer)
  - TXO (ESP8266) -> RXI (FTDI Programmer)
  - CHPD (ESP8266) -> 3.3V (FTDI Programmer)
  - GPIO0 (ESP8266) -> GND (FTDI Programmer)
  - VCC (ESP8266) -> 3.3V (FTDI Programmer)
  - GND (ESP8266) -> GND (FTDI Programmer)

FLASHING ESP8266 WITH NODEMCU

- Schematic of the connection between the ESP8266 and the FTDI Programmer:

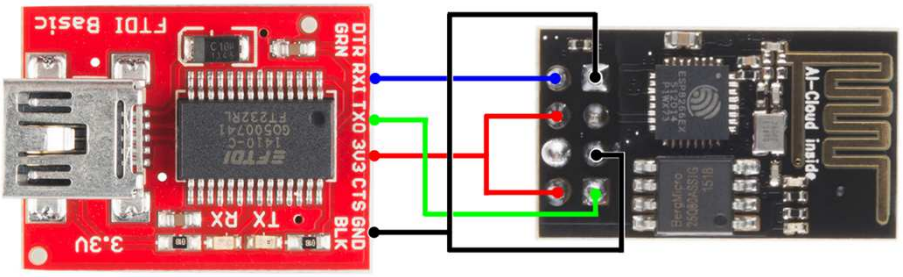

FLASHING ESP8266 WITH NODEMCU

- After connecting the ESP8266 module to the FTDI programmer, open the ESP8266Flasher and this window should appear:

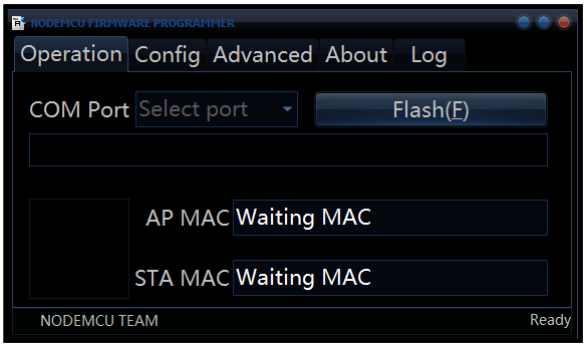

FLASHING ESP8266 WITH NODEMCU

- In the **Advanced** tab of the ESP8266Flasher, adjust the baud rate, flash size, flash speed, SPI Mode. The recommended settings are shown in the picture below, but you might have to change some of these settings.



FLASHING ESP8266 WITH NODEMCU

- From the device manager on your computer, find the serial port for your FTDI programmer. Right click on the desired serial port and go to properties. In the **Port Settings** tab, adjust the baud rate and other settings.
- The recommended settings are shown in the picture, but you might have to change some of these settings.

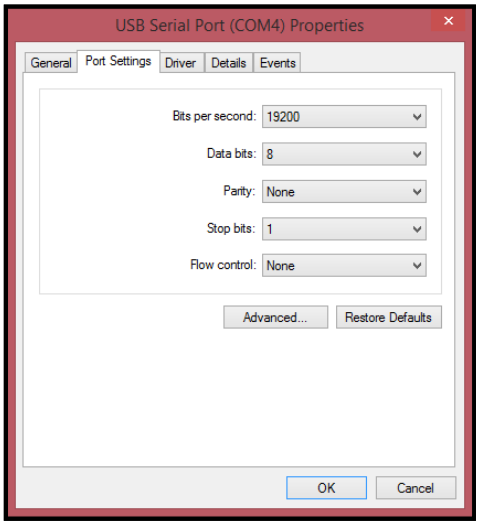

FLASHING ESP8266 WITH NODEMCU

- Reset the ESP8266 (by connecting the reset pin to ground and then disconnecting it). Then press the flash button in the **Operation** tab and it should start the flashing process. After finishing the process, a green circle with a check icon will appear.

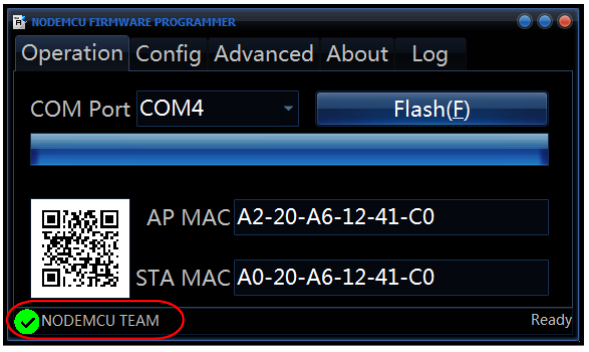

ESPLORER

- Change the baud rate for the serial port from **device manager** to 115200 (recommended setting).
- Reset the ESP8266 (by connecting the reset pin to ground and then disconnecting it).
- Run ESPLorer.

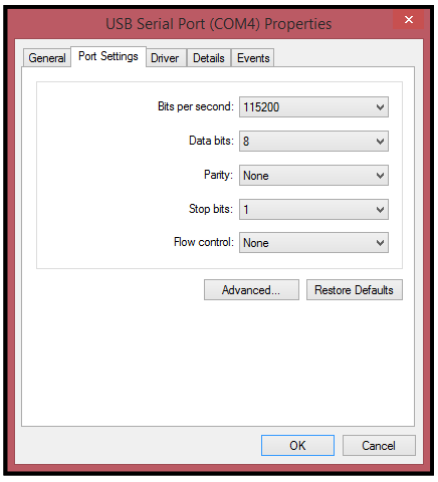

ESPLORER

- The connection for the ESP8266 and FTDI Prorammer for this part is as follows:
  - RXI (ESP8266) -> TXO (FTDI Programmer)
  - TXO (ESP8266) -> RXI (FTDI Programmer)
  - CHPD (ESP8266) -> 3.3V (FTDI Programmer)
  - VCC (ESP8266) -> 3.3V (FTDI Programmer)
  - GND (ESP8266) -> GND (FTDI Programmer)

ESPLORER

- Schematic of the connection between the ESP8266 and the FTDI Programmer:

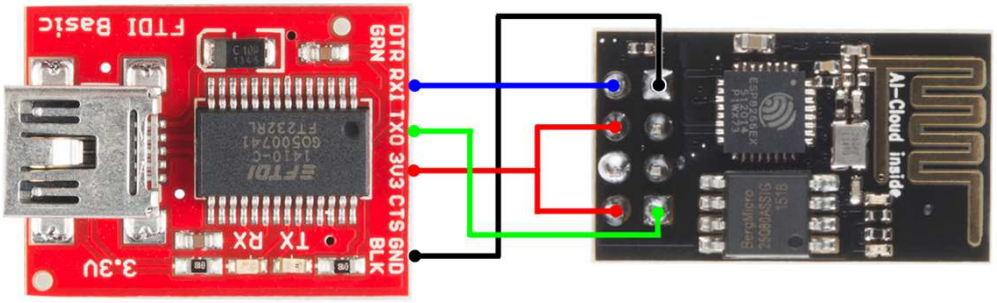

ESPLORER

- The ESPLorer window is divided into two sections: the right side is the NodeMCU window and the left side is the Micropython Window.

Micropython

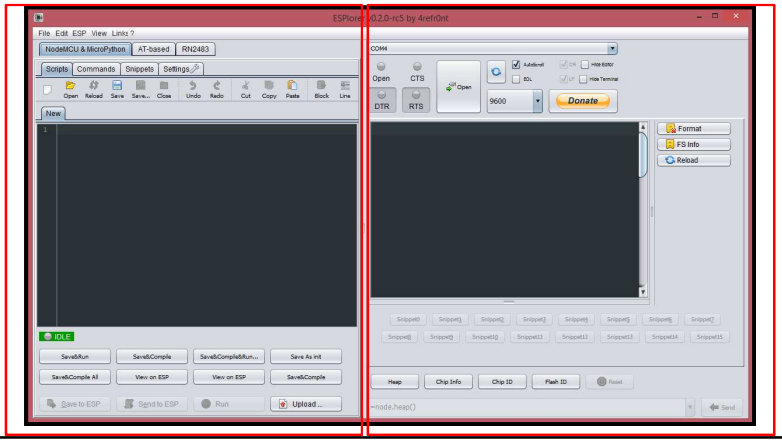

NodeMCU

ESPLORER

- From the NodeMCU window, choose the right serial port, select DTR and RTS, set the baud rate (recommended setting: 9600) and then open the port.
- You might need to reset the ESP8266 (by connecting the reset pin on the ESP8266 to ground and then disconnecting it) to get the program to communicate with the MCU.

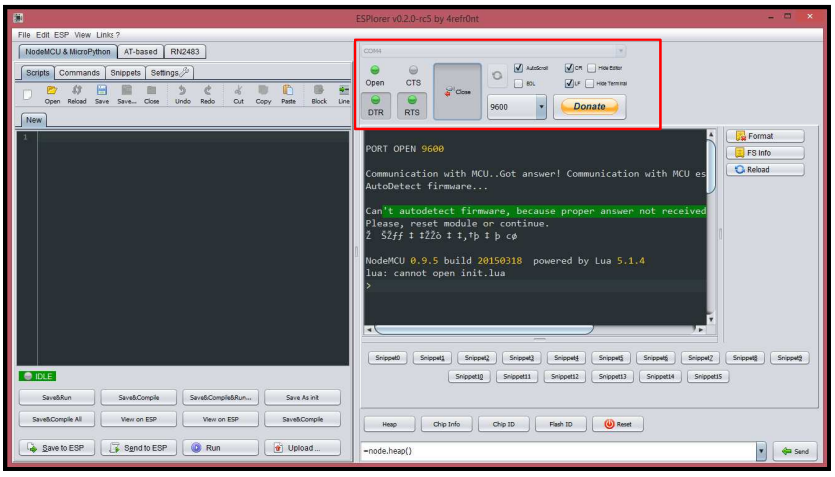

ESPLORER

- Copy the code from the config file (which holds the configuration) into the Micropython window. The config file can be found in the folder. In this file, we:
  - Declare an array of WiFi Access Points
  - Connect the ESP module to the desired WiFi network by setting the SSID and password
  - Set the IP Address for the host PC
  - Get the chip ID that can be used to differentiate between different objects
  - Set a standard endpoint prefix (topic) so that we do not have any collisions on the broker
- Save the file as config.lua in ESPLorer root folder.

ESPLORER

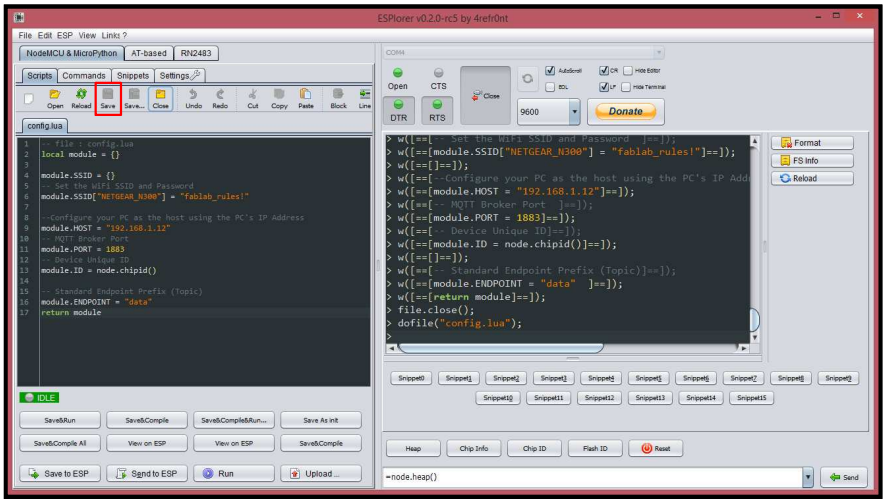

ESPLORER

- Open a New file.
- Copy the code from the setup file (which holds the WiFi setup) into the Micropython window. The setup file can be found in the folder. In this file, we are going to iterate over the available WiFi Access Points, and if there is one AP that we have the password for, we'll try to connect to it.
- Save the file as setup.lua in the ESPLorer root folder.

ESPLORER

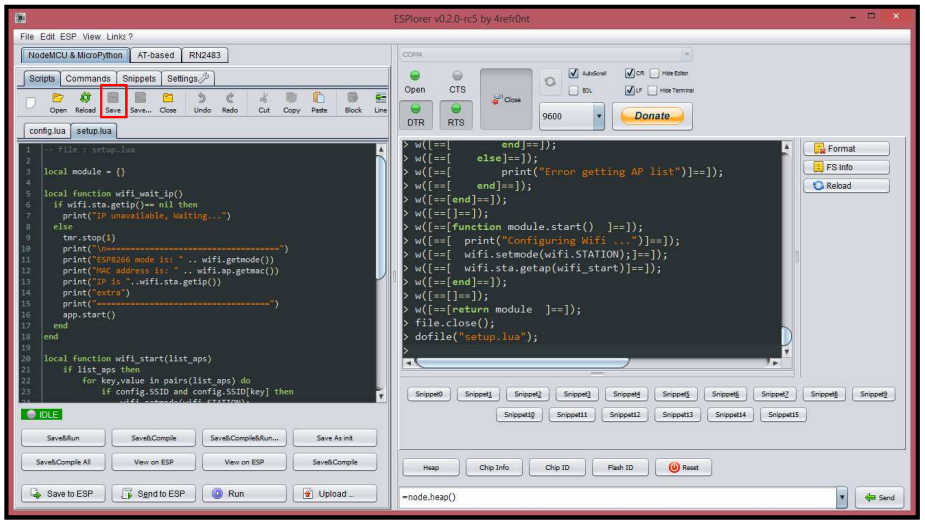

ESPLORER

- Open a New file.
- Copy the code from the uartComs file (which holds the UART Communication Setup) into the Micropython window. The uartComs file can be found in the folder. In this file, we are setting up the UART communication between the ESP8266 and other devices, so that the ESP8266 is able to receive data from other devices through UART connection.
- Save the file as uartComs.lua in the ESPLorer root folder.

ESPLORER

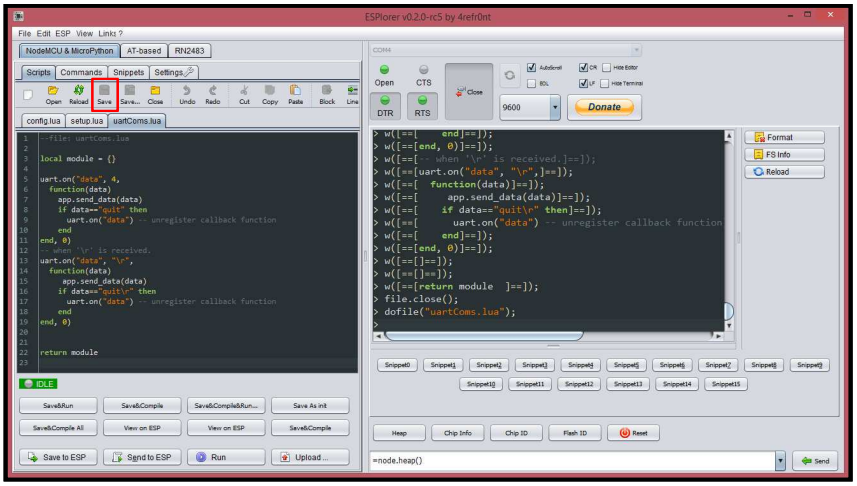

ESPLORER

- Open a New file.
- Copy the code from the application file (which holds our main code) into the Micropython window. The application file can be found in the folder. In this file, we are:
  - Creating a callback function for when we receive a message
  - Connecting to the Broker
  - Subscribing to the topic(endpoint prefix)/NodeID endpoint to receive targeted messages
  - Setting a recurring ping function that wil send the node ID to topic/ping so that the broker knows the device is alive.
- Save the file as application.lua in the ESPLorer root folder.

ESPLORER

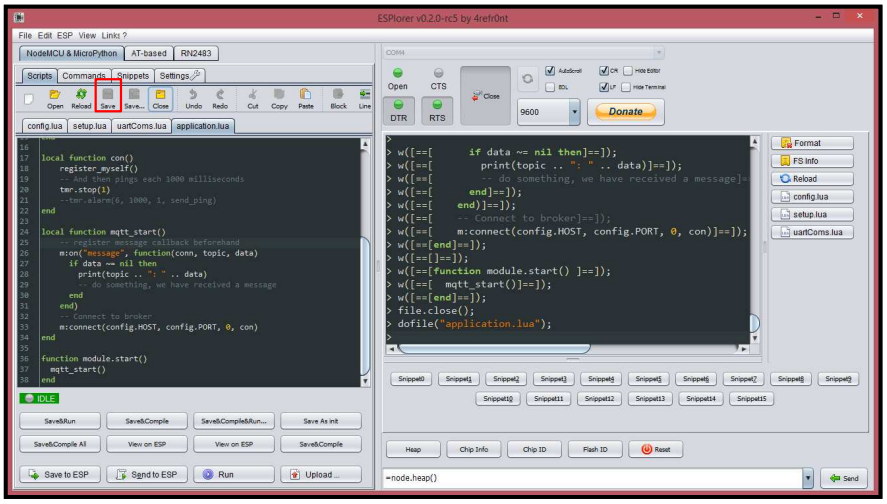

ESPLORER

- Save the config file to ESP.

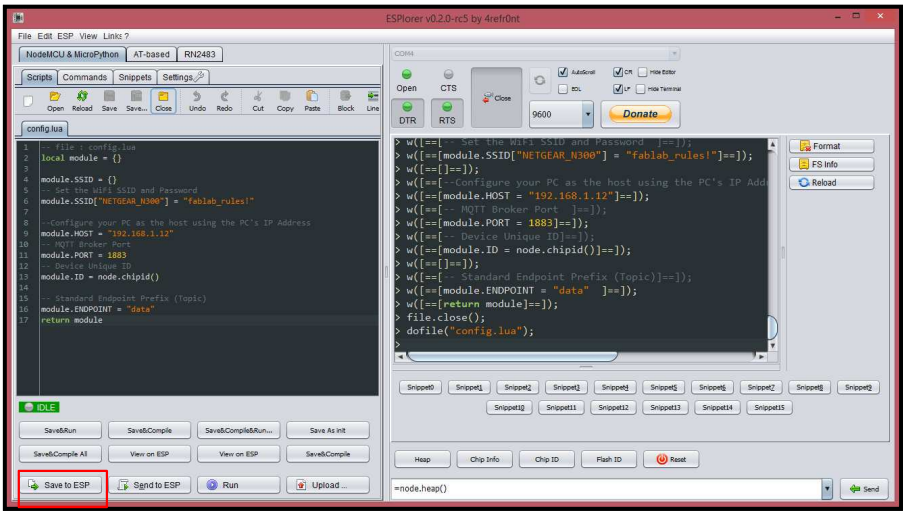

ESPLORER

- Save the setup file to ESP.

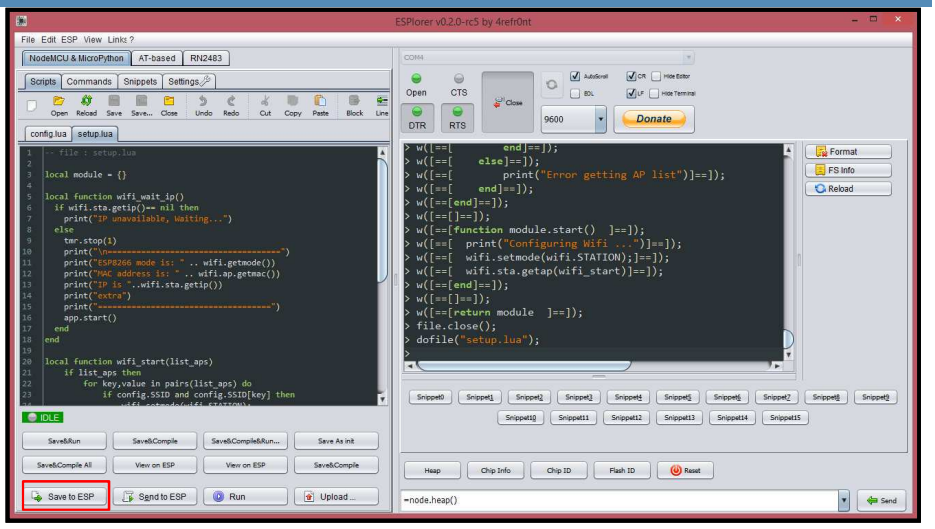

ESPLORER

- Save the uartComs file to ESP.

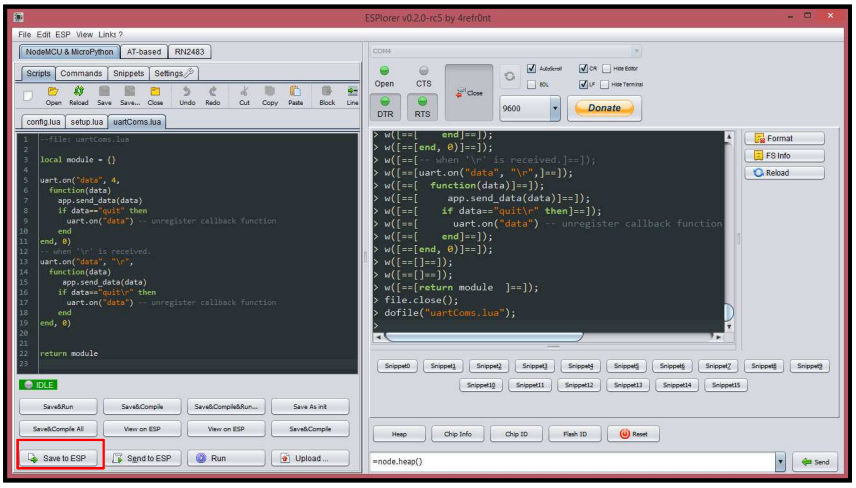

ESPLORER

- Save the application file to ESP.

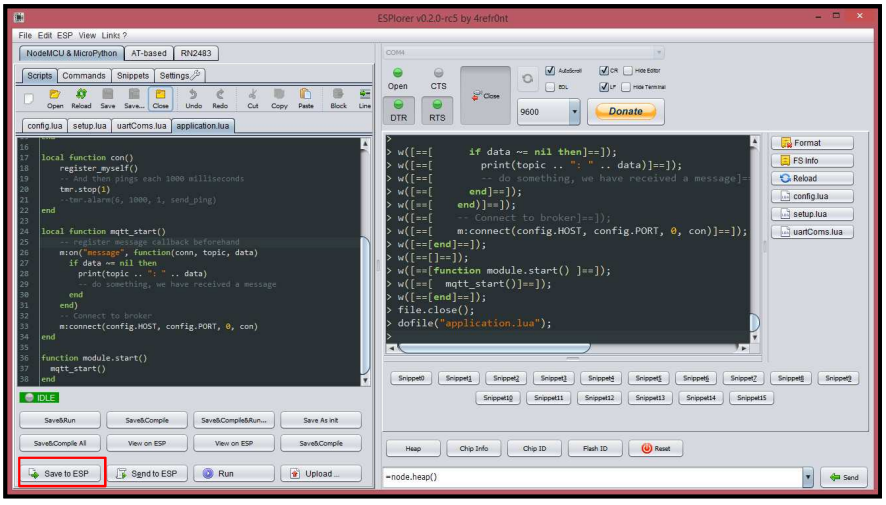

RUNNING MOSQUITTO

- Open command prompt. In the command prompt, navigate to the root folder where mosquitto is downloaded. In the command prompt window, write the command **mosquitto –v**. This will run mosquito in verbose mode, allowing you to see console messages.
- You can use the command **mosquitto** to start the broker manually or the command **mosquitto –h** for help.

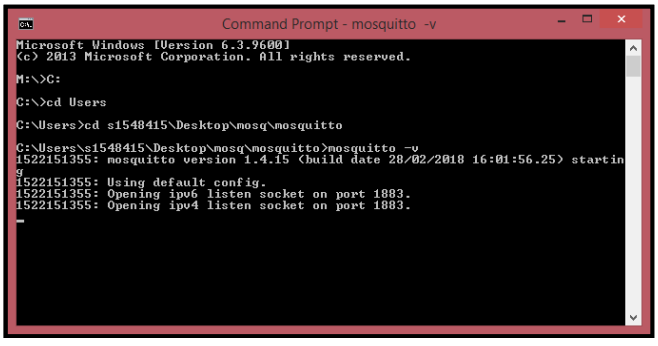

ESPLORER

- Open a New file.
- Copy the code from the test file (which holds the same content as the init.lua file) into the Micropython window. The test file can be found in the folder. It is good practice to use test.lua to test that the device works properly and then use init.lua at the end when you are sure of the code. The init.lua file on the NodeMCU is automatically played on startup. This means that everything placed in this file will be executed the moment NodeMCU starts.
- Save the file as test.lua in the ESPLorer root folder.

ESPLORER

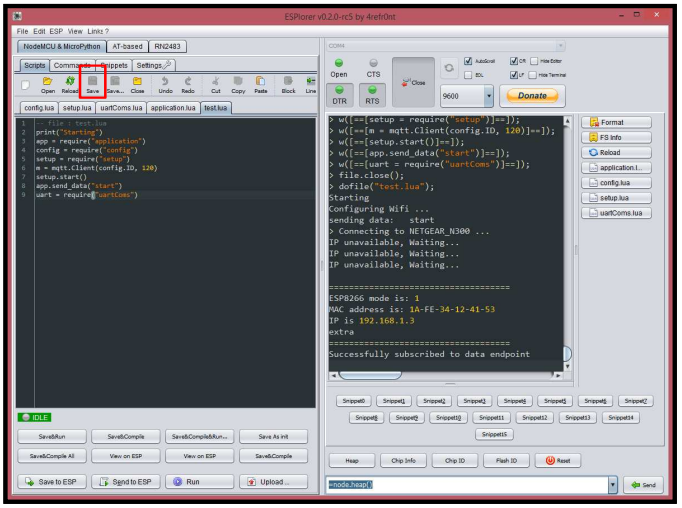

ESPLORER

- Save the test file to ESP.

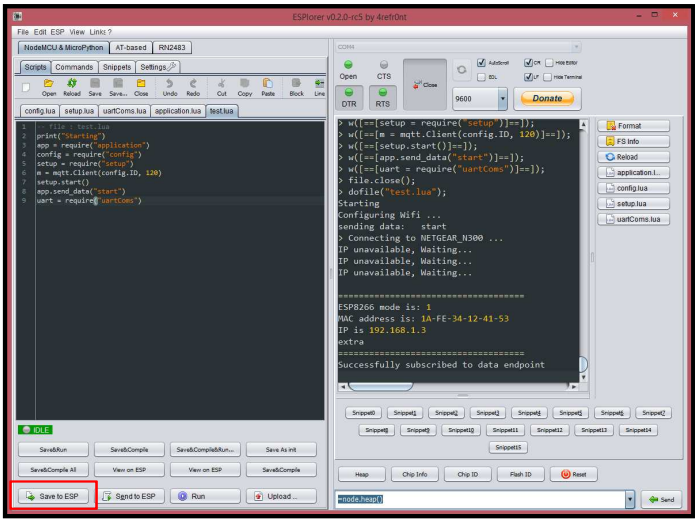

RUNNING MOSQUITTO SUBSCRIBER

- Open another command prompt window. In the command prompt, navigate to the root folder where mosquitto is downloaded. In the command prompt window, write the command **mosquitto_sub –h 127.0.0.1 –i testSub –t data**. This will subscribe to your topic, and you will be able to see any messages sent to the ESP8266. (-h is the hostname, -i is the client_id, -t is the message_topic).
- **Note:** You need to set the message_topic according to what you have set in your code. In this case, it was "data".

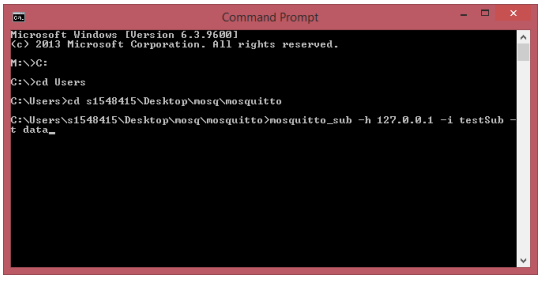

ESPLORER (SERIAL PRINT)

- Write in the serial port on NodeMCU Window in ESPLorer and press on **Send.**

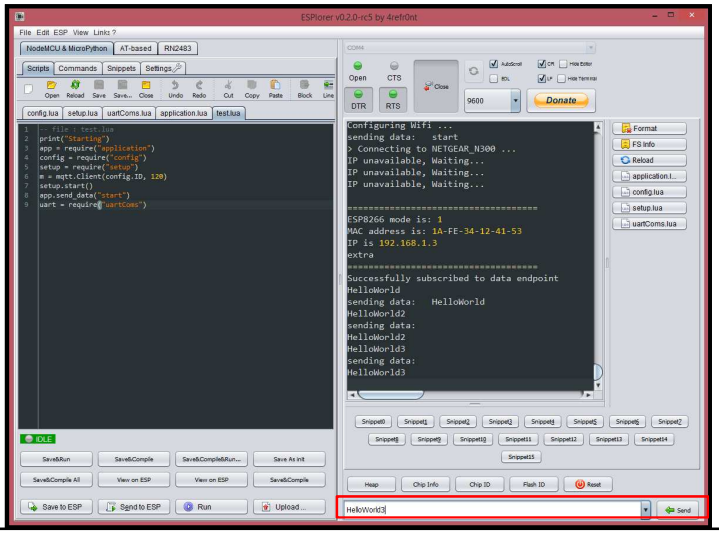

ESPLORER (SERIAL PRINT)

- Check that you receive the message on the mosquitto subscriber

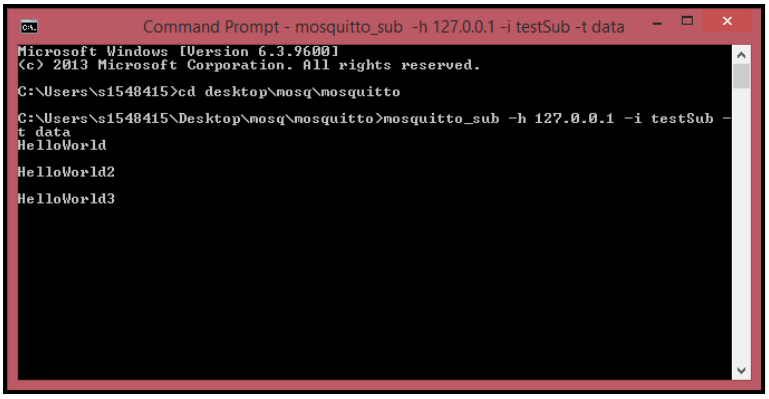

ESPLORER

- After checking that you receive correctly, it is time to upload the init.lua file on the ESP8266.
- Open a new file.
- Copy the code from the init file into the Micropython window. The init file can be found in the folder.
- Save the file as init.lua in the ESPLorer root folder.

ESPLORER

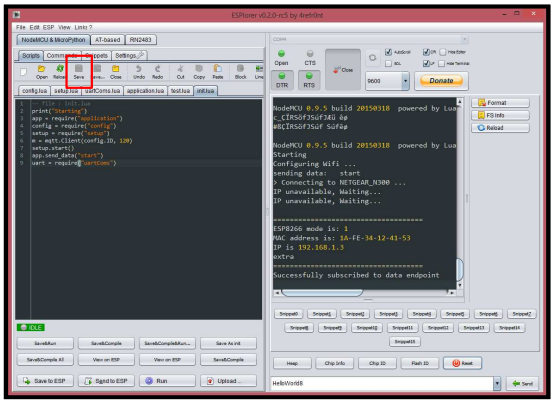

ESPLORER

- Save the init file to ESP.

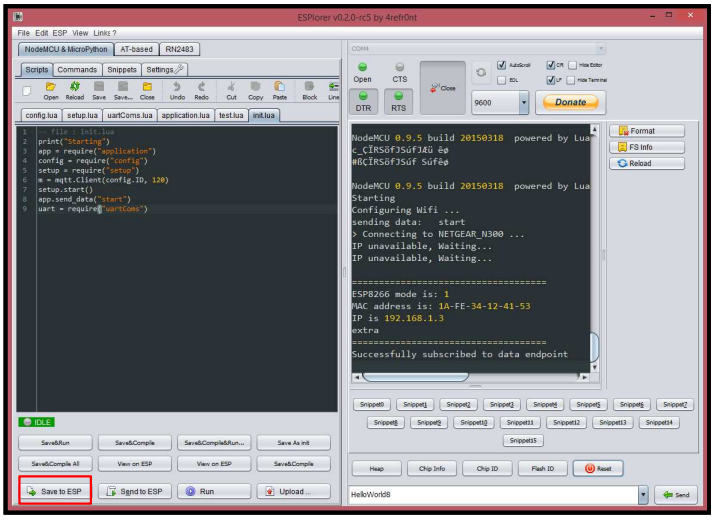

FORMATTING THE ESP8266

- To format the ESP8266 and delete all the files stored on it, you need to flash it with a blank binary file.
- Set the baud rate for the serial port from device manager to 19200 (recommended setting).
- Connect the ESP8266 to the FTDI Programmer as follows:
  - RXI (ESP8266) -> TXO (FTDI Programmer)
  - TXO (ESP8266) -> RXI (FTDI Programmer)
  - CHPD (ESP8266) -> 3.3V (FTDI Programmer)
  - GPIO0 (ESP8266) -> GND (FTDI Programmer)
  - VCC (ESP8266) -> 3.3V (FTDI Programmer)
  - GND (ESP8266) -> GND (FTDI Programmer)
- Open the ESP8266Flasher and adjust the settings in the **advanced** tab as shown in the picture below (recommended settings).

FORMATTING THE ESP8266

- The recommended settings for resetting the ESP8266 is as follows:



FORMATTING THE ESP8266

- In the **config** tab, add the blank file, choose it, untick the NODEMCU firmware and set the address of the blank file to the same address where you put the NODEMCU firmware.
- The blank binary file can be found in the folder (blank_1MB.bin).

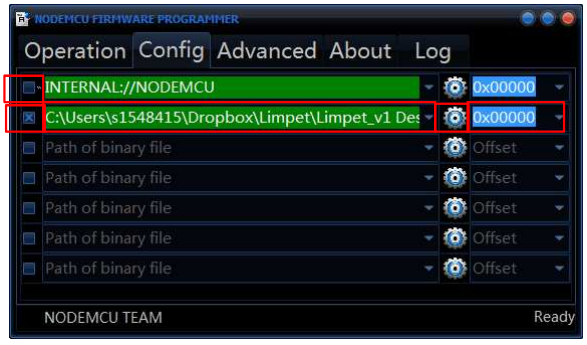

FORMATTING THE ESP8266

- After adding the blank file to the config tab and adjusting the settings in the advanced tab, navigate to the **operation** tab. Reset the ESP8266 and then press on the **flash** button.
- When it is done flashing, you will see a green tick at the bottom of the ESP8266Flasher.

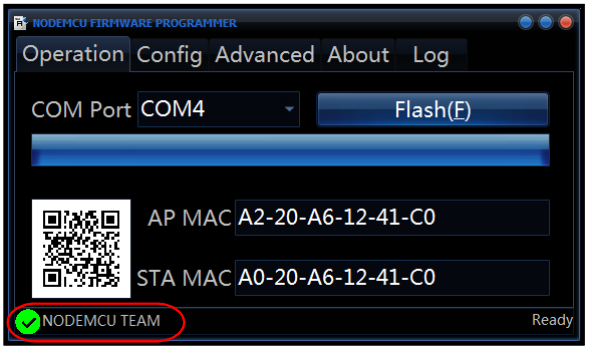

FORMATTING THE ESP8266

- After formatting the ESP8266, you can then reflash it with NodeMCU by following the same steps as stated previously, and then you will be able to repeat the whole process and upload new files to the ESP8266.

Appendix F

Printed Circuit Boards Design

F.1 Infrared Handheld Transceiver Schematic

Software: Eagle PCB Design Software

Authors: Mohammed E. Sayed

Infrared Transceiver Schematic

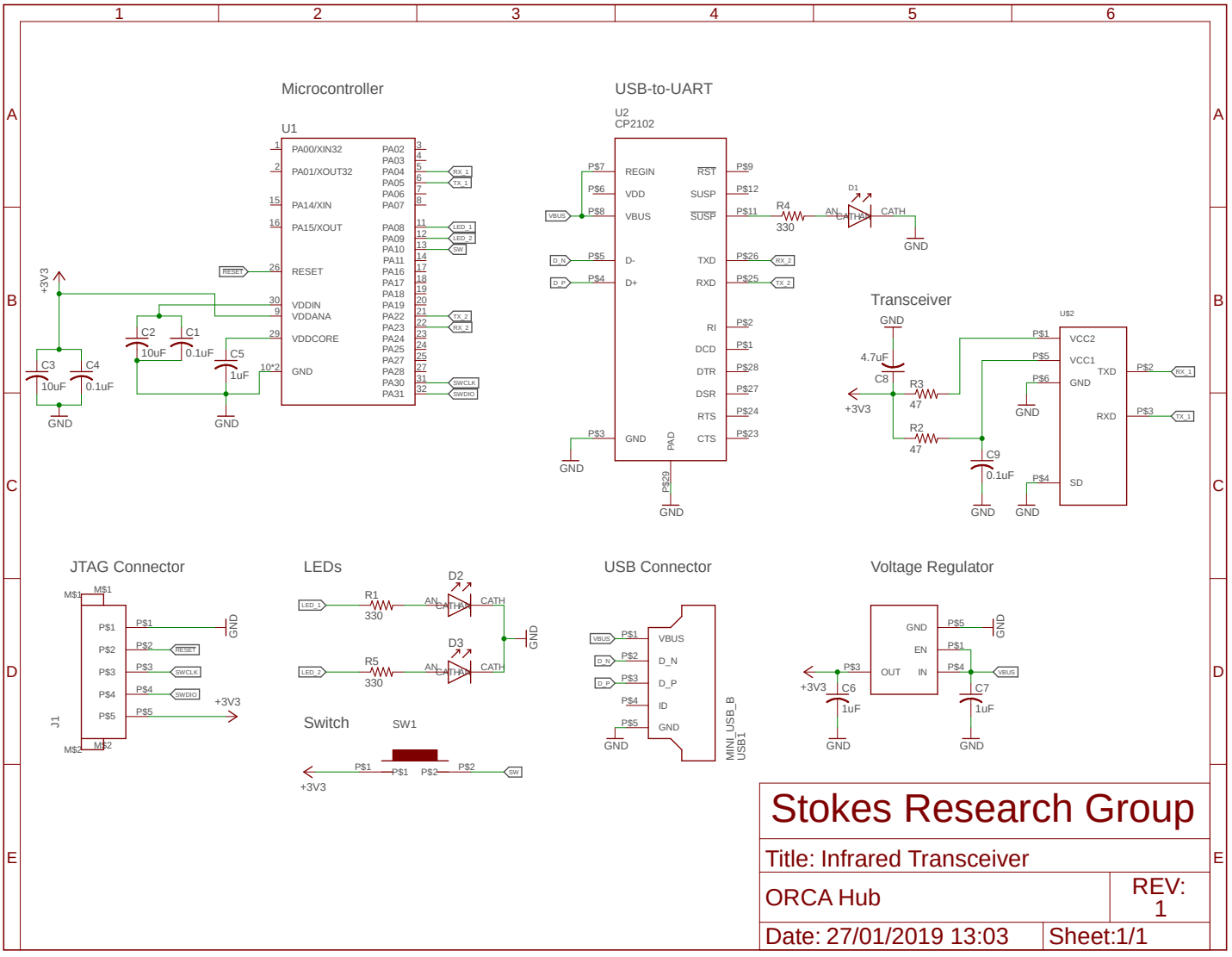

Stokes Research Group

Title: Infrared Transceiver

ORCA Hub

REV: 1

Date: 27/01/2019 13:03

Sheet:1/1

F.2 Infrared Handheld Transceiver PCB Layout

Software: Eagle PCB Design Software

Authors: Mohammed E. Sayed

Infrared Transceiver PCB Layout 

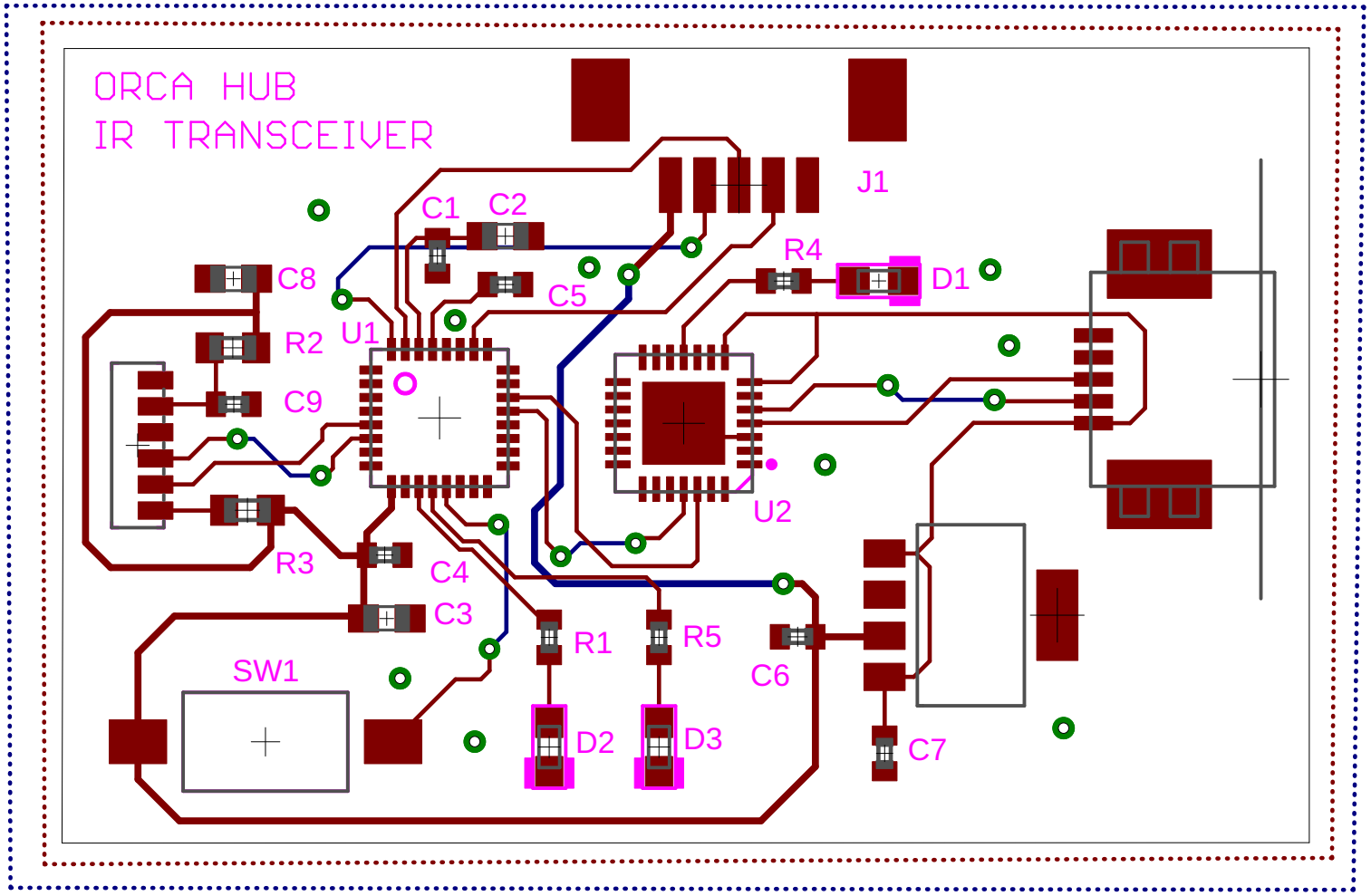
ORCA HUB
IR TRANSCEIVER
J1
C1
C2
C5
C8
R2
U1
C9
R3
C4
C3
SW1
R1
R5
D2
D3
R4
D1
U2
C6
C7

F.3 Sensing Module Schematic

Software: Eagle PCB Design Software

Authors: Mohammed E. Sayed

Sensing Module Schematic 

Communication

ESP8266

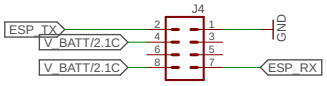

Connectors

JTAG (Programmer)

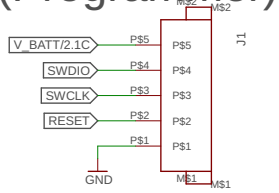

Battery Charger Connector

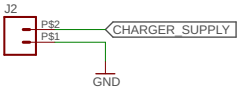

Microcontroller

SAMD21 MCU

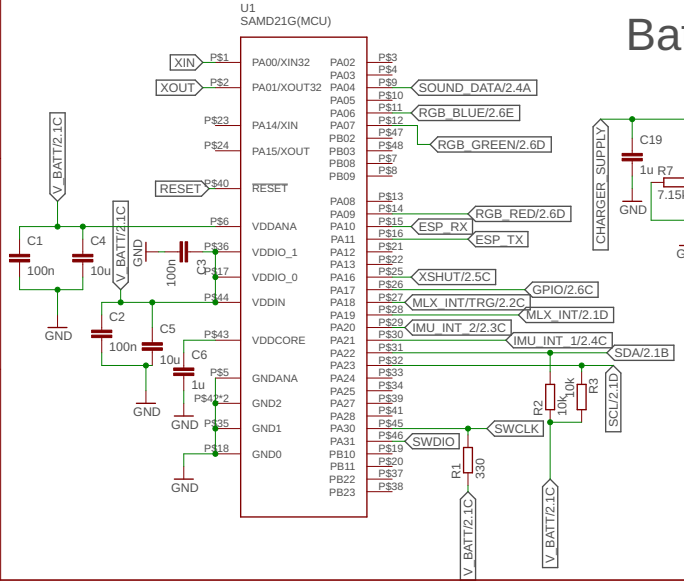

Power

Battery Charger

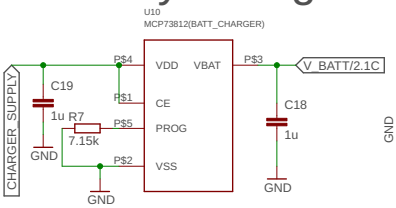

Battery Holder



Oscillator

Crystal Unit

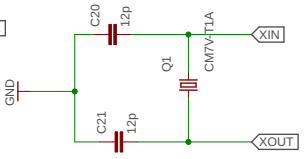

Stokes Research Group	
Title: Limpet ver. 1	
Author: Mohammed E. Sayed	REV: 1
Date: 20/05/2018 13:22	Sheet: 1/2

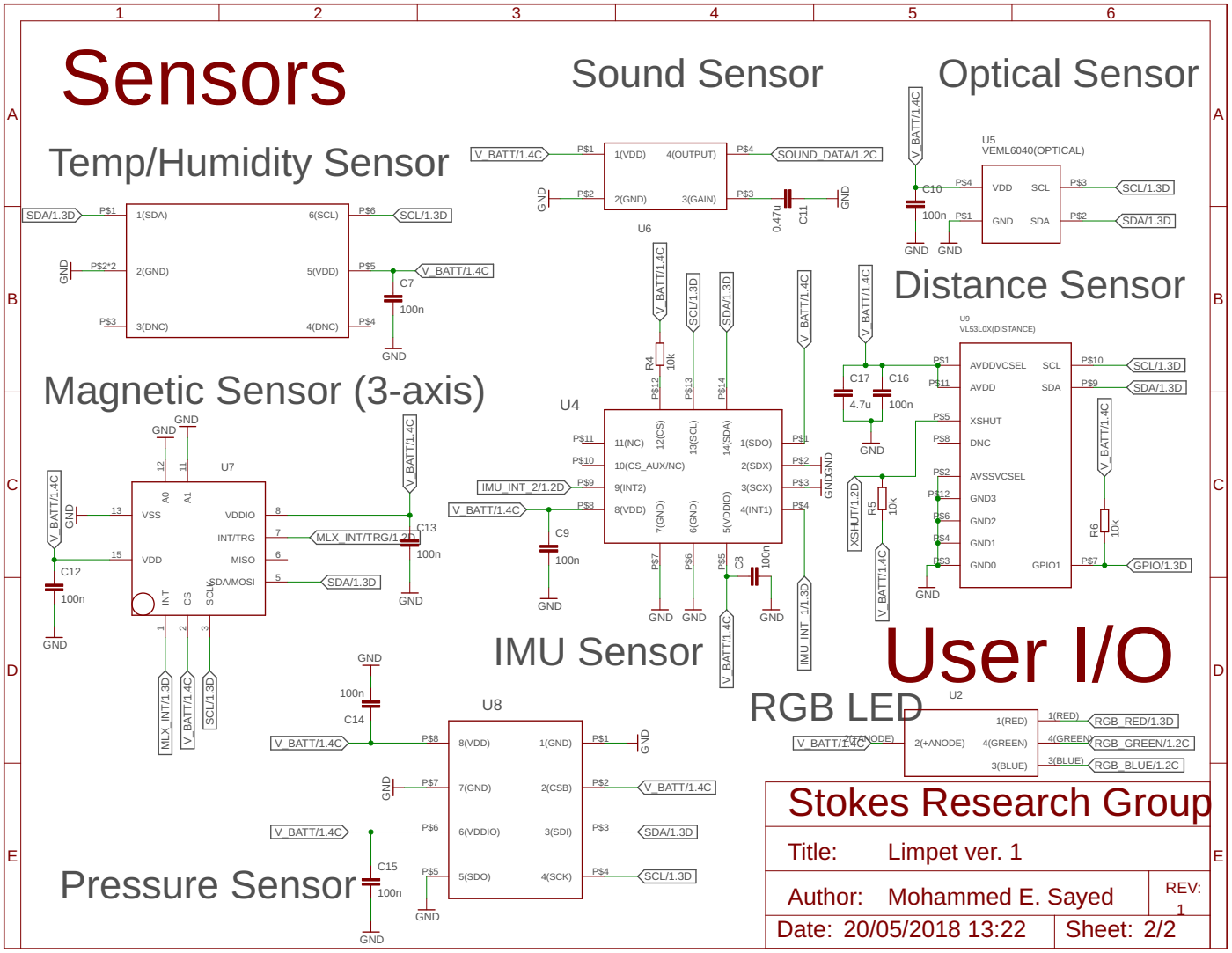
Sensors
Temp/Humidity Sensor
Magnetic Sensor (3-axis)
Pressure Sensor
Sound Sensor
IMU Sensor
Optical Sensor
Distance Sensor
User I/O
RGB LED
U2
U4
U5
VEML6040(OPTICAL)
U6
U7
U8
U9
VL53L0X(DISTANCE)
SDA/1.3D
SCL/1.3D
V_BATT/1.4C
GND
C7
100n
C12
C13
C14
C15
C16
C17
C8
C9
C10
C11
R4
R5
R6
10k
4.7u
0.47u
SOUND_DATA/1.2C
MLX_INT/TRG/1.2D
IMU_INT_2/1.2D
IMU_INT_1/1.3D
XSHUT/1.2D
GPIO/1.3D
RGB_RED/1.3D
RGB_GREEN/1.2C
RGB_BLUE/1.2C
Stokes Research Group
Title: Limpet ver. 1
Author: Mohammed E. Sayed
REV: 1
Date: 20/05/2018 13:22
Sheet: 2/2

F.4 Sensing Module PCB Layout

Software: Eagle PCB Design Software

Authors: Mohammed E. Sayed

Sensing Module PCB Layout

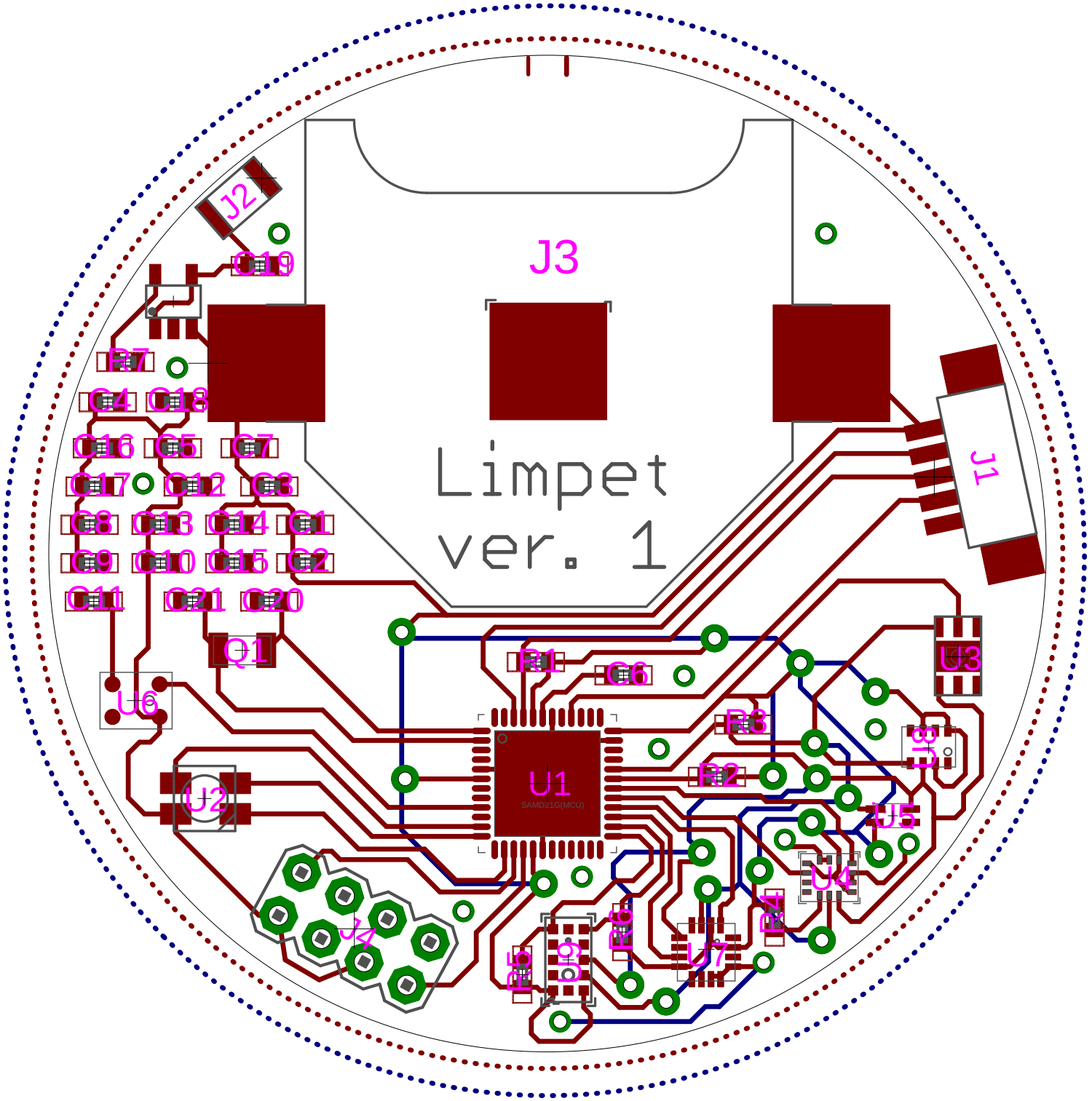
J3
Limpet
ver. 1
J2
J1
C19
R7
C4
C18
C16
C5
C7
C17
C12
C3
C8
C13
C14
C1
C9
C10
C15
C2
C11
C21
C20
Q1
U6
U2
U1
SAMD21G(MCU)
R1
C6
R3
R2
U3
U5
U4
J4
U7

F.5 Power Driver Module Schematic

Software: Eagle PCB Design Software

Authors: Mohammed E. Sayed

Power Driver Module Schematic 

Microcontroller (SAMD21G18)

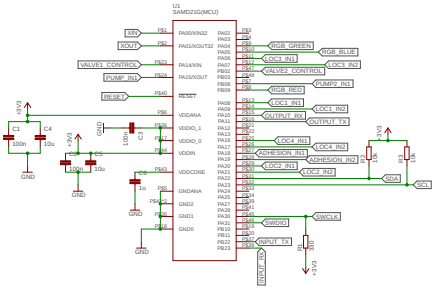

Communication Connector

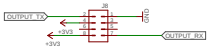

Pump Controller

U6

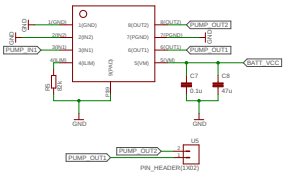

Locomotion Module 2 Controller

U9

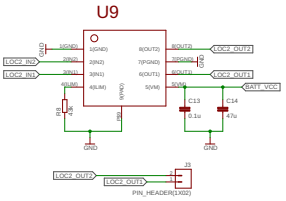

3V3 Regulator

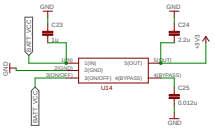

Adhesion Module Controller

U7

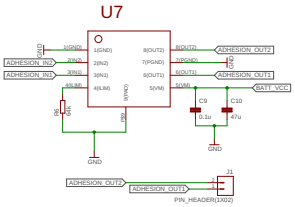

Locomotion Module 3 Controller

U10

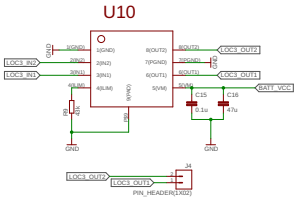

5V Regulator

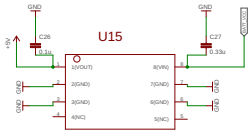

Crystal Oscillator

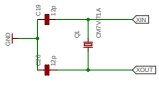

JTAG (Programmer)

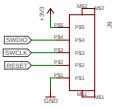

Valve 1 Controller

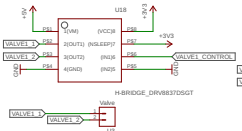

Valve 2 Controller

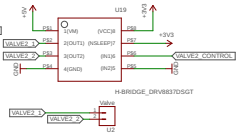

Board Connector

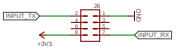

Locomotion Module 1 Controller

U8

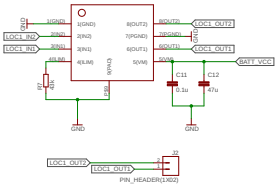

Locomotion Module 4 Controller

U11

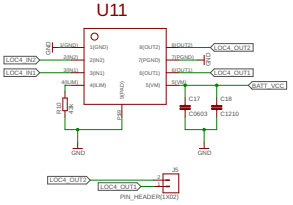

Battery Connector



Pump 2 Controller

U16

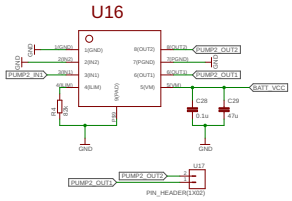

Pressure Sensor

U4



IrDA Transceiver

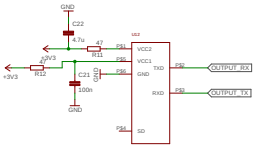

RGB LED

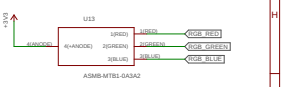

Stokes Research Group	
TITLE: Power Driver PCB	
AUTHOR: Mohammed E. Sayed	REV:
Date: 09/04/2019 15:19	Sheet: 1/1

F.6 Power Driver Module PCB Layout

Software: Eagle PCB Design Software

Authors: Mohammed E. Sayed

Power Driver Module PCB Layout 

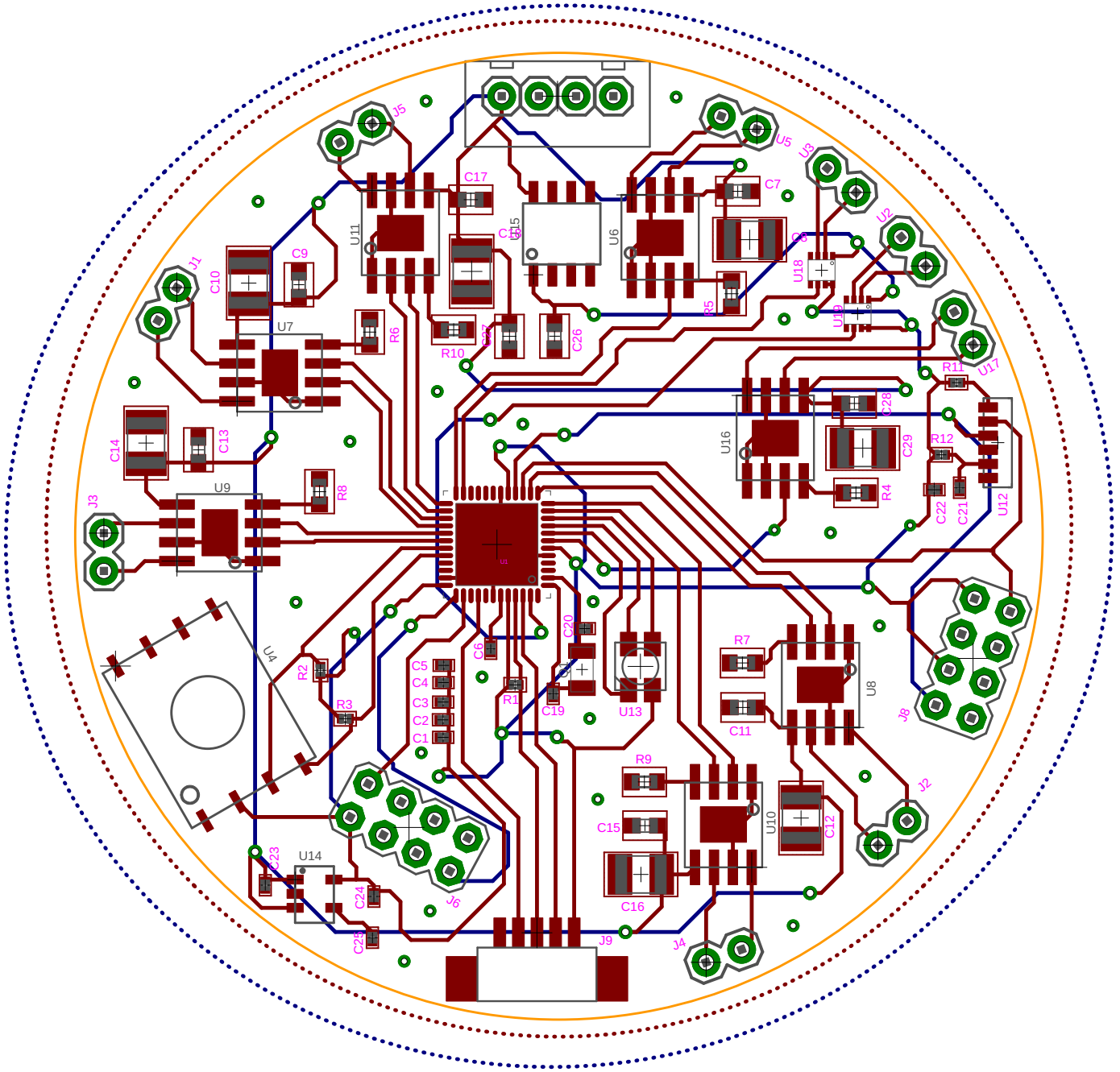
J5
U5
U3
C17
C7
U11
U15
U6
C8
U2
J1
C9
C10
U18
U7
R6
R10
C27
C26
R5
U19
R11
U17
C28
C14
C13
U16
C29
R12
U9
R8
R4
C22
C21
U12
J3
U1
C20
U4
R2
C6
R7
C5
C4
C3
C2
C1
R1
C19
U13
U8
R3
C11
J8
R9
J2
C15
U10
C12
U14
C23
C24
J6
C16
C25
J9
J4

Appendix G

Journal: The Limpet: A ROS-Enabled Multi-Sensing Platform for the ORCA Hub

Journal: Sensors

Publisher: MDPI

Section: Sensing in Oil and Gas Applications

Sensors Journal Paper 

sensors

MDPI

Article

The Limpet: A ROS-Enabled Multi-Sensing Platform for the ORCA Hub

Mohammed E. Sayed [1], Markus P. Nemitz [1,†], Simona Aracri [1,†], Alistair C. McConnell [1], Ross M. McKenzie [1,2] and Adam A. Stokes [1,*]

[1] School of Engineering, Institute for Integrated Micro and Nano Systems, The University of Edinburgh, Scottish Microelectronics Centre, Alexander Crum Brown Road, King's Buildings, Edinburgh EH9 3FF, UK; m.mohammed@ed.ac.uk (M.E.S.); m.nemitz@ed.ac.uk (M.P.N.); simona.aracri@ed.ac.uk (S.A.); alistair.mcconnell@ed.ac.uk (A.C.M.); r.m.mckenzie@ed.ac.uk (R.M.M.)

[2] Engineering and Physical Sciences Research Council (EPSRC) Centre for Doctoral Training (CDT) in Robotics and Autonomous Systems, School of Informatics, The University of Edinburgh, Edinburgh EH9 3LJ, UK

* Correspondence: Adam.Stokes@ed.ac.uk; Tel.: +44-131-650-5611

† These authors contributed equally to this work.

Received: 20 August 2018; Accepted: 10 October 2018; Published: 16 October 2018



Abstract: The oil and gas industry faces increasing pressure to remove people from dangerous offshore environments. Robots present a cost-effective and safe method for inspection, repair, and maintenance of topside and marine offshore infrastructure. In this work, we introduce a new multi-sensing platform, the Limpet, which is designed to be low-cost and highly manufacturable, and thus can be deployed in huge collectives for monitoring offshore platforms. The Limpet can be considered an instrument, where in abstract terms, an instrument is a device that transforms a physical variable of interest (measurand) into a form that is suitable for recording (measurement). The Limpet is designed to be part of the ORCA (Offshore Robotics for Certification of Assets) Hub System, which consists of the offshore assets and all the robots (Underwater Autonomous Vehicles, drones, mobile legged robots etc.) interacting with them. The Limpet comprises the sensing aspect of the ORCA Hub System. We integrated the Limpet with Robot Operating System (ROS), which allows it to interact with other robots in the ORCA Hub System. In this work, we demonstrate how the Limpet can be used to achieve real-time condition monitoring for offshore structures, by combining remote sensing with signal-processing techniques. We show an example of this approach for monitoring offshore wind turbines, by designing an experimental setup to mimic a wind turbine using a stepper motor and custom-designed acrylic fan blades. We use the distance sensor, which is a Time-of-Flight sensor, to achieve the monitoring process. We use two different approaches for the condition monitoring process: offline and online classification. We tested the offline classification approach using two different communication techniques: serial and Wi-Fi. We performed the online classification approach using two different communication techniques: LoRa and optical. We train our classifier offline and transfer its parameters to the Limpet for online classification. We simulated and classified four different faults in the operation of wind turbines. We tailored a data processing procedure for the gathered data and trained the Limpet to distinguish among each of the functioning states. The results show successful classification using the online approach, where the processing and analysis of the data is done on-board by the microcontroller. By using online classification, we reduce the information density of our transmissions, which allows us to substitute short-range high-bandwidth communication systems with low-bandwidth long-range communication systems. This work shines light on how robots can perform on-board signal processing and analysis to gain multi-functional sensing capabilities, improve their communication requirements, and monitor the structural health of equipment.

Keywords: communication fail-over; fault diagnosis; Limpet; on-board processing; ORCA Hub; real-time condition monitoring; remote sensing; robots; robot sensing systems; ROS Interface

1. Introduction

1.1. Challenges Facing Offshore Industries

The international offshore energy industry currently faces the challenges of: a fluctuating oil price, significant and expensive decommissioning commitments for old infrastructure, and small margins on the traded commodity price per kWh of offshore renewable energy [1]. Furthermore, the number of people available to work in offshore industries has reduced because graduates are shifting to less hazardous places onshore, and the current workforce is ageing. As the oil and gas requirements increase with the rapid growth of the world's population, advanced technologies will become vital, and the cost of operation of these technologies will significantly rise due to the harsh and inaccessible nature of the environment. There have been several reported accidents and explosions of offshore rigs, with the most widely reported tragedy being the Deep Horizon oil spill in the Gulf of Mexico [2], which triggered the biggest debate from governments, academia, environmentalists and major companies of the oil and gas industry to look for safer ways to inspect, repair and maintain offshore platforms [3].

1.2. Application of Robotics in Offshore Industries

Operators are seeking more cost-effective and safe methods for inspection, repair, and maintenance of their topside and marine offshore infrastructure. Robots are seen as key enablers in this regard. Robots can be deployed in the air, on the rig or in the subsea, where they can be used to remotely monitor pipelines, corrosion, natural gas leaks, equipment conditions and real-time reservoir status. Hence, they can improve health, safety, and environment (HSE) and increase the production and cost efficiency.

1.3. Offshore Robotics for Certification of Assets (ORCA Hub)

The UK Robotics and Artificial Intelligence Hub for Offshore Robotics for Certification of Assets (ORCA Hub) is a 3.5 year EPSRC funded, multi-site project with a vision to use teams of robots and autonomous intelligent systems (AIS) on remote energy platforms to enable cheaper, safer and more efficient working practices [1]. The ORCA Hub brings together top industrial companies (Total, Chevron, BP, and many others) with academia (University of Edinburgh, Heriot-Watt University, University of Oxford, Imperial College London, and University of Liverpool). The long-term vision for the ORCA Hub is an offshore platform that is completely autonomous and being operated and inspected from the shore, which will decrease the number of people working offshore. The ORCA Hub System constitutes the offshore platform, assets, sensors, and the heterogeneous robotic systems (topside, aerial, and marine robots) interacting with the platform as shown by Figure 1. In abstract terms, the proposed system is a sensor network with static nodes (Limpet agents) and mobile nodes (UAVs, drones, legged robots). We used Robot Operating System (ROS) as the software middleware for the proposed system, and, as such, the different nodes within the ORCA Hub System are referred to as 'robots' in this work following the concepts defined in ROS.

The ORCA Hub System provides remote solutions using robotics and Artificial Intelligence (AI) that are readily integratable with existing and future assets and sensors, and that can operate and interact safely in autonomous or semi-autonomous modes in complex and cluttered environments [1]. The ORCA Hub System aims at achieving tasks that are not possible with a single robot due to the complex nature of offshore platforms. It includes many components such as robotic autonomy, mobility, manipulation, sensor processing, autonomous mapping, navigation, multimodal interfaces,

and human-machine collaboration. In this work, we focus on the sensing aspect of the ORCA Hub System. Sensing is a key element to the ORCA Hub System as it is important in asset monitoring, fault detection, mapping, environmental monitoring and helping other robots navigate around the platform.

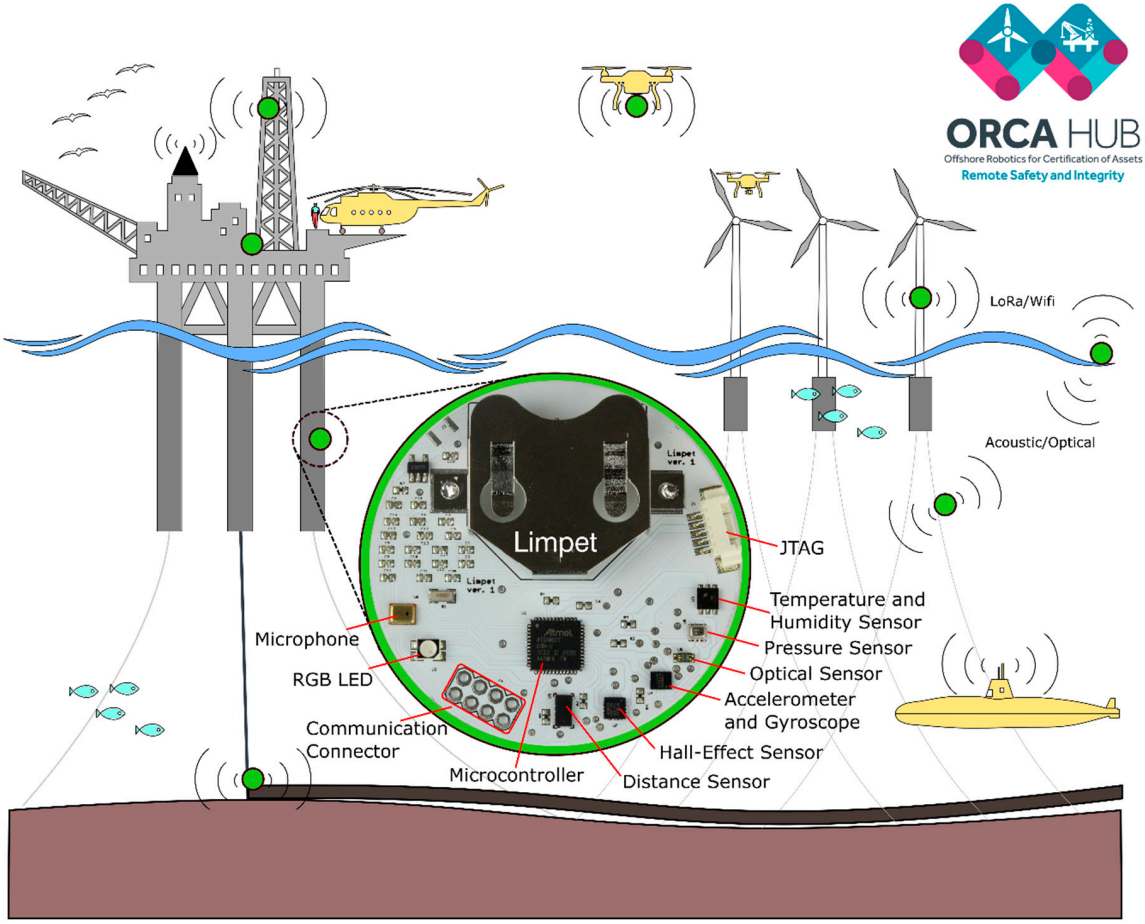

Figure 1. A conceptual overview of the ORCA Hub System. The Limpet, a part of the heterogeneous collection of robots that comprise the system, is shown in detail. The field robots and the Limpet communicate to each other, and the ORCA System controller, using Robot Operating System (ROS).

1.4. Offshore Robotics (Current-State-of-the-Art and Challenges)

Robots on offshore platforms face many challenges. Some of these challenges include the absence of protection against saltwater spray and direct sunlight, harsh weather conditions involving rain, hail and high speed winds, extreme ambient temperature, high humidity levels, and dangerous atmospheric conditions resulting from gases, which can be explosive, toxic and corrosive [4]. For a robot to be suitable for operation on offshore platforms, there are some requirements regarding hardware, software, and communication. Some of the hardware requirements for offshore robots include making the electronics suitable for harsh environments and equipping the robot with highly reliable sensors to perceive its surroundings [4]. An example of the standards that an offshore robot must comply with is the ATEX directive 2014/34/EU (Appareils destinés à être utilisés en ATmosphères EXplosibles) in the European Union, DSEAR (The Dangerous Substances and Explosive Atmospheres Regulations of 2002) in Britain, and HAZLOC (Hazardous locations) in the United States of America. These standards cover any piece of equipment that is intended to be used in a potentially explosive atmosphere. Offshore robots also have requirements for software development including the ability to control the robot from remote locations, ease of programming new inspection and manipulation tasks without the use of experts, and the capability to alert remote operators when sensor values detected are abnormal [4].

Communication requirements mainly includes the ability to communicate and transmit data to a remote control station or to neighboring systems. As a result, of the harsh offshore conditions, remote sensing is becoming extremely valuable. Recent advances in the Internet of Things (IoT) and the cloud computing model provide support for remote sensing [5].

Currently, the majority of offshore robotics are used for subsea tasks, such as mapping of the seabed and inspecting underwater equipment and pipelines using AUVs and ROVs [6–12]. However, offshore robots for topside operations have started to gain the interest of researchers in recent years. Bengel et al. [13] were the first to demonstrate the application of robots for inspection and maintenance tasks in offshore platforms with their work on the MIMROex inspection robot. The Sensabot [14], which is developed by the National Robotics Engineering Center, is a tele-operated offshore inspection robot designed to withstand extreme weather conditions and harsh environment. Kyrkjebo et al. [15] developed the SINTEF Topside Robotic System, which can enable operators to control and monitor processes on the platform from onshore. Another robotic system developed by Galassi et al. [16] for offshore inspection and monitoring of offshore platforms is DORIS. DORIS moves through a rail and carries different sensors, where it can process the sensor data or store it for future analysis. The sensors can identify abnormalities such as intrudes in restricted areas, smoke, fire, liquid and gas leakages [16]. The robot has an embedded manipulator that allows it to take samples and read instruments. Walloid, which is a 4-arm quasistatic robot designed for offshore platform topside automation developed by Moghaddam et al. [17], is capable of climbing walls of different materials. In 2009, Bengel et al. [18] developed another mobile offshore inspection robot equipped with a robotic arm, a camera and several application sensors such as a microphone, gas sensor and fire sensor. The robotic prototype can autonomously execute pre-programmed inspection tasks in automatic mode.

1.5. Fault Detection and Condition Monitoring Systems

A potential application for robots on offshore platforms is fault detection and condition monitoring systems. Condition monitoring techniques help describe types of faults that can occur to a system, and the observable signs generated by these faults. Offshore implementation of fault detection and condition monitoring is challenging due to the complexity of remote sensing, data collection, data processing and data analysis. Condition monitoring systems play an important role in reducing maintenance and operational costs in offshore structures and, therefore, real-time condition monitoring and fault detection is essential [19,20].

In this work, we show a use case of condition monitoring for offshore wind turbines. However, the approach presented here is applicable to other offshore structures in oil and gas platforms such as rotating machinery, gears valves and cooling fans. Different techniques for condition monitoring of wind turbines have been proposed in the literature [21–26]. Some of these techniques for fault diagnosis of wind turbines are based on piezoelectric impact sensors [27], acoustic emission sensors [28], fiber Bragg grating sensor system [29,30], piezoceramic and impedance sensing [31,32]. However, real-time condition monitoring of wind turbines and fault detection has not been studied in detail, due to the harsh environments surrounding wind turbines, which makes experimental research challenging. Our work introduces a novel method to achieve real-time condition monitoring and fault detection for offshore wind turbines by combining signal-processing methods with remote sensing. The reliability of the monitoring system is enhanced by conducting all the data processing and analysis on the microcontroller, and transmitting data using high-range low-bandwidth communication systems only in the event of the presence of a fault.

1.6. The Limpet

In this work, we introduce our new multi-sensing platform, the Limpet, which is low-cost and designed for manufacturability. Our system is inspired by patella vulgate [33], commonly known as Limpet, which is an aquatic snail with a conical shell that lives on rocks on land or in the sea. It has a strong shell that protects it from the external environment and predators, and it can adhere to

surfaces for long periods of time. The patella vulgata has an optic vesicle at the end of its tentacles that provides sensory function, and allows it to sense light and darkness levels [33]. We developed our bio-inspired system, the Limpet, for inspection and monitoring of offshore energy platforms. We embedded permanent magnets in the protective housing of the Limpet to enable it to attach to metallic surfaces. The protective housing acts as a shell that can protect the circuitry from the harsh offshore weather conditions. We can also integrate the Limpet with the ROS. The integration of the Limpet with ROS is essential, as it allows the Limpet to communicate with other robots that constitute the ORCA Hub system. The Limpet is designed to be one part (sensing) of the larger ORCA Hub System, where the system aims at realizing complex tasks that would not be possible with a single robot system.

We show how the Limpet is modelled as an instrument of sensing and measurement in Section 2.1. We discuss the design of the Limpet and how we integrate it with ROS in Sections 2.2 and 2.3, respectively. We include a detailed description of the experimental setup we designed to conduct all our experiments in Section 3.1. We describe the offline and online classification of faults using the Limpet and the signal-processing components involved in these classifications in Sections 3.2 and 3.3, respectively. We give an overview of the different communication strategies involved in this work and how we managed to achieve each strategy in Section 3.4. We give an overview of the signal processing and analysis tools used in this work in Section 3.5. We demonstrate and discuss the results of the experiments conducted in Section 4. We discuss how our approach can be applied to other sensors and other faults in Sections 5.1 and 5.2, respectively. We compare on-board computation to offline computation in Section 5.3. We describe the different parameters that affect our measurements and explain how we try to reduce them in Section 5.4.

2. Design and Fabrication of the Limpet

2.1. Instrument Model

The instrument model [34] is a simple generalized model accepted by the sensors community to describe an instrument or a measuring device. In abstract terms, an instrument is a device that transforms a physical variable of interest (measurand) into a form that is suitable for recording (measurement) as shown by Figure 2A. An example of a basic instrument is a ruler. In this case, the measurand is the length of some object, and the measurement is the number of units (meters, inches, etc.) that represents the length.

The measurand (physical process) is represented by an observable physical measurement variable (X). There is a wide range of physical measurement variables. Common physical measurement variables include: force, temperature, humidity, acceleration, velocity, pressure, frequency, time, length, capacitance, resistance, etc. It is important to know that the physical measurement variable (X) does not necessarily have to be the measurand but can simply be related to the measurand. For example, the mass of an object is often measured by the process of weighing. In this case, the measurand is the mass but the physical measurement variable is the downward force the mass exerts in the Earth's gravitational field. Another example is vibration detection. A robot can detect the measurand vibration by measuring force or by relating the measurand to another physical measurement variable such as acceleration. Both implementations will allow the detection of vibration; however, the accelerometer is much cheaper than the force sensor. There are also other situations where a single measurement variable contains information about multiple measurands. We refer to this capability as multi-functional sensing. One example is Infrared (IR) light. IR light has been used by robots for proximity measurements and communication with other robots [35]. Receiving signals from an IR transmitter requires sensors, such as photodiodes that transduce IR light into electric signals. Therefore, communication using IR light can be considered a sensing task. Another example is the use of the magnetic flux density from a single hall-effect sensor to detect whether the robot had a successful movement, collision or rotation measurands [36].

The key element of the instrument model is the sensor. The function of the sensor is to convert the physical measurement variable X into a signal variable S. Signal variables can be manipulated in a transmission system, such as an electrical or mechanical circuit, which means that they can be transmitted to an output device that is remote from the sensor. In our work, we use this property to be able to transmit the signal variable to a remote device using different communication or transmission systems. Typical signal variables include voltage displacement, current, force, frequency, light, pressure, etc. The output from the sensor is transmitted to a display or recording device, and the observed output is known as the measurement (M).

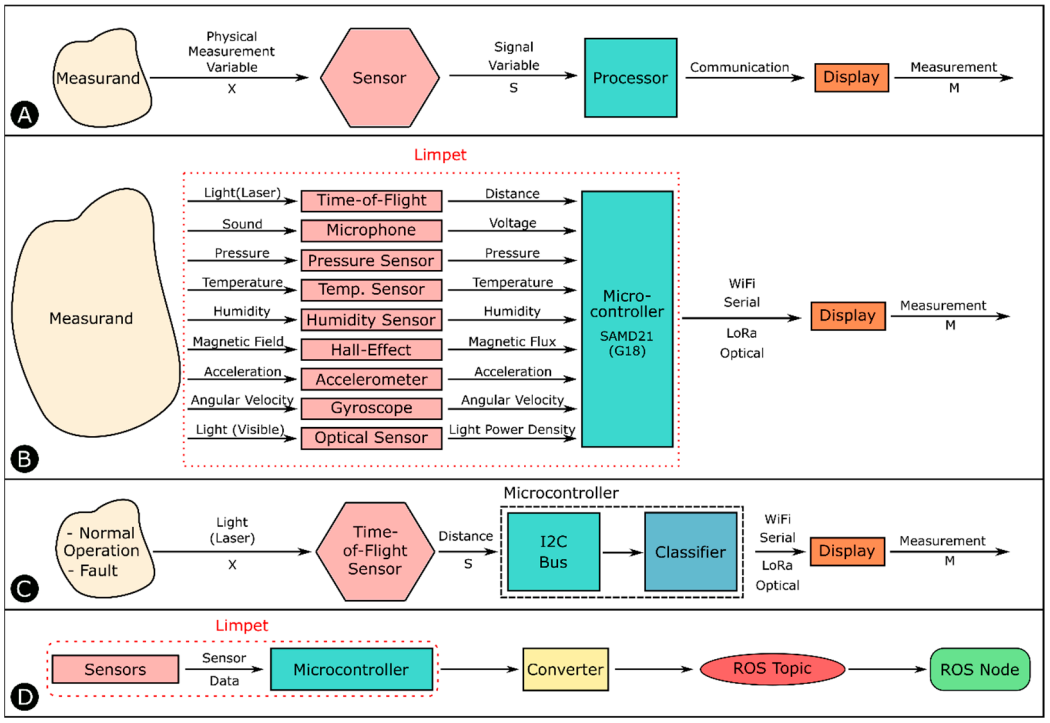

Figure 2. (**A**) Instrument model. (**B**) The Limpet system overview showing the nine sensing modalities and their corresponding signal variables. The Limpet can use several communication strategies to transmit the signal variables. (**C**) Instrument model for the Limpet for distance-based fault detection. We detect normal operation or fault measurands by using a time-of-flight sensor that converts the time of arrival of the reflected light into a distance measurement. (**D**) Architecture of the Limpet interface with ROS.

2.2. Design of the Limpet

2.2.1. System Design

We equipped the Limpet with nine exteroceptive sensing modalities. The sensors incorporated in the Limpet are temperature, pressure, humidity, optical, distance, sound, magnetic field, accelerometer, and gyroscope. We conducted a literature survey to understand what parameters are relevant to offshore environments and monitoring of offshore structures and chose the sensors accordingly. We also got input from the industrial partners involved in the ORCA Hub project on the parameters that are interesting to monitor for the offshore platforms. These discussions influenced the choice of sensing modalities on the Limpet system. The main purpose of the Limpet is to monitor the offshore assets and the environmental conditions surrounding them. The Limpet can be modelled as an instrument, where each of its sensors converts a physical measurement variable into a corresponding signal variable as shown by Figure 2B. The signal variables are fed to the on-board microcontroller, which can then transmit the signal variable using one of several communication systems. In this work, we give one example of the multi-functional capabilities of the Limpet. Table 1 describes how the

physical measurement from each sensor on the Limpet can be related to different measurands on offshore platforms. The table is based on the instrument model described in Figure 2A. It gives an example of a few potential measurands, and not all the measurands possible with each sensor, and it gives an overview of the multi-functionality that can be achieved with each sensor on the Limpet.

Table 1. The different physical measurements from each sensor on the Limpet and their relation to different possible measurands.

Sensor	Physical Measurement Variable	Signal Variable	Measurands
Accelerometer	Acceleration	Acceleration	Inclination, Collision, Vibration, Free-Fall Detection, Movement Acceleration
Gyroscope	Angular Velocity	Angular Velocity	Tilt Detection, Orientation
Temperature	Temperature	Temperature	Ambient Temperature, Over-heating, Fire Detection
Humidity	Humidity	Humidity	Relative Humidity
Microphone	Sound	Voltage	Speech Recognition, Noise Cancellation, Audible Fault Detection
Pressure	Pressure	Pressure	Ambient Pressure
Hall-Effect	Magnetic Field	Magnetic Flux Density	Locating Pipelines, Corrosion Detection
Optical	Light (Visible)	Distance	Ambient Light Intensity, Local Communication, Color Detection
Distance (Time-of-Flight)	Light (Laser)	Distance	Fault Detection, Proximity, Collision Detection, Object Identification

In this work, we demonstrate fault detection in equipment, specifically in wind turbines. We achieve the fault detection using a distance sensor, which is a Time-of-Flight (ToF) sensor. Not only does the distance sensor achieve condition monitoring and fault detection remotely, it gives an extra parameter, distance, which can be extremely useful in different applications (e.g., blade deflection monitoring), or when integrating it with other robots. The approach we used requires a sensor that is capable of remotely detecting the mechanical rotation of the wind turbine. For example, this approach can be performed using a magnetic sensor to measure magnetic reluctance. However, using a magnetic sensor would require the blades to be metallic. An accelerometer could also be used, by attaching it to the blade to monitor the speed and vibration, but the number of faults that can be detected are limited. A combination of a photodiode and phototransistor is another way to achieve fault detection in wind turbines, but it requires a complex setup and would only give indication of one parameter, which is absence of blade.

Figure 2C indicates the instrument model for the Limpet as considered in this work. The measurands normal operation and fault can be related to the physical measurement variable light. We use the distance sensor on the Limpet, which converts the physical measurement variable light to a signal variable distance, which is fed into the microcontroller's I^2C bus. We use the microcontroller to process the sensor data on-board and check them against a classifier. We use the distance measurements to classify if the machine is operating normally, or if there is a fault in the machine hindering its performance. The Limpet can send the data to a PC using one of several different communication systems. We can then use spectral analysis on the data to further reduce the information density and classify the type of fault detected.

The primary communication method of the Limpet is Wi-Fi. The Limpet uses Wi-Fi to transmit its data to a PC. We incorporated an ESP8266, which is a System-on-a-Chip (SOC) Wi-Fi module with integrated TCP/IP protocol stack capable of giving any microcontroller access to the Wi-Fi network, on the Limpet. We use Mosquitto [37], which implements a messaging protocol known as Message Queuing Telemetry Transport (MQTT), to send the data wirelessly from the Limpet to the PC. MQTT is

a light-weight publish/subscribe messaging protocol used for remote communication. The received data can then be plotted in a real-time basis using MATLAB or saved on the PC and processed later.

We designed the Limpet to have robust communication. We can use multiple communication methods with the Limpet, including serial, Wi-Fi, LoRa and optical communication. LoRa is a digital wireless data communication technology that enables long-range transmission with low power consumption [38]. LoRa technology is provided by the LoRa Alliance, which is a non-profit association of more than 500 member companies that are developing and promoting LoRaWAN open standard for IoT. We achieve optical communication with a combination of the RGB LED and the optical sensor on the Limpet. Wi-Fi and serial communication do not allow agent-to-agent communication, unlike LoRa and optical communication. We incorporated a communication fail-over mechanism on the Limpet. If the primary communication method (Wi-Fi) fails for any reason, the functions of the Wi-Fi are assumed by a secondary communication module, which makes the system more fault-tolerant and robust in communication and data transmission.

The Limpet has an on-board programming port (JTAG). We programmed the Limpet using a SEGGER J-Link programmer together with a JTAG Adapter (Olimex ARM-JTAG-20-10). We programmed it in C/C++ using Atmel Studio 7. We used the standard Universal Asynchronous Receiver-Transmitter (UART) protocol for communication. The UART protocol uses a high idle line, which is pulled low at the start of a message.

Cost and functionality were the most important factors that we considered when designing the Limpets. Our rationale behind the system design was to keep the costs as low as possible without sacrificing functionality. The Limpet has a diameter of 50 mm, a height of 7 mm and weighs 17 g with, and 10 g without, the battery. We designed the Limpets to have a size and weight ideal for ease of fabrication, manufacturing, and assembly. The total cost of electronic components used in the design of the Limpet is about £22.

2.2.2. Electrical Design

The Limpet consists of a single two-layer Printed Circuit Board (PCB) and a detachable Li-Ion coin cell battery. We designed a fully integrated PCB incorporating a low–power microcontroller (ATSAMD21G18A), RGB LED (LTST-N683EGBW), battery holder (BK-877) for a rechargeable Li-ion battery (LIR2477), charging IC (MCP73812T), charger connector, programming port [JTAG] (Molex 532610571), and a communication connector as shown by Figure 1. The PCB includes several exteroceptive sensors, which are: Temperature and Humidity Sensor (Si7006), IMU [Accelerometer and Gyroscope] Sensor (LSM6DS3), Optical Sensor (VEML6040), Sound Sensor (SPU0414HR5H-SB), 3-Axis Magnetic Sensor (MLX90393), Pressure Sensor (BMP280), Distance Sensor (VL53L0). Figure S1 shows the PCB schematic. The communication connector is connected to UART of the microcontroller. Therefore, we can use this connector to connect the Limpet to different communication systems. We designed the Limpet to use a single PCB for control, communication, and sensing.

The sensors on the Limpet, except for the microphone, are controlled by the microcontroller through the I^2C bus. The microphone is an omnidirectional Micro-Electro-Mechanical System (MEMS) sensor, with an analogue output and a frequency range of 100 Hz to 10 KHz. In this work, we use the distance sensor for fault detection. The distance sensor on the Limpet is the smallest range sensor on the market today. It is a ToF laser-ranging module that can measure sub-mm distances for a range between 0 and 2.2 m. We also demonstrate the use of the optical sensor for local communication between two Limpets.

The Limpet could be used in a wide variety of areas, which leads to a wide range of temperatures that the components must be tolerant too. The datasheets of the sensors used show that they can be used in a wide range of temperatures. We designed the Limpet for the North Atlantic region which has a water temperature range of between 6 °C and 17 °C. This temperature range was within the allowed range of all the components used on the Limpet. The sensors used on the Limpet also have a wide humidity range. Some of the sensors used are splash resistant such as the IMU, hall-effect,

and optical sensors. If we were to deploy the Limpet for field tests, it would require encapsulation to ensure resistance to extreme temperature and humidity conditions and saltwater spray. As noted in Section 1.4, the casing would have to comply with the regulations used in the specific area it would be deployed in.

We power the Limpet by a rechargeable 3.6 V 160 mAh lithium-ion coin cell battery. We can recharge the battery using a 6Vdc plug-in power supply. We included header pins on the PCB for connecting the power supply to recharge the battery. The Limpet has a battery life @160 mAh of 0.87 to 1600 h. We calculated the minimum battery life by assuming the Limpet has all the sensors, RGB LED, microcontroller and Wi-Fi communication continuously on. The Limpet will consume approximately 182.9 mA (ESP8266 consumes 135 mA, RGB LED consumes 20 mA, sensors consume 20.9 mA, microcontroller consumes 7 mA), which allows for a battery life of about 0.87 h or 52.2 min. We calculated the maximum battery life by assuming the Limpet is in sleep mode, where it consumes an average current of 0.1 mA. In this mode, the battery life of the Limpet can reach about 1600 h or 67 days. In the application presented in this work, the Limpet battery life is expected to last an average of 20 h if it is used for continuous monitoring. If we program the Limpet to sample once every hour, the battery life can go up to an average of 120 h.

2.2.3. Mechanical Design

We designed the PCB of the Limpet using Eagle PCB Design Software and fabricated them on double-sided Cu-FR4-Cu 0.1 mm boards using an external company called Minnitron Ltd. (Kent, UK). We purchased all electronic components from RS Components and Digi-key Electronics. We soldered the components on the PCB using a reflow soldering process. In this process, we cut solder paste stencils from vinyl using a Laser Cutter (Epilog Laser Fusion 32).

We fabricated the protective housing from an optically clear, semi-rigid polyurethane resin. We developed the housing by casting the resin in a 3D printed mold. We did not cover the surfaces of the sensors by resin to keep them exposed to the external physical measurement variables. A picture of the encapsulated Limpet and the mold can be found in Figures S2 and S3.

We designed the Limpet explicitly for manufacturability; it consists of a single PCB and therefore mass manufacture is a simple case of placing a batch order with a PCB foundry. The PCB consists of surface mount components, except for the communication connector, and can be autonomously populated with pick-and-place machines at the point of manufacture. Systems that are made of a single PCB with mostly surface components allow for scaling up to huge collectives of agents easily without sacrificing functionality [39]. Assembly of one Limpet takes seconds as it is a matter of only connecting the coin cell battery. Once the battery is connected, there is no need to remove the battery from the Limpet again as it can be charged on-board. As a result, of the Limpet being highly manufacturable and easy to assemble, it is easy to mass-produce Limpet agents and deploy them in huge collectives.

2.3. ROS Interface

We can interface the Limpet with ROS, and the architecture of this interface is shown by Figure 2D. The sensor data are fed into the microcontroller, and the microcontroller then sends out the data to a converter. The converter is a custom-written python script on the remote PC, which receives the data from the Limpet through one of the communication strategies (Wi-Fi/LoRa/serial) and converts this data into a ROS protocol. We can publish this data to a ROS topic, and any ROS node can subscribe to that topic to read the sensor data. The different sensors on the Limpet have different physical measurement variables. When these measurement variables are fed into the microcontroller, it adds a label to the data to differentiate data from the different sensors (e.g., distance, temperature, pressure, etc.). The data are published to the relative ROS topic based on this label as shown by the overview in Figure S4. ROS nodes can subscribe to relevant topics to gain access to the sensor data. Interfacing the Limpet with ROS enables it to interact with other robots in the ORCA System that are running ROS, where the interaction between them can result in a more complex and useful behavior. Figure S5

depicts the results from integrating the Limpet with ROS. It shows a screenshot of the data published to the distance ROS Topic, and a graph of the distance measurement from the ROS Topic during normal operation of the fan.

3. Experimental Design

The work presented here focuses on the sensing capabilities of the Limpet. In this work, we use the ToF sensor to demonstrate how distance measurements can be used to detect faults in the operating conditions of machines or equipment. We show how a measurement variable can be indirectly related to the measurand and demonstrate an example of how the Limpet could be used for condition monitoring. The approach presented in this work can used for monitoring different offshore structures. This section discusses the design of the experiments that we used to demonstrate the capabilities of a single Limpet in fault detection and condition monitoring.

3.1. Design of the Distance-Based Fault Detection Experimental Setup

The experimental setup consists of a platform containing the Limpet and a custom-designed fan with four blades rotating in front of the Limpet as shown by Figure 3A. We designed the fan blades by cutting a pattern out of an acrylic sheet using a laser cutter. We attached the fan blades to a stepper motor to achieve rotation. We used the fan to mimic a small wind turbine. We placed the fan 85 mm from the Limpet. We use the ToF sensor on the Limpet to measure distance to the fan blades as they are rotate. We controlled the speed of rotation of the fan by controlling the speed of rotation of the stepper motor. When a blade passes in front of the Limpet, the blade is intercepted by the ToF sensor, and a distance measurement is recorded. We programed the Limpet to interpret the absence of a blade as a zero measurement. Figure 3B shows a schematic of how the distance measurement was determined for the fan for normal operating conditions. It shows the distance profile, which depicts the distance measurement for each blade passage in front of the Limpet. The frequency of detection of the fan blades is 1.25 Hz under normal conditions. The fan has four blades, and each blade corresponds to a peak on the graph. In our case, the zero value represents the absence of a blade in front of the Limpet. We recorded the distance profile over a period of 3.2 s, which corresponds to the frequency of rotation of the fan. The difference in width between the peaks is due to the error in detection of the edges of the blade, which is discussed further in Section 5.4.

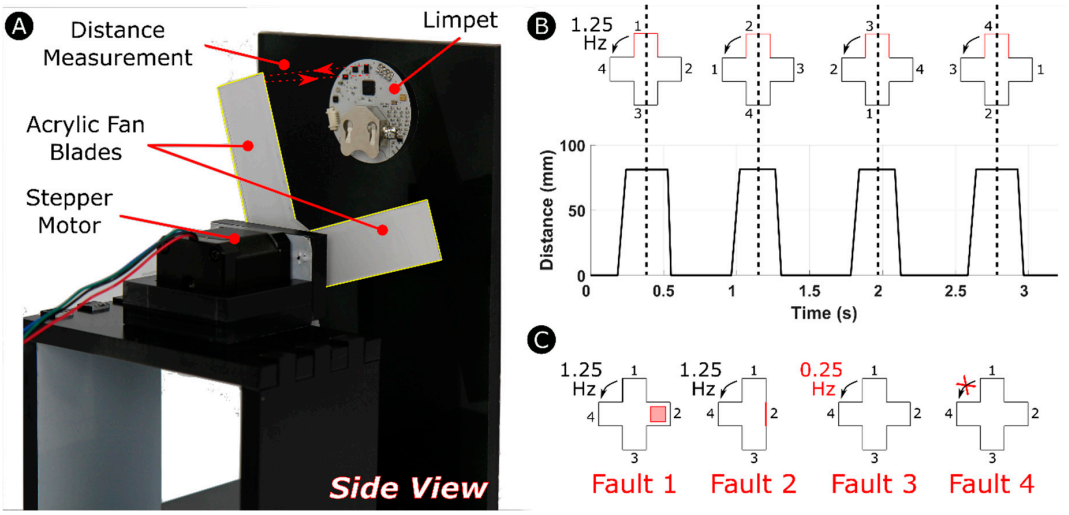

Figure 3. (**A**) Experimental setup for distance-based fault detection. We fixed the Limpet in place and used the fan to mimic a small wind turbine. (**B**) Schematic of the fan and distance profile for normal operation mode. Each peak corresponds to one of the four fan blades detected. (**C**) Schematic of the faults introduced to the system.

To evaluate the capability of distance-based fault detection using the Limpet, we divided the work into two parts: offline classification and online classification of faults. We tested the offline classification approach using two different communication techniques: serial and Wi-Fi. We performed the online classification approach using two different communication techniques: LoRa and optical. We conducted five experiments for each of the four communication systems. We conducted each of the five experiments separately for each communication system. We conducted all the experiments under normal laboratory conditions. We designed one of the five experiments to be normal operation of the fan. In the other four experiments, we introduce a fault to the system and check if the Limpet is capable of detecting this fault. Thus, we tested the detection of the fault using both approaches (offline and online classification). The faults introduced to the system are listed below and a schematic of these faults are shown by Figure 3C.

- **Fault 1:** We attach an object of 15 mm thickness to one of the four blades.
- **Fault 2:** We remove one of the four blades of the fan.
- **Fault 3:** We reduce the frequency of detection of a fan blade from 1.25 Hz to 0.25 Hz.
- **Fault 4:** We immobilize the rotation of the fan for a certain period during its normal operation.

3.2. Design of the Offline Classification Experiments

Figure 4A gives an overview of the components included in the offline classification process of the system. First, we conduct the distance measurement experiment with the Limpet and record the data (distance measurement, timestamp). We transmit the data from the Limpet to the PC in a real-time manner using a high-bandwidth communication system such as serial or Wi-Fi communication. Since there is no memory limitation, as the data are not stored on the microcontroller in the offline classification approach, we recorded the sensor data over a period of 300 s. We then process the data on the PC using MATLAB. We apply a Median Absolute Deviation (MAD) algorithm to remove any outliers from the dataset. We then apply a low-pass filter (simple moving average) to the data to remove the white noise. We also down-sample the data after application of the low-pass filter. In the presence of a fault, given this processed dataset, we apply spectral analysis to classify the type of fault. This offline classification process is used as a learning basis for online classification on the Limpet.

To test for other faults, we conducted two additional experiments using Wi-Fi and serial communication (offline classification); these were: sampling at a rate lower than the Nyquist Frequency, and immobilizing the fan twice during the 300 s measurement period.

When we conducted the experiments for Wi-Fi and serial communication on normal operation of the fan, we calculated the average and standard deviation of the distance measurements recorded over a period of ten min. We used these values as learning values for the microcontroller when performing the online classification process.

3.3. Design of the Online Classification Experiments

Figure 4B gives an overview of the online classification process. In the online classification approach, the Limpet does all the processing and analysis on-board, and then takes an autonomous decision based on the classification result. The Limpet starts sampling the distance to the fan using the ToF sensor. The Limpet stores several distance measurements into its memory (120 measurements). The Limpet processes the data, by first removing any outliers from the sensor data. The data are then down-sampled according to the down-sampling frequency to accord with the limitations of the microcontroller on the Limpet. The Limpet classifies the dataset using a sliding window algorithm. The sliding window algorithm is used to process data streams, where the input is presented as a sequence of items, and the function of interest is computed over a fixed-size window in the stream [40,41]. The Limpet detects the first rising edge and the fourth falling edge and calculates the period between them. This period is checked against the frequency of normal operation stored in the microcontroller's memory. The distance measurements are also compared to the average value

and standard deviation of normal operation, which were stored in the microcontroller after training the classifier offline.

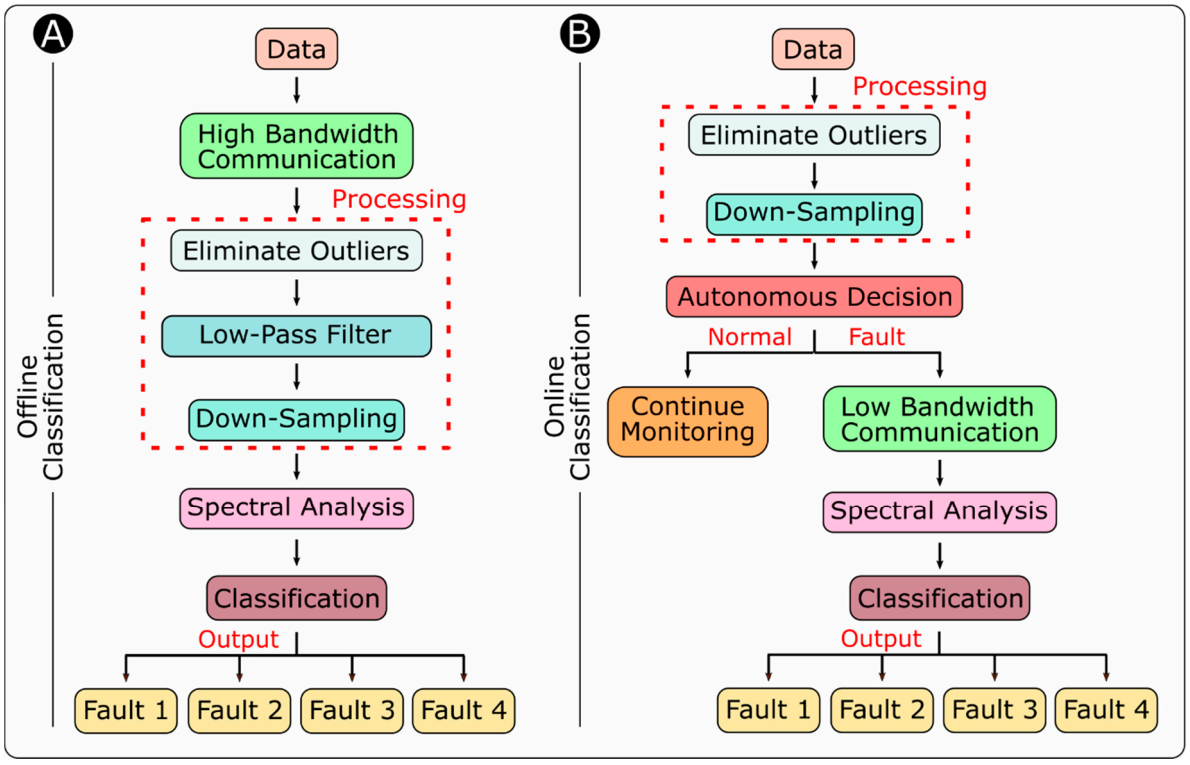

Figure 4. Overview of the signal-processing components for (**A**) Offline Classification and (**B**) Online Classification.

According to the offline training of the classifier, the distance measurement for each blade must fall within a range of average ± standard deviation. The parameters of the class representations (average, standard deviation, time period) were trained offline and do not change during operation. These parameters are stored on the Read-Only Memory (ROM) of the microcontroller. The amount of ROM used depends mainly on the number of points (120) in the dataset and their size (distance is 8-bit, time is 16-bit, distance index is 8-bit). After the Limpet checks the dataset for the presence of any faults, it makes an autonomous decision based on the result of the classification. Autonomy is the ability of a system to make its own decision and to act on its own without external intervention [42]. Within autonomy, there are many variations concerning where and how decisions are made, and actions are invoked. An automatic system carries out several fixed and prescribed activities, where there may be options, but they are fixed in advance and follow a rigid cycle [42]. An adaptive system uses feedback from the environment to improve its performance [42]. A completely autonomous system makes decisions based on the system's view of the situation at the time of decision and its current view of the environment [42]. Decisions made by completely autonomous systems mimic human-level decisions.

Since the Limpet carries out several prescribed activities or checks during online classification, it can be considered an automatic system. If the dataset is within the specified range and frequency, the Limpet continues monitoring the system, but if the dataset fails any of the checks, the Limpet classifies the measurements as faulty operation. The Limpet then transmits the processed data using low-bandwidth communication systems such as LoRa and optical communication to the PC, where spectral analysis is performed to classify the fault detected. For optical communication, we placed another Limpet in front of the Limpet that is part of the distance-based fault detection

experimental setup. We aligned the second Limpet such that it does not block the distance sensor of the first Limpet, but at the same time with its optical sensor aligned with the RGB LED of the first Limpet.

3.4. Overview of the Communication

In this work, we use four different communication methods (Wi-Fi, serial, LoRa, optical) to transmit the sensor data from the Limpet to the PC. Figure S6 gives an overview of the communication strategies involved in this work and how they are achieved. For serial and Wi-Fi communication, the communication bandwidth is high, and we can send the sensor data from the Limpet continuously in real time to the PC. We can then analyze the data on the PC using analysis tools such as MATLAB. In this regard, the Limpet is only making a measurement and transmitting it instantly to the PC without doing any processing on the data, which means serial and Wi-Fi communication are not computationally demanding on the Limpet. We transmit the data from the Limpet over Wi-Fi using the ESP8266, and serially using SparkFun's FTDI Basic Breakout-3.3 V, which is a serial to USB convertor.

LoRaWAN is a new wide area network (WAN) technology that allows for long-range communication, but with a limited bandwidth. Low power WAN combines robust modulation and low data rate to achieve long-range communication. LoRaWAN is one of the most successful tools in low power WAN technologies. It is a network stack rooted in the LoRa physical layer. LoRaWAN features a low data rate (a maximum of 27 kb/s with spreading factor 7 and 500 kHz channel) and long-range communication (2–5 km in urban areas and 15 km in suburban areas). There is a tradeoff between the spreading factor (SF) and communication range in LoRa. The higher the SF, which means the slower transmission, the longer the communication. Depending on the spreading factor used (7 to 12), LoRaWAN data rate ranges from 0.3 kb/s to 27 kb/s [43]. LoRa has a much lower communication bandwidth than serial and Wi-Fi communication. Thus, when we use LoRa technology with the Limpet for communication, the limited bandwidth limits the ability to send the sensor data continuously in real time to the PC. Therefore, if the dataset is large, processing and analysis of the data need to be done before transmission to allow for only small amounts of data to be transmitted. This on-board processing and analysis approach requires higher computational power than serial and Wi-Fi communication. We used the LoPy, which is a MicroPython enabled Wi-Fi, Bluetooth and LoRa development board, to gain access to the LoRa network. The LoPy transmits the data from the Limpet to The Things Network, which is a network that uses LoRaWAN to allow for devices to talk to the Internet without 3G or Wi-Fi.

Optical communication has the lowest bandwidth among the four communication strategies. The processing and analysis also need to be done before the transmission of data. In our case, we transmitted data using the on-board RGB LED. We transmit the data by pulse-width modulating (PWM) the LED to different levels, where each level corresponds to a number from 0 to 9. We pulse-width modulate the RGB LED from 0 to 255 in steps of 25, which allows for ten different intensity levels corresponding to each of the numbers (0 to 9). We used the different LED colors to correspond to different measurements such as time, distance, and index of measurement. We can use the other LED colors for other sensor measurements such as pressure, temperature, etc. Our optical communication protocol transmits a single digit at a time. Therefore, we programmed the Limpet to divide all the measurements into single digits and transmit the digits one after the other. The intensity of the transmission (PWM level) and the LED color (measurement type) allows us to reconstruct the transmitted data from the RGB LED.

We used the optical sensor on the Limpet as a receiver. We used it to read the light intensity (indication of the transmitted number) and color power density (indication of measurement type), to interpret the data transmitted using the RGB LED. Before we conducted any experiments using optical communication, we ran a calibration experiment for the light sensor using two Limpets. We PWM the RGB LED from 0 to 255 in steps of 25 on one Limpet. We pulse-width modulated the red LED first, followed by the green LED and the blue LED. We used the optical sensor on the other Limpet to read the light intensity and color power density of the LED for each PWM level, and the results are

shown by Figure S7. Plots of the power density versus time for different numbers transmitted using the red, green, and blue LED are shown by Figures S8, S9 and S10, respectively. We used the results of this calibration experiment as a reference to interpret the data transmitted by the Limpet during the experiments with optical communication. We used the red LED to send distance measurements, the green LED to send timestamps, and the blue LED to send the index of the data point. Figure S11 shows a plot of the power density from each LED for each of the numbers transmitted. The data transfer speed achieved in our optical communication lies in the range of 6 bps to 53 bps.

There is an extra step involved in the optical communication, which is the calibration and use of the optical sensor to infer the transmitted data. This extra step implies a higher computational power demand for optical communication. Optical communication cannot be used for long-range communication, where the optical communication range in this work is in the region of a few 10 s of cm. The optical communication range is a function of both the intensity of the RGB LED and the sensitivity of the optical sensor. Optical communication can be useful for communication with underwater vehicles, as it was discovered that blue light can propagate in seawater better than other frequencies of light [44]. In field conditions, the amount of ambient light intensity has an impact on the optical communication system.

3.5. Overview of the Classification Techniques

3.5.1. Signal-Processing Tools

To eliminate outliers from the input signal, we applied a MAD Algorithm. MAD algorithm is used in statistics as a measure of the variability of a sample of quantitative data. MAD is more resilient to outliers in a dataset than the standard deviation. Since MAD is more robust to scale estimates than the standard deviation, it is better applied to data that is not normally distributed, which is the case in this work. Consider an input signal $x = [x_1, \ldots, x_N]$ with length N. MAD is defined as the median of the absolute deviations from the dataset's median, and is given by

$$\text{MAD} = median\ (|x_i - \ median(x)|),\ i = 1, \ldots, N \tag{1}$$

In this work, we considered data points greater than 3 median absolute deviations from the dataset's median as outliers, and we replaced them with the mean of the dataset.

After the successful elimination of outliers, we applied a low-pass filter to the data to remove white noise from the input signal. We applied a simple moving average filter to smooth out the short-term fluctuations in the data. In this stage, we calculate the mean from an equal number of data points on either side of a central value. By doing so, the variations in the mean are associated with the variations in the data instead of being shifted in time.

For an input signal x and a positive integer k, the moving average y is computed by sliding a window of length k along x. Each element of y is the local mean of the corresponding values in the input signal x within the window, and signal y is the same size as x. For a signal x made up of k scalar observations, the mean μ and the moving average y are given by

$$u = \frac{1}{k} \sum_{i=1}^{k} x_i \tag{2}$$

$$y = [u_i, \ldots, u_N] \tag{3}$$

We have chosen a moving average sliding window of size (k = 8) as the distance sensor records 8 data points for each blade passage in front of the sensor due to sampling frequency we set for the sensor (25 Hz). The time series after application of the low-pass filter varies within a narrower range as compared to the signal after elimination of outliers.

After elimination of outliers and noise, we reduce the input signal $x = [x_1, \ldots, x_N]$ with length N in size to accord with the computational limitations of the microcontroller. We reduce the length of the signal (N) by dividing the signal into L parts, each of which contains $M = \frac{N}{L}$ measurements. The value of each element x'_M of the down-sampled signal x' is given by

$$x'_m = \frac{1}{M} \sum_{i=M(l-1)}^{Ml} x_i,\ l = 1, \ldots, L \tag{4}$$

In this work, we down-sample the full distance measurement for one complete fan rotation to 8 measurements (M = 8) corresponding to the four peaks in the distance profile. We conduct the same process on the timestamp and index information sent with the original data. Down-sampling has an impact on the classifier's detection rate. The higher the down-sampling frequency on the input signal, the worse the detection rate becomes. Down-sampling potentially removes important features in the signal that can help the classifier discriminate between signals constituting normal operation or a fault. However, the higher the down-sampling frequency, the lower the memory required to store values of the cumulative distance matrix. Memory reductions are useful since it lowers the requirements for our low-cost microcontroller. Therefore, there is a tradeoff between memory reduction and classifier performance. In this work, we were able to achieve good classification performance with suitable memory usage as shown in the Results Section. We determined the down-sampling frequency after conducting multiple experiments for normal operation of the fan and studying the signal for characterizing features in the distance profile. We conducted each experiment for a period of 300 s, during which we recorded 7322 data points. Among the recorded data, 802 data points corresponded to the detection of rising and falling edges, i.e., 401 peaks. Therefore, the down-sampling frequency is calculated to be ~9 (7322/802).

3.5.2. Analysis Tools

After processing the input signal, we use spectral analysis to classify the fault detected. Spectral analysis has been used extensively in literature for fault detection [45,46]. We first apply a fast Fourier Transform (FFT) algorithm to the processed signal, which divides the time signal into its frequency components. These components are single sinusoidal oscillations at different frequencies, where each component has its own phase and amplitude. The FFT algorithm is the Discrete Fourier Transform (DFT) of a sequence. FFT computes the same results as DFT but can do it more quickly. In terms of time complexity, which is described as the amount of time needed to run an algorithm based on its computational complexity and expressed using big O notation, DFT takes **O(N^2)** arithmetical operations, while FFT takes **O(N log N)** arithmetical operations for an input signal with N points. The N-point DFT equation for a finite-duration sequence $x(n)$ is given by

$$X(f) = \sum_{n=1}^{N} x(n) e^{-j\frac{2\pi}{N}(f-1)(n-1)},\ 1 \le f \le N \tag{5}$$

Following the application of the FFT algorithm, we compute the power spectral density function (PSD) of the signal. The PSD shows the variation of power as a function of frequency, which could be used to detect abnormal system behavior. Thus, observing the PSD of the recorded sensor data will enable classifying the fault using a single parameter. The power spectral density for a signal $x(n)$ with N points is given by

$$P(f) = \frac{1}{N} |X(f)|^2 \tag{6}$$

For a periodic rectangular pulse function, the FFT divides the pulse signal into several harmonics (sine waves) to approximate the pulse signal. Adding more sine waves of increasingly higher frequencies improves the approximation of the rapid changes (discontinuity) in the pulse signal. In the frequency domain, a periodic rectangular pulse function results in a sinc() function centered

around the dominant frequency. As the duty cycle or pulse-width of the signal is varied, the sinc() function changes. As the duty cycle is decreased, the width of the of the sinc() function broadens (i.e., it becomes less localized in frequency). Thus, if a function changes rapidly in time, the signal must contain high frequency component to allow for such a rapid change.

4. Results

Distance-Based Fault Detection

Figure 5 depicts the results of the experiments for Wi-Fi (offline classification), LoRa and optical communication (online classification). The results from the experiments we conducted using serial communication (offline classification) were similar to the results from the Wi-Fi experiments. Figure 5 shows the distance profile resulting from each of the four faults introduced to the system. We constructed the distance profile for LoRa and optical communication (dotted lines) from the down-sampled results of the experiments (markers). Every two consecutive points (markers) on the graph represent a single peak or a fan blade. The distance profiles are shown within a period (T) of 3.2 s (corresponding to the frequency of rotation of the fan during normal operation). When a fault is introduced to the fan and stepper motor system, its distance profile looks distinctly different as compared to the distance profile of normal operation. Each fault also possesses a distinctive power spectral density plot as compared to other faults.

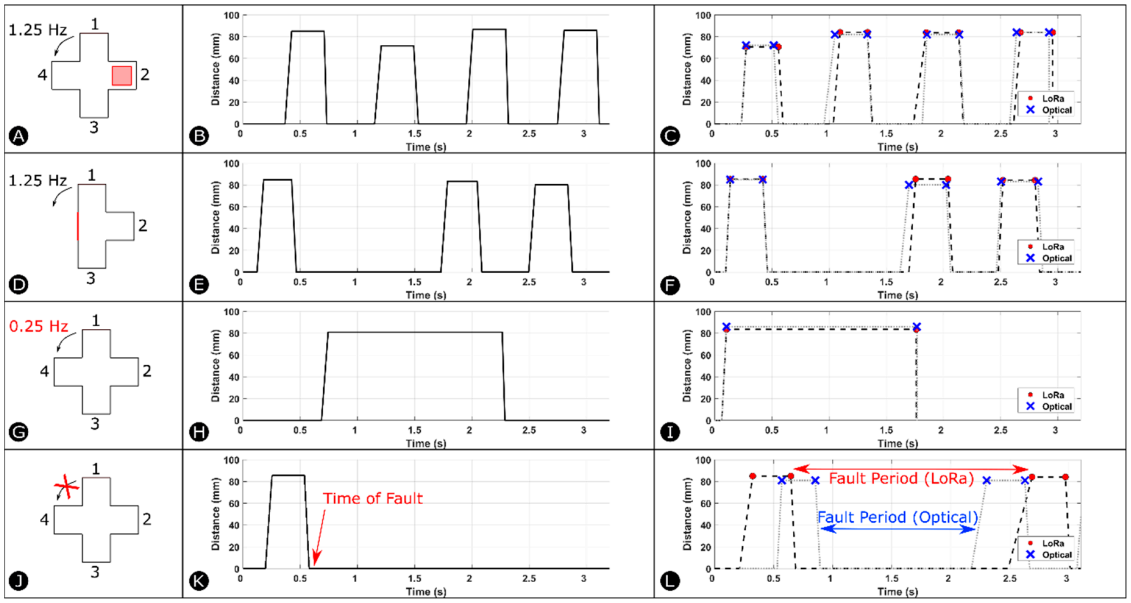

Figure 5. Schematic of (**A**) Fault 1, (**B**) Fault 2, (**C**) Fault 3, (**D**) Fault 4. Distance Profile of Wi-Fi communication experiment for (**E**) Fault 1, (**F**) Fault 2, (**G**) Fault 3, (**H**) Fault 4. Distance Profile of LoRa and optical communication experiments for (**I**) Fault 1, (**J**) Fault 2, (**K**) Fault 3, (**L**) Fault 4.

Figure 5A shows a schematic of Fault 1. Figure 5E shows the distance profile acquired using Wi-Fi communication, and Figure 5I shows the distance profile for LoRa and optical communication, after we introduce Fault 1 to the system. As seen in both Figures, one of the peaks in the distance profile has an amplitude lower than the other peaks as a result of the object attached (extra thickness) to it. Figure 5B shows a schematic of Fault 2. The results for Wi-Fi communication, and LoRa and optical communication are shown by Figure 5F,J, respectively. The results of the three communication systems show that one of the peaks in the distance profile is missing as compared to normal operation. Figure 5C shows a schematic of Fault 3, where we reduced the frequency of detection of the fan blade to 0.25 Hz. The distance profile for Wi-Fi, LoRa and optical communication shows only a single peak within 3.2s as shown by Figure 5G,K, as the frequency of blade detection is lower than normal

operation. Figure 5D shows a schematic of Fault 4, where we immobilized the fan during its normal operation. The distance profile for Wi-Fi communication shows the absence of any peaks after the introduction of the fault to the system as shown by Figure 5H. Figure 5L shows the down-sampled results and the distance profile for LoRa and optical communication. The graph shows that two of the peaks are missing corresponding to where the fault is present. The fault period is slightly different for LoRa and optical communication experiments. The fault duration is also different for LoRa and optical communication as compared to Wi-Fi communication. For Wi-Fi communication, we recorded the distance measurements for a long period, and, thus the fault was introduced over a larger time window.

The raw sensor data we recorded from the Limpet during each of the five experiments using Wi-Fi communication are shown by Figure S12. The data after elimination of outliers, application of a low-pass filter, and down-sampled results can be found in Figures S13, S14 and S15, respectively. For serial communication, the raw sensor data, data after elimination of outliers, results of the low-pass filter and down-sampled results can be found in Figures S16, S17, S18 and S19, respectively. Figure S20 shows the distance profile from the serial communication experiments within a period (T) of 3.2 s.

Figure 6 shows the power spectral density plots for each of the four faults. We obtained these results from the experiments using Wi-Fi communication. During normal operation, the spectral analysis gives a single output signal (peak) at a frequency of 1.3 Hz as shown by Figure S21, which corresponds to the dominating harmonic frequency that best describes the signal in the time domain. In the time domain, the distance profile is a periodic rectangular pulse signal, therefore, in the frequency domain the harmonics exist around the same frequency. This collection of similar harmonics results in a peak in the frequency domain that is distributed around the dominating frequency. Figure 6A shows the power spectral density graph resulting from the introduction of Fault 1 to the system. There is a large peak at a frequency of 1.3 Hz, and three smaller peaks at frequencies of 0.35 Hz, 0.7 Hz and 1 Hz. The peak at 1.3 Hz represents the dominant harmonic in the time domain signal, while the other peaks are present because of the harmonics introduced to the system due to the presence of Fault 1. The PSD divides the signal into its single sinusoidal components at the different frequencies. In this case, the time domain signal is more complex, since the pulse signal is not periodic anymore. Therefore, the harmonics in this signal are more complex and introduce lower frequency components to describe the signal in the frequency domain. Figure 6B shows the power spectral density graph resulting from the introduction of Fault 2 to the system. There is a large peak at a frequency of 1.3 Hz, and three smaller peaks at frequencies of 0.35 Hz, 0.7 Hz and 1.1 Hz. The peak at 1.3 Hz represents the dominating harmonic in the time domain signal, while the other peaks are present because of the harmonics introduced to the system due to the presence of Fault 2. The absence of the peak in the time domain signal introduces new harmonics in the spectrum represented by the lower frequency components. This power spectrum is distinct from the power spectrum of Fault 1, as the power in the lower frequency harmonics is higher due to the larger difference in the amplitude between the peaks in the distance profile. The spectral analysis of Fault 3 shown by Figure 6C depicts a single large peak at a frequency of 0.25 Hz, which corresponds to the lower frequency of detection of the fan blades. The signal is a periodic rectangular pulse signal, and thus, results in a spectral plot with a peak around the dominant frequency. Since the duty cycle is increased as compared to normal operation, the peak is narrower and larger in the frequency domain. The spectral analysis of Fault 4 shown by Figure 6D depicts a large peak at a frequency of 1.3 Hz representing the normal fan operation and another peak at a lower frequency representing the break of rotation of the fan. The amplitude of the peaks depends on the length of the jam introduced to the system. Figure S22 shows the power spectral density plots from the Wi-Fi experiments plotted against time.

Figures S23 and S24 show the power spectral density plots from the serial communication experiments plotted against frequency and time, respectively. The results of the spectral analysis on the serial communication experiments are similar to the spectral analysis of the Wi-Fi experiments. Figure S25 shows the optical sensor data, which is obtained from the transmission of measurements using the RGB LED during the optical communication experiments, and which shows the

down-sampled results from the experiments and the spectral analysis performed on the data for both LoRa communication and optical communication after we introduce the four faults to the system. The frequency of the peaks in the power spectral density graph of LoRa and optical communication experiments are similar to those of serial and Wi-Fi experiments. The only difference is the amount of power or energy in each peak. The power in the sinusoidal oscillations is much higher in serial and Wi-Fi experiments as the results were recorded over a larger period. The results from the two additional experiments (jamming the fan twice and a lower rate of sampling) we conducted using Wi-Fi communication and serial communication are shown by Figures S26–S29.

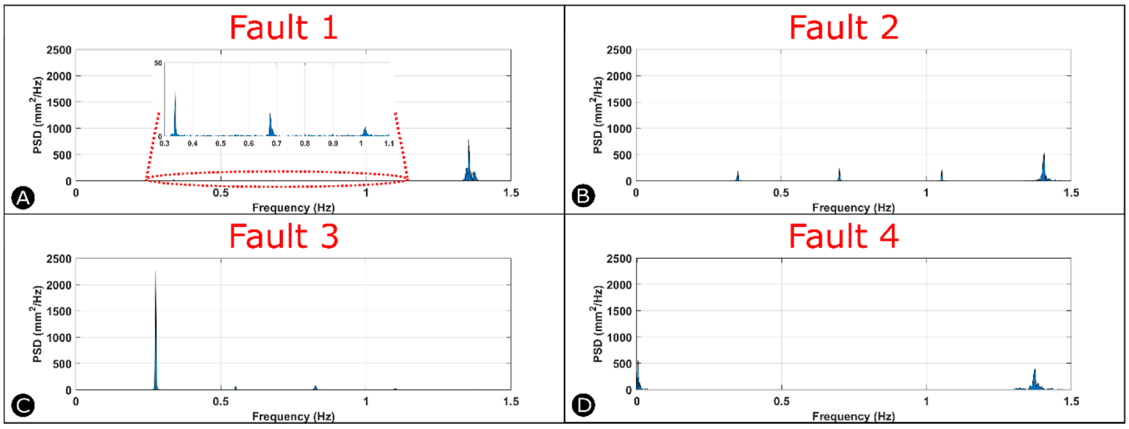

Figure 6. Spectral analysis of the data after introducing (**A**) Fault 1, (**B**) Fault 2, (**C**) Fault 3 and (**D**) Fault 4 to the system.

5. Discussion

In this paper, we combined ideas from the fields of offshore robotics, remote sensing and signal processing and designed a system to demonstrate that low-cost hardware can be a useful tool to monitor offshore energy platforms. The signal-processing techniques we used in this work were explicitly adapted to operate on our low-cost hardware. We introduced a down-sampling method to reduce the time taken to run the classifier and to decrease the size required in memory on the microcontroller. We performed a sliding window algorithm on-board as a rapid test of the system's functionality. The same approach can be applied to other faults and other sensors, which we discuss in Sections 5.1 and 5.2, respectively. We discuss, in Section 5.3, the advantages and disadvantages of on-board computation as compared to offline computation. We discuss possible interferences to our measurements, and how we reduce them, in Section 5.4.

5.1. Applicability to Other Faults

The classification approach we adopted is a generic solution to condition monitoring and not specific to the faults we introduced to the system in this work. Our method depends on the change in normal operation conditions of equipment, where the change is associated with the presence of a fault in the system. We trained our classifier offline with conditions related to normal operation of the fan. The offline classification determines multiple parameters for normal operation including average distance to the fan blades, standard deviation of distance measurements, and frequency of rotation of the fan. These parameters are then transferred to the Limpet for online classification and do not change during operation. During the online classification, the Limpet checks the parameters of the class representations (average, standard deviation, period) to the parameters of normal operation stored on the microcontroller's memory. If any of the parameters fails the check, the Limpet classifies the measurement as a faulty operation. Thus, any fault that changes the normal operation conditions of the fan, which in turn results in a change in these parameters, will be detected and flagged as faulty operation by the Limpet. We believe that our method is applicable to several different fault types.

We test our approach by introducing four specific faults to the system to determine if the Limpet can detect these faults. Examples of other faults that could be detected for wind turbines or rotating machinery are bending of blades, change of distance between blades, or undesirable vibration or oscillation of blades.

5.2. Applicability to Other Sensors

In this work, we have shown how we can use a single sensor to monitor the state of equipment by measuring several measurands, as well as how we can process the data and analyze it on-board to improve communication requirements. Our method is dependent on distinct measurement profiles associated with each measurand. The method also depends on time-varying measurements. We think that this approach is applicable to other sensors and systems, if the measurement profile is (i) a time-varying measurement and (ii) distinctly different from other profiles. Thus, this method could be used by other sensors to identify different types of faults with equipment or to monitor different parameters on offshore platforms. It could also be easily adapted to other low-cost systems.

5.3. On-Board Data Processing vs. Offline Processing

By processing and analyzing data on-board using the microcontroller, we can improve the communication and power requirements of the system while still being able to perform same analysis. Data transmission does not need to occur continuously, but only in the case of a particular event. This design allows us to use communication systems with high transmission distance, but low bandwidth (such as LoRaWAN), and increase battery life of systems as the data transmission link is the most power-consuming part of a system. Offline processing involves continuously transmitting data and analyzing it to detect the presence of any faults. This approach is time-consuming, reduces battery life and requires high communication bandwidth, which lowers transmission distance. The major drawback of our approach is that low-cost hardware is limited in its computational power. As such, we are restricted to the types of algorithms that could be used on the system.

5.4. Mitigation of Interferences

By processing and analyzing data on-board using the microcontroller, we can improve the communication and power requirements of the system while still being able to perform same analysis. Data transmission does not need to occur continuously, but only in the case of a particular event. This design allows us to use communication systems with high transmission distance, but low bandwidth (such as LoRaWAN), and increase battery life of systems as the data transmission link is the most power-consuming part of a system. Offline processing involves continuously transmitting data and analyzing it to detect the presence of any faults. This approach is time-consuming, reduces battery life and requires high communication bandwidth, which lowers transmission distance. The major drawback of our approach is that low-cost hardware is limited in its computational power. As such, we are restricted to the types of algorithms that could be used on the system. Several parameters impact the sensor measurements and interferes with the classification process. Five of these parameters are: (1) Displacement of the Limpet during the experiment, which will affect the distance measurement to the equipment and will impact the classification process; (2) Change in the distance between the Limpet and the fan for the different set of experiments; (3) The target surface used for the fan blades. Different target surfaces will reflect light (laser) differently and might thus affect the distance measurements; (4) Presence of objects behind the experimental setup or fan. The distance sensor can detect distances up to 2 m, and the presence of any objects behind the fan would affect the distance measurement level (zero) for absence of fan blades; and (5) The Field of View (FoV) of the distance sensor, which is the angle at which the receiver on the sensor is sensitive to electromagnetic radiation. The distance sensor has a FoV of 25°, which causes it to detect the edge of the fan blade before the blade center is opposite the sensor. This error results in a larger number of distance measurements versus time as

each blade passes in front of the limpet, and therefore, the blade appears wider than its actual width when observed by the receiver of the sensor.

In our work, we reduce the effect of these parameters on our measurements in five ways: (1) We fixed the Limpet in place on a small wall in front of the fan to reduce any displacement by the Limpet; (2) We fixed the stepper motor in place in the experimental setup to minimize the errors in measurement by having the fan always at the same distance from the Limpet for all the experiments; (3) We used a white acrylic surface for the fan blades, as white targets cause maximum reflectance; (4) We place an acrylic sheet at a distance of 2.5 m behind the fan and setup, which is out of the range of measurement of the distance sensor, and thus ensures the same measurement level for absence of blades; and (5) We compute the moving average of our sensor measurements with a sliding window of size (8) to reduce the effect that the FoV introduces on our measurements.

6. Conclusions

In this work, we introduce a new multi-sensing platform, the Limpet, which is part of the ORCA Hub System. We embedded the Limpet circuitry in a protective housing to protect it from the harsh offshore weather conditions. We have integrated the Limpet with ROS, which allows it to be used with other robots within the ORCA Hub System, where the interaction between different robots results in more complex and useful behavior. We designed the Limpet to be low-cost and highly manufacturable, which enables us to deploy it in huge collectives for inspecting offshore energy platforms. We show how the Limpet could be used for fault detection in wind turbines, by detecting multiple measurands from a single sensor. This demonstrates one of the possible multi-sensing capabilities of the Limpet. We demonstrate this approach using four different communication systems. We also show how we can do the processing and analysis of the data from the sensor on-board using the microcontroller, which can improve our communication requirements. The signal-processing techniques that we used in this paper are generally applicable to time-variant measurements; however, they must be applied to time-varying, distinct, and systematically reoccurring measurements to augment the sensing capabilities of a robot. We train the classifier offline and transfer its parameters to the Limpet for online classification. During online classification, the Limpet takes an autonomous decision of either transmitting the data or continuing the monitoring process based on whether a fault is detected or not. We apply spectral analysis to the data to classify the type of fault detected. This work shines light on how robots can perform on-board signal processing and analysis to gain multi-functional sensing capabilities, improve their communication requirements, and monitor the structural health of equipment.

Supplementary Materials: The following are available online at http://www.mdpi.com/1424-8220/18/10/3487/s1.

Author Contributions: Created the system and is the lead author of the work, M.E.S.; Worked on the introduction literature, experimental design and advised on the development of the classifier, M.P.N.; Worked on the experimental design, introduction literature, classification and analysis and advised on the development of the classifier, S.A.; ROS Interface, A.C.M. and R.M.M.; Lead advisor and primary editor of the manuscript, A.A.S.

Funding: Markus Nemitz gratefully acknowledges support from the CDT in Intelligent Sensing and Measurement (EP/L016753/1), UK. Adam A. Stokes, Simona Aracri and Alistair C. McConnell acknowledge support from the EPSRC ORCA Hub (EP/R026173/1). Ross M. McKenzie acknowledges support from EPSRC via the Robotarium Capital Equipment, and CDT Capital Equipment Grants (EP/L016834/1).

Acknowledgments: The authors thank the members of the Stokes Research Group at The University of Edinburgh and the members of the ORCA Hub project for useful conversations and feedback on this article.

Conflicts of Interest: The authors declare no competing financial interest.

References

1. Hastie, H.; Lohan, K.; Chantler, M.; Robb, D.A.; Ramamoorthy, S.; Petrick, R.; Vijayakumar, S.; Lane, D. The ORCA Hub: Explainable Offshore Robotics through Intelligent Interfaces. In Proceedings of the 13th Annual ACM/IEEE International Conference on Human Robot Interaction, Chicago, IL, USA, 5–8 March 2018.
2. Griggs, J.W. BP Gulf of Mexico oil spill. *Energy Law J.* **2011**, *32*, 57.
3. Shukla, A.; Karki, H. Application of robotics in offshore oil and gas industry—A review Part II. *Robot. Auton. Syst.* **2016**, *75*, 508–524. [CrossRef]
4. Chen, H.; Stavinoha, S.; Walker, M.; Zhang, B.; Fuhlbrigge, T. Opportunities and Challenges of Robotics and Automation in Offshore Oil & Gas Industry. *Intell. Control Autom.* **2014**, *5*, 136–145.
5. Mois, G.; Folea, S.; Sanislav, T. Analysis of Three IoT-Based Wireless Sensors for Environmental Monitoring. *IEEE Trans. Instrum. Meas.* **2017**, *66*, 2056–2064. [CrossRef]
6. Yuh, J.; Lakshmi, R. An intelligent control system for remotely operated vehicles. *IEEE J. Ocean. Eng.* **1993**, *18*, 55–62. [CrossRef]
7. Elvander, J.; Hawkes, G. ROVs and AUVs in support of marine renewable technologies. In Proceedings of the 2012 Oceans, Hampton Roads, VA, USA, 14–19 October 2012; pp. 1–6.
8. Raine, G.A.; Lugg, M.C. *ROV Inspection of Welds—A Reality*; Underwater Intervention: Houston, TX, USA, 1995.
9. Whitcomb, L.L. Underwater robotics: Out of the research laboratory and into the field. In Proceedings of the 2000 IEEE International Conference on Robotics and Automation (ICRA), San Francisco, CA, USA, 24–28 April 2000; Volume 1, pp. 709–716.
10. Bessa, M.S.W. Controlling the dynamic positioning of a ROV. In Proceedings of the Oceans 2003, San Diego, CA, USA, 22–26 September 2003; Volume 2.
11. Hagen, P.E.; Fossum, T.G.; Hansen, R.E. Applications of AUVs with SAS. In Proceedings of the OCEANS 2008, Quebec City, QC, Canada, 15–18 September 2008; pp. 1–4.
12. Costa, M.J.; Goncalves, P.; Martins, A.; Silva, E. Vision-based assisted teleoperation for inspection tasks with a small ROV. In Proceedings of the 2012 Oceans, Hampton Roads, VA, USA, 14–19 October 2012; pp. 1–8.
13. Bengel, M.; Pfeiffer, K. *Mimroex Mobile Maintenance and Inspection Robot for Process Plants*; Fraunhofer Institute for Manufacturing Engineering and Automation IPA: Stuttgart, Germany, 2007.
14. NREC/CMU. Sensabot: A Safe and Cost-Effective Inspection Solution. *J. Pet. Technol.* **2012**, *64*, 32–34. [CrossRef]
15. Kyrkjebo, E.; Liljebäck, P.; Transeth, A.A. A Robotic Concept for Remote Inspection and Maintenance on Oil Platforms. In Proceedings of the ASME 28th International Conference on Ocean, Offshore and Arctic Engineering, Honolulu, HI, USA, 31 May–5 June 2009; pp. 667–674.
16. Galassi, M.; Røyrøy, A.; Carvalho, G.; Freitas, G.; From, P.J.; Costa, R.R.; Lizarralde, F.; Hsu, L.; de Carvalho, G.H.; de Oliveira, J.F. DORIS—A Mobile Robot for Inspection and Monitoring of Offshore Facilities. In Proceedings of the Congresso Brasileiro de Automática, Belo Horizonte, Brazil, 20–24 September 2014.
17. Moghaddam, A.F.; Lange, M.; Mirmotahari, O.; Høvin, M. Novel Mobile Climbing Robot Agent for Offshore Platforms. *Int. J. Mech. Aerosp. Ind. Mechatron. Manuf. Eng.* **2012**, *6*, 1353–1359.
18. Bengel, M.; Pfeiffer, K.; Graf, B.; Bubeck, A.; Verl, A. Mobile robots for offshore inspection and manipulation. In Proceedings of the 2009 IEEE/RSJ International Conference on Intelligent Robots and Systems, St. Louis, MO, USA, 11–15 October 2009; pp. 3317–3322.
19. Nichols, J.M. Structural health monitoring of offshore structures using ambient excitation. *Appl. Ocean Res.* **2003**, *25*, 101–114. [CrossRef]
20. Hillis, A.J.; Courtney, C.R.P. Structural health monitoring of fixed offshore structures using the bicoherence function of ambient vibration measurements. *J. Sound Vib.* **2011**, *330*, 1141–1152. [CrossRef]
21. Yang, W.; Tavner, P.J.; Wilkinson, M.R. Condition monitoring and fault diagnosis of a wind turbine synchronous generator drive train. *IET Renew. Power Gener.* **2009**, *3*, 1–11. [CrossRef]
22. Kryter, R.C.; Haynes, H.D. Condition monitoring of machinery using motor current signature analysis. In Proceedings of the Power Plant Dynamics, Control and Testing Symposium, Knoxville, TN, USA, 15–17 May 1989; Volume 20.

23. Cardoso, A.J.M.; Saraiva, E.S. Computer-aided detection of airgap eccentricity in operating three-phase induction motors by Park's vector approach. *IEEE Trans. Ind. Appl.* **1993**, *29*, 897–901. [CrossRef]
24. Hameed, Z.; Hong, Y.S.; Cho, Y.M.; Ahn, S.H.; Song, C.K. Condition monitoring and fault detection of wind turbines and related algorithms: A review. *Renew. Sustain. Energy Rev.* **2009**, *13*, 1–39. [CrossRef]
25. Lu, B.; Li, Y.; Wu, X.; Yang, Z. A review of recent advances in wind turbine condition monitoring and fault diagnosis. In Proceedings of the 2009 IEEE Power Electronics and Machines in Wind Applications, Lincoln, NE, USA, 24–26 June 2009; pp. 1–7.
26. Shin, S.-H.; Kim, S.; Seo, Y.-H.; Shin, S.-H.; Kim, S.; Seo, Y.-H. Development of a Fault Monitoring Technique for Wind Turbines Using a Hidden Markov Model. *Sensors* **2018**, *18*, 1790. [CrossRef] [PubMed]
27. Yuji, T.; Bouno, T.; Hamada, T. Suggestion of Temporarily for Forecast Diagnosis on Blade of Small Wind Turbine. *IEEJ Trans. Power Energy* **2006**, *126*, 710–711. [CrossRef]
28. Buono, T.; Yuji, T.; Hamada, T.; Hideaki, T. Failure Forecast Diagnosis of Small Wind Turbine using Acoustic Emission Sensor. *KIEE Int. Trans. Electr. Mach. Energy Convers. Syst.* **2005**, *5*, 78–83.
29. Schroeder, K.; Ecke, W.; Apitz, J.; Lembke, E.; Lenschow, G. A fibre Bragg grating sensor system monitors operational load in a wind turbine rotor blade. *Meas. Sci. Technol.* **2006**, *17*, 1167–1172. [CrossRef]
30. Tian, S.; Yang, Z.; Chen, X.; Xie, Y. Damage Detection Based on Static Strain Responses Using FBG in a Wind Turbine Blade. *Sensors* **2015**, *15*, 19992–20005. [CrossRef] [PubMed]
31. Oh, K.-Y.; Park, J.-Y.; Lee, J.-S.; Epureanu, B.I.; Lee, J.-K. A Novel Method and Its Field Tests for Monitoring and Diagnosing Blade Health for Wind Turbines. *IEEE Trans. Instrum. Meas.* **2015**, *64*, 1726–1733. [CrossRef]
32. Ruan, J.; Ho, S.C.M.; Patil, D.; Song, G. Structural health monitoring of wind turbine blade using piezoceremic based active sensing and impedance sensing. In Proceedings of the 11th IEEE International Conference on Networking, Sensing and Control, Miami, FL, USA, 7–9 April 2014; pp. 661–666.
33. Marshall, D.J.; Hodgson, A.N. Structure of the Cephalic Tentacles of Some Species of Prosobranch Limpet (Patellidae and Fissurellidae). *J. Molluscan Stud.* **1990**, *56*, 415–424. [CrossRef]
34. Webster, J.G. *The Measurement, Instrumentation and Sensors Handbook*, 1st ed.; CRC Press LLC: Boca Raton, FL, USA, 1999; Volume 104.
35. Farrow, N.; Klingner, J.; Reishus, D.; Correll, N. Miniature six-channel range and bearing system: Algorithm, analysis and experimental validation. In Proceedings of the 2014 IEEE International Conference on Robotics and Automation (ICRA), Hong Kong, China, 31 May–7 June 2014; pp. 6180–6185.
36. Nemitz, M.P.; Stokes, A.A.; Marcotte, R.J.; Sayed, M.E.; Ferrer, G.; Hero, A.O.; Olson, E.B. Multi-Functional Sensing for Swarm Robots Using Time Sequence Classification: HoverBot, an Example. *Front. Robot. AI* **2018**, *5*, 55. [CrossRef]
37. Light, R.A. Mosquitto: Server and client implementation of the MQTT protocol. *J. Open Source Softw.* **2017**, *2*, 265. [CrossRef]
38. Sornin, N.; Luis, M.; Eirich, T.; Kramp, T.; Hersent, O. *LoRaWAN Specification*; LoRa Alliance: Fremont, CA, USA, 2015.
39. Nemitz, M.P.; Sayed, M.E.; Mamish, J.; Ferrer, G.; Teng, L.; McKenzie, R.M.; Hero, A.O.; Olson, E.; Stokes, A.A. HoverBots: Precise Locomotion Using Robots That Are Designed for Manufacturability. *Front. Robot. AI* **2017**, *4*, 55. [CrossRef]
40. Wang, J.; Wang, R.; Li, T. Analysis of the data streams trend in sensor network based on sliding window. In Proceedings of the 2012 IEEE International Conference on Computer Science and Automation Engineering (CSAE), Zhangjiajie, China, 25–27 May 2012; pp. 224–228.
41. Vafaeipour, M.; Rahbari, O.; Rosen, M.A.; Fazelpour, F.; Ansarirad, P. Application of sliding window technique for prediction of wind velocity time series. *Int. J. Energy Environ. Eng.* **2014**, *5*, 105. [CrossRef]
42. Dennis, L.A.; Fisher, M.; Aitken, J.M.; Veres, S.M.; Gao, Y.; Shaukat, A.; Burroughes, G. Reconfigurable Autonomy. *KI Künstliche Intelligenz* **2014**, *28*, 199–207. [CrossRef]
43. Adelantado, F.; Vilajosana, X.; Tuset-Peiro, P.; Martinez, B.; Melia-Segui, J.; Watteyne, T. Understanding the Limits of LoRaWAN. *IEEE Commun. Mag.* **2017**, *55*, 34–40. [CrossRef]
44. Jin, M.H.-C.; Pierce, J.M.; Lambiotte, J.C.; Fite, J.D.; Marshall, J.S.; Huntley, M.A. Underwater Free-Space Optical Power Transfer: An Enabling Technology for Remote Underwater Intervention. In Proceedings of the Offshore Technology Conference, Houston, TX, USA, 30 April–3 May 2018.

45. Benbouzid, M.E.H. A review of induction motors signature analysis as a medium for faults detection. *IEEE Trans. Ind. Electron.* **2000**, *47*, 984–993. [CrossRef]
46. Pineda-Sanchez, M.; Puche-Panadero, R.; Martinez-Roman, J.; Sapena-Bano, A.; Riera-Guasp, M.; Perez-Cruz, J. Partial Inductance Model of Induction Machines for Fault Diagnosis. *Sensors* **2018**, *18*, 2340. [CrossRef] [PubMed]



© 2018 by the authors. Licensee MDPI, Basel, Switzerland. This article is an open access article distributed under the terms and conditions of the Creative Commons Attribution (CC BY) license (http://creativecommons.org/licenses/by/4.0/).

Appendix H

Journal: Linbots: Soft Modular Robots Utilising Voice Coils

Journal: Soft Robotics

Publisher: Mary Ann Liebert, Inc.

Soft Robotics Journal Paper

SOFT ROBOTICS
Volume 6, Number 2, 2019
Mary Ann Liebert, Inc.
DOI: 10.1089/soro.2018.0058

SoRo
Soft Robotics

ORIGINAL ARTICLE

Linbots: Soft Modular Robots Utilizing Voice Coils

Ross M. McKenzie,[1,2,*] Mohammed E. Sayed,[1,*] Markus P. Nemitz,[1,3] Brian W. Flynn,[1] and Adam A. Stokes[1]

Abstract

Robots performing automated tasks in uncontrolled environments need to adapt to environmental changes. Through building large collectives of robots, this robust and adaptive behavior can emerge from simple individual rules. These collectives can also be reconfigured, allowing for adaption to new tasks. Larger collectives are more robust and more capable, but the size of existing collectives is limited by the cost of individual units. In this article, we present a soft, modular robot that we have explicitly designed for manufacturability: Linbots. Linbots use multifunctional voice coils to actuate linearly, to produce audio output, and to sense touch. When used in collectives, the Linbots can communicate with neighboring Linbots allowing for isolated behavior as well as the propagation of information throughout a collective. We demonstrate that these collectives of Linbots can perform complex tasks in a scalable distributed manner, and we show transport of objects by collective peristalsis and sorting of objects by a two-dimensional array of Linbots.

Keywords: soft, modular, voice coils, Linbots, robots, soft robotics

Introduction

Large robotic collectives allow for robust behavior

There has been major interest in modular robotic systems over the past years. This interest is due to the hypothesis that multiple low-cost units are more robust than a single, advanced robot.[1,2] Modular robot collectives can be reconfigured for different tasks,[1,3–5] setting them apart from monolithic robots. Collectives of modular robots have greater capability than the sum of their parts.[6] This increased capability allows modular collectives to be used for tasks that are not possible with monolithic robots such as reconfigurable furniture[7] and modeling cell collectives.[8] Although modular actuators can also be combined into a single system for tasks such as controllable surfaces,[9–11] collectives of modular robots have the advantages of reconfigurability and inbuilt sensing and computation.

The capability of a modular robot collective is dependent on the number of units within it.[1] The size of a collective robotic system, however, is often limited by cost, with larger groups sacrificing the functionality of individual robots to keep costs low. Creating low-cost robots with more capabilities is one of the key challenges in collective robotics. In this work, we developed modular, soft robots, demonstrated in Supplementary Video S1 designed for manufacturability and which use multifunctional components to reduce hardware costs.

Multifunctional hardware can lower costs

The use of multifunctional hardware is demonstrated by the Kilobot.[12] The Kilobot is the lowest cost ($\sim$\$15) robot currently available. It uses an actuation mechanism based on cheap vibrational motors. It also uses a single infared radiation (IR) sensor for both proximity sensing and communication. Through pulsing its IR transmitter, a Kilobot is able to communicate with others and by measuring the intensity of

[1]Scottish Microelectronics Centre, School of Engineering, Institute for Integrated Micro and Nano Systems, The University of Edinburgh, Edinburgh, United Kingdom.
[2]EPSRC CDT in Robotics and Autonomous Systems, Edinburgh Centre for Robotics, Edinburgh, United Kingdom.
[3]Department of Computer Science and Engineering, University of Michigan, Ann Arbor, Michigan.
*These authors contributed equally to this work.

© Ross M. McKenzie *et al*. 2018; Published by Mary Ann Liebert, Inc. This Open Access article is distributed under the terms of the Creative Commons License (http://creativecommons.org/licenses/by/4.0), which permits unrestricted use, distribution, and reproduction in any medium, provided the original work is properly cited.

incoming IR communications. It is also capable of detecting how close other Kilobots are to it. This use of a single piece of hardware for multiple functionalities reduces the cost of robots.

Building a robot with an extensible architecture allows extra sensors to be easily added to the robot.[13] This architecture allows the user to define the required abilities of each robot and keeps the cost-to-volume ratio balanced with respect to the task at hand. The base of the robot can then be repurposed for different tasks.

The HoverBot[14] uses a Hall-effect sensor for both odometry and navigation.[15] This swarm robot is made of a single printed circuit board (PCB) with electromagnetic coils and uses an air table with embedded permanent magnets for low-cost locomotion. Absent magnets on the air table create magnetic landmarks that can be detected by the HoverBots. This dual use of a Hall-effect sensor allows the number of required sensors and the cost of each HoverBot to be reduced.

Our Linbot uses a voice coil system for actuation, audio output, sensing, and communication. This voice coil system is based on the Wormbot.[16]

Voice coils for actuation, communication, and sensing

Voice coil systems are electromagnetic systems that are based on the same fundamental principles as loudspeakers; their method of actuation is detailed in Supplementary Figure S1. The voice coil system consists of an actuating electromagnetic coil and a permanent magnet, which are attached together by a soft body that functions as a spring. The electromagnet can repel or attract the permanent magnet and this force stretches or compresses the body of the robot, creating linear motion. The voice coils are hybrid hard/soft systems. Hybrid systems can take advantage of rigid components while still being able to partially conform to their environment.[17]

Voice coils have been shown to be a useful actuation system for soft robotics.[16] The voice coil systems are multifunctional components that demonstrate different behaviors over a range of different control signal frequencies. In addition to actuation capabilities at low frequencies, the voice coils can function as loudspeakers at audible sound frequencies and can be used for communications at higher frequencies.[16] This communication is based on inductive data transmission.[18]

We also utilize the permanent magnets in our voice coil system for sensing. The soft body of the robot deforms when it is actuated or when it is subjected to external force and we measure this deformation by monitoring a three-axis Hall-effect sensor, which responds to the relative position of the permanent magnets that are embedded on the top of the robot. This approach allows us to perform both proprioceptive sensing and tactile sensing.[19]

Building soft modular systems with voice coils

The simple linear action of voice coil systems is similar to the action of myocytes (muscle cells). Myocytes can only perform a simple action, contraction, and respond to simple inputs, signals from a nerve.[20] Many of these simple pairs of myocytes and nerves, placed at different positions and orientations, can produce complex actions such as prehensile movement or skeletal locomotion. Stacking units in this way can produce useful behavior for robotic applications.[21–24] In this article, we provide two examples of stacking: first, peristaltic locomotion, which has been a major interest for soft robotic researchers.[25–28] Second, we rearrange the units used for peristaltic locomotion into a grid to create a peristaltic table that is capable of moving objects over the surface.[29,30] Two-dimensional (2D) matrices of actuators have been created by Kim *et al*.,[9] Stanley *et al*.,[10] and Follmer *et al*.,[11] and these arrays could be adapted to allow a system designer to make a peristaltic table.

In this article, we have combined both computation and sensing into actuators that we arrange in a 2D array to create a fully distributed and modular peristaltic table.

To allow voice coils to function similarly to nerve/myocyte pairs, they need onboard computation to control their behavior. By including this functionality, we have created linear modular robots that can be stacked together. We have developed low-cost robots—Linbots—that can be configured to produce different forms of useful behavior. Our Linbots are capable of communication, actuation, sensing, and proprioception all through their central voice coil system.

Linbot Design

Design of the hardware

Figure 1A shows an individual Linbot unit. The main body of each Linbot is made up of the voice coil system, which includes the following: electromagnetic coils wound around a reel; permanent magnets embedded in a holder; and a spring consisting of connected bent legs resembling a Chinese lantern. A sketch of the Linbot, including its main components, is shown in Supplementary Figure S1. The magnet holder is attached to the spring via a circular, acrylic top layer. The coil reel is attached to the spring via the PCB, which serves as the bottom layer.

The Linbot can be extended or contracted axially from its rest position, depending on the polarity of current applied to the electromagnetic coil in the voice coil system. A sketch of the actuation mechanism is shown in Supplementary Figure S1. The sensing capability of the Linbots is achieved by a combination of a three-axis Hall-effect sensor incorporated in the PCB and the permanent magnets in the voice coil system. The Hall-effect sensor can track the motion of the magnets in three dimensions. This allows the Linbot to function as a tactile sensor since a change in displacement due to the addition or removal of objects on the Linbot can be easily detected.

Design of the voice coil system.

We made the magnet holder, reel, and spring from acetate sheets using kirigami. Kirigami involves cutting a pattern out of the sheets and folding it into the desired configuration, the 2D patterns are shown in Supplementary Figure S2. We use kirigami as it allows our components to be low cost and highly manufacturable.[31] The electromagnetic coils consist of two 12-turn coils used for the transmission circuit, and a larger 200-turn coil used for the actuation and receiver circuit. A circuit diagram of the coils is shown in Supplementary Figure S3. Supplementary Figures S4 and S5 show the block diagram and circuit schematic of the transmission and receiver circuits.

We used permanent neodymium magnets in our voice coil system. The internal components of the voice coil system are shown in Figure 1C. Supplementary Figure S6 shows a labeled picture of the custom-built coil-winding machine used for producing the actuation coils of the Linbots.

Design of the control electronics.

We designed a fully integrated PCB incorporating a transmission circuit, receiver

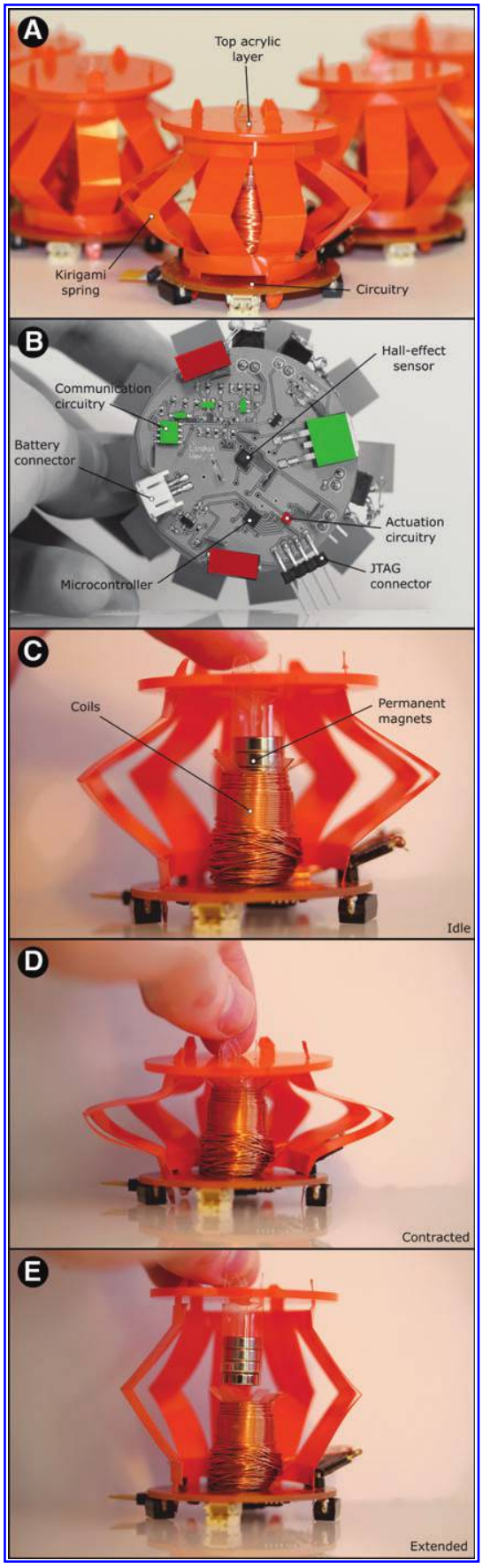

circuit, microcontroller (STM8S), voltage regulator, H-bridge (DRV8837), and Hall-effect sensor (MLX90393) as shown in Figure 1B. The PCB schematic is provided in Supplementary Figure S7. We designed each Linbot to use a single PCB for control, sensing, and communication. The PCB is powered by a 450 mAh 7.4 V lithium polymer battery. Our communication system utilizes electromagnetic induction for data transmission, where the transmission coil generates an alternating magnetic field that induces a voltage in the receiver coil. Further information on the electronic design is detailed in The Electronic Design of the Linbot section of Supplementary Data.

Design of the control software

We wrote the control software in C and used standard peripheral libraries from ST,[32] including I^2C libraries for the Hall-effect sensor and universal asynchronous receiver/transmitter (UART) for communications. The Hall-effect measurements of magnetic field are used to calculate the displacement of the top half of the Linbot from its rest state.

We use the standard UART protocol[33] for magnetic communication to take advantage of the libraries provided by ST. The UART protocol uses a high idle line, which is pulled low at the start of a message. However, with the Linbot system, if two robots have their transmitters switched in, then all communications will be blocked. Therefore, we need our robots to switch their transmitters off when they are not sending any data. This requirement can lead to an extra byte, with a 0 value, being received at the end of each transmission. To avoid the extra bytes affecting the received data, we check for and remove these erroneous bytes.

Experimental Design

Design of the experiments to characterize an individual Linbot

This section discusses the design of the experiments used to demonstrate the capabilities of a single Linbot.

Quantifying output force. To evaluate the output force of the Linbots, we designed a controllable experimental setup with a scale, ruler, and clamp, shown in Figure 2A. Before starting the experiment, we zero the scale with a Linbot, a battery, and a ruler on it. We programmed the Linbot to extend periodically with maximum force. We used a clamp from a retort stand to restrict the height of the Linbot to different relative lengths. Since each of our hand-folded springs has a different rest length, we compare the force to the relative length rather than the absolute length. The relative length is given by the following:

$$x_r = \frac{x}{x_0}, \tag{1}$$

where x_r is the extension, x is the absolute length, and x_0 is the rest length. x_0 is measured before starting the experiment. We

FIG. 1. System overview. **(A)** A side view of a Linbot showing the kirigami spring and top acrylic layer. **(B)** A Linbot PCB. **(C)** A cutaway of a Linbot. The coil interacts with the permanent magnets and either pulls or pushes the kirigami spring. The circuitry is embedded on the *bottom side*. **(D)** A Linbot contracting. **(E)** A Linbot extending. PCB, printed circuit board.

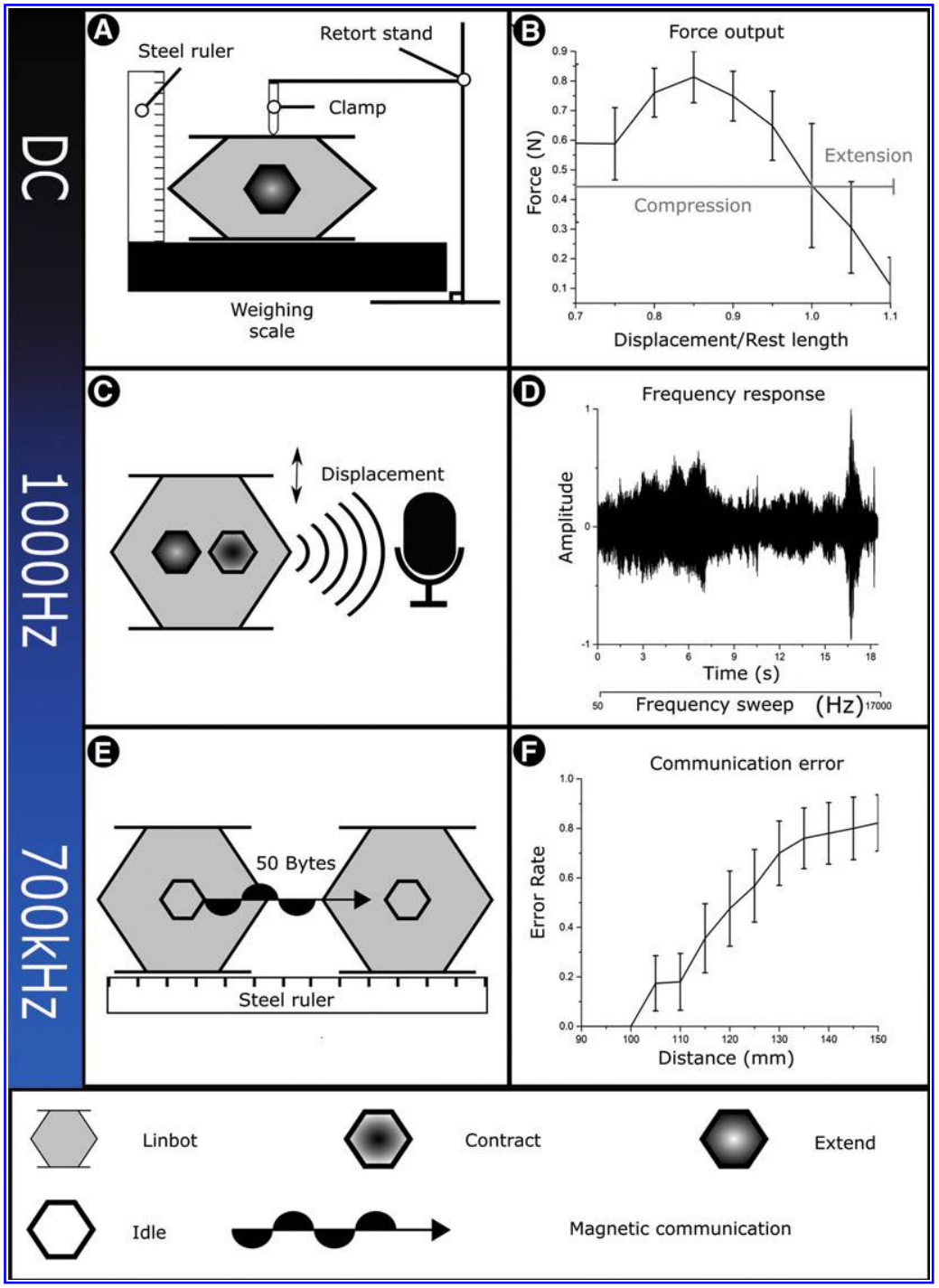

FIG. 2. Frequency-dependent functionality. **(A)** A schematic of our experiment to quantify the force output. This experiment involved control frequencies of hertz or lower. **(B)** The force output of the Linbot against relative length. The force output shown in the figure is a combination of the electromagnetic and spring forces of the voice coil. This shows that the Linbot has the highest force output around its rest length. **(C)** A schematic of our frequency response experiment. This experiment involved control frequencies of tens of hertz up to tens of kilohertz. **(D)** The sound wave produced by the Linbot during the last 18 s of a frequency test, shown in Supplementary Video S3. **(E)** A schematic of our experiment to evaluate the communication between Linbots. This experiment involved control frequencies of hundreds of kilohertz. **(F)** The byte error rate. This shows that the Linbots can communicate without error with up to 100 cm between their centers.

increase the extension in steps of 0.05 from 0.65 to 1.1; these extensions represent the full range of motion for the Linbots. Using relative length will introduce some error to the experiments as the electromagnetic force from the voice coil will depend on absolute length. The measured mass on the scale was used to calculate the force output of the Linbot at each extension. This output force is a combination of the spring force and electromagnetic force.

We repeated the experiment on a sample of five different Linbots as a screening experiment; this sample size allowed us to measure more than half of the available Linbot population (nine in total). We recorded the average force from these experiments and standard deviation at each extension. One repeat of this experiment is shown in Supplementary Video S2.

Frequency response analysis. The primary function of the voice coil system is linear actuation at low frequencies, but can also be used across a wide frequency range to provide audio output or communicate with neighbors. In this experiment, we programmed the microcontroller to vary the coil frequency from 7 Hz to 13.5 kHz. We then recorded sound produced by the Linbot. The experimental setup is depicted in Figure 2C.

To test pulse-width-modulation (PWM) control of the Linbot, we used the microcontroller to provide a PWM signal to the coil. We then observed the effect of changing the duty cycle on the actuation scheme. We first sweep through duty cycles from 0% to 100% and then from 100% to 0%. Next, we step the Linbot between set duty cycles of 10%, 20%, 40%, and 80%. We recorded the experiments using an 18-mp Canon EOS 100D camera and an EF-S 18–55 mm f/3.5–5.6 IS STM lens. We ran this experiment once to demonstrate the capabilities of the Linbots and the output is shown in Supplementary Videos S3 and S4.

Feasibility of tactile sensing. We designed an experiment to demonstrate the tactile sensing capabilities of the Linbot by showing that the Hall-effect sensor can be used to track the movement of the magnets in three dimensions. The Z axis of the Hall-effect sensor can be used to measure force parallel to the direction of motion of a Linbot. The X and Y axes of the sensor can measure the shear force between the two halves of the Linbot. In this experiment, the top half of the Linbot is moved along the positive and negative directions of the X, Y, and Z axes. A combination of the different LEDs on the Linbot is used to display the direction of displacement. The schematic of the experiment is shown in Supplementary Figure S8. The experiment was run once to demonstrate the capabilities of the Linbots and is shown in Supplementary Video S5.

Design of the communication experiment

We designed an experiment to investigate bidirectional communication between two Linbots and to evaluate the error rate in data transmission at different communication distances. The experimental setup is shown in Figure 2E. We demonstrate communication between the Linbots using on–off keying of a 700 kHz carrier signal. The coils were not modified for demonstrating communication in any of the experiments.

In this experiment, we tested the communication between two Linbots at varying distances from one another. We increased the distance between the Linbots in steps of 5 mm from 90 to 150 mm. We measured the distance from the centers of the Linbots. The experiment is divided into two parts, where at each distance, the first Linbot transmits a stream of data and the second Linbot receives the transmitted data, then the second Linbot transmits a stream of data and the first Linbot receives the transmitted data. The transmitted information consists of 50 bytes of data. We set these data to be the numbers 11–211 in incremental steps of 4. This array of numbers varies the shape of the signal.

The Linbot that receives the transmitted data knows the series of bytes it should be receiving, and when it receives a byte it checks the value against its expected value. If the value is different from the expected value, the Linbot interprets the byte as a faulty byte. In the experiment, the orange light depicts a Linbot in transmission mode and a green light depicts a Linbot in receiver mode. After receiving the stream of bytes, if there is a fault in the received data, the Linbot uses a combination of its LEDs to depict the number of faulty bytes received. The Linbot flashes a blue LED once for every 10 faulty bytes and flashes an orange LED once for the remaining single faulty bytes.

The number of wrong bytes received is used to calculate the error rate at each communication distance. If the Linbot does not receive any transmitted data because it is outside the communication range, the error rate is considered to be 1. Once a distance is reached where both Linbots have an error rate of 1, all larger distances for that pair are assumed to be 1.

Due to the large number of Linbots, we decided to perform a screening experiment by sampling more than 50% of the population, so that we could gain a good understanding of the overall capability of the Linbots. We chose five Linbots at random, from the population of nine, and used each one for two tests at each range. To separate the effects of transmission strength from the receiving sensitivity for each Linbot, we chose to test each Linbot twice, in a different pairing. By taking into account all of the permutations we calculated that we needed 500 binary tests of communication at each range. This experiment is shown in Supplementary Video S6.

Design of the Linbot collective experiments

Design of the peristaltic conveyor. In addition to the experiments that show the capabilities of one or two Linbots, we performed additional demonstrations to show how the Linbots can perform collective behaviors. For the first demonstration, we designed a peristaltic conveyor to show how a collective of our Linbots can use simple individual behaviors to perform a more complex task. The system is shown in Figure 3D. The conveyor used nine Linbots arranged in a straight line within a platform. The current used to power the Linbot communication controls the maximum range of the communication. Based on the range of around 100 mm seen in the communication test, we placed the Linbots 80 mm apart. This spacing only allowed nearest neighbor communication.

The platform consists of two parts: a backboard to prevent objects from falling off the conveyor and a base to hold the Linbots. The conveyor was given a 4° roll so that conveyed objects rest against the backboard, and a 1° pitch, so that these objects are moved uphill. For this experiment, we programmed the Linbot as a finite state machine to respond to either contact by an object or receiving a message from a neighbor. On detecting communication from another Linbot, the receiving Linbot contracts. When the Linbot contracts or

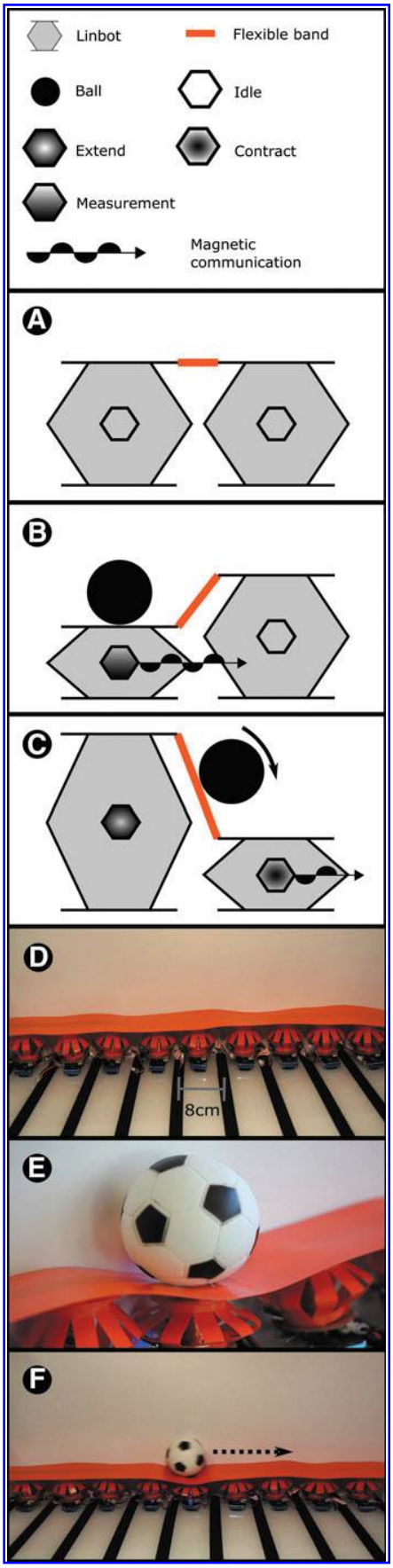

is compressed, it turns on its communication and transmits information to its neighboring Linbot. The Linbot then expands to push the object to the next Linbot. Multiple Linbots performing this sequence create a traveling wave along the conveyor from one side to the other.

After expansion, each Linbot enters an unresponsive state for a set amount of time to avoid responding to the signal from the succeeding Linbot in the conveyor. This mechanism ensures that the wave travels only in one direction, carrying the object with it. Schematics of the mechanism are shown in Figure 3A–C. We used a small toy ball that weighs 40 g for this experiment. This experiment is shown in Supplementary Video S7.

Design of the peristaltic sorter. To demonstrate how Linbots can be reconfigured to perform other tasks, we designed a peristaltic sorter using the Linbots. The layout of the Linbots for this sorter is shown in Figure 4A. In this demonstration, nine Linbots are arranged in a 3×3 array and are capable of sorting objects by their weight. A 2.5 g ball and a 40 g ball were used to demonstrate the sorting technique in this experiment. The 2.5 g ball should be moved to the left, and the 40 g ball should be moved downward.

As the sorter configuration uses multiple, nondormant Linbots within the communication range of one another, we needed to use an addressing system to control if a received command activates a Linbot. To implement the addressing system before starting the sorting task, when the Linbot collective is turned on, the bottom left Linbot is pressed. Pressing a Linbot will cause it to propagate a message through the collective, allowing each Linbot to know how far away, on the grid, it is from the Linbot pressed. The process is repeated with the top left Linbot. Based on the grid distances given by the bottom left and top left Linbot, each Linbot will have unique coordinates. Each Linbot will also know the relative position of the other coordinates on the grid. This addressing system is demonstrated in Figure 4C–E.

When a Linbot detects a weight placed on it, it increments a counter related to the class of the weight it believes is on top of it. When the counter of a class reaches a threshold, the Linbot sends a message to its neighbors causing them to actuate. This buildup and discharge behavior is inspired by action potentials in heart muscle cells.[34]

The message transmitted by the Linbot under a weight contains the coordinates of the signaling Linbot and the direction to move the weight. The neighboring Linbots actuate based on their relative position to the instructing Linbot. This actuation leads to the ball rolling off the edge of the grid in the

FIG. 3. Peristaltic conveyor. **(A)** Schematic of two Linbots at rest within the peristaltic conveyor. **(B)** Schematic of the same Linbots within the conveyor detecting a weight placed on the first Linbot. At this point, it communicates with its neighbor. **(C)** Schematic of the two Linbots after the first Linbot sends the communication signal. This communication causes the second Linbot to contract, while the first Linbot extends. The actuation changes the slope of the flexible band and causes the weight to roll off and onto the second Linbot. The second Linbot then communicates to its next neighbor along the conveyor. This process is repeated to create a traveling wave along the conveyor. **(D)** The conveyor at rest. **(E)** A close-up of a ball traveling along the conveyor. **(F)** The conveyor moving a ball from one side to the other.

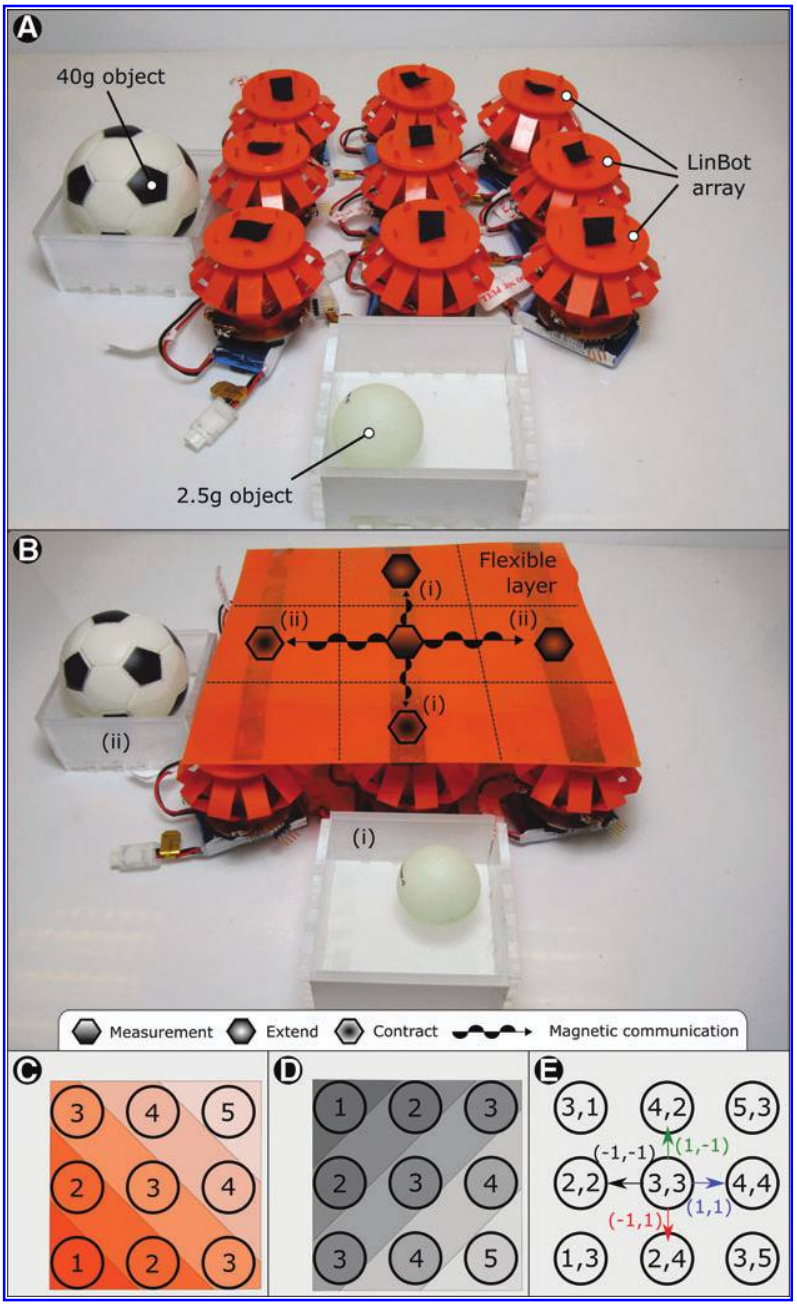

FIG. 4. Peristaltic sorter and addressing system. **(A)** The peristaltic sorter without the flexible layer on *top* of it, showing the Linbot array. **(B)** The peristaltic sorter with the flexible layer attached. The behavior of the sorter is shown with the central Linbot detecting the weight of an object and its neighbors actuating to roll the object in the desired direction based on weight. (i) Behavior of the sorter for the 2.5 g object. (ii) Behavior of the sorter for the 40 g object. All the Linbots in the sorting system had the same controller. **(C)** Shows the allocation of the first coordinate of the addressing system, based on communication hops from the *bottom left* Linbot. **(D)** Shows the allocation of the second coordinate of the addressing system, based on communication hops from the *top left* Linbot. **(E)** The final addresses for the peristaltic sorter. Vectors between neighboring Linbots in this coordinate scheme are shown around the central Linbot.

desired direction. The Linbots all have the same controller and can function in any role or position within the system. The setup and behavior of the sorter are depicted in Figure 4B. This behavior is similar to the peristaltic conveyor, detailed in the Design of the Communication Experiment section, and rolls the ball in the correct direction.

Results and Discussion

Fabrication and assembly

We designed the Linbots to have a size and weight appropriate for ease of fabrication, manufacturing, and assembly. They each have an inner diameter of 50 mm, an outer diameter of 70 mm, and a height of 50 mm at the rest position. This size allowed us to fit all of the electronic components on one side of the PCB while also allowing large numbers of Linbots to be space efficient. Each Linbot weighs 33 g, and the battery used for each Linbot also weighs 33 g. The Linbots are designed for manufacturability and the total bill of materials is £13.64. Further information about the components and assembly can be found in The Fabrication of the Linbot section of Supplementary Data, and in the supplementary ZIP folder containing CAD files and PCB schematics.

Results of the individual Linbot characterization experiments

Quantifying force output. We expected the force output to be the sum of spring force and magnetic force between the

electromagnets and permanent magnets. When the coil and magnet are fully separated, the force is given by the following:

$$F \simeq kd + \mu \frac{q_{coil} q_{pmag}}{4\pi(d + r_0)^2}, \quad (2)$$

where F is the total force, k is the spring constant, d is the distance from rest position, μ is the permittivity of air, q_{coil} is the pole strength of the electromagnetic coil, q_{pmag} is the pole strength of the permanent magnets, and r_0 is the initial distance between center of the coil and center of the magnets. q_{coil} is given by the following:

$$q_{coil} = \frac{NIA}{L}, \quad (3)$$

where N is the number of turns, I is the current through the coil, A is the cross-sectional area of the coil, and L is the length of the coil.

When the permanent magnets enter the coil, the magnetic force between them drops, reaching zero when their centers align. At the beginning, we expect a positive force trending down linearly due to the spring force dominating. Once the centers of the permanent magnets move away from the center of the coil, we expect a rapid increase that overtakes the decrease of the spring force. Once the permanent magnets are separated from the electromagnet, further behavior will be an inverse-square relationship, summed with a negative linear term as the spring force starts pulling the magnet back.

We see this expected behavior in the results from our force test, shown in Figure 2B. One repeat of the experiment is recorded in Supplementary Video S2. The results have a standard deviation of between 0.05 and 0.21 N, and this variance is likely caused by differences during construction, leading to a spread of restoring forces in the springs for each Linbot. The springs can also exhibit some asymmetry, diverting the force from being vertically upward, leading to a reduction in measured force output.

The rest length of the Linbots used in the experiment ranged 46.5–51.0 ± 0.5 mm. Removing this variance would require using a machine to fold the springs of each Linbot. The error seen in this experiment is acceptable as these robots are soft and have not been designed to require a high level of precision to achieve their tasks; instead, they rely on compliance to adapt to the environment. The maximum force output was 0.81 N, which suggests that the Linbots could lift objects with masses below ~83 g. For objects near this limit, lifting would require a controller that actuates such that it does not allow the Linbot to compress below 0.85 relative length. Below this relative length, the force output drops off and the Linbot may be unable to lift as heavy an object.

Frequency response analysis. We expected the Linbots to actuate at a low control frequency and transition to sound output as the frequency reaches audible levels. At high frequency, we also expect to use PWM to produce forces smaller than the maximum actuation force, and therefore, partial actuation. We demonstrated that the Linbots can actuate up to high frequencies and act as a loudspeaker. The waveform for the output sound is shown in Figure 2D, and its frequency spectrum is shown in Supplementary Figure S9. We also show this behavior in Supplementary Video S3. The video shows the Linbot actuating at increasing frequencies and then transitioning to sound output at the highest frequencies. Our use of a PWM actuation signal produced the expected partial actuation behavior. The partial actuation behavior resulting from the PWM signal is demonstrated in Supplementary Video S4.

Feasibility of tactile sensing. We designed the Linbots to be able to sense the displacement of their top half relative to their bottom half. We expected accurate classification of movement for positive and negative movements along three orthogonal axes. We demonstrated this ability in Supplementary Video S5. The video shows the Linbot being moved in six orthogonal directions, the direction of movement is displayed via the LED color combinations, shown in Supplementary Figure S8.

Evaluation of the communication between Linbots

We expected each pair of Linbots to show a very high successful transmission rate at separation distances below their maximum transmission range, as the receiving circuits have a threshold for signal strength that is set above the background noise. The background noise level from the receiver circuit is shown by Supplementary Figure S12. As they reach their maximum communication range, we expected their success rate to decrease sharply. This decrease is due to the received transmission strength approaching the threshold of the receiver, which is detailed in The Fabrication of the Linbot section of Supplementary Data. As some signals are pushed over or under the threshold by random noise, we would expect many faulty bytes. Once above the maximum transmission range, we expect none of the bytes to be received, as the transmission strength would always be below the signal threshold.

Due to variation in the construction of the coils, the transmission strength and receiving sensitivity vary in each Linbot. This variation gives each pair of Linbots a different maximum transmission range. The effect of this variation was expected to give rise to a high success region before any pairs reach their maximum range, then a distance where the average success rate is below 1 and has a high error due to some pairs having started their rapid decrease, while others have not. The average success rate should then decrease to zero as more pairs move past their maximum range.

The results of the communication test between the Linbots are shown in Figure 2F. The experiment is shown in Supplementary Video S6. We demonstrated that the Linbots can communicate with each other over at least 100 cm, giving us our expected high success region. Beyond that, the average success rate started to decline with a high error rate as expected. The shortest maximum transmission range seen was 105 mm, while the longest was over 150 mm. One Linbot did not reach a maximum transmission range. This unexpectedly high maximum range is the reason the mean error rate only reaches ~0.8.

The results of these communication experiments are used to quantify the maximum distance for reliable communications and acted as a guideline for the separation distance between Linbots in the following experiments that used collectives of robots.

Results of the Linbot collective experiments

Peristaltic conveyor. We expected a collective of Linbots to be able to generate a sufficiently powerful peristaltic wave

to roll a ball up a gradient. Our Linbot collective achieved this task and the result can be seen in Supplementary Videos S7 and S8. These videos show the Linbots rolling a ball along the conveyor by using collective behavior. We used a delay of 0.45 s before each Linbot propagated the wave, and this delay led to the ball traveling at an average of 18 cm/s across the conveyor. A close-up of the ball moving along the conveyor and the conveyor moving the ball from one side to the other is shown in Figure 3E and F, respectively.

This conveyor would be suitable for any objects that slide or roll but would have trouble moving adhesive objects. The peristaltic wave used could have been faster, as the video shows the ball sometimes getting slowed by falling into the trough of the wave. A faster wave also increases the chance that the ball would fall behind the wave and stop. The speed of the wave is limited by the gradient created for the ball to roll down. This gradient is determined by the actuation range of the Linbots and the spacing between them. In this experiment, the angle of the rising slope of the peristaltic wave is $\sim 12°$, including the opposing 3° pitch of the conveyor. Increasing the range of motion of the Linbots or reducing the distance between them would allow for a faster peristaltic wave.

Two-dimensional peristaltic sorting table. We designed the Linbot collectives to be able to sense the difference between two balls, one weighing 2.5 g and the other 40 g. We also expected that they would move the 2.5 g balls off the grid to the left side and the 40 g ball off the grid to the bottom side. Our collective behaved as expected. This behavior is depicted in Figure 4B and can be seen in Supplementary Videos S9 and S10. The videos show the Linbots rolling the two balls in the correct directions.

The signal used to classify the balls is shown in Supplementary Figures S10 and S11. The difference in signal between the two balls means that comparing the signal to a threshold spaced between the two will correctly classify a ball every time. These figures also show that the rest length of a Linbot is changed even after removing the weight placed on them. In the experiment, we removed the effect of this change on the signal by resetting the base Hall-effect reading after a weight is removed. The Linbots in this sorter have identical controllers that use the relative positions of Linbots to determine actions. This distributed control means that the controller is not reliant on the size of the sorter.

Scope for Development

Vibrational sorting

The high actuation frequency of the Linbots allows them to be used for vibrational sorting. Vibrating collections of objects allow them to be sorted by firmness or density. A single Linbot with a slanted plate attached to the top can produce the vibrations needed to sort objects. The peristaltic sorter could also be adapted for a mixture of vibrational and peristaltic sorting.

Communication range

Our use of inductive data transmission for the Linbots means that communication is only possible between nearby Linbots. In the future, the frequency of the carrier wave used could be increased to create far-field communication between Linbots and to enable long-range communication between dispersed Linbots.

Wireless charging

Through adding a rectifier and LiPo balance circuit to the Linbot, its battery could be charged through inductive power transfer. This would involve placing the Linbot in a strong alternating magnetic field, whose power would be coupled into the main coil of the Linbot.

Wireless programming

By writing a program to allow Linbots to be programmed via UART, we could allow for wireless programming of the Linbots. This modification would reduce the time needed to program the Linbots as an antenna could be used to program them simultaneously. It would also allow new programs and controllers to be propagated through a collective by the Linbots themselves.

Additional sensors

By connecting I^2C sensors to Linbot PCB I^2C bus pins, we can tailor the Linbots to new tasks. For example, to make an array of Linbots respond to the distance from objects, IR range sensors can be added to a Linbot PCB.

Learned behavior

In large Linbot collectives, each individual robot can affect the state of other Linbots with whom it does not have a direct communication link. This complication leads to difficulties in writing effective controllers. Machine learning algorithms could be applied to allow Linbots to learn the dynamics of their collective and even to have individually tailored controllers.

Self-synchronization

If we have a task that requires synchronization, we can design our Linbot controllers to create a global clock. Using phase rate equalization, any detectable pulses can be used to synchronize the Linbots.[35] We can create these pulses with periodic broadcasts from a Linbot to neighboring Linbots. We can also use the periodic actuation of a Linbot, which can detect the actuation of neighboring Linbots through tactile signals from a flexible layer on top of them.

A larger peristaltic sorter

Further robots could be added to make the peristaltic sorter larger without needing to rewrite the controller. This larger sorter could be used to examine large-scale behaviors of Linbots.

Locomoting Linbot collectives

A Linbot collective could be reconfigured for locomotion, similar to the Wormbot.[16] The peristaltic conveyor could also be inverted to produce waves that would enable the whole assembly to locomote across a surface. Reducing the weight of the Linbots by decreasing the battery size would allow for more robust locomotion. A 2D Linbot collective designed for

locomotion would be capable of steering in response to sensory information.

Miniaturized Linbots

The Linbots could be miniaturized for use in different applications such as tactile displays or implantable devices. By converting the circuitry into one integrated circuit, the volume of a Linbot could be reduced to about a cubic centimeter. At this size, the Linbots could use the magnets and coils from the smallest commercially available solenoids, while still using off-the-shelf batteries.

Making the robot even smaller would preclude the use of available batteries. This means that either a miniature battery would need to be manufactured or the robot would need to run on miniature charged capacitors and an external power source. At smaller scales, the coil would need to be changed from being a wound wire to a planar coil cut into a PCB, and the magnets would need to be fabricated rather than bought. The limit at this level would be the minimum size of integrated circuits, which means the Linbot cannot be smaller than a few millimeters in size.

Conclusions

Modular robotic collectives are more robust than monolithic systems. Often modular systems are limited in their functionality due to cost. Soft, modular robots also often require an outside pressure or vacuum source. We present our Linbots, our combination of untethered, reconfigurable robots with soft robotics. Our Linbots demonstrate communication, actuation, tactile sensing, proprioception, and sound synthesis. The linear motion of our Linbots sets them apart from existing modular robots and allows them to be used for tasks that require peristaltic motion.

We demonstrated the abilities of individual Linbots as well as their ability to communicate with one another. We used a Linbot collective to convey a ball up a slope using a peristaltic wave. We then reconfigured this Linbot collective to demonstrate sorting. The collective was able to sort two balls based on weight and transfer them to desired bins.

Our use of multifunctional hardware allows the system to be low cost without sacrificing functionality. The soft nature of our Linbots allows them to conform to their surroundings. Our Linbots provide a low-cost modular platform that can be configured for different real-world tasks. In addition, our multifunctional voice coil system can be adapted to other modular or swarm robotic systems. Our work supports the move toward reconfigurable, modular robotic platforms as useful tools for both academia and industry.

Funding

This study was supported by EPSRC via the Robotarium Capital Equipment and CDT Capital Equipment Grants (EP/L016834/1), and the CDT in Robotics and Autonomous Systems. M.P.N. gratefully acknowledges support from the CDT in Intelligent Sensing and Measurement (EP/L016753/1), United Kingdom. A.A.S. acknowledges support from the EPSRC ORCA Hub (EP/R026173/1).

Authors' Contribution

R.M.M., designing and developing the Linbot, developing the experimental scheme, writing and revising the article. M.E.S., designing and developing the Linbot, developing the experimental scheme, writing and revising the article. M.P.N., writing parts of the article/developing the figures, revising the article, and contributing to Linbot PCB design. B.W.F., advised on building the Linbot system. A.A.S., lead advisor and primary editor of the article.

Author Disclosure Statement

No competing financial interests exist.

References

1. Yim M, Shen W, Salemi B, *et al*. Modular self-reconfigurable robot systems [Grand Challenges of Robotics]. IEEE Robot Autom Mag 2007;14:43–52.
2. Clune J, Mouret J-B, Lipson H. The evolutionary origins of modularity. Proc R Soc Lond B Biol Sci 2013;280:1755.
3. Belke CH, Paik J. Mori: A Modular Origami Robot, IEEE ASME Trans Mechatronics 2017;22:2153–2164.
4. Neubert J, Rost A, Lipson H. Self-soldering connectors for modular robots. IEEE Trans Robot 2014;30:1344–1357.
5. Stoy K. Reconfigurable robots, in Springer Handbook of Computational Intelligence, Kacprzyk J, Pedrycz W. (Eds). Berlin, Heidelberg: Springer Berlin Heidelberg, 2015, pp. 1407–1421.
6. Mahon ST, Roberts JO, Sayed ME, *et al*. Capability by stacking: The current design heuristic for soft robots. Biomimetics 2018;3:16.
7. Sproewitz A, Billard A, Dillenbourg P, *et al*. Roombots-mechanical design of self-reconfiguring modular robots for adaptive furniture. In ICRA, Kobe, Japan, 2009:4259–4264.
8. Vergara A, Lau Y-S, Mendoza-Garcia R-F, *et al*. Soft modular robotic cubes: Toward replicating morphogenetic movements of the embryo. PLoS One 2017;12:1–17.
9. Kim S-R, Lee D-Y, Koh J-S, *et al*. Fast, compact, and lightweight shape-shifting system composed of distributed self-folding origami modules. In ICRA, Stockholm, Sweden, 2016:4969–4974.
10. Stanley AA, Okamura AM. Controllable surface haptics via particle jamming and pneumatics. IEEE Trans Haptics 2015;8:20–30.
11. Follmer S, Leithinger D, Olwal A, *et al*. inFORM: dynamic physical affordances and constraints through shape and object actuation. UIST, St. Andrews, UK, 2013:417–426.
12. Rubenstein M, Ahler C, Nagpal R. Kilobot: A low cost scalable robot system for collective behaviors. In ICRA, St. Paul, MN, 2012:3293–3298.
13. Skjetne C, Haddow PC, Rye A, *et al*. The ChIRP robot: A versatile swarm robot platform. RiTA, Denver, CO, 2013: 71–82.
14. Nemitz MP, Sayed ME, Mamish J, *et al*. HoverBots: Precise locomotion using robots that are designed for manufacturability. Front Robot AI 2017 Nov;4(55):00055.
15. Nemitz MP, Marcotte RJ, Sayed ME, *et al*. Multi-functional sensing for swarm robots using time sequence classification: HoverBot, an example. Front Robot AI 2018;5:55.
16. Nemitz MP, Pavel M, Barraclough TW, *et al*. Using voice coils to actuate modular soft robots: Wormbot, an example. Soft Robot 2016;3:198–204.
17. Stokes A, Shepherd R, Morin S, *et al*. A hybrid combining hard and soft robots. Soft Robot 2014;1:70–74.
18. Kim S, Knoll T, Scholz O. Feasibility of inductive communication between millimeter-sized wireless robots. IEEE Trans Robot 2007;23:605–609.

19. Paulino T, Ribeiro PC, Neto M, *et al*. Low-cost 3-axis soft tactile sensors for the human-friendly robot Vizzy. In ICRA, Singapore, 2017:966–971.
20. Scott W, Stevens J, Binder-Macleod SA. Human skeletal muscle fiber type classifications. Phys Ther 2001;81:1810–1816.
21. Robertson MA, Paik J. New soft robots really suck: Vacuum-powered systems empower diverse capabilities. Sci Robot 2017;2:eaan6357.
22. Acome E, Mitchell SK, Morrissey TG, *et al*. Hydraulically amplified self-healing electrostatic actuators with muscle-like performance. Science 2018;359:61–65.
23. Kellaris N, Venkata VG, Smith GM, *et al*. Peano-{HASEL} actuators: Muscle-mimetic, electrohydraulic transducers that linearly contract on activation. Sci Robot 2018;3: eaar3276.
24. Angatkina O, Chien B, Pagano A, *et al*. A metameric crawling robot enabled by Origami and smart materials. In ASME 2017 Conference on Smart Materials, Adaptive Structures and Intelligent Systems, Snowbird, UT, 2017: 3836–3846.
25. Wei T, Stokes A, Webb B. A soft pneumatic Maggot robot. In Biomimetic and Biohybrid Systems. Cham, 2016:375–386.
26. Menciassi A, Gorini S, Pernorio G, *et al*. A SMA actuated artificial earthworm. In ICRA, New Orleans, LA, 2004: 3282–3287.
27. Fukuda T, Hosokai H, Otsuka M. Autonomous pipeline inspection and maintenance robot with inch worm mobile mechanism. In ICRA, Raleigh, NC, 1987:539–544.
28. Boxerbaum AS, Shaw KM, Chiel HJ, *et al*. Continuous wave peristaltic motion in a robot. Int J Robot Res 2012;31: 302–318.
29. Stommel M, Xu WL, Lim PPK, *et al*. Soft peristaltic actuation for the harvesting of Ovine Offal. Robot Intelligence Technology and Applications 3: Results from the 3rd International Conference on Robot Intelligence Technology and Applications Kim J, Yang W, Jo J, Sincak P, Myung H. (Eds). Cham: Springer International Publishing, 2015, pp. 605–615.
30. Stommel M, Xu W. Optimal, efficient sequential control of a soft-bodied, peristaltic sorting table. IEEE Trans Autom Sci Eng 2016;13:858–867.
31. Sung C, Rus D. Automated fabrication of foldable robots using thick materials. In Robotics Research: Volume 1 Bicchi A, Burgard W. (Eds). Cham: Springer International Publishing, 2018, pp. 253–266.
32. STMicroelectronics, Home Page. [Online]. Available: www.st.com/content/st_com/en.html. Accessed February 11, 2018.
33. Osborne A. An Introduction to Microcomputers: Basic Concepts, first ed., Osborne/McGraw-Hill, 1980.
34. Cheney N, Clune J, Lipson H. Evolved electrophysiological soft robots. ALIFE 2014;14:222–229.
35. Brandner G, Schilcher U, Bettstetter C. Firefly synchronization with phase rate equalization and its experimental analysis in wireless systems. Comp Netw 2016;97:74–87.

Address correspondence to:
Adam A. Stokes
Scottish Microelectronics Centre
School of Engineering
Institute for Integrated Micro and Nano Systems
The University of Edinburgh
Alexander Crum Brown Road, King's Buildings
Edinburgh EH9 3FF
United Kingdom

E-mail: adam.stokes@ed.ac.uk

Appendix I

Journal: Limpet: A Modular, Untethered Soft Robot

Journal: Soft Robotics

Publisher: Mary Ann Liebert, Inc.

Limpet: A Modular, Untethered Robot

Mohammed E. Sayed[1], Jamie O. Roberts[1,2], Ross M. McKenzie[1,2], Simona Aracri[1], Anthony Buchoux[1], and Adam A. Stokes[1*]

[1]School of Engineering, Institute for Integrated Micro and Nano Systems, The University of Edinburgh, Scottish Microelectronics Centre, Alexander Crum Brown Road, King's Buildings, Edinburgh, UK, EH9 3FF

[2]Engineering and Physical Sciences Research Council (EPSRC) Centre for Doctoral Training (CDT) in Robotics and Autonomous Systems, School of Informatics, The University of Edinburgh, Edinburgh EH9 3LJ, UK

*** Author to whom correspondence should be addressed.**
Adam A. Stokes
Adam.Stokes@ed.ac.uk

Abstract

The ability to navigate complex unstructured environments and carry out inspection tasks requires robots to be capable of climbing inclined surfaces and to be equipped with a sensor payload. These features are desirable for robots that are used to inspect and monitor offshore energy platforms. Existing climbing robots mostly use rigid actuators, and robots that use soft actuators are not fully untethered yet. One of the major problems with current climbing robots are also not built in a modular fashion, which makes it harder to adapt the system to new tasks, to repair the system, to replace and reconfigure the modules. This work presents a 450 g and a 250 x 250 x 140 mm modular, untethered hybrid hard/soft robot - Limpet. The Limpet uses a hybrid electromagnetic module as its core module to allow adhesion and locomotion capabilities. The adhesion capability is based on negative pressure adhesion utilising suction cups. The locomotion capability is based on slip-stick locomotion. The Limpet also has a sensor payload with nine different sensing modalities, which can be used to inspect and monitor offshore structures and the conditions surrounding them. Since the Limpet is designed as a modular system, the modules can be reconfigured to achieve multiple tasks. To demonstrate its potential for inspection of offshore platforms, we show that the Limpet is capable of responding to different sensory inputs, repositioning itself within its environment, adhering to structures made of different materials, and climbing inclined surfaces.

Summary: An untethered hybrid hard/soft robot that is designed in a modular fashion, allowing the modules to be reconfigured for different tasks such as climbing inclined surfaces and responding to changes in its environment.

Keywords: Limpet, Modular, Hybrid, Untethered, Robot, Soft, Climbing, Adhesion, Sensors, Electromagnetic Actuator

1 Introduction

1.1 Offshore Environment Requirements

Offshore platforms are massively complex and unstructured environments. The environment consists of structures at different angles, steep inclines, and inverted surfaces. To navigate such unstructured environments efficiently and to be useful for inspection and exploration tasks, a robot must be have a good adhesion mechanism and be capable of multiple locomotion modalities such as walking, running, and climbing [1]. The ability to adhere and to climb these inclined surfaces increases the accessible areas of terrestrial robots in such environments, which improves the capability of the robot to do inspection and monitoring of the offshore platform. Adhering to and climbing on these unstructured offshore environments alone is not enough for the robot to carry out inspection tasks; it must also be equipped with a sensor payload.

1.2 Modularity, Stacking and Reconfigurability

Robots performing tasks in unstructured environments (e.g. offshore) need to adapt to variable constraints in their environment. Traditional robotics provide unique solutions to a specific real world application, but are usually hard to use in other applications due to the lack of their adaptive nature [2]. Modular robots or assemblies of modular units [3], [4], [13]–[15], [5]–[12] are easier to adapt to new tasks and make it easier to repair the system, to replace modules, and to control the robot. Modular robots are usually made of some primary structural actuated unit and some additional specialised units (e.g. grippers, sensor payload, feet, etc.) [16]. The interest in modular systems is due to the hypothesis that a single, advanced robot is more expensive and less robust than multiple low-cost modules [2], [16], [17]. Modular robots can be easily reconfigured for different tasks [2], [3], [14], [16], [18]–[20], making them different from monolithic robots. Modular robots provide the advantage of: reconfigurability; reusability; versatility; low-cost; robustness; ease of manufacturing over traditional robotic systems [2], [21]. The capability of a modular robotic system is usually dependent on the number of modules within it [16]. However, the number of modules is often limited by the cost of the unit, where systems with large number of modules sacrifice their functionality to keep the costs low. Creating low-cost modular robotic systems with higher capabilities is a key challenge in modular robotics. The use of hardware for multifunctional purposes is a great way to keep costs of the system low. Examples include the Kilobot system [22] and the Hoverbot system [23], [24]. The capability of single modules are limited, but modular robots consisting of multiple units have increased capability compared to the sum of their parts [25]. By stacking modules, we can increase the overall capability and the range of behaviours and motions of a system, and thus, utilise it to perform useful tasks. The term “stacking” refers to the ability to combine functional units to develop a system that has greater capability and complexity than the sum of its individual units [25]. There are multiple examples of systems where higher capability was achieved by stacking functional modules together [26], [27], [36]–[45], [28], [46]–[48], [29]–[35].

1.3 Climbing Robots

Climbing robots can be used for a wide range of applications in unstructured environments (e.g. offshore). The two key features for climbing robots are adhesion and locomotion mechanisms. Recent work on climbing robots have adapted different bio-inspired and engineered adhesion mechanisms. The adhesion mechanisms include gecko-inspired adhesion (via long-range molecular forces) [49]–[51], magnetic adhesion [52]–[57], electroadhesion [1], [58]–[64], adhesive materials [65] and negative pressure adhesion [66], [67]. Geckos adhere to surfaces via Van der Waals forces using a large number of very fine hair structures [68]. Gecko-inspired adhesion has been utilised by climbing robots of different scales to move on smooth inclined surfaces [69]–[75]. Magnetic adhesion relies on generating

a magnetic force using permanent magnets, electromagnets or electro-permanent magnets. Magnetic adhesion has the advantage of facile control, but it works only on ferromagnetic surfaces. Electroadhesion is achieved by using an applied electric field, and it can be tuned by changing the input voltage modulation [1]. Electroadhesion requires a large input voltage, and it also uses power tethers [1]. Adhesive materials for climbing robots are not very reliable and they require smooth and clean surfaces [65]. The most widely adopted adhesion mechanism for climbing robots is negative pressure adhesion using suction cups. This adhesion method has higher reliability, simpler design and easier application than other adhesion methods. Adhesion in nature based on suction can be seen in many different animals including northern clingfish [76], limpet [77], octopus [78], [79], and squid [80]. The suction mechanism demonstrates effectiveness both in terrestrial [39], [81] and aquatic environments [82]. Suction mechanisms have also been applied by robots in other applications, such as picking objects with variable shape and size [83]. It is important to have sensory feedback on the adhesion module, to inform the status of adhesion of the system and to implement closed-loop control systems that can enable robots to maintain their adhesion for longer periods of time.

Locomotion types of climbing robots include crawlers [84]–[87], wheels [88], [89], and legs [1], [90]–[96]. Crawler-type climbing robots can move relatively fast, but are not adequate for rough environments as they cannot cross obstacles easily. The most common strategy for locomotion is using a two-wheel differential drive, where each wheel is powered by an electric motor. Wheeled robots are capable of achieving high velocities, do not need actuator calibration, and are platform independent. Wheeled locomotion, however, has a negative impact on the battery life and the cost of the robot. Another main disadvantage of using wheeled locomotion for robots that use suction force adhesion is the need to maintain an air gap between the robot base and the surface the robot is moving on. This feature will create some problems for the robot like loss of pressure or friction with the surface [97]. Legged robots allow the creation of a stable and strong adhesion force to the surface, and they can cope well with cracks or obstacles in their environment [97]. The disadvantage of legged robots is that they achieve low speeds and may require complex control. There has been various other climbing robots based on different adhesion and locomotion mechanisms reported recently [65], [98]–[106].

1.4 The Limpet

In this work, we introduce our modular, untethered hybrid robot - Limpet - which uses a multi-functional electromagnetic module (EMM) and a sensing module to achieve increased capability and reconfigurability while keeping the costs low. The modularity of the Limpet allows it to climb inclined surfaces, adhere to different structures and sense and respond to changes in its environment. **Video S1** shows an overview of the Limpet system and its capabilities. The Limpet is being developed as part of the Offshore Robotics for Certification of Assets (ORCA Hub) in the UK. The ORCA Hub is a 3.5 year EPSRC funded multi-site project aiming to use teams of robots and autonomous intelligent systems (AIS) on remote energy platforms to enable cheaper, safer and more efficient working practices [107]. The ORCA Hub is a collaboration between five universities (University of Edinburgh, Heriot-Watt University, University of Liverpool, Imperial College London, and University of Oxford) and top industrial companies (Total, Chevron, British Petroleum, Tharsus, and many others). The ORCA Hub aims to assist industry to move towards an offshore platform that is operated, inspected, and certified by autonomous robots. Sensing is a key component to the ORCA Hub, as it is important for inspection, monitoring structural and asset health, fault detection, environmental monitoring, mapping and helping other robots navigate around the platform. The Limpet comprises the sensing aspect of the ORCA Hub.

We based our untethered modular robot presented in this paper on version 1 of the Limpet [108] and the Linbot system [109]. We developed version 1 of the Limpet as a multi-sensing platform for monitoring offshore platforms. The Limpet version 1 was designed to be low-cost and highly

manufacturable, and thus can be deployed in huge collectives for monitoring the offshore platforms. Version 1 of the Limpet is an integrated Printed Circuit Board (PCB) with nine sensing modalities. We integrated it with Robot Operating System (ROS), to allow it to interact with other robots on the offshore platform. We demonstrated how the Limpet version 1 can be used to achieve real-time condition monitoring for offshore structures, by combining remote sensing with signal-processing techniques, where the Limpet detects a fault in the operation of an offshore asset by running an on-board classifier [108]. We developed the Linbots to show a collective of low-cost robots that can be reconfigured to achieve different useful tasks. The Linbot is a soft, modular robot that uses a multi-functional electromagnetic module for linear actuation, communication, sound output and tactile sensing. The Linbot and the Limpet version 1 are not capable of locomotion or adhesion. In this paper, we define the Limpet version 1 as the sensing module. The EMM used for the Linbot system is utilised in this paper to achieve locomotion and adhesion for version 2 of the Limpet. The following sections describe the design and evaluation of version 2 of the Limpet system and all its modules.

The Limpet system is inspired by patella vulgata [110], commonly known as Limpet, which is an aquatic snail with a conical shell that lives on rocks on land or in the sea. The patella vulgata has a strong shell that protects it from the external environment and predators. It can alternate between different adhesion mechanisms depending on the required period and strength of adhesion [77]. Suction is the primary adhesion mechanism used by patella vulgata, where the suction force can reach up to 25N [111]. The shell of the patella vulgata also plays an important role in the adhesion mechanism. The patella vulgata clamps its shell to increase friction with the surface and prevent any dislodgements caused by shear forces [111]. Shell clamping against the surface makes use of the vertical adherence strength of the suction mechanism to create a frictional force that resists the shear force of hydrodynamic drag [111]. The patella vulgata has an optic vesicle at the end of its tentacles that provides sensory function, and enables it to sense light and darkness levels [110].

1.5 Objectives

Our objective in this work was to design a hybrid robot in a modular fashion – Limpet – such that the modules can be reconfigured to achieve different tasks such as climbing inclined surfaces, adhering to structures and sensing its environment. The primary purpose of this robot is to inspect and monitor offshore energy platforms and as such these tasks are vital to allow the robot to be useful in its environment. The robot consists of a sensing module, power driver module, and adhesion and locomotion modules based on EMMs. We explained the design procedure and fabrication techniques for each of the different modules in the Limpet system. We described the experimental methods used to characterize the performance of each of the different modules. It is important to characterize each of the modules in a modular robot to understand the capabilities of the single modules and how they can come together to create a more complex and useful system. Finally, we demonstrated the capability of the final Limpet system in climbing inclined surfaces, adhering to structures and responding to sensory input by reconfiguring the modules of the system.

2 Materials and Methods

2.1 System Design

The Limpet v2 uses a low-cost and manufacturable EMM as its core module. The EMM can actuate linearly, and it can produce sound output. We used the EMM to construct adhesion and locomotion modules, to give the Limpet the capability of locomotion, adhesion and sound communication. The Limpet is designed as a modular system with multi-sensing capabilities. The modular architecture allows the Limpet to achieve multiple complex tasks in its environments including climbing, adhesion and structural health monitoring. The Limpet is a hybrid system combining between hard and soft

materials. Hybrid systems can take advantage of rigid components while still being able to partially conform to their environment [42]. The soft materials in the Limpet system gives it the advantage of inherent compliance, low-cost manufacturing, and improved safety. The soft material compliance can immensely help robots in unstructured environments adapt to unexpected environmental changes such as slopes and obstacles. We have developed the Limpet as an untethered system. The dependence on electrical or pneumatic tethers limits the applications that can be performed by robots in their environment [30], [112]. For systems to be useful in field applications, all their vital components (e.g. actuation, power, communication and processing components) need to be fully integrated within their structure [112]. The experiments we conducted to characterise the different modules within the Limpet used power and pneumatic tethers. However, the final Limpet system combining all the modules was developed as an untethered system.

The Limpet system consists of a sensing module (Limpet version 1), a power driver module, an adhesion module, a locomotion module, and an outer protective shell as shown by **Figure 1**. The main purpose of the Limpet is to monitor the offshore assets and the environmental conditions surrounding the assets [108]. We equipped the Limpet with nine exteroceptive sensing modalities. The sensing modalities on the Limpet system are all incorporated on the sensing module. The sensors included on the Limpet are: temperature; pressure; humidity; optical; distance; sound; magnetic; accelerometer; gyroscope. Our choice of sensing modalities was based on the ability to measure parameters that are relevant to monitoring the environmental conditions on the offshore platform and monitoring the health of the offshore structures. The choice of sensing modalities was also influenced by discussions and input from industrial partners in the ORCA Hub project. Each sensor on the Limpet can convert a physical measurement variable into a corresponding signal variable, where the physical measurement variable can be related to multiple measurands (events) giving the Limpet multi-functional sensing capabilities [108]. **Table 1** gives an example of how each sensor can be used to detect multiple measurands in offshore platforms, and thus, gives an overview of the multi-functionality that can be achieved with the Limpet.

2.1.1 Sensing Modalities, Communication and Programming

The sensors on the sensing module, except for the sound sensor, are controlled by the microcontroller through the I^2C bus. The sound sensor has an analog output and is connected to an analog-to-digital converter on the microcontroller. Analog sensors produce a continuous analog output signal that is proportional to the measurand. Digital sensors, on the other hand, convert the measured signal into a digital output signal inside the sensor itself, and then transmit the digital signal. Digital sensors are usually preferred over analog sensors, as they are less susceptible to noise (undesirable variation in voltage). Small variations in the voltage of an analog signal can result in significant errors during the processing stage. Thus, digital sensors have a higher accuracy and throughput.

We designed the Limpet to have robust communication. It can transmit data to a PC or other nodes using one of several different communication systems, including WiFi, serial, LoRa, optical and infrared communication. WiFi and serial communication do not allow for communication with neighbouring Limpets, unlike LoRa, optical and infrared communication. Serial, WiFi, and infrared communication are high-bandwidth communication, and as such, we can send the sensor data from the Limpet continuously in real time to the PC. The data can then be analyzed on the PC using analysis tools such as Matlab. In this regard, the Limpet is only making a measurement using the sensors and transmitting it instantly to the PC without doing any processing on the data, which means serial and Wi-Fi communication are not computationally demanding on the Limpet. LoRa and optical communication have a much lower communication bandwidth than serial and Wi-Fi communication. Thus, when these communication technologies are used with the Limpet, their limited bandwidth limits the ability to send the sensor data continuously in real time to the PC. Therefore, if the dataset is large,

processing and analysis of the data need to be done on the microcontroller of the Limpet before transmission to allow for only small payloads of data to be transmitted [108]. This on-board processing and analysis approach requires higher computational power than serial, Wi-Fi, and infrared communication. Further information on the communication methods used with the Limpet and how each communication is achieved can be found in **Section S1** in the Supplementary Materials and Methods. Schematics of the architecture of the WiFi, serial and LoRa communication are shown by **Figure S1**, **Figure S2**, and **Figure S3**, respectively. In this work, we use the on-board infrared transceiver (IR) for robot-to-computer communication, where the data from the Limpet and the sensors can be sent via IR to the computer. We debugged the Limpet via Infrared using a custom-designed infrared handheld device. The custom-designed infrared handheld device consists of an infrared transceiver module (TFBS4711), a microcontroller (ATSAMD21E16), and a USB-to-UART convertor (CP2102).

The sensing module and power driver module have an on-board programming port (JTAG). We program the Limpet via a SEGGER J-Link programmer together with a JTAG Adapter (Olimex ARM-JTAG-20-10) using a serial wire debug interface. We program the Limpet in C/C++ using Atmel Studio 7, and the main code includes online libraries and custom-written sensor libraries. We used the standard Universal Asynchronous Receiver-Transmitter (UART) protocol for communication. The UART protocol uses a high idle line, which is pulled low at the start of a message.

2.1.2 Cost and Dimensions of the Limpet

Cost and functionality are the most important factors considered when developing robots. These properties have a great effect on the scalability of a system to large number of agents. Scaling up robot collectives without sacrificing functionality is a challenging problem. Low-cost robots are scalable, but current systems have limited capabilities, which limit the type of useful tasks that can be performed by robots in "real-world" scenarios. Our rationale behind the Limpet system was to keep the costs as low as possible without sacrificing functionality. The sensing module is an integrated PCB that has a diameter of 50 mm, a height of 3 mm and weighs 10g. The power driver module is a PCB with a diameter of 65 mm, a height of 3 mm and weighs 15g. The full Limpet system has a length of 250 mm, a width of 250 mm and a height of 140 mm. We designed the Limpet to have a size and weight ideal for ease of fabrication, manufacturing and assembly. The total cost of the Limpet system is about £112. The breakdown of the cost of the different components in the Limpet system is shown in **Table 2**.

2.2 Electrical Design

2.2.1 Design of the Control Electronics

2.2.1.1 Sensing Module

The sensing module is based on the Limpet v1 PCB [108]. The sensing module consists of a single two-layer PCB incorporating a low–power microcontroller (ATSAMD21G18A), a 32.768 KHz crystal oscillator (CM7V-T1A), RGB LED (LTST-N683EGBW), charging IC (MCP73812), programming port [JTAG] (Molex 532610571), and a communication connector as shown by **Figure 1** and **Figure S4**. The PCB includes several exteroceptive sensors, which are: temperature and humidity sensor (Si7006), inertial measurement unit (IMU) [Accelerometer and Gyroscope] sensor (LSM-6DS3), optical sensor (VEML6040), sound sensor (SPU0414HR5H-SB), 3-Axis magnetic sensor (MLX90393), pressure sensor (BMP280), distance sensor (VL53L0). The communication connector on the sensing module is connected to the UART of the microcontroller. Therefore, we can use this connector to connect the sensing module to multiple different communication systems. We connect the communication connector to the power driver module. The microcontroller on the sensing module is responsible for controlling the sensing capabilities, and sending control messages to the power driver module based on the sensory input. The schematic of the sensing module is shown by **Figure S5**.

2.2.1.2 Power Driver Module

The power driver module consists of a single two-layer PCB incorporating a low–power microcontroller (ATSAMD21G18A), H-bridge drivers (DRV8871 and DRV8837), solenoid valve, air pump, barbed absolute pressure sensor (HSCMANN015PA2A3), 3.5V voltage regulator (LP2985IM5), 5V voltage regulator (MC78L05ACDR2G), 32.768 KHz crystal oscillator (CM7V-T1A), infrared transceiver (TFBS4711), connection to sensing module, battery connector, programming port and a communication connector. We use the microcontroller to control the frequency of the actuation of the electromagnetic modules. We control the direction of the actuation of the electromagnetic modules by the H-bridge driver using the microcontroller. The air pump and solenoid valve are also controlled by the microcontroller through an H-bridge. The microcontroller on the power driver module is responsible for controlling the adhesion and locomotion capabilities. The pressure sensor is used as a feedback component for the closed loop controller of the adhesion system. The sensing module sends all the on-board sensor data to the power driver PCB, which then sends it to the computer through the IR transceiver or any other communication system (serial, WiFi, LoRa, optical) connected to the communication connector. A labelled picture and the PCB schematic of the power driver module is shown by **Figure S6** and **Figure S7**, respectively.

2.2.2 Power System

The Limpet system is powered by a 450 mAh 11.1V lithium polymer (Li-Po) battery. The Li-Po battery is a rechargeable battery and has dimensions of 49 x 28.5 x 16 mm. In this Limpet version, we detach the Li-Po batteries for charging. The Limpet has a minimum battery life of 26 minutes and a maximum of 4500 hours. We calculated the minimum battery life by assuming the Limpet has all the sensors, RGB LED, microcontroller, infrared communication and electromagnetic module continuously on. The Limpet will consume approximately 1060 mA (communication consumes 10 mA, RGB LED consumes 20 mA, sensors consume 23 mA, microcontroller consumes 7 mA, electromagnetic module consumes 1000 mA), which allows for a battery life of about 26 minutes. We calculated the maximum battery life by assuming the Limpet is in sleep mode, where it consumes an average current of 0.1 mA. In this mode, the battery life of the Limpet can reach about 4500 hours (188 days). The other Limpet capabilities have different current consumption levels and thus can change the battery life. For example, when the limpet is static and adhered to a surface, the Limpet will have a battery lifetime of 50 hours. In this mode, the pressure sensor consumes 2.1 mA to achieve the closed loop control of the adhesion system, and the microcontroller consumes 7 mA.

2.3 Mechanical Design

2.3.1 Design of the Electromagnetic Module (EMM)

The Limpet is designed as a modular system consisting of an adhesion module, locomotion module, sensing module and power driver module. The main unit of the Limpet is the electromagnetic module, which is used as the core unit of the adhesion and locomotion modules. **Figure 2** shows our EMM. The EMM is an electromagnetic system that is based on the same fundamental principles of loudspeakers. The EMM consists of an actuating electromagnetic coil and permanent magnets, which are attached together using a soft body that functions as a spring. The electromagnetic coil can repel or attract the permanent magnet depending on the direction of the current applied to the coil, and this force stretches or compresses the body of the robot, creating linear motion. The EMM is a hybrid hard/soft system.

EMMs have been shown to be a useful system for soft robotics [32], [109]. They are multi-functional components that can generate different behaviours over a range of different control frequencies. At low frequencies, the EMM demonstrates linear actuation capabilities. At audible sound frequencies, the EMM acts as a loudspeaker and at even higher frequencies it can be used for communication [32],

[109], where the communication is based on inductive data transmission, in which the transmission coil generates an alternating magnetic field that induces a voltage in the receiver coil. In this work, we only focus on the actuation and sound capabilities of the EMM and do not utilise its communication capabilities.

Our EMM consists of: electromagnetic coils wound around a reel; permanent magnets embedded in a holder; and a spring consisting of connected bent legs resembling a Chinese lantern as shown by **Figure 2A**. The magnet holder and the coil reel are attached to the spring using laser-cut circular acrylic layers. The EMM can be extended or contracted axially from its rest position, depending on the polarity of current applied to the electromagnetic coil in the voice coil system. A sketch of the module and actuation mechanism is shown by **Figure S8**. The internal components of the electromagnetic module is shown by **Figure 2A**. Application of current to the coil allows the actuator unit to be contracted or extended along its central axis from its rest position; as shown by **Figure 2B** and **Figure 2C**. The applied current induces a magnetic field in the coil, which either attracts or repels the permanent magnets resulting in this actuation mechanism.

2.3.2 Design of the Adhesion Module

To navigate the offshore environment efficiently and be useful for inspection and monitoring of offshore structures, the Limpet will need to have a good adhesion mechanism that allows robust adhesion to different surfaces. We developed an adhesion module based on the EMM, where the adhesion mechanism is based on negative pressure adhesion. The adhesion module also includes a suction cup, vacuum pump, a micro solenoid valve and a pressure sensor. Negative pressure adhesion using suction cups provides the flexibility needed to seal on uneven or coarse surfaces. Our adhesion module is depicted in **Figure 3A**. **Figure 3B** shows a schematic representation of the adhesion system. We attach a T-connector to the suction cup. One side of the T-connector is connected to a pressure sensor. The other side of the T-connector is connected to a valve and pump. To attach to a surface, we program the EMM to push initially on the suction cup to flatten the suction cup and push out the air in the cavity between the cup and surface. We then open the valve and turn on the vacuum pump. The pump will remove any remaining air in the cavity and create a vacuum seal. After the seal is created, we close the valve and turn the pump off. To detach the suction cup, we open the solenoid valve to atmosphere, which causes air to rush into the cavity and break the seal. We use a microcontroller (ATSAMD21G18) to control the pressure sensor, solenoid valve and air pump in the adhesion system. We chose a commercial suction cup for our adhesion module. We compared the commercial suction cup with two different groups of suction cups, which we fabricated out of different soft materials. The two groups of suction cups are: custom-designed suction cups and replicas of the commercial suction cup. We used six different soft materials for each group of suction cups which are Dragon Skin 10, Dragon Skin 20, Dragon Skin 30, Ecoflex 00-10, Ecoflex 00-30, Ecoflex 00-50. A picture of the mould used to fabricate the custom-designed suction cups is shown by **Figure S9**. We designed an experimental setup to test the maximum vertical loading capacity and maximum horizontal loading capacity of the suction cups. A picture of the experimental setup and results of the tests can be found in **Figure S10** and **Figure S11**, respectively. We conducted the same test for the commercial suction cup and the results are shown by **Figure S12**. The commercial suction cup can handle a much higher loading capacity in both the vertical and horizontal direction, and, thus, we decided to use the commercial suction cup for our adhesion module in the Limpet. From our experiment, we also found out that the custom-made suction cups deteriorate quickly (3-4 days) and lose adhesion over time.

2.3.3 Design of the Locomotion Module

Locomotion is another important capability for inspection robots in offshore environments. We developed our locomotion module using the EMM and rubber feet as shown by **Figure 3C**. The locomotion is achieved by actuating the EMM at high frequencies, which results in vibrations. These

vibrations are converted into a forward force that causes movement. Our locomotion technique is thus based on slip-stick locomotion [22], [113]. By changing the amplitude and frequency of vibration, or number of locomotion modules, we are able to achieve movement in different directions.

2.3.4 Design of the Outer Body (Shell)

The shell acts as a protective housing for the Limpet components. The shell was fabricated using Ecoflex 00-50. We first developed a flat mould, which we used to make a 1 mm layer of Ecoflex 00-50. The soft layer was then bent into the right shape and used to cover the Limpet system components, with the sensing module exposed to the outer environment. The Ecoflex 00-50 is a soft material and as such can be manufactured at low cost and allows the Limpet to be inherently complaint to its environment. In addition to that, the Ecoflex is lightweight (reducing the overall weight of the Limpet), very strong (resistant to tearing) and very stretchy (capable of stretching multiple times of its original size without tearing and restores its original form without deforming).

2.4 Fabrication

2.4.1 Fabrication of the Printed Circuit Boards

We designed the sensing and power driver PCBs using Eagle PCB Design Software and fabricated them on double-sided Cu-FR4-Cu 0.1-mm boards. The sensing PCB and power driver PCB was fabricated using an external company called Minnitron Ltd. (Kent, UK). We purchased all electronic components from RS Components, Digi-key Electronics and Mouser Electronics. We soldered the components on the PCBs using a reflow soldering process. In this process, we cut solder paste stencils from vinyl using a Laser Cutter (Epilog Laser Fusion 32). We then stick the stencil on the PCB and apply solder paste on the stencil and PCB. We remove the stencil and manually place the components on their respective pads. Finally, we place the PCBs in an oven to reflow the solder.

2.4.2 Fabrication of the Electromagnetic Module (EMM)

We fabricated the magnet holder, reel, and spring from acetate sheets using kirigami. Kirigami involves cutting a pattern out of sheets and folding it into the desired 3D configuration. The 2D patterns for the coil reel, magnet holder and spring are shown by **Figure S13**. We use kirigami as it allows our components to be low cost and highly manufacturable [114].

The electromagnetic coil consists of a 280-turn 0.35 mm insulated copper wire. We used 12 mm permanent neodymium magnets for our EMMs. We produced the actuation coils for the EMM using a custom-built coil-winding machine, which is shown by **Figure S14**. We purchased the 0.35 mm insulated copper wire from RS Components and the 12 mm permanent neodymium magnets from First4magnets. We used our custom-built coil-winding machine to wind the coils around the coil reel. The resulting reel with wound coils has an internal diameter of 14.5 mm, an outer diameter of 18.5 mm, and a height of 20 mm. The coil winding machine feeds the copper wire onto a rotating coil reel holder and we deposit superglue on the wire as it rotates so that the coil holds its shape.

We fabricated the top and bottom layers of the EMM from a 2 mm acrylic sheet. We used acetate for the spring of the electromagnetic module. Acetate provides advantages of low-cost, lightweight, and high manufacturability. Acetate is also a widely available material. We cut the patterns for the kirigami components (coil reel, magnet holder, spring) and the acrylic layers using a laser cutter (Epilog Laser Fusion 32).

2.4.3 Fabrication of the Adhesion Module

We fabricated the adhesion module from an EMM, suction cup, vacuum pump, solenoid valve and pressure sensor. We used 12 mm permanent magnets and a 280-turn 0.35 mm insulated copper wire

coils for the EMM in the adhesion module. We drilled a hole in the suction cup and connected a plastic T-connector [3cm x 1.8cm x 0.6cm] to it. We used gorilla glue to seal the connection between the T-connector and the hole in the suction cup. We used a 1.6 mm diameter silicon tubing to connect the T-connector to the pressure sensor and the valve. We used the same silicon tubing to connect the valve and pump. The EMM was then glued on top of the T-connector and suction cup.

2.4.4 Fabrication of the Locomotion Module

We fabricated the locomotion module from an EMM. Similar to the EMM fabrication, we used 12 mm permanent magnets and a 280-turn 0.35 mm insulated copper wire coils for the locomotion module. We added round black soft-plastic feet to the bottom layer of the EMM. The plastic feet have a height of 7 mm and a diameter of 12 mm. We used 5 soft-plastic feet on the locomotion module, where one foot was in the center of the module and the four others where each on one of the edges of the module (right, left, top, bottom).

3 Experimental Design and Experimental Results

3.1 Characterisation of the Electromagnetic Module (EMM)

In this section, we discuss the design of the experiments we used to demonstrate the basic capabilities of the EMM. We conducted three different experiments: frequency response analysis, evaluation of the spring constant and measurement of the output force for different input actuation currents

We conducted an additional experiment to analyse the effect of the coil wire thickness on the joule heating in the coils for different currents fed into the coil. In this experiment, we placed the coils with different thicknesses in a custom-designed white acrylic box containing a temperature sensor. The temperature sensor was connected to a computational circuit consisting of a microcontroller and bypass capacitors. We fed current into the coils and measured the temperature rise as a result of the input current. A picture of the experimental setup and results of this experiment are shown by **Figure S15** and **Figure S16**, respectively. The results show that the amount of current drawn by the coils is proportional to the rate of temperature rise. We analysed the temperature rise of the coils for a period of 150 seconds each. Each graph shows the rise in temperature over time for each of the coils at a different current level (1A, 2A, 3A, 4A). The results also show that rate of temperature rise increases significantly as the wire thickness decreases.

3.1.1 Frequency Response Analysis

The EMM provides different capabilities over a wide frequency range. The primary function of the EMM is actuation at low frequencies, but it can also produce an audio output at higher frequencies. We designed an experiment in which we programmed the microcontroller to vary the coil frequency from 1 Hz to 15 KHz. We measured the height of actuation of the top part of the EMM using a RealSense Camera mounted above the module. The RealSense Camera can detect the depth, and this function was used to track the movement of the top half of the EMM in the frequency response experiment. We also used an omni-directional sound sensor (-22 dB) to record the audio output produced by the EMM at high frequencies. The experimental setup is shown by **Figure 4A**. We also designed an experiment to test the pulse-width scheme on the EMM and its effect on height of actuation by programming the microcontroller to provide a PWM signal to the coils of the EMM. We first sweep through duty cycles from 0% to 100% and then from 100% back to 0%. Following that, we increment the duty cycles applied to the EMM in steps of 20% from 0% to 100%, and measure the displacement at each step. We recorded the experiments using an 18-mp Canon EOS 100D camera and an EF-S 18–55mm f/3.5–5.6 IS STM lens. The frequency response of the EMM can be seen in **Video S2**. We also recorded the frequency response analysis experiment with a Sony PlayStation 3 eyetoy camera, which

provides a higher frame rate than the RealSense camera. The video from the eyetoy camera is shown by **Video S3**. A video of the PWM experiment can be found in **Video S4**. We conducted these experiments only once to show the capabilities of the EMM over the range of different frequencies.

In this experiment, we demonstrate that the EMM can actuate at a low frequency and transition to sound output as the frequency increases to audible levels as shown by **Video S2**. The video shows the EMM actuating at increasing frequencies and then transitioning from actuation to sound output at higher frequencies. The change in height of the EMM against actuation frequency at low actuation frequencies is shown by **Figure 4B**. As seen by the graph in **Figure 4B**, as the actuation frequency increases the period for the EMM to extend and contract fully decreases. As the frequency increases further, the change in height decreases as the EMM actuates at a very high speed. At even higher frequencies, the camera cannot pick up the change is height properly as the EMM is actuating at a frequency higher than the frame rate of the camera. The sound spectrogram for the EMM at audible frequency levels is shown by **Figure S17**. The spectrogram is based on the audio from seconds 24 to 42 in **Video S2**. The audio is sampled at a rate of 44,100 KHz and divided into windows of 8820 samples with an overlap of 2205 samples between neighbouring windows. Fast Fourier Transform (FFT) is conducted on each window. The amplitude of the powers in the FFT is then scaled [115] based on a Mel-Scale, which is a model of the sensitivity of the human ear to each frequency [116]. The resulting FFTs are used to create a heat map of frequency versus time called a Mel-Spectrogram.

We also demonstrate how we can control the height of actuation by changing the PWM signal level. We expected that the use of PWM will change the actuation current to produce forces smaller than the maximum actuation force, and therefore, partial actuation. Our use of a PWM actuation signal produced the expected partial actuation behavior. The partial actuation behavior resulting from the PWM signal is demonstrated in **Video S4**. The change in height of the EMM with respect to the PWM duty cycle is shown by **Figure S18**. The change in height has a linear relationship with the PWM duty cycle.

3.1.2 Evaluating the Spring Constant of the EMM

The output force of the EMM is a combination of a spring force and an electromagnetic force. To evaluate the output force from the kirigami spring, it is important to study the elasticity of the kirigami spring by measuring its spring constant. The spring constant represents the amount of force required to compress or extend a spring. The relationship between the force applied to the spring and the displacement is given by:

$$F = kx$$

Where F is the force applied, k is the spring constant, and x is the distance the spring is extended or compressed from its rest position. To evaluate the spring force, we designed an experimental setup to investigate the spring constant of the kirigami spring. Our experimental setup consists of the kirigami spring (without the coils and magnets), ruler, metal guide rails and weights as shown by **Figure 4C**. In our experiment, we placed weights on the kirigami spring and measured the displacement of the spring. We increased the weight from 0 to 120 g in steps of 20 g. We used the metal guide rails to avoid any bending of the top acrylic part of the spring when we place the weights on it. The experiment we conducted to identify the spring constant is shown by **Video S5**. The graph of the force applied against the extension is shown by **Figure 4D**. The spring constant can be calculated by measuring the slope of the graph. In this case, the kirigami spring has a spring constant of 45.5 N/m. Since we took the measurements of displacement using a ruler the standard error is ±0.5 mm**.**

3.1.3 Determining the Output Force for Different Actuation Currents

To determine the output force for different current levels supplied to the EMM, we designed a controllable experimental setup consisting of a force testing rig, force gauge and a hook as shown by **Figure 4C**. We designed the setup so that the force gauge and the EMM are fixed in place in the force testing rig, with the force gauge aligned perpendicularly above the EMM. We connected the EMM and the force gauge together with a hook and a laser-cut eye loop. We programmed the EMM to contract at maximum force and, thus, it pulls against the force gauge hook and gives a force measurement on the force gauge. We supplied the EMM with different current levels and measured the maximum force achieved at each current level. We increased the current from 0 to 1500 mA in steps of 50 mA. When the EMM pulls against the force gauge, it does not change its shape. Thus, the effect of the spring force does not affect the results in this experiment. The electromagnetic force measured in this experiment is the force at zero displacement of the EMM. We repeated the experiment five times. **Video S6** shows one repeat of the experiment we conducted to measure the output force for different actuation currents. The output force from the EMM is a sum of the spring force from the kirigami spring and electromagnetic force from the interaction of the coils and permanent magnets. The total force generated by the EMM is given by:

$$F_{output} = F_{spring} + F_{electromagnet}$$

The electromagnet force, when the coil and magnets are fully separated, is given by:

$$F_{electromagnet} = \mu \frac{q_{coil}\ q_{pmag}}{4\pi(d + r_o)^2}$$

Where μ is the permeability of free space, qcoil is the pole strength of the electromagnetic coil, qpmag is the pole strength of the permanent magnets, d is the distance from rest position, and ro is the distance between center of coil and center of magnets at rest position. qcoil is given by:

$$q_{coil} = \frac{NIA}{L}$$

Where N is the number of turns of the electromagnetic coil, I is the current supplied to the coil, A is the cross-sectional area of the coil, and L is the length of the coil. In this experiment, the EMM was pulling against the force gauge with maximum force. The EMM did not change its height. Thus, the effect of the spring force does not affect the results of this experiment. For the electromagnetic force, the force measured is the force at zero displacement (d). The results of the output force for different actuation currents is shown by **Figure 4F**. There is a linear relationship between the current supplied and the actuation force. The results of all the five experiments are within the measurement error of the force gauge (±0.02N). The maximum force achieved by the EMM in this experiment was 1.8 N, which suggests that a single module could lift objects with masses below ~184g when provided with an actuation current of 1500 mA.

3.2 Characterisation of the Adhesion Module

In this section, we discuss the design of the experiments we used to characterise the adhesion module of the EMM. We conducted two different experiments: strength of attachment to different surfaces and closed loop control of the adhesion system. The first experiment evaluates the adhesion force of our adhesion module on surfaces with different roughness, and gives a safety factor indication for the design of the adhesion module for different surfaces. The second experiment demonstrates the capability of our closed loop controller implemented on the adhesion module.

3.2.1 Strength of Attachment to Different Surfaces

To characterise the ability of our adhesion module to stick to different surfaces, we designed an experimental setup consisting of the adhesion module, surfaces with different average surface roughness, laser-cut acrylic weight rig and weights. We measured the average surface roughness of five different surfaces (acrylic, vinyl, copper, two different types of steel) using the Dektak XTL stylus profiler. The Dektak XTL provides a 2D roughness surface characterization by dragging a 2 µm stylus across the surface. The average surface roughness gives an indication of surface texture and overall profile height characteristics of a surface. For each surface, we repeated the surface roughness measurement five times, and used the average of the five measurements. We conducted the experiment by attaching the adhesion module to each surface and testing the maximum vertical and horizontal loading capacity on the module. We attached the weight rig to the adhesion module and start adding weights to the rig in steps of 10g until the adhesion module fails and detaches from the surface.

In this experiment, we observe that the adhesion force of the adhesion module decreases linearly with average surface roughness. **Figure 5A** shows the relationship between the vertical and horizontal adhesion force of the adhesion module and the average surface roughness. We measured the average surface roughness of five different target surfaces as shown by the points on the graph. We then plotted the best fit line through the points. We added a safety factor of 1.5 for the vertical and horizontal adhesion force. Taking into account the safety factor, the graph shows that on the surface with the highest measured surface roughness, the adhesion module can handle up to 26N in the vertical direction and up to 9N in the horizontal direction. These measurements indicate that the adhesion module can handle an average maximum weight of 920g in the horizontal direction if placed on a rough metallic surface. We used this measurement as a guide for the maximum allowed weight of the final Limpet system, if it is to be used for climbing rough surfaces in offshore environments.

3.2.2 Closed Loop Control of the Adhesion System

We designed a closed loop controller for our adhesion system. The closed loop controller monitors the pressure in the cavity between the suction cup and the surface. When the pressure reaches a certain threshold, which is lower than the pressure required to detach the suction cup (atmospheric pressure), the controller will open the valve and turn on the vacuum pump to restore the pressure in the cavity. The controller ensures that if any leakage occurs in the suction cup, the adhesion module will not detach from the surface. To test the efficiency of the controller, we designed an experimental setup where we induce a leakage in the suction cup by opening the solenoid valve to atmosphere and then monitoring the effect of the closed loop controller on restoring the suction cup pressure.

In this experiment, we first attach the adhesion module to the surface by pumping the air out of the cavity between the suction cup and the surface. At this point, the pressure of the suction cup is measured to be 435 mbar. The suction sup detaches from the surface when the pressure in the cavity reaches atmospheric pressure (1014 mbar). We developed a closed loop controller that monitors the pressure in the cavity, and if the pressure ever reaches 895 mbar, the controller will open the pump to restore the adhesion force to normal. In this experiment, we induced a leakage in the suction cup after attachment, by opening the valve to atmosphere, and monitor the pressure as it rises towards atmospheric pressure. When the pressure reaches 895 mbar, the pressure is restored back to 435 mbar as shown by **Figure 5B**. We repeated this procedure multiple times, and the closed loop controller was always successful in restoring the adhesion of the module and preventing detachment of the suction cup.

3.3 Characterisation of the Locomotion Module

In this section, we discuss the design of the experiments we used to characterise the locomotion module of the Limpet. This section is divided into two parts. In the first part, we designed an experiment to show the modularity aspect of our system, and how we can achieve simpler controllers and more complex systems by stacking basic modules (EMMs) together. In the second part, we conducted an experiment to track the movement of our final locomotion system as it moves in a pre-defined geometry in its environment. We also conducted an experiment to track the displacement of the top part of the final locomotion system as it moves in a straight line along one axis.

3.3.1 Effect of Stacking the Locomotion Modules

The locomotion using this module (EMM and rubber feet) can be achieved in multiple different ways depending on the number of modules used and the mechanical design of the system. The mechanical design of the system will affect the center of mass of the system. In this section, we designed an experiment to investigate the effect of stacking or combining basic functional modules (locomotion modules) to create a system that is more complex and has greater capability than the sum of its individual parts. We use three types of locomotion systems: using a single EMM, using two EMMs, and using four EMMs as shown in **Figure 3C**, **Figure 3D** and **Figure 3E**. In this experiment, we have an environment with four targets in each of the four cardinal directions. The aim of this experiment is to show how we can stack or combine locomotion modules to produce a system that can achieve greater capability with simpler control. In the first part of the experiment, we used a single locomotion module and show the effect of weight biasing on the ability of module to reach the targets. We used a 20g weight to achieve the change in directions using the single locomotion module. We used an actuation frequency of 4 Hz, and supplied the module with an actuation current of 300 mA. In the second part of this experiment, we demonstrate the capability of a system consisting of two combined locomotion modules and show the effect of both amplitude biasing and weight biasing on the performance of this system. For weight biasing, we change the direction of movement of the system using a 20g weight, while for amplitude biasing we actuate each of the locomotion modules in a different way to the other. The two locomotion modules are attached together using a 2mm acrylic piece. For this part of the experiment, one module was contracted fully while the other module was actuating at a frequency of 6.7 Hz. We supplied an actuation current of 750 mA to both modules. Finally, we designed a system with four different modules and used amplitude biasing on the system to try to reach the four targets, and we show the effect of this system on our controller and system design.

In this experiment, we observe that using one locomotion module to reach four targets in each cardinal direction requires a change in the mechanical structure of the module. We can bias the direction of movement by placing a weight at the edge of the EMM facing the desired direction of movement. We use a 20g weight for this experiment, and we repeat the experiment four times. In each repetition of the experiment, we have to manually change the location of the weight on the top acrylic layer of the module as shown by **Figure 6A-6D**. The weight tilts the EMM and shifts its center of mass allowing it to move to the desired direction. Thus, to use a single EMM as the final locomotion system, we would have to design a mechanical system that can shift the center of mass of the EMM towards the required direction, and we would have to develop a technique to allow the EMM to alter that mechanical system autonomously to achieve successful movement. This approach of using a single EMM would make the mechanical design and the controller of the Limpet very complex. The average speed of the single module in this experiment is 35.4 mm/s. **Video S7** shows the single locomotion module reaching the four targets by biasing the direction using an external weight. When we stack two EMM modules into one locomotion system, the system is capable of more complex motions with a simpler controller and design. The system can be biased in two ways. The center of mass of the system can be shifted using an external weight or using the combination of the two EMMs. The first method involves adding a 20g weight on either side of the space between the two EMMs. The weight tilts the system and results in a shift in the center of mass causing the locomotion system to move in the north

or south directions as shown by **Figure 6E** and **Figure 6F**. The second method involves programming the EMMs to have different behaviours, which will also result in a shift of the center of mass of the system. In our case, we program the EMM that is on the side closer to the target to actuate continuously in both directions, while the EMM further away from the target to be in continuous contraction at maximum force as shown by **Figure 6G** and **Figure 6H**. The average speed achieved by the system when biased by the weight is 70.7 mm/s. The average speed achieved by biasing the system using the combination of the EMMs is 31.4 mm/s. The results of the locomotion system composed of two EMMs is shown by **Video S8**. Based on the results of these two experiments, we decided to develop a locomotion system using four EMMs. We can use this locomotion system to achieve motion in all cardinal directions using only the EMMs as shown in **Figure 7**. We use the EMMs to shift the center of mass of the locomotion system and achieve movement in the required direction. Thus, this system simplifies our mechanical design and the controller required. The average speed achieved by this system is 37.1 mm/s. All the targets are reached successfully and simply by the locomotion system without using any external weight bias as shown in **Video S9**. The speed of the different systems is not an important comparison parameter, as we can control the speed of the system by changing the input current and actuation frequency of the different modules.

3.3.2 Evaluating the Locomotion

We observe that stacking functional blocks results in systems that are increasingly capable of a diverse range of complex motions and behaviors. We decided to use the locomotion system composed of four EMMs and explore it further. We conducted two different experiments to evaluate the locomotion of the system. We recorded both experiments using an 18-mp Canon EOS 100D camera and an EF-S 18–55mm f/3.5–5.6 IS STM lens.

In the first experiment, we programmed the system to travel in a rectangular path and we track the position of the system using AprilTags [117]. Each side of the rectangular path is achieved by actuating a different combination of locomotion modules at different frequencies. The locomotion system is programmed to move in a rectangular fashion and can achieve so with a slight deviation in one of the sides as shown in **Figure 8A** and **Video S10**. We supplied a current of 2A to the system in this experiment.

In the second experiment, we track the change in height of the top part of the locomotion system as it moves in a straight line along one axis as shown by **Video S11**. We track the displacement and change in height using a 3D printed black sphere that we attached to the top of the locomotion system. We developed a custom-written script that can track the black sphere against the white background and record the change in position of the sphere vertically and horizontally. The change in height versus horizontal displacement is shown by **Figure 8B**.

3.4 Demonstrations

In addition to the experiments that show the characterisation of the different modules included in the Limpet, we performed additional demonstrations to show how the modules can be configured to allow the Limpet to perform useful behaviours in its environment.

3.4.1 Untethered Sensory Control of the Limpet

In this experiment, we use the different sensors on the Limpet to control its locomotion and adhesion capabilities. We use the sound, distance, light, and IMU sensors to show an example of how the Limpet can respond to sensory input in its environment. These demonstrations shows how the Limpet can use this capability and the sensing measurements to map its environment and act upon changes in that environment. Such a capability is important for inspecting and monitoring offshore platforms. **Video**

S12 shows the Limpet responding to a light stimulus, where a change in the ambient light color will lead to movement in different directions. In this demonstration, we use the light sensor on the Limpet, which is capable of measuring ambient light intensity, and power density of red, green and blue light. **Video S13** shows how the Limpet can change its movement direction or enable and disable its adhesion mechanism based on a change in frequency of a sound input signal that is measured by the sound sensor on the Limpet. **Video S14** shows how the Limpet can respond to the presence of objects at different proximity from the Limpet using the on-board distance sensor. In **Video S15**, we poke the Limpet, which will cause it to start repositioning itself away and then adhering in place at the new position. We use the IMU sensor for this demonstration, where poking the Limpet will result in a small change in the acceleration and gyro data. This small change is picked up by the Limpet, which responds to this change by repositioning itself in its environment.

3.4.2 Sound-Based Inter-Communication of Limpets

One of the capabilities of the EMM is generation of sound output. This capability can be used by the Limpets for communication with neighbouring Limpets. In this demonstration, we demonstrate how the sound capabilities of the EMM in the Limpet can be used for communication with other neighbouring Limpets. One Limpet generates a sound signal (distress signal), and the neighbouring Limpet around it will start moving away from that Limpet. The result of this demonstration is shown by **Video S16**. This capability can be used in a situation where other communication systems (e.g. WiFi and LoRa) are down, and the Limpet needs to communicate to its neighbours. The idea behind this capability is that the Limpet can send out command signals to its neighbours, which can be for example, to start inspecting and mapping the structure for faults.

3.4.3 Climbing

To highlight the modularity aspect of the Limpet system and to show its capability in unstructured offshore environments, we reconfigured the modules of the Limpet to enable it to climb an inclined surface. A side view and a top view of the Limpet climbing the surface is shown by **Video S17**. In this experiment, we reconfigured our electromagnetic and adhesion modules as shown by **Figure S19**. The Limpet configuration includes two vertical adhesion modules, and two horizontal electromagnetic modules connected between the adhesion modules. We programmed the Limpet to follow a sequence of steps as follows:

- Top adhesion module adheres to the surface by activating its pump, closing its valve, and extending itself to push the suction cup on the surface.
- Bottom adhesion module contracts to lift its suction cup off the surface.
- Horizontal EMMs contract, which brings the bottom adhesion module closer to the top one.
- Bottom adhesion module adheres to the surface by activating its pump, closing its valve, and extending itself to push the suction cup on the surface.
- Top adhesion module detaches from the surface by opening its valve to atmosphere and contracting to lift its suction sup off the surface.
- Horizontal EMMs extend, which pushes the top adhesion module further away from the bottom one.
- Top adhesion module adheres to the surface by activating its pump, closing its valve and extending itself to push the suction cup on the surface.
- The motion is then repeated multiple times to achieve the vertical locomotion on the surface.

4 Discussion

In this work, we present an untethered hybrid robot that integrates a sensing module, power driver module, adhesion and locomotion modules based on EMMs. The robot is designed in a modular fashion, equipped with nine exteroceptive sensing modalities, and features capabilities of simple and untethered control, adhering to different structures and materials (acrylic, vinyl, copper, steel), walking on horizontal surfaces, climbing inclined surfaces and sensing its environment.

The Limpet is a useful system for carrying out inspection tasks offshore as it capable of navigating on surfaces at different angles. Current climbing robots focus on the climbing capabilities and have limited or no sensing abilities on-board. Also, the existing systems mostly use rigid actuators, which does not allow the robot to easily conform to its environment and adds complexity in the task planning phase. Soft climbing robots that have been reported [64] are not fully untethered systems yet, which limits their capability to carry out useful tasks in such extreme environments. The Limpet uses hybrid actuators, which has the advantages of rigid components and can still partially conform to its environment. The Limpet is also developed as a fully, untethered system, which removes the limitations associated with power and communication tethers in performing tasks and allows for autonomous deployment of the system. The Limpet is equipped with nine sensing modalities, which allows it to sense its environment and monitor the conditions of the different offshore structures. The Limpet is developed in a modular fashion, which makes it easier to adapt the system to new tasks, to repair the system, to replace and reconfigure the modules.

One major drawback of the locomotion technique of the Limpet is that there is no real form of on-board odometry, which makes moving accurately and precisely for a long duration of time or for large distances a challenging task. However, we can achieve odometry using a combination of the AprilTags surrounding the system and an off-board communication system (e.g. Infrared Transceiver), to accurately estimate the change in position and achieve more precise movement over long distances. Another limitations with the current system is the high power consumption of electromagnetic modules when holding force. We try to minimise this power consumption by minimising the time in which electromagnetic modules hold their force. For adhesion, the module is provided with a single power impulse to help with the adhesion process and then the pump kicks in and the electromagnetic module is switched off. For the locomotion, the electromagnetic module is provided with power impulses in both directions, and we minimise the time between pulses to minimise the holding force period of the module.

We can easily alter the speed of the locomotion system, as the speed is a function of the current supplied, frequency of actuation of the EMMs and the weight of the system. However, there are some limitations to increasing the speed, as faster actuation consumes higher power and affects the battery lifetime. Power consumption during deployment life is a very important consideration for the Limpet system to be used in offshore environments. The speed achieved in vertical climbing is smaller than that achieved in horizontal motion, as the adhesion and locomotion forces are used to overcome the gravity force of the robot during climbing. The adhesion capability of the Limpet relies on materials and surface textures, and works best on flat surfaces. The adhesion can be used on rough and uneven surfaces, but will achieve shorter periods of adhesion. The Limpet system presented in this work has a short battery life. The battery life can be increased by using larger batteries, but those batteries have larger weight and will affect the adhesion force and the climbing speed of the system.

5 Conclusion

Existing climbing robots mostly use rigid actuators, and robots that use soft actuators are not fully untethered yet. Current climbing robots are also not built in a modular fashion, which makes it harder to adapt the system to new tasks, to repair the system, to replace and reconfigure the modules. In this work, we present an untethered hybrid soft/hard robot - the Limpet – that is designed in a modular

fashion. The modules of the Limpet can be reconfigured to achieve different tasks giving it the ability to of climb inclined surfaces, adhering to different structures and sensing its environment. The Limpet uses a hybrid electromagnetic module as its core unit to allow adhesion and locomotion capabilities. The adhesion capability is based on negative pressure adhesion utilising suction cups. The locomotion capability is based on slip-stick locomotion. The Limpet also has a sensor payload with nine different sensing modalities, which can be used to inspect and monitor offshore structures and the conditions surrounding them. To demonstrate its potential for inspection of offshore platforms, we show that the Limpet is capable of responding to different sensory inputs, repositioning itself within its environment, adhering to structures made of different materials, and climbing inclined surfaces.

6 Figure Captions

Figure 1. System Overview. The Limpet is a modular, untethered hybrid hard/soft robot consisting of a sensing module, locomotion module, adhesion module, power driver module, outer soft shell.

Figure 2. Electromagnetic Module (EMM). (A) A labelled picture of the EMM and a cross-sectional view of the EMM at rest position (l) showing the kirigami spring, coils, magnets, top and bottom acrylic layers. The coils interact with the magnets and either push or pull the kirigami spring. (B) An EMM extending resulting in an increase in length of the module ($l + \Delta l$). (C) An EMM contracting resulting in a decrease in length of the module ($l - \Delta l$).

Figure 3. Adhesion Module and Locomotion Modules. (A) A labelled picture of the adhesion module showing the EMM, suction cup, T-connector, and pneumatic and power tethers. (B) A schematic representation of the adhesion system. (C) A side view picture and bottom view picture of the locomotion module based on the EMM. (D) A picture of the combination of two locomotion modules based on the EMMs. (E) A picture of 4 EMMs stacked together into a locomotion system.

Figure 4. Characterisation of the Electromagnetic Module (EMM). (A) Schematic of the experimental setup used to characterize the frequency response of the EMM. At low frequencies, the EMM demonstrates linear actuation capabilities and acts as a loudspeaker at higher frequencies. We used a depth camera to track the height of actuation at low frequencies, and a microphone to detect the sound output at higher frequencies. (B) Results of the frequency response analysis experiment showing the change in height of the EMM against the actuation frequency. (C) A labelled picture of the experimental setup used to measure the spring constant of the kirigami spring of the EMM. (D) Results of the spring constant evaluation experiment showing the extension of the spring against the force applied to the spring. (E) A labelled picture of the experimental setup used to measure the output electromagnetic force from the EMM for different current levels supplied to it. (F) Results of the experiment used to evaluate the output force from the EMM against the current supplied to the EMM. The experiment was repeated five times, and the results of all the five experiments are within the measurement error of the force gauge (± 0.02N).

Figure 5. Characterisation of the Adhesion Module. (A) Results of the adhesion force of the adhesion module on different surfaces. The graph shows the maximum vertical and horizontal adhesion force of the module for surfaces with different surface roughness, and a safety factor of 1.5 for the vertical and horizontal adhesion forces. (B) A graph demonstrating our closed loop control of the adhesion module. We induce a leakage in the suction cup, which causes the pressure in the cavity between the suction cup and surface to rise. When the pressure reaches a certain threshold, which is lower than the pressure required to detach the suction cup, the valve will open and the pump will switch back on to restore the pressure in the cavity.

Figure 6. Modularity and Stacking of the Locomotion Modules. (Ai-Di) Schematic of the experimental setup used to analyse a single locomotion module and its ability to reach four different targets within its environment. We add a weight on one side of the locomotion module to bias it to move in that direction. (Aii-Dii) Images of the single locomotion module with the weight on top of it reaching the targets at the different cardinal directions. (Ei-Fi) Schematic of the experimental setup used to analyse a locomotion system made up of 2 EMMs, where the system is biased to move by adding a weight on top of it. (Gi-Hi) Schematic of the experimental setup used to analyse a locomotion system made up of 2 EMMs, where the system is biased to move by actuating the 2 EMMs in different manners to each other. (Eii-Fii) Images of the double locomotion system trying to reach targets in the North and South directions by manually adding a weight to different sides of the module. (Gii-Hii) Images of the double locomotion system trying to reach targets in the East and West directions by actuating one module in both directions, while only extending the other module.

Figure 7. A Locomotion System Composed of a Stack of Four Locomotion Modules. (A-D) Schematic of how each locomotion module within the locomotion system is actuated to achieve movement in the different directions. In each case, two of the modules are idle, one module is actuating in both directions, while the final module is contracting to bias the direction of the movement.

Figure 8. Characterisation of the Locomotion System with the Four Locomotion Modules. (A) The path of the locomotion system after being programmed to travel in a rectangular path and the position of the system is tracked using AprilTags. (B) Tracking the vertical displacement of the locomotion system as it moves horizontally in a straight line.

7 List of Supplementary Materials

Figure S1: Architecture of the WiFi Communication
Figure S2: Architecture of the Serial Communication
Figure S3: Architecture of the LoRaWAN Communication
Figure S4: Labelled Picture of the Sensing Module
Figure S5: A Circuit Schematic of the Sensing Module
Figure S6: Labelled Picture of the Power Driver Module
Figure S7: A Circuit Schematic of the Power Driver Module
Figure S8: Sketch of the EMM and the Actuation Mechanism
Figure S9: Custom-Designed Suction Cup Mould
Figure S10: Vertical Loading Capacity of the Suction Cups
Figure S11: Horizontal Loading Capacity of the Suction Cups
Figure S12: Horizontal and Vertical Loading Capacity on Commercial Suction Cup
Figure S13: 2D Patterns of the EMM components
Figure S14: Custom-Built Coil-Winding Machine
Figure S15: Experimental Setup for Heat Dissipation Measurements for Different Coils Thickness
Figure S16: Experimental Results of the Heat Dissipation Experiment
Figure S17: Sound Spectrogram of the EMM at Audible Frequency Levels
Figure S18: PWM Experiment Results
Figure S19: Configuration of the Limpet System for Vertical Climbing

Video S1: Overview of the Limpet System
Video S2: Frequency Response Analysis
Video S3: Frequency Response Analysis at a Higher Frame Rate
Video S4: Pulse-Width Modulation of the Electromagnetic Module
Video S5: Evaluation of the Spring Constant of the Electromagnetic Module
Video S6: Determining the Output Force for Different Actuation Currents

Video S7: Single Locomotion Module
Video S8: Locomotion System with Two Locomotion Modules
Video S9: Locomotion System with Four Locomotion Modules
Video S10: Locomotion System Following a Rectangular Shaped Path
Video S11: Tracking the Height of Displacement of the Locomotion System
Video S12: Untethered Control of the Limpet Using Light Sensor
Video S13: Untethered Control of the Limpet Using Sound Sensor
Video S14: Untethered Control of the Limpet Using Distance Sensor
Video S15: Untethered Control of the Limpet Using IMU Sensor
Video S16: Sound-Based Inter-Communication of Limpets
Video S17: Climbing an Inclined Surface

8 Acknowledgements

Adam A. Stokes and Simona Aracri acknowledge support from the EPSRC ORCA Hub (EP/R026173/1). Ross M. McKenzie and Jamie O. Roberts acknowledge support from EPSRC via the Robotarium Capital Equipment, and CDT Capital Equipment Grants (EP/L016834/1) and the CDT in Robotics and Autonomous Systems at Heriot-Watt and The University of Edinburgh. Anthony Buchoux acknowledges support from the ESPRC New Engineering Concepts from Phase Transitions: A Leidenfrost Engine (EP/P005705/1).

9 Author Disclosure Statement

The authors declare no competing financial interest.

10 Author Contributions

M.E.S. designed and created the system, designed and conducted the experiments, analyzed the data and is the lead author of the work. J.O.R. helped in the design and creation of the system, assisted in designing the experiments. R.M.M. helped in the design of the electromagnetic module and conducting the experiments. S.A. helped in analyzing the data. A.B. helped with conducting the surface roughness measurements. A.A.S. directed the project and edited the manuscript.

References

[1] S. D. de Rivaz, B. Goldberg, N. Doshi, K. Jayaram, J. Zhou, and R. J. Wood, 'Inverted and vertical climbing of a quadrupedal microrobot using electroadhesion', *Sci. Robot.*, vol. 3, no. 25, p. eaau3038, Dec. 2018.

[2] S. S. R. Chennareddy, A. Agrawal, and A. Karuppiah, 'Modular Self-Reconfigurable Robotic Systems: A Survey on Hardware Architectures', *J. Robot.*, vol. 2017, pp. 1–19, Mar. 2017.

[3] S. Li *et al.*, 'Particle robotics based on statistical mechanics of loosely coupled components', *Nature*, vol. 567, no. 7748, pp. 361–365, Mar. 2019.

[4] D. Rus and M. Vona, 'A physical implementation of the self-reconfiguring crystalline robot', in *IEEE international conference on robotics and automation (ICRA)*, 2000, vol. 2, pp. 1726–1733.

[5] M. Yim, D. G. Duff, and K. D. Roufas, 'PolyBot: a modular reconfigurable robot', in *IEEE international conference on robotics and automation (ICRA)*, 2000.

[6] J. W. Suh, S. B. Homans, and M. Yim, 'Telecubes: mechanical design of a module for self-reconfigurable robotics', in *IEEE international conference on robotics and automation (ICRA)*, 2002, pp. 4095–4101.

[7] B. Salemi, M. Moll, and W. Shen, 'SUPERBOT: A Deployable, Multi-Functional, and Modular Self-Reconfigurable Robotic System', in *2006 IEEE/RSJ International Conference on Intelligent Robots and Systems*, 2006.

[8] G. G. Ryland and H. H. Cheng, 'Design of iMobot, an intelligent reconfigurable mobile robot with novel locomotion', in *2010 IEEE International Conference on Robotics and Automation*, 2010.

[9] K. Gilpin, A. Knaian, and D. Rus, 'Robot pebbles: One centimeter modules for programmable matter through self-disassembly', in *2010 IEEE International Conference on Robotics and Automation*, 2010.

[10] J. Zhao, X. Cui, Y. Zhu, and S. Tang, 'A new self-reconfigurable modular robotic system UBot: Multi-mode locomotion and self-reconfiguration', in *2011 IEEE International Conference on Robotics and Automation*, 2011.

[11] J. W. Romanishin, K. Gilpin, and D. Rus, 'M-blocks: Momentum-driven, magnetic modular robots', in *2013 IEEE/RSJ International Conference on Intelligent Robots and Systems*, 2013.

[12] J. Baca, S. G. M. Hossain, P. Dasgupta, C. A. Nelson, and A. Dutta, 'ModRED: Hardware design and reconfiguration planning for a high dexterity modular self-reconfigurable robot for extra-terrestrial exploration', *Rob. Auton. Syst.*, vol. 62, no. 7, pp. 1002–1015, Jul. 2014.

[13] X. Jia, M. Frenger, Z. Chen, W. R. Hamel, and M. Zhang, 'An alligator inspired modular robot', in *2015 IEEE International Conference on Robotics and Automation (ICRA)*, 2015, pp. 1949–1954.

[14] S. Murata, E. Yoshida, A. Kamimura, H. Kurokawa, K. Tomita, and S. Kokaji, 'M-TRAN: self-reconfigurable modular robotic system', *IEEE/ASME Trans. Mechatronics*, vol. 7, no. 4,

pp. 431–441, Dec. 2002.

[15] A. Brunete, J. E. Torres, and M. Hernando, ‘Arquitectura para robots modulares multiconfigurables heterogéneos de tipo cadena’, *Arquit. Control Para Robot. Sección publicaciones la Esc. Técnica Super. Ing. Ind. (ETSII), Univ. Politécnica Madrid*, pp. 151–167, 2007.

[16] M. Yim *et al.*, ‘Modular Self-Reconfigurable Robot Systems [Grand Challenges of Robotics]’, *IEEE Robot. Autom. Mag.*, vol. 14, no. 1, pp. 43–52, Mar. 2007.

[17] J. Clune, J.-B. Mouret, and H. Lipson, ‘The evolutionary origins of modularity’, *Proc. R. Soc. B Biol. Sci.*, vol. 280, no. 1755, pp. 20122863–20122863, Jan. 2013.

[18] C. H. Belke and J. Paik, ‘Mori: A Modular Origami Robot’, *IEEE/ASME Trans. Mechatronics*, vol. 22, no. 5, pp. 2153–2164, Oct. 2017.

[19] J. Neubert, A. Rost, and H. Lipson, ‘Self-Soldering Connectors for Modular Robots’, *IEEE Trans. Robot.*, vol. 30, no. 6, pp. 1344–1357, Dec. 2014.

[20] K. Stoy, ‘Reconfigurable Robots’, in *Springer Handbook of Computational Intelligence*, J. Kacprzyk and W. Pedrycz, Eds. Springer, 2015, pp. 1407–1419.

[21] A. Brunete, A. Ranganath, S. Segovia, J. P. de Frutos, M. Hernando, and E. Gambao, ‘Current trends in reconfigurable modular robots design’, *Int. J. Adv. Robot. Syst.*, vol. 14, no. 3, p. 172988141771045, May 2017.

[22] M. Rubenstein, C. Ahler, and R. Nagpal, ‘Kilobot: A low cost scalable robot system for collective behaviors’, in *2012 IEEE International Conference on Robotics and Automation*, 2012, pp. 3293–3298.

[23] M. P. Nemitz *et al.*, ‘HoverBots: Precise Locomotion Using Robots That Are Designed for Manufacturability’, *Front. Robot. AI*, vol. 4, p. 55, Nov. 2017.

[24] M. P. Nemitz *et al.*, ‘Multi-Functional Sensing for Swarm Robots Using Time Sequence Classification: HoverBot, an Example’, *Front. Robot. AI*, vol. 5, p. 55, May 2018.

[25] S. T. Mahon *et al.*, ‘Capability by Stacking: The Current Design Heuristic for Soft Robots’, *Biomimetics*, vol. 3, no. 3, p. 16, Jul. 2018.

[26] S.-R. Kim, D.-Y. Lee, J.-S. Koh, and K.-J. Cho, ‘Fast, compact, and lightweight shape-shifting system composed of distributed self-folding origami modules’, in *2016 IEEE International Conference on Robotics and Automation (ICRA)*, 2016, pp. 4969–4974.

[27] A. A. Stanley and A. M. Okamura, ‘Controllable Surface Haptics via Particle Jamming and Pneumatics’, *IEEE Trans. Haptics*, vol. 8, no. 1, pp. 20–30, Jan. 2015.

[28] S. Follmer, D. Leithinger, A. Olwal, A. Hogge, and H. Ishii, ‘inFORM: Dynamic Physical Affordances and Constraints through Shape and Object Actuation’, in *ACM Symposium on User Interface Software and Technology (UIST)*, 2013.

[29] M. A. Robertson and J. Paik, ‘New soft robots really suck: Vacuum-powered systems empower diverse capabilities’, *Sci. Robot.*, vol. 2, no. 9, p. eaan6357, Aug. 2017.

[30] M. T. Tolley *et al.*, ‘A Resilient, Untethered Soft Robot’, *Soft Robot.*, vol. 1, no. 3, pp. 213–223, Sep. 2014.

[31] D. Keithly *et al.*, ‘A cephalopod-inspired combustion powered hydro-jet engine using soft actuators’, *Extrem. Mech. Lett.*, vol. 20, pp. 1–8, Apr. 2018.

[32] M. P. Nemitz, P. Mihaylov, T. W. Barraclough, D. Ross, and A. A. Stokes, ‘Using Voice Coils to Actuate Modular Soft Robots: Wormbot, an Example’, *Soft Robot.*, vol. 3, no. 4, pp. 198–204, Dec. 2016.

[33] R. F. Shepherd *et al.*, ‘Multigait soft robot’, *Proc. Natl. Acad. Sci.*, vol. 108, no. 51, pp. 20400–20403, Dec. 2011.

[34] E. Acome *et al.*, ‘Hydraulically amplified self-healing electrostatic actuators with muscle-like performance.’, *Sci.* , vol. 359, no. 6371, pp. 61–65, Jan. 2018.

[35] C. Laschi, M. Cianchetti, B. Mazzolai, L. Margheri, M. Follador, and P. Dario, ‘Soft Robot Arm Inspired by the Octopus’, *Adv. Robot.*, vol. 26, no. 7, pp. 709–727, Jan. 2012.

[36] C. Christianson, N. N. Goldberg, D. D. Deheyn, S. Cai, and M. T. Tolley, ‘Translucent soft robots driven by frameless fluid electrode dielectric elastomer actuators’, *Sci. Robot.*, vol. 3, no. 17, p. eaat1893, Apr. 2018.

[37] S. Li, D. M. Vogt, D. Rus, and R. J. Wood, ‘Fluid-driven origami-inspired artificial muscles.’, *Proc. Natl. Acad. Sci. U. S. A.*, vol. 114, no. 50, pp. 13132–13137, Dec. 2017.

[38] B. Mosadegh *et al.*, ‘Control of soft machines using actuators operated by a Braille display.’, *Lab Chip*, vol. 14, no. 1, pp. 189–99, Jan. 2014.

[39] S. Sareh *et al.*, ‘Anchoring like octopus: biologically inspired soft artificial sucker’, *J. R. Soc. Interface*, vol. 14, no. 135, p. 20170395, Oct. 2017.

[40] R. K. Katzschmann, A. D. Marchese, and D. Rus, ‘Hydraulic Autonomous Soft Robotic Fish for 3D Swimming’, in *Experimental Robotics*, Springer, Cham, 2016, pp. 405–420.

[41] M. Wehner *et al.*, ‘An integrated design and fabrication strategy for entirely soft, autonomous robots’, *Nature*, vol. 536, no. 7617, pp. 451–455, Aug. 2016.

[42] A. A. Stokes, R. F. Shepherd, S. A. Morin, F. Ilievski, and G. M. Whitesides, ‘A Hybrid Combining Hard and Soft Robots’, *Soft Robot.*, vol. 1, no. 1, 2013.

[43] N. Kellaris, V. Gopaluni Venkata, G. M. Smith, S. K. Mitchell, and C. Keplinger, ‘Peano-HASEL actuators: Muscle-mimetic, electrohydraulic transducers that linearly contract on activation’, *Sci. Robot.*, vol. 3, no. 14, p. eaar3276, Jan. 2018.

[44] N. W. Bartlett *et al.*, ‘A 3D-printed, functionally graded soft robot powered by combustion.’, *Science (80-.).*, vol. 349, no. 6244, pp. 161–5, Jul. 2015.

[45] B. Mosadegh *et al.*, ‘Pneumatic Networks for Soft Robotics that Actuate Rapidly’, *Adv. Funct. Mater.*, vol. 24, no. 15, pp. 2163–2170, Apr. 2014.

[46] T. Wei, A. Stokes, and B. Webb, ‘A Soft Pneumatic Maggot Robot’, in *Biomimetic and Biohybrid Systems*, Springer, Cham, 2016, pp. 375–386.

[47] A. Nemiroski *et al.*, ‘Arthrobots’, *Soft Robot.*, vol. 4, no. 3, pp. 183–190, Sep. 2017.

[48] G. Agarwal, M. A. Robertson, H. Sonar, and J. Paik, ‘Design and Computational Modeling of a Modular, Compliant Robotic Assembly for Human Lumbar Unit and Spinal Cord Assistance’, *Sci. Rep.*, vol. 7, no. 1, p. 14391, Dec. 2017.

[49] K. Autumn *et al.*, ‘Adhesive force of a single gecko foot-hair’, *Nature*, vol. 405, no. 6787, pp. 681–685, Jun. 2000.

[50] K. Autumn, A. Dittmore, D. Santos, M. Spenko, and M. Cutkosky, ‘Frictional adhesion: A new angle on gecko attachment.’, *J. Exp. Biol.*, vol. 209, no. Pt 18, pp. 3569–79, Sep. 2006.

[51] M. Sitti and R. S. Fearing, ‘Synthetic gecko foot-hair micro/nano-structures for future wall-climbing robots’, in *2003 IEEE International Conference on Robotics and Automation*, 2003, vol. 1, pp. 1164–1170.

[52] F. Ochoa-Cardenas and T. J. Dodd, ‘Design of an active magnetic wheel with a varying Electro-Permanent Magnet adhesion mechanism’, in *2015 IEEE/RSJ International Conference on Intelligent Robots and Systems (IROS)*, 2015, pp. 3340–3345.

[53] J. C. Grieco, M. Prieto, M. Armada, and P. Gonzalez de Santos, ‘A six-legged climbing robot for high payloads’, in *Proceedings of the 1998 IEEE International Conference on Control Applications (Cat. No.98CH36104)*, vol. 1, pp. 446–450.

[54] M. Eich and T. Vogele, ‘Design and control of a lightweight magnetic climbing robot for vessel inspection’, in *2011 19th Mediterranean Conference on Control & Automation (MED)*, 2011, pp. 1200–1205.

[55] Z. Xu and P. Ma, ‘A wall-climbing robot for labelling scale of oil tank’s volume’, *Robotica*, vol. 20, no. 02, pp. 209–212, Mar. 2002.

[56] W. Shen, J. Gu, and Y. Shen, ‘Permanent magnetic system design for the wall-climbing robot’, in *IEEE International Conference Mechatronics and Automation, 2005*, vol. 4, pp. 2078–2083.

[57] W. Shen, J. Gu, and Y. Shen, ‘Proposed wall climbing robot with permanent magnetic tracks for inspecting oil tanks’, in *IEEE International Conference Mechatronics and Automation, 2005*, vol. 4, pp. 2072–2077.

[58] H. Wang, A. Yamamoto, and T. Higuchi, ‘Electrostatic-motor-driven electroadhesive robot’, in *2012 IEEE/RSJ International Conference on Intelligent Robots and Systems*, 2012, pp. 914–919.

[59] R. Liu, R. Chen, H. Shen, and R. Zhang, ‘Wall Climbing Robot Using Electrostatic Adhesion Force Generated by Flexible Interdigital Electrodes’, *Int. J. Adv. Robot. Syst.*, vol. 10, no. 1, p. 36, Jan. 2013.

[60] H. Wang and A. Yamamoto, ‘Analyses and Solutions for the Buckling of Thin and Flexible Electrostatic Inchworm Climbing Robots’, *IEEE Trans. Robot.*, vol. 33, no. 4, pp. 889–900, Aug. 2017.

[61] A. Yamamoto, T. Nakashima, and T. Higuchi, ‘Wall Climbing Mechanisms Using Electrostatic Attraction Generated by Flexible Electrodes’, in *2007 International Symposium*

on Micro-NanoMechatronics and Human Science, 2007, pp. 389–394.

[62] H. Prahlad, R. Pelrine, S. Stanford, J. Marlow, and R. Kornbluh, 'Electroadhesive robots—wall climbing robots enabled by a novel, robust, and electrically controllable adhesion technology', in *2008 IEEE International Conference on Robotics and Automation*, 2008, pp. 3028–3033.

[63] H. Wang, A. Yamamoto, and T. Higuchi, 'A Crawler Climbing Robot Integrating Electroadhesion and Electrostatic Actuation', *Int. J. Adv. Robot. Syst.*, vol. 11, no. 12, p. 191, Dec. 2014.

[64] G. Gu, J. Zou, R. Zhao, X. Zhao, and X. Zhu, 'Soft wall-climbing robots', *Sci. Robot.*, vol. 3, no. 25, p. eaat2874, Dec. 2018.

[65] K. A. Daltorio, A. D. Horchler, S. Gorb, R. E. Ritzmann, and R. D. Quinn, 'A small wall-walking robot with compliant, adhesive feet', in *2005 IEEE/RSJ International Conference on Intelligent Robots and Systems*, 2005, pp. 3648–3653.

[66] J. Zhu, D. Sun, and S.-K. Tso, 'Development of a Tracked Climbing Robot', *J. Intell. Robot. Syst.*, vol. 35, no. 4, pp. 427–443, 2002.

[67] H. Kim *et al.*, 'Development of a wall-climbing robot using a tracked wheel mechanism', *J. Mech. Sci. Technol.*, vol. 22, no. 8, pp. 1490–1498, Aug. 2008.

[68] K. Autumn and A. M. Peattie, 'Mechanisms of Adhesion in Geckos', *Integr. Comp. Biol.*, vol. 42, no. 6, pp. 1081–1090, Dec. 2002.

[69] S. Kim, M. Spenko, S. Trujillo, B. Heyneman, D. Santos, and M. R. Cutkosky, 'Smooth Vertical Surface Climbing With Directional Adhesion', *IEEE Trans. Robot.*, vol. 24, no. 1, pp. 65–74, Feb. 2008.

[70] M. P. Murphy, C. Kute, Y. Mengüç, and M. Sitti, 'Waalbot II: Adhesion Recovery and Improved Performance of a Climbing Robot using Fibrillar Adhesives', *Int. J. Rob. Res.*, vol. 30, no. 1, pp. 118–133, Jan. 2011.

[71] O. Unver, A. Uneri, A. Aydemir, and M. Sitti, 'Geckobot: a gecko inspired climbing robot using elastomer adhesives', in *Proceedings 2006 IEEE International Conference on Robotics and Automation, 2006. ICRA 2006.*, pp. 2329–2335.

[72] Y. Li, A. Ahmed, D. Sameoto, and C. Menon, 'Abigaille II: toward the development of a spider-inspired climbing robot', *Robotica*, vol. 30, no. 01, pp. 79–89, Jan. 2012.

[73] M. Greuter, G. Shah, G. Caprari, F. Tâche, R. Siegwart, and M. Sitti, 'Toward Micro Wall-Climbing Robots Using Biomimetic Fibrillar Adhesives', in *Proceedings of the 3rd International Symposium on Autonomous Minirobots for Research and Edutainment (AMiRE 2005)*, Berlin/Heidelberg: Springer-Verlag, 2006, pp. 39–46.

[74] E. W. Hawkes, D. L. Christensen, and M. R. Cutkosky, 'Vertical dry adhesive climbing with a 100x bodyweight payload', in *2015 IEEE International Conference on Robotics and Automation (ICRA)*, 2015, pp. 3762–3769.

[75] W. A. Breckwoldt, K. A. Daltorio, L. Heepe, A. D. Horchler, S. N. Gorb, and R. D. Quinn,

'Walking inverted on ceilings with wheel-legs and micro-structured adhesives', in *2015 IEEE/RSJ International Conference on Intelligent Robots and Systems (IROS)*, 2015, pp. 3308–3313.

[76] D. K. Wainwright, T. Kleinteich, A. Kleinteich, S. N. Gorb, and A. P. Summers, 'Stick tight: suction adhesion on irregular surfaces in the northern clingfish', *Biol. Lett.*, vol. 9, no. 3, pp. 20130234–20130234, May 2013.

[77] A. M. SMITH, 'The Role of Suction in the Adhesion of Limpets', *J. Exp. Biol.*, vol. 161, no. 1, pp. 151–169, 1991.

[78] W. M. Kier and A. M. Smith, 'The Structure and Adhesive Mechanism of Octopus Suckers', *Integr. Comp. Biol.*, vol. 42, no. 6, pp. 1146–1153, Dec. 2002.

[79] J. Gray, H. W. Lissmann, and R. J. Pumphrey, 'The Mechanism of Locomotion in the Leech (Hirudo Medicinalis Ray)', *J. Exp. Biol.*, vol. 15, no. 3, 1938.

[80] J. Hou, E. Wright, R. H. C. Bonser, and G. Jeronimidis, 'Development of Biomimetic Squid-Inspired Suckers', *J. Bionic Eng.*, vol. 9, no. 4, pp. 484–493, Dec. 2012.

[81] H. Bing-Shan, W. Li-Wen, F. Zhuang, and Z. Yan-zheng, 'Bio-inspired Miniature Suction Cups Actuated by Shape Memory Alloy', *Int. J. Adv. Robot. Syst.*, vol. 6, no. 3, p. 29, Sep. 2009.

[82] P. R. Bandyopadhyay, J. D. Hrubes, and H. A. Leinhos, 'Biorobotic adhesion in water using suction cups', *Bioinspir. Biomim.*, vol. 3, no. 1, p. 016003, Mar. 2008.

[83] Z. Zhakypov, F. Heremans, A. Billard, and J. Paik, 'An Origami-Inspired Reconfigurable Suction Gripper for Picking Objects With Variable Shape and Size', *IEEE Robot. Autom. Lett.*, vol. 3, no. 4, pp. 2894–2901, Oct. 2018.

[84] H. R. Choi, S. M. Ryew, T. H. Kang, J. H. Lee, and H. M. Kim, 'A wall climbing robot with closed link mechanism', in *Proceedings. 2000 IEEE/RSJ International Conference on Intelligent Robots and Systems (IROS 2000) (Cat. No.00CH37113)*, vol. 3, pp. 2006–2011.

[85] P. G. Backes, Y. Bar-Cohen, and B. Joffe, 'The multifunction automated crawling system (MACS)', in *Proceedings of International Conference on Robotics and Automation*, vol. 1, pp. 335–340.

[86] N. Elkmann, T. Felsch, M. Sack, J. Saenz, and J. Hortig, 'Innovative service robot systems for facade cleaning of difficult-to-access areas', in *IEEE/RSJ International Conference on Intelligent Robots and System*, vol. 1, pp. 756–762.

[87] J. Zhu, D. Sun, and S.-K. Tso, 'Application of a Service Climbing Robot with Motion Planning and Visual Sensing', *J. Robot. Syst.*, vol. 20, no. 4, pp. 189–199, Apr. 2003.

[88] S. Park, H. D. Jeong, and Z. S. Lim, 'Design of a mobile robot system for automatic integrity evaluation of large size reservoirs and pipelines in industrial fields', in *Proceedings 2003 IEEE/RSJ International Conference on Intelligent Robots and Systems (IROS 2003) (Cat. No.03CH37453)*, vol. 3, pp. 2618–2623.

[89] X. Gao and K. Kikuchi, 'Study on a Kind of Wall Cleaning Robot', in *2004 IEEE*

International Conference on Robotics and Biomimetics, pp. 391–394.

[90] R. T. Pack, J. L. Christopher, and K. Kawamura, 'A Rubbertuator-based structure-climbing inspection robot', in *Proceedings of International Conference on Robotics and Automation*, vol. 3, pp. 1869–1874.

[91] R. Lal Tummala *et al.*, 'Climbing the walls [robots]', *IEEE Robot. Autom. Mag.*, vol. 9, no. 4, pp. 10–19, Dec. 2002.

[92] S. P. Krosuri and M. A. Minor, 'A multifunctional hybrid hip joint for improved adaptability in miniature climbing robots', in *2003 IEEE International Conference on Robotics and Automation (Cat. No.03CH37422)*, vol. 1, pp. 312–317.

[93] J. Xiao, N. Xi, J. Xiao, and J. Tan, 'Multi-sensor referenced gait control of a miniature climbing robot', in *Proceedings 2003 IEEE/RSJ International Conference on Intelligent Robots and Systems (IROS 2003) (Cat. No.03CH37453)*, vol. 3, pp. 3656–3661.

[94] J. Xiao, J. Xiao, N. Xi, and W. Sheng, 'Fuzzy system approach for task planning and control of micro wall climbing robots', in *IEEE International Conference on Robotics and Automation, 2004. Proceedings. ICRA '04. 2004*, 2004, p. 5033–5038 Vol.5.

[95] B. E. Shores and M. A. Minor, 'Design, Kinematic Analysis, and Quasi-Steady Control of a Morphic Rolling Disk Biped Climbing Robot', in *Proceedings of the 2005 IEEE International Conference on Robotics and Automation*, pp. 2721–2726.

[96] W. Brockmann, 'Concept for Energy-autarkic, Autonomous Climbing Robots', in *Climbing and Walking Robots*, Berlin, Heidelberg: Springer Berlin Heidelberg, 2006, pp. 107–114.

[97] M. F. Silva, J. A. T. Machado, and J. K. Tar, 'A Survey of Technologies for Climbing Robots Adhesion to Surfaces', in *2008 IEEE International Conference on Computational Cybernetics*, 2008, pp. 127–132.

[98] G. La Rosa, M. Messina, G. Muscato, and R. Sinatra, 'A low-cost lightweight climbing robot for the inspection of vertical surfaces', *Mechatronics*, vol. 12, no. 1, pp. 71–96, Feb. 2002.

[99] M. Murphy, W. Tso, M. Tanzini, and M. Sitti, 'Waalbot: An Agile Small-Scale Wall Climbing Robot Utilizing Pressure Sensitive Adhesives', in *2006 IEEE/RSJ International Conference on Intelligent Robots and Systems*, 2006, pp. 3411–3416.

[100] C. Menon, M. Murphy, and M. Sitti, 'Gecko Inspired Surface Climbing Robots', in *2004 IEEE International Conference on Robotics and Biomimetics*, pp. 431–436.

[101] K. Sangbae, A. T. Asbeck, M. R. Cutkosky, and W. R. Provancher, 'SpinybotII: climbing hard walls with compliant microspines', in *ICAR '05. Proceedings., 12th International Conference on Advanced Robotics, 2005.*, pp. 601–606.

[102] D. Longo and G. Muscato, 'A modular approach for the design of the Alicia ^{3} climbing robot for industrial inspection', *Ind. Robot An Int. J.*, vol. 31, no. 2, pp. 148–158, Apr. 2004.

[103] H. L. Rodriguez, B. Bridge, and T. P. Sattar, 'Climbing Ring Robot For Inspection of Offshore Wind Turbines', in *Advances in Mobile Robotics*, 2008, pp. 555–562.

[104] K. A. Daltorio, T. E. Wei, S. N. Gorb, R. E. Ritzmann, and R. D. Quinn, 'Passive Foot Design and Contact Area Analysis for Climbing Mini-Whegs', in *Proceedings 2007 IEEE International Conference on Robotics and Automation*, 2007, pp. 1274–1279.

[105] K. A. Daltorio, S. Gorb, A. Peressadko, A. D. Horchler, R. E. Ritzmann, and R. D. Quinn, 'A Robot that Climbs Walls using Micro-structured Polymer Feet', in *Climbing and Walking Robots*, Berlin, Heidelberg: Springer Berlin Heidelberg, 2006, pp. 131–138.

[106] T. Kang, H. Kim, T. Son, and H. Choi, 'Design of quadruped walking and climbing robot', in *Proceedings 2003 IEEE/RSJ International Conference on Intelligent Robots and Systems (IROS 2003)*, 2003, vol. 1, pp. 619–624.

[107] H. Hastie *et al.*, 'The ORCA Hub: Explainable Offshore Robotics through Intelligent Interfaces', in *13th Annual ACM/IEEE International Conference on Human Robot Interaction*, 2018.

[108] M. Sayed *et al.*, 'The Limpet: A ROS-Enabled Multi-Sensing Platform for the ORCA Hub', *Sensors*, vol. 18, no. 10, p. 3487, Oct. 2018.

[109] R. M. McKenzie, M. E. Sayed, M. P. Nemitz, B. W. Flynn, and A. A. Stokes, 'Linbots: Soft Modular Robots Utilizing Voice Coils', *Soft Robot.*, p. soro.2018.0058, Dec. 2018.

[110] D. J. Marshall and A. N. Hodgson, 'Structure of the Cephalic Tentacles of Some Species of Prosobranch Limpet (Patellidae and Fissurellidae)', *J. Molluscan Stud.*, vol. 56, no. 3, pp. 415–424, Aug. 1990.

[111] G. K. Ellem, J. E. Furst, and K. D. Zimmerman, 'Shell clamping behaviour in the limpet Cellana tramoserica.', *J. Exp. Biol.*, vol. 205, no. Pt 4, pp. 539–47, Feb. 2002.

[112] S. I. Rich, R. J. Wood, and C. Majidi, 'Untethered soft robotics', *Nat. Electron.*, vol. 1, no. 2, pp. 102–112, Feb. 2018.

[113] P. Vartholomeos and E. Papadopoulos, 'Analysis, design and control of a planar micro-robot driven by two centripetal-force actuators', in *Proceedings 2006 IEEE International Conference on Robotics and Automation, 2006. ICRA 2006.*, pp. 649–654.

[114] C. Sung and D. Rus, 'Automated Fabrication of Foldable Robots Using Thick Materials', in *Robotics Research*, A. Bicchi and W. Burgard, Eds. Springer Proceedings in Advanced Robotics, 2018, pp. 253–266.

[115] M. Slaney, 'Auditory Toolbox Version 2', 1993.

[116] S. S. Stevens, J. Volkmann, and E. B. Newman, 'A Scale for the Measurement of the Psychological Magnitude Pitch', *J. Acoust. Soc. Am.*, vol. 8, no. 3, pp. 185–190, Jan. 1937.

[117] E. Olson, 'AprilTag: A robust and flexible visual fiducial system', in *2011 IEEE International Conference on Robotics and Automation*, 2011, pp. 3400–3407.

Limpet: A Modular, Untethered Soft Robot

Mohammed E. Sayed[1], Jamie O. Roberts[1,2], Ross M. McKenzie[1,2], Simona Aracri[1], Anthony Buchoux[1], and Adam A. Stokes[1*]

Figures

[1]School of Engineering, Institute for Integrated Micro and Nano Systems, The University of Edinburgh, Scottish Microelectronics Centre, Alexander Crum Brown Road, King's Buildings, Edinburgh, UK, EH9 3FF

[2]Engineering and Physical Sciences Research Council (EPSRC) Centre for Doctoral Training (CDT) in Robotics and Autonomous Systems, School of Informatics, The University of Edinburgh, Edinburgh EH9 3LJ, UK

*** Author to whom correspondence should be addressed.**

Figure 1


Sensing Module
Locomotion Module
Adhesion Module
Power Driver Module

Figure 2

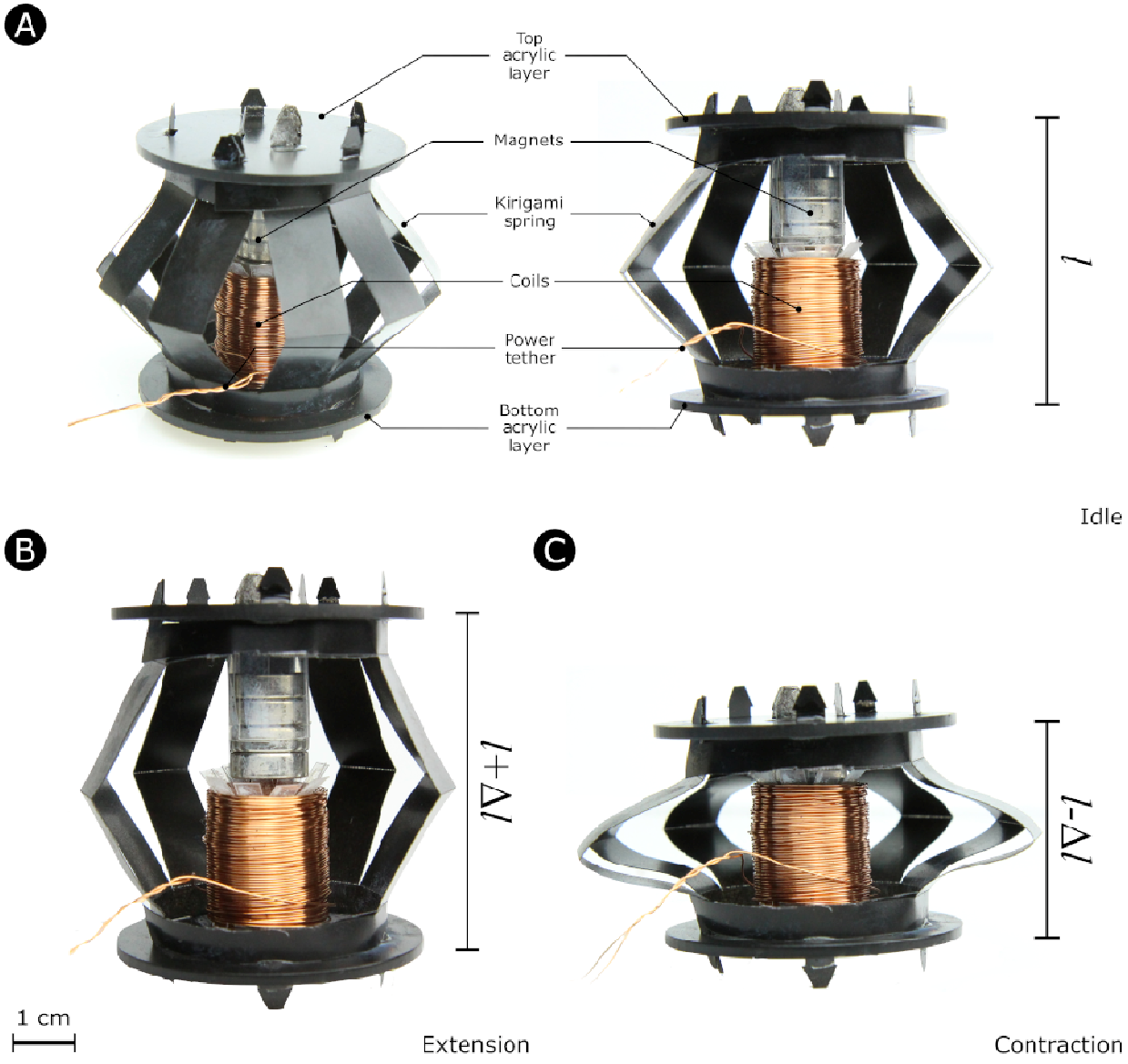
A
Top acrylic layer
Magnets
Kirigami spring
Coils
Power tether
Bottom acrylic layer
l
Idle
B
l+Δl
C
l-Δl
1 cm
Extension
Contraction

Figure 3

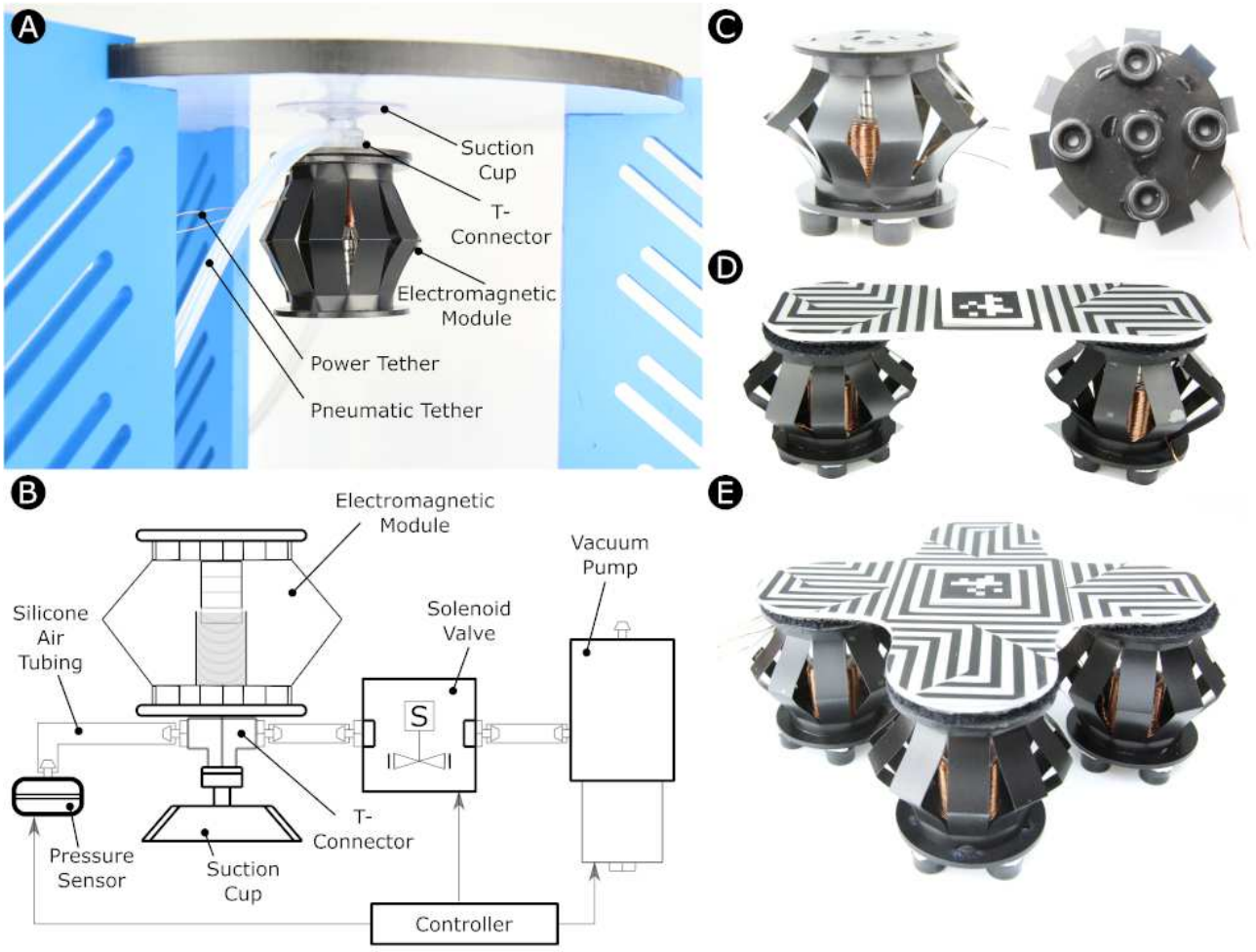
A
Suction Cup
T-Connector
Electromagnetic Module
Power Tether
Pneumatic Tether
B
Electromagnetic Module
Vacuum Pump
Silicone Air Tubing
Solenoid Valve
S
T-Connector
Pressure Sensor
Suction Cup
Controller
C
D
E

Figure 4

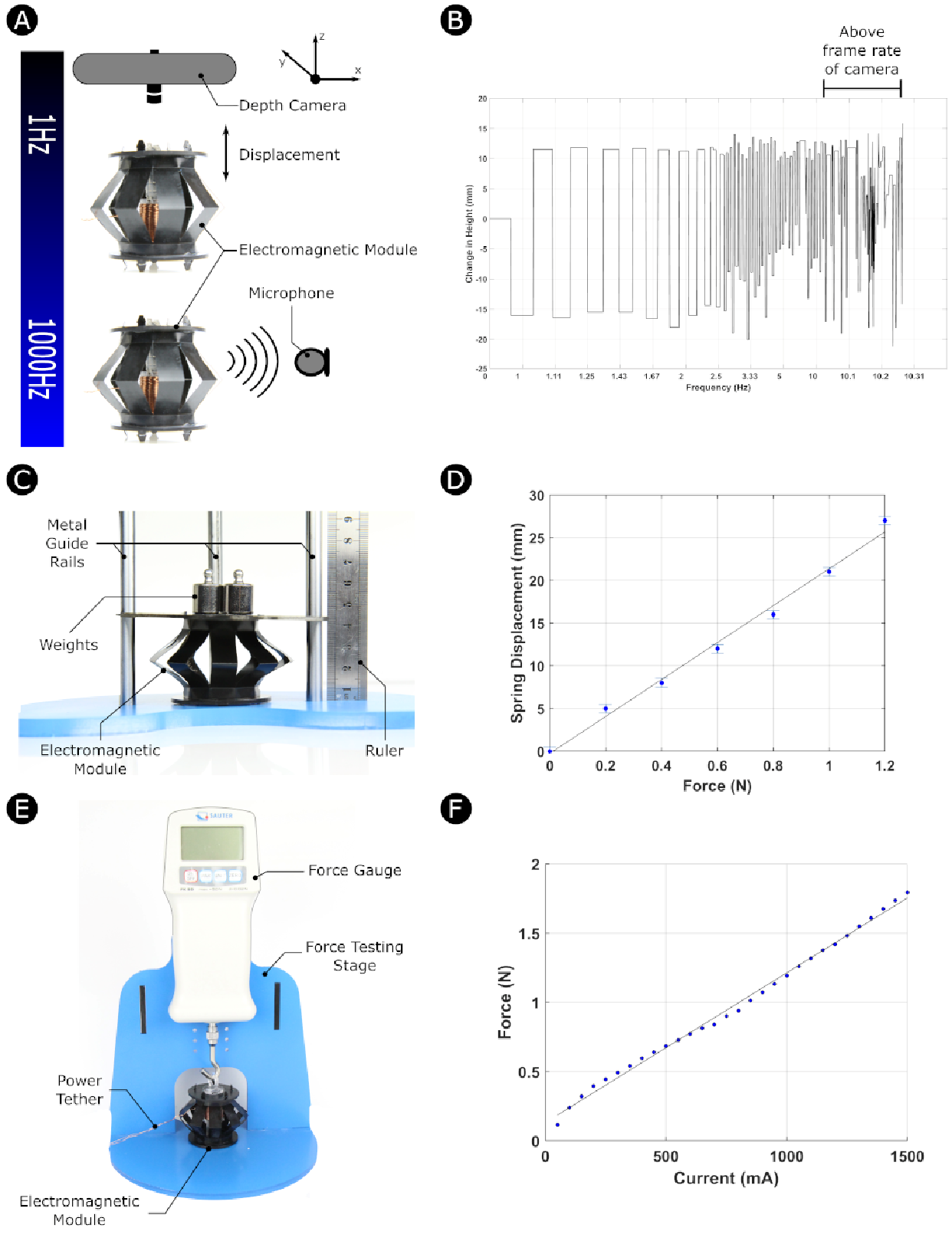
A
1HZ
1000HZ
Depth Camera
Displacement
Electromagnetic Module
Microphone
B
Above frame rate of camera
Change in Height (mm)
Frequency (Hz)
C
Metal Guide Rails
Weights
Electromagnetic Module
Ruler
D
Spring Displacement (mm)
Force (N)
E
Force Gauge
Force Testing Stage
Power Tether
Electromagnetic Module
F
Force (N)
Current (mA)

Figure 5

A

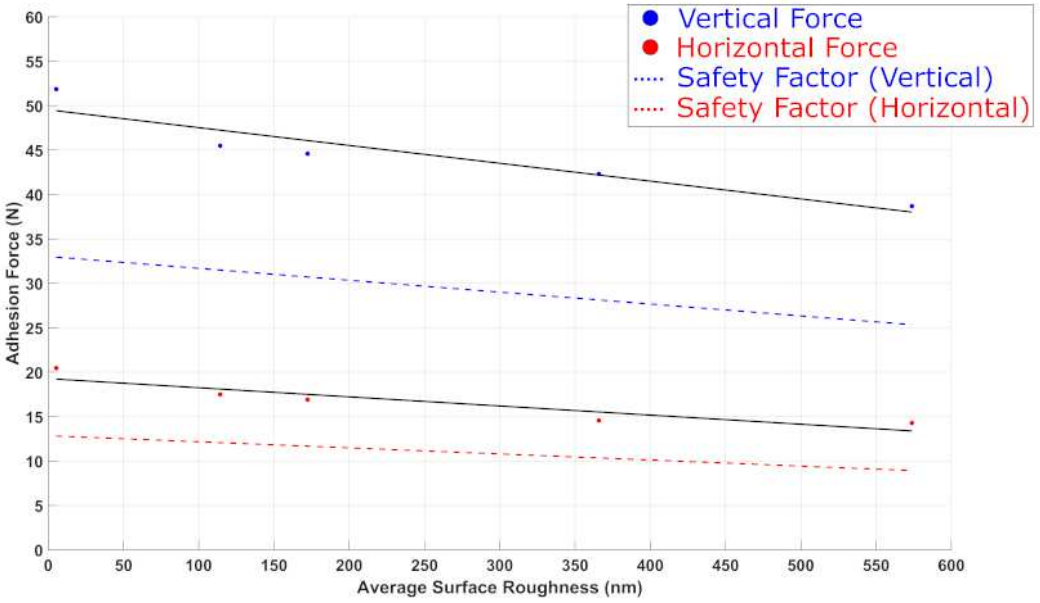
Vertical Force
Horizontal Force
Safety Factor (Vertical)
Safety Factor (Horizontal)
Adhesion Force (N)
Average Surface Roughness (nm)

B

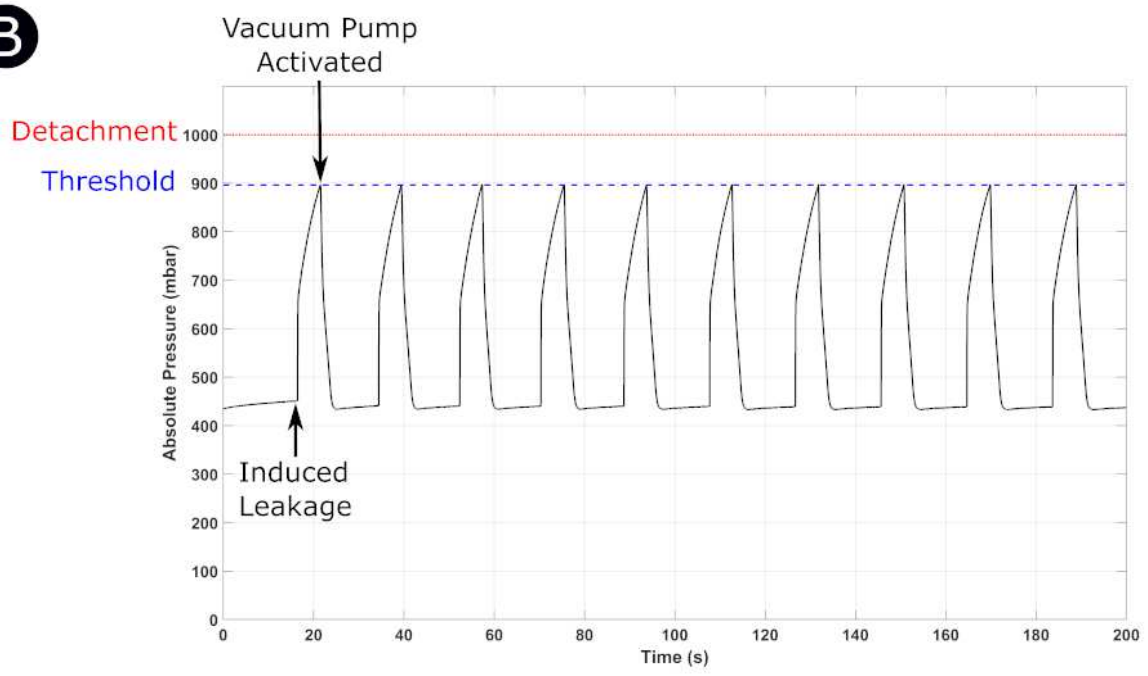
Vacuum Pump Activated
Detachment Threshold
Induced Leakage
Absolute Pressure (mbar)
Time (s)

Figure 6

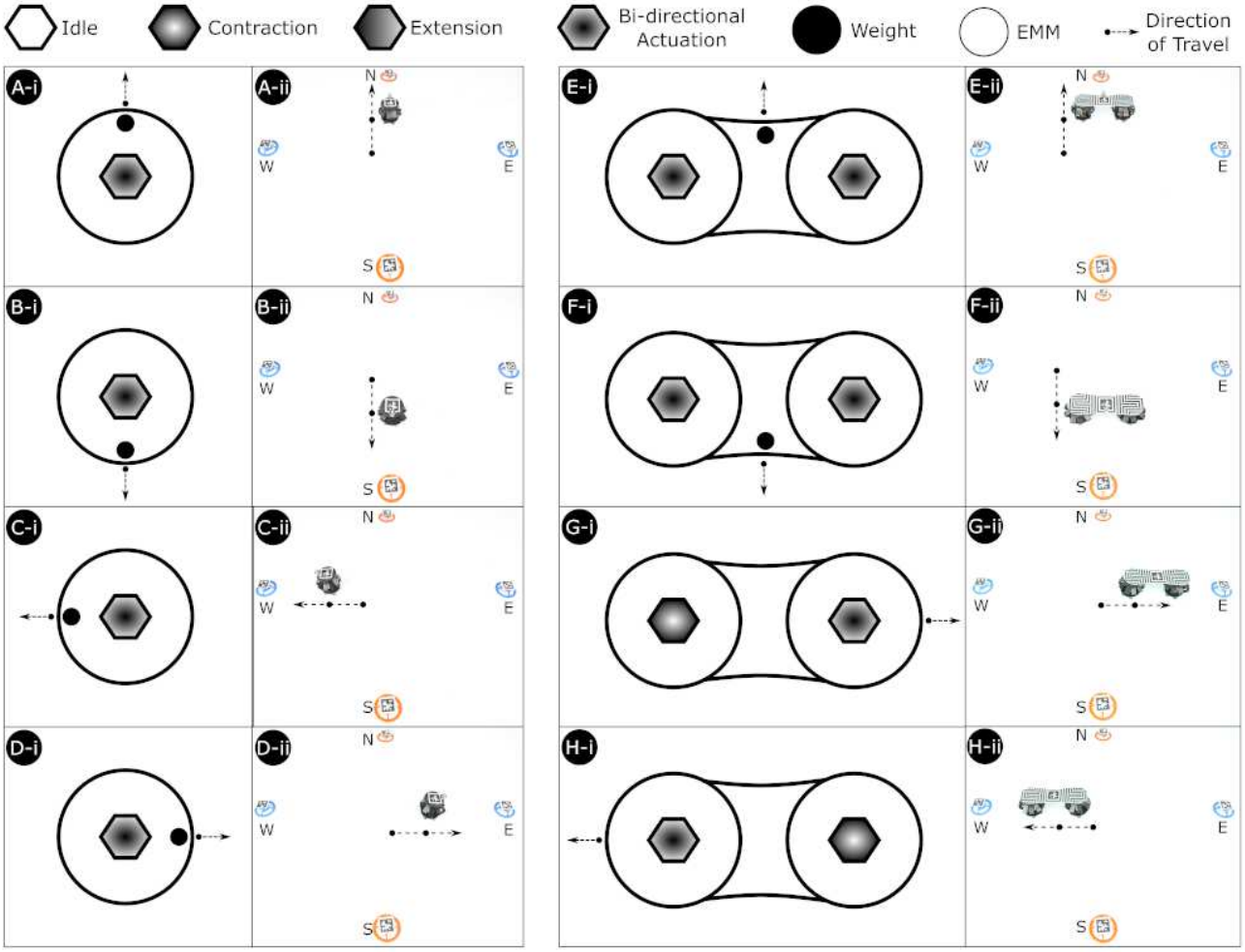
Idle
Contraction
Extension
Bi-directional Actuation
Weight
EMM
Direction of Travel
A-i
A-ii
B-i
B-ii
C-i
C-ii
D-i
D-ii
E-i
E-ii
F-i
F-ii
G-i
G-ii
H-i
H-ii
N
W
E
S

Figure 7

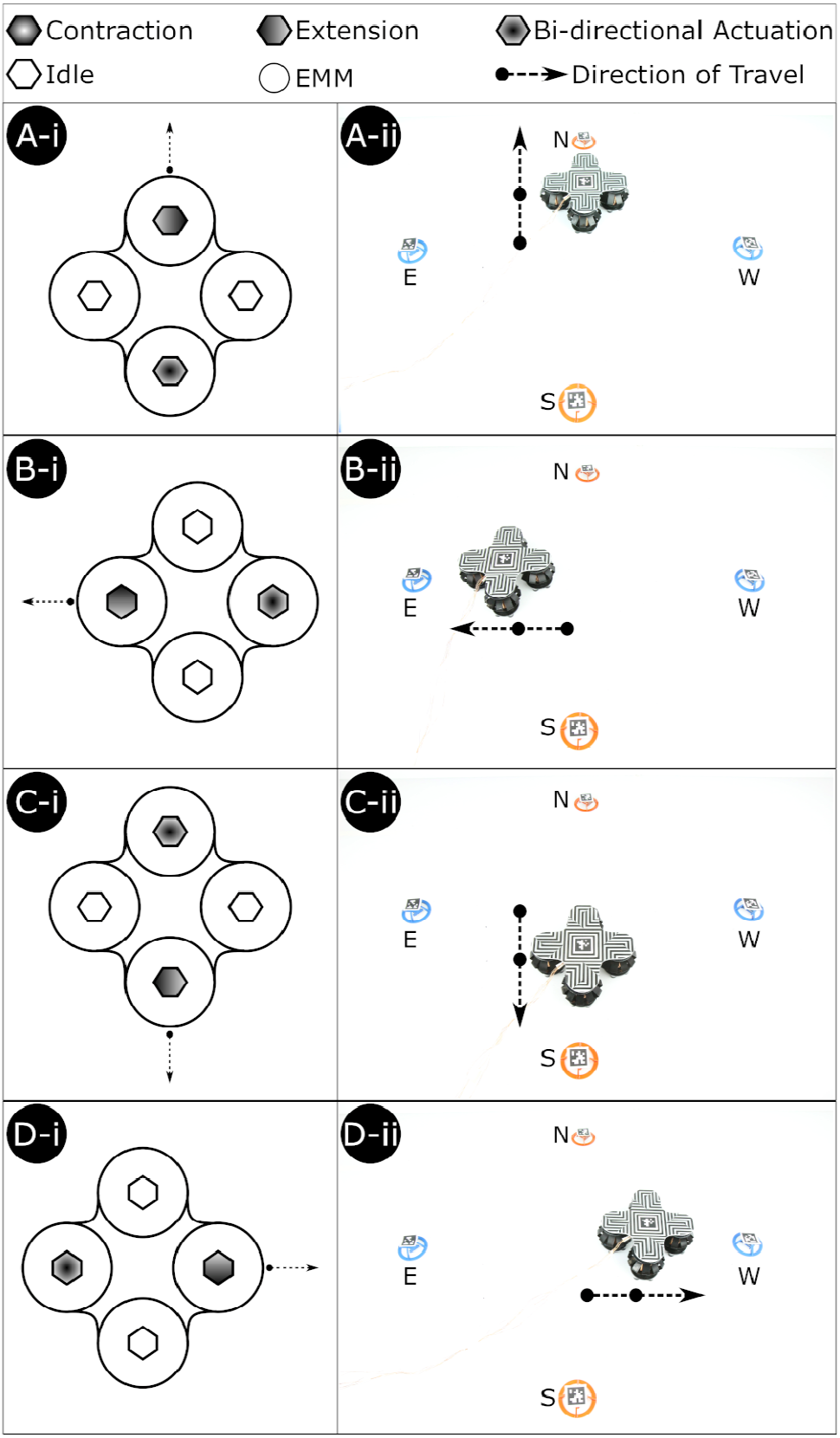
Contraction
Extension
Bi-directional Actuation
Idle
EMM
Direction of Travel
A-i
A-ii
N
E
W
S
B-i
B-ii
N
E
W
S
C-i
C-ii
N
E
W
S
D-i
D-ii
N
E
W
S

Figure 8

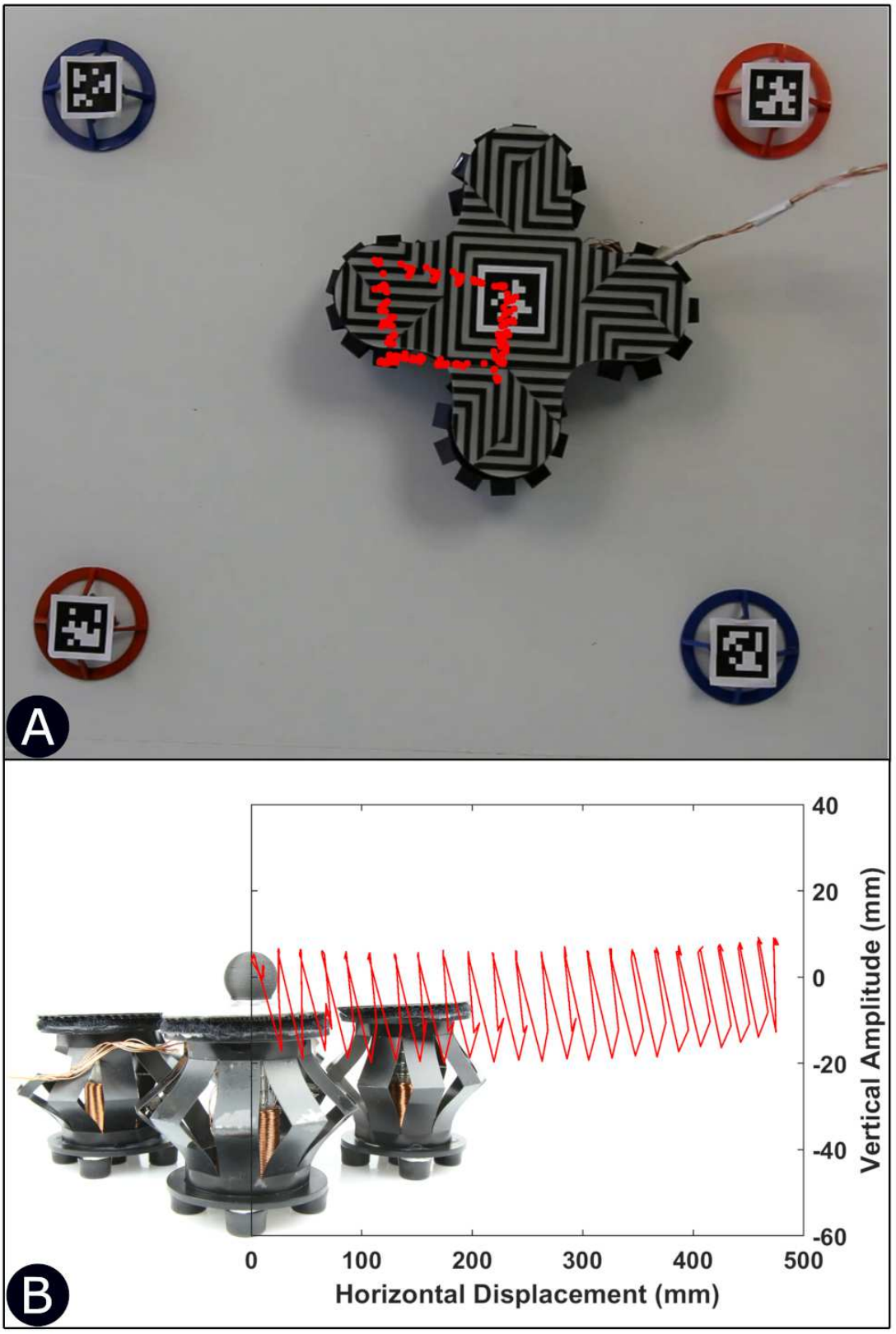
A
B
40
20
0
-20
-40
-60
Vertical Amplitude (mm)
0
100
200
300
400
500
Horizontal Displacement (mm)

Limpet: A Modular, Untethered Soft Robot

Mohammed E. Sayed[1], Jamie O. Roberts[1,2], Ross M. McKenzie[1,2], Simona Aracri[1], Anthony Buchoux[1], and Adam A. Stokes[1*]

Tables

[1]School of Engineering, Institute for Integrated Micro and Nano Systems, The University of Edinburgh, Scottish Microelectronics Centre, Alexander Crum Brown Road, King's Buildings, Edinburgh, UK, EH9 3FF

[2]Engineering and Physical Sciences Research Council (EPSRC) Centre for Doctoral Training (CDT) in Robotics and Autonomous Systems, School of Informatics, The University of Edinburgh, Edinburgh EH9 3LJ, UK

*** Author to whom correspondence should be addressed.**

Table 1: Measurands (events) from the sensors on the Limpet and some application examples.

Sensor	Physical Measurement Variable	Signal Variable	Measurands	Application Examples
Accelerometer	Acceleration	Acceleration	Inclination, Collision, Vibration, Free-Fall Detection, Movement Acceleration	Monitoring conductor motion and vibration; monitoring floating production storage and offloading vessel movement
Gyroscope	Angular Velocity	Angular Velocity	Tilt Detection, Orientation	Monitoring the orientation and angle of drilling equipment; monitoring floating production storage and offloading vessel tilt and roll
Temperature	Temperature	Temperature	Ambient Temperature, Over-heating, Fire Detection	Overheating of structures and equipment
Humidity	Humidity	Humidity	Relative Humidity	Monitoring humidity levels that can cause problems related to corrosion of components and issues to materials used as additives
Microphone	Sound	Voltage	Speech Recognition, Noise Cancellation, Audible Fault Detection	Monitoring vibration of vessels, pipes, structures; Structural health monitoring of platform and structures
Pressure	Pressure	Pressure	Ambient Pressure	Flow and pressure measurement in vessels
Hall-Effect	Magnetic Field	Magnetic Flux Density	Locating Pipelines, Corrosion Detection	Monitoring corrosion in pipes and wind turbines
Optical	Light (Visible)	Light Intensity	Ambient Light Intensity, Local Communication, Colour Detection	Monitoring the level of debris in the air
Distance (Time-of-Flight)	Light (Laser)	Distance	Fault Detection, Proximity, Collision Detection, Object Identification	Monitoring vibration of structures, pipes, vessels, conductors; Structural Health monitoring of wind turbines

Table 2: Cost summary of the Limpet and its components

Category	Components	Cost (£)
Sensing Module	Electronic Components	22
Power Driver Module	Electronic Components	47.96
Electromagnetic Module (EMM)	Coils	1.22
	Magnets	3.08
	Acetate	0.054
	Acrylic	0.5
Adhesion Module	EMM	4.854
	Suction Cup	0.18
	Silicon Tubing	0.8
	Vacuum Pump	8.23
	Solenoid Valve	2
Locomotion Module	EMM	4.854
	Rubber Feet (x5)	0.773
Limpet	Adhesion Module (x1)	16.064
	Locomotion Module (x4)	22.508
	Sensing Module (x1)	22
	Power Driver Module (x1)	47.96
	Outer Body (Shell) (x1)	3.8
Total Cost	Limpet	112.3

Limpet: A Modular, Untethered Soft Robot

Mohammed E. Sayed[1], Jamie O. Roberts[1,2], Ross M. McKenzie[1,2], Simona Aracri[1], Anthony Buchoux[1], and Adam A. Stokes[1*]

SUPPLEMENTAL INFORMATION

[1]School of Engineering, Institute for Integrated Micro and Nano Systems, The University of Edinburgh, Scottish Microelectronics Centre, Alexander Crum Brown Road, King's Buildings, Edinburgh, UK, EH9 3FF

[2]Engineering and Physical Sciences Research Council (EPSRC) Centre for Doctoral Training (CDT) in Robotics and Autonomous Systems, School of Informatics, The University of Edinburgh, Edinburgh EH9 3LJ, UK

*** Author to whom correspondence should be addressed.**

Supplemental Materials and Methods

S1. Design of the Communications for the Limpet

In order to use WiFi for transmission of data from the Limpet to a node (e.g. PC), we use an ESP8266, which is a low-cost System-on-a-Chip (SOC) WiFi module with integrated TCP/IP protocol stack capable of giving any microcontroller access to the WiFi network. We use a software development kit (SDK), known as NodeMCU, to program the chip directly. NodeMCU is a Lua-based firmware, where Lua is lightweight multi-paradigm programming language that is used for embedded applications. To send and receive the messages between the ESP8266 and the PC, we use Eclipse Mosquitto [S1], which implements a messaging protocol known as Message Queuing Telemetry Transport (MQTT). MQTT is a lightweight publish/subscribe messaging protocol used for remote communication as shown by Figure S1. In this case, the Limpet is the publisher and the PC subscribes to the MQTT topic to receive the Limpet data. The received data can then be plotted in a real-time basis, or saved on the PC and processed later.

We transmit the data from the Limpet serially using SparkFun's FTDI Basic Breakout-3.3V, which is a serial to USB convertor. The communication between the Limpet and the FTDI Basic Breakout occurs over Universal Asynchronous Receiver/Transmitter (UART). The transmitting UART (Limpet) converts parallel data from the microcontroller into serial format, transmits it in serial to the receiving UART (FTDI), which converts the serial data back into parallel form for the PC. The UART transmits the data asynchronously, which means there is no clock synchronisation between sending data from the transmitting device and receiving data by the receiver. In UART, instead of the clock signal, the transmitting device adds a start bit and a stop bit to the data being sent, which defines the beginning and end of the data packet for the receiving UART. A schematic of the serial communication is shown by Figure S2.

LoRaWAN is a new long range wide area network (WAN) technology that allows for long-range communication with low power consumption, but with a limited bandwidth [S2]. There is a tradeoff between the spreading factor (SF) and communication range in LoRa. The higher the SF, which means a slower transmission, the longer the communication range. Depending on the spreading factor used (7 to 12), LoRaWAN data rate ranges from 0.3 kb/s to 27 kb/s [S3]. We used the LoPy, which is a MicroPython enabled Wi-Fi, Bluetooth and LoRa development board, to gain access to the LoRa network. In LoRa communication, devices or nodes send small data packets to a gateway, which can be several kilometers away from the node, using the LoRaWAN wireless protocol. The gateway then uses traditional communication methods (Ethernet, WiFi, mobile network) to forward the packets to a network server, which validates the packets and forwards it to an application server. Since the Limpet is designed to be used in offshore energy platforms, where data security is important and internet connectivity is low, we have developed a local network for the LoRaWAN communication for the Limpets. The local LoRaWAN network can be used in any environment and allows the data packets to be secure. The local network developed uses the LoRa Server project provided by CableLabs [S4]. The architecture of the LoRa network is shown by Figure S3. The Limpet sends the sensor data through the UART to the LoPy nodes, which send these data packets to the LoRa gateway using the LoRaWAN wireless protocol. The gateway runs a packet-forwarder software, which is responsible for forwarding the incoming packets to a network server using a User Datagram Protocol (UDP). The network server and the LoRa gateway are given IP addresses through a local Domain Name

System (DNS) server. The LoRa Gateway Bridge, which runs on the local machine or PC that runs the network server, is responsible for transforming the packet-forwarder UDP Protocol into an MQTT Protocol. We used Eclipse Mosquitto as the MQTT Broker. The MQTT messages are forwarded to the LoRa Server, which is the LoRaWAN network server component running on the local machine. The LoRa Server manages the state of the network, where it handles the join requests by the devices and has knowledge of which devices are active on the network. The LoRa App Server component implements a LoRaWAN application-server compatible with the LoRa Server component. It provides a web-interface and APIs for management of users, organizations, applications, gateways and devices. The data payload sent by the devices can then be published from the LoRa App Server to an application using MQTT protocol.

Optical communication has a low bandwidth, and thus, the processing and analysis need to be done before transmission of the data. For optical communication, we use the on-board RGB LED for transmission of data. We transmit the data by pulse-width modulating (PWM) the LED to different levels, where each level corresponds to a number from 0 to 9. We pulse-width modulate the RGB LED from 0 to 255 in steps of 25, which allows for ten different intensity levels corresponding to each of the numbers (0 to 9). We use the different LED colors to correspond to different measurements in a single experiment. The optical communication protocol transmits a single digit at a time. Therefore, we programmed the Limpet to divide any measurements into single digits and transmit the digits one after the other. The intensity of the transmission (PWM level) and the LED color (measurement type) allows reconstruction of the transmitted data from the RGB LED. We use the optical sensor on the Limpet as a receiver, where it detects the light intensity (indication of the transmitted number) and color power density (indication of measurement type), to interpret the data transmitted using the RGB LED. The data transfer speed achieved in our optical communication protocol lies in the range of 6 bps to 53 bps. Optical communication cannot be used for long-range communication, where the optical communication range in our system is in the region of a few 10s of cm. The optical communication range is a function of both the intensity of the RGB LED and the sensitivity of the optical sensor. In field conditions, the amount of ambient light intensity has an impact on the optical communication system.

The Limpet possesses an infrared data transceiver module. The module supports IrDA communication protocol with data rates up to 115200 bits per second and a transmission range of up to 8m. The module consists of an infrared emitter, a PIN photodiode and a low-power CMOS control IC. In this work, we use the infrared transceiver (IR) for robot-to-computer communication, where the data from the Limpet and the sensors can be sent via IR to the computer.

Supplemental References

[S1] R. A. Light, “Mosquitto: server and client implementation of the mqtt protocol,” *Journal of Open Source Software*, vol. 2, no. 13, 2017.

[S2] N. Sornin, M. Luis, T. Eirich, T. Kramp, and O. Hersent, *LoRaWAN Specification*. LoRa Alliance.

[S3] F. Adelantado, X. Vilajosana, P. Tuset-Peiro, B. Martinez, J. Melia-Segui, and T. Watteyne, “Understanding the limits of lorawan,” *IEEE Communication Magazine*, vol. 55, no. 9, p. 34, 2017.

[S4] CableLabs, “Lora server, open-source lorawan network-server.”

Supplemental Figures

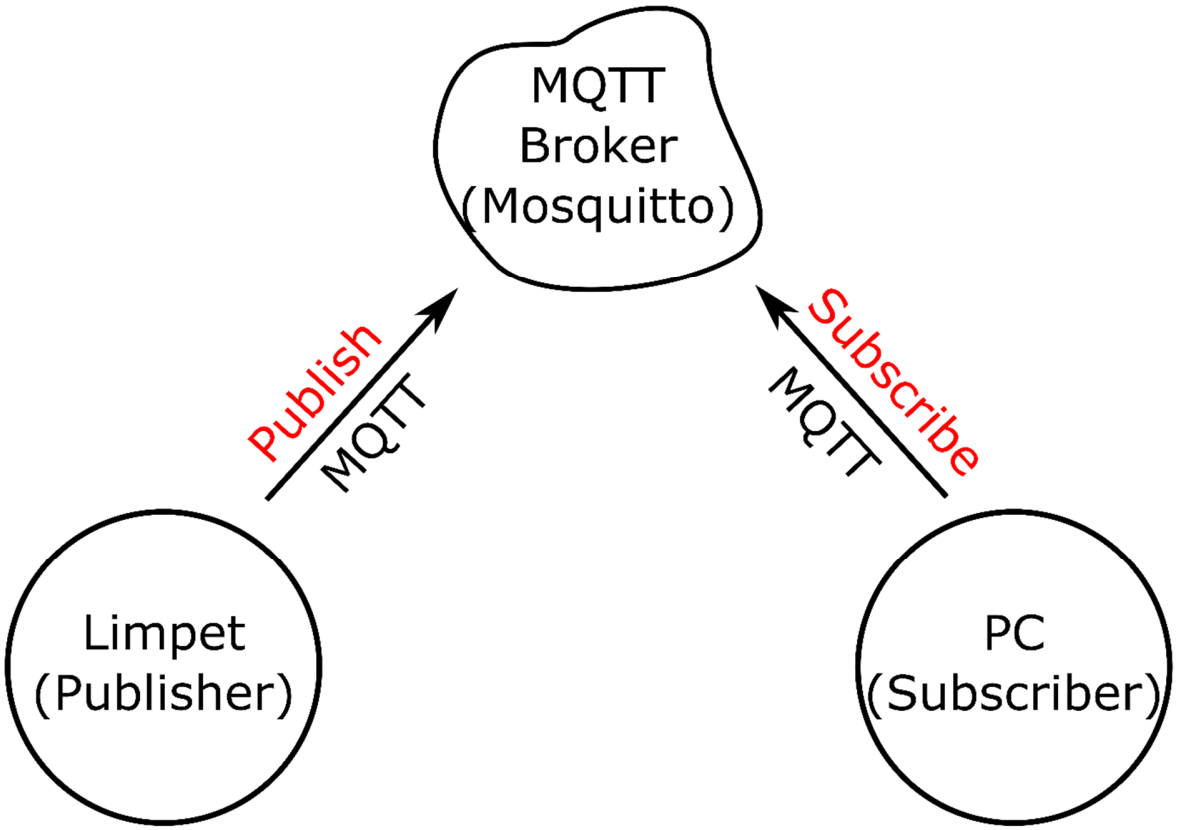

Figure S1: Architecture of the WiFi Communication. In the WiFi communication strategy using MQTT protocol, the Limpet is the publisher, where it publishes the different sensor data, and the subscriber is the PC, where it can subscribe to the MQTT topic to receive the sensor data. The nodes (Limpet and PC) communicate with a server, known as MQTT Broker. We use Mosquitto as the MQTT Broker.

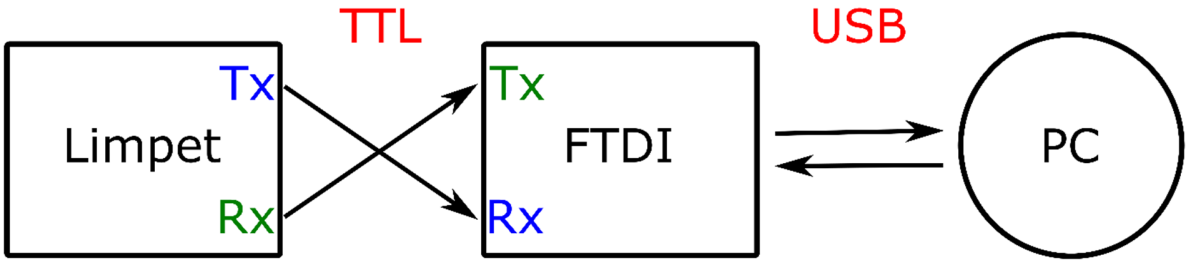

Figure S2: Architecture of the Serial Communication. The Limpet sends the data serially to the computer using the FTDI Basic Breakout, which converts the TTL communication from the Limpet to USB signals for the PC.

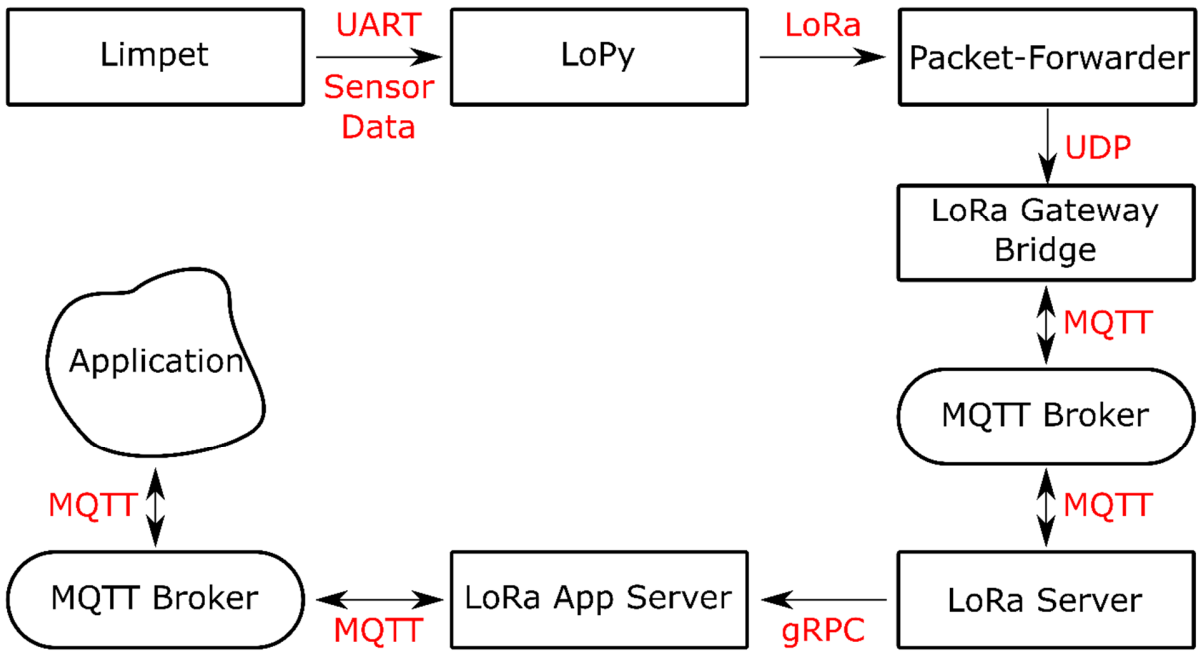

Figure S3: Architecture of the LoRaWAN Communication. The Limpet sends the sensor data packets to the LoPy node through the UART. The LoPy sends these data packets to the LoRa gateway using the LoRaWAN wireless protocol. The gateway runs an implementation of the packet-forwarder software, which forwards the data packets to a network server (LoRa Server) using a UDP protocol. The LoRa Gateway Bridge transfers the packet-forwarder UDP protocol into messages over MQTT. The MQTT broker routes the MQTT messages between the nodes. The MQTT messages are forwarded to the LoRa server, which provides the LoRaWAN network server component. The LoRa App Server implements a LoRaWAN application server and provides a web interface and APIs. The data packets or payload can be published from the LoRa App Server to an application using the MQTT protocol. The application handles the application payloads sent by the Limpets.

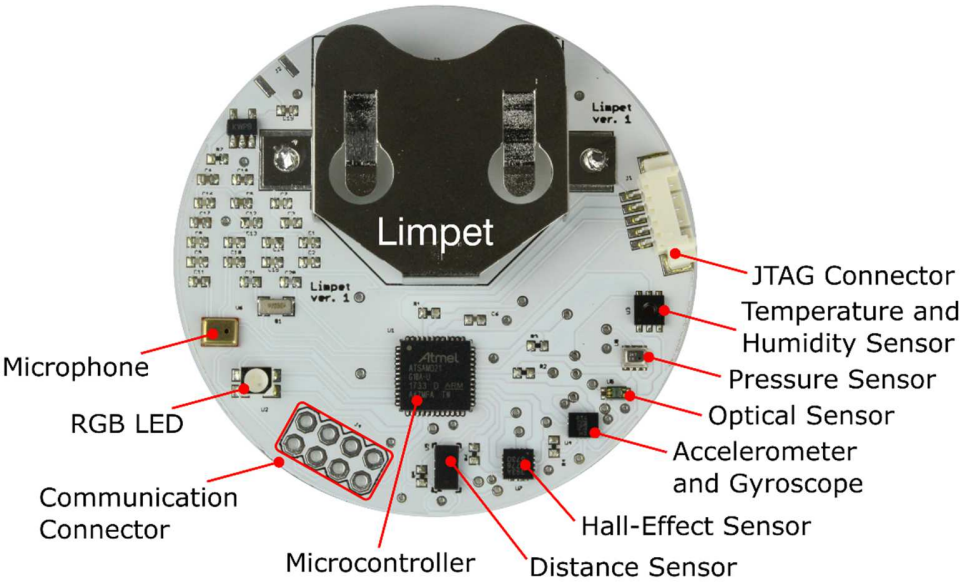

Figure S4: Labelled Picture of the Sensing Module. A labelled picture of the sensing PCB showing the different on-board sensing modalities, microcontroller and RGB LED.

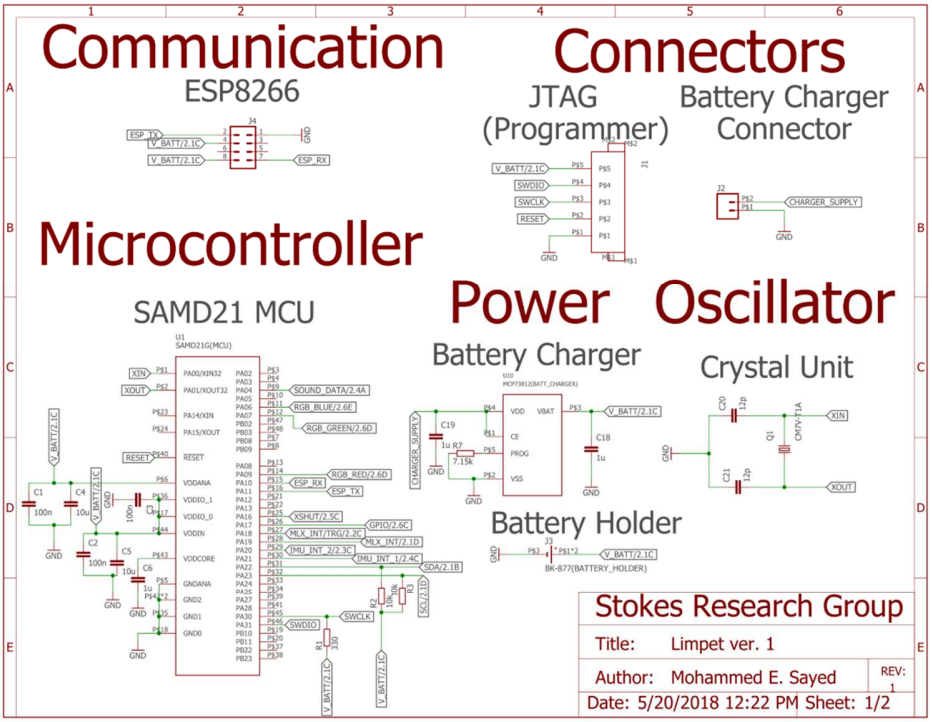

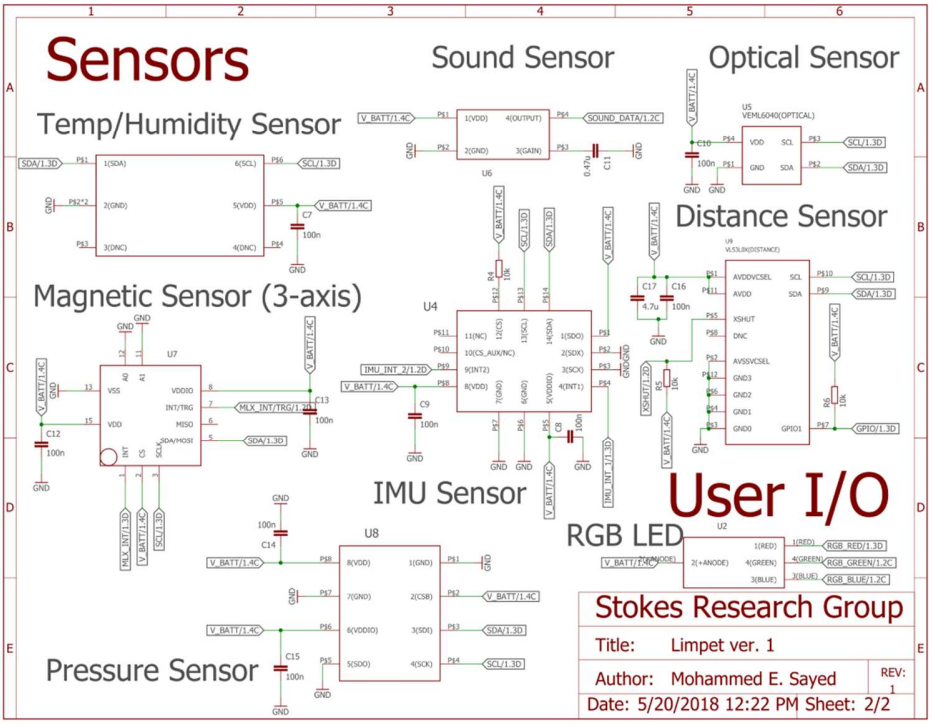

Figure S5: A Circuit Schematic of the Sensing Module.

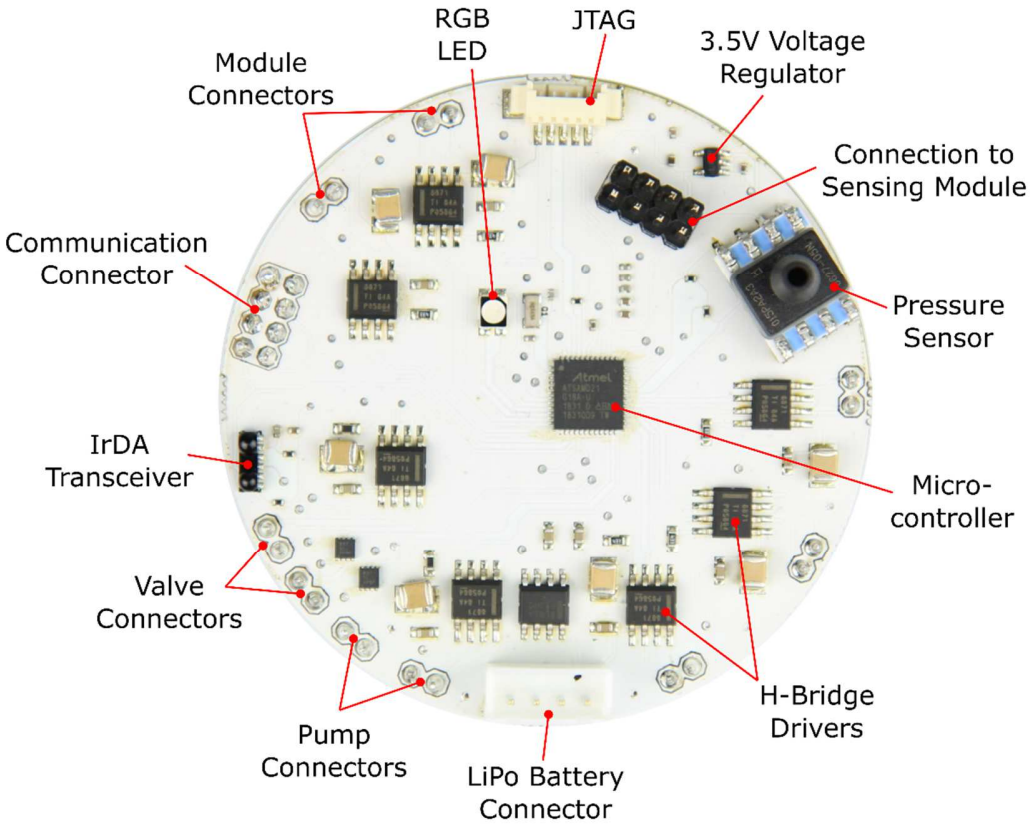

Figure S6: Labelled Picture of the Power Driver Module. A labelled picture of the power driver PCB showing the pressure sensor, h-bridges, infrared transceiver, RGB LED, board-to-board connector, communication connector, JTAG, battery connector, microcontroller, valve connector, and pump connector.

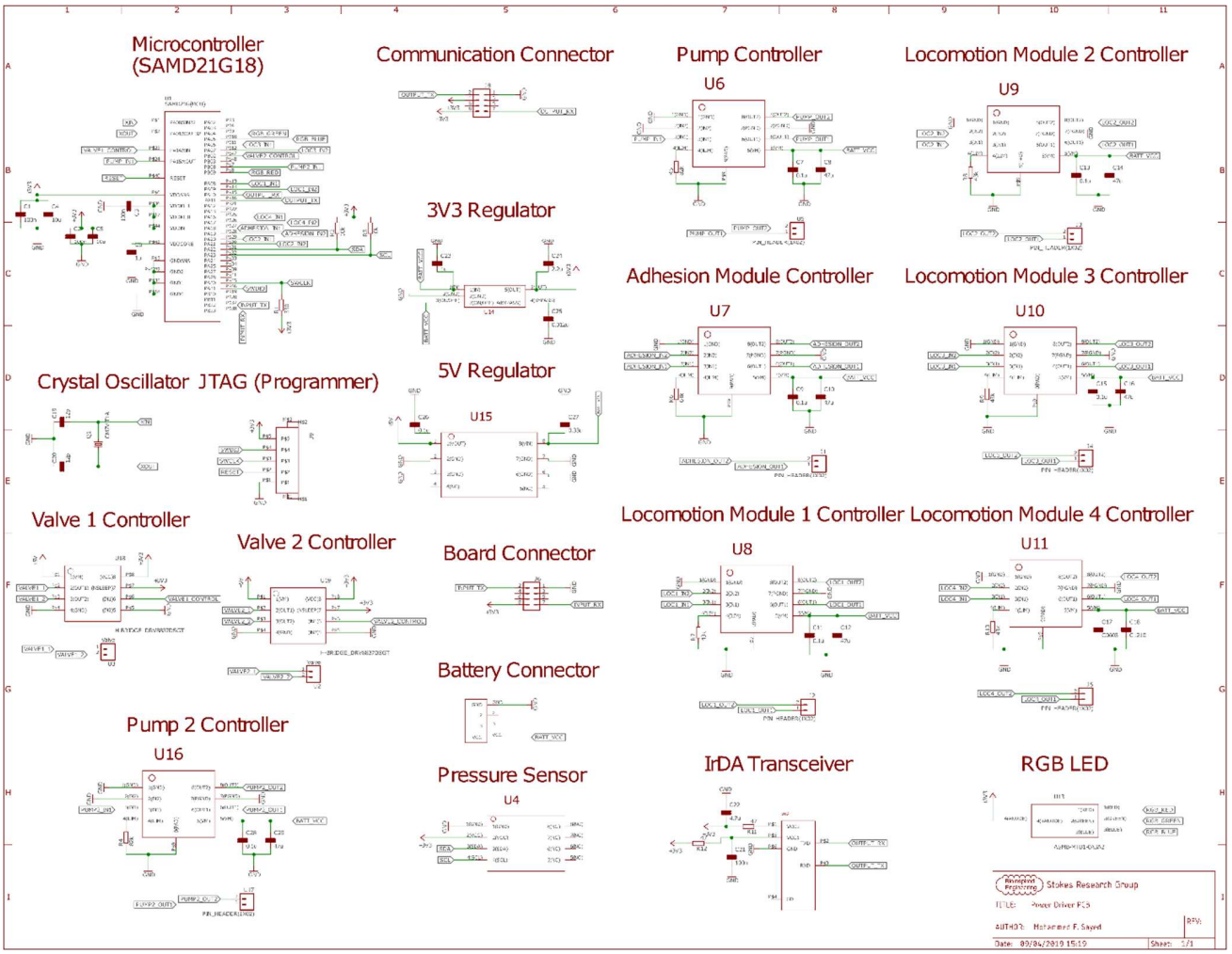

Figure S7: A Circuit Schematic of the Power Driver Module.

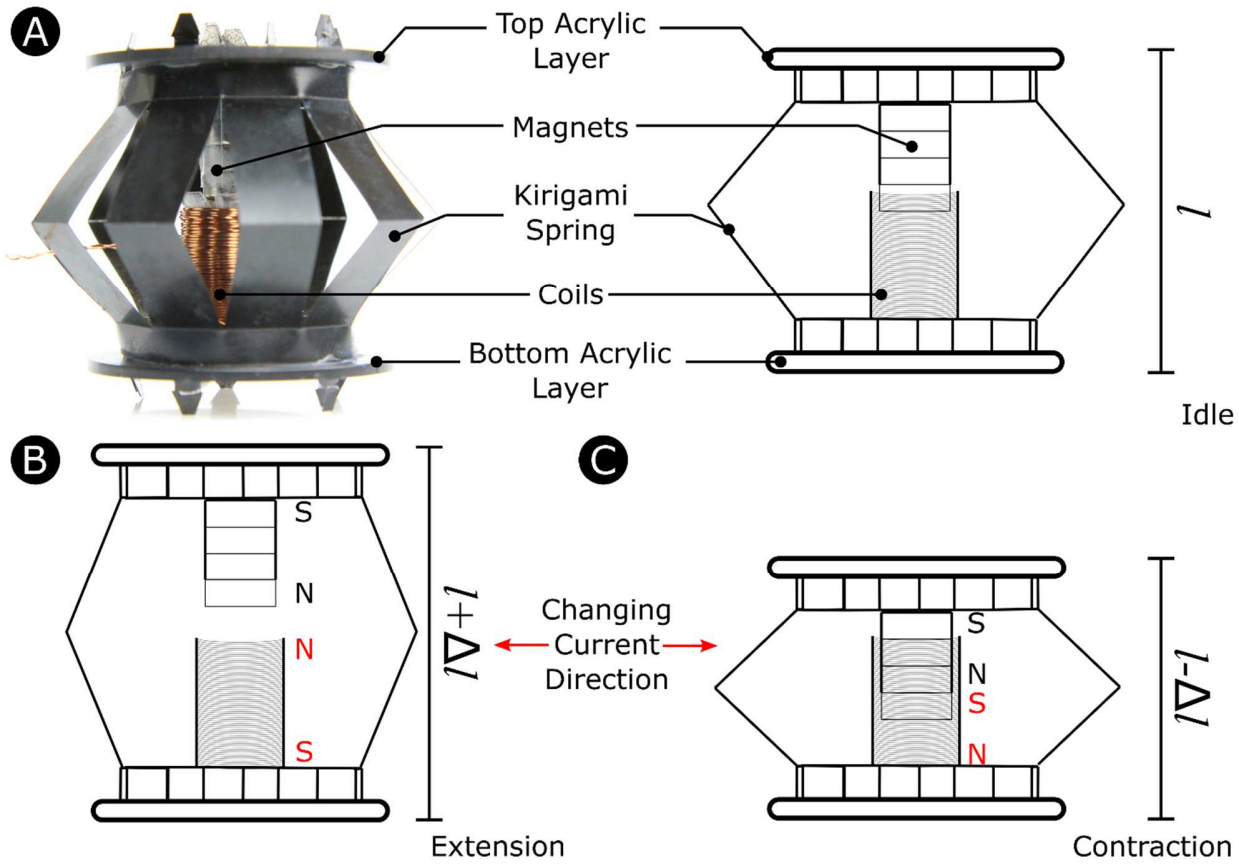

Figure S8: Sketch of the EMM and the Actuation Mechanism. A labelled picture and sketch of the EMM showing all its components, and a sketch of the actuation mechanism.

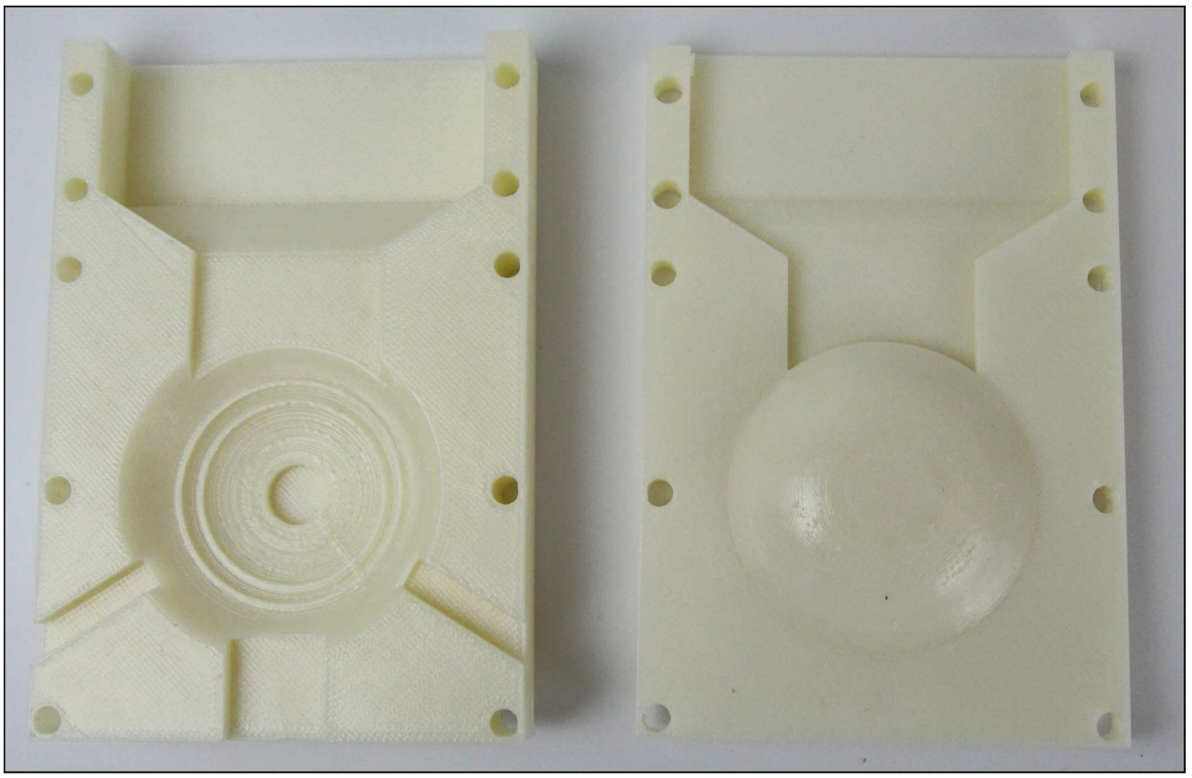

Figure S9: Picture of the Mould Used to Fabricate the Custom-Designed Suction Cups.

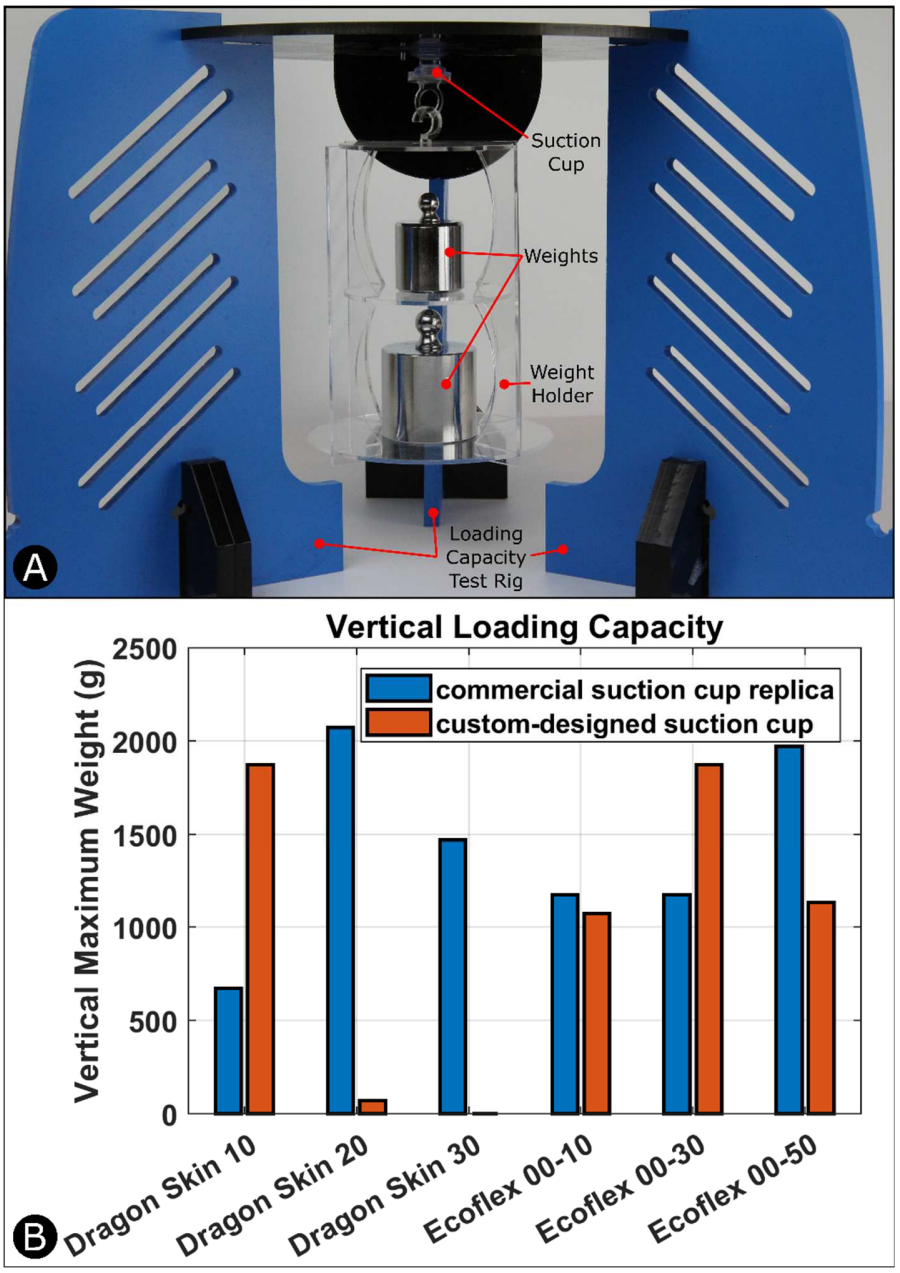

Figure S10: Vertical Loading Capacity of the Suction Cups. (A) A labelled picture of the experimental setup used to test the vertical loading capacity of suction cups. In this experiment, we fabricated two different groups of suction cups, custom-designed suction cups and replicas of the commercial suction cup, out of different soft materials: Dragon Skin 10, Dragon Skin 20, Dragon Skin 30, Ecoflex 00-10, Ecoflex 00-30, Ecoflex 00-50. (B) Results of the vertical loading capacity experiment showing the maximum loading capacity for the suction cups fabricated out of the different soft materials.

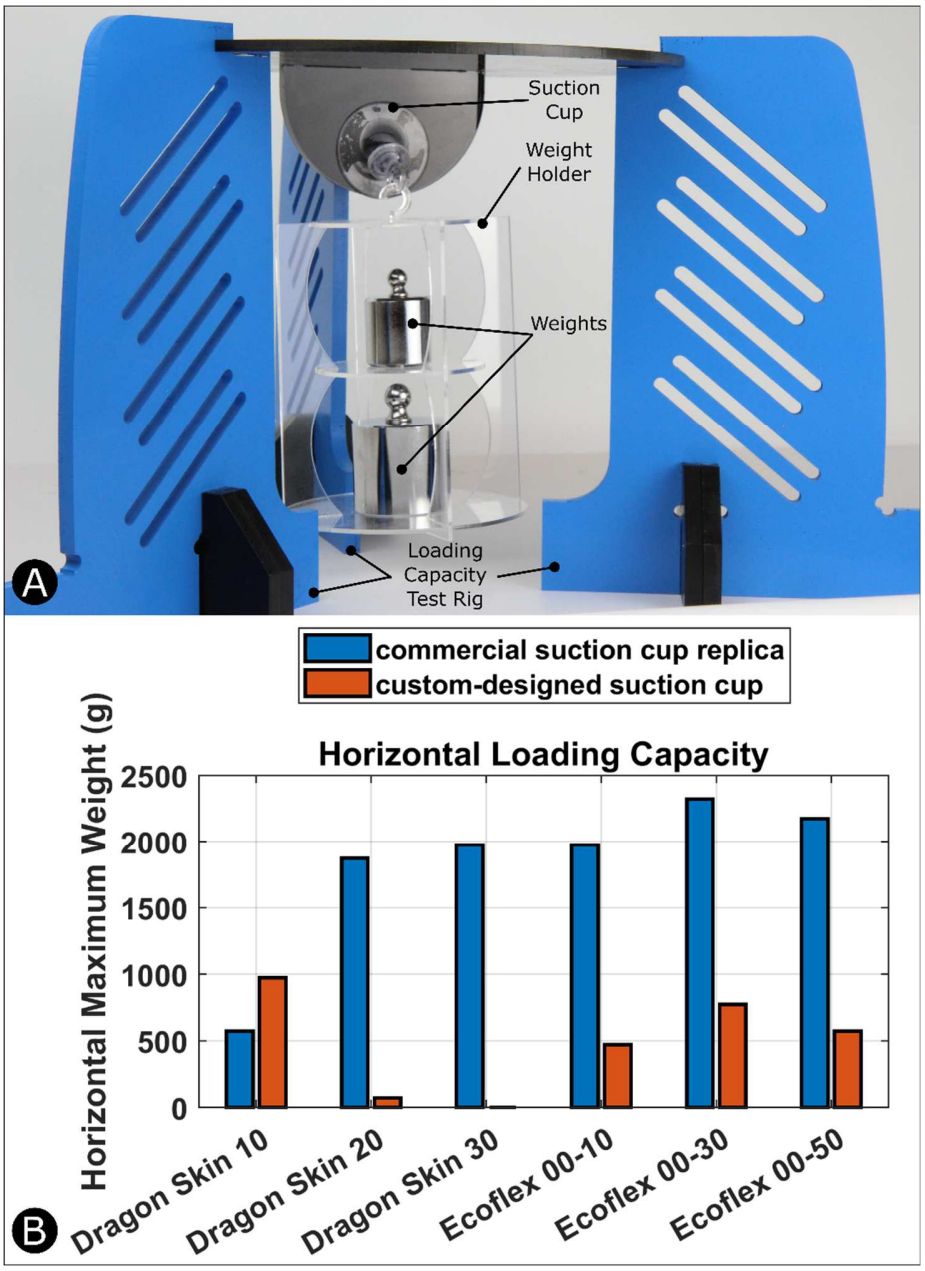

Figure S11: Horizontal Loading Capacity of the Suction Cups. (A) A labelled picture of the experimental setup used to test the horizontal loading capacity of suction cups. In this experiment, we fabricated two different groups of suction cups, custom-designed suction cups and replicas of the commercial suction cup, out of different soft materials: Dragon Skin 10, Dragon Skin 20, Dragon Skin 30, Ecoflex 00-10, Ecoflex 00-30, Ecoflex 00-50. (B) Results of the horizontal loading capacity experiment showing the maximum loading capacity for the suction cups fabricated out of the different soft materials.

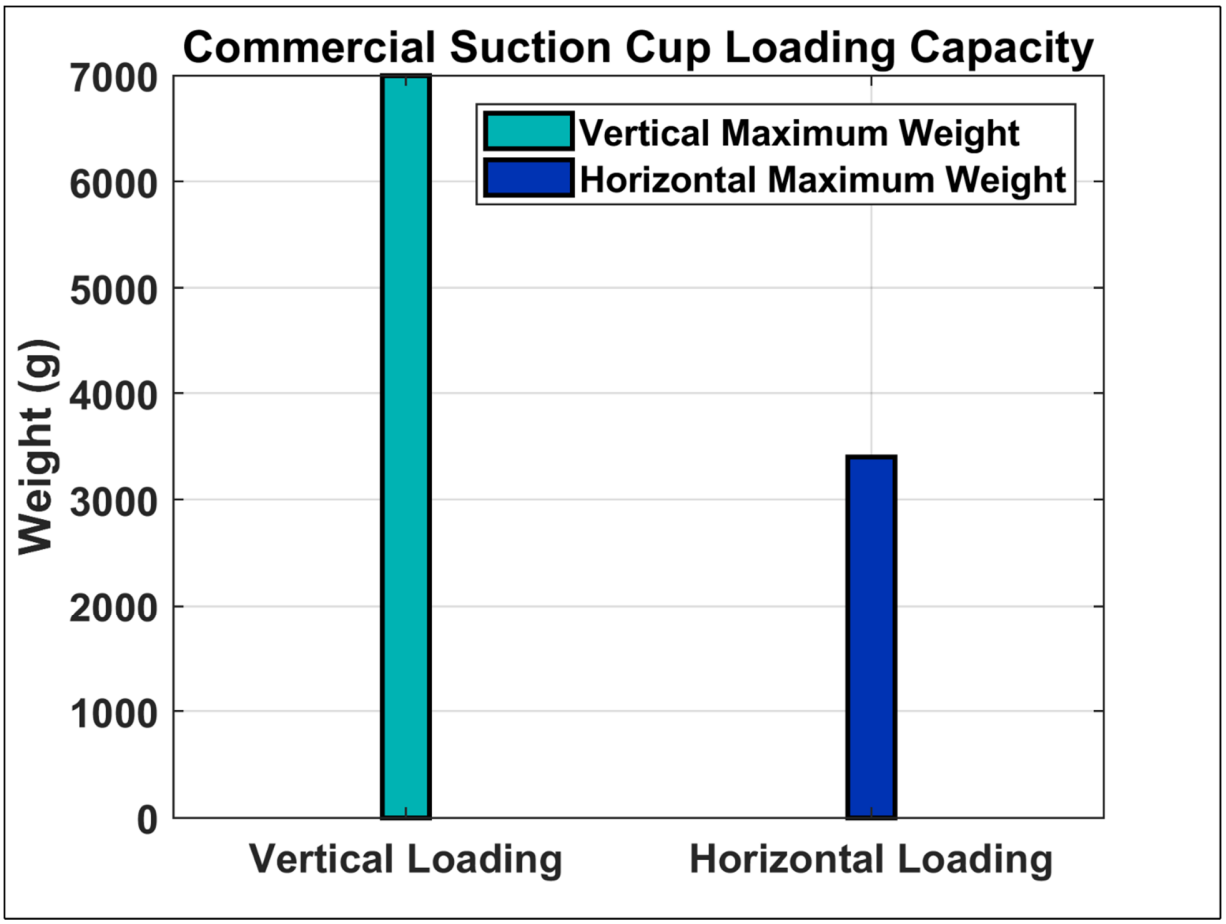

Figure S12: Horizontal and Vertical Loading Capacity on Commercial Suction Cup. Maximum vertical and horizontal loading capacity on the commercial suction cup used for the Limpet. The graphs show the loading capacity of the suction cup before we make any changes to it.

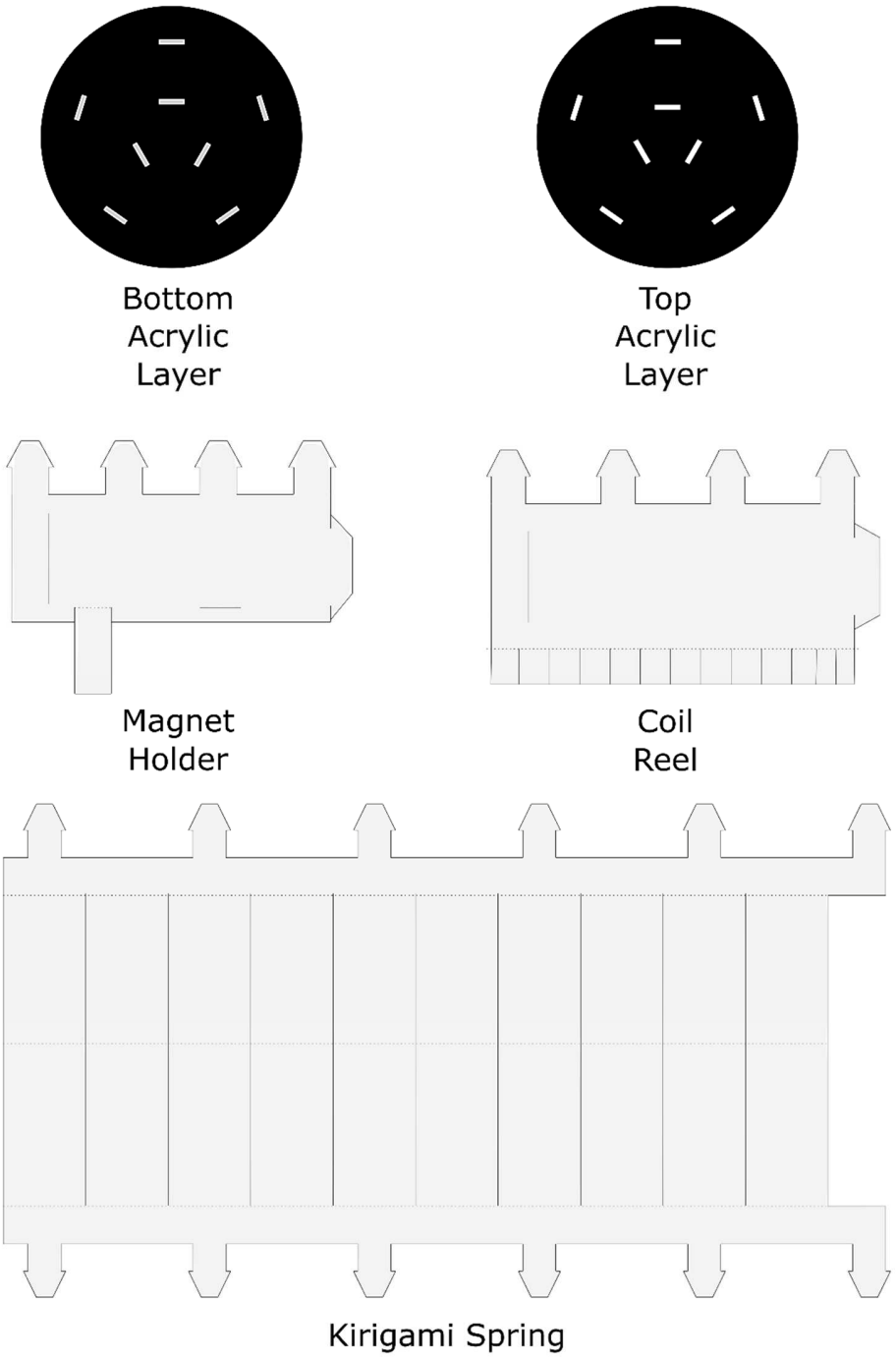

Figure S13: 2D Patterns of the EMM components. 2D design of the top acrylic layer, bottom acrylic layer, magnet holder, coil reel and kirigami spring of the EMM.

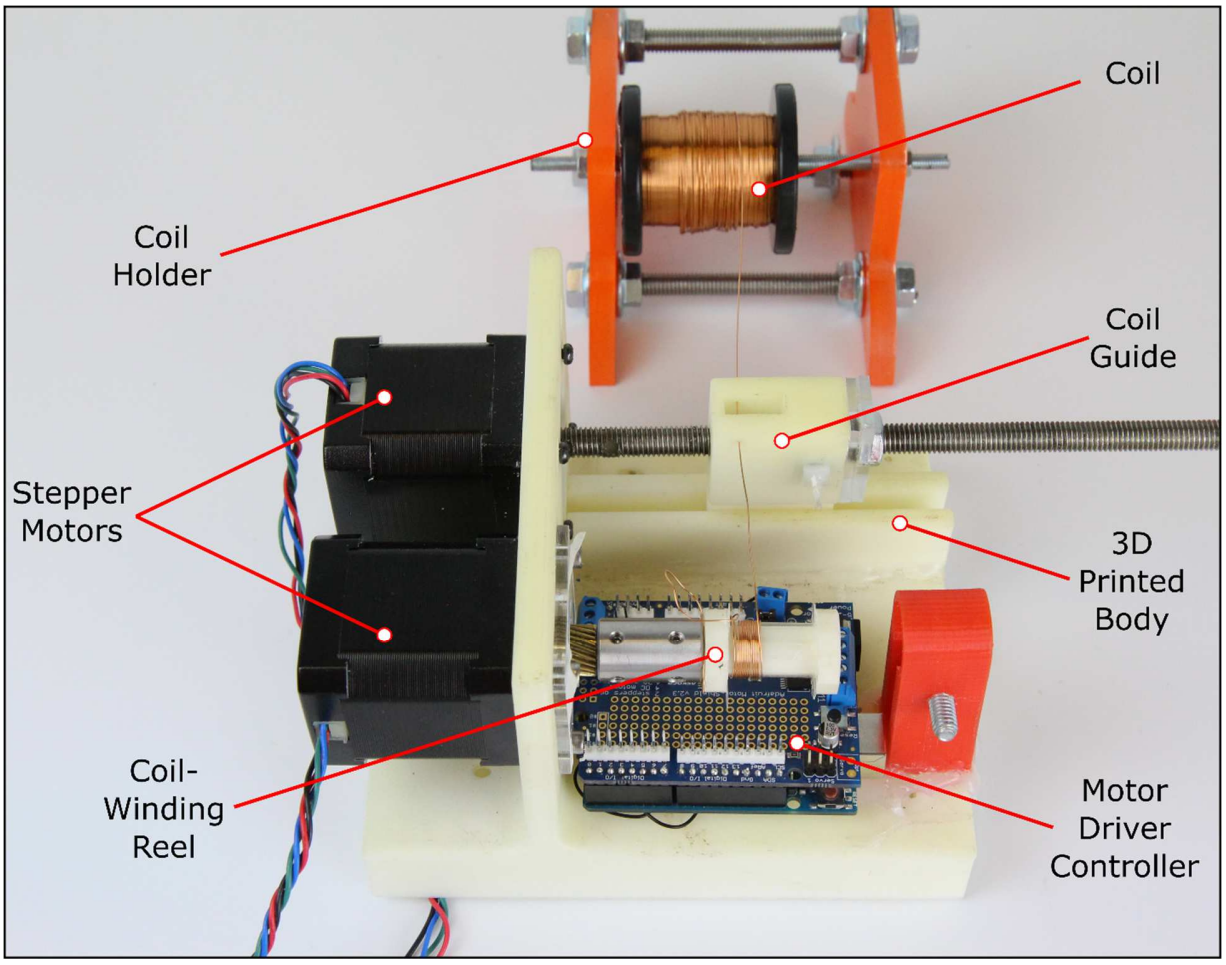

Figure S14: Custom-Built Coil-Winding Machine. A labelled picture of the custom-built coil-winding machine used to produce the coils in the electromagnetic modules (EMMs).

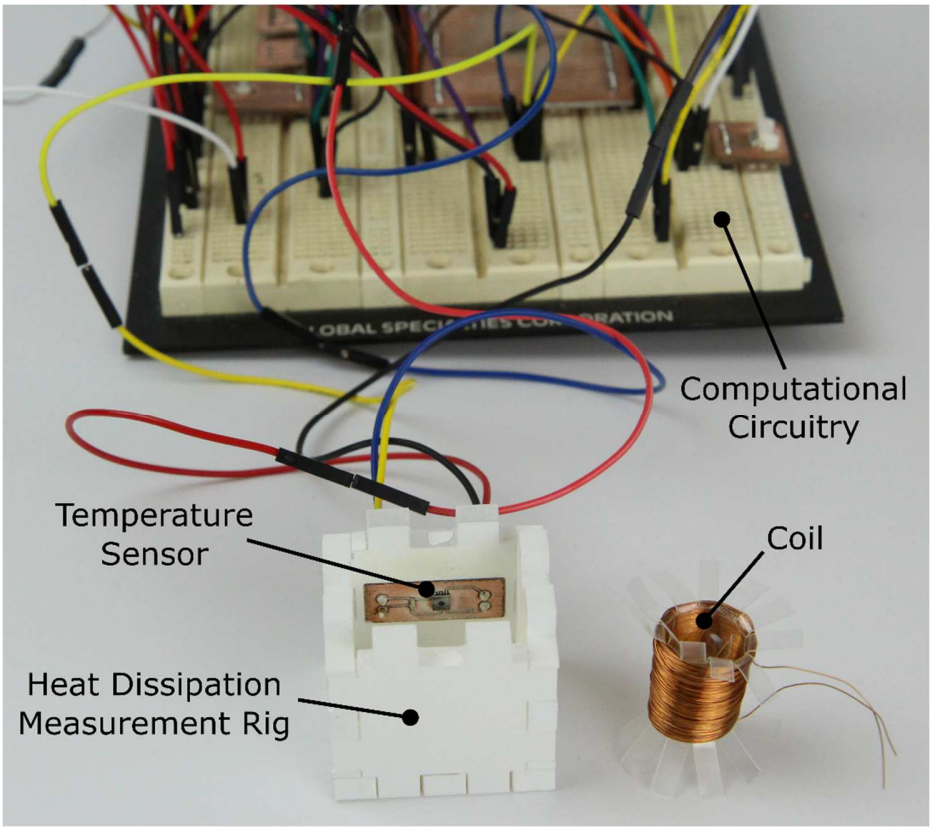

Figure S15: Experimental Setup for Heat Dissipation Measurements for Different Coils Thickness. A picture of the experimental setup we used to analyse the effect of the coil wire thickness on the joule heating in the coils for different currents fed into the coil. We placed the coils in a custom-designed white acrylic box containing a temperature sensor. The temperature sensor is connected to a computational circuit consisting of a microcontroller and bypass capacitors. We feed current into the coil and measure the temperature rise as a result of the current.

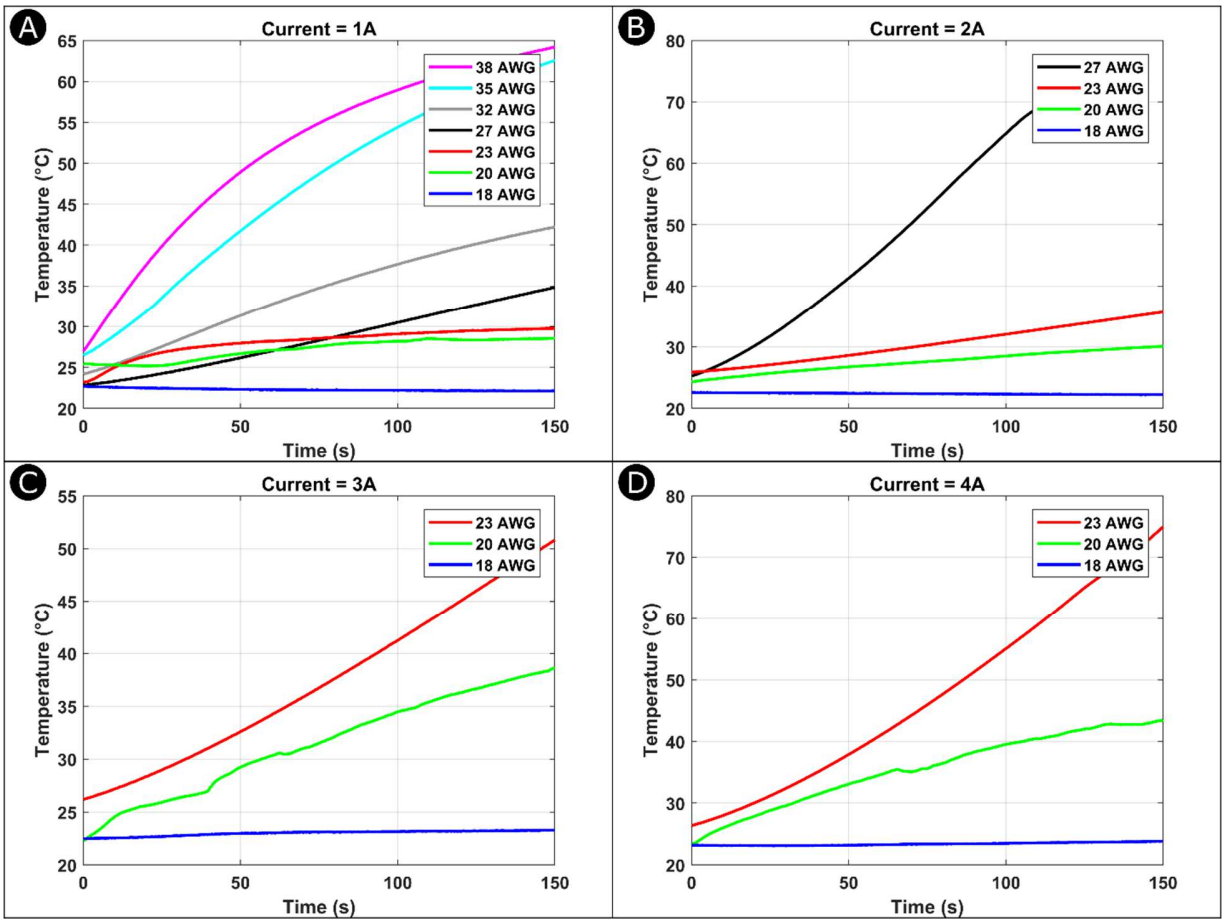

Figure S16: Experimental Results of the Heat Dissipation Experiment. Results of the heat dissipation experiments showing the rise in temperature due to different currents for the different coil thicknesses. These measurements show that the amount of current drawn by the coils is proportional to the rate of temperature rise. We analysed the temperature rise of the coils for a period of 150 seconds each. Each graph shows the rise in temperature over time for each of the coils at a different current level (1A, 2A, 3A, 4A).

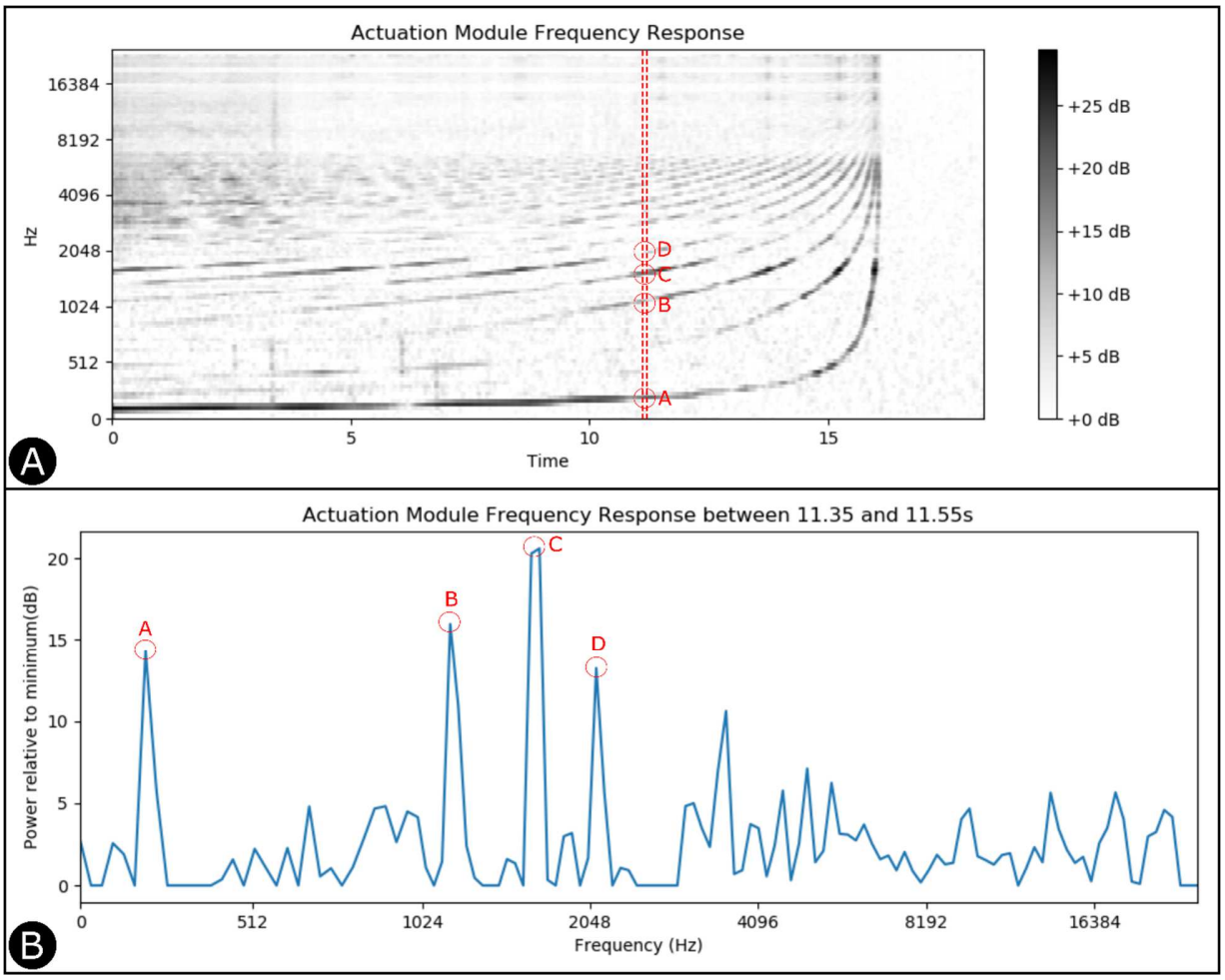

Figure S17: Sound Spectrogram of the EMM at Audible Frequency Levels. (A) A Mel-Spectrogram of the audio from seconds 24 to 42 of Video S2. The frequency axis is linear under 1000 Hz and is in log base 2 scale above 1000 Hz. (B) A vertical slice of the Mel spectrogram representing a Mel-Scaled FFT of the audio from 11.35s-11.55s of Video S2.



Figure S18: PWM Experiment Results. Results of the PWM test of the EMM showing the change in height of the EMM against the PWM duty cycle.

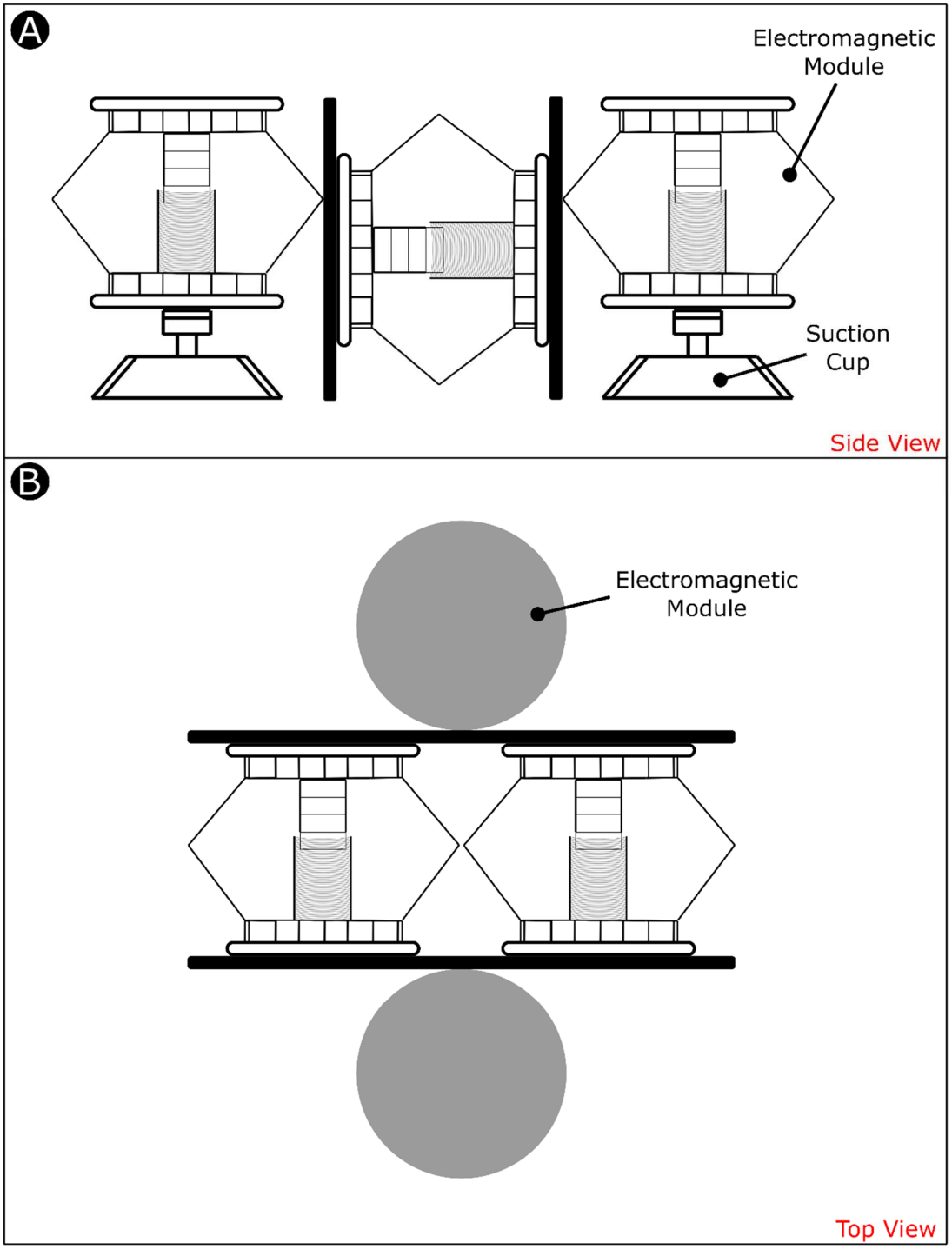

Figure S19: Configuration of the Limpet System for Climbing. (A) Side view and (B) Top view of the configuration used for the Limpet system to achieve climbing on a surface.

Video Captions

Video S1: Overview of the Limpet System.

Video S2: Frequency Response Analysis. A video showing the effect of varying the control frequencies on the EMM. The EMM actuates at low control frequencies, and as the frequency increases, the EMM transitions to producing sound.

Video S3: Frequency Response Analysis at a Higher Frame Rate. A video showing the frequency response of the EMM using a camera with a higher frame rate.

Video S4: Pulse-Width Modulation of the Electromagnetic Module. A labelled video showing a pulse-width-modulated (PWM) signal applied to the EMM to observe the effect of changing the duty cycle on the actuation height. The EMM sweeps through duty cycles from 0-100% and then from 100-0%. The EMM then steps between set duty cycles of 20%, 40%, 60%, 80% and 100%.

Video S5: Evaluation of the Spring Constant of the Electromagnetic Module. A video showing the experiment conducted to evaluate the spring constant of the EMM, where weights are added on the spring and the change in height measured.

Video S6: Determining the Output Force for Different Actuation Currents. A labelled video showing the setup for the quantification of force output from the EMM. The video shows the output force for different current levels supplied to the EMM.

Video S7: Single Locomotion Module. A video showing a single locomotion module reaching targets in the four cardinal directions in an environment. We bias the direction of movement of the module by changing the position of the weight on top of it.

Video S8: Locomotion System with Two Locomotion Modules. A video showing a locomotion system composed of two locomotion modules reaching targets in the four cardinal directions in an environment. We bias the direction of movement of the module by changing the

position of the weight on top of it or changing the actuation pattern of the two modules with respect to each other.

Video S9: Locomotion System with Four Locomotion Modules. A video showing a locomotion system composed of four locomotion modules reaching targets in the four cardinal directions in an environment. We bias the direction of movement of the module by changing the actuation pattern of the locomotion modules with respect to each other.

Video S10: Locomotion System Following a Rectangular Shaped Path. A video showing the tracking of the locomotion system as it moves in a pre-programmed rectangular shape.

Video S11: Tracking the Height of Displacement of the Locomotion System. A video showing the locomotion system moving horizontally on a surface in a straight line. The black sphere on the locomotion system is used to track the height of movement of the locomotion system as it moves along the surface.

Video S12: Untethered Control of the Limpet Using Light Sensor. A video showing the Limpet responding to a change in the LED colour by changing direction of movement.

Video S13: Untethered Control of the Limpet Using Sound Sensor. A video showing the Limpet responding to a change in sound frequency by changing direction of movement.

Video S14: Untethered Control of the Limpet Using Distance Sensor. A video showing the Limpet responding to the presence of an object in close proximity by repositioning itself.

Video S15: Untethered Control of the Limpet Using IMU Sensor. A video showing the Limpet repositioning itself when it is poked or touched.

Video S16: Sound-Based Inter-Communication of Limpets. A video showing one Limpet generating a sound signal (distress signal), and the neighbouring Limpet repositioning itself away from the first Limpet.

Video S17: Climbing an Inclined Surface. A video showing the top and side views of the Limpet climbing a surface.

Technical Files

The authors have provided a zip-file for CAD files and Bill of Materials.

Appendix J

Journal: Long Necked Turtle: A Soft/Hard Hybrid Mobile Robotic Platform for IoT Node Distribution

Journal: Frontiers in Robotics and AI

Publisher: Frontiers

Long Necked Turtle: A Soft/Hard Hybrid Mobile Robotic Platform for IoT Node Distribution

Alistair C. McConnell[1], Mohammed E. Mohammed[1], Jamie O. Roberts[1], Simona Aracri[1], Ross M. McKenzie[1], Adam A. Stokes[1*]

[1]University of Edinburgh, United Kingdom

Submitted to Journal:
Frontiers in Robotics and AI

Specialty Section:
Multi-Robot Systems

Article type:
Original Research Article

Manuscript ID:
485139

Received on:
15 Jul 2019

Frontiers website link:
www.frontiersin.org

In review

Conflict of interest statement

The authors declare that the research was conducted in the absence of any commercial or financial relationships that could be construed as a potential conflict of interest

Author contribution statement

ACM, MES and JOR contributed equally to this all sections of this work.
SA contributed to the experimentation and writing of this work.
RMM contributed to the design and fabrication of the system.
AAS contributed to the design and writing of this work.

Keywords

Soft IoRT, Turtlebot, Multi-robot system, IoT robot deployment, Robust robotics, Networked robotics

Abstract

Word count: 203

Monitoring structural and environmental conditions is a critical task in the oil and gas industry. Given the inherent risk of the task, there has been a drive to remove humans from hazardous offshore environments. Robots have been proposed to be an effective replacement for personnel in these environments.
A major challenge that robots will face on offshore installations is the unstructured nature of the environment. Task planning in such conditions requires increased computational complexity and is resource intensive.
In this work, we present the Long Necked Turtle (LNT), a mobile soft/hard hybrid robotic platform designed to function as part of an Internet of Robotic Things (IoRT) network by robustly mounting an IoT sensor node. We demonstrate how our platform navigates an area and locates a target to place the sensor node: the `Limpet'.
Using the data provided by the Limpet, the soft manipulator robustly places the Limpet on the target.
Our platform has been developed for the ORCA Hub (Offshore Robotics for Certification of Assets), and provides an initial test of how soft robotics can be used as part of an IoRT network in the oil and gas industry by transporting and placing the Limpet sensor node, to enable remote monitoring of assets.

Contribution to the field

In this work, we present the Long Necked Turtle (LNT), a mobile soft/hard hybrid robotic platform designed to function as part of an Internet of Robotic Things (IoRT) network by robustly mounting an IoT sensor node. We demonstrate how our platform navigates an area and locates a target to place the sensor node: the `Limpet'. Using the data provided by the Limpet, the soft manipulator robustly places the Limpet on the target. The work contributes an important step in the IoRT area by demonstrating a robust mobile platform that can expand its own IoRT network using IoT Limpet sensors.

Funding statement

This work was supported by EPSRC ORCA Hub (EP/L016753/1), EPSRC via Robotarium Capital Equipment and CDT Capital Equipment Grants (EP/L016834/1).

Ethics statements

Studies involving animal subjects

Generated Statement: No animal studies are presented in this manuscript.

Studies involving human subjects

Generated Statement: No human studies are presented in this manuscript.

Inclusion of identifiable human data

Generated Statement: No potentially identifiable human images or data is presented in this study.

in review

Data availability statement

Generated Statement: The datasets generated for this study are available on request to the corresponding author.

In review

frontiers

Long Necked Turtle: A Soft/Hard Hybrid Mobile Robotic Platform for IoT Node Distribution

Alistair C. McConnell [1†], Mohammed E. Sayed [1†], Jamie O. Roberts [1†], Simona Aracri [1], Ross M. McKenzie [1] and Adam A. Stokes [1*]

[1] *School of Engineering, Institute for Micro and Nano Systems, The University of Edinburgh, Edinburgh, UK*

[†] *The authors that contributed equally to this work.*

Correspondence*:
Adam A. Stokes, School of Engineering, Institute for Micro and Nano Systems, The University of Edinburgh, Scottish Microelectronics Centre, Alexander Crum Brown Road, King's Buildings, Edinburgh, UK, EH9 3FF
Adam.Stokes@ed.ac.uk

In review

ABSTRACT

Monitoring structural and environmental conditions is a critical task in the oil and gas industry. Given the inherent risk of the task, there has been a drive to remove humans from hazardous offshore environments. Robots have been proposed to be an effective replacement for personnel in these environments. A major challenge that robots will face on offshore installations is the unstructured nature of the environment. Task planning in such conditions requires increased computational complexity and is resource intensive. In this work, we present the Long Necked Turtle (LNT), a mobile soft/hard hybrid robotic platform designed to function as part of an Internet of Robotic Things (IoRT) network by robustly mounting an IoT sensor node. We demonstrate how our platform navigates an area and locates a target to place the sensor node: the 'Limpet'. Using the data provided by the Limpet, the soft manipulator robustly places the Limpet on the target. Our platform has been developed for the ORCA Hub (Offshore Robotics for Certification of Assets), and provides an initial test of how soft robotics can be used as part of an IoRT network in the oil and gas industry by transporting and placing the Limpet sensor node, to enable remote monitoring of assets.

Keywords: Soft IoRT, turtlebot, multi-robot system, IoT robot deployment, robust robotics, networked robotics

1 INTRODUCTION

1.1 Hazards and Opportunities in Offshore Industries

Oil platforms, wind turbines, tidal barrages and any offshore platforms, all face harsh and dangerous environmental conditions that degrade their structures. The cost of decommissioning old infrastructure, a fluctuating oil price and expensive maintenance costs, when comparing to sites on land Lo (2018), create the perfect storm of potential failures and rising costs Wood (2014). All offshore industries are facing pressure to maintain their output in line with consumer demand. Achieving this requires constructing more platforms and extending the life of the current ones Hastie et al. (2018). Failures in offshore platforms can

be catastrophic, recent examples are the Deep Horizon oil spill in the Gulf of Mexico and the Piper Alpha disaster in the North Sea. In both of these incidents, there was considerable loss of life and environmental damage Griggs (2011). As a result people are trying to find safer ways to inspect, repair and maintain offshore platforms Shukla and Karki (2016).

1.1.1 Applications of Robotics in Offshore Industries

To thoroughly monitor offshore infrastructure, frequent inspections need to be conducted of both the topside and underwater sections of the platforms. These inspections can be done manually by visually inspecting the areas for faults and taking in-situ measurements. This method has inherent problems relating to the aforementioned issues such as fewer workers and extremely hazardous environments. As infrastructure ages, the frequency of these inspections is required to increase, due to the degradation in the structural material, which leads to both weakened and uneven surfaces.

Robots are currently being used for underwater inspection and maintenance in a twofold manner: Remote Operated Vehicles (ROVs) Costa et al. (2012) and Autonomous Underwater Vehicles (AUVs) Elvander and Hawkes (2012). Aerial vehicles controlled by an operator are also used for topside inspection. Another approach are climbing robots that have been designed to scale the platforms to perform the inspection tasks Moghaddam et al. (2012), although these robots have not been used in large-scale deployment.

These inspection methods can only be used periodically as they are expensive to deploy as all require trained operators and ships to launch from. Although providing essential information, they do not offer any form of real-time monitoring.

The potential for fire or explosion on any offshore platforms can be considered one of the most dangerous scenarios Miller (1991), and for this reason, any potential robot that has to operate in this area, would need to comply with the ATEX directive 2014/34/EU in the European Union and with the DSEAR in Britain.

From these points, we can extract the need for robots to be used to monitor offshore platforms frequently or on-demand, autonomously or semi-autonomously, deployable from the platform, able to traverse stairs and uneven terrain, ATEX or DSEAR certified and able to manipulate surfaces robustly and delicately. These robots would need to be part of an IoT network on the platform to fully monitor it.

1.1.2 Challenges for Robots on Offshore Platforms

For this work, we focus on the top-side of the offshore platforms. There are multiple mobile robots currently in the market, all come in a broad range of prices, functionality, connectivity and locomotion.

The ANYmal Fankhauser and Hutter (2018), developed by ANYbotics is a 30kg quadruped robot, designed for autonomous function in challenging environments. Capable of dynamic running with maximum speed of 1m/s and carrying capacity of 10kg.

The Husky Unmanned Ground Vehicle Clearpath Robotics (2018), created by Clearpath Robotics is a 50kg tracked robot designed to navigate complex and challenging terrains autonomously, with a maximum speed of 1m/s and capable of carrying a maximum payload of 75kg.

The TurtleBot3 TurtleBot (2018), designed by Open Robotics is a wheeled robot created as an educational tool capable of manoeuvring along flat terrain. This 1kg robot has a maximum speed of 0.22m/s and maximum payload of 15kg.

In review

All of these examples can be characterised as hard robots, which posses several advantages such as precise positioning and rapid locomotion. They also have several disadvantages including expensive to build or purchase, complex control methods and mechanically rigid Raibert et al. (2008).

Soft robotics provides an alternative to the traditional hard robotics. They have several advantages including mechanical compliance, low cost, lightweight and simplistic controls enabled by the nature of the materials used Albu-Schaffer et al. (2008); Trivedi et al. (2008). They can also have several disadvantages, such as they are generally slower and cannot compete with the load carry capabilities of their hard robotic counterparts Fankhauser and Hutter (2018).

As well as for locomotion, soft robotics can be used as a form of robotic grasping. There are two distinct categories of soft robotic grasping Bicchi and Kumar (????): (1) Fingertip grasp, when an object is pinched between two or more contact points and (2) Enveloping grasps, where the fingers and palm wrap around an object.

To enable grasping a soft robotic actuator must be used. There are multiple forms currently in existance: PneuNet Bending Ilievski et al. (2011), Fiber-Reinforced Galloway et al. (2013), Pneumatic Artificial Muscles Chou and Hannaford (1996), Dielectric Elastomer Keplinger et al. (2012) and Particle Jamming Actuators Brown et al. (2010). For this work, we used the PneuNet bending actuators to provide the grasping method for the robot.

We incorporate both hard and soft robotics in this paper to overcome the negative attributes of each type of robot. The idea of a mobile hybrid robot has been successfully applied in previous works. Stokes et al. (2014) Stokes et al. (2014) showed the advantages of the speed that is provided by hard robotics and all-terrain locomotion and compliant gripping of the soft robotics. A hybrid robotic arm has been demonstrated by McKenzie et al. (2017) McKenzie et al. (2017) where the speed and positioning of a hard robot were complemented with the versatility of a soft end effector. A hybrid soft/hard object retreval robot has been shown by Dorobantu et al. (2018).

In review

2 THE LONG NECKED TURTLE AND THE LIMPET

One way to monitor structures is to deploy a collective of static sensor nodes to create a full IoT network. Mounting a sensor node requires accurate knowledge of several factors such as the shape of the surface, the shape and weight of the sensor and a compliant limb/manipulator to place the sensor on the surface. For this reason, these sensors are often positioned by hand instead of by an automated process. We have developed a soft/hard robotic hybrid that can navigate autonomously within a given area, use the Limpet Sayed et al. (2018) sensor to find the ideal placement point for the Limpet and then, take advantage of the compliant nature of the soft robotic gripper to conform to the irregularities in the surface. The computational complexity of the task planning is reduced by the use of a soft gripper. The LNT can be seen in Fig 1.

Location of Figure 1

2.1 Design of the Hardware

2.1.1 The Limpet

Limpet node shown in Fig 1 is a multi-sensing platform designed for structural and environmental monitoring of offshore platforms. Its sensing capabilities consist of nine exteroceptive sensors which are temperature, pressure, humidity, optical, distance, sound, magnetic field, accelerometer and gyroscope.

For this work, we used the data collected by the Time of Flight sensor to measure the distance between the Limpet and the target area. The Limpet can use multiple methods of communication including wired, Wi-Fi and LoRa Alliance (2018). We transmit data from the Limpet to the LNT over Wi-Fi using the ESP8266 module, which is a System-on-a-chip (SoC) modules giving any microcontroller access to the Wi-Fi network. Fig 1(g) shows the Limpet mounted in its encapsulation while grasped by the LNT. The encapsulation that has been designed to protect it from damage and provide the ability to be mounted via the integrated magnets.

2.1.2 The Design of the Soft Gripper

The key aspect of this work is the soft gripper of the robot. We wanted a design that would be able to hold the Limpet securely while it was traversing the terrain and afterwards to be able to robustly mount the Limpet on an uneven or fragile surface. We designed the soft gripper to be able to collect the Limpet in its encapsulated form using four contact points in line with the 'fingertip grasp' method, transport it to the area of mounting, direct it to find the best mounting point and then, place it. We created a soft robotic gripper that comprised of four PneuNets in a cross shape and was controlled by a single pneumatic line. The CAD files are included in the supplemental material. This single line of control reduced the complexity of the robot, while providing suitable strength and compliance to carry and place the Limpet. The Limpet being held in the soft gripper of the LNT can be seen in Fig 1(f). Using a soft actuator allowed us to place the Limpet onto the wall regardless of its shape, as the soft actuator would conform to the tilted surface.

2.1.3 The Design of the Robotic Arm

The requirements of the arm include stability and accuracy. We based the arm of the LNT on the DoBot arm used by McKenzie et al. (2017) McKenzie et al. (2017). The initial arm used three stepper motors at the base of the arm connected through a set of linkages to provide the movement and lift capabilities. This system had a limited lifted capacity. We designed a 2-DOF arm using servo motors to provide more torque and therefore increase the lifting capacity.

2.1.4 The Design of the On-Board Controller

The on-board controller of the platform takes the form of an Intel NUC8i7HVK, running Linux. The Intel NUC is compact, 220×140×44mm. The Intel NUC, shown in Fig 1(c) is mounted on the first layer of the scaffolding.

2.1.5 The Design of the Mobile Base

The body is based on a wheeled hard robot (iRobot Create)Jones (2006), which has been modified with a acrylic superstructure that the computer, arm and camera are mounted on. The wheeled robot, shown in Fig 1(a), is capable of travelling up to 500mm/s on a smooth, flat surface, unloaded the robot is capable of carrying up to 3kg payload. The robot contains multiple sensors such as a front bump sensor, front mounted IR sensor, cliff sensors and drop sensor. The iRobot is operated via serial communication.

2.1.6 The Design of the Vision System

The navigation of the LNT uses an Intel RealSense D415 camera Intel (2018). This camera is a stereo depth camera that allows for 3D mapping and object recognition. In this work the camera has been used for:

- 3D mapping
- Detection of an AprilTag

In review

2.2 Design of the Control Software

The LNT control was provided by the Intel NUC and the microprocessor.

The data flow in the system is linear, where the RealSense camera and the Limpet send data over USB and Wi-Fi respectively, to the Intel NUC. This processes the data and sends the appropriate commands to the microprocessor via USB, which in turn, sends the commands to either the arm, soft gripper or mobile base.

2.2.1 Simultaneous localization and mapping (SLAM) Navigation

The navigation of the LNT was a combination of the SLAM navigation Temeltas and Kayak (2008) in the form of Real-Time Appearance-Based Mapping (RTAB-Map) Labbe and Michaud (2014) and a visual fiducial system the AprilTag Wang and Olson (2016). The RTAB-Map is a RGB-D Graph SLAM approach compatible with ROS. The SLAM approach was paired with the use of AprilTags. AprilTags are a form of opensource visual fiducial system that uses a 2D bar code 'tag' that allows for six degree of freedom localisation and provides a marker point for the wall. AprilTags have been used in land robotics navigation Wang and Olson (2016), but also in underwater navigation Westman and Kaess (2018).

2.2.2 Limpet to LNT Communication

The Limpet will communicate to the LNT through the use of a ESP8266 Wi-Fi module. This will allow the Limpet to send its data through a messaging protocol known as Message Queuing Telemetry Transport (MQTT) wirelessly from the Limpet to the Intel NUC. We use Mosquitto Light (2017) to implement the MQTT messaging protocol. The LNT can then act on the data it receives or store it for later processing. This messaging system allows for the Limpets and LNT to be incorporated into their own IoRT network.

Location of Figure 2

2.3 Full System Assembly

Fig 1 shows the complete LNT system. It was autonomously controlled by an Arduino Mega 2560, where the data from the vision system was processed by a python script running on the Intel NUC which in turn, then passed commands to the microcontroller. The microcontroller parsed commands to the motor controls, electro-pneumatic controls and to the mobile base. The total additional payload added to the wheeled base is 1.5kg. We use a Slackbot Slack (2018) which is a custom developed bot that functions with the Slack mobile application on a smart phone to send a start command, monitor what the system is doing and to allow us to perform an emergency shut down if required.

3 EXPERIMENTAL DESIGN

In this section, the design of the experiments used to verify the functionality of the LNT system as a mobile platform capable of robustly and autonomously mounting sensor nodes is explained. Fig 2 shows a schematic of the experimental setup used. The LNT was placed in an enclosed arena with an AprilTag and a steel plate affixed to one section of the wall.

3.1 3D Mapping of the Arena

The initial task of the LNT is to create a 3D map of its surrounding area. This would be done as follows:

- Begin scanning the arena

In review

- Once a full sweep has been completed repeat it once more
- Progress to search and location task

3.2 Design of the Search and Location Task

The second task that the LNT is required to complete is a search and location task. An AprilTag was placed on the test wall in the experimental area as a trigger for locating the wall, the LNT has to complete the following steps:

- Locate the AprilTag using the RealSense Camera
- Once located, approach the AprilTag to a minimum stopping distance
- Progress to placement task

This task is designed to ensure the navigation and locomotion systems function correctly.

3.3 Design of the Placement Task

Task three for the LNT is a placement task. Once the search and navigation task is completed the LNT will be required to complete the following steps:

- Position the soft gripper holding the Limpet within 100mm of the surface
- Traverse the wall with the Limpet monitoring the surface
- Extend the arm, open the soft robotic gripper and the release the Limpet onto the surface

In review

4 RESULTS AND DISCUSSION

4.1 Evaluation of the Systems Performance

Included in the supplemental material is a video of the system performing the experiments, the full data gathered by the Limpet sensor and the 3D map built up from the navigation system. To fully evaluate the performance of the LNT, we analysed the results of the tasks that had been performed, (1) 3D Mapping, (2) Search and Location, (3) Placement. We also reviewed the data gathered by the Limpet when it was used to scan and locate its target position on the wall.

4.1.1 3D Mapping

Shown in Fig 2(d),(e),(f) is the 3D map of the environment the LNT creates. This was the first task to be performed to both check the area for obstacles and to map the wall.

4.1.2 Search and Location

Location of Figure 3 Shown in Fig 3 is the progress of the LNT as it moves through its search and location task. The LNT begins its navigation in Fig 3(a) where it has located the AprilTag and has begun navigating towards it. We can see the LNT has arrived at the AprilTag in Fig 3(b). In both Fig 3(a)and(b) in the bottom right corner we show the view from the RealSense Camera.

4.1.3 Placement

In Fig 3(c) the LNT raises the soft gripper up the plate. Fig 3(d) shows the arm of the robot extending and placing the soft gripper against the wall and mounting the Limpet magnetically. In the bottom of Fig 3(c) and (d) the distance data taken from the Time of Flight sensor on the Limpet is shown.

The 3D mapping task was accomplished, the LNT created a 3D map of the area in an arc in from of itself showing the walls surrounding it and the location of the metallic plate on the wall. The search and location task was completed, the LNT managed to navigate around the arena while scanning for the AprilTag. Once the AprilTag was located the LNT drove towards it and stopped within 200mm of it. The view from the RealSense camera showed the AprilTag being located and marked as the LNT moved towards it. The placement task demonstrated the LNT extend its arm and plant the Limpet on the wall. The captured data from the Limpet showed the arm and soft actuator move up the wall and then extend forwards and place the Limpet.

5 CONCLUSION

Our system uses a conventional mobile robotic base and a soft gripper to deploy a sensor node in an unstructured environment. Our work demonstrates that integrating soft materials with conventional robotic platforms reduces the computational complexity in dynamic task planning, as the inherent compliance of the material reduces uncertainty in unstructured environment.

The LNT is capable of creating a 3D map of its surrounding area, moving rapidly over smooth surfaces, detecting a target (AprilTag), and placing the Limpet sensor node at the target.

Placement of sensors nodes would typically require an in-depth knowledge of the sensor node and properties of the surface. Our LNT uses its soft robotic gripper to both handle a sensor node, of which it has no previous knowledge of and robustly mount it on a wall.

The communication system for the LNT relies on a Slackbot for its initial command before it runs autonomously using its own IoT network with the Limpets to perform all necessary tasks. The LNT has is capable of carrying all of its necessary components, communications systems, motors, valves, a Limpet and a soft robotic gripper.

The LNT is currently tethered to a mains power supply for all its power requirements, this would be improved for the next version by using a battery pack. We intend to replace the current servo driven hard/soft arm with a fully soft robotic one, to allow the LNT to mount Limpets behind and within objects if a suitable surface is found.

We intend to further the IoT network by using a LoRaWAN based communications system for larger scale Limpet navigation and placement.

We show that this integration of hard robotics with soft robotic manipulation can lead to more complex tasks being achieved by simpler systems.

CONFLICT OF INTEREST STATEMENT

The authors declare that the research was conducted in the absence of any commercial or financial relationships that could be construed as a potential conflict of interest.

AUTHOR CONTRIBUTIONS

Alistair C. McConnell, Mohammed E. Sayed and Jamie O. Roberts contributed equally to this all sections of this work. Simona Aracri contributed to the experimentation and writing of this work. Ross M.McKenzie contributed to the design and fabrication of the system. Adam A. Stokes contributed to the design and writing of this work.

In review

FUNDING

This work was supported by EPSRC ORCA Hub (EP/L016753/1), EPSRC via Robotarium Capital Equipment and CDT Capital Equipment Grants (EP/L016834/1).

ACKNOWLEDGMENTS

The authors thank the Soft Systems Research Group at The University of Edinburgh.

REFERENCES

Albu-Schaffer, A., Eiberger, O., Grebenstein, M., Haddadin, S., Ott, C., Wimbock, T., et al. (2008). Soft robotics. *IEEE Robotics & Automation Magazine* 15, 20–30. doi:10.1109/mra.2008.927979

[Dataset] Alliance, L. (2018). LoRaWAN. https://lora-alliance.org/

Bicchi, A. and Kumar, V. (????). Robotic grasping and contact: a review. In *Proceedings 2000 ICRA. Millennium Conference. IEEE International Conference on Robotics and Automation. Symposia Proceedings* (IEEE). doi:10.1109/robot.2000.844081

Brown, E., Rodenberg, N., Amend, J., Mozeika, A., Steltz, E., Zakin, M. R., et al. (2010). Universal robotic gripper based on the jamming of granular material. *Proceedings of the National Academy of Sciences* 107, 18809–18814. doi:10.1073/pnas.1003250107

Chou, C.-P. and Hannaford, B. (1996). Measurement and modeling of McKibben pneumatic artificial muscles. *IEEE Transactions on Robotics and Automation* 12, 90–102. doi:10.1109/70.481753

[Dataset] Clearpath Robotics (2018). Husky unmanned ground vehicle. https://www.clearpathrobotics.com/husky-unmanned-ground-vehicle-robot/

Costa, M. J., Goncalves, P., Martins, A., and Silva, E. (2012). Vision-based assisted teleoperation for inspection tasks with a small ROV. In *2012 Oceans* (IEEE). doi:10.1109/oceans.2012.6404915

[Dataset] Dorobantu, V., Lippe, C., Ransohoff, L., Simeonoglou, E., DeCastro, J., Kress-Gazit, H., et al. (2018). A synergistic design leveraging the diverse functionalities of soft- and rigid-bodied robots. https://softroboticstoolkit.com/synergistic-design

Elvander, J. and Hawkes, G. (2012). ROVs and AUVs in support of marine renewable technologies. In *2012 Oceans* (IEEE). doi:10.1109/oceans.2012.6405139

Fankhauser, P. and Hutter, M. (2018). ANYmal: A unique quadruped robot conquering harsh environments. *Research Features* , 54–57

Galloway, K. C., Polygerinos, P., Walsh, C. J., and Wood, R. J. (2013). Mechanically programmable bend radius for fiber-reinforced soft actuators. In *2013 16th International Conference on Advanced Robotics (ICAR)* (IEEE). doi:10.1109/icar.2013.6766586

Griggs, J. W. (2011). BP Gulf of Mexico oil spill. *Energy Law Journal* 32, 57 – 81

Hastie, H. F., Lohan, K. S., Chantler, M. J., Robb, D. A., Ramamoorthy, S., Petrick, R., et al. (2018). The ORCA hub: Explainable offshore robotics through intelligent interfaces. *CoRR*

Ilievski, F., Mazzeo, A. D., Shepherd, R. F., Chen, X., and Whitesides, G. M. (2011). Soft robotics for chemists. *Angewandte Chemie International Edition* 50, 1890–1895. doi:10.1002/anie.201006464

[Dataset] Intel (2018). Realsense camera d415. https://realsense.intel.com/

Jones, J. L. (2006). Robots at the tipping point: the road to iRobot Roomba. *IEEE Robot. Automat. Mag.* 13, 76–78

In review

Keplinger, C., Li, T., Baumgartner, R., Suo, Z., and Bauer, S. (2012). Harnessing snap-through instability in soft dielectrics to achieve giant voltage-triggered deformation. *Soft Matter* 8, 285–288. doi:10.1039/c1sm06736b

Labbe, M. and Michaud, F. (2014). Online Global Loop Closure Detection for Large-Scale Multi-Session Graph-Based SLAM. In *Proceedings of the IEEE/RSJ International Conference on Intelligent Robots and Systems*. 2661–2666

Light, R. A. (2017). Mosquitto: server and client implementation of the MQTT protocol. *The Journal of Open Source Software* 2, 265. doi:10.21105/joss.00265

[Dataset] Lo, C. (2018). The economics of efficiency: offshore maintenance in the north sea. https://www.offshore-technology.com/features/featurethe-economics-of-efficiency-offshore-maintenance-in-the-north-sea-4844363/

McKenzie, R. M., Barraclough, T. W., and Stokes, A. A. (2017). Integrating soft robotics with ROS - A hybrid pick and place arm. *CoRR*

Miller, K. (1991). Piper alpha and the cullen report. *Industrial Law Journal* 20, 176–187. doi:10.1093/ilj/20.3.176

Moghaddam, A. F., Lange, M., Mirmotahari, O., and Hovin, M. E. (2012). Novel mobile climbing robot agent for offshore platforms. In *International Journal of Mechanical and Mechatronics Engineering*. vol. 6

Raibert, M., Blankespoor, K., Nelson, G., and Playter, R. (2008). BigDog, the rough-terrain quadruped robot. *IFAC Proceedings Volumes* 41, 10822–10825. doi:10.3182/20080706-5-kr-1001.01833

Sayed, M. E., Nemitz, M. P., Aracri, S., McConnell, A. C., McKenzie, R. M., and Stokes, A. A. (2018). The limpet: A ROS-enabled multi-sensing platform for the ORCA hub. *Sensors* 18

Shukla, A. and Karki, H. (2016). Application of robotics in offshore oil and gas industry - a review part II. *Robot. Auton. Syst.* 75, 508–524

[Dataset] Slack (2018). slack api. https://api.slack.com/bot-users

Stokes, A. A., Shepherd, R. F., Morin, S. A., Ilievski, F., and Whitesides, G. M. (2014). A hybrid combining hard and soft robots. *Soft Robotics* 1, 70–74. doi:10.1089/soro.2013.0002

Temeltas, H. and Kayak, D. (2008). SLAM for robot navigation. *IEEE Aerospace and Electronic Systems Magazine* 23, 16–19. doi:10.1109/maes.2008.4694832

Trivedi, D., Rahn, C. D., Kier, W. M., and Walker, I. D. (2008). Soft robotics: Biological inspiration, state of the art, and future research. *Applied Bionics and Biomechanics* 5, 99–117. doi:10.1080/11762320802557865

[Dataset] TurtleBot (2018). Turtlebot3. https://www.turtlebot.com/

Wang, J. and Olson, E. (2016). AprilTag 2: Efficient and robust fiducial detection. In *Proceedings of the IEEE/RSJ International Conference on Intelligent Robots and Systems (IROS)*

Westman, E. and Kaess, M. (2018). *Underwater AprilTag SLAM and calibration for high precision robot localization*. Tech. Rep. CMU-RI-TR-18-43, Carnegie Mellon University, Pittsburgh, PA

Wood, S. I. (2014). *UK Continental Shelf (UKCS) Maximising Recovery Review Final Report*. Tech. rep., Oil and Gas Authority

FIGURE CAPTIONS

In review

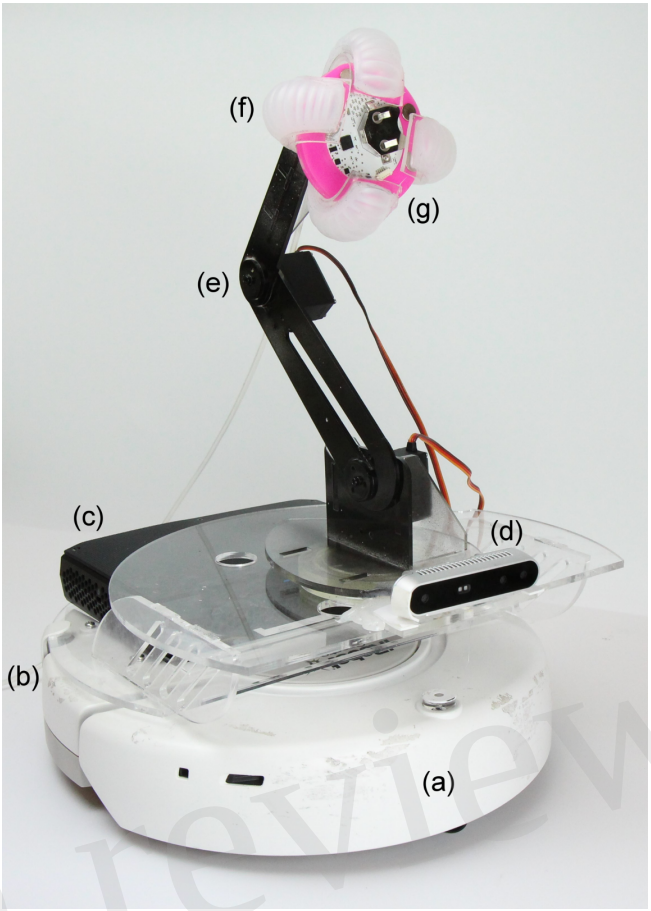

In review

Figure 1. A delineated image of the complete Turtle system. (a) iRobot Create Base. (b) Power and Control Hardware. (c) Intel NUC. (d) RealSense D415 Camera. (e) 2 Degree of Freedom Arm. (f) Soft Robotic Actuator. (g) Encapsulated Limpet.

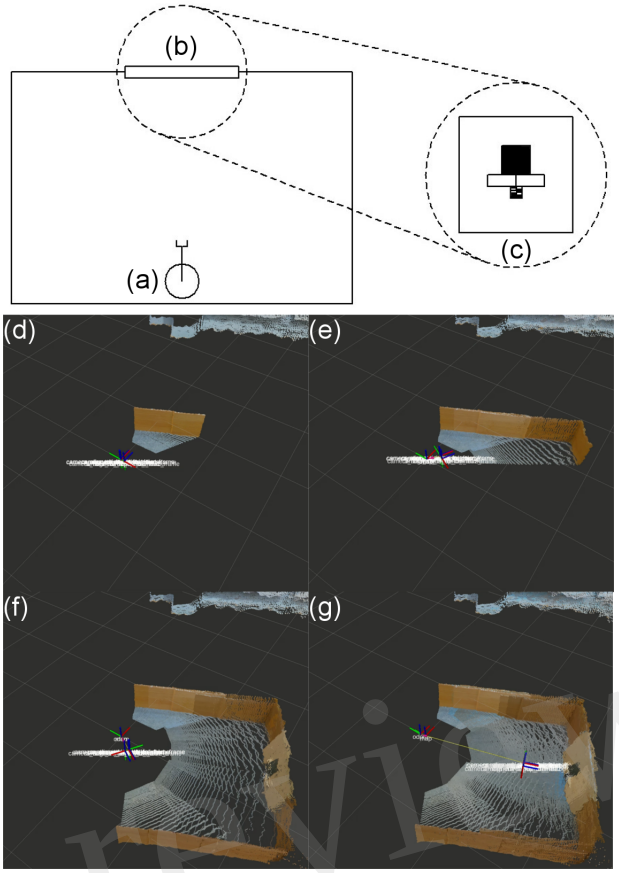

Figure 2. The layout of the test arena is shown in the top third of this figure where (a) shows the intial start point of the LNT, (b) the target area, (c) the breakdown of the target. The lower two thirds of the image show the 3D mapping of the arena (d) the LNT begins to map its surrounding area, (e) the LNT continues to turn, (f) a complete 180 degree arc in-front of the LNT has been mapped, (g) the LNT moves towards its target.

In review

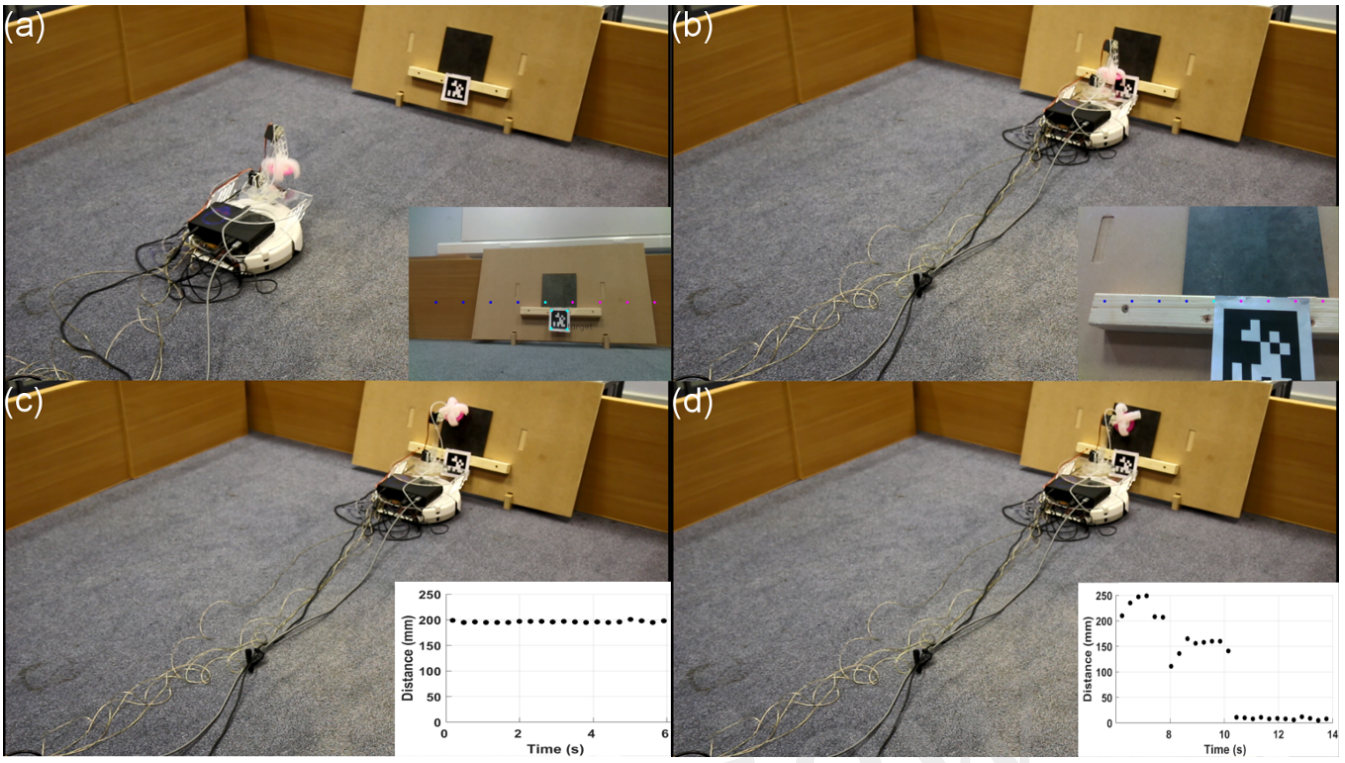

Figure 3. Still frames from the video of the LNT performing a search, location and placement tasks with the Limpet. (a) shows the LNTs progress searching and locating the target which it moves towards until in (b) it has reached the target and stops. Included in (a) and (b) in the bottom right of each frame is the view from the RealSense camera as it tracks the AprilTag. (c) shows the 2 DOF arm raising up to its mounting position and aiming the Limpet at the target area. In (d) the arm has extended and the soft actuator has placed the Limpet against the wall. Included in (c) and (d) is the data received from the Limpet regarding its distance from the target as the placement task proceeded.

In review

Figure 1.JPEG

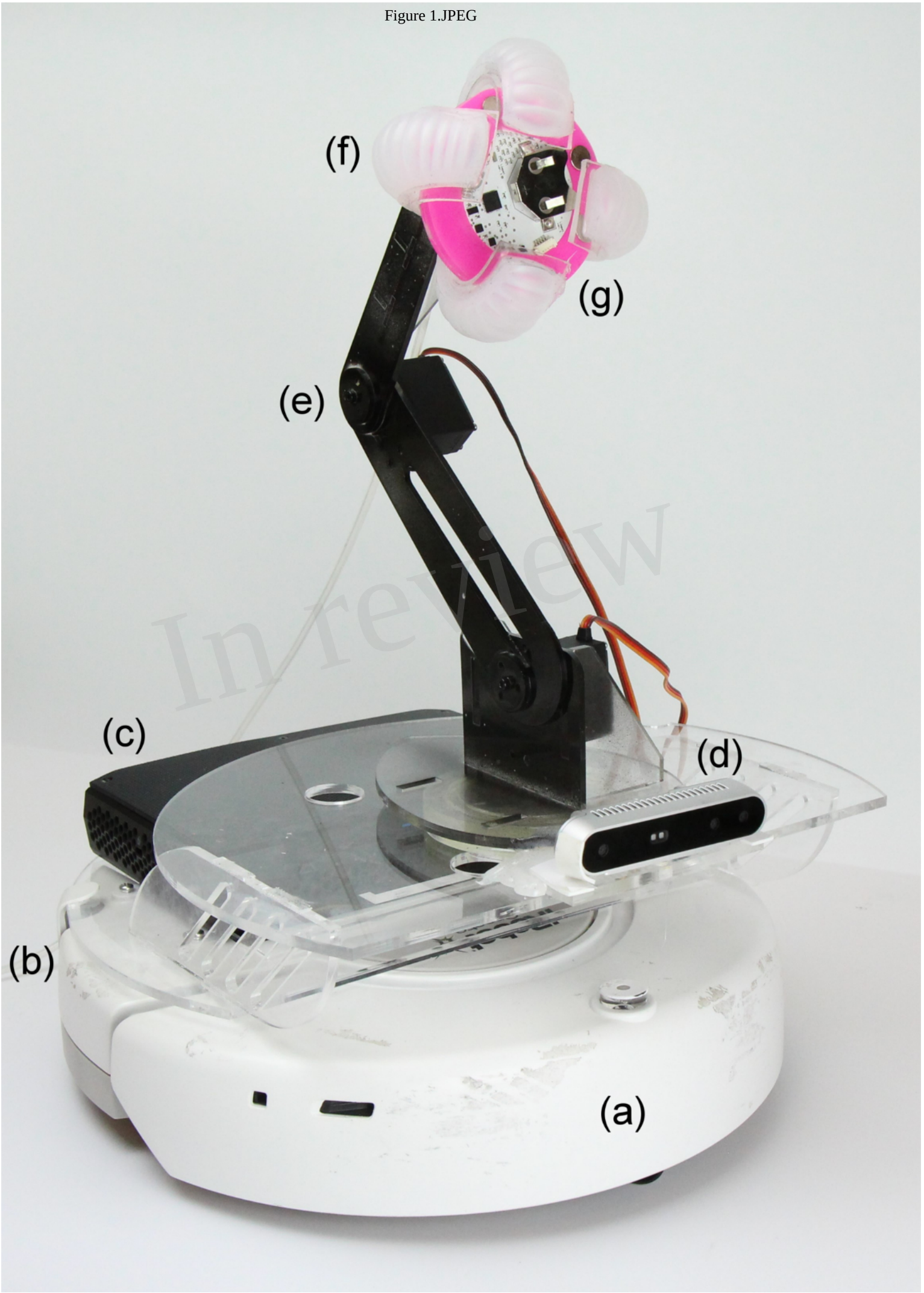

In review

Figure 2.JPEG

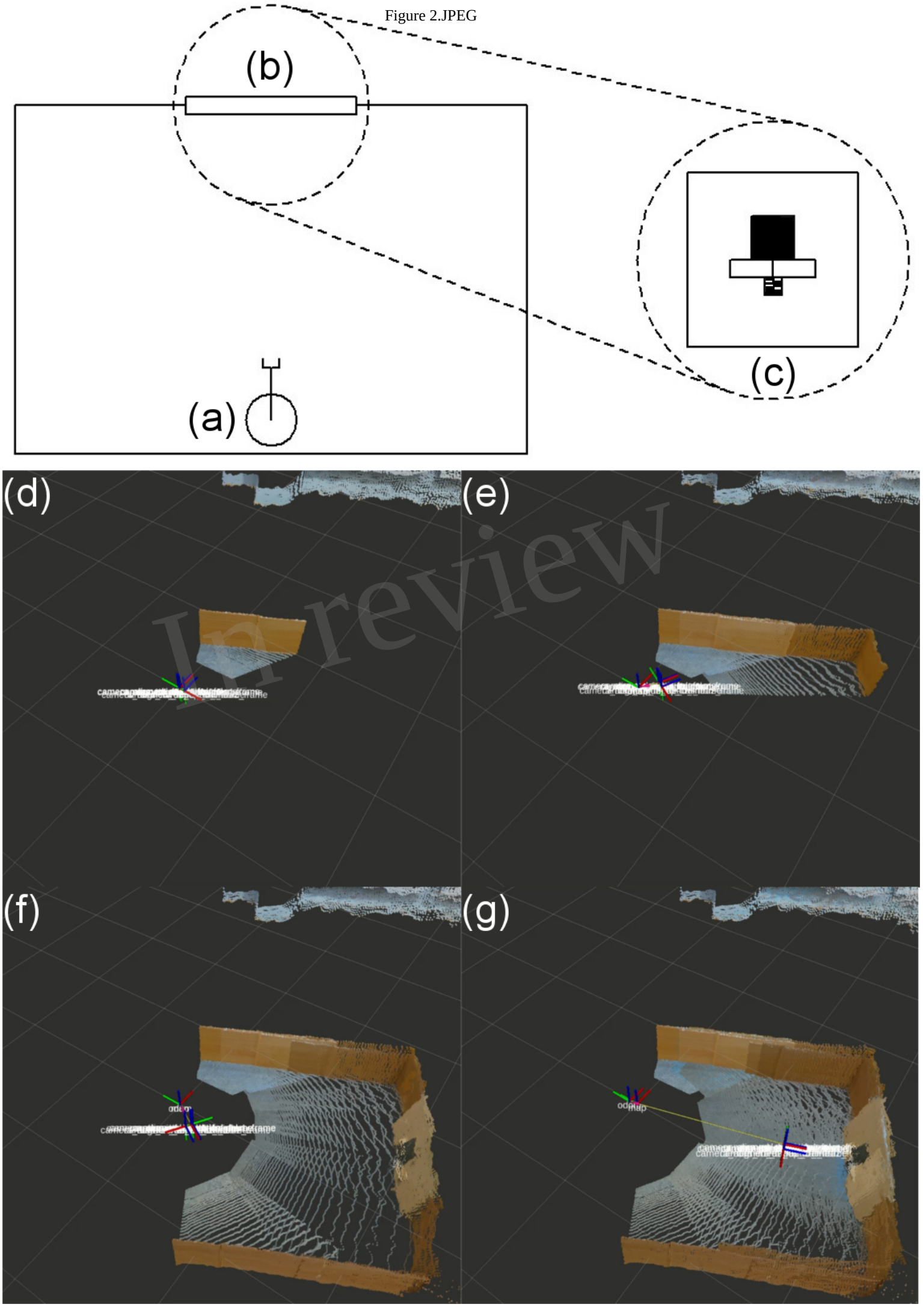

In review

Figure 3.JPEG

In review

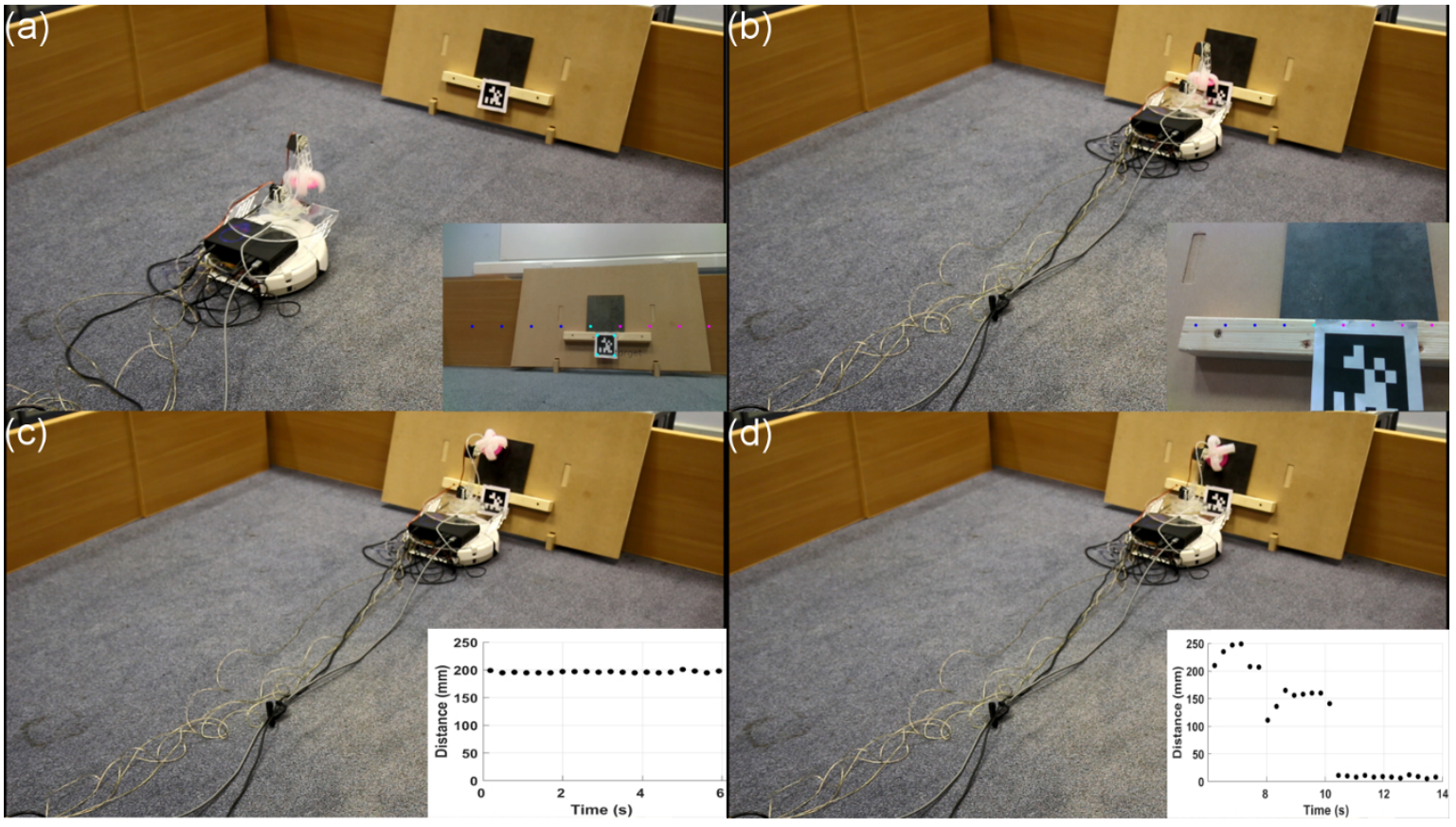

Appendix K

Conference Proceeding: Robust TDA-MAC for Practical Underwater Sensor Network Deployment: Lessons from USMART Sea Trials

Conference: Proceedings of the Thirteenth ACM International Conference on Underwater Networks and Systems (WUWNet '18)

WUWNet '18 Paper 

Robust TDA-MAC for Practical Underwater Sensor Network Deployment: Lessons from USMART Sea Trials

Nils Morozs*, Paul D. Mitchell, Yuriy Zakharov
Department of Electronic Engineering
University of York
York, YO10 5DD, UK
*nils.morozs@york.ac.uk

Rahul Mourya, Yvan R. Petillot, Tyler Gibney, Mauro Dragone
School of EPS
Heriot-Watt University
Edinburgh, EH14 4AS, UK

Benjamin Sherlock, Jeffrey A. Neasham, Charalampos C. Tsimenidis
School of Engineering
Newcastle University
Newcastle-upon-Tyne, NE1 7RU, UK

Mohammed E. Sayed, Alistair C. McConnell, Simona Aracri, Adam A. Stokes
Institute for Integrated Micro and Nano Systems
School of Engineering, University of Edinburgh
Scottish Microelectronics Centre
Edinburgh, EH9 3FF, UK

ABSTRACT

In this paper, we present the results of deploying the first test prototype of the USMART low cost underwater sensor network in sea trials in Fort William, UK, on 29/06/2018 and 03/07/2018. We demonstrate the first ever hardware implementation of the TDA-MAC protocol for data gathering in underwater acoustic sensor networks (UASNs). The results show a successful application of TDA-MAC to remote environmental monitoring, integrating a range of different sensor nodes developed by the Universities of Heriot-Watt, York, Newcastle and Edinburgh. We focus on the practical challenges and their mitigation strategies related to TDA-MAC to increase its robustness in real-world deployments, compared with theoretical and simulation-based studies. The lessons learned from the sea trials reported in this paper prompted several crucial modifications to TDA-MAC which, in turn, form a solid foundation for further work on the development of TDA-MAC based UASNs.

KEYWORDS

Medium Access Control, Sea Trials, TDA-MAC, Underwater Acoustic Network, Wireless Sensing

ACM Reference Format:
Nils Morozs*, Paul D. Mitchell, Yuriy Zakharov, Rahul Mourya, Yvan R. Petillot, Tyler Gibney, Mauro Dragone, Benjamin Sherlock, Jeffrey A. Neasham, Charalampos C. Tsimenidis, and Mohammed E. Sayed, Alistair C. McConnell, Simona Aracri, Adam A. Stokes. 2018. Robust TDA-MAC for Practical Underwater Sensor Network Deployment: Lessons from USMART Sea Trials. In *Proceedings of International Conference on UnderWater Networks and Systems (WUWNet'18).* ACM, New York, NY, USA, 8 pages. https://doi.org/10.1145/nnnnnnn.nnnnnnn

Permission to make digital or hard copies of part or all of this work for personal or classroom use is granted without fee provided that copies are not made or distributed for profit or commercial advantage and that copies bear this notice and the full citation on the first page. Copyrights for third-party components of this work must be honored. For all other uses, contact the owner/author(s).
WUWNet'18, Dec 2018, Shenzhen, China
© 2018 Copyright held by the owner/author(s).
ACM ISBN 978-x-xxxx-xxxx-x/YY/MM.
https://doi.org/10.1145/nnnnnnn.nnnnnnn

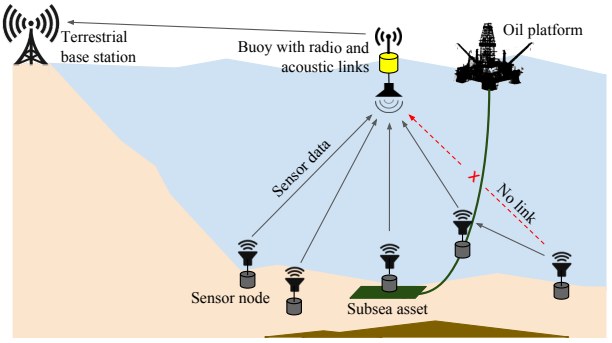

Figure 1: Underwater wireless sensor network deployment with a surface buoy used as the gateway node.

1 INTRODUCTION

The use of wireless sensor networks (WSNs) for remote monitoring of the ocean environment is becoming an increasingly popular research subject, owing to the modern developments in underwater acoustic modem technologies [2, 8]. It is investigated as a solution to a range of underwater sensing tasks, such as water pollution measurements [10], fish tracking [3], seismic monitoring [14] etc. The WSN approach to ocean monitoring provides significant advantages over the traditional deployment of data logging sensor nodes from dedicated ships, because WSNs allow flexible long term deployments and eliminate the need to retrieve the sensor nodes from the sea bed in order to collect the data. For example, Figure 1 shows a typical underwater WSN deployment scenario that is considered in this study. A buoy is used as the surface gateway node to gather the readings from sensor nodes deployed underwater via acoustic communications, and to relay these sensor readings to an on-shore base station via a wireless radio link.

In contrast with terrestrial wireless communication systems, underwater radio propagation is severely limited in range due to high absorption of electromagnetic (EM) waves in seawater, while optical communications suffer from both high absorption and optical

scattering [12]. Acoustic waves are the preferred practical medium of communication in the underwater environment; they exhibit significantly better propagation characteristics compared with EM waves. However, acoustic communications are fundamentally limited by the low sound propagation speed, approximately 1500 m/s in water, and by low bandwidth with carrier frequencies typically limited to tens of kHz, or lower for long range transmissions [8, 12].

The long propagation delays of acoustic signals present a significant challenge in Medium Access Control (MAC), i.e. coordinating transmissions of multiple acoustic communication nodes potentially spaced kilometres apart. Much of the well-established research on MAC in underwater acoustic networks (UANs) focuses on schedule-based TDMA protocols. There, the nodes are scheduled to transmit their packets in particular time slots such that they arrive at the intended receivers without collisions, e.g. [6, 11, 13]. Schedule-based MAC schemes do not involve contention for communication resources, thus removing the need for control signalling, e.g. Request-to-Send (RTS), Clear-to-Send (CTS), acknowledgements etc., in order to establish collision-free links. Therefore, they are capable of achieving high throughput by efficiently scheduling transmissions in a way that results in a stream of data packets separated by guard intervals at the intended receivers. However, the drawback of the scheduling protocols is their need for clock synchronization across different nodes, which is a challenging task in UANs due to long propagation delays, noisy time-varying multipath channels, and the signaling overhead that is not negligible compared with terrestrial radio systems [4, 8].

In [15] we designed TDA-MAC, a MAC protocol for scheduled data gathering in UANs which does not require clock synchonization across the sensor nodes. It focuses on UANs that consist of many low cost, low specification sensor nodes, that are currently being investigated in the EPSRC "Smart dust for large scale underwater wireless sensing (USMART)" project [1]. In particular, TDA-MAC has the following key features:

- scalability to large networks (up to hundreds of nodes),
- no requirement for clock synchronization,
- little control signalling overhead,
- low energy consumption,
- low computation requirements.

Between 27/06/2018 and 03/07/2018 we have undertaken a series of initial trials of the USMART sensor network test prototype, which implemented the TDA-MAC protocol for underwater acoustic data gathering, in Loch Linnhe, Fort William, UK. This was facilitated by the EPSRC ORCA Hub [7], and was a collaboration among the Universities of Heriot-Watt, York, Newcastle and Edinburgh. As a result of these trials we have learned crucial lessons and made several improvements to the TDA-MAC protocol to increase its robustness for future practical deployments. Therefore, the purpose of this paper is two-fold:

(1) To present the results of deploying the initial prototype of the USMART sensor network in sea trials;
(2) To discuss the key issues with TDA-MAC that we encountered in practice, compared with theory and simulations, and to list the improvements that we made in order to make TDA-MAC more robust in real-world deployments.

The rest of the paper is organized as follows: Section 2 introduces the TDA-MAC protocol and its application to data gathering in UANs; Section 3 gives the implementation details of the USMART sensor network prototype and the sea experiment setup; Section 4 presents the pressure and temperature sensing results from the sea trials; Section 5 discusses the practical considerations and improvements that we made to TDA-MAC based on the sea trials; finally, Section 6 concludes the paper and discusses further work.

2 DATA GATHERING USING TDA-MAC

In [15], we proposed the TDA-MAC protocol for centralized scheduling of data transmissions from sensor nodes connected to the same gateway node, such as in the scenario depicted in Figure 1. Its main advantage over other MAC protocols found in the literature is that it can achieve network throughputs close to the maximum channel capacity for a large number of nodes, without clock synchronization or any other advanced functionality at the sensor nodes. It achieves it by reducing the amount of control signalling at the data gathering stage to a single packet per full set of sensor readings regardless of the network size. Therefore, it shows great potential as a practical solution for efficient data gathering in UANs. Figure 2 gives a simple example that shows the packet flow in TDA-MAC. The gateway node transmits a broadcast data request (REQ) packet that is received by every sensor node at a different time (due to long, variable propagation delays). Each sensor node then waits for a specific (individually assigned) amount of time before transmitting their data packet back to the gateway node.

The gateway node assigns a transmit delay to every individual sensor node using the following iterative equation:

$$\tau_{\mathrm{tx}}[n] = \tau_{\mathrm{tx}}[n\text{-}1] + T_{\mathrm{dp}}[n\text{-}1] + T_{\mathrm{g}}[n\text{-}1] - 2(\tau_{\mathrm{p}}[n] - \tau_{\mathrm{p}}[n\text{-}1]), \tag{1}$$

where $\tau_{\mathrm{p}}[n]$ is the estimated propagation delay from the gateway node to the nth sensor node, $\tau_{\mathrm{tx}}[n]$ is the transmit delay assigned to the nth sensor node, $\tau_{\mathrm{tx}}[1] = 0$, i.e. the first node starts transmitting its data packet as soon as it receives the REQ packet from the gateway node, $T_{\mathrm{dp}}[n]$ is the duration of the nth node's data packet and $T_{\mathrm{g}}[n]$ is the guard interval after the nth node's data packet reception at the gateway node. The nodes in the $\boldsymbol{\tau}_{\mathrm{tx}} = (\tau_{\mathrm{tx}}[1], \tau_{\mathrm{tx}}[2], \ldots, \tau_{\mathrm{tx}}[N])$ and $\boldsymbol{\tau}_{\mathrm{p}} = (\tau_{\mathrm{p}}[1], \tau_{\mathrm{p}}[2], \ldots, \tau_{\mathrm{p}}[N])$ vectors are sorted from the shortest to the longest propagation delay from

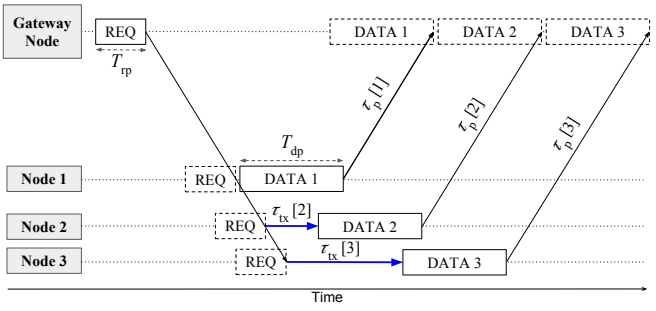

Figure 2: TDA-MAC packet flow example, where a single gateway node gathers data from 3 sensor nodes [16].

Algorithm 1 TDA-MAC algorithm implementation on a sensor node; TDI - transmit delay instruction, REQ - data request packet

```
if PING packet received from gateway node then
    Transmit PING packet back to gateway node
end if
if TDI packet received from gateway node then
    Store transmit delay allocated to this node
end if
if REQ packet received from gateway node then
    Schedule packet transmission with allocated delay
end if
```

the gateway node. In some cases, transmit delays calculated using (1) may be negative. Then they are set to zero before continuing to iterate over the rest of the nodes in $\boldsymbol{\tau}_{\text{tx}}$.

The only prerequisite for implementing TDA-MAC is the knowledge of propagation delays between the gateway and sensor nodes, which is measured using a sequence of ping signals during the initial network deployment. Afterwards, during the normal operation of the network, the gateway node can continuously monitor the accuracy of the estimated propagation delays by measuring the error in the timing of the received data packets. For full details of the initialization process and operation of TDA-MAC, see [15].

The guard interval $T_g[n]$ is an important design parameter that is used to avoid packet collisions due to inaccuracies in propagation delay estimates, slow variations in node positions and the multipath spread. For example, a 100 ms guard interval can tolerate approximately up to 150 m changes in relative node positions before the transmit delays have to be adjusted by sending out updated transmit delay instructions (TDI) to the nodes in question.

One of the advantages of TDA-MAC compared with other schedule-based MAC protocols is the simplicity of implementation at the sensor nodes, which lends itself well to large scale, low cost sensor network deployments. Algorithm 1 shows the functionality required at the sensor nodes to enable TDA-MAC data gathering. It consists of three basic operations, responding to one of the three types of packet received from the gateway node.

3 USMART SENSOR NETWORK PROTOTYPE

In this section we give details of the initial USMART sensor network prototype built for the ORCA Hub sea trials that took place in Fort William, UK between 27/06/2018 and 03/07/2018. The network consisted of multiple different sensor nodes and a gateway node gathering their data using TDA-MAC. Table 1 summarizes the key components used in the experiments discussed in this paper, while the rest of this section describes them in more detail.

3.1 Acoustic Nanomodems

Figure 3 shows the miniature, low-cost, low-power "Nanomodems" developed at Newcastle University which measure 42 mm diameter by 60 mm long. Operating in the acoustic frequency band 24-28 kHz, the modems utilise a simple but highly robust spread spectrum modulation scheme based on binary orthogonal keying using chirp waveforms (chirp-BOK). This achieves data transmission at 40 bps over ranges up to 2 km transmitting a source level of 168 dB re 1μPa @ 1m (0.5 W), while the receiver power consumption is < 10 mW. The range between devices can be measured using ping packets to a resolution of 10 cm. Interfacing to a PC or other processor platform is via RS232 at 9600 baud. Implementation of a robust spread spectrum receiver with minimal energy and processor cost has been enabled by several innovations in sparse signal processing to reduce the computational load whilst maintaining high processing gain and immunity to the severe multipath distortions commonly found in the underwater channel. These devices were developed to provide a communication and positioning building block for large scale, cost effective WSNs to be constructed subsea.

Table 1: Summary of the hardware used in the experiments

Module	Description
Acoustic Nanomodems	Miniature, low-cost, low-power acoustic modems developed at Newcastle University, 24-28 kHz frequency range, 168 dB re 1μPa @ 1m source level (Figure 3)
Evologics SONOBOT	Autonomous surface vehicle carrying gateway/sensor nodes (Figure 6)
DS18B20 sensor	Temperature (T) sensor, integrated into sensor node v1 via OneWire interface
MS5837-30BA sensor	Temperature + pressure (T+P) sensor, integrated into sensor node v2 via I^2C
Sensor node v1a (SNv1a)	Raspberry Pi 3B+, Nanomodem, DS18B20 T sensor, 5V Li-Ion battery (Figure 4a)
Sensor node v1b (SNv1b)	MicroPython pyBoard v1.1 development board with STM32F405RG microcontroller, Nanomodem, DS18B20 T sensor, 4xAA battery pack (same design as Figure 4a)
Sensor node v2 (SNv2)	Raspberry Pi Zero, Nanomodem, MS5837-30BA T+P sensor, 5V Li-Ion battery, watertight case from BlueRobotics (Figure 4b)
Limpet sensor node (LSN)	Sensor node (PCB) with 9 exteroceptive sensors (temperature, pressure, humidity, optical, distance, sound, magnetic field, accelerometer and gyroscope), Nanomodem, 3.6V Li-Ion Battery, MAX3232 (RS-232 To TTL adapter), watertight case from BlueRobotics (Figure 4c)
Gateway node	Repurposed SNv1a (with Raspberry Pi), running gateway node software via SSH

3.2 Sensor Nodes

Throughout the preparations for the sea trials we developed 4 different types of sensor nodes:

- **Sensor node v1a (SNv1a)**, shown in Figure 4a, comprises a Raspberry Pi 3B+, a 5V (10000 mAh) Li-Ion power supply, a GPS module for positioning, a DS18B20 temperature sensor, all these contained in a waterproof (IP67) enclosure. A Nanomodem is connected to the Raspberry Pi via RS232

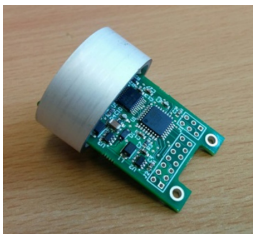

(a) PCB + transducer



(b) Encapsulated

Figure 3: Acoustic "Nanomodems" developed by Newcastle University

and hangs several meters below water surface using the 5 m cable seen in Figure 4a.

- **Sensor node v1b (SNv1b)** follows the same design as SNv1a, except it uses the STM32F405RG microcontroller on the MicroPython pyBoard v1.1 as the computing unit, and is powered by a 4×AA battery pack.
- **Sensor node v2 (SNv2)**, shown in Figure 4b, is a more recent, robust design compared with SNv1a/b. It consists of a Raspberry Pi Zero, a 5V (10000 mAh) Li-Ion power supply, a DS18B20 temperature sensor, MS5837-30BA pressure + temperature sensor, all contained in a watertight (up to 1000 m depth) enclosure by BlueRobotics.
- **Limpet sensor node (LSN)**, shown in Figure 4c, uses the same enclosure as SNv2, but incorporates a novel Limpet sensor platform developed by the University of Edinburgh, described in detail in Subsection 3.3.

3.3 Limpet Node

The Limpet is a multi-sensing platform, which is designed to be low-cost and highly manufacturable, and thus can be deployed in large collectives for monitoring offshore energy platforms [17]. It is designed to be one part of a heterogeneous collection of field robots (drones, UAVs, mobile legged robots etc.) that together comprise The Offshore Robotics for Certification of Assets (ORCA Hub) system for asset certification and management [7]. The Limpet is equipped with nine exteroceptive sensors: temperature, pressure, humidity, optical, distance, sound, magnetic field, accelerometer and gyroscope. The total cost of the electronic components used in the design of the Limpet is approx. £22. The Limpet consists of a single two-layer Printed Circuit Board (PCB) and a detachable Li-Ion coin cell battery. It is a fully integrated PCB incorporating a low-power microcontroller (ATSAMD21G18A), RGB LED (LTSTN683EGBW), battery holder (BK-877) for a rechargeable Li-ion battery (LIR2477), charging IC (MCP73812T), charger connector, programming port [JTAG] (Molex 532610571), and a communication connector as shown in Figure 4c. The sensors on the Limpet, except for the microphone, are controlled by the microcontroller through the I^2C bus. The Limpet is powered with a rechargeable 3.6V 160 mAh Lithium-Ion coin cell battery and has a battery life @160 mAh of 0.87 to 1600 hours.

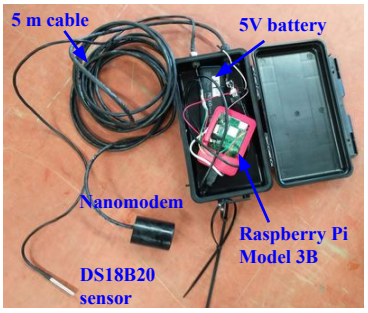

(a) Sensor node, version 1a (SNv1a)

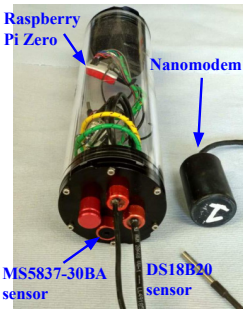

(b) Sensor node, version 2 (SNv2)

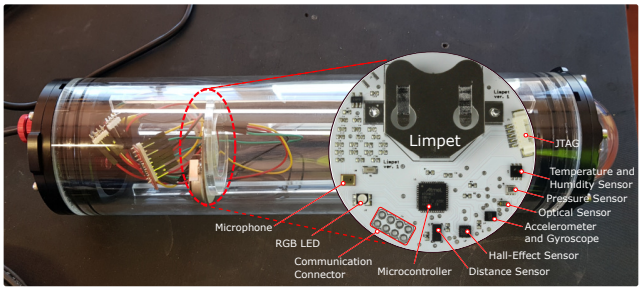

(c) Limpet sensor node (LSN)

Figure 4: Sensor nodes used in the sea trials

3.4 Gateway Node

Figure 5 shows a screenshot of the GUI written in Python 2.7 to be used at the gateway node. It controls the acoustic Nanomodem via the serial port interface using a USB-RS232 adapter. The "Start sensing" button initiates the TDA-MAC protocol which starts by pinging every sensor node sequentially and noting the measured propagation delays. It then proceeds to send the TDI packet to

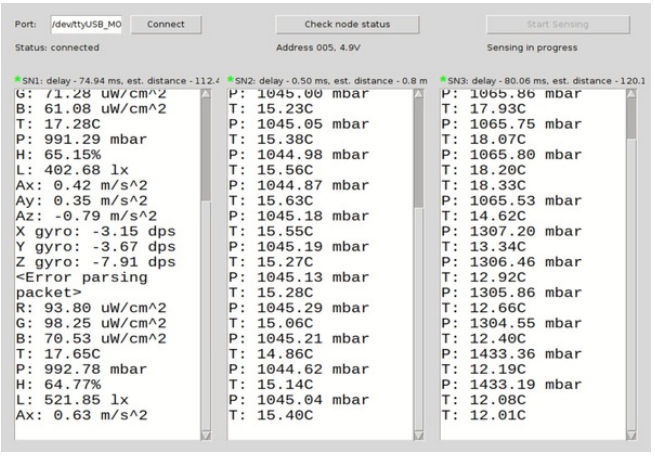

Figure 5: TDA-MAC Python GUI on the gateway node, recorded during an experiment with one Limpet sensor node (LSN) and 2 pressure & temperature nodes (SNv2)

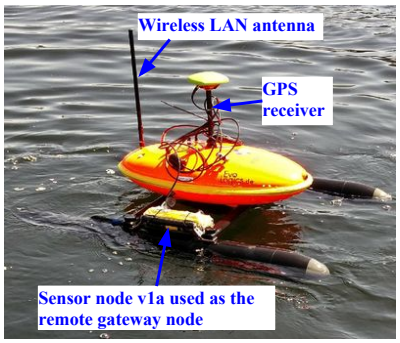

Figure 6: Evologics SONOBOT - autonomous surface vehicle with the gateway node (repurposed SNv1a) attached to it

every sensor node which contains the delay value that the given node has to wait before transmitting data as shown in Figure 2. When it receives a data packet from any sensor node, it displays its contents in the corresponding text panel. For example, in Figure 5 it is gathering data from 3 sensor nodes - one LSN and two SNv2. The first sensor node is cycling through the different sensor types available on the Limpet, while the other two nodes only have a temperature and pressure sensor available.

This gateway node software was executed both directly on a PC/laptop for initial tests, and remotely on a repurposed Raspberry Pi based sensor node (SNv1a) mounted on the Evologics SONOBOT surface vehicle as shown in Figure 6. Since the SONOBOT vehicle was equipped with a Wi-Fi access point, it allowed us to connect to the Raspberry Pi computer using a Wi-FI repeater on the pier and run the gateway node software via SSH.

4 UASN EXPERIMENT RESULTS

In this section we discuss the examples of successful deployment of the initial USMART sensor network prototype described in Section 3. Table 2 summarises the setup of the two experiments reported in this section.

Table 2: Description of the reported experiments

Date	Experiment
29/06/18	**#1** Gateway node on SONOBOT ≈100 m away from the pier, SNv2 × 2 deployed from pier approx. 120 and 130 m away from the SONOBOT
29/06/18	**#2** Gateway node on SONOBOT ≈100 m away from pier, SNv2 on SONOBOT, SNv2 and LSN deployed from pier approx. 110 and 120 m away from the SONOBOT

4.1 Temperature and Pressure Sensing Results

Figure 7a shows a plot of the temperature and pressure data recorded live on 29/06/2018 in Experiment #1 from Table 2. The gateway node was deployed on the SONOBOT vehicle with an SSH connection to the laptop on shore. It was gathering data from two sensor nodes (SNv2) by alternating between pressure and temperature readings

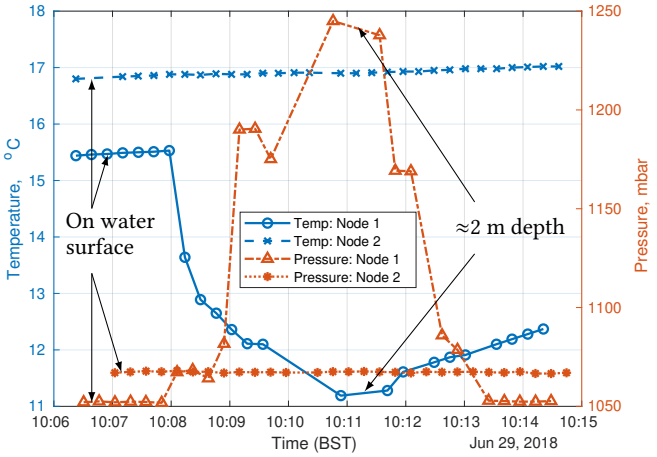

(a) Experiment #1, 29 June 2018, Fort William, UK

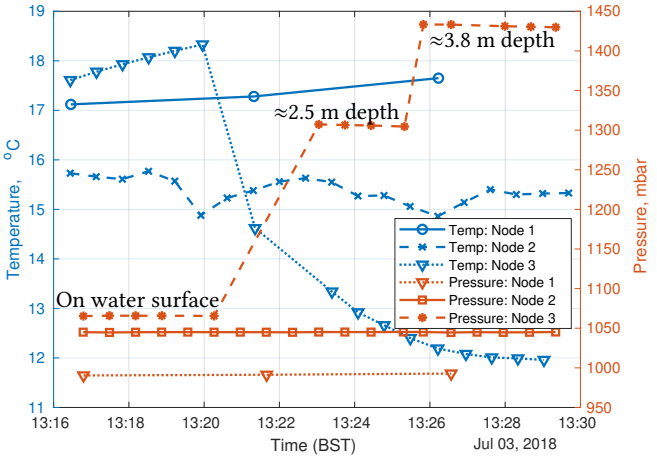

(b) Experiment #2, 3 July 2018, Fort William, UK

Figure 7: Live temperature and pressure sensor readings with one of the nodes having adjustable depth, obtained via TDA-MAC in sea experiments described in Table 2

using a modified broadcast REQ packet structure, which included a sensor type field. This was due to the limited payload length of the current Nanomodem packet structure (7 bytes). In future versions of the USMART sensor nodes, many types of sensor readings will be integrated into a single data packet if needed.

Both Nanomodems were submerged several metres underwater, while Node 2 sensor payload was attached to the pier above water and Node 1 was attached to a pulley for adjustable depth. This enabled us to test the sensors in a live TDA-MAC trial by submerging Node 1 approx. 2 m underwater to observe the changes in pressure and temperature above and below the surface. Despite some packet loss, in particular when Node 1 was submerged deeper and the acoustic Nanomodem was close to sea bottom, most of the sensor data was successfully delivered to the gateway node via TDA-MAC to monitor the changes in pressure and temperature in real-time.

Figure 7b shows the results from Experiment #2 from Table 2, a similar experiment but with three sensor nodes. In this case the majority of the packets were also successfully delivered to the gateway node. The plot includes only 3 pressure and temperature sensor readings from Node 1, because this was the Limpet sensor node (LSN) which cycled through all of the different sensors it integrated in addition to temperature and pressure as described in Subsection 3.3. The live GUI output from this experiment is shown in Figure 5, where the gateway node was receiving many different types of sensor readings from Node 1, while the other two nodes were alternating between pressure and temperature.

4.2 Throughput and Packet Loss Performance

Table 3 summarizes the network performance at the MAC level in the two sea experiments discussed in the previous subsection. 20% of the sensor data packets were lost in Experiment #1, and 10% in Experiment #2. Packet loss occurred due to several factors such as:

- obstructed signal paths and disturbance of the water column due to boat and ship traffic;
- challenging multipath propagation with signal reflections from the harbour infrastructure and the sea bed;
- collisions between data packets at the gateway node, and between data and REQ packets at sensor nodes due to errors in packet scheduling.

However, 10/20% packet loss does not account for the overall loss in network throughput shown in Table 3. The raw bitrate of the Nanomodems is 40 bps as described in Subsection 3.1. Part of this channel capacity is occupied by the header and footer data, e.g. the synchronisation waveform, node address, CRC, etc. This leaves the channel capacity in terms of the data payload at approximately 27 bps, if the maximum packet length of 7 bytes is used.

The sensor network achieved the total throughput of 37% and 24% of the maximum 27 bps channel capacity, which is far lower than the near-optimal channel utilization of TDA-MAC achieved in simulation experiments in [15, 16]. The factors that contributed to the throughput loss in the reported sea experiments, in addition to the packet loss, are the following (most to least significant):

- The guard intervals between the scheduled packet slots were increased to 1 s in Experiment #1 and 3 s in Experiment #2 to accommodate for sporadic errors in packet timing;
- The small number of nodes, compared with simulations, resulted in the increase in proportion of channel airtime used for control signalling, i.e. REQ packet for every 2/3 data transmissions, e.g. instead of 100 in simulations;
- The data payload was 6 bytes which reduced the maximum channel capacity by ≈5%, compared with the 7-byte payload;

The maximum achievable throughput of the TDA-MAC protocol was derived in [15]. For fixed length data packets and guard intervals, it is given by the following expression:

$$\gamma_{\max} = \frac{NT_{\mathrm{dp}}}{T_{\mathrm{rp}} + 2\min_{n}\{\tau_{\mathrm{p}}[n]\} + N(T_{\mathrm{dp}} + T_{\mathrm{g}})}, \tag{2}$$

where $\gamma_{\max}$ is the network throughput normalized by the channel capacity, T_{dp} is the data packet duration, T_{rp} is the REQ packet duration, $\tau_{\mathrm{p}}[n]$ is the propagation delay to the nth node, T_{g} is the guard interval, and N is the number of sensor nodes. It shows that the increase in the guard interval T_{g} and the decrease in the number of nodes N have a direct negative impact on the maximum achievable network throughput of TDA-MAC.

Although the high throughput capability of TDA-MAC was not fully exploited in the sea trials due to large guard intervals, these experiments provided valuable data that helped us identify practical considerations of the TDA-MAC protocol that needed to be addressed. In Section 5 we look more closely at the practical issues with TDA-MAC encountered in the sea trials and what actions we took to make the protocol more robust in real-world deployments.

Table 3: Throughput and packet loss in TDA-MAC sea trials

Exp.	Packet loss	Throughput	
#1	20%	10 bps	13 packets/min
#2	10%	6.6 bps	7.9 packets/min

5 PRACTICAL CONSIDERATIONS AND IMPROVEMENTS TO TDA-MAC

In addition to the two sea experiments reported in this paper, our TDA-MAC protocol implementation was tested in a large number of initial and intermediate experiments in the lab environment over-air, in an anechoic water tank at Newcastle University, and in a large water tank and Loch Linnhe at the Underwater Centre in Fort William, UK. During these experiments we have discovered several issues which provide additional challenges for TDA-MAC in practical deployments, compared with theory and simulations. Table 4 lists all of the practical considerations that came to light during these trials, strategies to overcome them and modifications we made to the original version of TDA-MAC proposed by us in [15] and described in Section 2.

First, the network discovery and setup stage requires additional robustness features due to occasional loss of ping packets used for ranging and TDI control packets used to instruct the nodes about their individual transmit delays, the single parameter per sensor node which achieves TDA-MAC scheduling. The first simple modification that we made to TDA-MAC was to introduce several attempts at a successful ping exchange with every sensor node to establish a connection and measure the link propagation delay (actions 1, 2 in Table 4). For example, if the gateway node did not receive a ping response from a sensor node, it waits for a timeout period, e.g. 3 seconds, and retransmits the ping packet. If it fails to receive a ping response after 5 successive attempts, it is highly unlikely that it has a usable link with this node; therefore the latter has to be connected via multi-hop links, if multi-hop networking functionality designed in [16] is available.

The original TDA-MAC design involves the gateway node transmitting TDI packets in the "packet train" manner to every sensor node in order to streamline the network setup stage and make the protocol insensitive to long propagation delays by avoiding bi-directional communication at this stage. However, in practice the loss of a TDI packet at the sensor node results in significant disruption in the subsequent data gathering stage. For example, in one of the initial experiments, one of the sensor nodes had failed

Table 4: Solutions and mitigation strategies for practical issues with TDA-MAC

Practical Issue	Impact	Solution / Mitigation Strategy
Loss of ping packets	Unverified presence of a link; unknown propagation delay	1) 5 attempts at ping exhange per sensor node 2) Nodes that did not respond are either excluded from TDA-MAC data gathering, or connected via other nodes using multi-hop TDA-MAC*
Loss of TDI packets	Wrong transmit times at sensor nodes; packet collisions	3) ACK packet must be sent by sensor node to confirm TDI 4) 5 attempts at sending TDI and receiving the ACK from sensor node 5) Sensor node “activates" the link, i.e. responds to subsequent data requests (REQ), only if it receives a TDI 6) Nodes that did not send ACK are either excluded from TDA-MAC data gathering, or connected via other nodes using multi-hop TDA-MAC*
Loss of REQ packets	Loss of sensor readings	7) Verify packet timing at all nodes to check if REQ-data collisions occur 8) Re-estimate propagation delays between gateway and sensor nodes 9) Re-estimate processing delays, e.g. signal processing & sensing, by timing data packet arrivals 10) Send out updated TDI to one or more sensor nodes, if there was a change 11) Increase guard interval if the above measures failed
Loss of data packets	Loss of sensor readings	12) Perform actions 7-11 to avoid REQ-data and data-data collisions 13) Modify REQ packet structure to target specific nodes, not only broadcast 14) Consistently unresponsive nodes can be reconnected via multi-hop links*
Packet decoding and sensor reading delays	Late transmissions resulting in data packet collisions	15) Enforce a minimum transmit delay for any sensor node in (1), e.g. 1 sec 16) Take precise time of the REQ packet arrival, incorporating/estimating a packet processing delay 17) Measure the sensor reading delay and subtract it from overall Tx delay

* In these trials, the sensor nodes without a link to the gateway node are excluded from the TDA-MAC process. However, the solution to this connectivity issue via multi-hop TDA-MAC is demonstrated in simulation in [16].

to receive the TDI packet from the gateway node; as a result, when it received the subsequent REQ packets asking it to send its data, it did not know what its individually assigned transmit delay was, and instead transmitted its data with the default delay of zero, thus causing persistent packet collisions with other sensor nodes. This has prompted further modifications to TDA-MAC (3-6 in Table 4), which crucially incorporate TDI acknowledgement packets from the sensor nodes, and a link activation process whereby only the sensor nodes that received a valid TDI packet are allowed to transmit to the gateway node. These updates are depicted in Figure 8.

Despite establishing a more robust TDA-MAC network discovery and setup stage, as described above, there are still many factors in

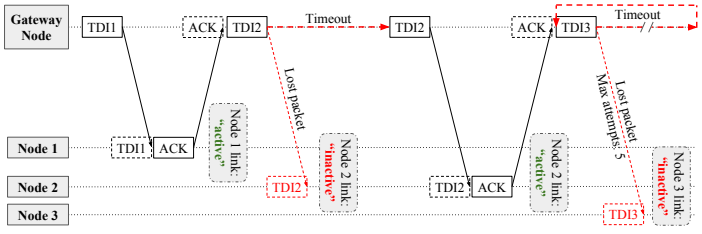

Figure 8: A modified TDA-MAC network setup stage, robust to control packet loss, incorporates TDI ACK packets and link activation triggered by TDI packet reception

a practical deployment that result in the errors in packet timing which, if greater than the guard interval between consecutive packet slots, cause collisions. In our TDA-MAC sea trials the following implementation issues gave rise to packet collisions:

- Sensor reading delays: it can take up to 750 ms to get a reading from the DS18B20 sensor [9], whereas the MS5837-30BA sensor returns the readings near-instantly [5].
- Signal processing delays: in many cases, in particular on lower cost nodes, there will be a delay between the end of an acoustic reception and the moment when the packet is decoded and passed to the higher layer.
- Software crashes, e.g. serial/UART port issues, resulted in inaccurate detection of the REQ packet arrival times, which in turn caused scheduling errors of the data packets.
- Different sensor node hardware incurred different software execution time and delay function precision, e.g. the less powerful microcontroller based sensor node (SNv1b) consistently transmitted its readings approx. 1 second late, because its software execution time and the delay function precision of 1 second (as opposed to 1 microsecond on Raspberry Pi) were initially unaccounted for.
- Packet collisions are also possible due to significant changes in node positions and an insufficient guard interval to compensate for them. In these cases, re-estimating the propagation delays and sending updated TDI packets is required.

Algorithm 2 Updated TDA-MAC implementation on a sensor node; blue italic text highlights new features

```
1:  if PING packet received from gateway node then
2:      Transmit PING packet back to gateway node
3:  end if
4:  if TDI packet received from gateway node then
5:      Store transmit delay, mark link as "active"
6:      Send ACK to gateway node
7:  end if
8:  if REQ packet received from gateway node then
9:      if link is marked "active" and REQ is addressed to this node
        then
10:         Note precise time of REQ arrival
11:         Take sensor readings, and note the sensor reading delay
12:         Schedule packet transmission with allocated delay
13:     end if
14: end if
```

Accurate local timing of the received REQ packets and data transmissions at sensor nodes is crucial in avoiding scheduling errors due to practical factors such as those listed above. Some of these issues were alleviated by further modifications to the TDA-MAC protocol. For example, enforcing a minimum transmit delay, e.g. 1 s instead of zero, allows the sensor reading, signal processing and software execution delays to occur without a negative effect on scheduling. There is also scope for modifying the REQ packet structure to include useful content, e.g. addressing particular nodes rather than always broadcasting, and including corrections to TDIs for some of the nodes. Other issues we discussed above were specific to our implementation, and can be solved by a more precise, lower level implementation of the protocol, compared with the prototype presented in this paper, e.g. using GPIO interface and interrupt routines to accurately detect packet start and end times.

Algorithm 2 summarizes all the key changes to the TDA-MAC implementation at the sensor nodes discussed in this section. It highlights the new features designed to increase the robustness of TDA-MAC in practical deployments in blue italic text, and can be directly compared with the original TDA-MAC protocol implementation in Algorithm 1.

6 CONCLUSIONS AND FURTHER WORK

The sea trials discussed in this paper demonstrated the first ever implementation of the TDA-MAC protocol in practice, and the first test prototype of the low cost sensor network that is being developed in the EPSRC USMART project. We showed a successful application of TDA-MAC based underwater acoustic networking to remote environmental monitoring, integrating a range of different sensor nodes developed by the Universities of Heriot-Watt, York, Newcastle and Edinburgh.

Furthermore, the experiments we performed during these sea trials have revealed a number of practical challenges that were not addressed during the development of the TDA-MAC protocol in theory and simulations. These practical issues prompted several crucial modifications to the TDA-MAC protocol to make it robust in real-world deployments. We presented the details of the updated network setup stage, and a list of modifications and troubleshooting actions required for a successful TDA-MAC data gathering stage of the network operation.

The initial USMART network prototype and the lessons learned from the sea trials reported in this paper form a solid foundation for further work on the development of TDA-MAC based UASNs, including larger networks, i.e. more sensor nodes, and the development of multi-hop functionality, such as that proposed in [16].

ACKNOWLEDGMENTS

This work was supported by the UK Engineering and Physical Sciences Research Council (EPSRC) through the USMART project (EP/P017975/1). Furthermore, Y.R. Petillot, M. Dragone, A.C. McConnell, S. Aracri and A.A. Stokes acknowledge support from the EPSRC ORCA Hub (EP/R026173/1).

REFERENCES

[1] 2018. EPSRC USMART (EP/P017975/1). https://research.ncl.ac.uk/usmart/
[2] G. Acar and A. E. Adams. 2006. ACMENet: an underwater acoustic sensor network protocol for real-time environmental monitoring in coastal areas. *IEE Proceedings - Radar, Sonar and Navigation* 153, 4 (2006), 365–380.
[3] B.J. Boom, Jiyin He, S. Palazzo, P.X. Huang, C. Beyan, Hsiu-Mei Chou, Fang-Pang Lin, C. Spampinato, and R.B. Fisher. 2014. A research tool for long-term and continuous analysis of fish assemblage in coral-reefs using underwater camera footage. *Ecological Informatics* 23, Supplement C (2014), 83 – 97.
[4] N. Chirdchoo, W.S. Soh, and K.C. Chua. 2008. MU-Sync: A Time Synchronization Protocol for Underwater Mobile Networks. In *Proceedings of the ACM International Workshop on Underwater Networks (WuWNet 2008)*. 8.
[5] TE Connectivity. 2015. Ultra Small Gel Filled Pressure Sensor. MS5837-30BA datasheet.
[6] R. Diamant and L. Lampe. 2011. Spatial Reuse Time-Division Multiple Access for Broadcast Ad Hoc Underwater Acoustic Communication Networks. *IEEE Journal of Oceanic Engineering* 36, 2 (2011), 172–185.
[7] H. Hastie, K. Lohan, M. Chantler, D.A. Robb, S. Ramamoorthy, R. Petrick, S. Vijayakumar, and D. Lane. 2018. The ORCA Hub: Explainable Offshore Robotics through Intelligent Interfaces. In *Proceedings of the ACM/IEEE International Conference on Human Robot Interaction (HRI 2018)*.
[8] J. Heidemann, M. Stojanovic, and M. Zorzi. 2011. Underwater sensor networks: applications, advances and challenges. *Philosophical Transactions of the Royal Society of London A: Mathematical, Physical and Engineering Sciences* 370, 1958 (2011), 158–175.
[9] Maxim Integrated. 2015. Programmable Resolution 1-Wire Digital Thermometer. DS18B20 datasheet.
[10] A. Khan and L. Jenkins. 2008. Undersea wireless sensor network for ocean pollution prevention. In *Proceedings of the International Conference on Communication Systems Software and Middleware and Workshops (COMSWARE 2008)*.
[11] K. Kredo II, P. Djukic, and P. Mohapatra. 2009. STUMP: Exploiting Position Diversity in the Staggered TDMA Underwater MAC Protocol. In *Proceedings of IEEE INFOCOM 2009*.
[12] L. Lanbo, Z. Shengli, and C. Jun-Hong. 2008. Prospects and problems of wireless communication for underwater sensor networks. *Wireless Communications and Mobile Computing* 8, 8 (2008), 977–994.
[13] S. Lmai, M. Chitre, C. Laot, and S. Houcke. 2017. Throughput-efficient super-TDMA MAC transmission schedules in ad hoc linear underwater acoustic networks. *IEEE Journal of Oceanic Engineering* 42, 1 (2017), 156–174.
[14] A. K. Mohapatra, N. Gautam, and R. L. Gibson. 2013. Combined Routing and Node Replacement in Energy-Efficient Underwater Sensor Networks for Seismic Monitoring. *IEEE Journal of Oceanic Engineering* 38, 1 (2013), 80–90.
[15] N. Morozs, P.D. Mitchell, and Y. Zakharov. 2018. TDA-MAC: TDMA Without Clock Synchronization in Underwater Acoustic Networks. *IEEE Access* 6 (2018), 1091–1108.
[16] N. Morozs, P.D. Mitchell, and Y. Zakharov. 2018. Unsynchronized dual-hop scheduling for practical data gathering in underwater sensor networks. In *Proceedings of the IEEE International Conference on Underwater Communications and Networking (UComms 2018)*.
[17] M.E. Sayed, M.P. Nemitz, S. Aracri, A.C. McConnell, R.M. McKenzie, and A.A. Stokes. 2018. The Limpet: A ROS-Enabled Multi-Sensing Platform for the ORCA Hub. *Sensors* 18, 10 (2018), 3487.

Appendix L

Poster: A Multi-Sensing Robotic Platform for Inspection of Offshore Infrastructures

Conference: Engineering Graduate Conference at The University of Edinburgh 2018

Authors: Mohammed E. Sayed, John Thompson and Adam A. Stokes

Engineering Graduate Conference Poster 

A Multi-Sensing Robotic Platform for Inspection of Offshore Infrastructures

Mohammed E. Sayed[1], John Thompson[2] and Adam A. Stokes[3]

THE UNIVERSITY OF EDINBURGH

IMNS INTEGRATED MICRO AND NANO SYSYRM

1. Introduction

The number of people available to work in offshore industries has reduced as graduates are shifting to less hazardous places onshore and the current workforce is ageing. Therefore, operators are seeking more cost effective and safe methods for inspection, repair and maintenance of their topside and marine offshore infrastructure. Robots are seen as key enablers in this regard as they can help improve platform safety, reduce operation costs and reduce the risk to human life [1].

Current challenges facing the offshore industry is the design of low-cost agents that are highly manufacturable, small in size and have low power consumption in order to be able to mass-produce the agents and deploy them in large collectives for inspecting offshore infrastructures. Another challenge that faces robots in offshore environments is the design of robust agents that are able to survive the harsh environment with minimal human intervention.

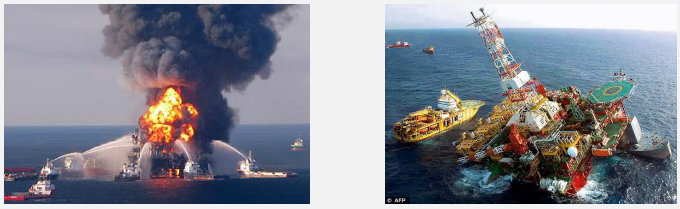

Fig 1. Common Offshore Incidents (e.g. Deep Water Horizon in Louisiana, 2010 and Petrobras' P36 in Rio De Janeiro, 2001)

2. Aims and Objectives

The underlying motivation of this project is the development of a new large-scale robotic system for inspection of offshore infrastructures. The project is divided into three parts and the main objectives of these parts are:

- Developing a manufacturable, low cost and robust multi-sensing robotic platform for inspection of offshore infrastructures.
- Developing a reversible adhesion mechanism for attachment of the robotic agent to multiple surfaces.
- Developing a collective of robotic agents to explore multi-sensor data fusion and dynamic repositioning of robotic agents.

3. Multi-Sensing Robot

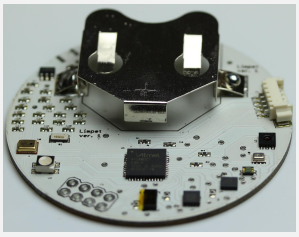

Fig 3.1 Picture of the Limpet PCB

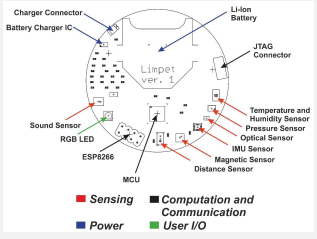

Fig 3.2 Schematic of the Limpet PCB

Robots designed for manufacturability enable scaling up to large robot collectives [2]. I developed a new multi-sensing robotic platform "Limpet" which is low cost, low power and manufacturable, and it has several (9) exteroceptive sensing modalities to monitor environmental and physical parameters in offshore platforms. The robot is made water resistant and more robust by encapsulating it in a soft material (protective housing), to protect it from harsh offshore conditions. The Limpet incorporates an ESP8266 chip, which allows it to send its data over Wi-Fi using MQTT protocol. The Limpet PCB is 52 mm in diameter and costs an average of £25. The robot design takes inspiration from limpets, which are aquatic snails with conical shells that live on rocks, on land or in sea [3].

4. Adhesion Mechanism



Fig 4.1 Picture of the Limpet PCB encapsulated in PDMS

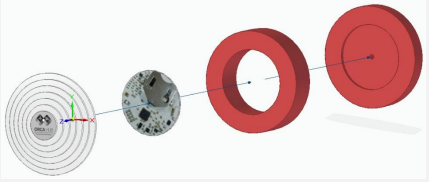

Fig 4.2 Exploded CAD view of the Limpet showing the different parts of the system. The bottom part incorporates the permanent magnets

The first version of the Limpet incorporates permanent magnets for adhesion to metal surfaces. The primary attachment mechanism of the aquatic animals is based on a suction mechanism [3]. For the second version of the Limpet, I will develop a new reversible adhesion mechanism based on a suction membrane that will enable the Limpet to stick to multiple different surfaces (metal surfaces, composite materials, ceramic surfaces or walls).

5. Collective of Robots

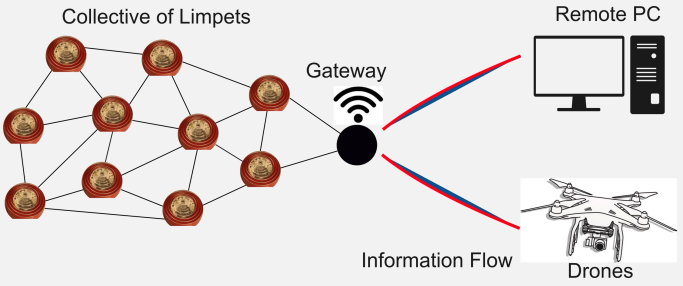

Fig 5. A Limpet collective data transmission schematic

I will be building a team of Limpets (>10) and operating them together in a collective to monitor and inspect offshore infrastructures. The Limpets will cooperate together to pass their data through the network to a centralized PC or to control drones. The drones will get instructions to reposition the Limpets to different locations, creating a dynamic multi-sensing robotic platform. The Limpets will also be used as a low cost multisensory platform to perform multi-functionality with individual sensors and to show how the data from multiple sensors can be fused together to enable solving complex tasks and scenarios.

6. Future Work

- Reversible adhesion mechanism
- Wireless charging of Limpets
- Multi-sensor data fusion
- Multi-functionality with individual sensors
- Deployment and repositioning of agents using drones

REFERENCE

[1] H. Chen, S. Stavinoha, M. Walker, B. Zhang and T. Fuhlbrigge, "Opportunities and Challenges of Robotics and Automation in Offshore Oil & Gas Industry", Intelligent Control and Automation, vol. 05, no. 03, pp. 136-145, 2014.

[2] M. Nemitz, M. Sayed, J. Mamish, G. Ferrer, L. Teng, R. McKenzie, A. Hero, E. Olson and A. Stokes, "HoverBots: Precise Locomotion Using Robots That Are Designed for Manufacturability", Frontiers in Robotics and AI, vol. 4, 2017.

[3] A. Smith, "The role of suction in the adhesion of limpets", Journal of Experimental Biology, no. 161, pp. 151-169, 1991.

1- Ph.D. Candidate, Stokes Research Group, University of Edinburgh, (m.mohammed@ed.ac.uk)
2- Assistant Supervisor, Digital Communications, University of Edinburgh, (john.thompson@ed.ac.uk)
2- Principal Supervisor, Stokes Research Group, University of Edinburgh, (adam.stokes@ed.ac.uk)

Stokes Research Group
Bioinspired Engineering

Appendix M

Poster: The Limpet: An Adaptable Multi-Sensor Inspection Robot

Conference: ORCA Hub Industry Engagement Day

Authors: Mohammed E. Sayed, Alistair C. McConnell, Simona Aracri and Adam A. Stokes

Industry Engagement Day Poster

The Limpet: An Adaptable Multi-Sensor Inspection Robot

M. E. Sayed, A.C. McConnell, S. Aracri, A. A. Stokes, School of Engineering, Institute for Integrated Micro and Nano Systems, The University of Edinburgh



The Limpet is a bioinpired robot (Patellogastropoda), low cost (£20), portable (50mm ⌀), capable of 5 different communication methods (acoustic, LoRa, WiFi, serial, optical), equipped with 9 exteroceptive modalities (Accelerometer, Gyroscope, Temperature Sensor, Humidity Sensor, Microphone, Pressure Sensor, Hall-Effect Sensor, Optical Sensor, Distance (Time-of-Flight) Sensor), low power consuming (0.1/182.9mA), long living (67 days/52 mins) with a rechargeable Li-Ion coin cell battery

Adaptability

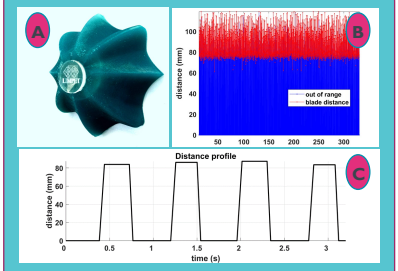

A) Standard WiFi Limpet encapsulation. B) Raw distance data for turbine blade passage detection. C) Edge processing output for turbine blade passage detection

The Context

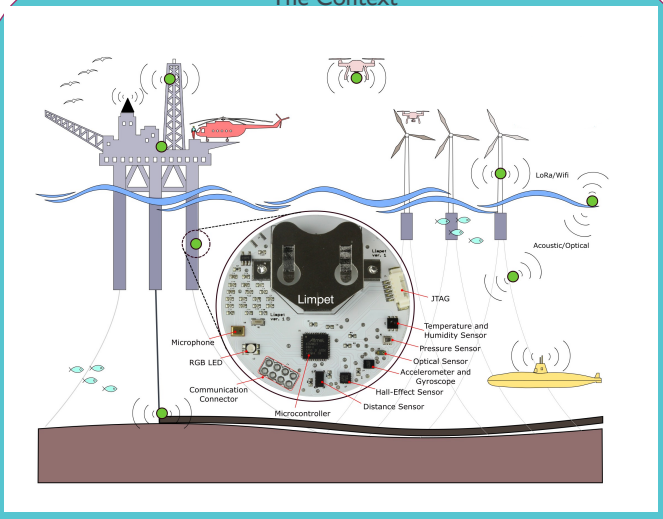

Conceptual overview of the Limpet in the ORCA Ecosystem. The Limpet is shown in detail including its exteroceptive sensors and varied methods of communication.

Capabilities

- Edge processing functionality
- Structural health monitoring
- Long term monitoring
- Communication failover scheme
- Robustness for sensor failure
- Multi-environmental deployment (remote/hazardous areas)
- Designed for mass manufacturing
- Low cost
- Smart sensing

Future Work

- Energy Harvest
- Adhesion

For further information on the Limpet:
stokesresearchgroup.com

Research Outputs

Journal Paper

M. E. Sayed, M. P. Nemitz, S. Aracri, A. C. McConnell, R. M. McKenzie , A. A. Stokes. (2018). The Limpet: A ROS-Enabled Multi-Sensing Platform for the ORCA Hub. Sensors (submitted)

Conference Paper

N. Morozs, P. D. Mitchell, Y. Zakharov, R. Mourya, Y. R. Petillot, T. Gibney, M. Dragone, B. Sherlock, J. A. Neasham, C. C. Tsimenidis, M. E. Sayed, A. C. McConnell, S. Aracri, A. A. Stokes. (2018). Robust TDA-MAC for Practical Underwater Sensor Network Deployment: Lessons from USMART Sea Trials. WUWNet'18, Dec 2018, Shenzhen, China (submitted)

Conference Talk

S. Aracri, M. E. Sayed, J. O. Roberts, A. C. McConnell, A. A. Stokes. (2018). Limpet: an Autonomous Bioinspired Robot for Environmental Monitoring. 19th Biennial Seminar on Water Resources and Environmental Management

HERIOT WATT UNIVERSITY · THE UNIVERSITY of EDINBURGH · UNIVERSITY OF LIVERPOOL · Imperial College London · UNIVERSITY OF OXFORD · INDUSTRIAL STRATEGY · UK Research and Innovation · EDINBURGH CENTRE FOR ROBOTICS

Appendix N

Code

Programming Language: C/C++, Matlab

Programs: Atmel Studio 7, Matlab

This section contains the code for the pressure sensor (BMP280), hall-effect sensor (MLX90393), optical sensor (VEML6040), optical sensor (VEML6040), temperature and humidity sensor (Si7006), sound sensor (SPU0414HR5H), distance sensor (VL53L0X), IMU sensor (LSM6DS3), RGB LED, Limpet version 1 main function, serial control of the Limpet, Limpet acoustic communication protocol, time-stamping the Limpet data, stepper motor control, ESP8266 Config.lua, ESP8266 Setup.lua, ESP8266 uartComs.lua, ESP8266 Application.lua, ESP8266 Init.lua, distance-based fault detection offline classification (WiFi communication), distance-based fault detection offline classification (Serial communication), optical sensor calibration for online classification using optical communication, distance-based fault detection online classification (LoRa communication), LoPy board setup (LoRa communication), optical sensor calibration Matlab code, optical sensor light intensity interpretation Matlab code, distance-based fault detection offline classification Matlab code, untethered distance control of Limpet version 2, untethered light control of Limpet version 2, untethered sound control of Limpet version 2, untethered IMU control of Limpet version 2, untethered control of direction of Limpet version 2, climbing code for Limpet version 2.

The labelled code file can be found here.

